Title

Measuring Cellular Mechanics with Quantitative Phase Microscopy

Author

Nguyen, Thang Le

Publication Date

2022

Peer reviewed|Thesis/dissertation

UNIVERSITY OF CALIFORNIA

Los Angeles

Measuring Cellular Mechanics with Quantitative Phase Microscopy

A dissertation submitted in partial satisfaction of the requirements for the degree Doctor of Philosophy in Bioengineering

by

Thang L. Nguyen

2022

ABSTRACT OF DISSERTATION

Measuring Cellular Mechanics

with Quantitative Phase Microscopy

by

Thang L. Nguyen

Doctor of Philosophy in Bioengineering

University of California, Los Angeles, 2022

Professor Michael Alan Teitell, Chair

Quantitative phase imaging (QPI) is a label-free microscopy approach using the phase shift of light as it passes through transparent objects, like mammalian cells, to quantify biomass distribution and changes in biomass over time and space. QPI has seen immense interest and advances in hardware and software leading to numerous applications in biology and expansions in utility within the last decades. This dissertation presents a subset of those studies applied to questions of cellular biology and biophysics along with an overview of the QPI field as whole. The initial proportion of this thesis is devoted to modeling and dissecting various biomechanical properties of cellular mechanics including cellular viscoelasticity and work across varying cell types and biological perturbations using purely QPI. This is followed by an in-depth review of the field of QPI including the development and lineages of the various QPI approaches along with the advances in QPI made

in the field of cellular biology, biophysics, and diagnostics. Finally, we conclude this thesis with a review of the ongoing technical and biological advances made in QPI along with perspectives on the directions that QPI field maybe proceeding towards. Demonstrating that QPI is not only a robust tool in probing cellular biology and biophysics already but is also expanding its' capabilities towards more applications in and interrogating fundamental questions about biology.

The dissertation of Thang L. Nguyen is approved.

Alexander Hoffman

Pei-Yu Chiou

Amy Catherine Rowat

Michael Alan Teitell, Committee Chair

University of California, Los Angeles

2022

DEDICATION

I dedicate this thesis to my parents, lab members, collaborators, and advisers for all their help and support.

TABLE OF CONTENTS

LIST OF TABLES AND FIGURES

Chapter 1

Chapter 2

ACKNOWLEDGEMENTS

Chapter 2 is a reprinted version of a published manuscript with permission from Nguyen, Thang L, et al. " Cell viscoelasticity is linked to fluctuations in cell biomass distributions." Scientific Reports, 10, 7403 (2020). https://doi.org/10.1038/s41598-020-64259-y

Chapter 3 is a version of a manuscript currently in preparation by Nguyen, Thang L, et al. " Quantifying biomechanical work in proliferating cancer cells."

Chapter 4 is a version of a manuscript currently in review by Nguyen, Thang L, et al. “Quantitative Phase Imaging: Recent Advances and Expanding Potential in Biomedicine.” ACS Nano.

Appendix II is a version of a reprinted published manuscript with permission from Yokota, Tomohiro, et al. “Type V Collagen in Scar Tissue Regulates the Size of Scar after Heart Injury." Cell, Volume 182, Issue 3, 2020, Pages 545-562.e23, ISSN 0092-8674, https://doi.org/10.1016/j.cell.2020.06.030

Appendix III is a version of a reprinted published manuscript with permission from, Patananan, Alexander N, et al. “Pressure-Driven Mitochondrial Transfer Pipeline Generates Mammalian Cells of Desired Genetic Combinations and Fates." Cell Reports, Volume 33, Issue 13, 2020, 108562, ISSN 2211-1247, https://doi.org/10.1016/j.celrep.2020.108562

Appendix IV is a version of a reprinted published manuscript with permission from, Pezhouman, Arash, et al. “Transcriptional, Electrophysiological, and Metabolic Characterizations of hESC-

Derived First and Second Heart Fields Demonstrate a potential role of TBX5 in cardiomyocyte maturation." Front. Cell Dev. Biol., 17 December 2021. https://doi.org/10.3389/fcell.2021.787684

Appendix V is a version of reprinted published manuscript with permission from, Yu, Jingyi, et al. “Topological Arrangement of Cardiac Fibroblasts Regulates Cellular Plasticity." Circulation Research. 2018; 123:73–85 https://doi.org/10.1161/CIRCRESAHA.118.312589

VITA

Education

University of California: Los Angeles, Los Angeles, CA

Henry Samueli School of Engineering

Bioengineering

Bachelor of Science, 2014

Awards

Whitcome Fellowship (2018)

Publications and Proceedings

Nguyen, T.L., Patananan, A.N., Sercel, S., Ahsan, F., Zangle, T.A., and Teitell, M.A. Quantification of biophysical work via QPI. (in preparation)

Tebon, P.J.*, Wang, B.*, Markowitz, A.L., Murray, G., Nguyen, H.T.L., Tavanaie, N., Nguyen, T.L., Boutros, P.C., Teitell, M.A.*, and Soragni, A.* High-speed Live Cell Interferometry for Screening Bioprinted Organoids. (BioRxiv, 2021)

Nguyen, T.L., Pradeep, S., Judson-Torres, R.L., Reed, J., Teitell, M.A., and Zangle, T.A. Quantitative Phase Imaging: Recent Advances and Expanding Potential in Biomedicine. (ACS Nano, in review)

Pezhouman, A., Nguyen, N.B., Sercel, A.J., Nguyen, T.L., Drarei, A., Sabri, S., Chapski, D., Patananan, N.A., Ernst, J., Plath, K., Vondriska, T.M., Teitell, M.A., and Ardehali, R. Transcriptional, Electrophysiological, and Metabolic Characterizations of hESC-Derived First and Second Heart Fields Demonstrate a Potential Role of TBX5 in Cardiomyocyte Maturation. (Frontiers in Cell and Developmental Biology, 2021 Dec 17)

Patananan, A.N., Sercel, A.J., Wu, T.-H., Ahsan, F.M., Torres Jr., A., Kennedy, S.A.L., Vandiver, A., Collier, A.J., Mehrabi, A., Van Lew, J., Zakin, L., Rodriguez, N., Sixto, M., Tadros, W., Lazar, A., Sieling, P.A., Nguyen, T.L., Dawson, E.R., Braas, D., Golovato, J., Cisneros, L., Vaske, C., Plath, K., Rabizadeh,

S., Niazi, K., Chiou, P.-Y., and Teitell, M.A. Pressure-Driven Mitochondrial Transfer Pipeline Generates Mammalian Cells of Desired Genetic Combinations and Fates. (Cell Reports, 2020 Dec 29)

Yokota, T., McCourt, J., Ma, F., Ren, S., Li, S., Kim, T.-H., Kurmangaliyev, Y.Z., Nasiri, R., Ahadian, S., Nguyen, T., Tan, X.H.M., Zhou, Y., Wu, R., Rodriguez, A., Cohn, W., Wang, Y., Whitelegge, J., Ryanzantsev, S., Khadamhosseini, A., Teitell, M.A., Chiou, P.-Y., Birk, D.E., Rowat, A.C., Crosbie, R.H., Pellegrini, M., Seldin, M., Lusis, A.J., and Deb, A. Type V Collagen in Scar Tissue Regulates the Size of Scar after Heart Injury. (Cell, 2020 August 6)

Nguyen, T.L., Polanco, E.R., Patananan A.N., Zangle, T.A., and Teitell, M.A. Cell viscoelasticity is linked to fluctuations in cell biomass distributions. (Scientific Reports, 2020 May 4)

Yu, J., Seldin, M.M., Fu, K., Li, S., Lam, L., Wang, P., Wang, Y., Huang, D., Nguyen, T.L., Wei, B., Kulkarni, R.P., Di Carlo, D., Teitell, M., Pellegrini, M., Aldons, L.J., and Deb, A. Topological Arrangement of Cardiac Fibroblasts Regulates Cellular Plasticity (Circulation Research, 2018 April 24)

Zhu, X., Man, T., Nguyen, T., Haw, T. X., Liu, T., Wen, X., Tetitell, M.A., and Pei-Yu, C. Parallel Nanomechanical Indentation Platform Using Quantitative Phase Imaging (Optical MEMS, 2018)

Conferences Poster Presentation and Talk

Nguyen, T.N. and Teitell T.A., (2018) *Molecular changes in cancer quantified by interferometry*. Molecular Biology Institute Retreat, Santa Barbara, CA.

Nguyen, T.N., Polanco, E.R., Zangle, T.A., and Teitell T.A., (2017) *Mitotic effect on cell stiffness quantified by QPM measurements of intracellular disorder.* UC Bioengineering Symposium, Los Angeles, CA.

Nguyen, T.N., Zangle, T.A., and Teitell T.A., (2016) *Quantifying the effects of cell division on mass redistribution dynamics in multicellular clusters using live cell interferometry*. Biophysical Society Meeting, Anaheim, CA.

Aftab, S., Brohaugh, S., Cheung, G., Nguyen, T., and Kim, H.J., (2014) *Pipettebot: A low cost automated pipetting robot*. UCLA Bioengineering Capstone Design Symposium, Los Angeles, CA.

Chapter 1. Introduction

Quantitative phase imaging (QPI) is a label-free microscopy technique that measures cell properties and behaviors, through cellular biomass via the phase shift of light as it passes through matter, this phase shift is caused by the retardation of light as it passes through a material of differing refractive index[1] and is described by the equation:

$$\phi = \frac{2\pi}{\lambda}\int_{z=0}^{h} n(z)dz \quad (1)$$

where ϕ is the phase shift of light. n is the refractive index of the sample, h, height of the sample, and z is the direction of integration. This measured phase shift is directly proportional to the dry biomass content of the sample[2]. This dry mass includes all mass with different refractive index from a reference which is in most case water. This can be seen in the increase of refractive index of a protein solution with a proportional increase in protein concentration[3]. This relationship between refractive index versus mass concentration is called the specific refractive increment[1, 4] with the average specific refractive increment, α, for the contents of mammalian cells being around 0.185 $\mu m^3/pg$[1], changing within ~6%[5]. The total cell dry mass within a given area, m, can then be calculated using the specific refractive increment, α, of a sample as[2]:

$$m = \frac{\lambda}{2\pi\alpha}\int \phi dA \quad (2)$$

where A is the area of the cell. This ability of QPI to measure quantitative biophysical features of the cell allows it a variety of applications and potential in biomedicine.

Branches of QPI methods

Traditional imaging detectors measure amplitude of incident light and not phase so all QPI methods created must address this need to recover phase shift information from light. There are many QPI approaches or lineages for this including interferometry[6, 7], wavefront sensing[8, 9], phase

retrieval[10, 11], and digital holography[12]. In interferometry, phase information is generated via splitting of light incident on a sample into two paths a sample and a reference path before recombining them at a detector. The magnitude of the resulting interference images is related to phase shift of light passing through the sample compared to the reference via the interference between the light from these two paths. Examples of interferometry techniques include the Michelson[13] (Figure 1) and Mach-Zehnder interferometer[14] which are respectively a reflective and transmission imaging setup.

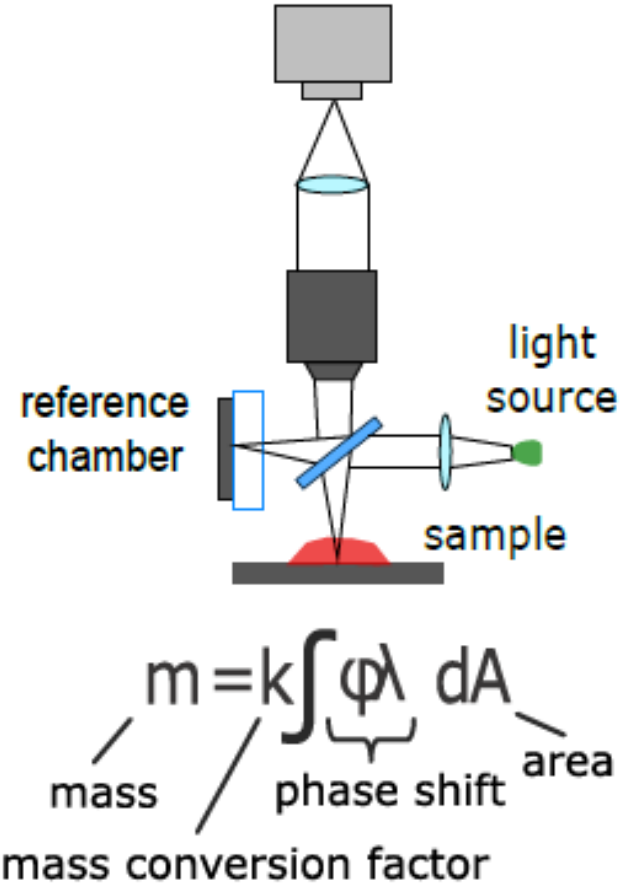

FIGURE 1 Schematic of a reflective interferometer setup called the Michelson interferometer. Phase shift information is obtained by cellular sample via the splitting of the incident light into a

reference and sample path which is later recombined to generate an image of constructive and destructive interference.

A related QPI imaging lineage is wavefront sensing which are approaches that seek to recover the aberrations in a wavefront caused by phase delays within a sample. Some wavefront sensing methods include Shack Hartmann wavefront sensing[15] and Ronchi sensing[16] with early wavefront sensing using lateral shearing interferometry[16, 17]. Lateral shearing wavefront imaging make use of incident wave that are sheared into two identical but tilted wave fronts that then interfere. These resulting single-direction phase gradient when paired with multiwave interferometry techniques[18] can generate 2D gradient maps needed to recapitulate QPI images. Another QPI lineage is phase retrieval methods which refers to non-interferometric methods that are computationally reconstruct the phase shift from intensity images. These phase retrieval methods can be classified as either iterative or deterministic[19] with iterative methods using iterative computation to the phase problem[20]. One widely used iterative phase retrieval method is the Gerchberg-Saxton algorithm. Deterministic methods solve for phase images without iteration with a commonly used approach based on the transport of intensity (TIE) equation which relates phase data at the in-focus plane to the axial derivative of intensity distribution[21].

The last branch of QPI we will discuss is digital holography which captures the interference between a reference and the off-axis sample beam with a digital camera placed at a known distance in front of the image plane. The interferogram is reconstructed through diffraction theory to recover the complex object wavefront, which includes the phase shift and intensity modulation of the light. Digital holography methods are based on those of holography as established by Gabor[22]

where light from a point source when interfering with secondary waves from light scattered by an object can produces a negative photograph of a 3D image. All these QPI lineages have benefited greatly from the increasing availability of high end computing allowing for greater digital image acquisition and data processing allowing for convergence of QPI branches like with quadriwave lateral shearing interferometry which combines principles of wavefront sensing with interferometry and phase retrieval algorithms[9].

Advantages and applications of QPI

Advantages QPI have include being label-free and containing quantitative information about phase in each pixel of the captured images. Paired with the specific refractive increment[5], which is the refractive index of a material is related to its mass, of cellular mass which is around 1.8 – 2.0 x 10-4 m^3/kg [2, 3, 5], QPI can generate biomass distribution images of individual cells or clusters (Figure 2a) at individual instances or through a time lapse set of images (Figure 2b) through its' phase shift information. These time-lapsed images can be used to extract information on cellular mass over time (Figure 2c) [4, 23-26]. Additionally, repeated QPI measurements of dry cell mass over time can provide dry mass accumulation or loss rates to quantify cell growth (Figure 2d)[7, 27-32], or the decrease in mass that occurs during cell death[33-38] . These type of mass accumulation measurements have also been paired up with a number of extracellular perturbations including changes in available glucose[29] or introduction of small molecule inhibitors like tunicamycin to induce cell stress[7]. Allowing for the development of QPI-based screens for agents that may cause changes in cell growth rate and cytotoxicity[7, 39]. Furthermore QPI has also been applied to study other cellular properties including motion (Figure 2e), migration, and metastatic potential[40].

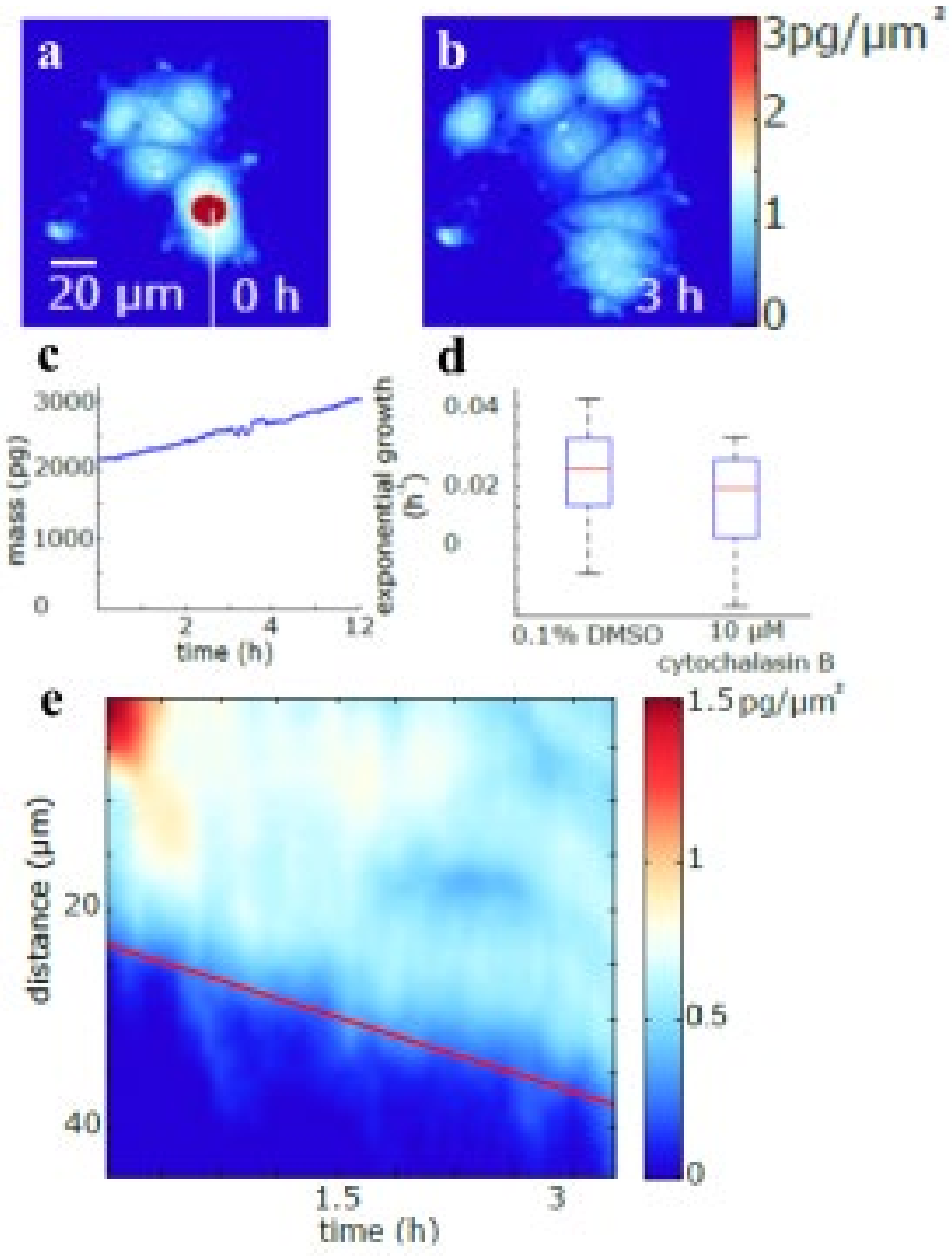

FIGURE 2 QPI imaging captures information of mass accumulation and motion. QPI images at (**a**) beginning and (**b**) end of 3h time lapse of MCF-7 cells. Time lapsed QPI images used to to measure (**c**) dry biomass over time for MCF-7 cluster and can be used to extract (**d**) mass

accumulation rate differences when treated with a drug treatment. Motion in QPI data can also be captured shown via a (**e**) kymograph of travel by the leading edge of the cluster represented in the white line in (**a**).

Due to QPI's flexibility it has been applied to study variety cell types and applications including primary human melanocytes[41], human pluripotent stem cells (hPSCs)[42], immune cells[43], and many others. For example, where other growth rate measurements like proliferation rates may be constrained due to limits on cellular replication like cells that are not proliferative like in hypertrophic cardiomyocytes or primary cells due to the Hayflick limit, QPI is able to work around this due to being a direct mass measurement as well as being to make such measurements on a very short time scale. This allows for mass accumulation measurements on the aforementioned hypertrophic cardiomyocytes and what media conditions may illicit hypertrophy (Figure 3a) as well as allow QPI to interrogate primary and primary cell derived samples (Figure 3b). This allows QPI a great advantage over the many other growth and mass measurement techniques and uniquely positons it to interrogate other biological questions of size, growth, and cellular mass.

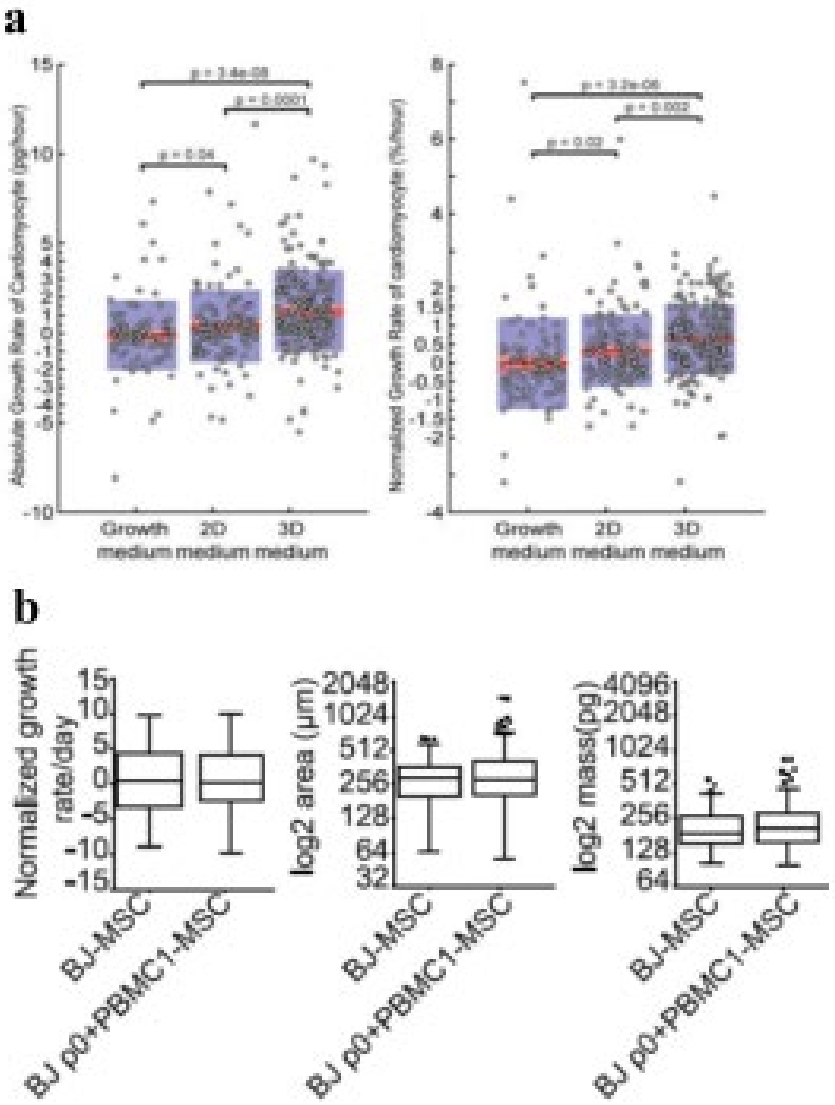

FIGURE 3 Cellular growth applications of QPI in situations inconvenient to proliferation assays. (**a**) Measurement of mass accumulation rate for cardiomyocytes under different media conditions meant to induce hypertrophy (Reproduced with permission from [44], © 2018 Wolters Kluwer Health). (**b**) Determined there was no noticeable size or growth differences in primary BJ fibroblast derived MSC vs. those of the rho0 + cell line mitochondria (Reproduced under Creative Commons Attribution (CC BY) license with permission from [45], © 2020 Patananan *et al.*).

Cellular mass and mass accumulation are not the only properties measured with QPI as shown by QPI's ability to quantify cellular motion as well (Figure 2e). What sets QPI apart from other simpler microscopy techniques like phase contrast or bright field is QPI's ability to measure not only motion external or full displacement of individual cells but also the intracellular motion as well by detecting the fluctuation of internal mass redistribution and motion. While typical microscopy techniques might only be able to quantify differences in displacement by wild type fibroblast (Figure 4a) vs collagen knockout ones (Figure 4b), QPI is able to quantify the differences internal as well (Figure 4c). This difference in internal mass redistribution and motion can also be applied to determine physiological differences between cell types shown by internal mass redistribution being able to determine differences between cardiomyocytes of two different heart fields (Figure 4d). This demonstrates QPI's capability to extract even more information from its' already extensive information on cellular mass and mass accumulation allowing for prospectively extensive characterization cellular properties via different examination and manipulation of QPI cellular mass information.

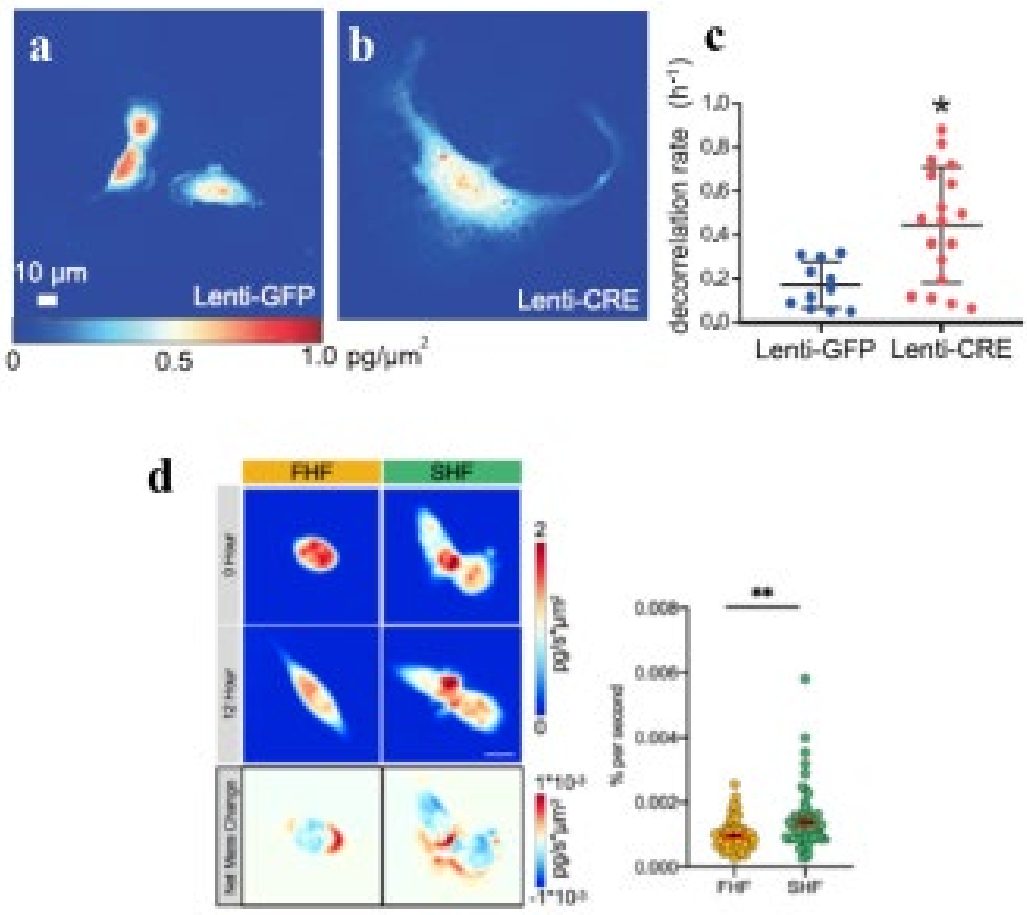

FIGURE 4 QPI applications of internal redistribution and intercellular mass motion. QPI phase images of (**a**) GFP labeled wildtype and (**b**) collagen V knockout fibroblasts. (**c**) The two types of cells show marked differences in their internal redistribution of mass quantified as a decorrelation rate (Reproduced with permission from [46],© 2020 Elsevier). (**d**) Cardiomyocytes that comprise the first (FHF) and second (SHF) heart field show drastic differences in mass redistribution (Reproduced under Creative Commons Attribution (CC BY) license with permission from [47], © 2021 Pezshouman *et al.*).

Applications of QPI in biophysics

An emerging application of QPI is in the realm of biophysics due to QPI's ability to measure intracellular mass distributions and redistributions over time revealing information on cell movement and intracellular transport phenomena. These measurements of the movement of mass between cell regions enable applications in intracellular transport, while measurements of the shape and structure of a cell over time enable measurements of cell mechanics. An example of such applications can be found in measurements of label-free diffusion coefficients of organelles and vesicles in neurons and cardiomyocytes[48]. However, there are many more properties that can be teased out and this thesis is devoted to further probing out these various biomechanical properties with QPI and examining the state of the field QPI as whole in this regard.

References

1. Barer, R.; Joseph, S., Refractometry of Living Cells. *Quarterly Journal of Microscopical Science* **1954,** *s3-95* (32), 399.

2. Zangle, T. A.; Teitell, M. A., Live-Cell Mass Profiling: An Emerging Approach in Quantitative Biophysics. *Nature Methods* **2014,** *11* (12), 1221-8.

3. Barer, R.; Tkaczyk, S., Refractive Index of Concentrated Protein Solutions. *Nature* **1954,** *173* (4409), 821-822.

4. Barer, R., Determination of Dry Mass, Thickness, Solid and Water Concentration in Living Cells. *Nature* **1953,** *172* (4389), 1097-1098.

5. Zhao, H.; Brown, P. H.; Schuck, P., On the Distribution of Protein Refractive Index Increments. *Biophysical Journal* **2011,** *100* (9), 2309-17.

6. Zangle, T. A.; Teitell, M. A.; Reed, J., Live Cell Interferometry Quantifies Dynamics of Biomass Partitioning During Cytokinesis. *PLoS One* **2014,** *9* (12).

7. Reed, J.; Chun, J.; Zangle, T. A.; Kalim, S.; Hong, J. S.; Pefley, S. E.; Zheng, X.; Gimzewski, J. K.; Teitell, M. A., Rapid, Massively Parallel Single-Cell Drug Response Measurements Via Live Cell Interferometry. *Biophysical Journal* **2011,** *101* (5), 1025-31.

8. Platt, B. C.; Shack, R., History and Principles of Shack-Hartmann Wavefront Sensing. *J Refract Surg* **2001,** *17* (5), S573-7.

9. Bon, P.; Maucort, G.; Wattellier, B.; Monneret, S., Quadriwave Lateral Shearing Interferometry for Quantitative Phase Microscopy of Living Cells. *Opt Express* **2009,** *17* (15), 13080-94.

10. Tian, L.; Waller, L., Quantitative Differential Phase Contrast Imaging in an Led Array Microscope. *Optics Express* **2015,** *23* (9), 11394-403.

11. Streibl, N., Phase Imaging by the Transport Equation of Intensity. *Optics Communications* **1984,** *49* (1), 6-10.

12. Muller, P.; Cojoc, G.; Guck, J., Drymass: Handling and Analyzing Quantitative Phase Microscopy Images of Spherical, Cell-Sized Objects. *BMC Bioinformatics* **2020,** *21* (1), 226.

13. Weart, S. R., Selected Papers of Great American Physicists : The Bicentennial Commemorative Volume of the American Physical Society 1976. American Institute of Physics: New York, 1976; p 176 p.

14. Mach, L.; Zehnder, L.; Clark, C., The Interferometers of Zehnder and Mach. 2017.

15. Jim, S. In *History of the Shack Hartmann Wavefront Sensor and Its Impact in Ophthalmic Optics*, Proc.SPIE, 2014.

16. Ronchi, V., 40 Years of History of Grating Interferometer. *Applied Optics* **1964,** *3* (4), 437-&.

17. Bates, W. J., A Wavefront Shearing Interferometer. *Proceedings of the Physical Society* **1947,** *59* (6), 940-950-2.

18. Primot, J.; Sogno, L., Achromatic 3-Wave (or More) Lateral Shearing Interferometer. *Journal of the Optical Society of America a-Optics Image Science and Vision* **1995,** *12* (12), 2679-2685.

19. Zuo, C.; Li, J.; Sun, J.; Fan, Y.; Zhang, J.; Lu, L.; Zhang, R.; Wang, B.; Huang, L.; Chen, Q., Transport of Intensity Equation: A Tutorial. *Optics and Lasers in Engineering* **2020,** *135*.

20. Latychevskaia, T., Iterative Phase Retrieval for Digital Holography: Tutorial. *Journal of the Optical Society of America a-Optics Image Science and Vision* **2019,** *36* (12), D31-D40.

21. Bostan, E.; Froustey, E.; Rappaz, B.; Shaffer, E.; Sage, D.; Unser, M., Phase Retrieval by Using Transport-of-Intensity Equation and Differential Interference Contrast Microscopy. *2014 IEEE International Conference on Image Processing (ICIP)* **2014**, 3939-3943.

22. Gabor, D., A New Microscopic Principle. *Nature* **1948,** *161* (4098), 777-778.

23. Davies, H. G.; Wilkins, M. H. F.; Chayen, J.; Lacour, L. F., The Use of the Interference Microscope to Determine Dry Mass in Living Cells and as a Quantitative Cytochemical Method. *Quarterly Journal of Microscopical Science* **1954,** *95* (3), 271-&.

24. Barer, R., Interference Microscopy and Mass Determination. *Nature* **1952,** *169* (4296), 366-367.

25. Davies, H. G.; Wilkins, M. H. F., Interference Microscopy and Mass Determination. *Nature* **1952,** *169* (4300), 541-541.

26. Mitchison, J. M.; Passano, L. M.; Smith, F. H., An Integration Method for the Interference Microscope. *Quarterly Journal of Microscopical Science* **1956,** *s3-97* (38), 287.

27. Mir, M.; Wang, Z.; Shen, Z.; Bednarz, M.; Bashir, R.; Golding, I.; Prasanth, S. G.; Popescu, G., Optical Measurement of Cycle-Dependent Cell Growth. *Proceedings of the National Academy of Sciences of the United States of America* **2011,** *108* (32), 13124-9.

28. Kemper, B.; Bauwens, A.; Vollmer, A.; Ketelhut, S.; Langehanenberg, P.; Muthing, J.; Karch, H.; von Bally, G., Label-Free Quantitative Cell Division Monitoring of Endothelial Cells by Digital Holographic Microscopy. *Journal of Biomedical Optics* **2010,** *15* (3).

29. Popescu, G.; Park, Y.; Lue, N.; Best-Popescu, C.; Deflores, L.; Dasari, R. R.; Feld, M. S.; Badizadegan, K., Optical Imaging of Cell Mass and Growth Dynamics. *American Journal of Physiology-Cell Physiology* **2008,** *295* (2), C538-C544.

30. Tian, L.; Liu, Z. J.; Yeh, L. H.; Chen, M.; Zhong, J. S.; Waller, L., Computational Illumination for High-Speed in Vitro Fourier Ptychographic Microscopy. *Optica* **2015,** *2* (10), 904-911.

31. Rappaz, B.; Cano, E.; Colomb, T.; Kuhn, J.; Depeursinge, C.; Simanis, V.; Magistretti, P. J.; Marquet, P., Noninvasive Characterization of the Fission Yeast Cell Cycle by Monitoring Dry Mass with Digital Holographic Microscopy. *Journal of Biomedical Optics* **2009,** *14* (3).

32. Cooper, K. L.; Oh, S.; Sung, Y.; Dasari, R. R.; Kirschner, M. W.; Tabin, C. J., Multiple Phases of Chondrocyte Enlargement Underlie Differences in Skeletal Proportions. *Nature* **2013,** *495* (7441), 375-378.

33. Pavillon, N.; Kuhn, J.; Moratal, C.; Jourdain, P.; Depeursinge, C.; Magistretti, P. J.; Marquet, P., Early Cell Death Detection with Digital Holographic Microscopy. *PLoS One* **2012,** *7* (1), e30912.

34. Vicar, T.; Raudenska, M.; Gumulec, J.; Balvan, J., The Quantitative-Phase Dynamics of Apoptosis and Lytic Cell Death. *Sci Rep* **2020,** *10* (1), 1566.

35. Zuo, C.; Sun, J. S.; Li, J. J.; Zhang, J. L.; Asundi, A.; Chen, Q., High-Resolution Transport-of-Intensity Quantitative Phase Microscopy with Annular Illumination. *Scientific Reports* **2017,** *7*.

36. Kemper, B.; von Bally, G., Digital Holographic Microscopy for Live Cell Applications and Technical Inspection. *Applied Optics* **2008,** *47* (4), A52-A61.

37. Kemper, B.; Carl, D.; Schnekenburger, J.; Bredebusch, I.; Schafer, M.; Domschke, W.; von Bally, G., Investigation of Living Pancreas Tumor Cells by Digital Holographic Microscopy. *Journal of Biomedical Optics* **2006,** *11* (3).

38. Zuo, C.; Chen, Q.; Qu, W. J.; Asundi, A., Noninterferometric Single-Shot Quantitative Phase Microscopy. *Optics Letters* **2013,** *38* (18), 3538-3541.

39. Kuhn, J.; Shaffer, E.; Mena, J.; Breton, B.; Parent, J.; Rappaz, B.; Chambon, M.; Emery, Y.; Magistretti, P.; Depeursinge, C.; Marquet, P.; Turcatti, G., Label-Free Cytotoxicity Screening Assay by Digital Holographic Microscopy. *Assay and Drug Development Technologies* **2013,** *11* (2), 101-107.

40. Kandel, M. E.; Lu, W.; Liang, J.; Aydin, O.; Saif, T. A.; Popescu, G., Cell-to-Cell Influence on Growth in Large Populations. *Biomedical Optics Express* **2019,** *10* (9), 4664-4675.

41. McNeal, A. S.; Belote, R. L.; Zeng, H.; Urquijo, M.; Barker, K.; Torres, R.; Curtin, M.; Shain, A. H.; Andtbacka, R. H.; Holmen, S.; Lum, D. H.; McCalmont, T. H.; VanBrocklin, M. W.; Grossman, D.; Wei, M. L.; Lang, U. E.; Judson-Torres, R. L., Braf(V600e) Induces Reversible Mitotic Arrest in Human Melanocytes Via Microrna-Mediated Suppression of Aurkb. *Elife* **2021,** *10*.

42. Zangle, T. A.; Chun, J.; Zhang, J.; Reed, J.; Teitell, M. A., Quantification of Biomass and Cell Motion in Human Pluripotent Stem Cell Colonies. *Biophysical Journal* **2013,** *105* (3), 593-601.

43. Zangle, T. A.; Burnes, D.; Mathis, C.; Witte, O. N.; Teitell, M. A., Quantifying Biomass Changes of Single Cd8+T Cells During Antigen Specific Cytotoxicity. *PLoS One* **2013,** *8* (7).

44. Yu, J. Y.; Seldin, M. M.; Fu, K.; Li, S.; Lam, L.; Wang, P.; Wang, Y. J.; Huang, D.; Nguyen, T. L.; Wei, B. W.; Kulkarni, R. P.; Di Carlo, D.; Teitell, M.; Pellegrini, M.; Lusis, A. J.; Deb, A., Topological

Arrangement of Cardiac Fibroblasts Regulates Cellular Plasticity. *Circulation Research* **2018,** *123* (1), 73-85.

45. Patananan, A. N.; Sercel, A. J.; Wu, T. H.; Ahsan, F. M.; Torres, A.; Kennedy, S. A. L.; Vandiver, A.; Collier, A. J.; Mehrabi, A.; Van Lew, J.; Zakin, L.; Rodriguez, N.; Sixto, M.; Tadros, W.; Lazar, A.; Sieling, P. A.; Nguyen, T. L.; Dawson, E. R.; Braas, D.; Golovato, J.; Cisneros, L.; Vaske, C.; Plath, K.; Rabizadeh, S.; Niazi, K. R.; Chiou, P. Y.; Teitell, M. A., Pressure-Driven Mitochondrial Transfer Pipeline Generates Mammalian Cells of Desired Genetic Combinations and Fates. *Cell Reports* **2020,** *33* (13).

46. Yokota, T.; McCourt, J.; Ma, F. Y.; Ren, S. X.; Li, S.; Kim, T. H.; Kurmangaliyev, Y. Z.; Nasiri, R.; Ahadian, S.; Nguyen, T.; Tan, X. H. M.; Zhou, Y. G.; Wu, R. M.; Rodriguez, A.; Cohn, W.; Wang, Y. B.; Whitelegge, J.; Ryazantsev, S.; Khademhosseini, A.; Teitell, M. A.; Chiou, P. Y.; Birk, D. E.; Rowat, A. C.; Crosbie, R. H.; Pellegrini, M.; Seldin, M.; Lusis, A. J.; Deb, A., Type V Collagen in Scar Tissue Regulates the Size of Scar after Heart Injury. *Cell* **2020,** *182* (3), 545-+.

47. Pezhouman, A.; Nguyen, N. B.; Sercel, A. J.; Nguyen, T. L.; Daraei, A.; Sabri, S.; Chapski, D. J.; Zheng, M. L.; Patananan, A. N.; Ernst, J.; Plath, K.; Vondriska, T. M.; Teitell, M. A.; Ardehali, R., Transcriptional, Electrophysiological, and Metabolic Characterizations of Hesc-Derived First and Second Heart Fields Demonstrate a Potential Role of Tbx5 in Cardiomyocyte Maturation. *Frontiers in Cell and Developmental Biology* **2021,** *9*.

48. Wang, Z.; Millet, L.; Chan, V.; Ding, H.; Gillette, M. U.; Bashir, R.; Popescu, G., Label-Free Intracellular Transport Measured by Spatial Light Interference Microscopy. *Journal of Biomedical Optics* **2011,** *16* (2), 026019.

Chapter 2. Cell viscoelasticity is linked to fluctuations in cell biomass distributions

Introduction

Viscoelastic properties of cells are important emerging biomarkers of disease state and progression[1]. The simplest approach to defining cell viscoelastic properties examines two parameters: stiffness and viscosity, which characterize the elastic and dissipative components of a cell's response to stress[2]. The elastic response has been used as a biomarker for cancer cells[3] or metastatic potential[4], and has been related to cell migration during embryogenesis[5]. Cell viscosity has been linked to multiple biological processes, such erythrocyte porous trafficking and deformability[6], diffusion[7, 8], and cell disease state[9, 10].

Most approaches to interrogate cell viscoelastic properties use induced deformations[11] or probes[12]. Approaches to measure the elastic component of cell viscoelasticity include atomic force microscopy (AFM)[13], optical laser tweezers[14], magnetic tweezers[15], pipette suction[16], uniaxial stretching rheometry[17], hydrodynamic stretching[18], and microrheology[19, 20]. The viscous response of cells has been measured using approaches that include microrheology[19, 20], electronic spin resonance[21], fluorescent rotor protein[22], AFM[23], pipette suction[16], and optical laser tweezers[24]. These measurements, however, can be strongly influenced by the specific region of a cell that is probed[25], alterations of the cytoskeletal network by an applied stress[26] or cell interactions with a probe[27]. All of these influences may bias measurements of cell viscoelasticity.

Therefore, we developed a contact-free, non-invasive approach that accurately measures cell viscoelastic properties based on quantitative phase imaging (QPI), a method that we refer to as quantitative phase rheology (QPR). QPI[28] is a microscopy technique used to measure the phase-shift or retardation of light due to its interactions with the relative dry mass, or the non-aqueous

biomass, of a cell[29]. Using an experimentally determined cell-average specific refractive index, we can relate the phase shift of light to cell biomass[30, 31]. QPI has been used to study cell growth[32], death[33], and responses to growth inhibition by chemotherapeutics or targeted inhibitors of biological processes[34-36].

Previous studies have used what we refer to as QPR to measure membrane viscoelastic properties of enucleated erythrocytes, including development of an analytical model linking observed vibration modes to viscoelastic properties through the autocorrelation of quantitative phase data[37, 38]. However, this model does not directly translate to the more complex structure of nucleated cells. In an application to nucleated cells, spatial and temporal autocorrelations of quantitative phase data from human pluripotent stem cell colonies indicated both a larger degree of spatial coordination and faster rate of temporal decorrelation for pluripotent cells compared to their differentiated progeny[39]. A more recent study found that spatial autocorrelations of quantitative phase data can be used to indicate the intracellular disorder of cells, a parameter related to cell stiffness in response to deformation to fluid shear[40]. Other work on QPR indicates that temporal autocorrelation of quantitative phase data relates to cellular transport properties including diffusion[41-43], and show a correlative relation to cellular stiffness[44]. However, there is currently no QPR method to concurrently model and measure both the elastic and viscous components of cell viscoelasticity.

In the present study, we report that the temporal autocovariance of quantitative phase data for cells at interphase of the cell cycle show a response similar to a mass spring damper system. The elastic and viscous coefficients describing this behavior correlate with viscous and elastic stiffness components of interphase

cells quantified by AFM measurements. We varied the cell stiffness of three different cell lines with cytochalasin B[45], an actin polymerization inhibitor, and show a high correlation between QPR results and AFM viscoelasticity measurements. Finally, to validate our measurements in cells of the same genetic origin during a cell state transition in which stiffness plays a physiological role, we apply QPR to a cellular model of the epithelial to mesenchymal transition (EMT)[46]. These results show that QPR measures of stiffness and viscosity correlate with EMT state. Overall, our results suggest that label-free QPR can be used to indicate cell stiffness and viscosity, significantly expanding the utility of QPI for monitoring cell behavior.

RESULTS

Autocovariance of cell QPI data exhibits damped oscillations

We used QPI to measure cellular biomass distribution over time (Fig. 1a-1c) and computed the autocovariance of these biomass distributions over time, $C_{\phi\phi}$, to quantify changes in the distribution of biomass caused by the motion of cellular structures (Fig. 1d). The autocovariance of the quantitative phase data (Fig. 1d) is well-fit by an equation describing damped harmonic oscillations ($R^2 = 0.99$). The fitting coefficients in this equation are related to an effective stiffness, k, and effective viscosity, μ. Assuming the spring and damper act in series, k is given by equation (9) (Methods) and μ can be found by dividing equation (9) by equation (5) (Methods).

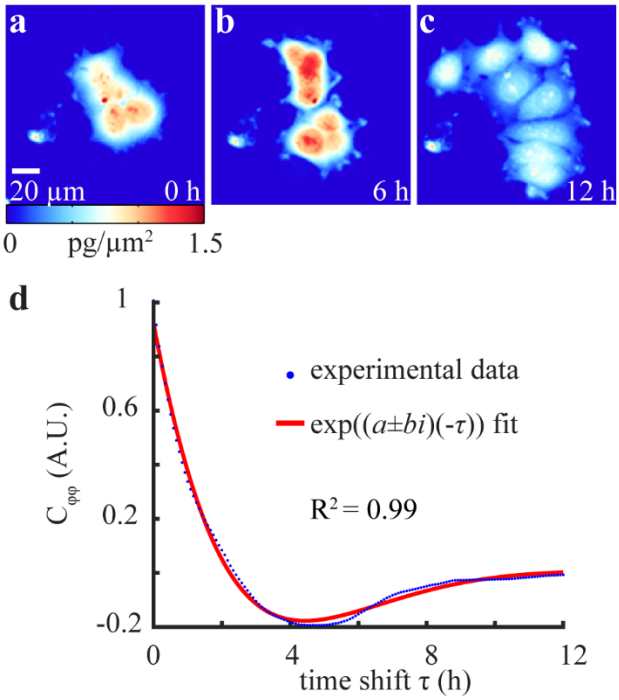

FIGURE 1 Autocovariance of QPI biomass-density over time displays underdamped oscillations. (**a-c**) QPI of MCF-7 cell cluster at 0, 6, and 12 h of imaging. (**d**) Autocovariance of QPI data over timeshift τ fitted to a complex exponential.

Automated detection and removal of cell division events in quantitative phase data

QPR detects large changes in both effective stiffness and viscosity during mitosis (Fig. S1). These changes are consistent with previously measured increases in cortical tension and cell stiffness during cell division and mitosis[47-49]. However, our QPR analysis averages values obtained over a period of approximately 5 h, so changes in cell stiffness due to single mitotic events are not resolved. To measure population-level differences, we therefore restrict our analysis to interphase cells.

We filtered QPI data to automatically detect the localized increase in biomass density that occurs during mitosis using a kernel consisting of a sigmoid function in time[50] and a disk in space. This kernel mimics the characteristic changes in cell phase shift that occur during mitotic cell rounding. When applied using an image processing filter (e.g. imfilter in Matlab), this kernel highlights regions of mitotic cells, without requiring any additional labels (Fig. S2 A-B). To validate this method of automatically detecting mitosis, we used FUCCI green fluorescence to mark mitotic cells (Fig. S2c). We observed >80% overlap between fluorescently labeled mitotic cells and cells with high values of the QPI mitosis filter, indicating robust detection of mitosis. We then calculated true positive versus false positive rates for detection of images that contain a division event (Fig. S2d). This allowed us to determine a filter threshold that gives a true positive rate of > 0.95.

We then applied our label-free QPI mitotic filter to our autocovariance analysis. We calculated autocovariance on all possible 5 h subsets of each cell cluster dataset. Any subset that was determined to contain images with a mitotic event were removed from the analysis. This automatic filtering eliminates cells in mitosis from QPI data to enable biomass-density decorrelation rate measurements for interphase cells only.

QPR measurements of elasticity and viscosity

We performed QPR with filtered elimination of mitotic events for MCF-7 (Fig. 2a), HeLa (Fig. 2b), and BT-474 (Fig. 2c) cells. These curves display significant heterogeneity as detected by the variable periods and amplitudes of oscillation seen in the autocovariance curves of individual clusters. For example, BT-474 cells displayed the highest frequency of oscillation ($b = 0.46 \pm 0.07$) and steepest exponential decay ($a = 0.63 \pm 0.05$) (Fig. 2c) compared to the other two cell lines,

whereas HeLa cells appear to have the lowest oscillation frequency and exponential decay (b = 0.24±0.11 and a = 0.52±0.12) (Fig. 2b). These qualitative differences correspond to a predicted lowest effective elasticity (aka stiffness) and viscosity for HeLa cells and a highest effective stiffness and viscosity for BT-474 cells. The standard deviation for stiffness from repeated measurements of single cells and clusters was 7-10%. The population standard deviation, however, was significantly larger, approximately 100%., indicating significant biological heterogeneity within each cell population.

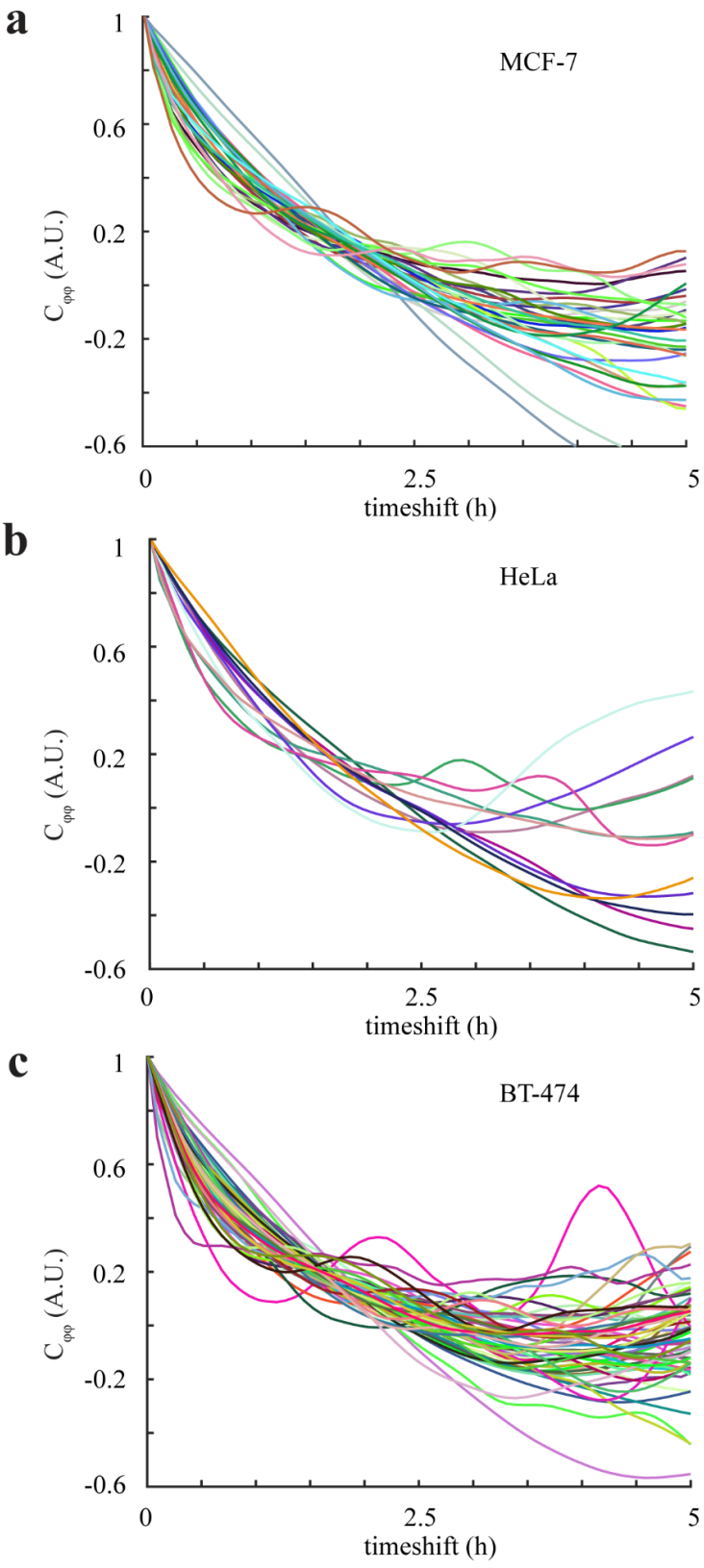
a
MCF-7
1
0.6
0.2
-0.2
-0.6
$C_{\varphi\varphi}$ (A.U.)
0
2.5
5
timeshift (h)
b
HeLa
1
0.6
0.2
-0.2
-0.6
$C_{\varphi\varphi}$ (A.U.)
0
2.5
5
timeshift (h)
c
BT-474
1
0.6
0.2
-0.2
-0.6
$C_{\varphi\varphi}$ (A.U.)
0
2.5
5
timeshift (h)

FIGURE 2 Autocovariance of QPI data from individual clusters and cells indicates significant heterogeneity. (**a**) Autocovariance of MCF-7 (*n*=31), (**b**) HeLa (*n*=12), and (**c**) BT-474 (*n*=51) cells in 0 μM cytochalasin B with individual cell or cluster traces shown.

To induce a change in cellular stiffness and viscosity, we used the actin polymerization inhibitor cytochalasin B to disrupt the cell cytoskeleton over a drug concentration range of 0-5 μM[51] and measured effective stiffness and viscosity with QPR (Fig. 3). These data display both significant cell-to-cell heterogeneity as well as the expected trend of decreasing stiffness and viscosity with increasing cytochalasin B concentrations. This is most easily detected in the population averaged autocovariance signal between control (R^2 = 0.99±0.01) and 5 μM (R^2 = 0.99±0.01) cytochalasin B treated MCF-7 cells (Fig. S3a), where the decay of the autocovariance for 5 μM treated cells is more rapid than the control, indicating a decrease in viscoelasticity. This result is consistent with similar data obtained using dynamic light scattering by others for the effect of lowered viscoelasticity on autocovariance values[52]. The stiffness change detected for HeLa (Fig. S3b) and BT-474 (Fig. S3c) cells was less dramatic under these cytochalasin B treatment conditions. Therefore, there are lower differences between the control (HeLa R^2 = 0.98±0.01, BT-474 R^2 = 0.98±0.01) and 5 μM perturbation autocovariance values (HeLa R^2 = 0.99±0.01, BT-474 R^2 = 0.99±0.01) for these cells than for MCF-7 cells. The individual autocovariance values for both control and 5 μM cytochalasin B treated cells fits the damped harmonic oscillation equations well, as quantified by average $R^2 > 0.98$ for all perturbations in all 3 cell types.

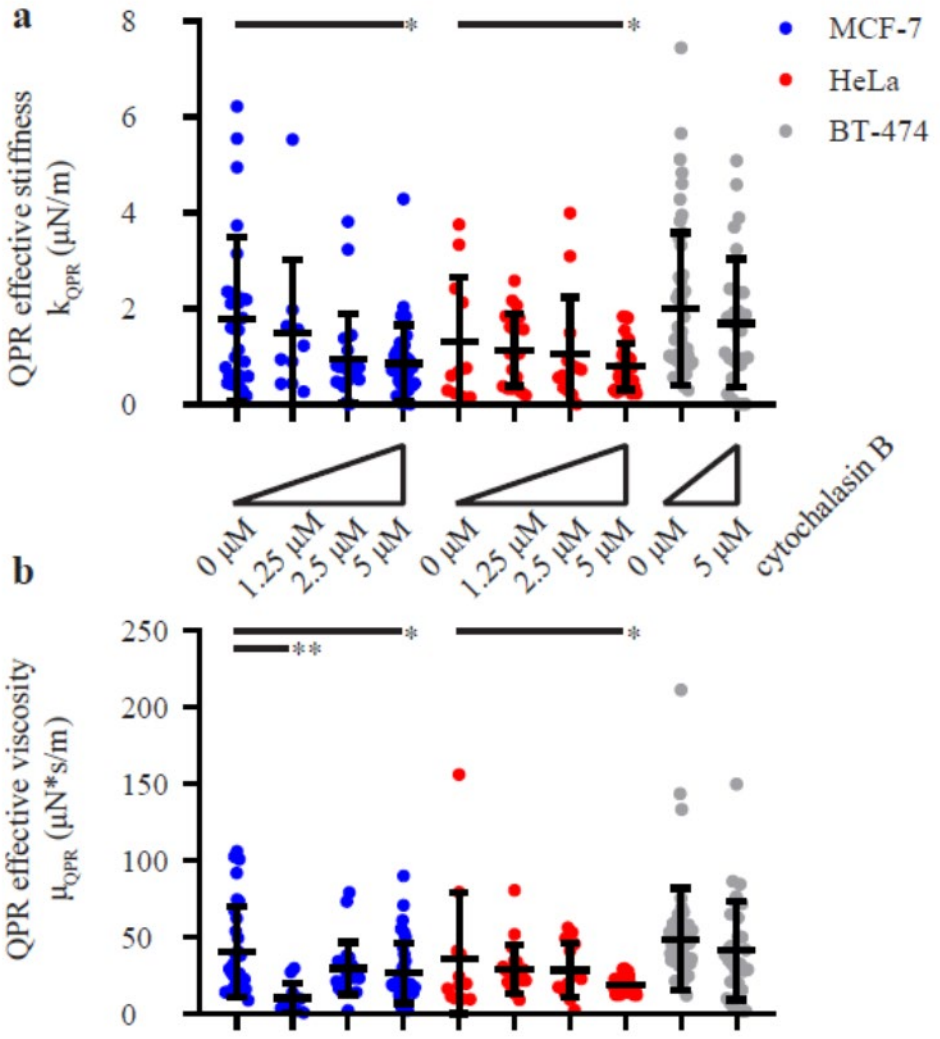

FIGURE 3 Population average QPR stiffness and viscosity values decrease with increasing cytochalasin B concentration. (**a**) QPR stiffness and (**b**) QPR viscosity of MCF-7, HeLa, and BT-474 over various 0-10 μM cytochalasin B concentration. QPR samples were collected at 0 μM (n=12), 1.25 μM (n=20), 2.5 μM (n=14), and 5 μM (n=25) for HeLa, at 0 μM (n=31), 1.25 μM (n=11), 2.5 μM (n=22), and 5 μM (n=34) for MCF-7, and at 0 μM (n=51) and 5 μM (n=31) for BT-474 cells. Error bars represent SD. * $p < 0.05$ and ** $p < 0.01$.

We then compared QPR with AFM data as AFM is a validated 'gold-standard' method for measuring cell viscoelastic properties. We obtained a strong correlation ($R^2 = 0.9$) between fit parameters for stiffness from QPR data compared with AFM measured stiffness values (Fig. 4a). QPR viscosity data also correlated well with AFM viscosity data with an R^2 of 0.89 (Fig. 4b). Additionally, the material relaxation time (Fig. S4) computed from QPR measurements (equation (10), Methods) compares well to those of AFM relaxation of deformation under constant load from published studies[53, 54]. Our measured values fall within the reported range[54, 55] for MCF-7 cells (23.2±3.9s), whereas the other cell types BT-474 (21.8±4.1s) and HeLa (38.0±8.3s) fall within the anticipated magnitudes for live cells, which ranges from seconds to one minute. These data indicate that QPR approaches provide reproducible and accurate label-free measurements of stiffness and viscosity.

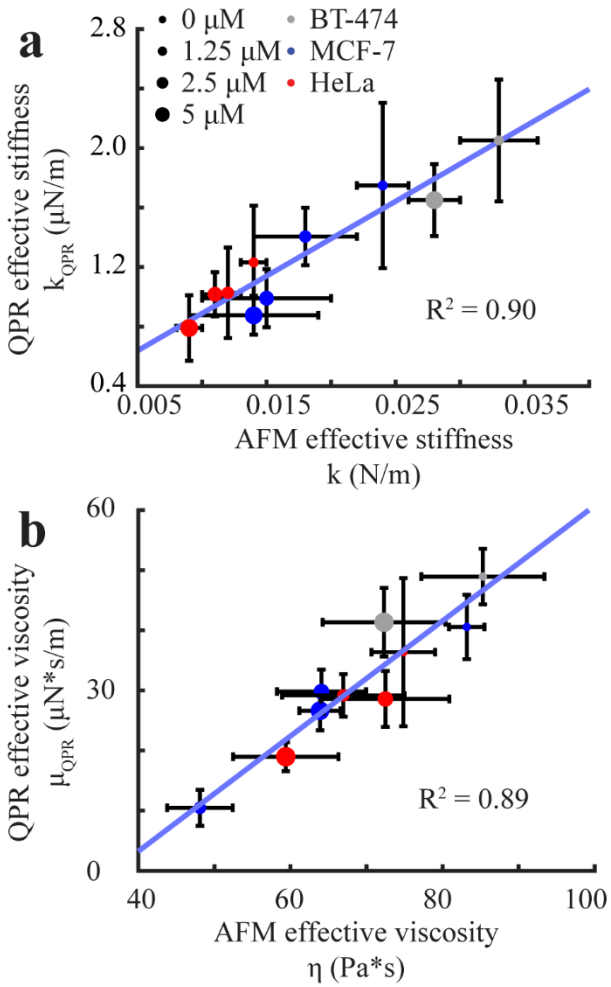

FIGURE 4 QPR predictions for stiffness and viscosity correlates with AFM data for multiple cell lines and drug concentrations. (**a**) QPR effective stiffness versus cell stiffness measured by AFM force curves for cells exposed to escalating doses of cytochalasin B. (**b**) QPR effective viscosity versus cell viscosity estimated with AFM by force dissipation. AFM data were collected at 0 µM (*n*=75), 1.25 µM (*n*=18), 2.5 µM (*n*=37), and 5 µM (*n*=133) for HeLa, at 0 µM (*n*=72), 1.25 µM (*n*=25), 2.5 µM (*n*=20), and 5 µM (*n*=66) for MCF-7, and at 0 µM (*n*=12) and 5 µM (*n*=28) for BT-474 cells. QPR samples were collected at the conditions and sample numbers indicated in Figure 3. Error bars represent SEM.

QPR measurements during EMT

We investigated whether QPR would be useful for measuring changes in effective stiffness and viscosity during changes in cell state. Therefore, we utilized our QPR approach for cells induced to undergo EMT. A shift from relatively stiff non-metastatic cancer cells to mechanically 'softer' cells with metastatic potential occurs during the EMT[56], making this cell state transition an important model system. We induced EMT in MCF-10A cells by TGF-β1 exposure and observed profound morphological changes by QPI compared with control, untreated cells (Fig. 5a) that were consistent with previous studies[57]. MCF-10A cells exposed to the TGF-β receptor-inhibitor SB431542 also showed unique morphological features in QPI compared to untreated control and TGF-β1 treated cells (Fig. 5a). Reduced steady-state expression of the epithelial biomarker, E-cadherin, and increased expression of the mesenchymal biomarker, vimentin, in TGF-β1-treated cells confirmed a transition to a mesenchymal state (Fig. 5b). Conversely, SB431542-treatment enforced an epithelial state, confirmed by unchanged E-cadherin and markedly reduced vimentin steady-state expression levels (Fig. 5b). Untreated cells had intermediate levels of both proteins, suggesting a mixed population of cells in epithelial and mesenchymal states. Measurements of cell biomass from QPI showed no statistically significant differences in biomass accumulation rates between cells in these different biophysical states (Fig. 5c). However, a clear difference in QPR stiffness (p-value < 0.05) (Fig. 5d) but not in viscosity (Fig. 5e), was obtained between SB431542-treated epithelial cells relative to untreated, mixed population, and TGF-β1-treated mesenchymal cells (Fig. 5a). Furthermore, an increase in E-cadherin expression in TGF-β1-treated cells corresponded with an increased stiffness that negatively correlates with vimentin expression (Fig. 5f). Overall, the data show that QPR stiffness could be an alternative, label-free physical biomarker

for distinguishing cells in an epithelial state from those in a mesenchymal state, as well as cells comprising a mixed heterogeneous population.

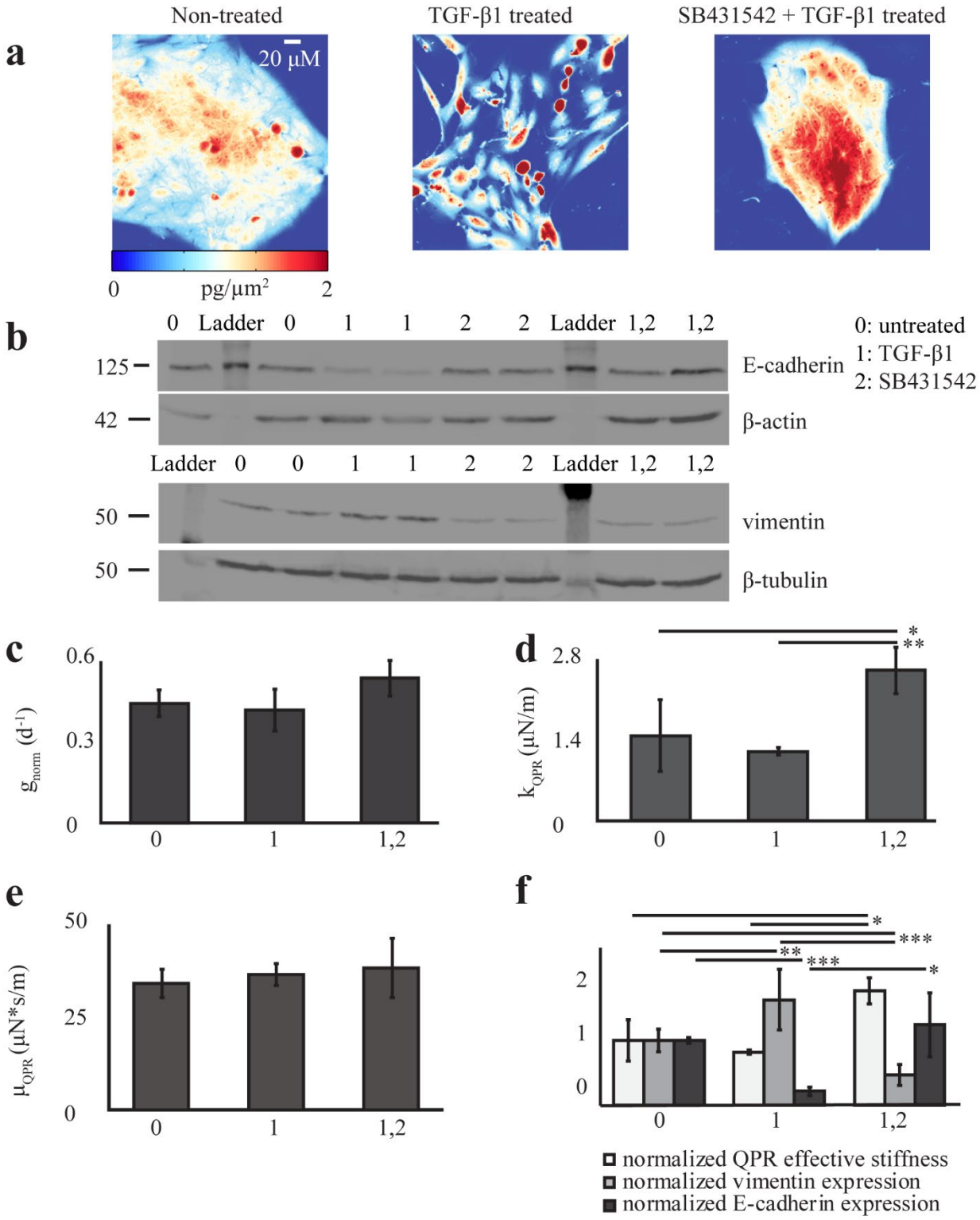

FIGURE 5 QPR quantifies changes in effective stiffness and viscosity during EMT. (**a**) Representative quantitative phase images of MCF-10A cells grown in control (non-treated) media, media supplemented with TGF-β1, and media supplemented with both TGF-β1 and SB431542. (**b**) Western blot of E-cadherin and vimentin expression in MCF-10A cells grown in untreated (control), TGF-β1, SB431542, or TGF-β1 + SB431542-containing media. β-actin and β-tubulin are loading controls, 2 independent biological replicates per sample. (**c**) Normalized growth rate, (**d**) QPR effective stiffness, and (**e**) QPR effective viscosity for MCF-10A cells grown in the listed conditions. (**f**) QPR stiffness, vimentin, and E-cadherin expression normalized to untreated cell values for MCF-10A cells grown in the listed conditions. Non-treated n=20, TGF-β1 n=41, and TGF-β1 + SB431542 n=37. Error bars are SEM. * $p < 0.05$, ** $p < 0.01$, and *** $p < 0.001$.

DISCUSSION

Movement of cell biomass, quantified as the autocovariance of quantitative phase imaging measurements, displays harmonic oscillatory motion (Fig. 2). A two-parameter viscoelastic model captures the oscillation and decay of this autocovariance (Fig. 1d). Fitting this model to experimental data enables the extraction of separate values of effective stiffness and viscosity of a cell (Fig. 3). Although there are previous methods to measure stiffness[40] with QPI data, our analysis method based on temporal measurements of cell biomass motion captures both stiffness and viscosity components of cell rheological properties. We refer to the measurement of these and other[40-43] rheological properties of a cell using QPI as QPR.

To use our QPR measurements to distinguish between different cell types, states and conditions, we assume a consistent stiffness over the measurement period of approximately 5 h. This assumption is not applicable during mitosis in which cell stiffness changes dramatically[49]. We therefore developed an automated method to detect cell divisions for their removal from quantitative phase imaging data. This enables QPR to automatically process live cell QPI data and extract cell rheological properties. Future work could examine improvements to the spatial and temporal resolution of QPR required to capture the magnitude of cell viscoelastic changes during mitosis

We observed a strong correlation between QPR measurements of cell stiffness (Fig. 4a) and viscosity (Fig. 4b) relative to AFM measurements. Relaxation times computed from QPR data are also within the same range observed previously with AFM (Fig S4)[54, 55]. This suggests that QPR measures cell viscoelasticity within a similar force and time regime as AFM measurements.

A physical interpretation of our results can be found in the model proposed by Qian[58] for single particle tracking within a Kelvin-Voight material. This model gives similar predictions to the series spring damper (Maxwell) material model we apply, suggesting that QPR is effectively tracking displacements of small particles of cell biomass immersed in a Maxwell material. When we applied the Kelvin-Voight model to our QPR data, we obtain a moderate fit to AFM viscosity values (R^2 =0.81, Fig. S5) compared to the fit for a Maxwell model (R^2 = 0.89, Fig. 4b). This indicates that a Maxwell material model is the more appropriate two-parameter, linear viscoelastic material model for interpreting QPR data. Although this two-parameter, linear model represents a simplistic view of cell viscoelasticity, this model nonetheless captures the essential features recorded in our data.

We note that this physical interpretation of the mathematical model includes an inertia term, despite describing the behavior of a low Reynolds number fluid. We keep this term, which arises in models of underdamped systems[58], to capture our observation of underdamped motion of cell biomass (Fig.1d and Fig. 2). This phenomenological assumption, rooted in observation, allows us to fit a two-parameter viscoelastic model and extract cell rheological properties from QPI data that correlate to AFM values. In terms of a potential physical meaning of this term, recent work indicates that inertia-like oscillations can occur in actively driven, viscoelastic fluids[59]. As the cell is an active material[60], we speculate that the inertia-like behavior we record in our system is due to a similar coupling between viscoelastic material properties and active force generation from cytoskeletal rearrangements. This suggests the need for future modeling based on a more sophisticated cell material model that can better incorporate these cellular mechanics.

Despite the correlation between AFM and QPR measurements of stiffness and viscosity, there is a large difference in magnitude of these values. This difference is partially explained by differences in probe size. The radius of the AFM probe tip is 500 nm, whereas the effective probe for QPR is the material within the cytoplasm. The observed difference in magnitude of QPR stiffness relative to AFM stiffness is ~10^4, suggesting a QPR probe size of ~5 nm. This probe size is within the range for a complex of average sized proteins that constitute the majority of mammalian cell biomass. For example, in eukaryotes a 'typical' ~3 nm in radius[61] protein has an average biomass of ~56 kDa[62]. The difference in magnitude of AFM and QPR measurements can therefore be explained by the difference in the cross sectional area of these probes. Furthermore, we model the cell as a purely linear viscoelastic material; however, in general, cell rheology is dependent on length scale, strain rate, and magnitude of applied force which may differ between these two approaches. In addition, AFM measures viscosity from viscous dissipation, whereas QPR measures an effective frictional coefficient felt by a particle due to the viscosity of a cell. These are technically two different properties that are closely related through viscosity. Our QPR method is most similar to passive particle tracking in microrheology[63], which provides a stiffness value from the expected relationship to passive particle motion. Microrheology measurements[64] when compared to AFM measurements[65] for mouse embryonic fibroblasts show large differences in measured magnitudes: 14 Pa for microrheology stiffness versus 7.7 kPa for AFM stiffness. A similar order of magnitude difference between AFM stiffness and microrheology stiffness was also obtained for MCF10A breast epithelial cells as well[66].

Additional parameters that may affect QPR measurements include the frequency of measurements[67] and the ratio of water content to cell volume of our samples[68, 69]. To interrogate

the effect of measurement frequency, we obtained QPR viscosity and elastic modulus data over a range of measurement frequencies for a single MCF-7 cell cluster and for a population ofcells (Fig. S6). We observed that both stiffness and viscosity values are within the standard error of the mean (SEM) for QPI measurements at frequencies less than 15 min per frame. However, for QPI measurement frequencies above ~30 min per frame, measurement accuracy and stability begins to deviate from the SEM. For water content effects, cells persist within a physiological range of 260-320 mOSM/kg[70], or within a range of ~60 mM for osmolality, with water losses of 10-15% or less[71]. Mechanisms[72] that maintain this homeostasis are tightly controlled and regulating both osmolality and water content losses. These values indicate, for the physiologically-relevant cell culture systems employed here, minimal osmolality or water content influences on QPR measurements. In addition, others have shown that significant stiffness changes require large changes in osmolality[69] of at least 150 mM or in water content to change cell volumes[68].

Overall, our results show the potential of a label-free and non-contact method that can measure cell rheological properties. As a transmitted light microscopy method, QPI is non-invasive and therefore minimizes the confounding effects of probes when examining biological processes in live cells. Because QPR builds on an existing quantitative phase imaging workflow, QPR can be integrated with other measurements already commonplace with quantitative phase techniques, such as cell biomass or biomass accumulation rate (Fig 5c). This and previous studies[40-43, 73] on alternative approaches to QPR suggests that the use of quantitative phase imaging data to measure cell structure[39, 40, 73] and how cell structure changes over time[41-44] provides powerful methods in biophysical research of cell state and state transitions.

METHODS

Cells and cell culture

MCF-7 and BT-474 human invasive ductal breast adenocarcinoma cells and MCF-10A immortalized human breast epithelial cells were purchased from the American Type Culture Collection (ATCC). HeLa human cervical adenocarcinoma cells expressing fluorescence ubiquitination cell cycle indicator (FUCCI)[74] plasmids were received from Dr. Ran Kafri (University of Toronto). FUCCI plasmids include mKO2-hCdt1, a monomeric fast-folding variant of Kusabira Orange fused to amino acids 30 – 120 of human Cdt1, and mAG-hGem, a monomeric version of Azami green fused to amino acids 1 – 100 of human Geminin[74]. MCF-7 cells were also transiently transfected with FUCCI mKO2-hCdt1 and mAG-hGem expression plasmids using the BacMam system (Fisher). We cultured MCF-7 cells in EMEM supplemented with 10% fetal bovine serum (FBS, Omega Scientific) and 10 mg/L human recombinant insulin (Sigma). BT-474 cells grew in Hybri-Care Medium (ATCC) reconstituted in cell culture grade water (Fisher) with 1.5 g/L sodium bicarbonate and 10% FBS (Omega Scientific). MCF-10A cells grew in MEGM Bulletkit media (Lonza) with cholera toxin (Sigma-Aldrich) at 100 ng/mL and without gentamycin-amphotericin B mix. HeLa cells were cultured in DMEM with 4.5 g/L glucose, L-glutamine, and sodium pyruvate (Cellgro) along with 1% penicillin streptomycin (Cellgro), 1% Q-max (Gibco), 1% non-essential amino acids (Gibco), and 10% FBS (Omega Scientific). We incubated cells with escalating doses of cytochalasin B (Sigma Aldrich) dissolved in DMSO solution or to 0.1% DMSO control, starting 4 h prior to experiments.

Quantitative phase and fluorescence Imaging

QPI of MCF-7, BT-474, and HeLa cells was performed as described in Yu *et al.*[75]. Fluorescence images were obtained with an EM-CCD C9100 camera (Hamamatsu Photonics) and an X-Cite Series 120 Q (Lumen Dynamics) source. Image collection occurred every 5 min for 12 h at 14 – 16 imaging locations containing cells plated with sufficient spacing to enable automated image processing and biomass segmentation.

Quantitative phase image analysis

Image processing was performed using custom MATLAB (MathWorks) scripts. Cells and cell clusters were identified and segmented using a local adaptive threshold based on Otsu's method[39, 76] and particle tracking code based on Grier *et al.*[50, 77]. Compensation for translational motion was done by finding the maximum two-dimensional cross correlation of each cell or cell cluster image against the immediately prior image. Manual detection of interphase, mitotic, and cell division boundaries was by visual inspection of image frames containing cells whose mean phase-shift increased, followed by splitting into two daughter cells then a decrease in mean phase-shift. Automated detection of an interphase-mitotic event boundary was by pattern matching biomass distribution images with a mitotic filter consisting of a one-dimensional sigmoid filter in time[78] and a two-dimensional disk filter of diameter 5 pixels in space. A mitotic filter value threshold of 0.6 A.U. for MCF-7, BT-474, and HeLa cells was chosen to maximize the true positive and minimize the false positive rates for entry into mitosis by validation with manual detection and fluorescence data.

AFM

AFM experiments were performed on a Bioscope Resolve BioAFM using a MLCT D triangular probe tip at 37°C (Bruker). Spring constants of cantilever tips measured 0.03-0.08 N/m and were calibrated with nanoscope measurement acquisition software (Bruker). Samples were incubated in media containing 0.1% DMSO or escalating doses of cytochalasin B for 4 h prior to the experiment with an additional 30 min of system equilibration with the cantilever submerged. The cantilever was calibrated using Nanoscope measurement acquisition software (Bruker). We analyzed force curves by finding the slope of the linear region of the curve measured during cantilever retraction of interphase cells in order to eliminate artifacts from pushing cells against the culture plate. This corresponded to the region from 20% to 80% of the maximum applied force on the cell (Fig. S7). Viscosity measurements were extracted from force curve data by calculating the area between the extended and retraction force curves as performed in Rebelo *et al.*[23] (Fig. S7, shaded region).

Biomass accumulation rate calculation

Quantitative phase biomass distribution images were summed over the projected area of each cell cluster to obtain the total biomass per cluster at specified time points. We calculated exponential biomass accumulation rates by taking the logarithm of the biomass over time data and fitting to a first order polynomial equation using MATLAB Polyfit (MathWorks).

EMT

One day before EMT induction, MCF-10A cells were placed in standard 6-well culture plates. Recombinant human TGF-β1 (Sigma-Aldrich) was added to the culture media at 5 ng/mL to induce EMT. Alternatively, the TGF-β receptor inhibitor SB-431542 (Sigma-Aldrich) was added to the culture media at 10 μM final concentration to enforce an epithelial phenotype on MCF-10A

cells. Cell exposure to these conditions for 7 d ensured full effects[46]. Cells re-plated for imaging or Western blot studies were cultured with no additives, 5 ng/mL TGF-β1, 10 μM SB-431532, or both agents together. We incubated cells with or without additives for 2 d before imaging or Western blot.

Western blot

MCF-10A cells were harvested and lysed in 2 mL of ice cold sample buffer containing 7 mL of 0.5 Tris-HCl (Sigma-Aldrich), 3 mL glycerol (Sigma-Aldrich), and 1 g of sodium dodecyl sulfate (SDS) (Sigma-Aldrich) mixed with 1.2 mg of bromophenol blue (Sigma-Aldrich). 30 ug of protein lysates with 3 μL β-mercaptoethanol (Sigma-Aldrich) were loaded on a 10% polyacrylamide gel (Sigma-Aldrich), electrophoresed, and then transferred to a nitrocellulose membrane (Fisher). Membranes were incubated overnight with primary antibodies against β-actin (Sigma-Aldrich, A2066), E-cadherin (Cell Signaling Technology, 14472s), β-tubulin (R&D Systems, MAB1195), or vimentin (Cell Signaling Technology, 5741s). This was followed by incubation for 2 h with a secondary antibody solution containing Li-Cor TBS blocking solution (Li-Cor) and either IRDye 800CW goat anti-rabbit (Li-Cor, 926-32211) and IRDye 680RD donkey anti-mouse (Li-Cor, 926-68072) or IRDye 800CW goat anti-mouse (Li-Cor, 926-68070) or IRDye 680RD donkey anti-rabbit (Li-Cor, 926-32214) antibodies and then imaging on a Li-Cor Odyssey FC (Li-Cor). Protein abundance was normalized to either β-tubulin or β-actin for quantification of western blot data.

Statistical analysis

Statistical analyses were performed using two-tailed Student's t-test with unequal variances and sample size (Welch's t-test).

Autocovariance calculation from quantitative phase data

To measure the similarity of quantitative phase data over time we used an unbiased estimate of autocovariance[79] of the phase-shift signal, which is an autocorrelation of the mean subtracted data. We normalized the temporal autocovariance to the number of data points used in each autocovariance window, referenced to the end of the time shift window (t_0), and defined as:

$$C_{\phi\phi}(x,y,t_0,\tau)=\frac{w\sum_{j=0}^{w-\tau/\Delta t}(\phi(x,y,t_0-j\Delta t)-\langle\phi(x,y,t_0)\rangle)\cdot(\phi(x,y,t_0-j\Delta t-\tau)-\langle\phi(x,y,t_0)\rangle)}{(w-\frac{\tau}{\Delta t})\sum_{j=0}^{w-\tau/\Delta t}(\phi(x,y,t_0-j\Delta t)-\langle\phi(x,y,t_0)\rangle)^2} \quad (1)$$

where x and y are position after removing rigid translational motion of the cell cluster, t_0 is the initial time or time of the first position in the time window, ϕ is phase shift, N is the number of data points used to calculate the signal, w is the number of images, Δt is time between measurements, and τ is time shift. The autocovariance was then averaged over a cell or cell cluster area as:

$$\langle C_{\phi\phi}(t_0,\tau)\rangle_{x,y}=\frac{1}{A}\sum_{\text{all } x,y \text{ in } A} C_{\phi\phi}(x,y,t_0,\tau) \quad (2)$$

where A is the area of a cell or cell cluster in pixels. We also took the average of the autocovariance through time for all times corresponding to interphase cells,

$$\langle C_{\phi\phi}(\tau)\rangle_{x,y,t}=\frac{1}{n}\sum_{\text{all interphase } t_0}\langle C_{\phi\phi}(t_0,\tau)\rangle_{x,y} \quad (3)$$

where n is the number of different end time points.

Predicted autocovariance of cell biomass distributions

Using biomass as a tracer for displacement and translating this equation into autocovariance space yields:

$$\left\langle C_{\phi\phi}(\tau)\right\rangle_{x,y,t} = \left(\frac{w}{w-\frac{\tau}{\Delta t}}\right)\left(1-\frac{\sum_{j=w-\tau/\Delta t}^{w}\phi(j\Delta t)\cdot\phi(j\Delta t)}{\sum_{j=0}^{w}\phi(j\Delta t)\cdot\phi(j\Delta t)}\right)\exp\left(\left(a\pm b\omega i\right)\left(-\tau\right)\right). \tag{4}$$

If we assume the observed damped oscillations are due to a series, harmonic a and b can be written as:

$$a = \frac{k}{2\mu} \tag{5}$$

$$b = \left(\frac{k}{\langle m\rangle}\right)^{1/2}\left(1-\frac{k\langle m\rangle}{4\mu^2}\right)^{1/2} \tag{6}$$

where k is the effective spring constant of the cell felt by the particle over the measurement period, μ is the effective damping coefficient from the viscous forces of the cell felt by the particle, and $\langle m\rangle$ is the average biomass of particles in our system. Assuming that the system is ergodic,

$$\left\langle \phi(j\Delta t)\right\rangle_{w-\tau/\Delta t}^{w} \approx \left\langle \phi(j\Delta t)\right\rangle_{0}^{w} \tag{7}$$

the autocovariance equation then reduces to:

$$\left\langle C_{\phi\phi}(\tau)\right\rangle_{x,y,t} = \exp((a\pm bi)(-\tau)). \tag{8}$$

This means that effective stiffness can be described as:

$$\frac{k}{\langle m\rangle} = a^2 + b^2 \tag{9}$$

and the effective viscosity can be found from dividing equation (9) by equation (5). Relaxation time t_{relax} was calculated as:

$$t_{relax} = \frac{1}{2a}\Delta t \tag{10}$$

where Δt is the time interval between measurements.

References

1. Bao, G.; Suresh, S., Cell and Molecular Mechanics of Biological Materials. *Nat Mater* **2003,** *2* (11), 715-25.

2. Moeendarbary, E.; Harris, A. R., Cell Mechanics: Principles, Practices, and Prospects. *Wiley Interdiscip Rev Syst Biol Med* **2014,** *6* (5), 371-88.

3. Cross, S. E.; Jin, Y. S.; Rao, J.; Gimzewski, J. K., Nanomechanical Analysis of Cells from Cancer Patients. *Nature nanotechnology* **2007,** *2* (12), 780-3.

4. Xu, W. W.; Mezencev, R.; Kim, B.; Wang, L. J.; McDonald, J.; Sulchek, T., Cell Stiffness Is a Biomarker of the Metastatic Potential of Ovarian Cancer Cells. *PLOS One* **2012,** *7* (10), e46609.

5. Barriga, E. H.; Franze, K.; Charras, G.; Mayor, R., Tissue Stiffening Coordinates Morphogenesis by Triggering Collective Cell Migration in Vivo. *Nature* **2018,** *554* (7693), 523-527.

6. Lim, C. T.; Zhou, E. H.; Quek, S. T., Mechanical Models for Living Cells--a Review. *J. Biomech.* **2006,** *39* (2), 195-216.

7. Einstein, A., The Motion of Elements Suspended in Static Liquids as Claimed in the Molecular Kinetic Theory of Heat. *Ann Phys-Berlin* **1905,** *17* (8), 549-560.

8. Wojcieszyn, J. W.; Schlegel, R. A.; Wu, E. S.; Jacobson, K. A., Diffusion of Injected Macromolecules within the Cytoplasm of Living Cells. *P Natl Acad Sci-Biol* **1981,** *78* (7), 4407-4410.

9. Eze, M. O., Membrane Fluidity, Reactive Oxygen Species, and Cell-Mediated-Immunity - Implications in Nutrition and Disease. *Med Hypotheses* **1992,** *37* (4), 220-224.

10. Zakim, D.; Kavecansky, J.; Scarlata, S., Are Membrane Enzymes Regulated by the Viscosity of the Membrane Environment. *Biochemistry* **1992,** *31* (46), 11589-11594.

11. Lekka, M.; Laidler, P.; Gil, D.; Lekki, J.; Stachura, Z.; Hrynkiewicz, A. Z., Elasticity of Normal and Cancerous Human Bladder Cells Studied by Scanning Force Microscopy. *Eur. Biophys. J.* **1999,** *28* (4), 312-6.

12. Wirtz, D., Particle-Tracking Microrheology of Living Cells: Principles and Applications. *Annual review of biophysics* **2009,** *38*, 301-26.

13. Haase, K.; Pelling, A. E., Investigating Cell Mechanics with Atomic Force Microscopy. *Journal of the Royal Society, Interface / the Royal Society* **2015,** *12* (104), 20140970.

14. Lincoln, B.; Erickson, H. M.; Schinkinger, S.; Wottawah, F.; Mitchell, D.; Ulvick, S.; Bilby, C.; Guck, J., Deformability-Based Flow Cytometry. *Cytometry A* **2004,** *59* (2), 203-9.

15. Amblard, F.; Yurke, B.; Pargellis, A.; Leibler, S., A Magnetic Manipulator for Studying Local Rheology and Micromechanical Properties of Biological Systems. *Rev Sci Instrum* **1996,** *67* (3), 818-827.

16. Hochmuth, R. M., Micropipette Aspiration of Living Cells. *J. Biomech.* **2000,** *33* (1), 15-22.

17. Desprat, N.; Richert, A.; Simeon, J.; Asnacios, A., Creep Function of a Single Living Cell. *Biophys. J.* **2005,** *88* (3), 2224-33.

18. Gossett, D. R.; Tse, H. T. K.; Lee, S. A.; Ying, Y.; Lindgren, A. G.; Yang, O. O.; Rao, J. Y.; Clark, A. T.; Di Carlo, D., Hydrodynamic Stretching of Single Cells for Large Population Mechanical Phenotyping. *Proceedings of the National Academy of Sciences of the United States of America* **2012,** *109* (20), 7630-7635.

19. Crocker, J. C.; Hoffman, B. D., Multiple-Particle Tracking and Two-Point Microrheology in Cells. *Methods Cell Biol* **2007,** *83*, 141-78.

20. Mason, T. G.; Weitz, D. A., Optical Measurements of Frequency-Dependent Linear Viscoelastic Moduli of Complex Fluids. *Physical Review Letters* **1995,** *74* (7), 1250-1253.

21. Mastro, A. M.; Babich, M. A.; Taylor, W. D.; Keith, A. D., Diffusion of a Small Molecule in the Cytoplasm of Mammalian Cells. *Proceedings of the National Academy of Sciences of the United States of America* **1984,** *81* (11), 3414-8.

22. Kuimova, M. K.; Yahioglu, G.; Levitt, J. A.; Suhling, K., Molecular Rotor Measures Viscosity of Live Cells Via Fluorescence Lifetime Imaging. *J. Am. Chem. Soc.* **2008,** *130* (21), 6672-+.

23. Rebelo, L. M.; de Sousa, J. S.; Mendes Filho, J.; Radmacher, M., Comparison of the Viscoelastic Properties of Cells from Different Kidney Cancer Phenotypes Measured with Atomic Force Microscopy. *Nanotechnology* **2013,** *24* (5), 055102.

24. Lugowski, R.; Kolodziejczyk, B.; Kawata, Y., Application of Laser-Trapping Technique for Measuring the Three-Dimensional Distribution of Viscosity. *Optics Communications* **2002,** *202* (1-3), 1-8.

25. Haga, H.; Sasaki, S.; Kawabata, K.; Ito, E.; Ushiki, T.; Sambongi, T., Elasticity Mapping of Living Fibroblasts by Afm and Immunofluorescence Observation of the Cytoskeleton. *Ultramicroscopy* **2000,** *82* (1-4), 253-8.

26. Reed, J.; Troke, J. J.; Schmit, J.; Han, S.; Teitell, M. A.; Gimzewski, J. K., Live Cell Interferometry Reveals Cellular Dynamism During Force Propagation. *Acs Nano* **2008,** *2* (5), 841-846.

27. Squires, T. M.; Mason, T. G., Fluid Mechanics of Microrheology. *Annual Review of Fluid Mechanics* **2010,** *42*, 413-438.

28. Popescu, G.; Park, Y., Quantitative Phase Imaging in Biomedicine. *J. Biomed. Opt.* **2015,** *20* (11), 111201.

29. Zangle, T. A.; Teitell, M. A., Live-Cell Mass Profiling: An Emerging Approach in Quantitative Biophysics. *Nat. Methods* **2014,** *11* (12), 1221-8.

30. Davies, H. G.; Wilkins, M. H. F., Interference Microscopy and Mass Determination. *Nature* **1952,** *169* (4300), 541-541.

31. Barer, R., Interference Microscopy and Mass Determination. *Nature* **1952,** *169* (4296), 366-367.

32. Mir, M.; Wang, Z.; Shen, Z.; Bednarz, M.; Bashir, R.; Golding, I.; Prasanth, S. G.; Popescu, G., Optical Measurement of Cycle-Dependent Cell Growth. *Proc. Natl. Acad. Sci. USA* **2011,** *108* (32), 13124-9.

33. Pavillon, N.; Kuhn, J.; Moratal, C.; Jourdain, P.; Depeursinge, C.; Magistretti, P. J.; Marquet, P., Early Cell Death Detection with Digital Holographic Microscopy. *PLoS One* **2012,** *7* (1), e30912.

34. Hejna, M.; Jorapur, A.; Song, J. S.; Judson, R. L., High Accuracy Label-Free Classification of Single-Cell Kinetic States from Holographic Cytometry of Human Melanoma Cells. *Scientific reports* **2017,** *7* (1), 11943.

35. Reed, J.; Chun, J.; Zangle, T. A.; Kalim, S.; Hong, J. S.; Pefley, S. E.; Zheng, X.; Gimzewski, J. K.; Teitell, M. A., Rapid, Massively Parallel Single-Cell Drug Response Measurements Via Live Cell Interferometry. *Biophys. J.* **2011,** *101* (5), 1025-31.

36. Mir, M.; Bergamaschi, A.; Katzenellenbogen, B. S.; Popescu, G., Highly Sensitive Quantitative Imaging for Monitoring Single Cancer Cell Growth Kinetics and Drug Response. *PLoS One* **2014,** *9* (2), e89000.

37. Park, Y.; Best, C. A.; Badizadegan, K.; Dasari, R. R.; Feld, M. S.; Kuriabova, T.; Henle, M. L.; Levine, A. J.; Popescu, G., Measurement of Red Blood Cell Mechanics During Morphological Changes. *Proc. Natl. Acad. Sci. USA* **2010,** *107* (15), 6731-6.

38. Popescu, G.; Park, Y.; Choi, W.; Dasari, R. R.; Feld, M. S.; Badizadegan, K., Imaging Red Blood Cell Dynamics by Quantitative Phase Microscopy. *Blood Cells Mol Dis* **2008,** *41* (1), 10-6.

39. Zangle, T. A.; Chun, J.; Zhang, J.; Reed, J.; Teitell, M. A., Quantification of Biomass and Cell Motion in Human Pluripotent Stem Cell Colonies. *Biophysical Journal* **2013,** *105* (3), 593-601.

40. Eldridge, W. J.; Steelman, Z. A.; Loomis, B.; Wax, A., Optical Phase Measurements of Disorder Strength Link Microstructure to Cell Stiffness. *Biophysical Journal* **2017,** *112* (4), 692-702.

41. Ceballos, S.; Kandel, M.; Sridharan, S.; Majeed, H.; Monroy, F.; Popescu, G., Active Intracellular Transport in Metastatic Cells Studied by Spatial Light Interference Microscopy. *J Biomed Opt* **2015,** *20* (11), 111209.

42. Wang, R.; Wang, Z.; Millet, L.; Gillette, M. U.; Levine, A. J.; Popescu, G., Dispersion-Relation Phase Spectroscopy of Intracellular Transport. *Opt Express* **2011,** *19* (21), 20571-9.

43. Kandel, M. E.; Fernandes, D.; Taylor, A. M.; Shakir, H.; Best-Popescu, C.; Popescu, G., Three-Dimensional Intracellular Transport in Neuron Bodies and Neurites Investigated by Label-Free Dispersion-Relation Phase Spectroscopy. *Cytometry A* **2017,** *91* (5), 519-526.

44. Ma, L. H.; Rajshekhar, G.; Wang, R.; Bhaduri, B.; Sridharan, S.; Mir, M.; Chakraborty, A.; Iyer, R.; Prasanth, S.; Millet, L.; Gillette, M. U.; Popescu, G., Phase Correlation Imaging of Unlabeled Cell Dynamics. *Scientific reports* **2016,** *6*.

45. Petersen, N. O.; Mcconnaughey, W. B.; Elson, E. L., Dependence of Locally Measured Cellular Deformability on Position on the Cell, Temperature, and Cytochalasin-B. *P Natl Acad Sci-Biol* **1982,** *79* (17), 5327-5331.

46. Zhang, J.; Tian, X. J.; Zhang, H.; Teng, Y.; Li, R.; Bai, F.; Elankumaran, S.; Xing, J., Tgf-Beta-Induced Epithelial-to-Mesenchymal Transition Proceeds through Stepwise Activation of Multiple Feedback Loops. *Sci Signal* **2014,** *7* (345), ra91.

47. Pourati, J.; Maniotis, A.; Spiegel, D.; Schaffer, J. L.; Butler, J. P.; Fredberg, J. J.; Ingber, D. E.; Stamenovic, D.; Wang, N., Is Cytoskeletal Tension a Major Determinant of Cell Deformability in Adherent Endothelial Cells? *Am J Physiol-Cell Ph* **1998,** *274* (5), C1283-C1289.

48. Matzke, R.; Jacobson, K.; Radmacher, M., Direct, High-Resolution Measurement of Furrow Stiffening During Division of Adherent Cells. *Nat. Cell Biol.* **2001,** *3* (6), 607-610.

49. Stewart, M. P.; Helenius, J.; Toyoda, Y.; Ramanathan, S. P.; Muller, D. J.; Hyman, A. A., Hydrostatic Pressure and the Actomyosin Cortex Drive Mitotic Cell Rounding. *Nature* **2011,** *469* (7329), 226-30.

50. Zangle, T. A.; Burnes, D.; Mathis, C.; Witte, O. N.; Teitell, M. A., Quantifying Biomass Changes of Single Cd8+ T Cells During Antigen Specific Cytotoxicity. *PLoS One* **2013,** *8* (7), e68916.

51. Rotsch, C.; Radmacher, M., Drug-Induced Changes of Cytoskeletal Structure and Mechanics in Fibroblasts: An Atomic Force Microscopy Study. *Biophys. J.* **2000,** *78* (1), 520-535.

52. Joo, C.; Evans, C. L.; Stepinac, T.; Hasan, T.; de Boer, J. F., Diffusive and Directional Intracellular Dynamics Measured by Field-Based Dynamic Light Scattering. *Optics Express* **2010,** *18* (3), 2858-2871.

53. Darling, E. M.; Zauscher, S.; Block, J. A.; Guilak, F., A Thin-Layer Model for Viscoelastic, Stress-Relaxation Testing of Cells Using Atomic Force Microscopy: Do Cell Properties Reflect Metastatic Potential? *Biophys. J.* **2007,** *92* (5), 1784-1791.

54. Kulkarni, A. H.; Chatterjee, A.; Kondaiah, P.; Gundiah, N., Tgf-Beta Induces Changes in Breast Cancer Cell Deformability. *Phys Biol* **2018,** *15* (6), 065005.

55. Yasaman, N.; Kuin Tian, P.; Chwee Teck, L., Correlating the Viscoelasticity of Breast Cancer Cells with Their Malignancy. *Convergent Science Physical Oncology* **2017,** *3* (3), 034003.

56. Calzado-Martin, A.; Encinar, M.; Tamayo, J.; Calleja, M.; Paulo, A. S., Effect of Actin Organization on the Stiffness of Living Breast Cancer Cells Revealed by Peak-Force Modulation Atomic Force Microscopy. *Acs Nano* **2016,** *10* (3), 3365-3374.

57. Wong, I. Y.; Javaid, S.; Wong, E. A.; Perk, S.; Haber, D. A.; Toner, M.; Irimia, D., Collective and Individual Migration Following the Epithelial-Mesenchymal Transition. *Nat Mater* **2014,** *13* (11), 1063-71.

58. Qian, H., Single-Particle Tracking: Brownian Dynamics of Viscoelastic Materials. *Biophys. J.* **2000,** *79* (1), 137-43.

59. Berner, J.; Muller, B.; Gomez-Solano, J. R.; Kruger, M.; Bechinger, C., Oscillating Modes of Driven Colloids in Overdamped Systems. *Nat Commun* **2018,** *9* (1), 999.

60. Chen, T.; Saw, T. B.; Mege, R. M.; Ladoux, B., Mechanical Forces in Cell Monolayers. *J. Cell Sci.* **2018,** *131* (24).

61. Moran, U.; Phillips, R.; Milo, R., Snapshot: Key Numbers in Biology. *Cell* **2010,** *141* (7), 1262-1262.

62. Kozlowski, L. P., Proteome-Pi: Proteome Isoelectric Point Database. *Nucleic Acids Res.* **2017,** *45* (D1), D1112-D1116.

63. Weihs, D.; Mason, T. G.; Teitell, M. A., Bio-Microrheology: A Frontier in Microrheology. *Biophys. J.* **2006,** *91* (11), 4296-305.

64. Wirtz, D., Particle-Tracking Microrheology of Living Cells: Principles and Applications. *Annual review of biophysics* **2009,** *38*, 301-326.

65. Lopez-Fagundo, C.; Livi, L. L.; Ramchal, T.; Darling, E. M.; Hoffman-Kim, D., A Biomimetic Synthetic Feeder Layer Supports the Proliferation and Self-Renewal of Mouse Embryonic Stem Cells. *Acta Biomater.* **2016,** *39*, 55-64.

66. Li, Y. X.; Schnekenburger, J.; Duits, M. H. G., Intracellular Particle Tracking as a Tool for Tumor Cell Characterization. *J. Biomed. Opt.* **2009,** *14* (6).

67. Hajjarian, Z.; Nia, H. T.; Ahn, S.; Grodzinsky, A. J.; Jain, R. K.; Nadkarni, S. K., Laser Speckle Rheology for Evaluating the Viscoelastic Properties of Hydrogel Scaffolds. *Scientific reports* **2016,** *6*.

68. Guo, M.; Pegoraro, A. F.; Mao, A.; Zhou, E. H.; Arany, P. R.; Han, Y.; Burnette, D. T.; Jensen, M. H.; Kasza, K. E.; Moore, J. R.; Mackintosh, F. C.; Fredberg, J. J.; Mooney, D. J.; Lippincott-Schwartz, J.; Weitz, D. A., Cell Volume Change through Water Efflux Impacts Cell Stiffness and Stem Cell Fate. *Proceedings of the National Academy of Sciences of the United States of America* **2017,** *114* (41), E8618-E8627.

69. Scarcelli, G.; Polacheck, W. J.; Nia, H. T.; Patel, K.; Grodzinsky, A. J.; Kamm, R. D.; Yun, S. H., Noncontact Three-Dimensional Mapping of Intracellular Hydromechanical Properties by Brillouin Microscopy. *Nat. Methods* **2015,** *12* (12), 1132-+.

70. Waymouth, C., Osmolality of Mammalian Blood and of Media for Culture of Mammalian Cells. *In Vitro Cell Dev B* **1970,** *6* (2), 109-&.

71. Bregestovski, P.; Waseem, T.; Mukhtarov, M., Genetically Encoded Optical Sensors for Monitoring of Intracellular Chloride and Chloride-Selective Channel Activity. *Front Mol Neurosci* **2009,** *2*, 15.

72. Lang, F.; Busch, G. L.; Ritter, M.; Volkl, H.; Waldegger, S.; Gulbins, E.; Haussinger, D., Functional Significance of Cell Volume Regulatory Mechanisms. *Physiol. Rev.* **1998,** *78* (1), 247-306.

73. Takabayashi, M.; Majeed, H.; Kajdacsy-Balla, A.; Popescu, G., Disorder Strength Measured by Quantitative Phase Imaging as Intrinsic Cancer Marker in Fixed Tissue Biopsies. *Plos One* **2018,** *13* (3), e0194320.

74. Sakaue-Sawano, A.; Kurokawa, H.; Morimura, T.; Hanyu, A.; Hama, H.; Osawa, H.; Kashiwagi, S.; Fukami, K.; Miyata, T.; Miyoshi, H.; Imamura, T.; Ogawa, M.; Masai, H.; Miyawaki, A., Visualizing Spatiotemporal Dynamics of Multicellular Cell-Cycle Progression. *Cell* **2008,** *132* (3), 487-498.

75. Yu, J.; Seldin, M. M.; Fu, K.; Li, S.; Lam, L.; Wang, P.; Wang, Y.; Huang, D.; Nguyen, T. L.; Wei, B.; Kulkarni, R. P.; Di Carlo, D.; Teitell, M.; Pellegrini, M.; Lusis, A. J.; Deb, A., Topological Arrangement of Cardiac Fibroblasts Regulates Cellular Plasticity. *Circ Res* **2018,** *123* (1), 73-85.

76. Otsu, N., Threshold Selection Method from Gray-Level Histograms. *Ieee T. Syst. Man Cyb.* **1979,** *9* (1), 62-66.

77. Crocker, J. C.; Grier, D. G., Methods of Digital Video Microscopy for Colloidal Studies. *J. Colloid Interf. Sci.* **1996,** *179* (1), 298-310.

78. Zangle, T. A.; Teitell, M. A.; Reed, J., Live Cell Interferometry Quantifies Dynamics of Biomass Partitioning During Cytokinesis. *PLoS One* **2014,** *9* (12), e115726.

79. Bendat, J. S.; Piersol, A. G., *Random Data : Analysis and Measurement Procedures*. 2013.

SUPPLEMENTARY INFORMATION

Supplementary Derivation

Supplementary Figures S1 – S5

Supplementary Unprocessed Western Blots (related to Fig. 5B)

Supplementary References

SUPPLEMENTARY DERIVATION

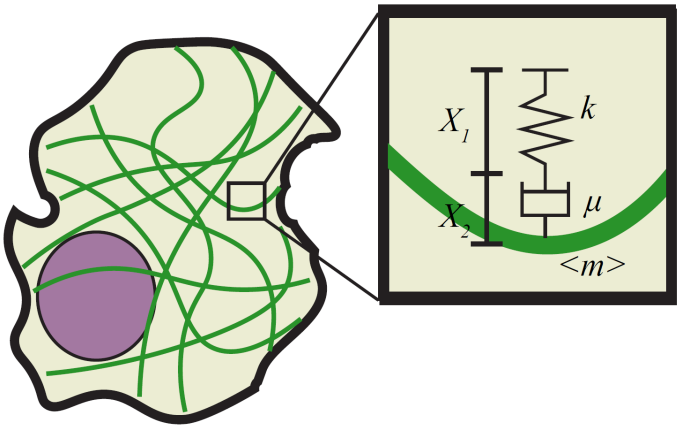

Summary:

We provide a derivation for how quantitative phase rheology (QPR) generates effective cell stiffness and viscosity using the autovariance of quantitative phase imaging (QPI) data. To do this, we establish a basic definition of the autovariance function and a basic equation that extracts stiffness and viscosity from dry mass, or non-aqueous biomass, displacement. We combine this definition and equation with QPI data to extract stiffness and viscosity regimes from the autovariance function.

Autocovariance

To measure the similarity of quantitative phase data over time we used an unbiased estimate of autocovariance[1] of the phase-shift signal, which is an autocorrelation of the mean subtracted data. We normalized the temporal autocovariance to the number of data points used in each autocovariance window, referenced to the end of the time shift window (t_0), and defined as:

$$C_{\phi\phi}(x,y,t_0,\tau)=\frac{w\sum_{j=0}^{w-\tau/\Delta t}(\phi(x,y,t_0-j\Delta t)-\langle\phi(x,y,t_0)\rangle)\cdot(\phi(x,y,t_0-j\Delta t-\tau)-\langle\phi(x,y,t_0)\rangle)}{(w-\frac{\tau}{\Delta t})\sum_{j=0}^{w-\tau/\Delta t}(\phi(x,y,t_0-j\Delta t)-\langle\phi(x,y,t_0)\rangle)^2} \quad \text{(S11)}$$

Where x and y are positions after removing rigid translational motion of a cell cluster, t_0 is the time, ϕ is phase-shift, N is the number of data points used to calculate the signal, w is the number of images, Δt is time between measurements, and τ is time lag. The autocovariance was then averaged over a cell or cell cluster area as:

$$\langle C_{\phi\phi}(t_0,\tau)\rangle_{x,y}=\frac{1}{A}\sum_{\text{all } x,y \text{ in } A}C_{\phi\phi}(x,y,t_0,\tau) \quad \text{(S12)}$$

where A is the area of a cell or cell cluster in imaging pixels. We also took the average of the autocovariance through time for all times corresponding to cells in interphase of the cell cycle,

$$\langle C_{\phi\phi}(\tau)\rangle_{x,y,t}=\frac{1}{n}\sum_{\text{all interphase } t_0}\langle C_{\phi\phi}(t_0,\tau)\rangle_{x,y} \quad \text{(S13)}$$

where n is the number of different end time points.

Two-parameter

We treat the cellular structures imaged by quantitative phase as particles immersed in a Maxwell liquid (Fig. 1A). Therefore, these structures feel the effect of a spring damper system in series described as the following system of equations:

$$\langle m \rangle \frac{d^2 X_{tot}}{dt^2} = -\mu \frac{dX_2}{dt} + f(t) \tag{S14}$$

$$kX_1 = \mu \frac{dX_2}{dt} \tag{S15}$$

$$X_{tot} = X_1 + X_2 \tag{S16}$$

where k is the long term effective spring constant of the cell felt by a particle, μ is the effective damping coefficient from the viscous forces of the cell felt by a particle, $f(t)$ is the applied impulse force, X_1 is the elastic displacement, X_2 is the viscous displacement, X_{tot} is the total displacement of the biomass, and $\langle m \rangle$ is the average biomass of particles in the system. We observe long timescales that are much greater than the average relaxation times of a cell (Fig. S3), so the long timescale effects dominate and the active force can be considered as applied nearly instantaneously. Rearranging equation (S4) in terms of only the elastic displacement X_1 or only the viscous displacement X_2 yields the following differential equations:

$$\langle m \rangle \frac{d^2 X_1}{dt^2} = -kX_1 - \frac{k\langle m \rangle}{\mu} \frac{dX_1}{dt} \tag{S17}$$

$$\langle m \rangle \frac{d^3 X_2}{dt^3} = -k \frac{dX_2}{dt} - \frac{k\langle m \rangle}{\mu} \frac{d^2 X_2}{dt^2} \ . \tag{S18}$$

Assuming that the total displacement X_{tot} contributes to the majority of biomass rearrangement and oscillation, we integrate eq (S8) over time, add it to eq (S7), and rearrange this equation of a damper spring system in series to obtain an inhomogeneous ordinary differential equation (ODE) for the total displacement:

$$\langle m \rangle \frac{d^2 X_{tot}}{dt^2} = -kX_{tot} - \frac{k\langle m \rangle}{\mu} \frac{dX_{tot}}{dt} + c_1 \tag{S19}$$

where c_1 could be seen as a buildup of stress from past deformation or a memory function. Solving for the general solution of equation (S9) gives a homogenous component and a particular solution by the method of undetermined coefficients:

$$X_{tot,\mathrm{h}}(t) = \left(X_{tot,0} - X_{tot,rest}\right)\exp\left(\left(\frac{k}{2\mu} \pm \left(\frac{k}{\langle m\rangle}\right)^{1/2}\left(1 - \frac{k\langle m\rangle}{4\mu^2}\right)^{1/2} i\right)t\right) \tag{S20}$$

$$X_{tot,p}(t) = \frac{c_1}{k} \equiv X_{tot,rest} \tag{S21}$$

where $X_{tot,0}$ is the initial displacement and $X_{tot,rest}$ is the long term resting displacement of our system. Because the relaxation timescale (Fig. S3) is over an order of magnitude lower than the period of measurement, the active force can be modeled as an instantaneous displacement represented as a delta function, δ, at some time, t_j, not equal to zero. Solution of this spring damper system without this active force yields:

$$X_{tot}(t) = \left(X_{tot,0} - X_{tot,rest}\right)\exp\left(\left(\frac{k}{2\mu} \pm \left(\frac{k}{\langle m\rangle}\right)^{1/2}\left(1 - \frac{k\langle m\rangle}{4\mu^2}\right)^{1/2} i\right)t\right) + X_{tot,rest}\ . \tag{S22}$$

With each individual impulse the displacement from the active force can be modeled as:

$$X_{tot}(t) = \left(X_{tot,0} - X_{tot,rest} + \delta(t - t_j)\right)\exp\left(\left(\frac{k}{2\mu} \pm \left(\frac{k}{\langle m\rangle}\right)^{1/2}\left(1 - \frac{k\langle m\rangle}{4\mu^2}\right)^{1/2} i\right)t\right) + X_{tot,rest} \tag{S23}$$

where t_j is the time of each impulse displacement. Assuming a linear viscoelastic material, the total displacement in time can be represented as the superposition of the various impulse displacements from the active forces, which then simplifies to:

$$X_{tot}(t) = \left(X_{tot,0} - X_{tot,rest} + \sum_{t_j \neq 0}^{T} \delta(t - t_j)\right)\exp\left(\left(\frac{k}{2\mu} \pm \left(\frac{k}{\langle m\rangle}\right)^{1/2}\left(1 - \frac{k\langle m\rangle}{4\mu^2}\right)^{1/2} i\right)t\right) + X_{tot,rest}$$

(S24)

where T is the period of observation. We then establish the relationship between biomass and displacement of biomass by:

$$\frac{DM(\vec{x},t)}{Dt} = \frac{\partial M(\vec{x},t)}{\partial t} + \vec{v}(\vec{x},t) \bullet \nabla M(\vec{x},t) \tag{S25}$$

where M is biomass as a function of position x and time t, and v is velocity as a function of x and t. We assume that the main contribution to the partial derivative of biomass with time is due to growth and since our measurement occurs over a short time interval, growth is negligible, therefore:

$$\frac{DM(\vec{x},t)}{Dt} = \vec{v}(\vec{x},t) \bullet \nabla M(\vec{x},t) \,. \tag{S26}$$

We further assume that the cell velocity, v, and biomass, M, fields are isotropic with no dependence on direction. Averaging over θ in polar coordinates yields:

$$\left\langle \frac{DM(r,t)}{Dt} \right\rangle_\theta = \left\langle v(r,t) \right\rangle_\theta \left(\frac{1}{r} \frac{\partial \left(r \left\langle M(r,t) \right\rangle_\theta \right)}{\partial r} \right) = \left\langle v(r,t) \right\rangle_\theta \left(\frac{1}{r} \left\langle M(r,t) \right\rangle_\theta + \frac{\partial \left\langle M(r,t) \right\rangle_\theta}{\partial r} \right).$$

(S27)

Assuming that this change in biomass over radial distance is small compared to the total biomass over a radial distance r we obtain:

$$\left\langle \frac{DM(r,t)}{Dt} \right\rangle_\theta = \left\langle v(r,t) \right\rangle_\theta \left(\frac{\left\langle M(r,t) \right\rangle_\theta}{r} \right) . \tag{S28}$$

Averaging over a radial distance and assuming that velocity, v, radial position, r, and biomass, M, do not correlate over the radial distance because the system is isotropic we obtain:

$$\left\langle \frac{DM(t)}{Dt} \right\rangle_{r,\theta} = \left\langle \left\langle v(r,t) \right\rangle_\theta \frac{\left\langle M(r,t) \right\rangle_\theta}{r} \right\rangle_r = \left\langle v(t) \right\rangle_{r,\theta} \left(\frac{\left\langle M(t) \right\rangle_{r,\theta}}{\left\langle r \right\rangle} \right) . \tag{S29}$$

Assuming this system is ergodic, the local spatial average of biomass is equal to the temporal average biomass, which is constant with respect to time, and therefore the average biomass over radial distance term is only a function of r, which we call $\kappa(r)$:

$$\kappa(r) \equiv \frac{\gamma(r)}{\langle r \rangle} \approx \frac{\langle M(t) \rangle_{r,\theta}}{\langle r \rangle} \tag{S30}$$

where $\gamma(r)$ is the local spatial average of the biomass, which is constant over time and is therefore only a function of radial position:

$$\left\langle \frac{DM(t)}{Dt} \right\rangle_{r,\theta} = \kappa(r) \langle v(t) \rangle_{r,\theta} = \kappa(r) \left\langle \frac{DX(t)}{Dt} \right\rangle_{r,\vartheta} . \tag{S31}$$

Since κ is independent of time, we can integrate and obtain:

$$\langle M(t) \rangle_{r,\theta} = \kappa(r) \langle X(t) \rangle_{r,\theta} . \tag{S32}$$

Thus, the ratio of biomass over initial biomass is equivalent to the displacement over initial displacement:

$$\frac{\langle M(t) \rangle_{r,\theta}}{\langle M(t_0) \rangle_{r,\theta}} = \frac{\kappa(r) \langle X(t) \rangle_{r,\theta}}{\kappa(r) \langle X(t_0) \rangle_{r,\theta}} = \frac{\langle X(t) \rangle_{r,\theta}}{\langle X(t_0) \rangle_{r,\theta}} . \tag{S33}$$

The biomass for a particular area is directly proportional to the phase-shift[2-5]:

$$M(\vec{x},t) = 1/\alpha \cdot \phi(\vec{x},t) \tag{S34}$$

where ϕ is phase-shift, and α is the specific refractive index, which is determined experimentally. Therefore, phase-shift data, ϕ, obtained via QPI can be used to obtain information about the displacement of cell biomass over time.

Predicted autocovariance of cell biomass distributions

Using biomass as a tracer for displacement and translating this equation into autocovariance space yields:

$$\left\langle C_{\phi\phi}(\tau)\right\rangle_{x,y,t} = \left(\frac{w}{w-\frac{\tau}{\Delta t}}\right)\left(1-\frac{\sum_{j=w-\tau/\Delta t}^{w}\phi(j\Delta t)\cdot\phi(j\Delta t)}{\sum_{j=0}^{w}\phi(j\Delta t)\cdot\phi(j\Delta t)}\right)\exp\left(\left(a\pm b\omega i\right)\left(-\tau\right)\right) \tag{S35}$$

where a and b are described in terms of coefficients as:

$$a = \frac{k}{2\mu} \tag{S36}$$

$$b = \left(\frac{k}{\langle m\rangle}\right)^{1/2}\left(1-\frac{k\langle m\rangle}{4\mu^2}\right)^{1/2} \tag{S37}$$

where w, τ, ϕ, and Δt are the same as in eq (S12), the average autocovariance function is the same as in eq (S3), and a and b are the coefficients described in eq (S26) and (S27). Assuming that the system is ergodic:

$$\left\langle\phi(j\Delta t)\right\rangle_{w-\tau/\Delta t}^{w} \approx \left\langle\phi(j\Delta t)\right\rangle_{0}^{w} \tag{S38}$$

$$\left\langle\phi(j\Delta t)\right\rangle_{w-\tau/\Delta t}^{w}\cdot\left\langle\phi(j\Delta t)\right\rangle_{w-\tau/\Delta t}^{w} \approx \left\langle\phi(j\Delta t)\right\rangle_{0}^{w}\cdot\left\langle\phi(j\Delta t)\right\rangle_{0}^{w} = c\left\langle\phi(j\Delta t)\right\rangle^{2} \tag{S39}$$

where

$$c = \frac{\sum_{j=0}^{w}\phi(j\Delta t)^2 - w\left\langle\phi(j\Delta t)\right\rangle^{2}}{w}\,. \tag{S40}$$

The autocovariance equation then reduces to:

$$\left\langle C_{\phi\phi}(\tau)\right\rangle_{x,y,t} = \exp((a\pm bi)(-\tau))\,. \tag{S41}$$

This means that the fitting parameter, a, describes the effective damping particles encounter within the cell, whereas the effective stiffness is described as:

$$\frac{k}{\langle m \rangle} = a^2 + b^2 . \tag{S42}$$

Relaxation time, τ_{relax}, was calculated as:

$$\tau_{relax} = \frac{1}{2a}\Delta t \tag{S43}$$

where Δt is the time interval between measurements.

SUPPLEMENTARY FIGURES

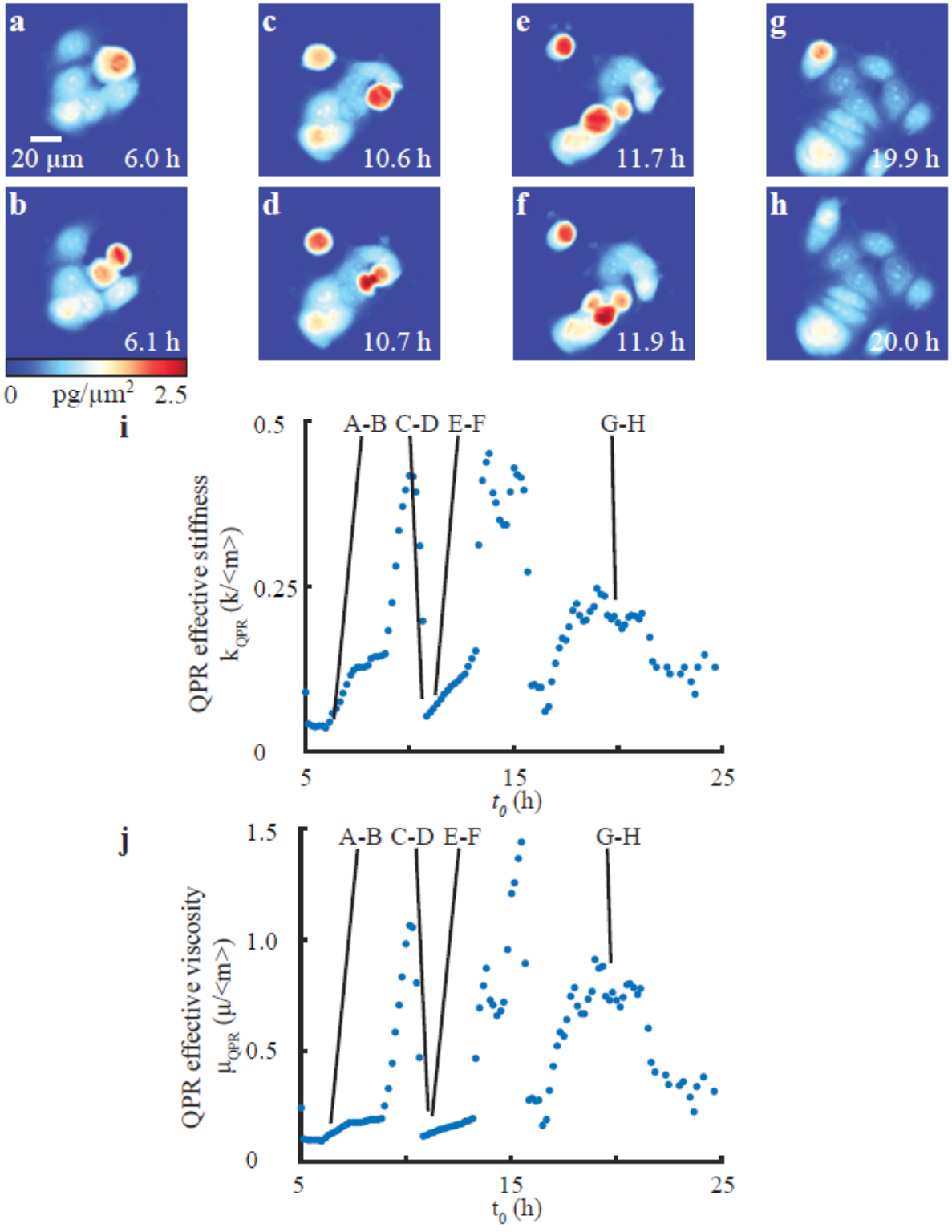

FIGURE S1 Cell division induces large mass fluctuations affecting QPR stiffness and viscosity measurements. (**a**, **c**, **e**, **g**) QPI of MCF-7 colonies before each mitosis plotted as 4 decorrelation rate peaks in (**i**). (**b**, **c**, **f**, **h**) QPI of MCF-7 colonies after each mitosis corresponding to the period after each trough in (**i**). (**i**) Time course of QPR stiffness measurement for MCF-7 cell colony in (**a**-**h**) with 4 cell divisions during 24 h of QPI. (**j**) Time course of QPR viscosity measurement for MCF-7 cell colony in (**a**-**h**) with 4 cell divisions over 24 h of QPI.

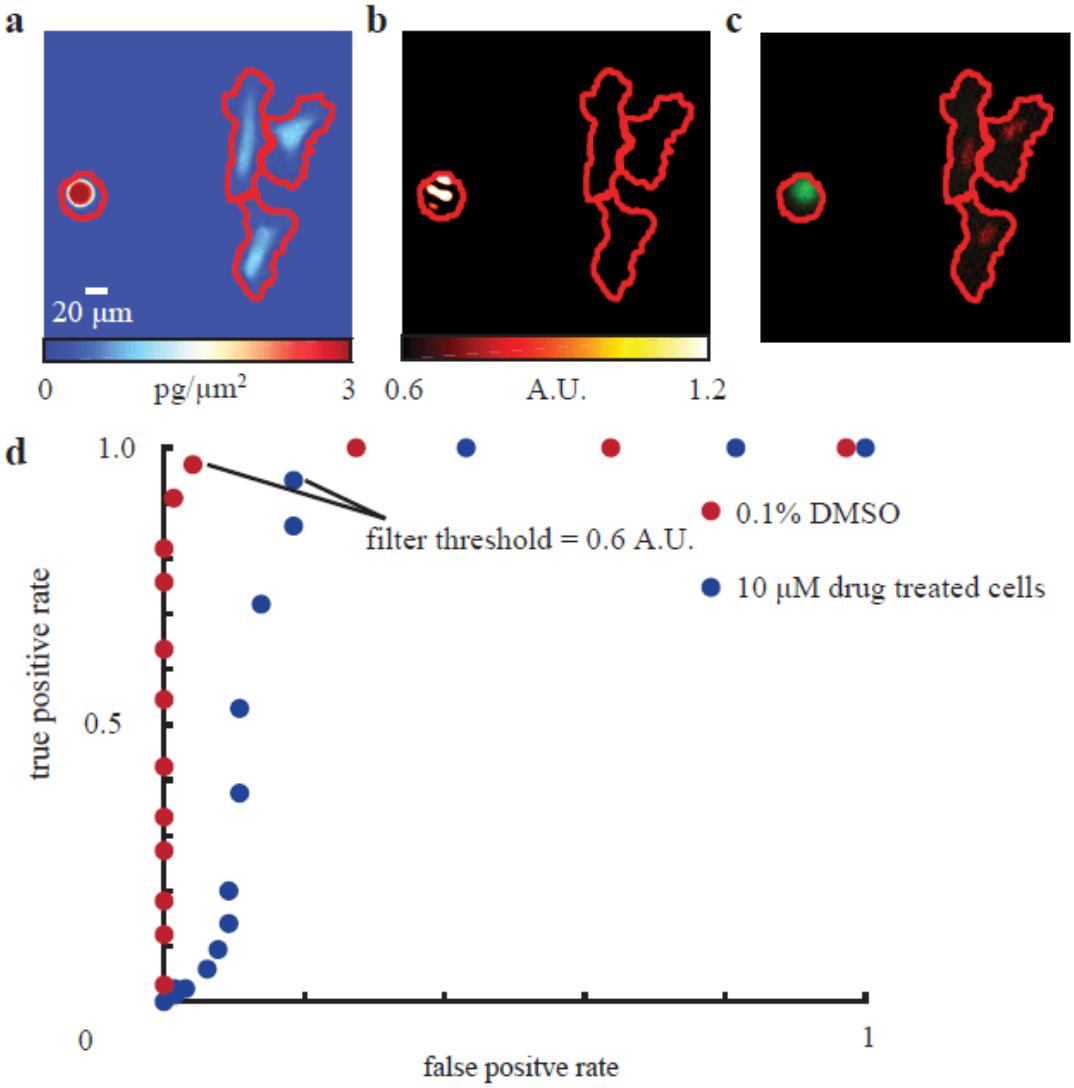

FIGURE S2 Assessment of cell division by fluorescence and QPI to remove mitotic events. (**a**) QPI of MCF-7 cells. (**b**) Filtered image of the same MCF-7 cells in (**b**) used to identify mitosis and cell division. The filter kernel consists of a sigmoid function in time and a disk in space to mimic and highlight round cells with a large phase shift in mitosis. (**c**) Simultaneous fluorescence image of MCF-7 cells in (**b** and **c**) expressing FUCCI fluorescence ubiquitination cell cycle indicator plasmids mKO2-hCdt1 and mAG-hGem. (**d**) ROC curves for detecting MCF-7 mitosis

and cell division events using the computational filter versus fluorescence in 0 and 10 μM concentrations of cytochalasin B.

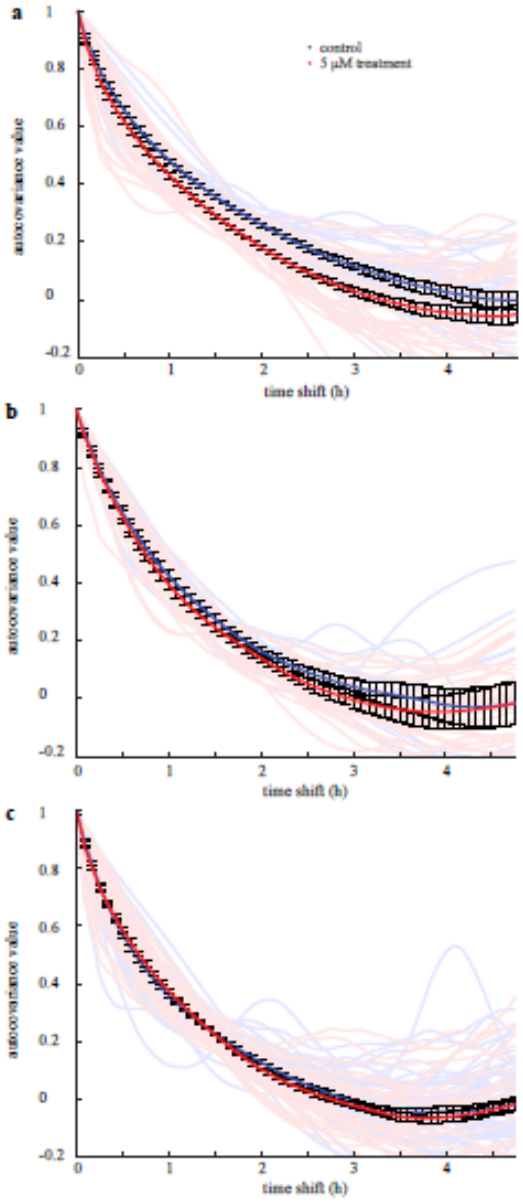

FIGURE S3 The average autocovariance of compliant (aka softer) cells decays more rapidly than for stiffer cells. (**a**) Individual and population averaged autocovariance curves for all 0 (R^2 = 0.99±0.01) and 5 μM (R^2 = 0.99±0.01) cytochalasin B treated MCF-7 cells analyzed. (**b**) Individual and population averaged autocovariance curves for 0 (R^2 = 0.98±0.01) and 5 μM (R^2 = 0.99±0.01)

cytochalasin B treated HeLa, and (**c**) 0 (R^2 = 0.98±0.01) and 5 μM (R^2 = 0.99±0.01) cytochalasin B treated BT-474 cells. Error bars represent SEM.

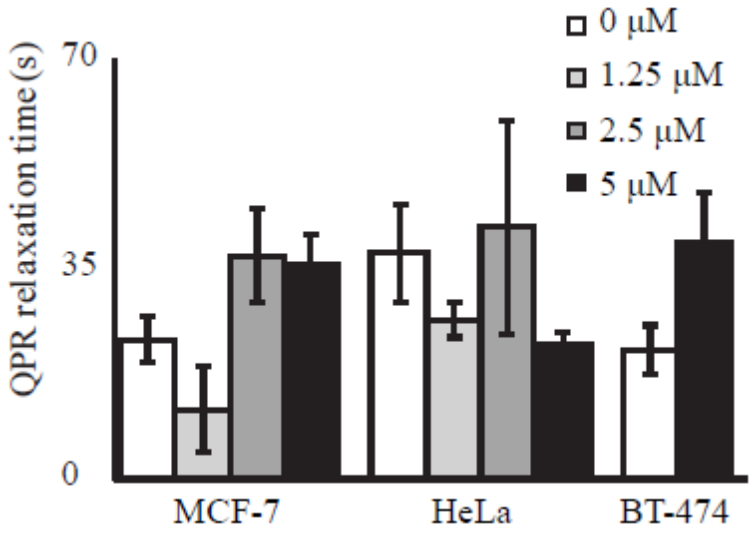

FIGURE S4 Interphase relaxation time calculated from QPR measurements are similar for multiple cell types and drug concentrations. Cells exposed to a range of cytochalasin B doses mainly display similar relaxation times despite changes in stiffness and viscosity. QPR samples were collected at 0 μM (*n*=12), 1.25 μM (*n*=20), 2.5 μM (*n*=14), and 5 μM (*n*=25) for HeLa, at 0 μM (*n*=31), 1.25 μM (*n*=11), 2.5 μM (*n*=22), and 5 μM (*n*=34) for MCF-7, and at 0 μM (*n*=51) and 5 μM (*n*=31) for BT-474 cells. Error bars represent SEM.

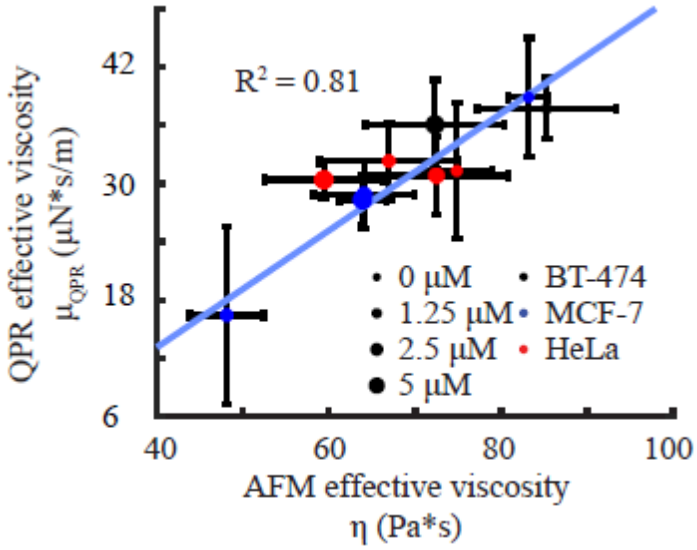

FIGURE S5 QPR predictions for viscosity using a Kelvin-Voight model show reduced correlation with AFM data relative to a Maxwell material model (Fig. 4b, $R^2 = 0.89$). QPR samples were collected at 0 μM (n=12), 1.25 μM (n=20), 2.5 μM (n=14), and 5 μM (n=25) for HeLa, at 0 μM (n=31), 1.25 μM (n=11), 2.5 μM (n=22), and 5 μM (n=34) for MCF-7, and at 0 μM (n=51) and 5 μM (n=31) for BT-474 cells. Error bars represent SEM.

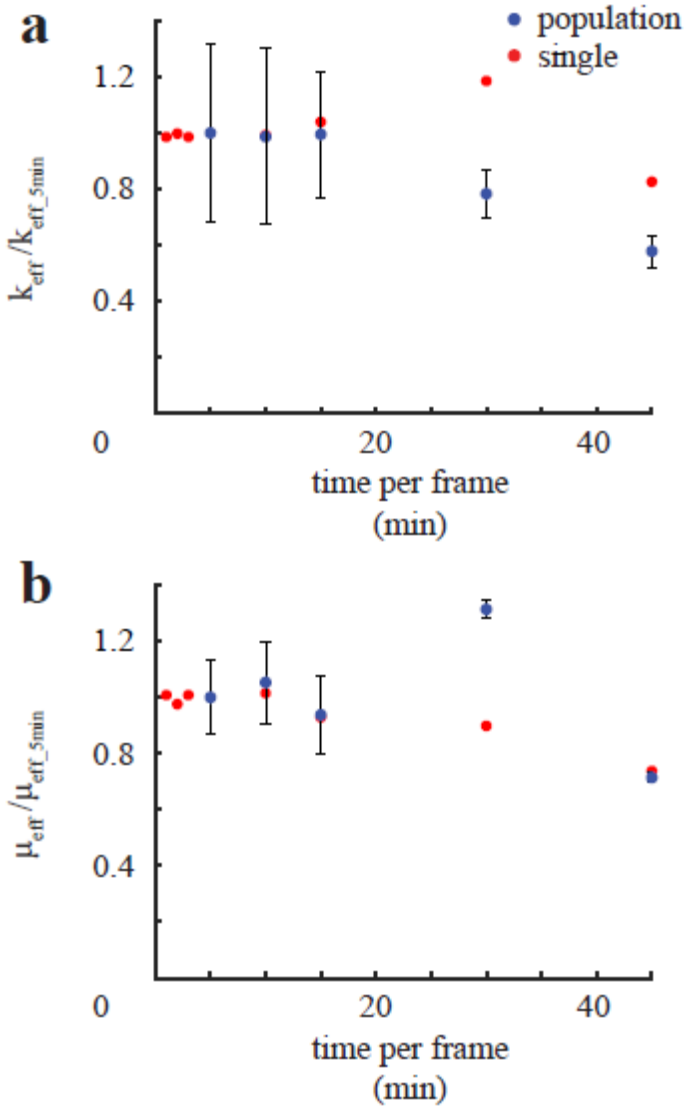

FIGURE S6 Effective viscoelastic modulus of MCF-7 cells at different measurement frequencies remains constant at an imaging rate under 15 minutes per frame. (**a**) Effective stiffness divided by effective stiffness at 5 minutes per frame for a range of QPI measurement frequencies. (**b**) Effective viscosity divided by effective viscosity at 5 minutes per frame for a range of QPI measurement frequencies. Blue represents the population average for analysis of MCF7 cells. A select MCF7 cluster was imaged at higher frequency and is shown in red. Error bars represent SEM.

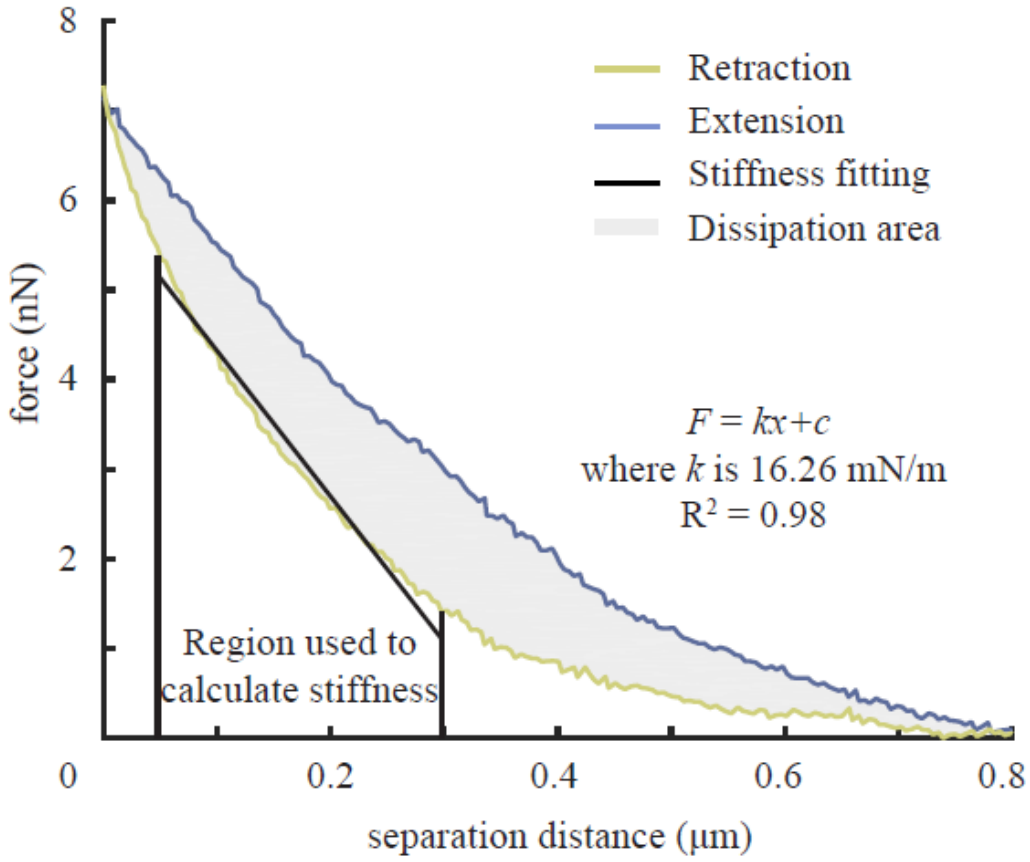

FIGURE S7 Representative AFM stiffness and viscosity measured using best fit of the retraction force curve and area difference between retraction and extend force curve. Data used for effective stiffness from AFM consists of the force data between 20% and 80% of maximum force signal, while viscosity measurements used data over 1 μm distance from contact with cell.

SUPPLEMENTARY UNPROCESSED WESTERN BLOTS

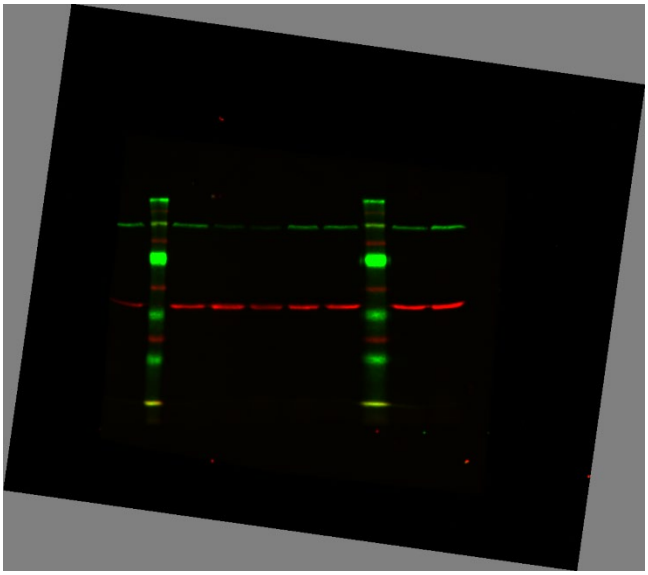

Western blot 1: Unprocessed immunoblot for E-cadherin (green) and β-actin (red) corresponding to Figure 5B.

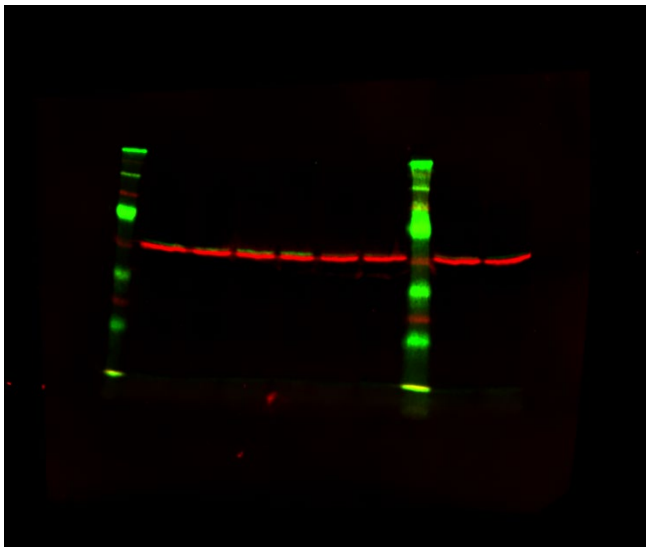

Western blot 2: Unprocessed immunoblot for vimentin (green) and β-tubulin (red) corresponding to Figure 5B.

SUPPLEMENTARY REFERENCES

1. Bendat, J. S.; Piersol, A. G., *Random Data : Analysis and Measurement Procedures*. 2013.

2. Davies, H. G.; Wilkins, M. H. F., Interference Microscopy and Mass Determination. *Nature* **1952,** *169* (4300), 541-541.

3. Barer, R., Interference Microscopy and Mass Determination. *Nature* **1952,** *169* (4296), 366-367.

4. Reed, J.; Chun, J.; Zangle, T. A.; Kalim, S.; Hong, J. S.; Pefley, S. E.; Zheng, X.; Gimzewski, J. K.; Teitell, M. A., Rapid, Massively Parallel Single-Cell Drug Response Measurements Via Live Cell Interferometry. *Biophysical Journal* **2011,** *101* (5), 1025-31.

5. Mir, M.; Wang, Z.; Shen, Z.; Bednarz, M.; Bashir, R.; Golding, I.; Prasanth, S. G.; Popescu, G., Optical Measurement of Cycle-Dependent Cell Growth. *Proc. Natl. Acad. Sci. USA* **2011,** *108* (32), 13124-9.

Chapter 3. Quantifying biomechanical work in proliferating cancer cells

Introduction

Cell energetics is important because of links to metabolism [1], maintenance of membrane potential [2], transport [3], and biosynthesis [4]. Despite its importance to the cell, it still remains insufficiently understood how energy is allocated into motion and mechanical processes versus biosynthesis and growth. The shuffling of energy via motion and mass production through the different spatial regime is of particular interest as cell lines have varying rates of motion and biosynthesis and thus may dissipate [5] or transfer motion into larger length scales [6] at different rates.

Common methods to study cellular energetics measure chemical potential energy as ATP level quantified with a luciferase assay [7] or fluorescence [8], or measure metabolic rate, for example, by measuring cellular oxygen consumption [9] or lactic acid production [10]. Viscous dissipation of energy which occurs due to cell deformation during cell spreading has been studied using a combination of fluorescence microscopy with comparison to a simplified computational model of the cell [11]. This study suggests that model of the cell as a viscous material can capture the dissipation of mechanical energy which occurs during changes in cell morphology. However, application of this method to study is limited by the need to create a suitable computational model and by the introduction of fluorescent labels that may affect cell behavior [12].

One solution is to use quantitative phase imaging (QPI) to measure time-dependent biomass distributions in cell clusters and compare these measurements to model predictions for the scaling of mass distribution fluctuations with spatial frequency. QPI is an imaging modality that quantifies the phase shift of light as it passes through and interacts with cell biomass [13]. Using an appropriate cellular average for the linear relationship between density and refractive index, the phase shift of

light throughout the cell then becomes proportional to its biomass [14, 15] resulting in an image of the cell dry mass distribution [16]. Previous biological applications of QPI include the measurement of cell growth [17] and death [18], membrane mechanical properties [19], cluster-scale mass motion [16], and bulk diffusion and advection within cells [20].

To address the need for non-invasive quantification of mechanical energy usage we assume that the majority of mechanical energy is dissipated at low length scales due to the highly viscous environment inside a cell [11]. We then extract the dissipation energy, or energy lost from motion in a viscous environment, from QPI data through a kinematic energy conservation analysis. We also examine how the energetic makeup of ATP production by cellular respiration and glycolysis from various cell lines alters the amount of energy spent in motion versus biosynthesis and the relative energetic efficiency of cell motion in cell clusters of varying size.

Results

Derivation of cellular work from QPI

Quantitative phase imaging can capture both the biochemical aspect of cellular work as quantified via net biomass accumulation (Fig. 1A) as well as the biomechanical portion captured in cellular motion (Fig. 1B). Values of net biomass accumulation grants information on the magnitude of biosynthesis processes between different cell lines (Fig. 1A) while cellular motion (Fig. 1B) gives us an idea on how much line might be focusing on motion. However, to compare how cells allocate their work to either biosynthesis or motion we must first have to develop a model to compare the two on the same magnitude.

We do this by first assuming that our change in energy is directly related to cellular biomass changes. Total energy of cell we assume is either stored biological represented as mass density (ρ^*) times the enthalpy per unit of biomass (h) or kinetically as ½ $\rho^* v^2$. To track this change in cellular energy we use a quantitative phase microscopy setup as depicted here (Fig. 1C). Assuming spatial isotropy, an isothermal system, and low influence of intracellular pressure gradients, the conservation of energy within a cell cluster in 2-dimensions is described by the following equation:

$$\frac{D}{Dt^*}(\rho^*(h+\frac{v^{*2}}{2})) = \rho^* \vec{f}^* \cdot \vec{v}^* + \nabla^* \tau^* v^* + kh\rho^* \tag{44}$$

where ρ*, h, v*, f*, τ*, k, t*, and ∇* represent the biomass density, enthalpy per mass, velocity, body forces, shear stress, localized mass accumulation rate, time, and spatial gradient respectively. We then assume that viscous forces dominate inertial forces and that the chemical potential energy dominates over kinetic energy within a cell. Therefore when we nondimensionalize Eq (1) we obtain:

$$\chi\left(\frac{\partial \rho}{\partial t} + \left(\vec{v} \cdot \nabla \rho\right)\right) = \frac{2a_{motor} LT\rho_0}{\mu} \rho \vec{f} \cdot \vec{v} + 2\nabla\left(\nabla \otimes v\right)v - \chi kT\rho \tag{45}$$

Where χ is the ratio of a Reynolds number over an Eckert number. Dividing through by chi gives an equation (Fig. 1D) that relates the mass density (Fig. 1E), change in mass density (Fig. 1F), and advection of mass (Fig. 1G) directly to the energy dissipation of the cell. With a spatial Fourier transform our nondimensionalized energy conservation (Fig. 1D) becomes a quadratic equation with the second order term corresponding to energy dissipation.

$$F\{\frac{\partial \rho}{\partial t} + \left(\vec{v} \cdot \nabla \rho\right)\} = G(q) = \left(\frac{2a_{motor} LT\rho_0}{\mu\chi}\left(F\{\vec{f} \cdot \vec{v}\}\right) - kT\right)\left(\eta(q)\right) + \frac{2|\omega|^2}{\chi} q^2 \tag{46}$$

The fitting terms in our model which can be grouped together as either the terms that relate the PSD (power spectral density) of mass distribution to the PSD of mass change which we call

coefficient of mass change (α) and parameter fitting the quadratic which we call the dissipation (β):

$$G(q) = \alpha \bullet \eta(q) + \beta q^2 \tag{47}$$

When this model is fitted to single cluster data like for a MCF-7 cluster (Fig. 1H) we obtain a very strong fitting (R^2 > 0.9) for this cluster with the population averaged fit of the entire cell line (Fig. 1I) having a similarly strong modeling (R^2 = 0.91). A reason why population fitting maybe preferred can be seen in clusters of other cell lines that are not as well modeled (R^2 < 0.5) by our derivation (Sup Fig. 1A). However, when we aggregate and average over many single cluster data together for a population averaged fit, our fitting better match the data the more we aggregate (Sup Fig. 1B-E) with the population sample having strongest fit (R^2 > 0.9) and having the most consistent parameters from fitting (Sup Fig. 1H). This held true for the various other cell lines we imaged including other breast cancer cell line like BT-474 (Fig. 2A), an embryonic kidney line HEK-293 (Fig. 2B), and an osteosarcoma line 143-BTK (Fig. 2C) along with its' various mitochondria mutant lines (Fig. 2D-F). With the strongest population averaged fit for the model being the BT-474 (Fig. 2A) with a R^2 of 0.96 and even the worse fitting cell line being 143 rho0 line (Fig. 2E) showing a relatively acceptable fitting (R^2 = 0.68).

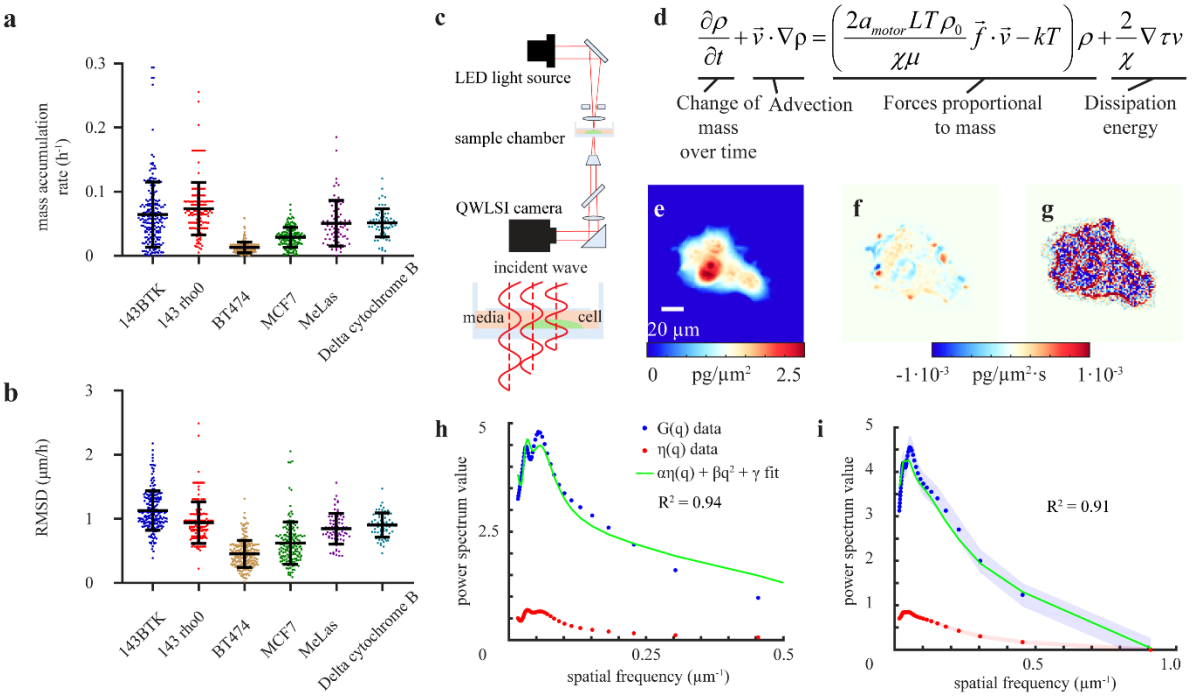

FIGURE 1 Quantitative phase imaging captures both biochemical and biomechanical information allowing a model of cellular work. QPI captures information on biosynthesis measured as the exponential constant of the mass accumulation rate (**a**) and motion measured as root mean square displacement (**b**) for wide variety of cell types (BT474, MCF7, HEK293, and 143BTK) and mitochondrial mutants of the 143 line (MeLas, delta cytochrome B, rho0). This data from captured from any (**c**) QPI setup could be used to model cellular work outlined from a (**d**) work balance equation. This derivation requires QPI information on (**e**) mass distribution, (**f**) mass change, and (**g**) advection of mass. The resulting fit in Fourier space for (**h**) a single MCF-7 and for an (**i**) entire population describes over 90% of the data.

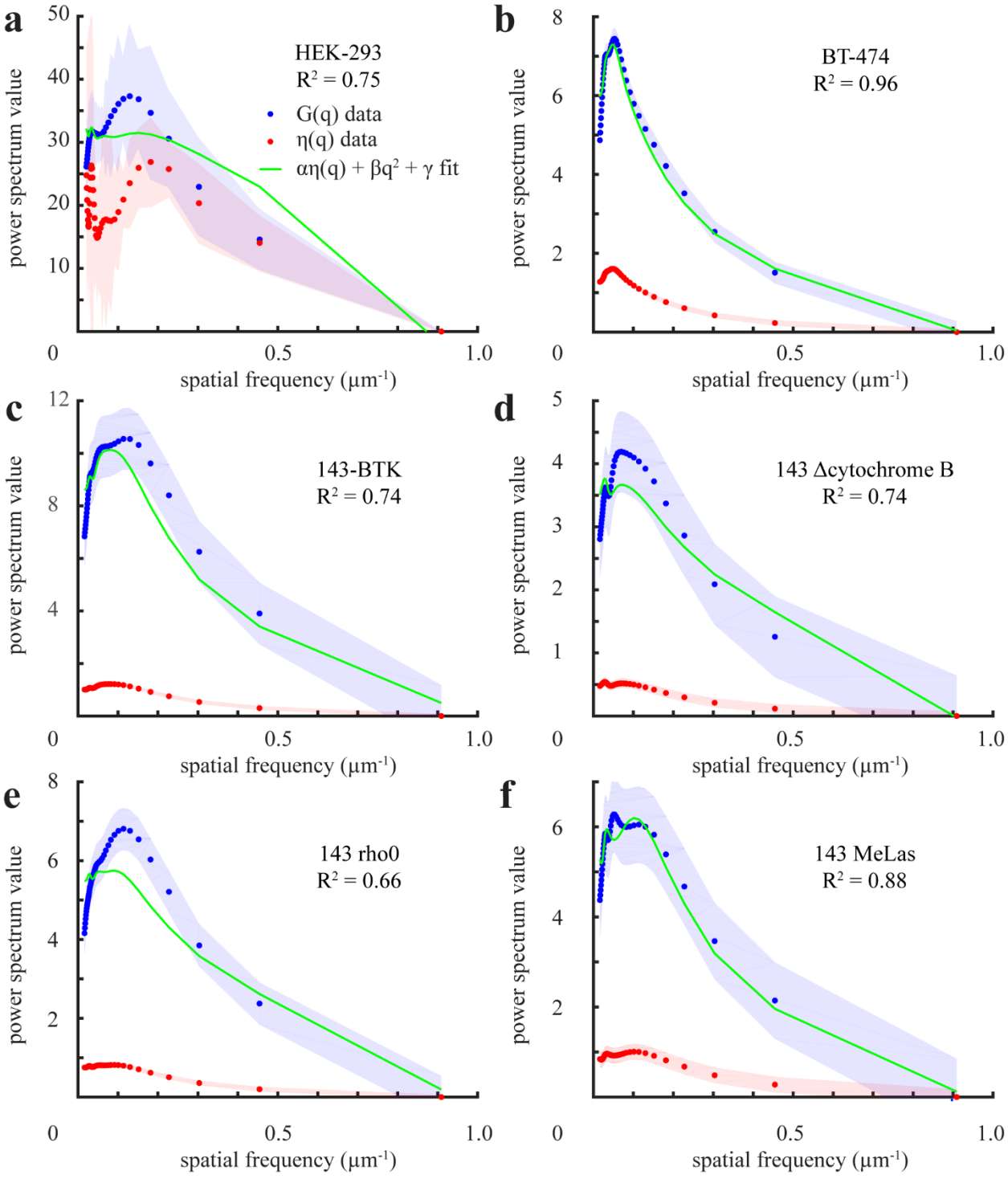

FIGURE 2 Model of cellular work consistent across different cellular lines and mitochondrial mutants. By using the Fourier transform of the mass distribution and mass change QPI data for various different cell line like (**a**) HEK-293, (**b**) BT-474, (**c**) 143-BTK, and different mitochondrial

mutants like (**d**) 143 delta cytochrome B, (**e**) 143 rho0, and (**f**) 143 MeLas we obtain various good ($R^2 > 0.65$) population fit to our model.

Correlation of QPI and metabolic properties

We validated the fitting terms in our model by correlating the various terms to other QPI properties along with cellular energetics properties (Fig. 3). The energetic properties were the rate of glycolysis and cellular respiration measured as either extra cellular acidification rate (ECAR) (Sup Fig. 2a) or oxygen consumption rate (OCR) (Sup Fig. 2b) along with a general net ATP production quantity calculated from the combination of using both measurements [21]. We found as expected that there was strong correlation between ECAR and ATP production normalized per pg with normalized growth ($R = 0.83$, $R= 0.91$), explained by glutamate production via glycolysis being a driver behind protein synthesis [22, 23], and motion ($R = 0.60$, $R = 0.64$) across all cell lines implying more energetically active cells spent more energy both in motion and biosynthesis. Some expected negative correlation we observed were between OCR and ECAR ($R = -0.86$) as well as the negative correlation between mean single cell mass and normalized mass accumulation ($R= -0.80$). Correlation of our fitting terms showed that there was a strong correlation between magnitude of dissipation (β) with RMSD ($R= 0.96$), mass fluctuations ($R= 0.86$), and normalized growth ($R= 0.82$). Similarly, there was a strong correlation between single cluster coefficient of mass change (alpha) to the various mass fluctuations properties of RMSD ($R= 0.52$), mass fluctuations ($R= 0.82$), and normalized growth ($R= 0.46$). Showing that there was a strong overlap between our properties of dissipation and coefficient of mass change and disambiguation of terms were needed.

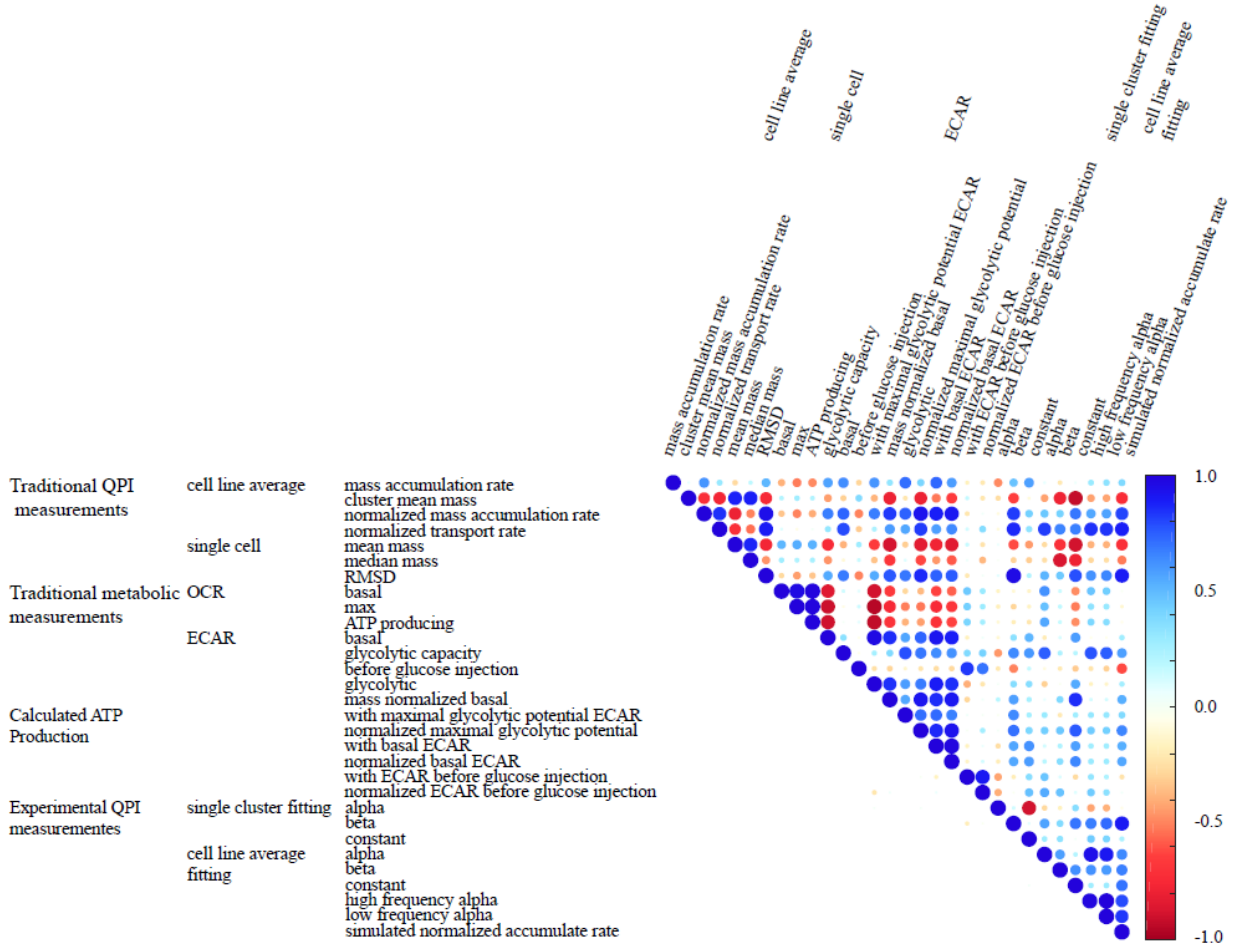

FIGURE 3 Correlation of experimental fitting parameters to traditional QPI and metabolic measurements. Correlation plot of the various traditional QPI parameters of mass accumulation, motion, and mass on both single cell and cluster scale along with metabolic information of cellular respiration (OCR), glycolysis (ECAR), and calculated ATP production generated from OCR and ECAR compared to novel QPI cellular work fitting parameters on both the cell cluster and population level.

Validation of QPI cellular work properties

In order to dissect the functional difference between the two terms of dissipation and coefficient of mass change we first examined the foundation of our dissipation term. This

dissipation term is supposed to be the energy dissipation via motion (Fig. 4A) and should therefore change if there was more mass motion or specifically more uncoordinated mass motion. We therefore modulated both amount of mass motion along with the cellular coordination of motion by examining the epithelial to meschenymal transition system in MCF-10A breast cancer cells where well-coordinated in the epithelial state (Fig. 4B) should expend less energy through motion than meschenymal cells (Fig. 4C) that are less coordinated. We find that while there was no significant difference in mass change coefficient (Fig. 4D) between the two states there was a significant difference ($p < 0.05$) in their dissipation (Fig. 4E). Another experimental setup were we increased the mass fluctuations but did not induce the same discoordination in motion but instead had net change mass accumulation was in a MCF-7 cytochalasin B treated system. Here we observed a significant change in coefficient of mass change ($p < 0.05$) (Fig. 4F) but not in dissipation (Fig. 4G) showing that there are different underlying mechanisms behind our two terms. Although there is still a strong correlation ($R^2 = 0.71$) between our dissipation term and cellular mass motion across the different cell lines (Fig. 4H) which makes sense since our dissipation is supposedly the energy dissipation via motion.

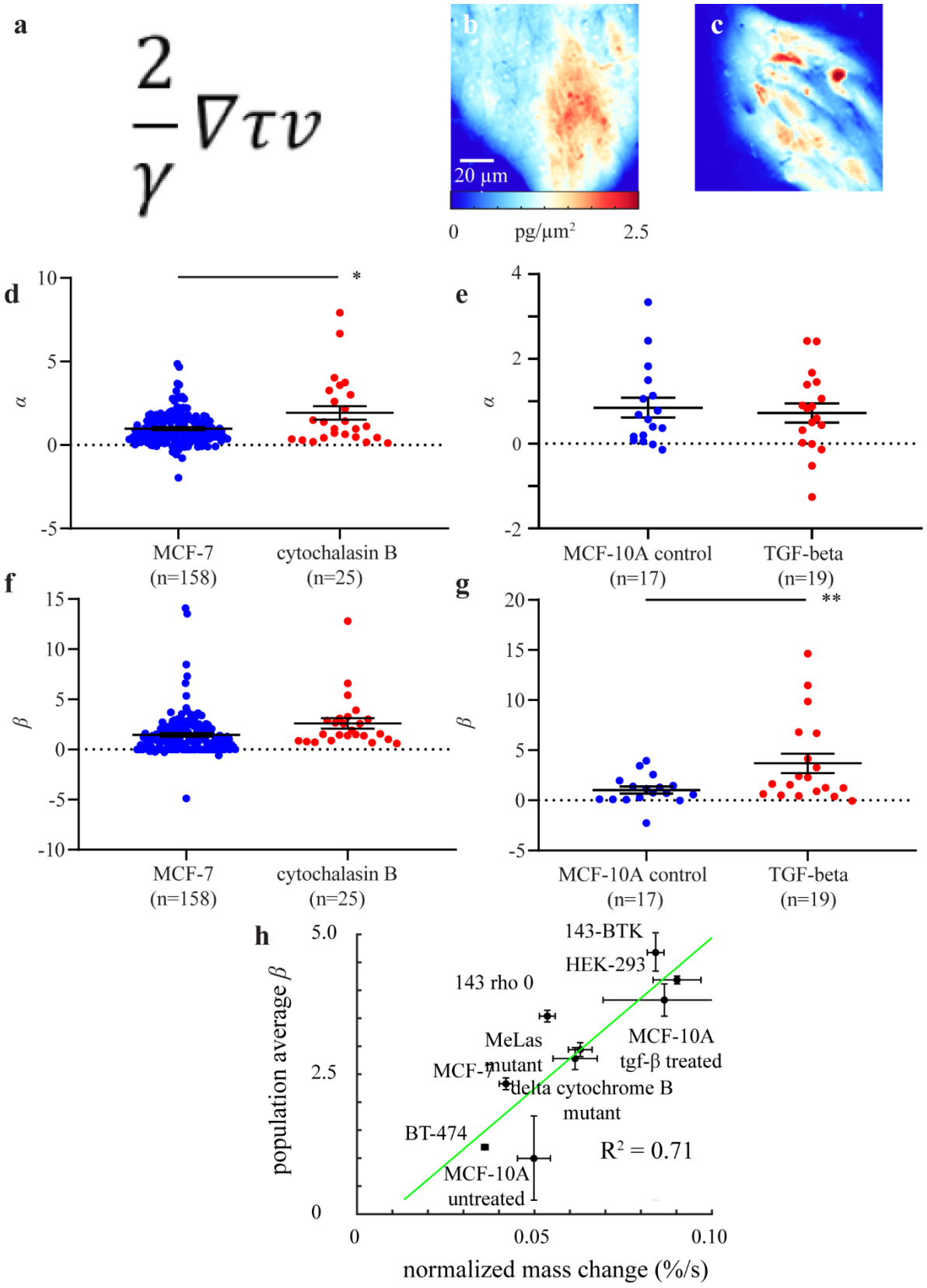
a
$\frac{2}{\gamma}\nabla\tau v$
b
20 µm
0
pg/µm²
2.5
c
d
α
MCF-7
(n=158)
cytochalasin B
(n=25)
*
e
α
MCF-10A control
(n=17)
TGF-beta
(n=19)
f
β
MCF-7
(n=158)
cytochalasin B
(n=25)
g
β
MCF-10A control
(n=17)
TGF-beta
(n=19)
**
h
population average β
normalized mass change (%/s)
143-BTK
HEK-293
143 rho 0
MeLas
mutant
MCF-7
MCF-10A
tgf-β treated
delta cytochrome B
mutant
BT-474
MCF-10A
untreated
R² = 0.71

FIGURE 4 Dissipation and coefficient of mass change are effected by different perturbations. (**a**) Dissipation of energy term from cellular work derivation can be distinguished from mass change coefficient via changing cell state as seen in the QPI images (**b**) MCF-10A transition with (**c**) tgf-beta treatment. Resulting in a nonsignificant change in (**d**) mass change coefficient but significant change in (**e**) dissipation. This is in contrast to the significant change in (**f**) mass change coefficient and not significant change in (**g**) dissipation from MCF-7 cell treatment with cytoskeletal disrupting agent cytochalasin B. Validating the theory that the dissipation term is the dissipation of energy via motion further evidenced in (**h**) the plot of population average dissipation vs average normalized mass change.

We next moved on to examining the mass change coefficient which in our derivation is comprised of two components biosynthesis and active transport (Fig. 5A). We attempted to isolate the active transport component via addition of the mass change coefficient (α) with the biosynthesis term (kT) obtaining (α+kT) which should be a measure of the active transport. We checked our assumption plotting the active transport component (α+kT) to the motion across all our different cell lines and conditions (Fig. 5B) and an exceptional strong correlation ($R^2 > 0.9$) between the two matching our theory. We then examined what portion of the biosynthesis term (kT) vs the active transport term (α+kT) comprised the majority of the cellular work in our various cell lines by dividing each net total work from both term (Fig. 5C). We found across the board that all the different cell lines spent at least 55% of their total work on motion with HEK293 line spending the most at nearly 80%. Cell lines that spent the most on biosynthesis were two of the mitochondrial mutants of the 143 lines spent nearly 42-43% of the work on building mass which was significantly higher than their parent line, which we would expect due to increased

glycolysis[23]. Another expected trend was seen in the transduced tgf-beta MCF-10A lines spending seemingly more of their work on motion compared to the epithelial line. All this shows that we were able to make comparisons of cellular work from biosynthesis and motion from our derivation.

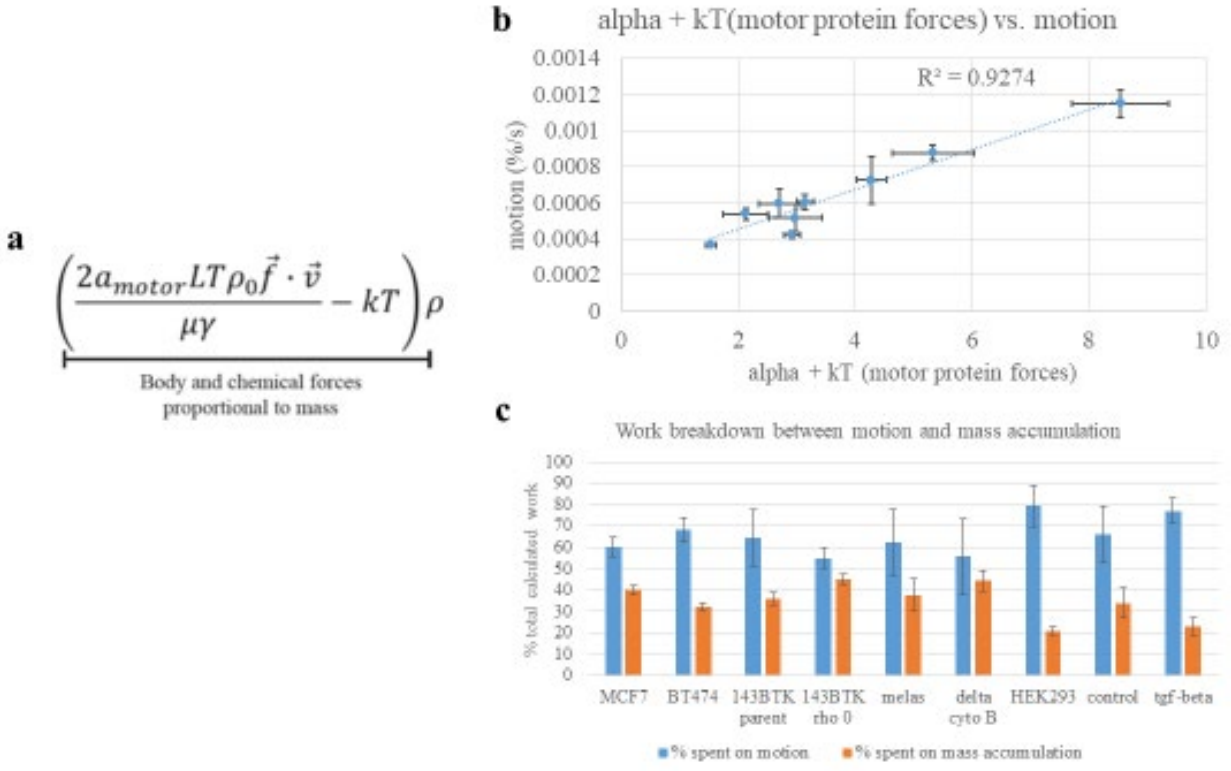

FIGURE 5 Separation and quantification of cellular work for biosynthesis and motion. (**a**) Mass change coefficient term is described by a biosynthesis and transport portion. (**b**) Transport portion of the mass change coefficient term is strongly related to motion across all cell lines. Once separated we compared the (**c**) percentage of cellular work being used for transport or biosynthesis across the cell lines HEK-293, BT-474, 143-BTK, MCF-10 A, different mitochondrial mutants 143 delta cytochrome B, 143 rho0, 143 MeLas, and tgf-beta treated MCF-10A.

Discussion

Many of our assumptions made to simplify the derivation like viscous forces dominating over inertial forces or that the chemical potential energy dominates over kinetic energy within a cell can be validated by literature on the of fluid dynamics within a cell, as seen viscous forces being dominate[24], or be can be seen in models of cytoskeletal networks for chemical potential energy being king[25]. Other assumptions like the spatial isotropy of mass can be seen as the reason why the population average fitting better matched the model (Fig. 2) than single cluster (Sup Fig. 1) given that any single cluster would be anisotropic given that individual cells have polarity[26] and can have preference for motion given an orientation[27]. This anisotropy of single cluster could be drowned out by the averaging over many clusters over an entire population which would start to approach our spatial isotropic assumption seen in our data resulting in better fits (Sup Fig. 1). This averaging over many clusters over many different points in time could also be the reason why other assumptions like intrinsic viscosity and enthalpy per unit mass become valid since they start to approach the average viscosity and enthalpy per unit mass of the cell line. Although removing certain assumptions may result in a better fit it would also result in a much more complicated model than our relative simplistic model that we have right now which already fits majority of our population experimental data (Fig. 1) and allows us to extract information on dissipation and work being done by the cell via the coefficient of mass change.

The one notable cell line that did not fit our model (Fig. 2) as well as the others was the 143 rho0 mutant line. It fitted the worst out of all cell line and conditions to our model which may be due to its' mitochondria deficiency when compared to the other lines. Even the other mitochondria mutants that did not have working mitochondria still had more mitoDNA intact than the 143 rho0 which may play some part in signaling the cell's physiological energetic response.

Or it could also be because that mutant line tended to also not like to aggregate resulting in the same breakdown of the model due to being more single cell as we outlined above.

The correlation of various QPI and metabolic parameters to our two new parameters of dissipation and coefficient of mass change (Fig. 3) results in certain relationships that we expect from theory. The strong connection between dissipation and coefficient of mass change with the different units of mass fluctuations and motion was to be expected given that both of the model terms were somewhat connected to motion. The interlinking between mass fluctuation and mass accumulation could also be explained given the need of cells to traffic more mass around as it underwent more biosynthesis. The relationship between metabolic properties of glycolysis with biosynthesis is well explained via glutamate production via glycolysis being a driver behind protein synthesis (ref) and served as check that we could indeed identify known biological relationship with QPI.

An explanation on why there was a significant change in mass change coefficient for cytochalasin B treatment but not dissipation for the MCF-7 cell line (Fig. 4) can be seen in the dual effect on structure and biosynthesis by cytochalasin B. The cytochalasin B treatment had significant detrimental effect on mass accumulation while as increasing the mass fluctuation in the cells due to disrupting the cytoskeletal network and lowering resistance to motion there. This decreases in biosynthesis and increase in fluctuations leads directly to the increases in mass change coefficient as described in our model while the negligible change in dissipation could be due to the loss of resistance to motion from the structural changes from cytochalasin B (ref). This is in direct contrast to the tgf-beta treatment of MCF-10A which saw no significant change in mass

accumulation but increases in mass motion and movement disorder resulting in the significant change in dissipation while not coefficient of mass change (Fig. 4).

The final breakdown of how cells spend their energy or cellular work (Fig. 5) showed that majority of work was spent in motion. It also showed that increasing glycolytic processes enough to significantly shift the percentage of work being used in biosynthesis as seen in the 143 mutant mitochondrial lines compared to the parent line. It was also possible that biological transition like EMT could induce a shift in cellular work in the opposite direction with the meschenymal tgf-beta treated cells using more cellular work on motion than the normal epithelial MCF-10A which can be explained in the biological shifting of priorities attributed to EMT[28]. Overall our derivation allows a simple process to use QPI data to compare and contrast the cellular work in terms of biochemical and biomechanical processes.

Methods

Cells and cell culture

MCF-7 and BT-474 human invasive ductal breast adenocarcinoma, HEK293 human embryo kidney, 143-BTK osteosarcoma, and MCF-10A immortalized human breast epithelial cells were purchased from the American Type Culture Collection (ATCC). 143 rho0 cells were generated from 143-BTK parent using DDC treatment and checked using uridine selection. 143-BTK MeLas mutant and 143BTK delta cytochrome B mutant were generated via method described by Patananan *et al.*[29] . MCF-7 cells were cultured in EMEM supplemented with 10% fetal bovine serum (FBS, Omega Scientific) and 10 mg/L human recombinant insulin (Sigma). BT-474 cells were grown in Hybri-Care Medium (ATCC) reconstituted in cell culture grade water (Fisher) with

1.5 g/L sodium bicarbonate and 10% FBS (Omega Scientific). MCF-10A cells grew in MEGM Bulletkit media (Lonza) with cholera toxin (Sigma-Aldrich) at 100 ng/mL and without gentamycin-amphotericin B mix. HEK293 were cultured in DMEM with 4.5 g/L glucose, L-glutamine, and sodium pyruvate (Cellgro) along with 1% penicillin streptomycin (Cellgro), 1% Q-max (Gibco), 1% non-essential amino acids (Gibco), and 10% FBS (Omega Scientific). 143-BTK parent, 143-BTK MeLas mutant, 143BTK delta cytochrome B mutant, and 143 rho0 cells were grown in the same media supplemented with 0.05 mg/mL uridine. We incubated cells with escalating doses of cytochalasin B (Sigma Aldrich) dissolved in DMSO solution or to 0.1% DMSO control, starting 4 h prior to experiments.

Quantitative phase imaging

Imaging of all cell lines were performed as described in Nguyen *et al.*[30]. Images were collected once every 10 min for 48 h over 20 – 30 imaging locations with sufficient spacing between cells to enable automated image processing and segmentation.

Quantitative phase image analysis

Image processing was performed using custom MATLAB (MathWorks) scripts. Cells and cell clusters were identified and segmented using a local adaptive threshold based on Otsu's method[31, 32] and particle tracking code based on Grier *et al.*[33, 34]. Compensation for translational motion was done by finding the maximum two-dimensional cross correlation of each cell or cell cluster image against the immediately prior image.

Biomass accumulation rate calculation

Quantitative phase biomass distribution images were summed over the projected area of each cell cluster to obtain the total biomass per cluster at specified time points. We calculated exponential biomass accumulation rates by taking the logarithm of the biomass over time data and fitting to a first order polynomial equation using MATLAB Polyfit (MathWorks).

EMT

MCF-10A cells were placed in standard 6-well culture plates and applied with recombinant human TGF-β1 (Sigma-Aldrich) to the culture media at 5 ng/mL one day after to induce EMT. Alternatively, the TGF-β receptor inhibitor SB-431542 (Sigma-Aldrich) was added to the culture media at 10 μM final concentration to enforce an epithelial phenotype on MCF-10A cells. Cell exposure to these conditions for 7 d ensured full effects[35]. Cells re-plated for imaging were cultured with no additives, 5 ng/mL TGF-β1, 10 μM SB-431532, or both agents together. We incubated cells with or without additives for 2 d before imaging.

Statistical analysis

Statistical analyses used two-tailed Student's t-test with unequal variances and sample size (Welch's t-test).

Mitochondrial Oxygen Consumption (OCR) and Extracellular Acidification Rate (ECAR) Measurements

OCR and ECAR was measured using a Seahorse XF96 Extracellular Flux Analyzer (Agilent). For all cell lines, 1 – 2 x105 cells per well were seeded onto 2 different V3 96-well plate (Agilent, Cat.

101085-004) and grown overnight before analysis. A mitochondrial stress test quantified OCR at basal respiration and after the sequential addition of mitochondrial inhibitors oligomycin, carbonyl cyanide-p-trifluoromethoxyphenylhydrazone (FCCP), and rotenone, while a glycolytic stress quantified ECAR before addition of glucose, after addition, with the addition of mitochondrial inhibitors oligomycin, and when added with 2-deoxyglucose.

RNA Extraction

All samples were grown in biological triplicates and technical duplicates to 70-80% confluence and purified using the RNeasy Mini Kit (Qiagen, Cat. # 74104) and RNase-free DNase (Qiagen, Cat. # 79254) following the manufacturer's protocols. All samples showed a A260/280 ratio > 1.99 (Nanodrop; Thermo Scientific). Prior to library preparation, quality control of the RNA was performed using the Advanced Analytical Technologies Fragment Analyzer (Advanced Analytical, Inc.) and analyzed using PROSize 2.0.0.51 software. RNA Quality Numbers (RQNs) were computed per sample between 8.1 and 10, indicating intact total RNA per sample prior to library preparation.

RNA-Seq Library Preparation

Strand-specific ribosomal RNA (rRNA) depleted RNA-Seq libraries were prepared from 1 µg of total RNA using the KAPA Stranded RNA-Seq Kit with Ribo-Erase (Kapa Biosystems, Roche). Briefly, rRNA was depleted from total RNA samples, the remaining RNA was heat fragmented, and strand-specific cDNA was synthesized using a first strand random priming and second strand dUTP incorporation approach. Fragments were then A-tailed, adapters were ligated, and libraries were amplified using high-fidelity PCR. All libraries were prepared in technical duplicates per

sample (n = 60 samples, 120 libraries total), and resulting raw sequencing reads merged for downstream alignment and analysis. Libraries were paired-end sequenced at 2x150 bp on an Illumina NovaSeq 6000.

RNA-Seq Pre-Processing

All samples were each sequenced in biological triplicates and technical duplicates (n = 30 total samples) to account for variation in extraction and culturing. Raw sequencing reads were converted into fastq files and filtered for low quality reads and Illumina sequencing adapter contamination using bcl2fastq (Illumina). Reads were then quasi-mapped and quantified to the *Homo sapiens* GENCODE 28 (GRCh38.p12, Ensembl 92, April 2018) transcriptome using the alignment-free transcript level quantifier Salmon v0.9.1 [36-38]. A quasi-mapping index was prepared using parameters *"salmon index -k 31 –type quasi"*, and comprehensive transcript level estimates were calculated using parameters *"salmon quant -l A –seqBias –gcBias --discardOrphansQuasi"*. Transcript level counts were collapsed to gene level (HGNC) counts, transcripts per million abundances (TPM) and estimated lengths using R Bioconductor package tximport v1.6.0 [39].

Gene Set Variation Analysis (GSVA)

GSVA on total transcripts was performed using R Bioconductor package GSVA v1.36.2 function gsva() with parameters ‘‘method = gsva, abs.ranking = FALSE, min.sz = 10, max.sz = 500, kcdf = “Poisson”’’ using a log2(TPM + 1) transformed gene expression matrix (Hanzelmann et al., 2013) and gene sets were acquired from the KEGG Database. GSVA scores were extracted and

correlated with QPM and metabolic data using the R Bioconductor package function corplot() with parameters “type = “upper”, sig.level = 0.01, tl.cex = .75, tl.col = “black””.

QPI cellular work calculations

A diffusion rate of cellular motion was extracted from QPI data using the method described in Ceballos *et al.*[40]. This diffusion value was then paired with QPI mass distribution images and used to simulate the expected motion purely due to diffusion through numerical methods 2nd order Runge Kutta. A total mass change image data was calculated by using 3 consecutive QPI mass distribution images and finding the rate of change in mass at each pixel using a best fit line for the 3 consecutive time points. This total mass change image data was subtracted from using the simulated diffusion motion to get a calculated mass motion due to advection image. All three images composited into new 5x5 (Sup. Fig. 2a) and were Fourier transformed in order to remove the effect of the frequency drop off (Sup. Fig. 2b). Frequency was then gated to the actual spatial frequencies of the image to remove drop off effect (Sup. Fig. 2c) was then collapsed down using polarity coordinates to generate fitting data for equation 4.

References and Notes

1. Rolfe, D. F.; Brown, G. C., Cellular Energy Utilization and Molecular Origin of Standard Metabolic Rate in Mammals. *Physiol. Rev.* **1997,** *77* (3), 731-58.

2. Nichols, C. G., Katp Channels as Molecular Sensors of Cellular Metabolism. *Nature* **2006,** *440* (7083), 470-6.

3. Gorlich, D.; Kutay, U., Transport between the Cell Nucleus and the Cytoplasm. *Annu. Rev. Cell. Dev. Biol.* **1999,** *15*, 607-60.

4. Russell, J. B.; Cook, G. M., Energetics of Bacterial Growth: Balance of Anabolic and Catabolic Reactions. *Microbiological reviews* **1995,** *59* (1), 48-62.

5. Dutta, D.; Palmer, X. L.; Kim, J.; Qian, S.; Stacey, M., Energy Dissipation Mapping of Cancer Cells. *Micron* **2018,** *105*, 24-29.

6. Rossen, N. S.; Tarp, J. M.; Mathiesen, J.; Jensen, M. H.; Oddershede, L. B., Long-Range Ordered Vorticity Patterns in Living Tissue Induced by Cell Division. *Nature Communications* **2014,** *5*.

7. Manfredi, G.; Yang, L.; Gajewski, C. D.; Mattiazzi, M., Measurements of Atp in Mammalian Cells. *Methods* **2002,** *26* (4), 317-26.

8. Yaginuma, H.; Kawai, S.; Tabata, K. V.; Tomiyama, K.; Kakizuka, A.; Komatsuzaki, T.; Noji, H.; Imamura, H., Diversity in Atp Concentrations in a Single Bacterial Cell Population Revealed by Quantitative Single-Cell Imaging. *Scientific reports* **2014,** *4*, 6522.

9. Gerencser, A. A.; Neilson, A.; Choi, S. W.; Edman, U.; Yadava, N.; Oh, R. J.; Ferrick, D. A.; Nicholls, D. G.; Brand, M. D., Quantitative Microplate-Based Respirometry with Correction for Oxygen Diffusion. *Anal. Chem.* **2009,** *81* (16), 6868-78.

10. Mookerjee, S. A.; Brand, M. D., Measurement and Analysis of Extracellular Acid Production to Determine Glycolytic Rate. *J Vis Exp* **2015,** (106), e53464.

11. Etienne, J.; Duperray, A., Initial Dynamics of Cell Spreading Are Governed by Dissipation in the Actin Cortex. *Biophys. J.* **2011,** *101* (3), 611-21.

12. Liu, H. S.; Jan, M. S.; Chou, C. K.; Chen, P. H.; Ke, N. J., Is Green Fluorescent Protein Toxic to the Living Cells? *Biochem. Biophys. Res. Commun.* **1999,** *260* (3), 712-7.

13. Zangle, T. A.; Teitell, M. A., Live-Cell Mass Profiling: An Emerging Approach in Quantitative Biophysics. *Nature methods* **2014,** *11* (12), 1221-8.

14. Barer, R., Interference Microscopy and Mass Determination. *Nature* **1952,** *169* (4296), 366-367.

15. Davies, H. G.; Wilkins, M. H. F., Interference Microscopy and Mass Determination. *Nature* **1952,** *169* (4300), 541-541.

16. Zangle, T. A.; Chun, J.; Zhang, J.; Reed, J.; Teitell, M. A., Quantification of Biomass and Cell Motion in Human Pluripotent Stem Cell Colonies. *Biophys. J.* **2013,** *105* (3), 593-601.

17. Mir, M.; Wang, Z.; Shen, Z.; Bednarz, M.; Bashir, R.; Golding, I.; Prasanth, S. G.; Popescu, G., Optical Measurement of Cycle-Dependent Cell Growth. *Proc. Natl. Acad. Sci. USA* **2011,** *108* (32), 13124-9.

18. Pavillon, N.; Kuhn, J.; Moratal, C.; Jourdain, P.; Depeursinge, C.; Magistretti, P. J.; Marquet, P., Early Cell Death Detection with Digital Holographic Microscopy. *PLoS One* **2012,** *7* (1), e30912.

19. Park, Y.; Best, C. A.; Badizadegan, K.; Dasari, R. R.; Feld, M. S.; Kuriabova, T.; Henle, M. L.; Levine, A. J.; Popescu, G., Measurement of Red Blood Cell Mechanics During Morphological Changes. *Proc. Natl. Acad. Sci. USA* **2010,** *107* (15), 6731-6.

20. Ceballos, S.; Kandel, M.; Sridharan, S.; Majeed, H.; Monroy, F.; Popescu, G., Active Intracellular Transport in Metastatic Cells Studied by Spatial Light Interference Microscopy. *J Biomed Opt* **2015,** *20* (11), 111209.

21. Mookerjee, S. A.; Gerencser, A. A.; Nicholls, D. G.; Brand, M. D., Quantifying Intracellular Rates of Glycolytic and Oxidative Atp Production and Consumption Using Extracellular Flux Measurements. *Journal of Biological Chemistry* **2017,** *292* (17), 7189-7207.

22. DeBerardinis, R. J.; Mancuso, A.; Daikhin, E.; Nissim, I.; Yudkoff, M.; Wehrli, S.; Thompson, C. B., Beyond Aerobic Glycolysis: Transformed Cells Can Engage in Glutamine Metabolism That Exceeds

the Requirement for Protein and Nucleotide Synthesis. *Proceedings of the National Academy of Sciences of the United States of America* **2007,** *104* (49), 19345-19350.

23. Hosios, A. M.; Hecht, V. C.; Danai, L. V.; Johnson, M. O.; Rathmell, J. C.; Steinhauser, M. L.; Manalis, S. R.; Vander Heiden, M. G., Amino Acids Rather Than Glucose Account for the Majority of Cell Mass in Proliferating Mammalian Cells. *Developmental Cell* **2016,** *36* (5), 540-549.

24. Huber, D.; Oskooei, A.; Solvas, X. C. I.; DeMello, A.; Kaigala, G. V., Hydrodynamics in Cell Studies. *Chemical Reviews* **2018,** *118* (4), 2042-2079.

25. Floyd, C.; Papoian, G. A.; Jarzynski, C., Quantifying Dissipation in Actomyosin Networks. *Interface Focus* **2019,** *9* (3).

26. Godde, N. J.; Galea, R. C.; Elsum, I. A.; Humbert, P. O., Cell Polarity in Motion: Redefining Mammary Tissue Organization through Emt and Cell Polarity Transitions. *Journal of Mammary Gland Biology and Neoplasia* **2010,** *15* (2), 149-168.

27. Wang, X.; Merkel, M.; Sutter, L. B.; Erdemci-Tandogan, G.; Manning, M. L.; Kasza, K. E., Anisotropy Links Cell Shapes to Tissue Flow During Convergent Extension. *Proceedings of the National Academy of Sciences of the United States of America* **2020,** *117* (24), 13541-13551.

28. Kalluri, R.; Weinberg, R. A., The Basics of Epithelial-Mesenchymal Transition. *Journal of Clinical Investigation* **2009,** *119* (6), 1420-1428.

29. Patananan, A. N.; Sercel, A. J.; Wu, T. H.; Ahsan, F. M.; Torres, A.; Kennedy, S. A. L.; Vandiver, A.; Collier, A. J.; Mehrabi, A.; Van Lew, J.; Zakin, L.; Rodriguez, N.; Sixto, M.; Tadros, W.; Lazar, A.; Sieling, P. A.; Nguyen, T. L.; Dawson, E. R.; Braas, D.; Golovato, J.; Cisneros, L.; Vaske, C.; Plath, K.; Rabizadeh, S.; Niazi, K. R.; Chiou, P. Y.; Teitell, M. A., Pressure-Driven Mitochondrial Transfer Pipeline Generates Mammalian Cells of Desired Genetic Combinations and Fates. *Cell Reports* **2020,** *33* (13).

30. Nguyen, T. L.; Polanco, E. R.; Patananan, A. N.; Zangle, T. A.; Teitell, M. A., Cell Viscoelasticity Is Linked to Fluctuations in Cell Biomass Distributions. *Scientific Reports* **2020,** *10* (1).

31. Zangle, T. A.; Chun, J.; Zhang, J.; Reed, J.; Teitell, M. A., Quantification of Biomass and Cell Motion in Human Pluripotent Stem Cell Colonies. *Biophysical Journal* **2013,** *105* (3), 593-601.

32. Otsu, N., Threshold Selection Method from Gray-Level Histograms. *Ieee T. Syst. Man Cyb.* **1979,** *9* (1), 62-66.

33. Crocker, J. C.; Grier, D. G., Methods of Digital Video Microscopy for Colloidal Studies. *J. Colloid Interf. Sci.* **1996,** *179* (1), 298-310.

34. Zangle, T. A.; Burnes, D.; Mathis, C.; Witte, O. N.; Teitell, M. A., Quantifying Biomass Changes of Single Cd8+ T Cells During Antigen Specific Cytotoxicity. *PLoS One* **2013,** *8* (7), e68916.

35. Zhang, J.; Tian, X. J.; Zhang, H.; Teng, Y.; Li, R.; Bai, F.; Elankumaran, S.; Xing, J., Tgf-Beta-Induced Epithelial-to-Mesenchymal Transition Proceeds through Stepwise Activation of Multiple Feedback Loops. *Sci Signal* **2014,** *7* (345), ra91.

36. Harrow, J.; Frankish, A.; Gonzalez, J. M.; Tapanari, E.; Diekhans, M.; Kokocinski, F.; Aken, B. L.; Barrell, D.; Zadissa, A.; Searle, S.; Barnes, I.; Bignell, A.; Boychenko, V.; Hunt, T.; Kay, M.; Mukherjee, G.; Rajan, J.; Despacio-Reyes, G.; Saunders, G.; Steward, C.; Harte, R.; Lin, M.; Howald, C.; Tanzer, A.; Derrien, T.; Chrast, J.; Walters, N.; Balasubramanian, S.; Pei, B.; Tress, M.; Rodriguez, J. M.; Ezkurdia, I.; van Baren, J.; Brent, M.; Haussler, D.; Kellis, M.; Valencia, A.; Reymond, A.; Gerstein, M.; Guigo, R.; Hubbard, T. J., Gencode: The Reference Human Genome Annotation for the Encode Project. *Genome Res* **2012,** *22* (9), 1760-74.

37. Mudge, J. M.; Harrow, J., Creating Reference Gene Annotation for the Mouse C57bl6/J Genome Assembly. *Mamm Genome* **2015,** *26* (9-10), 366-78.

38. Patro, R.; Duggal, G.; Love, M. I.; Irizarry, R. A.; Kingsford, C., Salmon Provides Fast and Bias-Aware Quantification of Transcript Expression. *Nat Methods* **2017,** *14* (4), 417-419.

39. Soneson, C.; Love, M. I.; Robinson, M. D., Differential Analyses for Rna-Seq: Transcript-Level Estimates Improve Gene-Level Inferences. *F1000Res* **2015,** *4*, 1521.

40. Ceballos, S.; Kandel, M.; Sridharan, S.; Majeed, H.; Monroy, F.; Popescu, G., Active Intracellular Transport in Metastatic Cells Studied by Spatial Light Interference Microscopy. *Journal of Biomedical Optics* **2015,** *20* (11).

SUPPLEMENTARY INFORMATION

Supplementary Derivation

Supplementary Figures S1-S2

SUPPLEMENTARY DERIVATION

Assumptions:

1. Isothermal
2. Spatial Isotropy
3. Low pressure influence $\nabla P \approx 0$
4. Average enthalpy per mass is an intrinsic value (e = constant)
5. Viscosity is an intrinsic value (μ = constant)
6. Newtonian fluid
7. Viscous forces dominate over inertial forces
8. Chemical potential dominates over kinetic potential

Conservation of Energy

Basic equations:

$$\frac{D}{Dt^*}\iiint_V \rho^*\left(e+\frac{\left|v^*\right|^2}{2}\right)dV = -\iint_S \vec{Q}\bullet\vec{n}dS + \iiint_V \rho^*\overrightarrow{f^*}\bullet\overrightarrow{v^*}dV + \iint_S \vec{\Sigma}\bullet\overrightarrow{v^*}dS + \iiint_V ke\rho^* dV \quad (1)$$

$$e = enthalpy\ per\ mass$$

$$v^* = velocity$$

$$Q = heat$$

$$f^* = body\ forces$$

$$\rho^* = \text{density}$$

$$\Sigma = surface\ force$$

Using Gauss theorem convert surface integral in (1) into volume integral

$$\iiint_V \frac{D}{Dt^*}\rho^*(e+\frac{\left|v^*\right|^2}{2})dV = -\iiint_V \nabla^* \bullet Q dV + \iiint_V \rho^* \overrightarrow{f^*} \bullet \overrightarrow{v^*} dV + \iiint_V \nabla^* \bullet \sigma v^* dV + \iiint_V ke\rho^* dV (2)$$

Since all terms are expressed as volume integral over arbitrary material volume the following true for every point in space:

$$\frac{D}{Dt^*}\rho^*(e+\frac{\left|v^*\right|^2}{2}) = -\nabla^* \bullet Q + \rho^* \overrightarrow{f^*} \bullet \overrightarrow{v^*} + \nabla^* \bullet \sigma v^* + ke\rho^* (3)$$

With Fick's law of heat conduction

$$Q = K\nabla^* T_{temperature} (4)$$

Since it is isothermal

$$\nabla^* T_{temperature} = 0 (5)$$

Then Q = 0

The surface forces can be broken down into a shear and pressure component with pressure being negligible from assumption:

$$\nabla^* \bullet \sigma v^* = \nabla^* \bullet P v^* + \nabla^* \bullet \tau^* v^* = (0) + \nabla^* \bullet \tau^* v^* = \nabla^* \bullet \tau^* v^* (6)$$

With Plugging (4) and (6) back into (3)

$$\frac{D}{Dt^*}\rho^*(e+\frac{\left|v^*\right|^2}{2}) = \rho^* \overrightarrow{f^*} \bullet \overrightarrow{v^*} + \nabla^* \bullet \tau^* v^* + ke\rho^* (7)$$

Expand the left hand side in (7)

$$\left(e+\frac{v^{*2}}{2}\right)\frac{D\rho^{*}}{Dt^{*}}+\frac{\rho^{*}}{2}\frac{D\left|v^{*}\right|^{2}}{Dt^{*}}=\rho^{*}\overrightarrow{f^{*}}\bullet\overrightarrow{v^{*}}+\nabla^{*}\bullet\tau^{*}v^{*}+ke\rho^{*}\left(8\right)$$

$$\left(e+\frac{v^{*2}}{2}\right)\left(\frac{\partial\rho^{*}}{\partial t^{*}}+\overrightarrow{v^{*}}\bullet\nabla\rho^{*}\right)+\frac{\rho^{*}}{2}\left(\frac{\partial v^{*2}}{\partial t^{*}}+\overrightarrow{v^{*}}\bullet\nabla v^{*2}\right)=\rho^{*}\overrightarrow{f^{*}}\bullet\overrightarrow{v^{*}}+\nabla^{*}\bullet\tau^{*}v^{*}+ke\rho^{*}\left(9\right)$$

Nondimensionalize (9)

$$v^{*}\sim v_{max}\equiv\frac{L}{T};\rho^{*}\sim\rho_{0};t^{*}\sim T;f^{*}\sim a_{motor};\nabla^{*}\sim\frac{1}{L}$$

$$\frac{e\rho_{0}}{T}\frac{\partial\rho}{\partial t}+\frac{e\rho_{0}v_{max}}{L}\left(\vec{v}\bullet\nabla\rho\right)+\frac{\rho_{0}{v_{max}}^{2}}{2T}\eta\frac{\partial v^{2}}{\partial t}+\frac{\rho_{0}{v_{max}}^{3}}{2L}\eta\left(\vec{v}\bullet\nabla\left(v^{2}\right)\right)+\frac{\rho_{0}{v_{max}}^{2}}{2T}v^{2}\frac{\partial\rho}{\partial t}+\frac{\rho_{0}{v_{max}}^{3}}{2L}v^{2}\left(\vec{v}\bullet\nabla\rho\right)$$

$$=\rho_{0}a_{motor}v_{max}\rho\vec{f}\bullet\vec{v}+\frac{\mu{v_{max}}^{2}}{L^{2}}\nabla\bullet\tau v-ke\rho_{0}\rho(10)$$

Divide (10) through by $\frac{\rho_{0}{v_{max}}^{3}}{2L}$ and consolidate derivatives

$$\frac{2e}{{v_{max}}^{2}}\frac{D\rho}{Dt}+v^{2}\frac{D\rho}{Dt}+\rho\frac{D(v^{2})}{Dt}=\frac{2a_{motor}L}{{v_{max}}^{2}}\rho\vec{f}\bullet\vec{v}+\frac{\mu}{\rho_{0}v_{max}L}\nabla\bullet\tau v-\frac{2e}{{v_{max}}^{2}}kT\rho\left(11\right)$$

Since viscous forces dominate over inertial forces we define our first nondimensional number:

$$\varepsilon_{1}\equiv\frac{\rho_{0}v_{max}L}{\mu}\ll1\left(12\right)$$

And chemical potential dominates over kinetic potential we define our second nondimensional number:

$$\varepsilon_2 \equiv \frac{v_{max}{}^2}{2e} \ll 1 (13)$$

Rewrite (11) in terms of (12) and (13)

$$\frac{\varepsilon_1}{\varepsilon_2}\frac{D\rho}{Dt} + \varepsilon_1 v^2 \frac{D\rho}{Dt} + \varepsilon_1 \rho \frac{D(v^2)}{Dt} = \frac{2a_{motor} LT\rho_0}{\mu} \rho \vec{f} \bullet \vec{v} + 2\nabla \bullet \tau v - \frac{\varepsilon_1}{\varepsilon_2} kT\rho (14)$$

Since we assume ε_1 and ε_2 to be small we dismiss the terms multiplied by those when considering O(1), however we don't know the ratio between the two which we will define as:

$$\gamma \equiv \frac{\varepsilon_1}{\varepsilon_2} (15)$$

Consider O(1):

$$\gamma \left(\frac{\partial \rho}{\partial t} + \left(\vec{v} \bullet \nabla \rho \right) \right) = \frac{2a_{motor} LT\rho_0}{\mu} \rho \vec{f} \bullet \vec{v} + 2\nabla \bullet \tau v - \gamma kT\rho (16)$$

Since we assume Newtonian fluid, the non-dimensionalized strain rate tensor becomes:

$$\tau = \left(\nabla \otimes v \right)^n = \left(\frac{1}{2} ((\nabla v) + (\nabla v)^T) \right)^n \quad (17)$$

In Cartesian coordinates ∇v is the Jacobian matrix where:

$$(\nabla v)_{ji} = \frac{\partial v_j}{\partial x_i} (18)$$

In 2 dimensions the strain rate tensor would then be:

$$\tau = \left(\frac{1}{2}\right)^n \left(\begin{bmatrix} \frac{\partial v_x}{\partial x} & \frac{\partial v_x}{\partial y} \\ \frac{\partial v_y}{\partial x} & \frac{\partial v_y}{\partial y} \end{bmatrix} + \begin{bmatrix} \frac{\partial v_x}{\partial x} & \frac{\partial v_y}{\partial x} \\ \frac{\partial v_x}{\partial y} & \frac{\partial v_y}{\partial y} \end{bmatrix} \right)^n = \frac{1}{2^n} \begin{bmatrix} 2\frac{\partial v_x}{\partial x} & \frac{\partial v_x}{\partial y} + \frac{\partial v_x}{\partial x} \\ \frac{\partial v_y}{\partial x} + \frac{\partial v_x}{\partial y} & 2\frac{\partial v_y}{\partial y} \end{bmatrix}^n \quad (19)$$

The evaluation of $\nabla \bullet \tau v$ value follows by:

$$\tau v = \frac{1}{2}\left(\begin{bmatrix} 2\frac{\partial v_x}{\partial x} & \frac{\partial v_x}{\partial y} + \frac{\partial v_y}{\partial x} \\ \frac{\partial v_y}{\partial x} + \frac{\partial v_x}{\partial y} & 2\frac{\partial v_y}{\partial y} \end{bmatrix} \right)\left(\begin{bmatrix} v_x \\ v_y \end{bmatrix} \right) = \frac{1}{2}\left(\begin{bmatrix} 2\frac{\partial v_x}{\partial x} v_x + (\frac{\partial v_x}{\partial y} + \frac{\partial v_y}{\partial x}) v_y \\ (\frac{\partial v_y}{\partial x} + \frac{\partial v_x}{\partial y}) v_x + 2\frac{\partial v_y}{\partial y} v_y \end{bmatrix} \right) \quad (20)$$

Since we assume spatial isotropy we can rewrite (20) as:

$$\frac{1}{2}\left(\begin{bmatrix} 2\frac{\partial v_x}{\partial x} v_x + (\frac{\partial v_x}{\partial y} + \frac{\partial v_y}{\partial x}) v_y \\ (\frac{\partial v_y}{\partial x} + \frac{\partial v_x}{\partial y}) v_x + 2\frac{\partial v_y}{\partial y} v_y \end{bmatrix} \right) = \frac{1}{2}\left(\begin{bmatrix} 2\frac{\partial v_x}{\partial x} v_x + \frac{\partial v_y}{\partial x} v_y + \frac{\partial v_x}{\partial y} v_y \\ \frac{\partial v_y}{\partial x} v_x + \frac{\partial v_x}{\partial y} v_x + 2\frac{\partial v_y}{\partial y} v_y \end{bmatrix} \right) \quad (21)$$

The divergence of (21) this is then:

$$\nabla \bullet \tau v = \frac{1}{2} \begin{bmatrix} \frac{\partial}{\partial x} \\ \frac{\partial}{\partial y} \end{bmatrix} \bullet \begin{bmatrix} 2\frac{\partial v_x}{\partial x} v_x + \frac{\partial v_y}{\partial x} v_y + \frac{\partial v_x}{\partial y} v_y \\ \frac{\partial v_y}{\partial x} v_x + \frac{\partial v_x}{\partial y} v_x + 2\frac{\partial v_y}{\partial y} v_y \end{bmatrix} =$$

$$2\frac{\partial^2 v_x}{\partial x^2} v_x + 2(\frac{\partial v_x}{\partial x})^2 + (\frac{\partial v_y}{\partial x})^2 + 2\frac{\partial v_y}{\partial x}\frac{\partial v_x}{\partial y} + \frac{\partial^2 v_x}{\partial y \partial x} v_y + \frac{\partial^2 v_y}{\partial y \partial x} v_x + \frac{\partial^2 v_y}{\partial x^2} v_y + +(\frac{\partial v_x}{\partial y})^2 + 2(\frac{\partial v_y}{\partial y})^2 + 2\frac{\partial^2 v_y}{\partial y^2} v_y$$

$$= \nabla \cdot v \nabla v + \nabla \cdot v (\nabla v)^T = \nabla \cdot \frac{1}{2} \nabla (v^2) + \nabla \cdot \frac{1}{2} \nabla^T (v^2)$$

Assuming an isotropic Newtonian fluid:

$$\nabla \cdot \frac{1}{2}\nabla(v^2) + \nabla \cdot \frac{1}{2}\nabla^T(v^2) = \nabla \cdot \nabla(v^2) = \nabla^2 v^2 \,(22)$$

Now Plugging (22) into (16) we get:

$$\gamma\left(\frac{\partial \rho}{\partial t} + \left(\vec{v} \bullet \nabla \rho\right)\right) = \frac{2a_{motor} LT\rho_0}{\mu}\rho\vec{f} \bullet \vec{v} + 2\nabla^2 v^2 - \gamma kT\rho\,(23)$$

We will Fourier transform (23) with respect to space with limits of integration for x and y being from 0 to L where L is the length of the viewing window:

$$\int_0^L \int_0^L \gamma\left(\frac{\partial \rho}{\partial t} + \left(\vec{v} \bullet \nabla \rho\right)\right)\exp(-iqx)dx\exp(-iqy)dy =$$

$$\int_0^L \int_0^L \frac{2a_{motor} LT\rho_0}{\mu}\rho\vec{f} \bullet \vec{v} + 2\nabla^2 v^2 - \gamma kT\rho\exp(-iqx)dx\exp(-iqy)dy$$

Where:

$$F\left\{\rho(x,t)\right\} \equiv \eta(q,t); F\left\{v(x,t)\right\} \equiv \omega(q,t); F\left\{f(\mathrm{x},t\right\} \equiv a(q,t)$$

$$\gamma\left(\frac{\partial \eta}{\partial t} + \omega * \eta qi\right) = \frac{2a_{motor} LT\rho_0}{\mu}\eta * a * \omega - 2q^2(\omega * \omega) - \gamma kT\eta\,(24)$$

Dividing by γ and move terms, and see that the convolution of ω with itself results in the multiplication with its complex conjugate giving the value of its magnitude squared.

$$\frac{\partial \eta}{\partial t} = \frac{2a_{motor} LT\rho_0}{\mu\gamma}\eta * a * \omega - kT\eta - \omega * \eta qi - \frac{2}{\gamma}q^2(\omega\bar{\omega})$$

$$= \frac{2a_{motor} LT\rho_0}{\mu\gamma}\eta * a * \omega - kT\eta - \omega * \eta qi - \frac{2}{\gamma}q^2\left|\omega\right|^2\,(25)$$

Taylor Approximations:

Since we defined: $F\{\rho(x,t)\} \equiv \eta(q,t)$, Then since dρ/dt is the derivative with respect to time, it should have no bearing in space thus:

$$F\left\{\frac{\partial\rho(x,t)}{\partial t}\right\} = \frac{\partial\eta(q,t)}{\partial t} \quad (26)$$

Also we know that:

$$\frac{\partial\rho(x,t)}{\partial t} = \lim_{\Delta t\to 0}\frac{\rho(x,t)-\rho(x,t+\Delta t)}{\Delta t} \quad (27)$$

Thus if we sample $\rho(x,t)$ close enough in time we can approximate the derivative of it

$$\frac{\rho(x,t)-\rho(x,t+\Delta t)}{\Delta t} = \frac{\Delta\rho(x,t)}{\Delta t} \equiv g(x,t) \approx \frac{\partial\rho(x,t)}{\partial t} \; for\; small\; \Delta t \quad (28)$$

Then

$$F\left\{\frac{\Delta\rho(x,t)}{\Delta t}\right\} \equiv G(q,t) \approx \frac{\partial\eta(q,t)}{\partial t} \quad (29)$$

Conservation of Mass:

$$\frac{D\rho}{Dt} = D_\rho\nabla^2\rho + k\rho \quad (30)$$

$$D_\rho = average\, diffusion\, coefficient\; for\, biomass$$

$$k = rate\, of\; metabolic\, change\, of\; biomass$$

Expanding the left hand side and rearranging in (31) we get:

$$\frac{\partial \rho}{\partial t} + \left(\vec{v} \bullet \nabla \rho\right) = D_\rho \nabla^2 \rho + k\rho (31)$$

$$\vec{v} \bullet \nabla \rho = D_\rho \nabla^2 \rho + k\rho - \frac{\partial \rho}{\partial t} (32)$$

With sufficiently small Δt we can Taylor approximate in time and plug equation (28) into (31):

$$\vec{v} \bullet \nabla \rho = D_\rho \nabla^2 \rho + k\rho - g\left(x,t\right) (33)$$

We know that the Laplacian can be written as:

$$\nabla^2 \rho = \nabla \bullet \nabla \rho = \frac{\partial}{\partial \vec{x}} \bullet \frac{\partial \rho}{\partial \vec{x}} (34)$$

With small enough Δx we can Taylor approximate (34) to:

$$\nabla^2 \rho \approx \sum_i \frac{\rho\left(x_i + \Delta x_i, t\right) - 2\rho\left(x_i, t\right) + \rho\left(r_i - \Delta x_i, t\right)}{{\Delta x_i}^2} \equiv b\left(x,t\right) (35)$$

Plugging D_ρ with the average bulk diffusion, k with the average normalized growth rate, and (35) into (33):

$$\vec{v} \bullet \nabla \rho = D_\rho b\left(x,t\right) + k\rho\left(x,t\right) - g\left(x,t\right) \equiv l\left(x,t\right) (36)$$

The Fourier transform of (36):

$$F\left\{l\left(r,t\right)\right\} \equiv L\left(q,t\right) \approx F\left\{\vec{v} \bullet \nabla \rho\right\} = \omega * \eta q i (37)$$

Plugging in (29) and (37) into (25):

$$G\left(q,t\right) = \frac{2a_{motor} LT\rho_0}{\mu\gamma} \eta * a * \omega - kT\eta - L\left(q,t\right) - \frac{2}{\gamma} q^2 \left|\omega\right|^2 (38)$$

Rearranging terms in (38) we get:

$$G(q,t)+L(q,t)=\frac{2a_{motor}LT\rho_0}{\mu\gamma}\eta*a*\omega-kT\eta-\frac{2}{\gamma}q^2\left|\omega\right|^2 \quad (39)$$

Where the imagery portion of (39) is:

$$\mathrm{Im}(G(q,t)+L(q,t)+kT\eta))=\mathrm{Im}(\frac{2a_{motor}LT\rho_0}{\mu\gamma}\eta*a*\omega) \quad (40)$$

The square of G and L would be:

$$\mathrm{Im}(G(q,t)+L(q,t))^2=\mathrm{Im}(\frac{2a_{motor}LT\rho_0}{\mu\gamma}\eta*a*\omega)^2-2\,\mathrm{Im}(kT\eta)\,\mathrm{Im}(\frac{2a_{motor}LT\rho_0}{\mu\gamma}\eta*a*\omega)+\mathrm{Im}(kT\eta)^2 \quad (41)$$

Now condense terms we get:

$$\mathrm{Im}(G(q,t)+L(q,t))^2=\alpha^2\,\mathrm{Im}(\eta*a*\omega)^2-2\alpha\phi\,\mathrm{Im}(\eta)\,\mathrm{Im}(\eta*a*\omega)+\phi^2\,\mathrm{Im}(\eta)^2 \quad (42)$$

Substituting (40) into (42):

$$\mathrm{Im}(G(q,t)+L(q,t))^2=\mathrm{Im}(G(q,t)+L(q,t)+\phi\eta)^2-2\phi\,\mathrm{Im}(\eta)\,\mathrm{Im}(G(q,t)+L(q,t)+\phi\eta)+\phi^2\,\mathrm{Im}(\eta)^2 \quad (43)$$

We can fit (43) to a surface to find the constant φ.

While the real portion of (39) contains the dissipation energy term:

$$\mathrm{Re}(G(q,t)+L(q,t)+\phi\eta)=\alpha\,\mathrm{Re}(\eta*a*\omega)-\frac{2}{\gamma}q^2\left|\omega\right|^2 \quad (44)$$

$$\mathrm{Re}(G(q,t)+L(q,t)+\phi\eta)^2=\alpha^2\,\mathrm{Re}(\eta*a*\omega)^2-2\alpha\,\mathrm{Re}(\eta*a*\omega)(\frac{2}{\gamma}q^2\left|\omega\right|^2)-(\frac{2}{\gamma}q^2\left|\omega\right|^2)^2 \quad (45)$$

Rearrange the terms in (44) and we can substitute to solve for dissipation energy in (45):

$$\mathrm{Re}(G(q,t)+L(q,t)+\phi\eta)+\frac{2}{\gamma}q^2\left|\omega\right|^2=\alpha\,\mathrm{Re}(\eta*a*\omega)(46)$$

Rewriting the body force term we get:

$$\alpha^2\left\|\eta*a*\omega\right\|^2=\alpha^2\left\|a\right\|^2\left\|\eta\right\|^2\left\|\omega\right\|^2=\alpha^2\left\|a\right\|^2\frac{\left\|L(q,t)\right\|^2}{q^2}(47)$$

$$\alpha^2\left\|a\right\|^2\frac{\left\|L(q,t)\right\|^2}{q^2}=(\alpha\,\mathrm{Re}(\eta*a*\omega))^2+(\alpha\,\mathrm{Im}(\eta*a*\omega))^2(48)$$

The power spectrum of the rearranged (40) gives:

$$\left\|G(q,t)+L(q,t)\right\|^2=\alpha^2\left\|\eta*a*\omega\right\|^2-2\alpha\,\mathrm{Re}(\eta*a*\omega)(\beta q^2\left|\omega\right|^2)-(\beta q^2\left|\omega\right|^2)^2$$
$$+2\,\mathrm{Re}(\phi\eta)*(\alpha\,\mathrm{Re}(\eta*a*\omega)+\beta q^2\left|\omega\right|^2)+2\,\mathrm{Im}(\phi\eta)*\alpha\,\mathrm{Im}(\eta*a*\omega)+(\phi\eta)^2(49)$$

Now condense and rearrange terms:

$$\left\|G(q,t)+L(q,t)\right\|^2=A^2\frac{\left\|L(q,t)\right\|^2}{q^2}-2AB\,\mathrm{Re}(\eta*a*\omega)(q^2)-B^2(q^2)^2$$
$$+2C\,\mathrm{Re}(\eta)*(A\,\mathrm{Re}(\eta*a*\omega)+Bq^2)+2AC\,\mathrm{Im}(\eta)*\mathrm{Im}(\eta*a*\omega)+C^2(\eta)^2+D(50)$$

Where:

$$\alpha\equiv A$$
$$\beta\left\|\omega\right\|^2\equiv B$$
$$\phi\equiv C$$
$$Cons.Integration\equiv D$$

SUPPLEMENTARY FIGURES

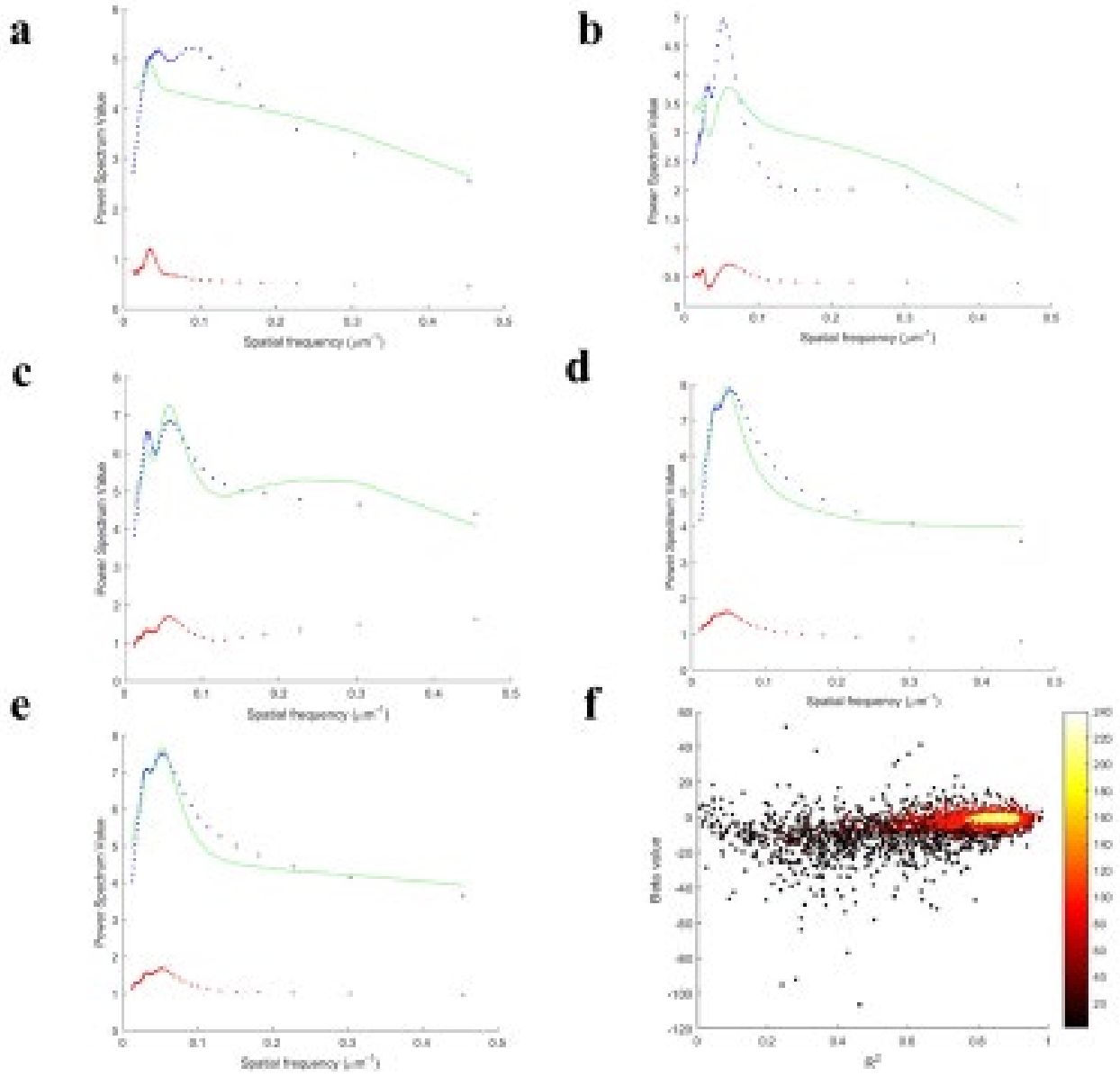

FIGURE S1 Dissipation modeling of cellular data show increasing fit with sample size. Fittings of the experiential spatial frequency power spectrum of the rate of mass change of BT474 cells to the theoretical energetic model using an averaged power spectrum of 1 (**a**), 5 (**b**), 10 (**c**), 50 (**d**), and the entire sample size of cells (**e**). (**f**) Plot of dissipation coefficient (beta) derived from model

fitting of the spatial frequency power spectrum of the rate of mass change vs. the goodness of fit (R^2) for averaged value of 1-240 BT-474 cells.

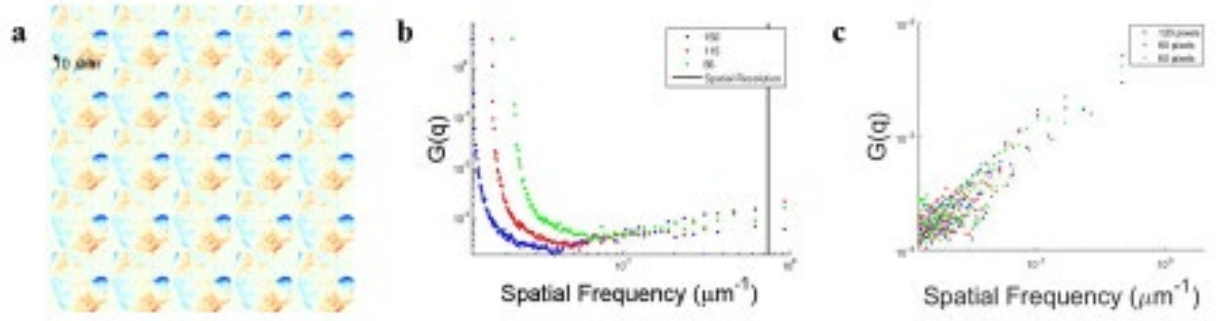

FIGURE S2 Correction of zeroth frequency drop off in power spectrum analysis. (**a**) QPI images were applied with 5x5 transformation before Fourier transformed. (**b**) This to was correct for the frequency drop off seen in the spatial frequency information of QPI data. (**c**) Power spectrum data when corrected using the 5x5 transform no longer show the effect of frequency drop off.

Chapter 4. Quantitative Phase Imaging: Recent Advances and Expanding

VOCABULARY

Phase (of light): Property that, along with amplitude (intensity), wavelength (color), and polarization, defines light as an electromagnetic wave. Shifts in phase are caused by a delay in propagation speed, as occurs when passing through a sample of higher refractive index.

Quantitative phase imaging (QPI): Method in which the phase shift of light as it interacts with matter is measured. Returns measurements of integrated refractive index through sample thickness at each pixel.

Interferometry: Method in which source light is split into a sample and reference beam, then recombined at or before the detector, generating interference patterns. Can be applied to acquire QPI data.

Wavefront sensing: Method that measures aberrations in the wavefront of light due to the distribution of phase shifts within the sample, typically without the reference beam used in interferometry.

Phase retrieval: A class of methods in which intensity images, often with some perturbations, e.g. partial defocusing, chromatic aberrations, partial illumination, plus knowledge of the optical transfer function are used to reconstruct the distribution of phase shifts through the sample.

Digital holography: Method in which a hologram is captured on a digital imaging sensor. The resulting digital hologram can be used to reconstruct QPI data.

Quantitative phase tomography: Method to measure the three-dimensional (3D) distribution of phase shifts within a sample. Returns measurements of average refractive index within each voxel.

INTRODUCTION

Advances in microscopy have driven advances in biology and medicine by enabling visualization and a greater perspective on the machinery of life. In this review, we discuss advances in quantitative phase imaging (QPI), a label-free microscopy technique that measures fundamental cell properties and behaviors, including mass, mechanical properties, growth, and intracellular transport. We discuss the history of QPI, technical aspects of its applications, and emerging developments that will shape future applications of this technology for addressing opportunities and challenges in biomedicine.

QPI methods measure the phase shift of light as it passes through a transparent sample. This phase shift is caused by light slowing down as it passes through a material with a higher refractive index than water[1] and can be written as:

$$\phi = \frac{2\pi}{\lambda}\int_{z=0}^{h} n(z)dz \tag{1}$$

where ϕ is the phase shift of light (in fractions of a wavelength) contributed by all elements in the sample of varying refractive index, n, through the height of the sample, h, in the z direction. This measured phase shift is directly proportional to the dry mass content of a biological sample[2]. Dry mass includes all mass excluding water and is therefore inclusive of biological macromolecules. For example, the increase of refractive index (real component) for a protein solution is proportional to the increase in protein concentration[3]. The slope of refractive index versus mass concentration defines this relationship and is called the specific refractive increment[1, 4]. The average specific refractive increment, α, for the typical contents of mammalian cells, including proteins, nucleic

acids, sugars, and lipids is ~0.185 μm^3/pg[1], a value that is correct to within ~6%[5]. The cell dry mass, m, can then be calculated using the specific refractive increment, α, of a sample by[2]:

$$m = \frac{\lambda}{2\pi\alpha}\int \phi dA \qquad (2)$$

where this integral is performed over A, the area of the cell. The ability of QPI to measure quantitative, biophysical features of the cell, such as mass, is central to its applications and potential in biomedicine.

Along with QPI, there are other widely used methods for leveraging the phase shift of light as it passes through a cell or other biological sample to generate image contrast. These include Zernike phase contrast microscopy[6, 7] and Nomarski differential interference contrast (DIC) microscopy[8]. In phase contrast microscopy, illumination of a sample is with a limited spatial frequency range (background light). The refractive index distribution of non-uniform structures within cells then causes this background light to diffract and undergo a phase shift relative to the unperturbed background light. Both this diffraction and phase delay helps to generate contrast in the resulting image. As a result, even minute differences in refractive index translate into amplitude changes in the resulting image. In DIC microscopy, image contrast arises by splitting the incident light based on orthogonal polarization and introducing a small lateral shear of one polarization angle relative to the other using a Nomarski-modified Wollaston prism. Recombination of this polarized light after passing through the sample at a second Wollaston prism causes interference based on the relative phase shift between the two polarization angles. The image intensity in DIC microscopy, therefore, relates to the gradient of phase in the shear direction. Both phase contrast and DIC microscopy enable label-free measurements of cell shape and position. However, the intensity of

images from phase contrast and DIC imaging do not linearly relate to the corresponding phase unless used as the basis for a phase retrieval method[9, 10]. As a result, and in contrast to QPI, phase contrast and DIC microscopy remain qualitative phase methods. As discussed further, the quantitative data available with QPI enables more precise statistical and incremental studies for probing biological mechanisms than are available with qualitative methods.

In this review, we introduce the fundamental problem of QPI and trace the development of methods to solve this problem (**Figure 1a**). With the ever-increasing availability of computational resources, these solutions have increasingly converged, leading to a number of key applications in quantitative biology and a dramatic increase in research interest in QPI (**Figure 1b**). Finally, we conclude by discussing four key ongoing areas of QPI research that we believe will have the greatest influence in the future.

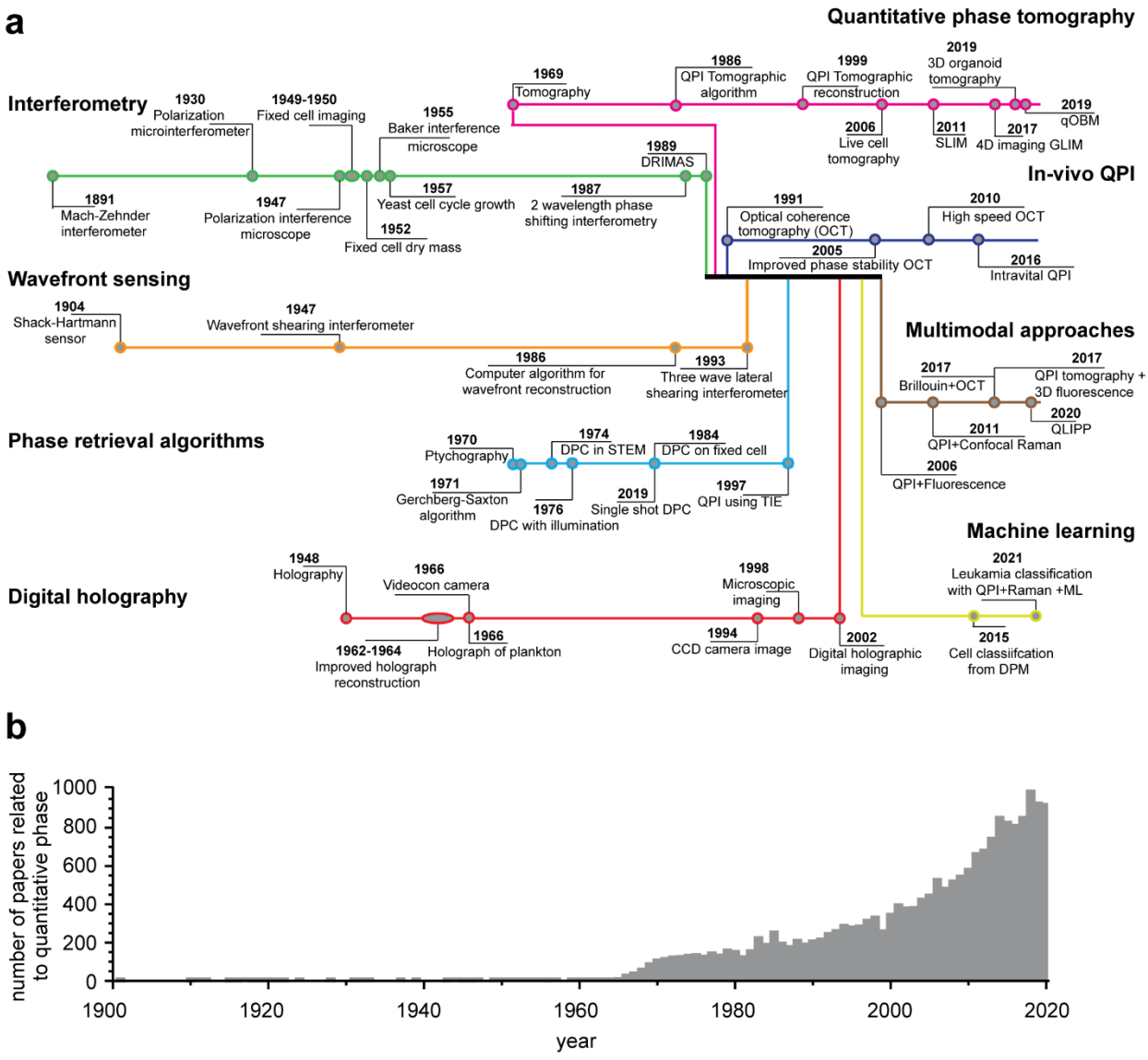

FIGURE 1 QPI has undergone a steady increase in interest driven by advances in different fields of optics. **(a)** Schematic of four main QPI approaches with interferometry (green timeline), wavefront sensing (orange timeline), phase retrieval algorithms (light blue timeline) and holography methods (red timeline) indicated. These methods have improved extensively over time with the emergence of greater computational resources (thick black line). The improved efficiency of computational resources led to technical advances in QPI that include quantitative phase tomography (magenta timeline), *in vivo* QPI (dark blue timeline), multi-modal approaches (brown

timeline), and machine learning methods (yellow-green timeline). **(b)** The growth in interest and advances in QPI over time depicted by the number of publications on Web of Science using search terms "Quantitative Phase Imaging" or "Quantitative Phase Microscopy" by year.

SOLVING THE FUNDAMENTAL PROBLEM OF QUANTITATIVE PHASE

QPI techniques seek to recover the phase shift of light that passes through a sample. However, conventional optical detectors recover only the amplitude of incident light, so additional optics and/or computations are necessary to recover phase shift information. This is the fundamental problem that all QPI methods must solve, which has stimulated the development of multiple QPI techniques. Here, we discuss the development of QPI in the context of these solutions, focusing on the four primary approaches that have had the largest impact on modern QPI methods and applications: interferometry[11, 12], wavefront sensing[13, 14], phase retrieval[15, 16], and digital holography[17]. While many of these approaches have integrated methods and concepts from electron, x-ray, and radio-wave techniques, here we use the term QPI to refer specifically to methods for phase retrieval based on visible light. We then discuss the convergence of these various techniques at the end of this section.

Interferometry

One method for computing phase information is interferometry. In interferometry, light incident on a sample is split into two paths, a sample path and a reference path, before recombining at a detector (**Figure 2a**). The amplitude of the resulting interference image relates to the phase shift of light passing through the sample with respect to the reference path by constructive and destructive interference between the light from these two paths. Interferometry was invented by

Albert Michelson and improved further in collaboration with Edward Morley and famously used for the Nobel prize winning 1887 Michelson-Morley experiment that provided evidence against the existence of the luminiferous aether[18] (**Figure 1a**). Major early improvements were the introduction of separate sample and reference cells in the Mach-Zehnder interferometer[19] and use of thin calcite films faced at 45º to enable micro-interferometry[20]. These dual path interferometers were followed by common-path interferometers where the reference beam and sample beam travel along the same path, reducing measurement sensitivity to vibration[21, 22]. A common-path interferometer microscope built by Dyson was used to image fixed biological specimens[23].

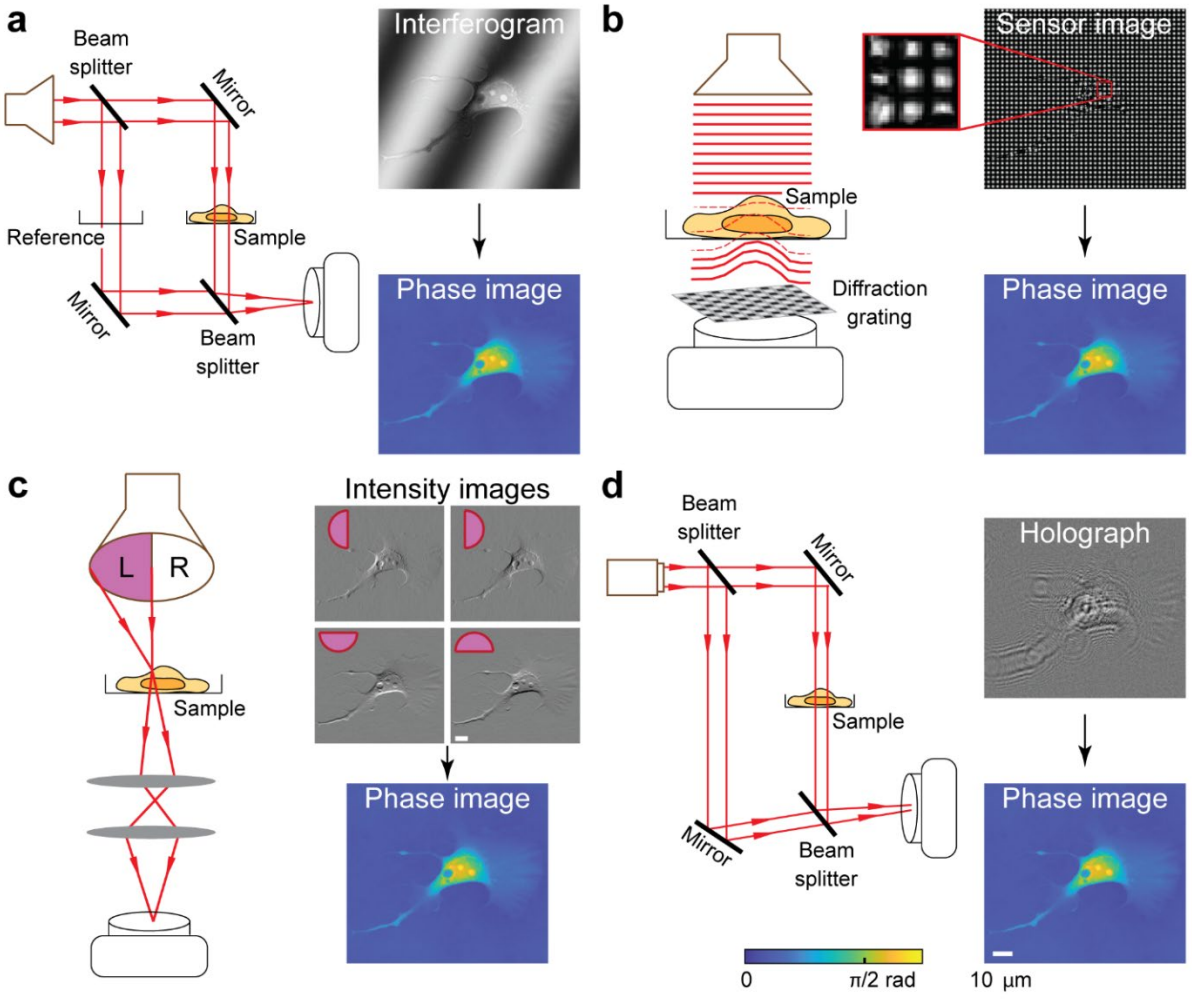

FIGURE 2 Examples of the four primary QPI lineages identified in **Figure 1**. **(a)** Mach-Zehnder interferometry uses interference between light passing through a sample and a reference beam to generate an interferogram that encodes phase information in image amplitude (e.g.[12]). An in-focus interferogram is then used to generate the phase image. **(b)** Wavefront sensing with quadriwave lateral shearing interferometry (QWLSI) uses a diffraction grating that captures gradients in phase shift as local distortions in the resulting intensity grid pattern on the camera sensor[14]. Sample images are compared to a reference wavefront image to determine the wavefront distortion due to the sample itself. This is numerically integrated to recover phase. **(c)** Differential phase contrast (DPC) microscopy, a deterministic phase retrieval method, images a sample using half-circle patterns of illumination that extend beyond the microscope objective numerical aperture. Light refraction through the sample then causes intensity increases (or decreases) in one half-circle image and decreases (or increases) in images with the opposing half-circle pattern. The normalized difference between these two images approximates the gradient of phase along one axis[15]. Multiple pairs of images are collected, and the phase is numerically integrated. **(d)** Digital holographic microscopy (DHM) computationally reconstructs the phase image from a slightly out-of-focus interferogram obtained using an interferometer[24]. A slightly off-axis reference beam is used to avoid the twin image problem, where the image and its conjugate sit on top of one another.

The next major advance in QPI towards biomedical applications was the calibration of a specific refractive increment[3] using varying specimen composition[25, 26] that enabled the calculation of cell dry mass. The earliest applications of cell dry mass measurements with interferometry mostly focused on regularly shaped organisms such as yeast and bacteria to simplify calculations[27, 28]. Early work on irregularly shaped cells used multiple images to find the total projected area and

average optical thickness, the product of which is proportional to total cell dry mass through the specific refractive increment[29]. The integration of the scanning optical microspectrograph with the interference microscope increased resolution[30], although not to the level of modern systems[31]. Other major improvements in interferometry focused on convenience for use in biological studies. This includes the polarization interference microscope that replaced the partially silvered reflecting layers of earlier common path systems with a birefringent layer[20]. The Baker interference microscope, which was used widely on mammalian cells, is a polarizing microscope modified into a two beam interferometer[32, 33]. Additional improvements include the use of a warmed stage to measure live yeast[34] or bacteria[28], and the replacement of uneven mercury lamp illumination with fiber optics. Although the relationship between amplitude and phase in interferometric images is straightforward, the required phase reference increases the complexity and number of optical elements, and increases susceptibility to vibrations[35] and instability of a light source[36]. Therefore, it was not until the introduction of digital cameras and image processing[37, 38] that interferometry provided truly quantitative data for internally complex mammalian cells.

Advances in a number of areas of interferometry-based QPI measurements benefit from the increasing use of computers. Automated image focusing has improved interference imaging accuracy and speed[39]. Single-wavelength interferometry cannot distinguish adjacent imaging pixels with a phase difference exceeding one quarter of a wavelength[2], but substantially larger phase shifts can be accurately measured by digitally combining images taken at two wavelengths[40]. Errors introduced from the unevenness of a reference surface can also be digitally corrected[41]. Phase shifting interferometry, in which multiple interference images are acquired at sub-wavelength shifts in the reference relative to the sample path length, corrects error due to external

disturbances[36]. Applications of this approach with the required temporal and spatial resolution to study subtle changes in the shape of cancer cells requires tight integration with computers for motion control and image processing[31]. Automated cell segmentation enables interferometry to measure the growth of many cells simultaneously in uniform[12] or mixed populations[42]. Automated segmentation has also improved the application of phase unwrapping, or removal of phase jumps of one wavelength (2π radians) created due to the inherent ambiguity in interpreting interferometry data, thereby reducing errors in dry mass measurements[43]. Overall, computer control of interference microscopes and digital image processing of the resulting data has revolutionized this 100+ year old method and led to a convergence with other methods, as discussed below. This also points towards the future of QPI, as the linkage to ever-expanding compute power enables increasingly sensitive approaches, and portends leveraging advances in machine learning.

Wavefront sensing

Wavefront sensing refers to approaches that seek to recover the aberrations in a wavefront caused by phase delays within a sample. Important wavefront sensing methods include Shack Hartmann wavefront sensing[44] and Ronchi sensing[45]. Of these, the Shack-Hartmann wavefront sensor is the most commonly used version, with construction that uses either an array of evenly spaced holes or a lens microarray for improved image quality. Either of these arrays creates a pattern of focused light spots on the camera sensor[46]. Aberrations in the light wavefront causes these spots to move, allowing reconstruction of the total phase shift through the sample.

The earliest work in wavefront sensing used lateral shearing interferometry[45, 47]. Lateral shearing wavefront imaging is similar to Nomarski DIC imaging in that the incident wave shears into two

identical but tilted wave fronts that then interfere. The resulting single-direction phase gradient from lateral shearing interference data lacks the necessary gradient information to generate a complete two dimensional phase-field and thus requires the use of multiwave interferometry techniques[48] that generate more than one gradient direction. Numerical reconstruction of the wavefront is possible, with such methods developed in 1986[49]. However, this method is computationally intensive, and was later used in practice on images captured using a three-wave shearing interferometer configuration[50]. Typical wavefront sensors lack the resolution needed for imaging cells. Quadriwave lateral shearing interferometry (QWLSI) uses a modified, micro-fabricated Hartmann mask, resulting in a pattern of dark spots that measures phase gradients along perpendicular directions[51], allowing the measurement of both intensity and phase (**Figure 2b**). Importantly, this mask enables high resolution images to support the live cell application of wavefront sensing in measurements of phase using QWLSI on erythrocyte cells[52].

Wavefront sensing has multiple advantages, such as higher sensitivity, speed and temporal resolution with less complex instrumentation than typical interferometry methods[14]. Importantly, wavefront sensing techniques do not require a reference arm[14], and therefore are less affected by vibrations and other disturbances than double-path systems. Wavefront sensing typically uses single image acquisition, resulting in high potential temporal resolution[53]. However, this approach has a trade-off with lower spatial resolution as the light from each phase measurement spot is spread over many pixels of a digital camera sensor. Thus, wavefront sensing is best for imaging high-speed cell dynamics requiring accurate phase information, but has a downside of lower spatial resolution. In applications to single cell imaging, QWLSI phase images require a low degree polynomial fitting to flatten the image background for accurate biomass measurements[54]. This

requirement and an inherent amount of both spatial and temporal noise due to the recovery of phase by numerical integration can impact cell segmentation. Overall, however, this approach can achieve high accuracy for measurements of the dry mass of cells, even at high cell densities[55].

Phase retrieval algorithms

Phase retrieval refers broadly to non-interferometric methods that computationally reconstruct the phase shift from a sequence of intensity images taken under varying conditions. The primary advantage of phase retrieval methods is that they can be performed using simpler optical systems, or used to enhance the performance of more complex optical systems. Phase retrieval methods can be classified as either iterative or deterministic[56]. Iterative methods use iterative computation to satisfy constraints in object and Fourier space between intensity images at the sample and detector plane to resolve the phase problem[57]. Iterative methods of phase retrieval were originally developed for electron microscopy to reconstruct the wavefront propagation between image and diffraction planes from the corresponding amplitude images[58]. The Gerchberg-Saxton (GS) algorithm was a widely used iterative phase retrieval method. The GS method seeks to iteratively approximate the source (e.g. illumination) and target (e.g. image) intensities and complex phase distribution from measured intensity images of the source and target. However, the GS algorithm typically requires a large number of iterations and can become stuck at local minima and therefore not converge to the real phase solution[59]. This was addressed by the introduction of the steepest gradient search[59] and input-output methods[60]. One common implementation of iterative phase retrieval is in Fourier ptychography[61-63]. Ptychography was developed to solve the phase problem in electron diffraction measurements[64]. Fourier ptychography recovers high spatial resolution (or large field of view) phase information at the object plane from a series of intensity images, such

as at varying angles, resulting in data from which a higher spatial frequency image can be reconstructed[65, 66]. Fourier ptychography has also been used to visualize the three-dimensional (3D) structures from light scattering signals[67] or complex transmittance functions[63].

Deterministic methods directly solve for phase images without iteration, enabling real time phase imaging. One commonly used approach is based on the transport of intensity (TIE) equation which relates phase data at the in-focus plane to the axial derivative of intensity distribution[68]. The TIE equation was proposed based on conservation of energy and describes the transport of energy in an optical field[16]. Differential phase contrast (DPC) microscopy, another commonly used deterministic imaging method, evolved from the idea of contrast enhancement by asymmetric illumination[69]. In DPC microscopy, multiple images of the specimen are obtained at different angles of half plane illumination to recover phase information[70] (**Figure 2c**). In this way, DPC imaging is similar to Schlieren imaging in which half plane illumination is used to remove half the spatial frequencies from the intensity image in one direction, giving phase gradients in orthogonal dimensions[71]. The earliest work on DPC imaging used a half plane electron source in a scanning transmission electron microscope (STEM)[72] and was later applied to imaging with visible light[73] and applied to increase contrast in images of fixed cells[74].

In contrast with interferometric methods, phase retrieval is typically less costly or uses more widely available optics, such as DIC[75], phase contrast[76, 77] or custom made imaging systems[15]. This is because phase retrieval algorithms eliminate the use of a reference based on knowledge, or approximation, of the optical transfer function of the imaging system[78]. Phase retrieval is also possible with partially coherent light sources[79-81]. However, the requirement of multiple images as

inputs for phase retrieval methods lowers the imaging temporal resolution compared to interference and wavefront sensing methods[54]. The use of iterative algorithms for phase retrieval also increases the overall workflow time.

As a primarily computational method, phase retrieval has benefited greatly from advances in compute power. The practical application of phase retrieval for QPI therefore began in the 1990s with extensive use of computing resources[82, 83]. Advances in optical systems further enhanced phase retrieval QPI, including the use of color-multiplexing to obtain phase data from a single image[84], lens-less phase retrieval with super-resolution reconstruction[85], and volumetric holography using asymmetric illumination[86]. Looking forward, phase retrieval stands to benefit greatly from future advances in computation. This is especially evident in recent applications of machine learning, where phase retrieval is possible without an optical physics model[87, 88]. A possible limitation that needs addressing as this field moves forward is that with more computation, more noise tends occur. Additionally, the opaquer the method, the harder it is to track down sources of error, a particular concern with machine learning approaches. Overall, however, these advances, combined with the ability to work from data acquired with diverse sets of optics, point towards a larger role for phase retrieval in the future of QPI.

Digital holography

Digital holography captures the interference between a reference and off-axis sample beam with a digital camera placed at a known distance in front of the image plane. Reconstruction of the resulting interferogram uses diffraction theory to recover the complex object wavefront, including the phase shift and intensity modulation of light passing through the sample. Digital holography

emerged from the establishment of holography by Gabor[89] for which he won the Nobel prize in 1971[90]. Gabor's work demonstrated that light from a point source interfering with secondary waves from light scattered by an object produces a negative photograph of a 3D image. However, a conjugate image is also superimposed on the reconstructed image, resulting in ambiguity due to the present of this twin image. It was later shown that use of an off-axis reference beam can separate the real and conjugate image[91 92]. Marine plankton provided an early application of live cells imaged using holography in a chamber with close proximity to a photographic plate[93].

The use of digital cameras[94,95] and numerical reconstruction[96] has greatly improved the accessibility of holography. Since the 1970s, holography has been used extensively for cell imaging[97]. Later, digital holography was introduced for 3D imaging enabling visualization of specimens with highly fluctuating phase profiles such as pollen[98]. Initial applications of holography to quantitative phase measurements were restricted to measuring the refractive index distribution of inorganic materials[99,]. The broader application of digital holography to QPI was enabled by the development of efficient computational reconstruction of holograms in the early 2000s[100] as well as developments in the field of electron microscopy[101]. This lead to digital holographic microscopy (DHM) of live neuron cells in culture with high phase accuracy[24]. Improved computational resources sped up the hologram reconstruction process for applications such as mapping the refractive index of cells[102, 103]. Even Schlieren images were generated from holography of patterns in inorganic materials[104], which were later used to measure optical thickness[105].

DHM has been implemented in multiple hardware configurations[106]. Of these, the Mach Zehnder interferometer[19] is the most widely used (**Figure 2d**), although this approach has the same

disadvantages of other double-path interferometers discussed previously. Traditionally, DHM requires spatially and temporally coherent laser light, leading to speckle noise. However, a number of white light and incoherent DHM alternatives are available, including spatial light interference microscopy (SLIM), a combination of digital holography and Zernike's phase contrast microscopy[107]. By processing a hologram of the 3D specimen wavefront, DHM also allows computational refocusing. However, this process can lead to errors in phase measurements, unless the proper refocusing plane is selected for repeatable measurements.

Evaluation and standardization of QPI methods

Each lineage of QPI methods has advantages and disadvantages compared to each other, which have diminished in magnitude over time from technological advances and verified standardizations. Briefly summarizing the four QPI lineages described above, interferometry is accurate but sensitive to reference arm noise; wavefront sensing has good temporal resolution and no reference arm, but has low spatial resolution; phase retrieval provides a large field of view and higher spatial resolution, but has low temporal resolution; and DHM has high temporal resolution, but is susceptible to noise from a reference arm.

A number of technical improvements address key limitations of these four QPI lineage approaches. For example, adapting DPC microscopy to work with multicolor illumination instead of separately imaging individual illumination patterns[108-111] achieved temporal resolution as high as 100 frames per second (fps)[112]. A high speed interferometry method using a diffraction grating generated a temporal resolution of 10^4 fps[111]. Recent developments in DHM systems enabled removal of a reference arm, for instance by using a self-referencing module[113]. It was shown that holography

could mathematically retrieve phase using single intensity images through an illumination control without a reference[114]. The use of coherent and partially coherent illumination can also help to reduce noise in QPI. Coherent illumination, such as from a laser, while useful for generating interference, has a disadvantage of being sensitive to noise from system optics, especially speckle noise[115]. Use of partially coherent illumination, such as from an LED or lamp, can eliminate these artifacts, at the cost of a moderate increase in difficulty aligning the optical system. Sub-Rayleigh resolution has been achieved by adjusting the illumination source[116]. Mach Zehnder interferometry has been adapted for biosensing within microchannels, increasing sensitivity[108, 109].

Another approach to generate improvements in QPI is to combine principles from different QPI lineages. For example, interferometry using a diffraction grating in a Mach Zehnder system can eliminate the need for a reference arm and increase phase sensitivity, by reducing measurement noise[110]. The use of iterative phase retrieval algorithms on single-shot holographs also enables the 3D reconstruction of QPI images without needing a reference standard[57]. The same iterative phase retrieval has also been successfully applied to transport of intensity algorithms using holographic microscopy[117]. The transport of intensity equation can be used to capture 3D QPI images at the diffraction limit using an electrically tunable microlens array, similar to that used in wavefront sensing, thereby significantly increasing temporal resolution[118].

Polystyrene beads are a widely used phase calibration standard for many QPI methods[119, 120] and have been used with DHM[121], QWLSI[14], and DPC[122] techniques. However, there is variability in the refractive index of polystyrene[123], and typically large refractive index differences between polystyrene beads relative to cell culture media, combined with sharp ‘imaging edges’ of these

round beads, can lead to phase unwrapping artifacts that are not usually encountered with live cell samples. Potential phase unwrapping artifacts using polystyrene bead calibration standards can be mitigated by, for example, mounting the beads within material with a closer refractive index[120, 124]. However, this approach also moves the calibration data range further from actual cell imaging conditions, which could impact experimental accuracy. Red blood cells have also been used as a phase calibration standard in the development of QPI methods because of their ready availability and fairly uniform shape and size[12, 125]. Typically, non-diseased RBCs show a population dry mass variation of ~15%[126]. However, as a biological sample, this can be more challenging to work with than an inanimate calibration standard. A number of studies have used USAF resolution test targets that are readily available because of their wide use in calibrating imaging systems[119, 127]. However, these standards are typically used for calibrating intensity images and are made of thin metal films, meaning that they do not function as pure phase objects. A phase specific calibration standard for QPI was developed and used in a comparison with atomic force microscopy (AFM), which showed that QPI has nanometer sensitivity over a wide range of spatial frequencies[62]. A 3D phase "phantom" that captures subcellular features of cells for calibration in 3D QPI methods has also been demonstrated[128], with further development and characterization of widely accessible standards an area that needs further attention to support continued advances in QPI.

QPI systems and image quality are defined by parameters including spatial and temporal resolution, phase measurement sensitivity, and signal-to-noise ratio (SNR). The SNR in QPI is measured as the signal over the standard deviation of the measured signal[129]. Noise in QPI measurements can be reduced, increasing the SNR, by increasing the number of measurements. This is especially important when using coherent illumination[54]. Analytic software packages for

assessing QPI measurements is another key system consideration. Some QPI approaches have available commercial analytic packages from Wyko Corporation, Phasics Corporation, Phase Holographic Imaging PHI, Inc. and other vendors, whereas additional analytical packages are custom-coded in MATLAB or Python. Table 1 summarizes the category of QPI hardware, key benefits, reported performance and available software of example methods from the four lineages of QPI discussed in this review.

Table 1. Example methods, key benefits, performance and software for different QPI lineages.

Lineage	**Example methods**	**Key improvements**	**Resolution**	**Accuracy**	**SNR**	**Software**
Interferometry	Mach Zehnder interferometer, Baker interferometer	No reference arm	100 fps[119], 250 fps[130]	2%[130], 0.5%[131]		Wyko Vision software[31, 132]
Wavefront sensing	Lateral shearing interferometry, QWLSI	Increased spatial resolution	10^4 fps[111]	2% (1 nm sensitivity)[14]	<8[133]	Phasics[14], MATLAB[134]
Phase retrieval algorithms	Iterative algorithms: Defocus methods (GS algorithm, Hybrid input-output algorithm, others), Fourier ptychographic microscopy. Deterministic methods: TIE, DPC	Increased temporal resolution	100 fps[112]	0.1-0.2[135]	<6[136, 137], <100[138]	Python[139], ImageJ[139], MATLAB[140, 141]
Digital holography	Same as interferometry, reconstruction in addition	Self-referencing module[113], less susceptible to noise	100 nm[142]	0.3 %[142]	Peak SNR< 55[143], SNR< 10[144]	HoloStudio (Holomonitor, phi)[145], Koala (Lyncee tech)[146], Python[17]

Computational convergence

Starting in the early 2000s, QPI began to rely increasingly on digital image acquisition and data processing, with the field also advancing from creative method combinations that were emerging from multiple technical lineages. For example, SLIM combines principles of digital holography

with phase contrast methods[107], and QWLSI combines the principles of wavefront sensing with interferometry and phase retrieval algorithms[14]. The combination of DHM with principles from lateral shearing interferometry addresses the twin image problem[147], and this combined approach can reconstruct optimally sampled QPI data[148]. Further improvements in computation and machine learning are enabling approaches analogous to QWLSI using an unstructured, random phase mask. These exciting developments point toward the future of QPI with increasing availability of computational resources and algorithms, including creative applications of machine learning, which will further advance quantitative studies in biology and medicine.

ADVANCES IN QUANTITATIVE BIOLOGY

As QPI approaches have advanced, so too have QPI applications. One advantage of QPI is that it is label-free. Therefore, QPI can study cell behavior with minimal impact, a feature that has been leveraged in a number of applications. As summarized above, there are also a number of other label-free microscopy approaches, including the more widely used methods of phase contrast and DIC microscopy. The primary advantage of QPI over these other approaches, however, is that, in contrast to phase contrast or DIC microscopy, the data contained in each pixel of a QPI image is a quantitative measure of the phase delay of light as it passes through that portion of a sample. Measurement of this phase delay can utilize any of the approaches already discussed above. Once this phase data is captured, its analyses can provide quantitative insights into numerous biological systems. Here we summarize key advances in the application of QPI to quantitative biology studies, ranging from applications that quantify the behavior of individual cells to emerging opportunities in clinical diagnostics.

QPI applications using measurements of cell mass or growth rate

The refractive index of a material is related to its mass through a quantity called the specific refractive increment[5]. For cells, a typical average value is 1.8 – 2.0 x 10-4 m^3/kg [2, 3, 5]. The phase shift measured by QPI is the integral of the difference in refractive index between a cell and its surroundings through the thickness of the cell's projected area. The measured phase shift of a cell is proportional to the mass of the cell's contents excluding water, which is the dry mass of the cell. This provides a quantitative measure of cell size, which can provide valuable information on cell viability, growth over time, replication, and function. Measuring cell volume is an alternative method to cell mass quantification that can be used to measure cell growth[149]. However, measurements of cell volume typically requires a simplifying assumption about cell shape (e.g. spherical mammalian cells, rod-shaped bacterial cells) and cell volume changes depend upon intra- and extracellular osmolality, which can be unrelated to internal dry mass amounts[150]. By contrast, dry mass is independent of osmolality and instead depends upon the balance of biosynthetic (anabolic) and degradative (catabolic) processes within a cell. In the early- to mid-1950s, several investigators began using QPI to measure the absolute total dry mass of live eukaryotic cells, including measurements of mass through the cell cycle [4, 25, 26, 34, 151] (**Figure 3**). Additionally, repeated QPI measurements of dry cell mass over time can provide dry mass accumulation or loss rates to quantify cell growth[12, 150, 152-156] (**Figure 3**), or the decrease in mass that occurs during cell death[157-162] . Below, we discuss example applications of QPI measurements of cell mass and growth in studies of basic biological processes, including in immunology and in the behavior of neurons.

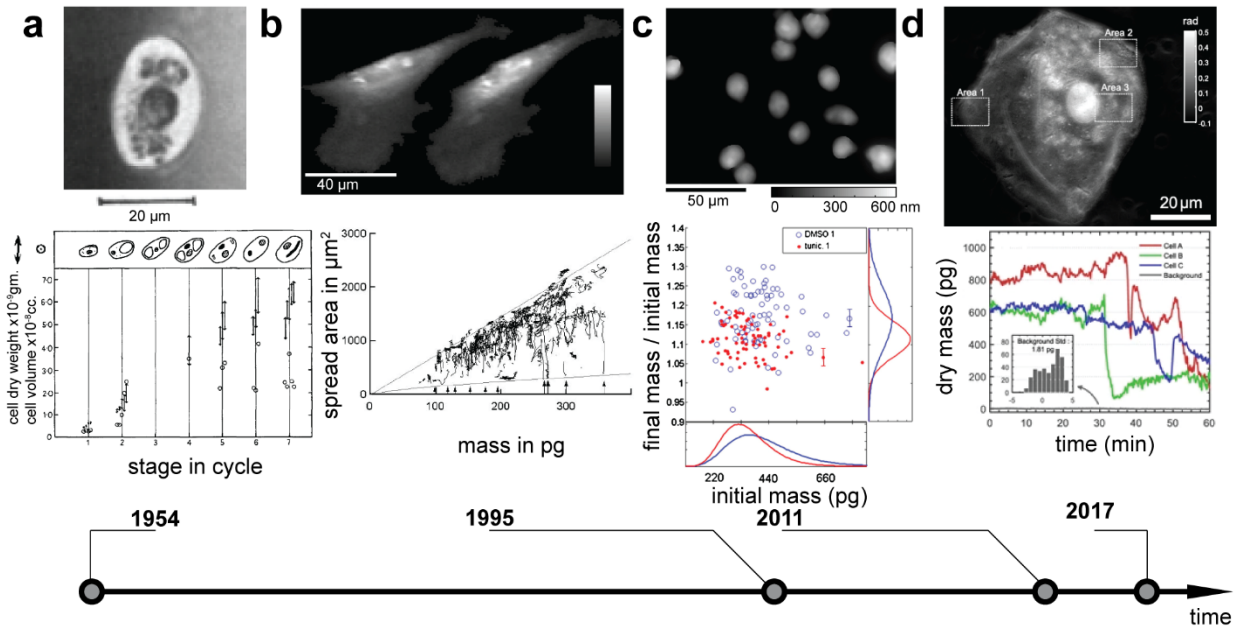

FIGURE 3 The evolution of complexity and information content from QPI measurements of cell dry mass and mass distributions within living cells. Representative images and data analysis are shown in a time series. **(a)** QPI film image of *Tradescantia bractea* pollen grain (top) along with QPI pollen grain dry mass measurements (bottom, upward arrowheads are no sucrose estimates and downward arrowheads show measurements with a 5% sucrose solution) and volume (circles) during different phases of development (Adapted with permission from [151],Copyright 1954 Company of Biologists Ltd.). **(b)** QPI of chicken fibroblasts with dry mass densities ranging from 0.01 (darkest grey) to 0.6 (white) pg/µm^2(top), processed to measure spread area relative to total cell mass (bottom) (Adapted with permission from [163], Copyright 1995 Company of Biologists Ltd.). **(c)** QPI of human H929 multiple myeloma cells (top) showing computationally processed data that simultaneously captures drug responses of hundreds of single cells, shown as initial cell mass versus normalized changes in mass during drug treatment (bottom) (Adapted and dataset with permission from [12], Copyright 2011 Elsevier). **(d)** High resolution QPI of a human buccal epithelial cell (top) and an example of changes in dry mass of HeLa cells undergoing

apoptosis triggered by exposure to cytotoxic paclitaxel (bottom) (Adapted with permission under Creative Commons Attribution (CC BY) license from [159], Copyright 2017 Zuo *et al.*).

Applications of QPI to studies of cell growth and associated biological processes

Several example studies discussed here demonstrate the utility of QPI measurements for providing insight into the regulation of cell size, growth and additional fundamental biological processes. In studies of cell size regulation, QPI measurements during fibroblast cell spreading revealed that the spread area is actively regulated by an undefined mechanism that adjusts the total area of spreading proportionally to the total cell mass[163]. Separately, dry mass quantification using SLIM during the cell cycle showed that osteosarcoma cells exhibit a mass-dependent growth that was best approximated by an exponential rather than a linear model of cell growth[152]. More precise QPI measurements of cell mass revealed oscillations in growth rate that were previously unappreciated, suggesting that a pure exponential model of cell growth is insufficient to explain the regulation of mammalian cell growth[164].

The impact of extracellular perturbations on cell size and growth have also been interrogated by QPI. For example, changes in available glucose[154], or the addition of small molecule inhibitors such as tunicamycin to induce cell stress[12], led to reproducible, QPI-quantifiable changes in cell dry mass and growth rate as indicators of cellular responses. These study results led to the use of QPI as a label-free method for screening different stimulants or inhibitors. Examples include QPI-based screens for agents that cause changes in cell growth rate and cytotoxicity[12, 165]. QPI has also been applied to study the influence of mechanical properties of the extracellular matrix on growth rate, migration, and metastatic potential of melanoma cells[166]. Long-term SLIM studies of cell

growth in epithelial and fibroblast co-cultures examined the influence of cell clusters on neighboring cells, with a few clusters, termed ‘influencer clusters’, showing a strong correlation between growth rate and distance, with potential implications for organogenesis and cancer cell metastasis[166].

QPI has also been applied to study the impact of genetic mutations on cell growth. For example, QPI was used to track the growth and division of primary human melanocytes for 30 days in culture[167]. This study found that proliferative arrest associated with oncogene expression, previously thought to be caused by G0 cell cycle phase senescence, was instead identified as a reversible and conditional mitotic arrest, an observation subsequently validated using clinical specimens. QPI was also used to confirm the impact of transcription factor YAP expression in HEK293 cells as a potential coordinating mechanism between cell and tissue size[168].Finally, QPI also has demonstrated utility for assessing whether different cell states, and transitions between cell states, alters the absolute dry mass or dry mass accumulation or loss rates of cells. One study quantified cell dry mass partitioning between daughter cells during and following cytokinesis and showed that mass asymmetry present at the time of cleavage furrow formation persisted through cytokinesis[11]. Addition of cytoskeleton-disrupting agents with differing mechanisms of action, including latrunculin A, blebbistatin, nocadozole, and cytochalasin B increased the number of daughter cell pairs exhibiting asymmetric dry mass partitioning. This suggested an absence of an active mass partitioning mechanism after cleavage furrow positioning and the requirement for mass adjustments by dynamic changes in cell growth rate, and/or cell cycle time, over the succeeding cell cycle. The lineage non-directed differentiation of human pluripotent stem cells (hPSCs)[169] was also interrogated using QPI measurements of absolute dry mass and changes in

growth and mass redistribution rates prior to and following the induction of differentiation. Study findings included that hPSCs grow at a consistent, exponential rate independent of colony size, with coordinated intra-colony mass movement ceasing with the onset of differentiation. In contrast, growth and proliferation rates decreased by only ~15% during early differentiation despite global changes in gene expression and energy metabolism, suggesting that the regulation of mass and proliferation are independent of pluripotency during early differentiation.

Applications of QPI to studies of immune cell behavior

Another example area of impact is the application of QPI measurements to gain insight into the functions of cells of the mammalian immune system. At the cellular level, the adaptive immune response requires rapid, massive cell growth to support the generation of both effector and long-lived memory cells. QPI, therefore, is well suited to studying the regulation and features of this process. For example, QPI measures of dry mass changes in a binary cytotoxic T lymphocyte (CTL) – cognate cancer- cell killing assay were illuminating. Study results revealed that the cancer cell mass decreased 20-60% over 1-4 h during a successful CTL attack, with a 4-fold increase in CTL mass accumulation rate at the start of killing and a 2-3 fold increase in CTL absolute mass relative to the mass of unresponsive T cells[42]. These results provide a kinetic, quantitative assessment of CTL activation in tumor cell killing and, potentially, a relatively rapid way to identify specific, activated patient-derived T cells for applications in cancer immunotherapy. Furthermore, QPI measurements of reconstituting donor T cells following hematopoietic stem cell transplantation showed mass changes correlated with immune reconstitution within the first few weeks post-transplant, a finding which could guide the withdrawal of immunosuppressive drugs and reduce the likelihood of graft-versus-host disease or cancer relapse[170].

In studies of B lymphocytes, QPI measurements also uncovered rapid mass accumulation and cell proliferation within the first 24 h of B cell activation accompanied by sustained AMP-kinase activation in the absence of energetic stress, an unexpected result because AMP-kinase activity strongly opposes anabolism and constrains mass accumulation in most biological contexts[171]. QPI was also used to measure variability in naïve B cell size and partitioning of mass between daughter cells during B cell expansion, providing support for an *in silico* model suggesting that intrinsic biological noise plays a key role in determining the extent of B cell proliferation, which ultimately determines which cells contribute to an immune response[172].

Applications of QPI to measure neuron behavior

Neuron growth and behavior is another impactful area for QPI applications. Many studies would benefit from imaging with a label-free method that avoids phototoxicity and photobleaching from long duration fluorescence imaging. As an example enablement, label-free QPI separately quantified neuronal body (soma) and projection (neurite) masses, which showed that most mass accumulation during a 5 d *in vitro* neuronal differentiation protocol goes towards the production of new neurite connections rather than strengthening of existing connections[173]. The process of neuronal branching has also been quantified using QPI plus machine learning as an alternative to fluorescent staining[174]. The high sensitivity of QPI has been leveraged to track the transport of individual vesicles within neuronal processes[175]. QPI has also been applied to measure long term (~1 min) responses of neurons to stimulation related to transmembrane ion fluxes[176] as well as short term (~0.1 ms)[164] fluctuations in neuron shape during neuronal spikes[111].

Applications of QPI in biophysics and biomechanics studies

In addition to measuring total cell mass, QPI can also measure the distribution of dry mass within cells. Measurements of intracellular mass distributions and redistributions over time can also reveal cell movement and intracellular transport phenomena. These two features of QPI data collection and analysis are foundational for applications in cell biophysics and biomechanics. In particular, measurements of the movement of mass between cell regions is enabling for applications in intracellular transport, whereas measurements of the shape and structure of a cell and how it changes over time is enabling for measurements of cell mechanics.

Applications of QPI in measuring the physical structure of a cell

Another biophysical application of QPI is to measure the structural features of individual cells and use this information to inform physical models. A recent study showed that the morphological differences in retinal nuclei of mice correspond to a pattern of nuclear architecture common to other nocturnal mammals[177]. Specifically, adult mouse retinal cells showed a spatially organized nuclear refractive index pattern, which contrasted with a more dispersed refractive index pattern uncovered in diurnal pig or immature mouse retinal cells. Simulations of light transmission found that the refractive index pattern in mouse retinal cells more effectively focused light and reduced scattering, suggesting a potential role in enhancing nocturnal vision. This result generated much discussion on the role of refractive index patterns in the nucleus. The appearance of a large phase shift through cell nuclei supports a physical model of a reduced nuclear refractive index[178], which has been validated in other studies reporting a lower refractive index in nuclei than in the cytoplasm[179-182]. These results were further supported by 3D QPI results that also showed a lower nuclear refractive index outside of the nucleolus[183, 184].

Applications of QPI in studies of intracellular transport

Intra- and inter-cellular transport of biomaterials are required for cell growth and function, with patterns of transport providing information on cell behavior, disease states, and cellular responses to changing environmental conditions. Two relatively common, non-QPI methods for studying cellular transport employ fluorescent labels typically attached to biomolecules, or to introduced particles, coupled with live cell imaging[185, 186], and label-free techniques, such as DIC microscopy[187]. Imaging of fluorescently tagged markers provides a high degree of specificity, and can be quite sensitive, but suffers the disadvantages of photobleaching, limiting transport study times, phototoxicity, which can induce cell stress and modify cell behavior, and autofluorescence, which excitation or emission filters may not completely remove[188]. These imaging limitations are irrelevant for QPI, although there is a loss of biomolecule specificity and sensitivity[187]. As discussed previously, QPI, unlike DIC and phase-contrast imaging, also quantifies the dry mass of cells and some tracked intra- and inter-cellular components, such as lipid droplets, revealing that lipid trafficking motion ranges from subdiffusive to active transport[189]. As a label-free method that provides additional quantitative data on cell behavior, QPI is a good option to consider for measurements of intracellular transport.

Imaging interferometry coupled to finite element analysis measured the intracellular transport of dry mass in fibroblasts at low resolution and showed that the kinetic energy of intracellular motility can be several hundred times greater than the kinetic energy of cellular translocation across a surface[190]. Recent improvements in image processing speed and methods are helping to increase the scope of intracellular transport studies available to QPI platform methods. For example, SLIM

measured the label-free diffusion of organelles and vesicles in hippocampal neurons and cardiomyocytes using a Laplace operator, with extended transport study time enabling extraction of diffusion coefficients[175]. SLIM also revealed the 3D time series movement of dry mass in neurons. Results were analyzed using dispersion-relation phase spectroscopy, a method to measure the spatiotemporal decay of the autocorrelation signal of phase[175], and revealed differences between transport in neuronal bodies and neurites, and also between longitudinal and transverse trafficking orientations[191]. Additional SLIM platform studies were inconsistent with purely passive diffusion and suggested advective transport of cargo within neuronal dendrites, also using the dispersion-relation phase spectroscopy analytic technique[175]. A holo-tomographic version of QPI combined with epifluorescence examined mitochondrial network and lipid droplet dynamics inside HeLa endocervical carcinoma cells. Features uncovered included the shape and dry mass dynamics of lipid droplets, endocytic structures, and a multi-organelle spinning phenomenon whose underlying mechanism remains undefined [192].

An alternative to QPI tracking of individual particles is phase correlation imaging. This method measures the temporal decorrelation time of QPI collected data based on fluctuations of cell refractive index as an indicator of intracellular mass transport. A549 lung carcinoma cells were imaged using SLIM and treated with an actin polymerization inhibitor, cytochalasin-D, which showed only small local effects, but also uncovered a distribution of correlation times that is qualitatively different for quiescent and senescent cells, without cell labeling, providing a creative method for identifying quiescent versus senescent cells within a cell population[193]. Another application of phase correlation imaging revealed that intracellular mass transport rates were significantly different for osteoblast cells with different levels of migratory capacity[194]. Studies of

aggressive, highly metastatic HeLa cells using SLIM and dispersion-relation phase spectroscopy revealed that mass transport in the cytoplasm was mainly active (ballistic, directed), compared to the nucleus which showed active and passive (diffusive) components, with faster mass transport in the cytoplasm than the nucleus[195].

Applications of QPI to cell migration assays

QPI provides a label-free alternative method to DIC or phase contrast microscopy for conventional cell motility or wound healing assays. An advantage of QPI in this application is that it additionally captures quantitative information on other cell features. For example, a commercially-available digital holographic cytometry version of QPI was equipped with semi-automated image acquisition, segmentation, and analysis software. Measurements of melanoma cell motility and metastatic potential were highly accurate in a comparison with field-standard measures of wound healing, transwell migration, and invasion assays, with the added benefits of identifying rare hypermotile metastatic cells and an ability to distinguish motility from cell division associated cell displacement[196]. Measurements of cell mass and morphology with the same system could similarly track kinetic epithelial-to-mesenchymal cell transitions in heterogeneous cultures[197]. Finally, optical diffraction tomography, a three-dimensional, label-free QPI-based imaging method, was used to study and quantify the dynamics of NIH3T3 cell migration in a wound healing assay, revealing single cell resolution of subcellular structure behavior and transport that underlies the mechanisms involved in gap closure and closure rate, with potential implications for pharmaceuticals development or re-purposing[198].

Applications of QPI for measuring biophysical cell properties

QPI can measure the distribution of mass within a cell, including the mass due to structural elements such as the cytoskeleton, and how this distribution changes over time. It is, therefore, possible to extract information about the biophysical properties of single cells[193-195], such as effective cell stiffness and cell viscosity, from QPI data. These viscoelastic properties, in turn, underlie cell structure, movement, and function and have increasingly served as biomarkers for diseases[199], cell states[200], and biological transitions[201]. A standard method for measuring cell viscous and elastic properties is to examine stiffness and elastic, dissipative responses to an applied stress. Numerous physically interactive methods have evolved to make such measurements, including by cell deformation using an AFM[202, 203], or by using external and intracellular introduced probes, as in particle tracking microrheology[203-205]. The use of probes[206] and applied stress[207], however, can affect cell behavior and impact measurements of cell viscoelasticity. Thus, the use of non-interactive techniques, such as those based on QPI, could circumvent or at least minimize these potential confounding influences.

QPI measurements of viscoelasticity divide into two main categories: (1) static measurements based on the spatial distribution and structure of mass within cells, including the cell cytoskeleton, and (2) dynamic measurements of changing cell mass distributions based on the temporal redistribution of mass. Early QPI dynamic measurements of viscoelasticity utilized sustained and rhythmic, temporal actuation and relaxation of magnetic beads as a form of spherical indenter, to induce local, transmitted stress on fibroblasts and observe the resulting mass redistribution and cell stiffening over time[31]. Actuated magnetic beads and QPI measurements also probed different cell types with and without cytoskeletal disruptions[207] (**Figure 4a**), whereas an optical stretching method was also applied in conjunction with DHM to examine differentiating marrow precursor

cells for changes in subcellular structure and refractive index[208]. A key disadvantage in these studies, however, is that they required the use of non-native probes. By contrast, probe-independent, noncontact studies of RBCs used QPI to measure fluctuations in cell shape, coupled to a mechanical model of the relatively simple discoid structure of RBCs. This method was then used to quantify changes in RBC membrane shear, area, and bending moduli during transitions from discoid to abnormal echinocyte and spherical shapes, with potential implications for circulation and oxygen delivery to tissues[209] (**Figure 4b**). However, this method requires a mechanical model, which in this case is limited to enucleated RBCs. More recent noncontact studies linked static QPI measurements of mass distribution in nucleated cells to spatial disorder strength, a measure of mass organization within cells including the cytoskeleton (**Figures 4c**), to HT-29 colon cancer cell shear stiffness[210] and the elastic moduli of two breast cancer cell lines (MCF-7 and BT-474 cells) [211]. Dynamic QPI measurements of mass redistribution rates for MCF-7, BT-474, and HeLa cells quantified both cell stiffness and elastic moduli during growth (**Figure 4d**) and during an epithelial-to-mesenchymal cell state transition[212]. Combined, these and future studies suggest a powerful and emerging opportunity for QPI to quantify cellular biophysical and biomechanical properties that traditional biochemical, molecular, and cell biology measurements alone cannot provide.

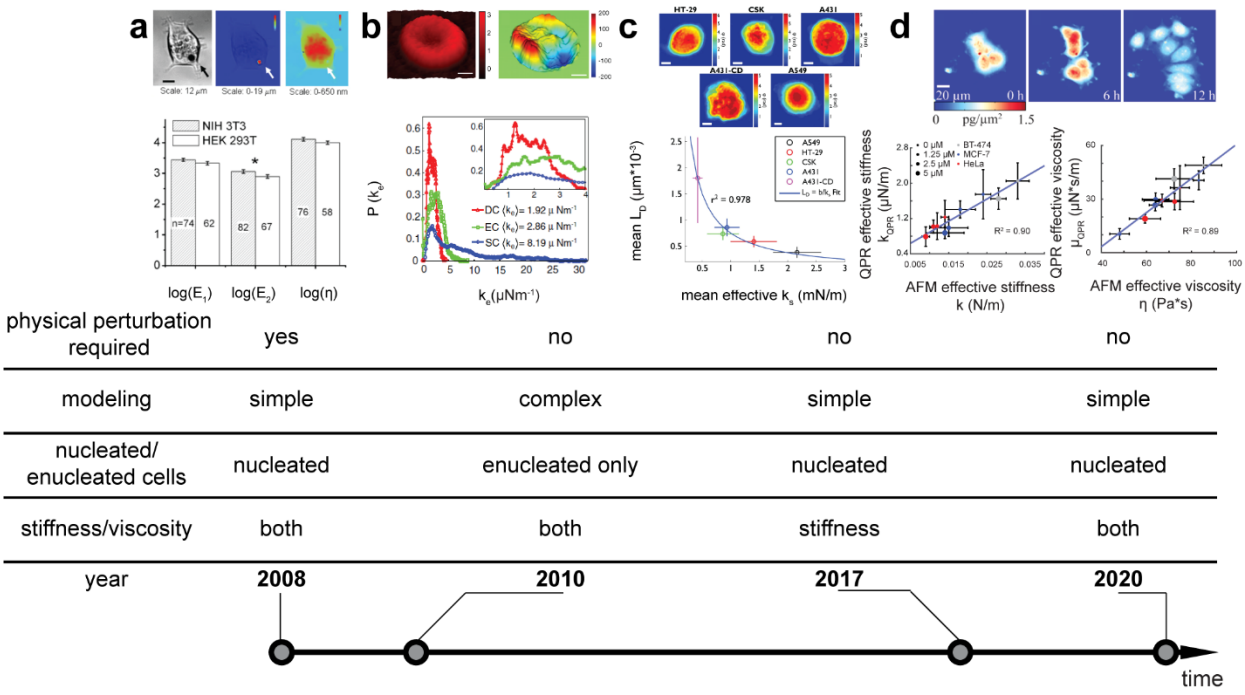

FIGURE 4 QPI biomechanics measurement evolution. **(a)** Early QPI biomechanical analyses required physical perturbations, such as actuation of a magnetic bead indenter on NIH3T3 fibroblasts (top) or HeLa carcinoma cells to extract Young's modulus (*E*; bottom) (Adapted with permission from [207], Copyright 2008 IOP Publishing Ltd.). **(b)** Detailed mechanical modeling from contactless measurements of biomechanical properties of red blood cells (RBCs; top left) using natural fluctuations in phase caused by membrane motion (top right) captures mechanical property variations (bottom) for populations of normal (DC), speculated (EC), and spherical (SC) shaped RBCs (Adapted with permission from [209], Copyright 2010 National Academy of Sciences, U.S.A.). Scale bar = 1.5 μm. **(c)**QPI phase (top-middle) of more complex cells HT-29 wild-type and shRNA (top left), HT-29 with CSK shRNA-mediated knock down (top middle), A431 epidermoid carcinoma control (top right) and cytochalasin D treated A431 (middle left) cells, and A549 lung adenocarcinoma cells (middle right) used to compute a mean phase disorder strength, related to intracellular cytoskeletal structure and independent measurements of shear stiffness (bottom)

(Adapted with permission from [210], Copyright 2017 Elsevier). **(d)** Time lapse QPI data (top) showing the redistribution of mass within single cells and cell clusters, which provides both resistance to deformation and decay terms. These terms were validated by comparisons with AFM measurements of stiffness (bottom left) and viscosity (bottom right) for MCF-7 and BT-474 breast carcinoma cells, and for HeLa endocervical carcinoma cells, treated with different concentrations of cytochalasin B (Adapted with permission under Creative Commons Attribution (CC BY) license from [212], Copyright 2020 Nguyen *et al.*).

Emerging QPI applications in preclinical and clinical studies

There are a growing number of potential applications for QPI in clinical studies, with current studies mainly at the technology development, applications and validation stages. There are at least two major directions under development for QPI aiming towards clinical applications (**Figure 5**), which are (1) measurements of cell dry mass changes in response to therapeutic agents (**Figure 5c**) and (2) measurements of cell morphologies and disease states (**Figures 5a, 5d**). These applications leverage QPI for quantitative and label-free measurements of individual cells and cell clusters.

QPI biomass applications in screening and drug therapy

Changes in dry cell mass detected by QPI has been used to measure single tumor cell sensitivity to cancer therapeutics[213]. The range of applications shown includes evaluating mitotic inhibitors with different mechanisms of action[214], examining the rate and extent of cancer cell escape and re-growth following senescence induction[215], and uncovering the response heterogeneity of a mixed sensitive and resistant cancer cell population to specific drug treatment[53]. Because QPI can track

the kinetics of dry mass growth responses of individual cells or clusters of cells within large populations of cells over time, heterogeneous cell responses to therapeutics are readily identified. For example, rare drug resistant diffuse large B cell lymphoma (DLBCL) cells within a population of DLBCL cells sensitive to a PI3-kinase inhibitor, idelalisib, were identifiable by continued mass accumulation and could, in concept, be isolated and recovered for further studies[53, 213, 216] Pre-clinical dry mass accumulation rate studies using patient derived xenografts predicted drug sensitivity for triple negative breast cancers, providing a potential QPI application for drug selection in the emerging area of personalized oncology[217, 218] (**Figure 5c**). A separate drug screening in breast cancer study applied QPI to capture drug sensitivity that was consistent with findings from current standard approaches, as well as multiple additional physiologically relevant parameters that characterized cell responses to therapy[219]. As discussed above, QPI measured viscoelasticity can differentiate between epithelial and mesenchymal states[212], a state transition that is a cardinal feature of cancer cell metastasis, and phase correlation imaging discriminated between quiescent and senescent cells, with potential implications for drug resistance and tumor reemergence[193].

QPI morphological applications in diagnostics

Anatomic pathologists have long used changes in cellular morphology and tissue architecture to diagnose disease, as changes in morphology represent changes in cell state and function as, for example, plasma membrane blebs can indicate dynamic cytoskeleton-regulated cell protrusions in apoptosis, cytokinesis, and cell movement[220]. Accordingly, diagnostic applications of QPI focus on cell state to provide a diagnostic tool with early attempts using features from QPI images to screen for cancerous tissue[221]. QPI tissue spatial correlation, a measure of refractive index map

correlation length that may represent nanoscale cell morphology in fixed tissue samples, provided a biomarker that distinguished between malignant and benign breast cancer biopsy samples[222]. When combined with dry mass measurements, QPI identified and classified different kinetic states for a population of melanoma cells in culture[223]. In applications with RBCs, morphology studies using QPI identified *Plasmodium falciparum* infection of RBCs[224] and suggested the possibility that QPI measurements of cell membrane dynamics could identify additional pathologies that cause or accompany other human diseases[223, 224] (**Figure 5a**). QPI using white light interferograms with red, green and blue wavelengths separated electronically helped determine morphological features of RBCs[225], as did using DHM with data clustering and discriminant analysis[226]. "Real time" QPI measurements of blood samples have been demonstrated, utilizing parallel computing strategies to calculate diagnostically relevant cell parameters without storing phase images, allowing for smaller electronic storage and data transmission requirements, which could benefit remote diagnoses of RBC diseases[227]. QPI has also been used to measure morphology changes in *HTori* thyroid cells during treatment with plasma from a nanosecond dielectric barrier discharge[228], changes in macrophages from chemically induced apoptosis and dynamic phagocytosis[162], and for sperm selection for bovine *in vitro* fertilization[229]. SLIM and tissue spatial correlation analysis was used to assess breast cancer fixed tissue microarrays and showed a 94% sensitivity and 85% specificity for cancer detection[230] (**Figure 5d**), independent of tissue staining quality.

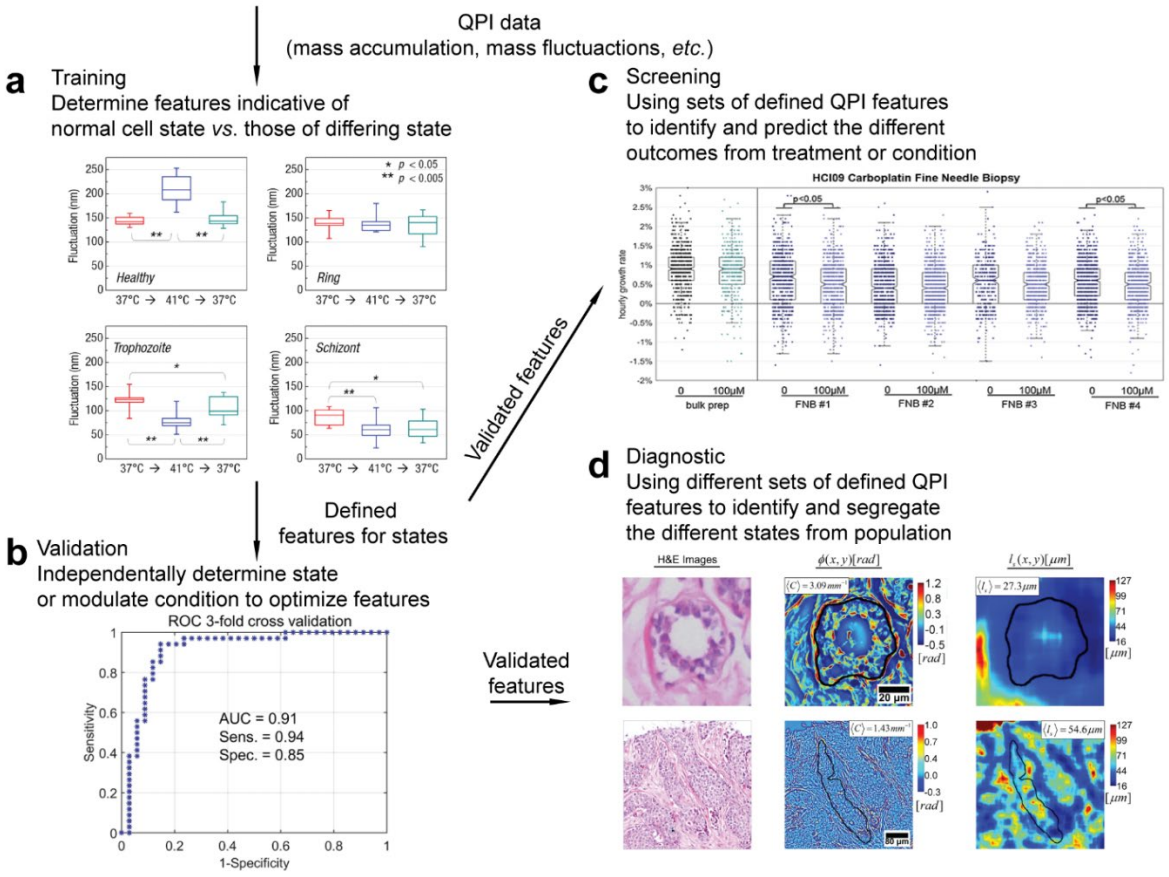

FIGURE 5 Progress towards QPI clinical applications as a screening and selection tool for treatments, and as a diagnostic tool to identify healthy versus diseased states. **(a)** Specific QPI features can be used to identify disease or changes from a healthy or control state. For example, QPI measured differences in RBC membrane fluctuations at 37°C and 41°C *in vitro* can distinguish between healthy and ring, trophozoite, or schizont diseased states with *P. falciparum* parasitic infection (Adapted with permission from [224], Copyright 2008 National Academy of Sciences, U.S.A.). **(b)** Once QPI features of interest are identified, validation is sought with an independent, orthogonal method, if available. For example, shown here is an area under the curve (AUC) or receiver operating characteristic (ROC) plot of the true positive (sensitivity) versus false positive (specificity) rate determining malignance from hematoxylin and eosin counter-stained tissue biopsy. This previously validated method is used to validate QPI determined malignant state for

breast tissue biopsies (Adapted with permission under Creative Commons Attribution (CC BY) license from[230], Copyright 2018 Majeed *et al.*). **(c)** Validation of a QPI measured feature in a specific context can broaden its utility. For example, validation of QPI measured changes in growth rate was successfully applied to identify effective treatments from a pool of candidate agents against carboplatin-resistant, patient-derived xenograft HCI09 breast carcinoma cells (Adapted with permission under Creative Commons Attribution (CC BY) license from [218], Copyright 2019 Murray *et al.*). **(d)** Example of QPI as a diagnostic tool, with spatial light interference microscopy (SLIM; middle and right columns) identification of benign (top row) versus malignant (bottom row) glandular tissue, validated by pathological classification of hematoxylin and eosin stained biopsy material (left column) (Adapted with permission under Creative Commons Attribution (CC BY) license from [230]. Copyright 2018 Majeed *et al.*).

ONGOING DEVELOPMENTS

Quantitative phase tomography

The transition from generating two-dimensional (2D) quantitative phase images to tomographic images that capture the 3D structure of specimens is an ongoing development in QPI. While 3D imaging is fairly common with fluorescent biomarkers using confocal or widefield microscopy and digital image processing reconstruction[231], the use of fluorescence tags has disadvantages that include photobleaching and phototoxicity with increased imaging time[232]. Imaging based on the inherent contrast provided by natural variation in refractive index eliminates these label-related problems. Tomography refers to the stacking of 2D planes or images acquired at multiple imaging angles to reconstruct 3D structures of specimens called tomographs. Although the principle of interferometric tomography was proposed in the 1960s[233] and experimentally demonstrated in the

1980s[234], tomographic image reconstruction was too computationally intensive to be routinely used for QPI until decades later[235]. Reconstruction of quantitative phase tomography from scattering images of polystyrene beads using Mach-Zehnder interferometry[236], and then polystyrene foam from DHM images was demonstrated[237], followed by measurements of the 3D refractive index and the absorbance profile of optical fibers using phase retrieval and tomographic reconstruction[238](**Figure 6a**).

Whereas 2D QPI measures the integral of Δn, the refractive index of the sample relative to the surrounding media through the thickness of the sample in each imaging pixel, Quantitative phase tomography maps Δn within each voxel. Advances in tomography have focused on increased precision and accuracy of 3D refractive index mapping using DHM assisted tomography[239] (**Figure 6b**). Tomography has also been developed from phase shifting interferometry[240], and light-emitting diode (LED) array microscopy, which forms the basis of DPC phase reconstruction[63, 241]. LED array systems are capable of an impressive 0.25 s acquisition time, made possible with optimized sample illumination[242] (**Figure 6c**). Another method for acquiring tomographic images for use in image reconstruction is by acquisition of holographic phase images at a series of angular projections using illumination with a rotating fiber optic, resulting in a 1 Hz imaging rate[243]. Intensity diffraction tomography using annular LED illumination has improved imaging speed, and achieved diffraction limited resolution[244].

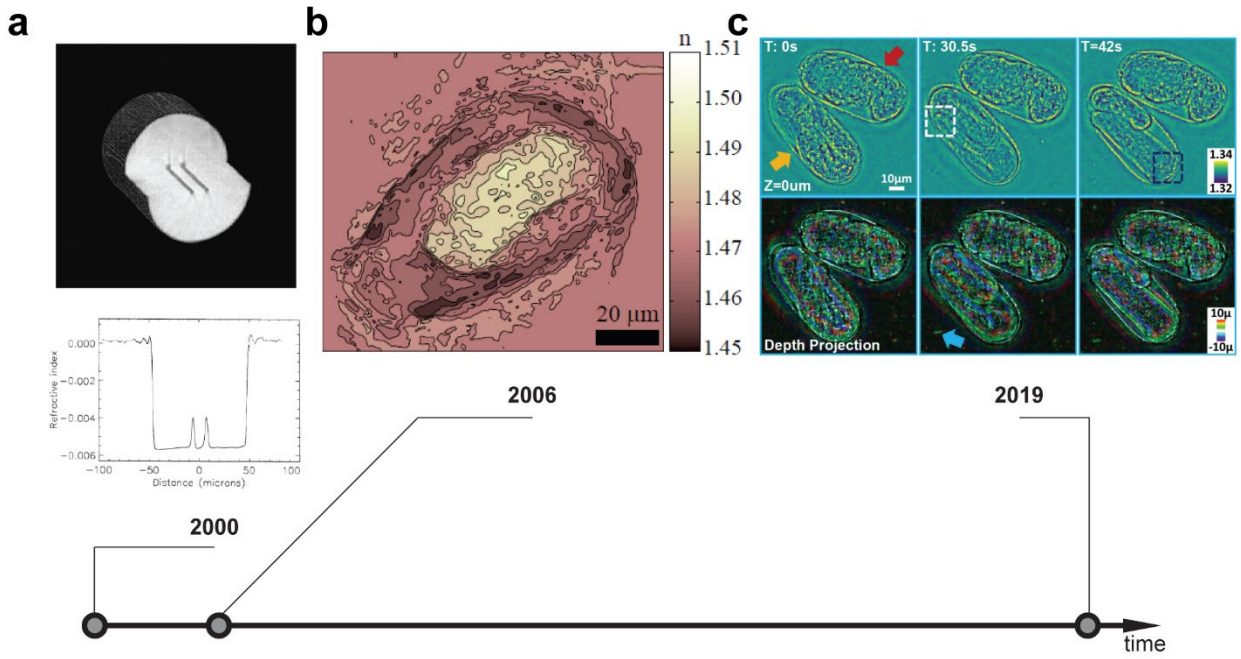

FIGURE 6 Progress in QPI tomography from applications with static optical fibers to multicellular organisms. **(a)** QPI tomography analysis of cross-sections of optical fibers (top). A common feature of QPI tomography is recovery of the 3D refractive index distribution, rather than the integrated refractive index through the sample thickness, as in 2D QPI. This is shown by the refractive index distribution measured as a line profile through the sample (bottom) (Reproduced from [238], Copyright 2000 Elsevier). **(b)** QPI tomography of single cell protozoan, *Hyalosphenia papilio*, with refractive index reconstructions shown as different 2D slices (Adapted from [239],©2006 The Optical Society). **(c)** Multiplexed intensity diffraction tomography of multicellular *Caenorhabditis elegans* embryos. Shown are in-focus refractive index (top row) and depth-coded projections of volumetric reconstruction (bottom row). Red and orange arrows indicate developmental stages of the embryos. Individual developing tissues, the buccal cavity (white box), intestine (blue box), and native bacteria (blue arrow), are visible (Reproduced with permission from [242], ©2019 The Optical Society).

A promising application of tomographic QPI to measure subcellular structures is the interrogation of biomolecular condensates, which are membrane-less organelles or organelle subdomains that have been implicated in a wide range of cell behaviors including bone metastasis [245] and autophagy[246]. The process of phase separation has been studied with 3D QPI with identification confirmed by fluorescence[247]. Future applications of QPI tomography can be combined with other QPI data analysis methods to reveal the essential biological mechanism(s) behind these structures. Another promising application of QPI tomography is the measurement of mass within multicellular specimens, such as whole animals[240] (see *in vivo* section, below), or 3D organoids that are often used as *in vitro* models of development or disease[248]. [245-247]Gradient light interference microscopy (GLIM) developed by combining aspects of DHM, DIC microscopy and low coherence interferometry enables 3D imaging of samples ranging from single cells to intact embryos for measurements of internal structures and their evolution in time[249]. Optical projection tomography uses DHM and analyzes movies of flowing samples to acquire images at multiple angles, resulting in reduced imaging time and a non-invasive solution for phase measurements of RBC aggregation[250], an offshoot of which is called limited-angle holographic tomography. White light diffraction tomography performed by deconvolution of QPI stacks generates high-resolution QPI data of intracellular structures[183]. Quantitative oblique back-illumination microscopy (qOBM) enables tomography of a wide range of samples, from thick highly scattering[248] to opaque[251] samples, by using multiple scattering paths generated within the sample to create an effective light source deep within the sample despite illuminating the sample in epi-mode. Overall, these selected example applications and approaches in quantitative phase tomography show that the ability to view and quantify sample features in 3D is very powerful. Since quantitative phase tomography is another QPI approach that relies heavily on computation for generating and processing 3D data,

this area will continue to benefit from ongoing advances in computing power and analytic software.

QPI in tissues and *in vivo*

There are ongoing efforts to apply QPI to tissue slices and the *in vivo* environment to limit the confounding effects of studying cell behavior *in vitro* (**Figure 7**). However, there exists several roadblocks to fully realizing this goal, including light scattering of thick samples, phase unwrapping errors due to long optical path lengths through thick tissues, and the small size of microscopes needed for imaging inside living organisms. One approach is to continue modifying techniques that have already been adapted for *in vivo* imaging for phase retrieval. A key example of this approach is the use of optical coherence tomography (OCT). OCT is a low-coherence interferometry method that leverages low temporal coherence to exclude scattered light outside a tissue slice of interest, coupled with backscattering of light, to image cross-sectional areas of tissues *in situ*[252, 253]. An early approach added phase retrieval to OCT to enable QPI of human cheek cells(**Figure 7a**)[254] and isolated chicken cardiomyocytes[255]. Phase sensitive OCT has also been extended into *in vivo* imaging of the human retina[256] and its' associated motion[257]. However, despite great improvements in phase stability, there is a still often a need for either manual or automatic phase unwrapping to correct for phase errors with this emerging technique.

Another adaptive approach is to use QPI methods developed in an *in vitro* setting to address issues of light scattering in thick samples and phase unwrapping and then translate them for *in vivo* imaging through miniaturization. This has led to attempts to miniaturize certain platforms, such as diffraction phase microscopy (DPM), into an endoscope (i.e., eDPM)[258], or to making a fiber optics

based qOBM system[259]. Demonstrations of these techniques have so far been limited to *ex vivo* imaging. The eDPM system has been used to measure stained white blood cells[258] and a similar holographic endoscope method was applied to mouse esophageal tumor samples[260], whereas the fiber optics qOBM imaging system has examined gliosarcoma cells from excised and formalin-fixed rat brain tissue(**Figure 7c**)[259]. The most definitive application of *in vivo* QPI has been DHM imaging of red blood cells in micro capillaries within the mesentery of live mice (**Figure 7b**)[261]. By using 2D holograms from different angles, Sung *et al.* was able to reconstruct a 3D tomogram via optical diffraction tomography [262]. Overall, work so far in this area points toward a bright future of applying various *in vitro* quantitative phase approaches to studies of mass regulation, biophysics, and the building of diagnostics based on QPI measurements of cells *in vivo*.

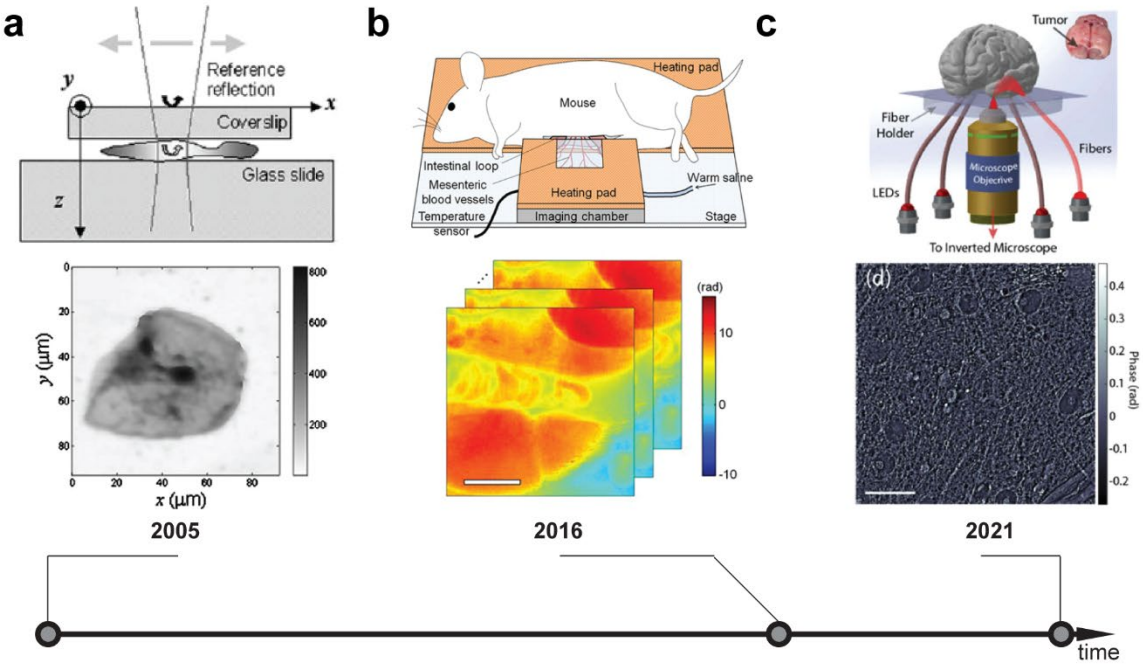

FIGURE 7 Progression of *in vivo* QPI approaches. **(a)** Sample preparation for an *in vivo* technique called spectral-domain optical coherence phase microscopy (SD-OCPM; top) which generated optical path difference maps for human epithelial check cells (bottom) (Adapted from

[254],© 2005 The Optical Society). **(b)** Diagram of live mouse heating stage setup for *in vivo* QPI (top). Representative QPI data from a live mouse mesentery showing mouse microvasculature represented as optical phase delay maps reconstructed from holograms (bottom) (Adapted with permission under Creative Commons Attribution (CC BY) license from [261], Copyright 2016 Kim *et al.*). Scale bar = 10 μm. **(c)** Schematic of a fiber-based quantitative oblique back-illumination microscopy (qOBM) platform for imaging tumor tissue in excised rat brain (top), thereby generating QPI images from deconvolution of intensity images (bottom) (Adapted from [259], © 2021 The Optical Society.). Scale bar = 50 μm.

Multimodality approaches

A key advantage of QPI is that it is label-free and captures data on all components that contribute to cell mass. However, a related limitation is that QPI data is not specific for any individual component of the cell. Therefore, a number of approaches and studies have combined QPI with other imaging modalities to learn more about cell structure and behavior (**Figure 8**). Two of the most promising connections are the combination of QPI with fluorescence detection through the tagging of specific molecules, and the combination of QPI with vibrational spectroscopy, for label-free measurements of chemical compositions within the cell.

Early combinations of fluorescence detection methods with QPI approaches[263] to interrogate RBCs measured physical and optical thickness[264], resolved substructures within cells[265], and identified and characterized the mass distribution of subcellular components[263, 266] (**Figure 8**). These initial approaches demonstrated QPI identification and measurement of different subcellular components within a cell that were manipulated to fluoresce. Fluorescence combined with QPI has also been

used to segregate different populations of cells in a mixed culture experiment[53], track the behavior of rare subpopulations of primary human cells *ex vivo*[167], or to determine different cell states[212] concurrently with mass accumulation and mass density measurements from niche cell populations. Dual fluorescence plus QPI combinations have also enabled biomechanical interrogations of cell responses to optical tweezers[267] and dual traction force and growth measurements[268]. The combination of SLIM and an epifluorescence traction stress imaging method, Hilbert phase dynamometry[269], was used to study mesenchymal stem cell growth and differentiation into osteocytes and adipocytes. Results showed that during osteogenesis and adipogenesis, greater force is exerted by these cell types on their growth substrates than by mesenchymal stem cells, which develop the least force and show the lowest growth rate[268].

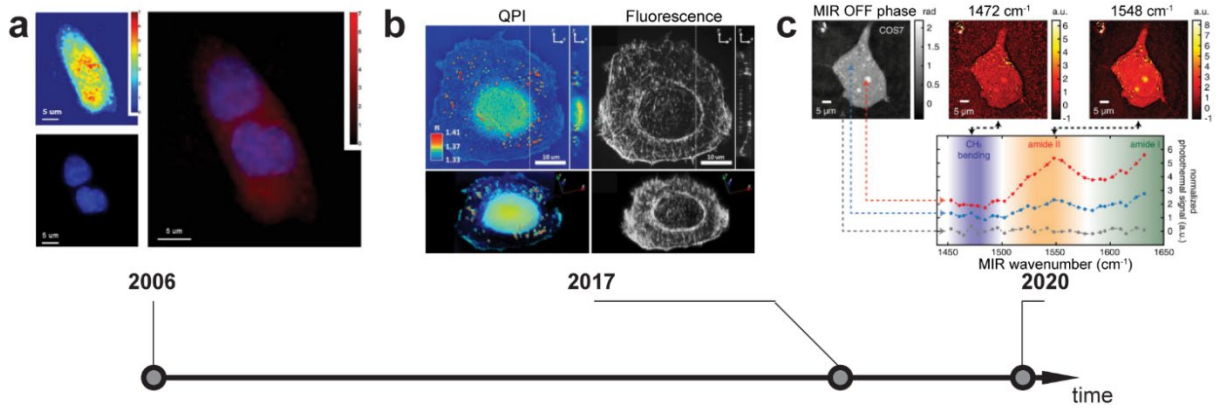

FIGURE 8 Examples of the opportunities available from coupling QPI with additional imaging modalities. **(a)** QPI of kidney cells paired with fluorescence detection enables the identification and quantification of dry mass changes, represented by phase shifts, within subcellular regions (right), such as the nucleus, identified by Hoechst staining (bottom left) (Reproduced with permission from [263], © 2006 The Optical Society). **(b)** Enhanced fast image acquisition of dual 3D fluorescence (top right) and refractive index measurements from tomographic QPI (top left). This accelerated approach provides the necessary capture speed in image scanning to reconstruct 3D

tomograms of A549 cells for both fluorescence (bottom right) and QPI (bottom left) measurements from z-step data (Adapted with permission from [270], © 2017 The Optical Society). **(c)** Molecular vibrational spectroscopy paired with QPI of COS7 cells (top left) examined for molecular signatures, such as CH_2 (top center) and peptide bending (top left), corresponding to subcellular phase shifts within the nucleus (orange), cytoplasm (blue), relative to empty space control (grey) (bottom) (Reproduced with permission from [271], © 2020 The Optical Society).

In general, combined 3D QPI/ 3D fluorescence techniques can differentiate subcellular components while rendering a map of cell refractive index[272] and identifying the refractive index of subcellular regions[273]. Combined 3D fluorescence detection and refractive index tomography on cells with fluorescently labelled nuclei, mitochondria and actin enabled registration of the refractive index profile with the labeled subcellular components[274]. Optical diffraction tomography has also been used in combination with 2D fluorescence to validate measurements of lipid content[272]. Moving towards the acquisition of functional data from 3D structure, studies using combinations of refractive index tomography with fluorescence sub-diffraction microscopy enable concurrent studies of cell biophysical properties and biochemical functions[265, 270]. Further advances include high-speed correlative 3D QPI/3D fluorescence techniques[270], which have evolved to enable 200 Hz imaging of 4D maps of cell structures[275]. With the addition of machine learning, more advances are possible due to the vast amount of morphological and molecular data collected by dual fluorescence QPI combination modalities, thereby enabling more complex analyses.

Another multimodal approach of interest is the combination of QPI with molecular vibrational spectroscopy to measure chemical composition (**Figure 8c**). Extracting chemical composition from QPI alone has been attempted as quantitative phase spectroscopy (QPS), but with limited success. QPS uses phase measurements over a range of wavelengths to estimate the component distributions in samples. This approach has been applied to measure hemoglobin[276] or BSA[277] concentrations in solution, and has been applied to measure healthy[277] and diseased[278] RBCs. This approach has also been extended to 3D tomography[279]. However, using this approach to decipher more complex cellular contents is limited by the relatively small variation in phase delay of biomolecules in visible light. Molecular vibrational spectroscopy techniques generate vibrational spectra of molecules measured from their linear absorption and inelastic light scattering[280]. These vibrational spectra are dependent on the chemical structure and environmental interactions of the molecules and thus can provide information on the chemical composition of materials. Raman spectroscopy, which is a type of vibrational spectroscopy, relies upon the inelastic scattering of photons to determine the vibrational modes of molecules, allowing for the detailed identification of chemical composition. However, use of scattering spectroscopy methods may generate an issue with limited signal in applications with live cells. To overcome this limitation typically requires either high illumination power, which induces phototoxicity, or metal probes for surface enhanced Raman, which can foul in solution environments. Nonetheless, label-free identification of chemical compositions within cells is an ideal complement to the less specific biomass information obtained with QPI.

Dual modality QPI plus molecular vibrational spectroscopy has been applied with a mid-infrared light source to characterize specific molecular contents with cellular mass distributions[271]. Raman

spectroscopy has been applied to characterize both the morphological dry mass and chemical composition within cells[281]. Combined Raman QPI approaches have also examined dry mass, mass density, and protein and lipid composition under ultraviolet radiation[282], and with the help of machine learning classified normal and cancerous tissues[283]. Combined, QPI with molecular vibrational spectroscopy enables the examination of chemical composition and biomass kinetics (**Figure 8c**), to further dissect core biological mechanisms and processes.

Brillouin microscopy is a noninvasive, label-free microscopy method to measure viscoelastic properties of cells and tissues[284] that has also been combined with QPI. Brillouin microscopy uses inelastic scattering to determine the viscoelasticity of heterogeneous materials of known density and refractive index. Brillouin microscopy was combined with optical coherence tomography to study biomechanical properties in tissues, including stiffness, elasticity and structural changes in embryos[285, 286]. Brillouin microscopy has also been combined with optical diffraction tomography and fluorescence microscopy to measure the refractive index, density and elasticity of specific fluorescently labelled structures inside cells[287].

As a label-free method based on brightfield microscopy, QPI can be added to other microscope imaging modalities beyond fluorescence and vibrational imaging methods. For example, quantitative label-free imaging with phase and polarization (QLIPP), a combination of defocused QPI and polarization microscopy, can measure volumetric phase, retardance and orientation, which is useful for studying structures in cells and tissue slices[288]. There is, therefore, a broad potential future for multimodality work in biological and potential clinical applications of QPI.

Machine learning

Machine learning has propelled many recent advances in QPI, such as improving phase reconstruction for QPI images, improving segmentation and tracking for processing QPI data, and improving data labeling and classification (**Figure 9**). In terms of pre-processing, machine learning can help improve the reliability of phase reconstruction algorithms. Most work applying machine learning to QPI uses convolution neural network (CNN) variants, such as U-Net[289]. CNN is well suited for phase recovery as it considers multiple pixels in the process of data condensation, unlike perceptron models that use individual pixel input[290]. For example, in the area of phase retrieval, machine learning has been used to reconstruct TIE results with a single intensity image, and can eliminate errors arising at the boundaries of images during TIE reconstructions as well as the impact of noise[87]. Machine learning can also benefit wavefront sensing[290, 291]. For example, a diffuser can be used to generate random speckles that then work as a wavefront sensor, when combined with a neural network trained on phase objects[292]. Phase unwrapping is often an issue in interferometric methods[43], and a one-step correction for phase unwrapping errors has therefore been introduced using machine learning methods[293]. Holographic image reconstruction has also been performed from single intensity images using machine learning, with validation on pap smears and human tissue samples[88].

Machine learning is also helpful in QPI data post-processing steps. Here, CNNs are the most widely used approaches as well. Machine learning networks have been designed to segment microscope images[294], and process cell tracking data, counting, and characterization[295]. Machine learning algorithms on unlabeled QPI images can compute or false-colorize staining patterns created by computer labelling of different organelles and components within cells. For example, machine learning can be used to identify lipid droplets in unlabeled QPI images[296]. A related

machine learning approach, called PhaseStain, was developed for label-free staining of QPI images[297]. This method has been extended for real-time staining and classification of sperm cells[298], identification of cells from subcellular components[299], and generation of pseudo-fluorescence images from label-free QPI data[297, 300]. The change in dry mass of subcellular structures has been measured over time using phase imaging with computational specificity (PICS), which segments QPI data with machine learning approaches[301].

One especially promising application of machine learning methods for QPI studies is in the classification and identification of cells and tissues. Classification schemes using machine learning algorithms can help reduce the time and labor involved in traditional pathology, while the label-free nature of QPI simplifies data collection. Statistical classification from QPI data was demonstrated using basic feature recognition algorithms for the classification of microorganisms[302, 303]. Similar classification schemes were later improved using machine learning approaches[304, 305]. Machine learning has since been used with QPI data for classifying specific cell death pathways[306]; categorizing the health and quality of human spermatozoa for *in vitro* fertilization[307 308]; screening red blood cells for hematologic disorders[309, 310] including sickle cell disease[311] and malaria[312]; and identifying and classifying microorganisms[313]. In cancer studies, machine learning has been applied to QPI data for scoring cancer cells as epithelial or mesenchymal in origin[314], phenotypic profiling of cancer and non-cancer cell lines[315], as a diagnostic tool in pancreatic cancer[316], and to quantify dynamic responses of melanoma cells to therapy[223] (**Figure 9d,e**). Machine learning with QPI in combination with data from additional techniques helps increase the accuracy of classification, as it increases the number of data inputs into selected classification methods. For example, QPI, fluorescence, and Raman spectroscopy

have been combined as inputs into a machine learning algorithm to detect macrophage activation[317]. Raman imaging and QPI combined with machine learning has also been applied to recognize stages of B cell acute lymphoblastic leukemia[318]. Overall, machine learning is poised to play an ever-increasing role in both the generation and interpretation of QPI data, and has already touched upon nearly every major application of QPI.

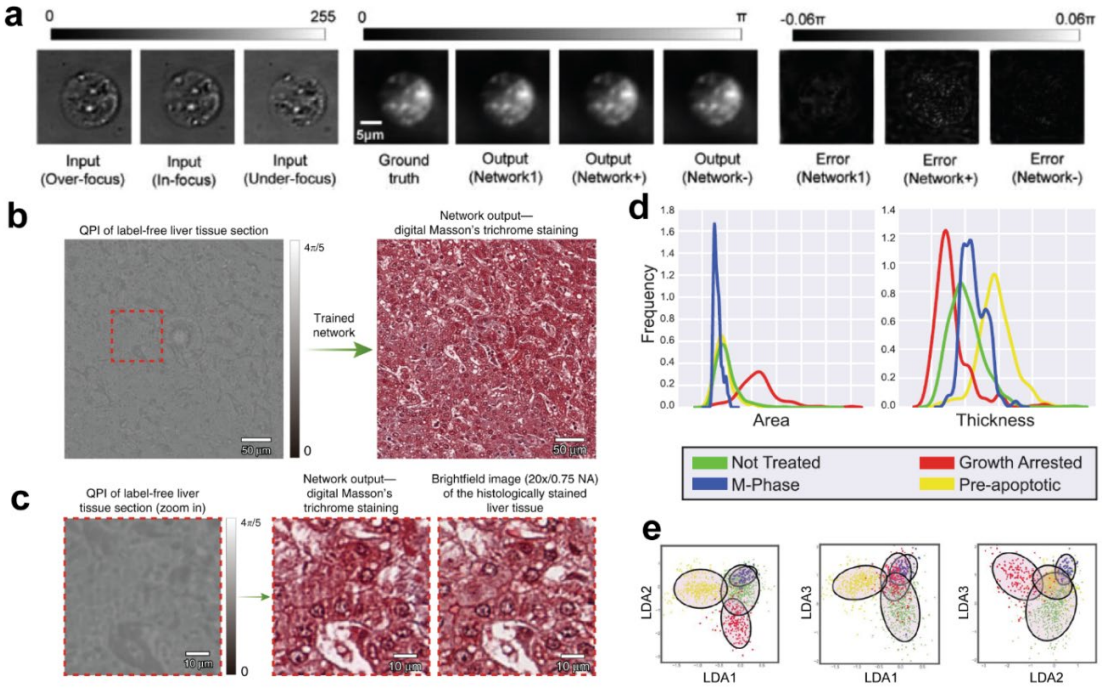

FIGURE 9 Machine learning has been applied to all three stages of a typical QPI processing and analysis pipeline: 1. computation of phase data, 2. labeling of phase images, and 3. feature-based cell classification. **(a)** Phase image reconstruction from a single over-focus or under-focus image using deep learning and transport of intensity (TIE) algorithm. The error of phase calculation using the combined deep learning TIE method is under 0.06 π for the 'Network+' learning-based method using one over-focus image and the 'Network-' method using an under-focus image when compared to the ground truth calculated from three images using TIE (Reproduced with permission from [87], Copyright 2020 Elsevier). **(b)** PhaseStain is a digital staining

method developed using deep learning on holographic microscopy images, to perform virtual staining of tissues from label-free QPI images. The stained images produced are similar to histological staining observed under a brightfield microscope. **(c)** A zoomed-in view comparing the liver tissue section stained using PhaseStain and Masson's trichrome staining (Reproduced with permission under Creative Commons Attribution (CC BY) license from [297], Copyright 2019 Rivenson *et al.*). **(d**, **e)** Machine learning to classify cell states during the epithelial-to-mesenchymal transition (EMT). M-phase, pro-apoptotic, and growth-arrested cell states occurring during EMT can be distinguished from untreated control cells using machine learning, utilizing cell features identified from QPI (Reproduced with permission under Creative Commons Attribution (CC BY) license from [223], Copyright 2017 Hejna *et al.*).

CONCLUSIONS AND PERSPECTIVE

QPI is an approach with a long history. However, the last two decades have seen great leaps in both the abilities and applications of QPI. The rapid recent development of QPI is from impressive advances in image processing capabilities enabled by digitalization and increasing computational power (**Figure 1a**). This development and application of computational tools has substantially increased the utility and power of QPI in its application to biomedicine and permitted the development and commercialization of prebuilt and user-friendly QPI platforms. Consequently, recent years have witnessed a surging interest in QPI, coupled to a dramatic increase in QPI enabled publications and discoveries (**Figure 1b**). This marked expansion of QPI applications is also being fueled by leveraging machine learning approaches and is increasingly impacting areas that are beginning to include disease diagnoses and measurements of biological state transitions. While exciting, this recent and rapid adoption of QPI platforms and associated published studies

has also highlighted the dearth of standardization tools and practices beyond the adaptation of polystyrene beads[124] as phase standards. Developing and circulating such tools will be critical for reproducible studies and validation of future QPI-based diagnostics and other applications.

Current areas of QPI utility include studies of cell size and its regulation, cellular diagnostics and screens, and biomechanics and biophysics. One key strength of QPI approaches includes label-free classification of key cellular behaviors such as programmed cell death pathways, differentiation, cell cycle progression, and immunological responses. Assessing these behaviors in the context of changes in biomass density, morphology, transport, and viscoelastic properties provides a deeper understanding of adaptations during cell or organismal life. A second key strength is the ability to study single cells or individual cell clusters over long periods of time. As techniques in single cell profiling continue development with increasing reports on molecularly distinct subpopulations of cells, QPI provides a platform for assessing distinct phenotypes and behaviors within these heterogeneous populations. Further development of multimodal approaches will be critical for merging the observations made using single cell molecular profiling with QPI single cell phenotyping.

Finally, although there have been a large number of studies pointing towards clinical utility of QPI, this approach is ready for more robust validation and testing with clinical samples. As a label-free approach that can quantify multiple physiologically relevant parameters describing the behavior of living cells, QPI is well positioned to work with clinical samples. QPI therefore has the potential to enable a wide range of clinical applications in functional and diagnostic medicine, both as an addition to current approaches that rely on staining and as an independent *ex vivo*

approach. Further work is therefore needed to build on the demonstrated capabilities of QPI to translate this technology to clinical utility and ultimately to improve the standard of patient care.

FUNDING SOURCES

This work was supported by the Whitcome Pre-doctoral Training Program and the UCLA Molecular Biology Institute (T.L.N), NIH grant CA246182, NIH-NCI Cancer Center Support Grant P30 CA016059 and the C. Kenneth and Dianne Wright Center for Clinical and Translational Research (J.R.), the University of Utah Office of the Vice President for Research and the Office of the Assistant Secretary of Defense for Health Affairs through the Breast Cancer Research Program under Award Number W81XWH1910065 (T.A.Z.), and by NIH grants R21CA227480, R01GM114188, R01CA185189, and P30CA016042 (M.A.T.).

CONFLICT OF INTEREST DISCLOSURE

The authors declare no competing financial interest.

REFERENCES

1. Barer, R.; Joseph, S., Refractometry of Living Cells. *Quarterly Journal of Microscopical Science* **1954,** *s3-95* (32), 399.

2. Zangle, T. A.; Teitell, M. A., Live-Cell Mass Profiling: An Emerging Approach in Quantitative Biophysics. *Nature Methods* **2014,** *11* (12), 1221-8.

3. Barer, R.; Tkaczyk, S., Refractive Index of Concentrated Protein Solutions. *Nature* **1954,** *173* (4409), 821-822.

4. Barer, R., Determination of Dry Mass, Thickness, Solid and Water Concentration in Living Cells. *Nature* **1953,** *172* (4389), 1097-1098.

5. Zhao, H.; Brown, P. H.; Schuck, P., On the Distribution of Protein Refractive Index Increments. *Biophysical Journal* **2011,** *100* (9), 2309-17.

6. Zernike, F., Phase Contrast, a New Method for the Microscopic Observation of Transparent Objects. *Physica* **1942,** *9* (7), 686-698.

7. Zernike, F., Phase Contrast, a New Method for the Microscopic Observation of Transparent Objects Part Ii. *Physica* **1942,** *9* (10), 974-986.

8. Lang, W., Nomarski Differential Interference-Contrast Microscopy. Carl Zeiss: 1982.

9. King, S. V.; Libertun, A.; Piestun, R.; Cogswell, C. J.; Preza, C., Quantitative Phase Microscopy through Differential Interference Imaging. *Journal of Biomedical Optics* **2008,** *13* (2), 024020.

10. Fu, D.; Oh, S.; Choi, W.; Yamauchi, T.; Dorn, A.; Yaqoob, Z.; Dasari, R. R.; Feld, M. S., Quantitative Dic Microscopy Using an Off-Axis Self-Interference Approach. *Optics Letters* **2010,** *35* (14), 2370-2372.

11. Zangle, T. A.; Teitell, M. A.; Reed, J., Live Cell Interferometry Quantifies Dynamics of Biomass Partitioning During Cytokinesis. *PLoS One* **2014,** *9* (12).

12. Reed, J.; Chun, J.; Zangle, T. A.; Kalim, S.; Hong, J. S.; Pefley, S. E.; Zheng, X.; Gimzewski, J. K.; Teitell, M. A., Rapid, Massively Parallel Single-Cell Drug Response Measurements Via Live Cell Interferometry. *Biophysical Journal* **2011,** *101* (5), 1025-31.

13. Platt, B. C.; Shack, R., History and Principles of Shack-Hartmann Wavefront Sensing. *J Refract Surg* **2001,** *17* (5), S573-7.

14. Bon, P.; Maucort, G.; Wattellier, B.; Monneret, S., Quadriwave Lateral Shearing Interferometry for Quantitative Phase Microscopy of Living Cells. *Opt Express* **2009,** *17* (15), 13080-94.

15. Tian, L.; Waller, L., Quantitative Differential Phase Contrast Imaging in an Led Array Microscope. *Optics Express* **2015,** *23* (9), 11394-403.

16. Streibl, N., Phase Imaging by the Transport Equation of Intensity. *Optics Communications* **1984,** *49* (1), 6-10.

17. Muller, P.; Cojoc, G.; Guck, J., Drymass: Handling and Analyzing Quantitative Phase Microscopy Images of Spherical, Cell-Sized Objects. *BMC Bioinformatics* **2020,** *21* (1), 226.

18. Weart, S. R., Selected Papers of Great American Physicists : The Bicentennial Commemorative Volume of the American Physical Society 1976. American Institute of Physics: New York, 1976; p 176 p.

19. Mach, L.; Zehnder, L.; Clark, C., The Interferometers of Zehnder and Mach. 2017.

20. Françon, M., Polarization Interference Microscopes. *Applied Optics* **1964,** *3* (9), 1033-1036.

21. Sagnac, G., Luminous Ether Demonstrated by the Effect of Relative Wind of Ether in a Uniform Rotation of an Interferometer. *Comptes Rendus Hebdomadaires Des Seances De L Academie Des Sciences* **1913,** *157*, 708-710.

22. Dyson, J., Common-Path Interferometer for Testing Purposes. *Journal of the Optical Society of America* **1957,** *47* (5), 386-390.

23. Dyson, J., An Interferometer Microscope. *Proceedings of the Royal Society of London. Series A. Mathematical and Physical Sciences* **1950,** *204* (1077), 170-187.

24. Marquet, P.; Rappaz, B.; Magistretti, P. J.; Cuche, E.; Emery, Y.; Colomb, T.; Depeursinge, C., Digital Holographic Microscopy: A Noninvasive Contrast Imaging Technique Allowing Quantitative Visualization of Living Cells with Subwavelength Axial Accuracy. *Optics Letters* **2005,** *30* (5), 468-470.

25. Barer, R., Interference Microscopy and Mass Determination. *Nature* **1952,** *169* (4296), 366-367.

26. Davies, H. G.; Wilkins, M. H. F., Interference Microscopy and Mass Determination. *Nature* **1952,** *169* (4300), 541-541.

27. Mitchison, J., The Growth of Single Cells: Ii. Saccharomyces Cerevisiae. *Experimental cell research* **1958,** *15* (1), 214-221.

28. Mitchison, J., The Growth of Single Cells: Iii. Streptococcus Faecalis. *Experimental cell research* **1961,** *22*, 208-225.

29. Davies, H. G.; Deeley, E. M., An Integrator for Measuring the "Dry Mass" of Cells and Isolated Components. *Experimental Cell Research* **1956,** *11* (1), 169-185.

30. Caspersson, T.; Carlson, L.; Svensson, G., A Scanning Interference Microscope Arrangement. *Experimental Cell Research* **1954,** *7* (2), 601-602.

31. Reed, J.; Troke, J. J.; Schmit, J.; Han, S.; Teitell, M. A.; Gimzewski, J. K., Live Cell Interferometry Reveals Cellular Dynamism During Force Propagation. *ACS Nano* **2008,** *2* (5), 841-846.

32. Ross, K. F. A., *Phase Contrast and Interference Microscopy for Cell Biologists*. Edward Arnold: London, 1967.

33. Smith, F. H., Two Half-Shade Devices for Optical Polarizing Instruments. *Nature* **1954,** *173* (4399), 362-363.

34. Mitchison, J. M.; Passano, L. M.; Smith, F. H., An Integration Method for the Interference Microscope. *Quarterly Journal of Microscopical Science* **1956,** *s3-97* (38), 287.

35. de Groot, P. J., Vibration in Phase-Shifting Interferometry. *Journal of the Optical Society of America A* **1995,** *12* (2), 354-365.

36. Ri, S.; Takimoto, T.; Xia, P.; Wang, Q.; Tsuda, H.; Ogihara, S., Accurate Phase Analysis of Interferometric Fringes by the Spatiotemporal Phase-Shifting Method. *Journal of Optics* **2020,** *22* (10).

37. Cherry, R. J., *New Techniques of Optical Microscopy and Microspectroscopy*. Macmillan International Higher Education: 1991.

38. Mitchison, J. M., The Growth of Single Cells: I. Schizosaccharomyces Pombe. *Experimental Cell Research* **1957,** *13* (2), 244-262.

39. Cohen, D. K.; Cochran, E. R.; Ayres, J. D. In *Development of an Automatic Focusing Mechanism for an Interference Microscope*, Proc.SPIE, 1989.

40. Creath, K., Step Height Measurement Using Two-Wavelength Phase-Shifting Interferometry. *Applied Optics* **1987,** *26* (14), 2810-2816.

41. Wyant, J. C.; Creath, K., Advances in Interferometric Optical Profiling. *International Journal of Machine Tools and Manufacture* **1992,** *32* (1), 5-10.

42. Zangle, T. A.; Burnes, D.; Mathis, C.; Witte, O. N.; Teitell, M. A., Quantifying Biomass Changes of Single Cd8+T Cells During Antigen Specific Cytotoxicity. *PLoS One* **2013,** *8* (7).

43. Kim, D. N.; Teitell, M. A.; Reed, J.; Zangle, T. A., Hybrid Random Walk-Linear Discriminant Analysis Method for Unwrapping Quantitative Phase Microscopy Images of Biological Samples. *Journal of Biomedical Optics* **2015,** *20* (11), 111211.

44. Jim, S. In *History of the Shack Hartmann Wavefront Sensor and Its Impact in Ophthalmic Optics*, Proc.SPIE, 2014.

45. Ronchi, V., 40 Years of History of Grating Interferometer. *Applied Optics* **1964,** *3* (4), 437-&.

46. Akondi, V.; Dubra, A., Accounting for Focal Shift in the Shack-Hartmann Wavefront Sensor. *Optics Letters* **2019,** *44* (17), 4151-4154.

47. Bates, W. J., A Wavefront Shearing Interferometer. *Proceedings of the Physical Society* **1947,** *59* (6), 940-950-2.

48. Primot, J.; Sogno, L., Achromatic 3-Wave (or More) Lateral Shearing Interferometer. *Journal of the Optical Society of America a-Optics Image Science and Vision* **1995,** *12* (12), 2679-2685.

49. Freischlad, K. R.; Koliopoulos, C. L., Modal Estimation of a Wave Front from Difference Measurements Using the Discrete Fourier Transform. *Journal of the Optical Society of America A* **1986,** *3* (11), 1852-1861.

50. Primot, J., Three-Wave Lateral Shearing Interferometer. *Applied Optics* **1993,** *32* (31), 6242-6249.

51. Primot, J.; Guerineau, N., Extended Hartmann Test Based on the Pseudoguiding Property of a Hartmann Mask Completed by a Phase Chessboard. *Applied Optics* **2000,** *39* (31), 5715-5720.

52. Curl, C. L.; Bellair, C. J.; Harris, P. J.; Allman, B. E.; Roberts, A.; Nugent, K. A.; Delbridge, L. M., Single Cell Volume Measurement by Quantitative Phase Microscopy (Qpm): A Case Study of Erythrocyte Morphology. *Cellular physiology and biochemistry : international journal of experimental cellular physiology, biochemistry, and pharmacology* **2006,** *17* (5-6), 193-200.

53. Huang, D.; Leslie, K. A.; Guest, D.; Yeshcheulova, O.; Roy, I. J.; Piva, M.; Moriceau, G.; Zangle, T. A.; Lo, R. S.; Teitell, M. A.; Reed, J., High-Speed Live-Cell Interferometry: A New Method for Quantifying Tumor Drug Resistance and Heterogeneity. *Analytical Chemistry* **2018,** *90* (5), 3299-3306.

54. Belanger, E.; Berube, J. P.; de Dorlodot, B.; Marquet, P.; Vallee, R., Comparative Study of Quantitative Phase Imaging Techniques for Refractometry of Optical Waveguides. *Optics Express* **2018,** *26* (13), 17498-17510.

55. Aknoun, S.; Yonnet, M.; Djabari, Z.; Graslin, F.; Taylor, M.; Pourcher, T.; Wattellier, B.; Pognonec, P., Quantitative Phase Microscopy for Non-Invasive Live Cell Population Monitoring. *Scientific Reports* **2021,** *11* (1), 4409.

56. Zuo, C.; Li, J.; Sun, J.; Fan, Y.; Zhang, J.; Lu, L.; Zhang, R.; Wang, B.; Huang, L.; Chen, Q., Transport of Intensity Equation: A Tutorial. *Optics and Lasers in Engineering* **2020,** *135*.

57. Latychevskaia, T., Iterative Phase Retrieval for Digital Holography: Tutorial. *Journal of the Optical Society of America a-Optics Image Science and Vision* **2019,** *36* (12), D31-D40.

58. Gerchberg, R. W., A Practical Algorithm for the Determination of Phase from Image and Diffraction Plane Pictures. *Optik* **1972,** *35*, 237-246.

59. Fienup, J. R., Reconstruction of an Object from the Modulus of Its Fourier Transform. *Optics Letters* **1978,** *3* (1), 27-29.

60. Fienup, J. R., Iterative Method Applied to Image Reconstruction and to Computer-Generated Holograms. *Optical Engineering* **1980,** *19* (3), 297-305.

61. Marrison, J.; Raty, L.; Marriott, P.; O'Toole, P., Ptychography - a Label Free, High-Contrast Imaging Technique for Live Cells Using Quantitative Phase Information. *Scientific Reports* **2013,** *3*.

62. Godden, T. M.; Muniz-Piniella, A.; Claverley, J. D.; Yacoot, A.; Humphry, M. J., Phase Calibration Target for Quantitative Phase Imaging with Ptychography. *Optics Express* **2016,** *24* (7), 7679-7692.

63. Tian, L.; Waller, L., 3d Intensity and Phase Imaging from Light Field Measurements in an Led Array Microscope. *Optica* **2015,** *2* (2), 104-111.

64. Hegerl, R.; Hoppe, W., Dynamische Theorie Der Kristallstrukturanalyse Durch Elektronenbeugung Im Inhomogenen Primärstrahlwellenfeld. *Berichte der Bunsengesellschaft für physikalische Chemie* **1970,** *74* (11), 1148-1154.

65. Konda, P. C.; Loetgering, L.; Zhou, K. C.; Xu, S. Q.; Harvey, A. R.; Horstmeyer, R., Fourier Ptychography: Current Applications and Future Promises. *Optics Express* **2020,** *28* (7), 9603-9630.

66. Zheng, G.; Shen, C.; Jiang, S.; Song, P.; Yang, C., Concept, Implementations and Applications of Fourier Ptychography. *Nature Reviews Physics* **2021,** *3* (3), 207-223.

67. Horstmeyer, R.; Chung, J.; Ou, X.; Zheng, G.; Yang, C., Diffraction Tomography with Fourier Ptychography. *Optica* **2016,** *3* (8), 827-835.

68. Bostan, E.; Froustey, E.; Rappaz, B.; Shaffer, E.; Sage, D.; Unser, M., Phase Retrieval by Using Transport-of-Intensity Equation and Differential Interference Contrast Microscopy. *2014 IEEE International Conference on Image Processing (ICIP)* **2014**, 3939-3943.

69. Kachar, B., Asymmetric Illumination Contrast: A Method of Image Formation for Video Light Microscopy. *Science* **1985,** *227* (4688), 766-768.

70. Mehta, S. B.; Sheppard, C. J. R., Quantitative Phase-Gradient Imaging at High Resolution with Asymmetric Illumination-Based Differential Phase Contrast. *Optics Letters* **2009,** *34* (13), 1924-1926.

71. Guenther, B. D., Phase Contrast Microscopy. In *Encyclopedia of Modern Optics*, Elsevier: Amsterdam, 2005; pp 103-111.

72. Dekkers, N.; De Lang, H., Differential Phase Contrast in a Stem. *Optik* **1974,** *41* (4), 452-456.

73. Stewart, W. C., On Differential Phase Contrast with an Extended Illumination Source. *Journal of the Optical Society of America* **1976,** *66* (8), 813-818.

74. Hamilton, D.; Sheppard, C., Differential Phase Contrast in Scanning Optical Microscopy. *Journal of microscopy* **1984,** *133* (1), 27-39.

75. Kwon, H.; Arbabi, E.; Kamali, S. M.; Faraji-Dana, M.; Faraon, A., Single-Shot Quantitative Phase Gradient Microscopy Using a System of Multifunctional Metasurfaces. *Nature Photonics* **2019,** *14* (2), 109-114.

76. Hai, N.; Rosen, J., Phase Contrast-Based Phase Retrieval: A Bridge between Qualitative Phase Contrast and Quantitative Phase Imaging by Phase Retrieval Algorithms. *Optics Letters* **2020,** *45* (20), 5812-5815.

77. Zhang, Y. a. n.; Pedrini, G.; Osten, W.; Tiziani, H. J., Phase Retrieval Microscopy for Quantitative Phase-Contrast Imaging. *Optik* **2004,** *115* (2), 94-96.

78. Sheppard, C. J. R., Defocused Transfer Function for a Partially Coherent Microscope and Application to Phase Retrieval. *Journal of the Optical Society of America A* **2004,** *21* (5), 828-831.

79. Anand, V.; Katkus, T.; Linklater, D. P.; Ivanova, E. P.; Juodkazis, S., Lensless Three-Dimensional Quantitative Phase Imaging Using Phase Retrieval Algorithm. *Journal of Imaging* **2020,** *6* (9).

80. Kou, S. S.; Waller, L.; Barbastathis, G.; Marquet, P.; Depeursinge, C.; Sheppard, C. J. R., Quantitative Phase Restoration by Direct Inversion Using the Optical Transfer Function. *Optics Letters* **2011,** *36* (14), 2671-2673.

81. Martinez-Carranza, J.; Falaggis, K.; Kozacki, T., Fast and Accurate Phase-Unwrapping Algorithm Based on the Transport of Intensity Equation. *Applied Optics* **2017,** *56* (25), 7079-7088.

82. Gureyev, T. E.; Nugent, K. A., Rapid Quantitative Phase Imaging Using the Transport of Intensity Equation. *Optics Communications* **1997,** *133* (1), 339-346.

83. Carol, J. C.; Nicholas, I. S.; Kieran, G. L.; Parameswaran, H. In *Quantitative Dic Microscopy Using a Geometric Phase Shifter*, Proc.SPIE, 1997.

84. Fan, Y.; Sun, J.; Chen, Q.; Pan, X.; Trusiak, M.; Zuo, C., Single-Shot Isotropic Quantitative Phase Microscopy Based on Color-Multiplexed Differential Phase Contrast. *APL Photonics* **2019,** *4* (12).

85. Kocsis, P.; Shevkunov, I.; Katkovnik, V.; Egiazarian, K., Single Exposure Lensless Subpixel Phase Imaging: Optical System Design, Modelling, and Experimental Study. *Optics Express* **2020,** *28* (4), 4625-4637.

86. Chia, Y. H.; Vyas, S.; Tsai, J. C.; Huang, Y. Y.; Yeh, J. A.; Luo, Y., Multiplane Differential Phase Contrast Imaging Using Asymmetric Illumination in Volume Holographic Microscopy. *Journal of Biomedical Optics* **2020,** *25* (12).

87. Wang, K.; Di, J.; Li, Y.; Ren, Z.; Kemao, Q.; Zhao, J., Transport of Intensity Equation from a Single Intensity Image Via Deep Learning. *Optics and Lasers in Engineering* **2020,** *134*.

88. Rivenson, Y.; Zhang, Y.; Gunaydin, H.; Teng, D.; Ozcan, A., Phase Recovery and Holographic Image Reconstruction Using Deep Learning in Neural Networks. *Light: Science & Applications* **2018,** *7*, 17141.

89. Gabor, D., A New Microscopic Principle. *Nature* **1948,** *161* (4098), 777-778.

90. Ash, E. A., Dennis Gabor, 1900-1979. *Nature* **1979,** *280* (5721), 431-433.

91. Leith, E. N.; Upatnieks, J., Reconstructed Wavefronts and Communication Theory. *JOSA* **1962,** *52* (10), 1123-1130.

92. Hariharan, P., *Basics of Holography*. Cambridge University Press: 2002.

93. Knox, C., Holographic Microscopy as a Technique for Recording Dynamic Microscopic Subjects. *Science* **1966,** *153* (3739), 989-90.

94. Goodman, J. W.; Lawrence, R. W., Digital Image Formation from Electronically Detected Holograms. *Applied Physics Letters* **1967,** *11* (3), 77-79.

95. Schnars, U.; Jüptner, W., Direct Recording of Holograms by a Ccd Target and Numerical Reconstruction. *Applied Optics* **1994,** *33* (2), 179-181.

96. Kim, M.-K., Applications of Digital Holography in Biomedical Microscopy. *Journal of the Optical Society of Korea* **2010,** *14* (2), 77-89.

97. Evans, E. A., Quantitative Reconstruction and Superresolution of Red-Blood-Cell Image Holograms. *Journal of the Optical Society of America* **1971,** *61* (8), 991-7.

98. Zhang, T.; Yamaguchi, I., Three-Dimensional Microscopy with Phase-Shifting Digital Holography. *Optics Letters* **1998,** *23* (15), 1221-1223.

99. Cuche, E.; Bevilacqua, F.; Depeursinge, C., Digital Holography for Quantitative Phase-Contrast Imaging. *Optics Letters* **1999,** *24* (5), 291-293.

100. Milgram, J. H.; Li, W., Computational Reconstruction of Images from Holograms. *Applied Optics* **2002,** *41* (5), 853-864.

101. Lichte, H.; Lehmann, M., Electron Holography—Basics and Applications. *Reports on Progress in Physics* **2007,** *71* (1), 016102.

102. Rappaz, B.; Marquet, P.; Cuche, E.; Emery, Y.; Depeursinge, C.; Magistretti, P. J., Measurement of the Integral Refractive Index and Dynamic Cell Morphometry of Living Cells with Digital Holographic Microscopy. *Optics Express* **2005,** *13* (23), 9361-9373.

103. Turko, N. A.; Shaked, N. T., Erythrocyte Volumetric Measurements in Imaging Flow Cytometry Using Simultaneous Three-Wavelength Digital Holographic Microscopy. *Biomedical Optics Express* **2020,** *11* (11), 6649-6658.

104. Story, J. B.; Ballard, G. S.; Gibbons, R. H., Schlieren Photographs from Holograms. *Journal of Applied Physics* **1966,** *37* (5), 2183-2184.

105. Tsuruta, T.; Itoh, Y., Hologram Schlieren and Phase-Contrast Methods. *Japanese Journal of Applied Physics* **1969,** *8* (1), 96.

106. Kemper, B.; Langehanenberg, P.; Kosmeier, S.; Schlichthaber, F.; Remmersmann, C.; von Bally, G.; Rommel, C.; Dierker, C.; Schnekenburger, J., Digital Holographic Microscopy: Quantitative Phase Imaging and Applications in Live Cell Analysis. In *Handbook of Coherent-Domain Optical Methods: Biomedical Diagnostics, Environmental Monitoring, and Materials Science*, Tuchin, V. V., Ed. Springer New York: New York, NY, 2013; pp 215-257.

107. Wang, Z.; Millet, L.; Mir, M.; Ding, H.; Unarunotai, S.; Rogers, J.; Gillette, M. U.; Popescu, G., Spatial Light Interference Microscopy (Slim). *Optics Express* **2011,** *19* (2), 1016-1026.

108. Janik, M.; Koba, M.; Celebanska, A.; Bock, W. J.; Smietana, M., Live E. Coli Bacteria Label-Free Sensing Using a Microcavity in-Line Mach-Zehnder Interferometer. *Sci Rep* **2018,** *8* (1), 17176.

109. Goodwin, M. J.; Besselink, G. A. J.; Falke, F.; Everhardt, A. S.; Cornelissen, J.; Huskens, J., Highly Sensitive Protein Detection by Asymmetric Mach-Zehnder Interferometry for Biosensing Applications. *ACS Appl Bio Mater* **2020,** *3* (7), 4566-4572.

110. Bhaduri, B.; Edwards, C.; Pham, H.; Zhou, R.; Nguyen, T. H.; Goddard, L. L.; Popescu, G., Diffraction Phase Microscopy: Principles and Applications in Materials and Life Sciences. *Advances in Optics and Photonics* **2014,** *6* (1), 57-119.

111. Ling, T.; Boyle, K. C.; Zuckerman, V.; Flores, T.; Ramakrishnan, C.; Deisseroth, K.; Palanker, D., High-Speed Interferometric Imaging Reveals Dynamics of Neuronal Deformation During the Action Potential. *Proc Natl Acad Sci U S A* **2020,** *117* (19), 10278-10285.

112. Phillips, Z. F.; Chen, M.; Waller, L., Single-Shot Quantitative Phase Microscopy with Color-Multiplexed Differential Phase Contrast (Cdpc). *PLoS One* **2017,** *12* (2), e0171228.

113. Fan, X.; Tang, Z.; O'Dwyer, K.; Hennelly, B. M., An Inexpensive Portable Self-Reference Module for Digital Holographic Microscopy. *Photonics* **2021,** *8* (7).

114. Baek, Y.; Park, Y., Intensity-Based Holographic Imaging Via Space-Domain Kramers–Kronig Relations. *Nature Photonics* **2021,** *15* (5), 354-360.

115. Rodrigo, J. A.; Alieva, T., Rapid Quantitative Phase Imaging for Partially Coherent Light Microscopy. *Opt Express* **2014,** *22* (11), 13472-83.

116. Liang, C.; Wu, G.; Wang, F.; Li, W.; Cai, Y.; Ponomarenko, S. A., Overcoming the Classical Rayleigh Diffraction Limit by Controlling Two-Point Correlations of Partially Coherent Light Sources. *Optics Express* **2017,** *25* (23).

117. Waller, L.; Luo, Y.; Yang, S. Y.; Barbastathis, G., Transport of Intensity Phase Imaging in a Volume Holographic Microscope. *Optics Letters* **2010,** *35* (17), 2961-2963.

118. Zuo, C.; Chen, Q.; Qu, W.; Asundi, A., High-Speed Transport-of-Intensity Phase Microscopy with an Electrically Tunable Lens. *Opt Express* **2013,** *21* (20), 24060-75.

119. Ahmad, A.; Dubey, V.; Butola, A.; Ahluwalia, B. S.; Mehta, D. S., Highly Temporal Stable, Wavelength-Independent, and Scalable Field-of-View Common-Path Quantitative Phase Microscope. *J Biomed Opt* **2020,** *25* (11).

120. Godden, T. M.; Suman, R.; Humphry, M. J.; Rodenburg, J. M.; Maiden, A. M., Ptychographic Microscope for Three-Dimensional Imaging. *Opt Express* **2014,** *22* (10), 12513-23.

121. Singh, D. K.; Ahrens, C. C.; Li, W.; Vanapalli, S. A., Label-Free Fingerprinting of Tumor Cells in Bulk Flow Using Inline Digital Holographic Microscopy. *Biomed Opt Express* **2017,** *8* (2), 536-554.

122. Cao, R.; Kellman, M.; Ren, D.; Eckert, R.; Waller, L., Self-Calibrated 3d Differential Phase Contrast Microscopy with Optimized Illumination. *Biomedical Optics Express* **2022,** *13* (3).

123. Wang, Z.; Marks, D. L.; Carney, P. S.; Millet, L. J.; Gillette, M. U.; Mihi, A.; Braun, P. V.; Shen, Z.; Prasanth, S. G.; Popescu, G., Spatial Light Interference Tomography (Slit). *Optics Express* **2011,** *19* (21), 19907-19918.

124. Kwee, E.; Peterson, A.; Halter, M.; Elliott, J., Practical Application of Microsphere Samples for Benchmarking a Quantitative Phase Imaging System. *Cytometry A* **2021,** *99* (10), 1022-1032.

125. Dubey, V.; Singh, G.; Singh, V.; Ahmad, A.; Mehta, D. S., Multispectral Quantitative Phase Imaging of Human Red Blood Cells Using Inexpensive Narrowband Multicolor Leds. *Appl Opt* **2016,** *55* (10), 2521-5.

126. Rappaz, B.; Barbul, A.; Emery, Y.; Korenstein, R.; Depeursinge, C.; Magistretti, P. J.; Marquet, P., Comparative Study of Human Erythrocytes by Digital Holographic Microscopy, Confocal Microscopy, and Impedance Volume Analyzer. *Cytometry Part A* **2008,** *73A* (10), 895-903.

127. Allier, C.; Herve, L.; Mandula, O.; Blandin, P.; Usson, Y.; Savatier, J.; Monneret, S.; Morales, S., Quantitative Phase Imaging of Adherent Mammalian Cells: A Comparative Study. *Biomed Opt Express* **2019,** *10* (6), 2768-2783.

128. Ziemczonok, M.; Kus, A.; Wasylczyk, P.; Kujawinska, M., 3d-Printed Biological Cell Phantom for Testing 3d Quantitative Phase Imaging Systems. *Scientific Reports* **2019,** *9*.

129. Popescu, G., *Quantitative Phase Imaging of Cells and Tissues*. McGraw-Hill: New York, 2011.

130. Chen, S.; Li, C.; Zhu, Y., Low-Coherence Wavelength Shifting Interferometry for High-Speed Quantitative Phase Imaging. *Opt Lett* **2016,** *41* (15), 3431-4.

131. Chen, S.; Li, C.; Zhu, Y., Sensitivity Evaluation of Quantitative Phase Imaging: A Study of Wavelength Shifting Interferometry. *Opt Lett* **2017,** *42* (6), 1088-1091.

132. Malinovski, I.; França, R. S.; Couceiro, I. B., Software for Imaging Phase-Shift Interference Microscope. *Journal of Physics: Conference Series* **2018,** *975*, 012034.

133. Velghe, S.; Guérineau, N.; Haïdar, R.; Toulon, B.; Demoustier, S.; Primot, J., Two-Color Multi-Wave Lateral Shearing Interferometry for Segmented Wave-Front Measurements. *Optics Express* **2006,** *14* (21), 9699-9708.

134. Baffou, G., Quantitative Phase Microscopy Using Quadriwave Lateral Shearing Interferometry (Qlsi): Principle, Terminology, Algorithm and Grating Shadow Description. *Journal of Physics D: Applied Physics* **2021,** *54* (29).

135. Komuro, K.; Nomura, T., Quantitative Phase Imaging Using Transport of Intensity Equation with Multiple Bandpass Filters. *Appl Opt* **2016,** *55* (19), 5180-6.

136. Komuro, K.; Yamazaki, Y.; Nomura, T., Transport-of-Intensity Computational Ghost Imaging. *Appl Opt* **2018,** *57* (16), 4451-4456.

137. Gupta, A. K.; Nishchal, N. K.; Banerjee, P. P., Transport of Intensity Equation Based Photon-Counting Phase Imaging. *OSA Continuum* **2020,** *3* (2).

138. Zhang, F.; Pedrini, G.; Osten, W., Phase Retrieval of Arbitrary Complex-Valued Fields through Aperture-Plane Modulation. *Physical Review A* **2007,** *75* (4), 043805.

139. Grant, S. D.; Richford, K.; Burdett, H. L.; McKee, D.; Patton, B. R., Low-Cost, Open-Access Quantitative Phase Imaging of Algal Cells Using the Transport of Intensity Equation. *R Soc Open Sci* **2020,** *7* (1), 191921.

140. Tian, L.; Li, X.; Ramchandran, K.; Waller, L., Multiplexed Coded Illumination for Fourier Ptychography with an Led Array Microscope. *Biomedical Optics Express* **2014,** *5* (7), 2376-2389.

141. Fitzpatrick, C. R. M.; Wilson, A.; Sawyer, T. W.; Christopher, P. J.; Wilkinson, T. D.; Bohndiek, S. E.; Gordon, G. S. D., Robustness to Misalignment of Low-Cost, Compact Quantitative Phase Imaging Architectures. *OSA Contin* **2020,** *3* (10), 2660-2679.

142. Balasubramani, V.; Kujawinska, M.; Allier, C.; Anand, V.; Cheng, C. J.; Depeursinge, C.; Hai, N.; Juodkazis, S.; Kalkman, J.; Kus, A.; Lee, M.; Magistretti, P. J.; Marquet, P.; Ng, S. H.; Rosen, J.; Park, Y.

K.; Ziemczonok, M., Roadmap on Digital Holography-Based Quantitative Phase Imaging. *J Imaging* **2021,** *7* (12).

143. Chen, L.; Chen, Z.; Singh, R. K.; Vinu, R. V.; Pu, J., Increasing Field of View and Signal to Noise Ratio in the Quantitative Phase Imaging with Phase Shifting Holography Based on the Hanbury Brown-Twiss Approach. *Optics and Lasers in Engineering* **2022,** *148*.

144. Charrière, F.; Colomb, T.; Montfort, F.; Cuche, E.; Marquet, P.; Depeursinge, C., Shot-Noise Influence on the Reconstructed Phase Image Signal-to-Noise Ratio in Digital Holographic Microscopy. *Applied Optics* **2006,** *45* (29), 7667-7673.

145. Alfoldi, R.; Balog, J. A.; Farago, N.; Halmai, M.; Kotogany, E.; Neuperger, P.; Nagy, L. I.; Feher, L. Z.; Szebeni, G. J.; Puskas, L. G., Single Cell Mass Cytometry of Non-Small Cell Lung Cancer Cells Reveals Complexity of in Vivo and Three-Dimensional Models over the Petri-Dish. *Cells* **2019,** *8* (9).

146. Kühn, J.; Shaffer, E.; Mena, J.; Breton, B.; Parent, J.; Rappaz, B.; Chambon, M.; Emery, Y.; Magistretti, P.; Depeursinge, C.; Marquet, P.; Turcatti, G., Label-Free Cytotoxicity Screening Assay by Digital Holographic Microscopy. *Assay and drug development technologies* **2013,** *11* (2), 101-107.

147. Ferraro, P.; Alferi, D.; De Nicola, S.; De Petrocellis, L.; Finizio, A.; Pierattini, G., Quantitative Phase-Contrast Microscopy by a Lateral Shear Approach to Digital Holographic Image Reconstruction. *Optics Letters* **2006,** *31* (10), 1405-1407.

148. Ferraro, P.; Del Core, C.; Miccio, L.; Grilli, S.; De Nicola, S.; Finizio, A.; Coppola, G., Phase Map Retrieval in Digital Holography: Avoiding the Undersampling Effect by a Lateral Shear Approach. *Opt Lett* **2007,** *32* (15), 2233-5.

149. Tzur, A.; Kafri, R.; LeBleu, V. S.; Lahav, G.; Kirschner, M. W., Cell Growth and Size Homeostasis in Proliferating Animal Cells. *Science* **2009,** *325* (5937), 167-171.

150. Cooper, K. L.; Oh, S.; Sung, Y.; Dasari, R. R.; Kirschner, M. W.; Tabin, C. J., Multiple Phases of Chondrocyte Enlargement Underlie Differences in Skeletal Proportions. *Nature* **2013,** *495* (7441), 375-378.

151. Davies, H. G.; Wilkins, M. H. F.; Chayen, J.; Lacour, L. F., The Use of the Interference Microscope to Determine Dry Mass in Living Cells and as a Quantitative Cytochemical Method. *Quarterly Journal of Microscopical Science* **1954,** *95* (3), 271-&.

152. Mir, M.; Wang, Z.; Shen, Z.; Bednarz, M.; Bashir, R.; Golding, I.; Prasanth, S. G.; Popescu, G., Optical Measurement of Cycle-Dependent Cell Growth. *Proceedings of the National Academy of Sciences of the United States of America* **2011,** *108* (32), 13124-9.

153. Kemper, B.; Bauwens, A.; Vollmer, A.; Ketelhut, S.; Langehanenberg, P.; Muthing, J.; Karch, H.; von Bally, G., Label-Free Quantitative Cell Division Monitoring of Endothelial Cells by Digital Holographic Microscopy. *Journal of Biomedical Optics* **2010,** *15* (3).

154. Popescu, G.; Park, Y.; Lue, N.; Best-Popescu, C.; Deflores, L.; Dasari, R. R.; Feld, M. S.; Badizadegan, K., Optical Imaging of Cell Mass and Growth Dynamics. *American Journal of Physiology-Cell Physiology* **2008,** *295* (2), C538-C544.

155. Tian, L.; Liu, Z. J.; Yeh, L. H.; Chen, M.; Zhong, J. S.; Waller, L., Computational Illumination for High-Speed in Vitro Fourier Ptychographic Microscopy. *Optica* **2015,** *2* (10), 904-911.

156. Rappaz, B.; Cano, E.; Colomb, T.; Kuhn, J.; Depeursinge, C.; Simanis, V.; Magistretti, P. J.; Marquet, P., Noninvasive Characterization of the Fission Yeast Cell Cycle by Monitoring Dry Mass with Digital Holographic Microscopy. *Journal of Biomedical Optics* **2009,** *14* (3).

157. Pavillon, N.; Kuhn, J.; Moratal, C.; Jourdain, P.; Depeursinge, C.; Magistretti, P. J.; Marquet, P., Early Cell Death Detection with Digital Holographic Microscopy. *PLoS One* **2012,** *7* (1), e30912.

158. Vicar, T.; Raudenska, M.; Gumulec, J.; Balvan, J., The Quantitative-Phase Dynamics of Apoptosis and Lytic Cell Death. *Sci Rep* **2020,** *10* (1), 1566.

159. Zuo, C.; Sun, J. S.; Li, J. J.; Zhang, J. L.; Asundi, A.; Chen, Q., High-Resolution Transport-of-Intensity Quantitative Phase Microscopy with Annular Illumination. *Scientific Reports* **2017,** *7*.

160. Kemper, B.; von Bally, G., Digital Holographic Microscopy for Live Cell Applications and Technical Inspection. *Applied Optics* **2008,** *47* (4), A52-A61.

161. Kemper, B.; Carl, D.; Schnekenburger, J.; Bredebusch, I.; Schafer, M.; Domschke, W.; von Bally, G., Investigation of Living Pancreas Tumor Cells by Digital Holographic Microscopy. *Journal of Biomedical Optics* **2006,** *11* (3).

162. Zuo, C.; Chen, Q.; Qu, W. J.; Asundi, A., Noninterferometric Single-Shot Quantitative Phase Microscopy. *Optics Letters* **2013,** *38* (18), 3538-3541.

163. Dunn, G. A.; Zicha, D., Dynamics of Fibroblast Spreading. *Journal of Cell Science* **1995,** *108*, 1239-1249.

164. Liu, X.; Oh, S.; Peshkin, L.; Kirschner, M. W., Computationally Enhanced Quantitative Phase Microscopy Reveals Autonomous Oscillations in Mammalian Cell Growth. *Proceedings of the National Academy of Sciences of the United States of America* **2020,** *117* (44), 27388-27399.

165. Kuhn, J.; Shaffer, E.; Mena, J.; Breton, B.; Parent, J.; Rappaz, B.; Chambon, M.; Emery, Y.; Magistretti, P.; Depeursinge, C.; Marquet, P.; Turcatti, G., Label-Free Cytotoxicity Screening Assay by Digital Holographic Microscopy. *Assay and Drug Development Technologies* **2013,** *11* (2), 101-107.

166. Kandel, M. E.; Lu, W.; Liang, J.; Aydin, O.; Saif, T. A.; Popescu, G., Cell-to-Cell Influence on Growth in Large Populations. *Biomedical Optics Express* **2019,** *10* (9), 4664-4675.

167. McNeal, A. S.; Belote, R. L.; Zeng, H.; Urquijo, M.; Barker, K.; Torres, R.; Curtin, M.; Shain, A. H.; Andtbacka, R. H.; Holmen, S.; Lum, D. H.; McCalmont, T. H.; VanBrocklin, M. W.; Grossman, D.; Wei, M. L.; Lang, U. E.; Judson-Torres, R. L., Braf(V600e) Induces Reversible Mitotic Arrest in Human Melanocytes Via Microrna-Mediated Suppression of Aurkb. *Elife* **2021,** *10*.

168. Mugahid, D.; Kalocsay, M.; Liu, X. L.; Gruver, J. S.; Peshkin, L.; Kirschner, M. W., Yap Regulates Cell Size and Growth Dynamics Via Non-Cell Autonomous Mediators. *Elife* **2020,** *9*.

169. Zangle, T. A.; Chun, J.; Zhang, J.; Reed, J.; Teitell, M. A., Quantification of Biomass and Cell Motion in Human Pluripotent Stem Cell Colonies. *Biophysical Journal* **2013,** *105* (3), 593-601.

170. Leslie, K. A.; Rasheed, M.; Sabo, R. T.; Roberts, C. C.; Toor, A. A.; Reed, J., Reconstituting Donor T Cells Increase Their Biomass Following Hematopoietic Stem Cell Transplantation. *Analyst* **2018,** *143* (11), 2479-2485.

171. Waters, L. R.; Ahsan, F. M.; ten Hoeve, J.; Hong, J. S.; Kim, D. N. H.; Minasyan, A.; Braas, D.; Graeber, T. G.; Zangle, T. A.; Teitell, M. A., Ampk Regulates Igd Expression but Not Energy Stress with B Cell Activation. *Scientific Reports* **2019,** *9*.

172. Mitchell, S.; Roy, K.; Zangle, T. A.; Hoffmann, A., Nongenetic Origins of Cell-to-Cell Variability in B Lymphocyte Proliferation. *Proc Natl Acad Sci U S A* **2018,** *115* (12), E2888-E2897.

173. Pradeep, S.; Tasnim, T.; Zhang, H.; Zangle, T. A., Simultaneous Measurement of Neurite and Neural Body Mass Accumulation Via Quantitative Phase Imaging. *Analyst* **2021,** *146* (4), 1361-1368.

174. Kandel, M. E.; Kim, E.; Lee, Y. J.; Tracy, G.; Chung, H. J.; Popescu, G., Multiscale Assay of Unlabeled Neurite Dynamics Using Phase Imaging with Computational Specificity. *ACS Sens* **2021,** *6* (5), 1864-1874.

175. Wang, Z.; Millet, L.; Chan, V.; Ding, H.; Gillette, M. U.; Bashir, R.; Popescu, G., Label-Free Intracellular Transport Measured by Spatial Light Interference Microscopy. *Journal of Biomedical Optics* **2011,** *16* (2), 026019.

176. Jourdain, P.; Boss, D.; Rappaz, B.; Moratal, C.; Hernandez, M. C.; Depeursinge, C.; Magistretti, P. J.; Marquet, P., Simultaneous Optical Recording in Multiple Cells by Digital Holographic Microscopy of Chloride Current Associated to Activation of the Ligand-Gated Chloride Channel Gaba(a) Receptor. *PLoS One* **2012,** *7* (12), e51041.

177. Solovei, I.; Kreysing, M.; Lanctot, C.; Kosem, S.; Peichl, L.; Cremer, T.; Guck, J.; Joffe, B., Nuclear Architecture of Rod Photoreceptor Cells Adapts to Vision in Mammalian Evolution. *Cell* **2009,** *137* (2), 356-68.

178. Yurkin, M. A., How a Phase Image of a Cell with Nucleus Refractive Index Smaller Than That of the Cytoplasm Should Look Like? A Comment on Two Papers by Steelman Et Al. And Schurmann Et Al.

Read the Responses to This Comment: E201800091 and E201800095. *Journal of Biophotonics* **2018,** *11* (6).

179. Schurmann, M.; Scholze, J.; Muller, P.; Guck, J.; Chan, C. J., Cell Nuclei Have Lower Refractive Index and Mass Density Than Cytoplasm. *Journal of Biophotonics* **2016,** *9* (10), 1068-1076.

180. Steelman, Z. A.; Eldridge, W. J.; Weintraub, J. B.; Wax, A., Is the Nuclear Refractive Index Lower Than Cytoplasm? Validation of Phase Measurements and Implications for Light Scattering Technologies. *Journal of Biophotonics* **2017,** *10* (12), 1714-1722.

181. Muller, P.; Guck, J., Response to Comment on "Cell Nuclei Have Lower Refractive Index and Mass Density Than Cytoplasm" a Comment on "How a Phase Image of a Cell with Nucleus Refractive Index Smaller Than That of the Cytoplasm Should Look Like?", E201800033. *Journal of Biophotonics* **2018,** *11* (6).

182. Steelman, Z. A.; Eldridge, W. J.; Wax, A., Response to Comment on "Is the Nuclear Refractive Index Lower Than Cytoplasm? Validation of Phase Measurements and Implications for Light Scattering Technologies" a Comment on "How a Phase Image of a Cell with Nucleus Refractive Index Smaller Than That of the Cytoplasm Should Look Like?", E201800033. *Journal of Biophotonics* **2018,** *11* (6).

183. Kim, T.; Zhou, R. J.; Mir, M.; Babacan, S. D.; Carney, P. S.; Goddard, L. L.; Popescu, G., White-Light Diffraction Tomography of Unlabelled Live Cells. *Nature Photonics* **2014,** *8* (3), 256-263.

184. Kim, K.; Guck, J., The Relative Densities of Cytoplasm and Nuclear Compartments Are Robust against Strong Perturbation. *Biophys J* **2020,** *119* (10), 1946-1957.

185. Liebel, M.; Ortega Arroyo, J.; Beltrán, V. S.; Osmond, J.; Jo, A.; Lee, H.; Quidant, R.; van Hulst, N. F., 3d Tracking of Extracellular Vesicles by Holographic Fluorescence Imaging. *Science Advances* **2020,** *6* (45), eabc2508.

186. Koslover, E. F.; Chan, C. K.; Theriot, J. A., Cytoplasmic Flow and Mixing Due to Deformation of Motile Cells. *Biophysical Journal* **2017,** *113* (9), 2077-2087.

187. Vicar, T.; Balvan, J.; Jaros, J.; Jug, F.; Kolar, R.; Masarik, M.; Gumulec, J., Cell Segmentation Methods for Label-Free Contrast Microscopy: Review and Comprehensive Comparison. *BMC Bioinformatics* **2019,** *20* (1), 360.

188. Jensen, E. C., Types of Imaging, Part 2: An Overview of Fluorescence Microscopy. *The Anatomical Record* **2012,** *295* (10), 1621-1627.

189. Kim, K.; Lee, S.; Yoon, J.; Heo, J.; Choi, C.; Park, Y., Three-Dimensional Label-Free Imaging and Quantification of Lipid Droplets in Live Hepatocytes. *Scientific Reports* **2016,** *6*.

190. Brown, A. F.; Dunn, G. A., Microinterferometry of the Movement of Dry Matter in Fibroblasts. *Journal of Cell Science* **1989,** *92 (Pt 3)*, 379-89.

191. Kandel, M. E.; Fernandes, D.; Taylor, A. M.; Shakir, H.; Best-Popescu, C.; Popescu, G., Three-Dimensional Intracellular Transport in Neuron Bodies and Neurites Investigated by Label-Free Dispersion-Relation Phase Spectroscopy. *Cytometry A* **2017,** *91* (5), 519-526.

192. Sandoz, P. A.; Tremblay, C.; van der Goot, F. G.; Frechin, M., Image-Based Analysis of Living Mammalian Cells Using Label-Free 3d Refractive Index Maps Reveals New Organelle Dynamics and Dry Mass Flux. *PLoS Biol* **2019,** *17* (12), e3000553.

193. Ma, L.; Rajshekhar, G.; Wang, R.; Bhaduri, B.; Sridharan, S.; Mir, M.; Chakraborty, A.; Iyer, R.; Prasanth, S.; Millet, L.; Gillette, M. U.; Popescu, G., Phase Correlation Imaging of Unlabeled Cell Dynamics. *Scientific Reports* **2016,** *6*, 32702.

194. Li, Y.; Di, J.; Wu, W.; Shang, P.; Zhao, J., Quantitative Investigation on Morphology and Intracellular Transport Dynamics of Migrating Cells. *Applied Optics* **2019,** *58* (34), G162-G168.

195. Popescu, G.; Park, Y.; Ceballos, S.; Kandel, M.; Sridharan, S.; Monroy, F.; Popescu, G., Nuclear Dynamics in Metastatic Cells Studied by Quantitative Phase Imaging. In *Quantitative Phase Imaging*, 2015.

196. Zhang, Y.; Judson, R. L., Evaluation of Holographic Imaging Cytometer Holomonitor M4(R) Motility Applications. *Cytometry A* **2018,** *93* (11), 1125-1131.

197. Kamlund, S.; Janicke, B.; Alm, K.; Judson-Torres, R. L.; Oredsson, S., Quantifying the Rate, Degree, and Heterogeneity of Morphological Change During an Epithelial to Mesenchymal Transition Using Digital Holographic Cytometry. *Applied Sciences* **2020,** *10* (14).

198. Lee, A. J.; Hugonnet, H.; Park, W.; Park, Y., Three-Dimensional Label-Free Imaging and Quantification of Migrating Cells During Wound Healing. *Biomedical Optics Express* **2020,** *11* (12), 6812-6824.

199. Park, K.; Lonsberry, G. E.; Gearing, M.; Levey, A. I.; Desai, J. P., Viscoelastic Properties of Human Autopsy Brain Tissues as Biomarkers for Alzheimer's Diseases. *IEEE Transactions on Biomedical Engineering* **2019,** *66* (6), 1705-1713.

200. Cross, S. E.; Jin, Y. S.; Rao, J.; Gimzewski, J. K., Nanomechanical Analysis of Cells from Cancer Patients. *Nature Nanotechnol* **2007,** *2* (12), 780-3.

201. Barriga, E. H.; Franze, K.; Charras, G.; Mayor, R., Tissue Stiffening Coordinates Morphogenesis by Triggering Collective Cell Migration in Vivo. *Nature* **2018,** *554* (7693), 523-527.

202. Haase, K.; Pelling, A. E., Investigating Cell Mechanics with Atomic Force Microscopy. *J R Soc Interface* **2015,** *12* (104), 20140970.

203. Wu, P. H.; Aroush, D. R. B.; Asnacios, A.; Chen, W. C.; Dokukin, M. E.; Doss, B. L.; Durand-Smet, P.; Ekpenyong, A.; Guck, J.; Guz, N. V.; Janmey, P. A.; Lee, J. S. H.; Moore, N. M.; Ott, A.; Poh, Y. C.; Ros, R.; Sander, M.; Sokolov, I.; Staunton, J. R.; Wang, N.; Whyte, G.; Wirtz, D., A Comparison of Methods to Assess Cell Mechanical Properties. *Nature Methods* **2018,** *15* (7), 491-+.

204. Mason, T. G.; Weitz, D. A., Optical Measurements of Frequency-Dependent Linear Viscoelastic Moduli of Complex Fluids. *Physical Review Letters* **1995,** *74* (7), 1250-1253.

205. Weihs, D.; Mason, T. G.; Teitell, M. A., Bio-Microrheology: A Frontier in Microrheology. *Biophysical Journal* **2006,** *91* (11), 4296-4305.

206. Squires, T. M.; Mason, T. G., Fluid Mechanics of Microrheology. *Annual Review of Fluid Mechanics* **2010,** *42*, 413-438.

207. Reed, J.; Frank, M.; Troke, J. J.; Schmit, J.; Han, S.; Teitell, M. A.; Gimzewski, J. K., High Throughput Cell Nanomechanics with Mechanical Imaging Interferometry. *Nanotechnology* **2008,** *19* (23).

208. Chalut, K. J.; Ekpenyong, A. E.; Clegg, W. L.; Melhuish, I. C.; Guck, J., Quantifying Cellular Differentiation by Physical Phenotype Using Digital Holographic Microscopy. *Integrative Biology* **2012,** *4* (3), 280-284.

209. Park, Y.; Best, C. A.; Badizadegan, K.; Dasari, R. R.; Feld, M. S.; Kuriabova, T.; Henle, M. L.; Levine, A. J.; Popescu, G., Measurement of Red Blood Cell Mechanics During Morphological Changes. *Proceedings of the National Academy of Sciences of the United States of America* **2010,** *107* (15), 6731-6736.

210. Eldridge, W. J.; Steelman, Z. A.; Loomis, B.; Wax, A., Optical Phase Measurements of Disorder Strength Link Microstructure to Cell Stiffness. *Biophysical Journal* **2017,** *112* (4), 692-702.

211. Eldridge, W. J.; Ceballos, S.; Shah, T.; Park, H. S.; Steelman, Z. A.; Zauscher, S.; Wax, A., Shear Modulus Measurement by Quantitative Phase Imaging and Correlation with Atomic Force Microscopy. *Biophysical Journal* **2019,** *117* (4), 696-705.

212. Nguyen, T. L.; Polanco, E. R.; Patananan, A. N.; Zangle, T. A.; Teitell, M. A., Cell Viscoelasticity Is Linked to Fluctuations in Cell Biomass Distributions. *Scientific Reports* **2020,** *10* (1).

213. Chun, J.; Zangle, T. A.; Kolarova, T.; Finn, R. S.; Teitell, M. A.; Reed, J., Rapidly Quantifying Drug Sensitivity of Dispersed and Clumped Breast Cancer Cells by Mass Profiling. *Analyst* **2012,** *137* (23), 5495-8.

214. Huang, D.; Roy, I. J.; Murray, G. F.; Reed, J.; Zangle, T. A.; Teitell, M. A., Identifying Fates of Cancer Cells Exposed to Mitotic Inhibitors by Quantitative Phase Imaging. *Analyst* **2019,** *145* (1), 97-106.

215. Saleh, T.; Tyutyunyk-Massey, L.; Murray, G. F.; Alotaibi, M. R.; Kawale, A. S.; Elsayed, Z.; Henderson, S. C.; Yakovlev, V.; Elmore, L. W.; Toor, A.; Harada, H.; Reed, J.; Landry, J. W.; Gewirtz, D. A., Tumor Cell Escape from Therapy-Induced Senescence. *Biochem Pharmacol* **2019,** *162*, 202-212.

216. Murray, G. F.; Guest, D.; Mikheykin, A.; Toor, A.; Reed, J., Single Cell Biomass Tracking Allows Identification and Isolation of Rare Targeted Therapy-Resistant Dlbcl Cells within a Mixed Population. *Analyst* **2021,** *146* (4), 1157-1162.

217. Murray, G. F.; Turner, T. H.; Leslie, K. A.; Alzubi, M. A.; Guest, D.; Sohal, S. S.; Teitell, M. A.; Harrell, J. C.; Reed, J., Live Cell Mass Accumulation Measurement Non-Invasively Predicts Carboplatin Sensitivity in Triple-Negative Breast Cancer Patient-Derived Xenografts. *ACS Omega* **2018,** *3* (12), 17687-17692.

218. Murray, G. F.; Tumer, T. H.; Guest, D.; Leslie, K. A.; Alzubi, M. A.; Radhakrishnan, S. K.; Harrell, J. C.; Reed, J., Qpi Allows in Vitro Drug Screening of Triple Negative Breast Cancer Pdx Tumors and Fine Needle Biopsies. *Frontiers in Physics* **2019,** *7*.

219. Polanco, E. R.; Moustafa, T. E.; Butterfield, A.; Scherer, S.; Cortes-Sanchez, E.; Bodily, T.; Welm, B. E.; Bernard, P. S.; Zangle, T. A., Multiparametric Quantitative Phase Imaging for Real-Time, Single Cell, Drug Screening in Breast Cancer. *bioRxiv* **2021**.

220. Fackler, O. T.; Grosse, R., Cell Motility through Plasma Membrane Blebbing. *Journal of Cell Biology* **2008,** *181* (6), 879-884.

221. Wang, Z.; Tangella, K.; Balla, A.; Popescu, G., Tissue Refractive Index as Marker of Disease. *Journal of Biomedical Optics* **2011,** *16* (11).

222. Takabayashi, M.; Majeed, H.; Kajdacsy-Balla, A.; Popescu, G., Tissue Spatial Correlation as Cancer Marker. *Journal of Biomedical Optics* **2019,** *24* (1).

223. Hejna, M.; Jorapur, A.; Song, J. S.; Judson, R. L., High Accuracy Label-Free Classification of Single-Cell Kinetic States from Holographic Cytometry of Human Melanoma Cells. *Scientific Reports* **2017,** *7*.

224. Park, Y.; Diez-Silva, M.; Popescu, G.; Lykotrafitis, G.; Choi, W.; Feld, M. S.; Suresh, S., Refractive Index Maps and Membrane Dynamics of Human Red Blood Cells Parasitized by Plasmodium Falciparum.

Proceedings of the National Academy of Sciences of the United States of America **2008,** *105* (37), 13730-5.

225. Mehta, D. S.; Srivastava, V., Quantitative Phase Imaging of Human Red Blood Cells Using Phase-Shifting White Light Interference Microscopy with Colour Fringe Analysis. *Applied Physics Letters* **2012,** *101* (20).

226. Liu, R.; Dey, D. K.; Boss, D.; Marquet, P.; Javidi, B., Recognition and Classification of Red Blood Cells Using Digital Holographic Microscopy and Data Clustering with Discriminant Analysis. *Journal of the Optical Society of America a-Optics Image Science and Vision* **2011,** *28* (6), 1204-10.

227. Pham, H. V.; Bhaduri, B.; Tangella, K.; Best-Popescu, C.; Popescu, G., Real Time Blood Testing Using Quantitative Phase Imaging. *PLoS One* **2013,** *8* (2).

228. Ohene, Y.; Marinov, I.; de Laulanie, L.; Dupuy, C.; Wattelier, B.; Starikovskaia, S., Phase Imaging Microscopy for the Diagnostics of Plasma-Cell Interaction. *Applied Physics Letters* **2015,** *106* (23).

229. Rubessa, M.; Kandel, M. E.; Schreiber, S.; Meyers, S.; Beck, D. H.; Popescu, G.; Wheeler, M. B., Morphometric Analysis of Sperm Used for Ivp by Three Different Separation Methods with Spatial Light Interference Microscopy. *Systems Biology in Reproductive Medicine* **2020,** *66* (1), 26-36.

230. Majeed, H.; Nguyen, T. H.; Kandel, M. E.; Kajdacsy-Balla, A.; Popescu, G., Label-Free Quantitative Evaluation of Breast Tissue Using Spatial Light Interference Microscopy (Slim). *Scientific Reports* **2018,** *8* (1), 6875.

231. Erhardt, A.; Zinser, G.; Komitowski, D.; Bille, J., Reconstructing 3-D Light-Microscopic Images by Digital Image Processing. *Applied Optics* **1985,** *24* (2), 194-200.

232. Pawley, J. B., *Handbook of Biological Confocal Microscopy*. Springer: New York, NY, 2005.

233. Wolf, E., Three-Dimensional Structure Determination of Semi-Transparent Objects from Holographic Data. *Optics Communications* **1969,** *1* (4), 153-156.

234. Radon, J., On the Determination of Functions from Their Integral Values Along Certain Manifolds. *IEEE Transactions on Medical Imaging* **1986,** *5* (4), 170-176.

235. Richmond, C., Sir Godfrey Hounsfield. *BMJ : British Medical Journal* **2004,** *329* (7467), 687-687.

236. Fercher, A. F.; Bartelt, H.; Becker, H.; Wiltschko, E., Image Formation by Inversion of Scattered Field Data: Experiments and Computational Simulation. *Appl Opt* **1979,** *18* (14), 2427-39.

237. Peter, C.; Wolfgang, L.; Dirk Van, D.; Jean-Pierre, G.; Michel, S.; Jose, B. In *Quantitative Phase Tomography by Holographic Reconstruction*, Proc.SPIE, 1999.

238. Barty, A.; Nugent, K. A.; Roberts, A.; Paganin, D., Quantitative Phase Tomography. *Optics Communications* **2000,** *175* (4), 329-336.

239. Charrière, F.; Pavillon, N.; Colomb, T.; Depeursinge, C.; Heger, T. J.; Mitchell, E. A. D.; Marquet, P.; Rappaz, B., Living Specimen Tomography by Digital Holographic Microscopy: Morphometry of Testate Amoeba. *Optics Express* **2006,** *14* (16), 7005-7013.

240. Choi, W.; Fang-Yen, C.; Badizadegan, K.; Oh, S.; Lue, N.; Dasari, R. R.; Feld, M. S., Tomographic Phase Microscopy. *Nature Methods* **2007,** *4* (9), 717-9.

241. Chen, M.; Tian, L.; Waller, L., 3d Differential Phase Contrast Microscopy. *Biomedical Optics Express* **2016,** *7* (10), 3940-3950.

242. Matlock, A.; Tian, L., High-Throughput, Volumetric Quantitative Phase Imaging with Multiplexed Intensity Diffraction Tomography. *Biomedical Optics Express* **2019,** *10* (12), 6432-6448.

243. Kuś, A.; Dudek, M.; Kemper, B.; Kujawińska, M.; Vollmer, A., Tomographic Phase Microscopy of Living Three-Dimensional Cell Cultures. *Journal of Biomedical Optics* **2014,** *19* (4), 046009.

244. Li, J.; Matlock, A.; Li, Y.; Chen, Q.; Zuo, C.; Tian, L., High-Speed in Vitro Intensity Diffraction Tomography. *Advanced Photonics* **2019,** *1* (06).

245. Esposito, M.; Fang, C.; Cook, K. C.; Park, N.; Wei, Y.; Spadazzi, C.; Bracha, D.; Gunaratna, R. T.; Laevsky, G.; DeCoste, C. J.; Slabodkin, H.; Brangwynne, C. P.; Cristea, I. M.; Kang, Y. B., Tgf-Beta-Induced Dact1 Biomolecular Condensates Repress Wnt Signalling to Promote Bone Metastasis. *Nature Cell Biology* **2021,** *23* (3), 257-+.

246. Choi, W. H.; Yun, Y.; Park, S.; Jeon, J. H.; Lee, J.; Lee, J. H.; Yang, S. A.; Kim, N. K.; Jung, C. H.; Kwon, Y. T.; Han, D.; Lim, S. M.; Lee, M. J., Aggresomal Sequestration and Stub1-Mediated Ubiquitylation During Mammalian Proteaphagy of Inhibited Proteasomes. *Proceedings of the National Academy of Sciences of the United States of America* **2020,** *117* (32), 19190-19200.

247. Hong, Y.; Dao, K. P.; Kim, T.; Lee, S.; Shin, Y.; Park, Y.; Hwang, D. S., Label-Free Quantitative Analysis of Coacervates Via 3d Phase Imaging. *Advanced Optical Materials* **2021,** *9* (20).

248. Ledwig, P.; Robles, F. E., Epi-Mode Tomographic Quantitative Phase Imaging in Thick Scattering Samples. *Biomedical Optics Express* **2019,** *10* (7), 3605-3621.

249. Nguyen, T. H.; Kandel, M. E.; Rubessa, M.; Wheeler, M. B.; Popescu, G., Gradient Light Interference Microscopy for 3d Imaging of Unlabeled Specimens. *Nature Communications* **2017,** *8* (1), 210.

250. Funamizu, H.; Aizu, Y., Three-Dimensional Quantitative Phase Imaging of Blood Coagulation Structures by Optical Projection Tomography in Flow Cytometry Using Digital Holographic Microscopy. *Journal of Biomedical Optics* **2018,** *24* (3), 1-6.

251. Ledwig, P.; Robles, F. E., Quantitative 3d Refractive Index Tomography of Opaque Samples in Epi-Mode. *Optica* **2021,** *8* (1), 6-14.

252. Huang, D.; Swanson, E. A.; Lin, C. P.; Schuman, J. S.; Stinson, W. G.; Chang, W.; Hee, M. R.; Flotte, T.; Gregory, K.; Puliafito, C. A.; et al., Optical Coherence Tomography. *Science* **1991,** *254* (5035), 1178-81.

253. Fujimoto, J. G.; Pitris, C.; Boppart, S. A.; Brezinski, M. E., Optical Coherence Tomography: An Emerging Technology for Biomedical Imaging and Optical Biopsy. *Neoplasia* **2000,** *2* (1-2), 9-25.

254. Joo, C.; Akkin, T.; Cense, B.; Park, B. H.; de Boer, J. E., Spectral-Domain Optical Coherence Phase Microscopy for Quantitative Phase-Contrast Imaging. *Optics Letters* **2005,** *30* (16), 2131-2133.

255. Choma, M. A.; Ellerbee, A. K.; Yang, C. H.; Creazzo, T. L.; Izatt, J. A., Spectral-Domain Phase Microscopy. *Optics Letters* **2005,** *30* (10), 1162-1164.

256. Jonnal, R. S.; Kocaoglu, O. P.; Wang, Q.; Lee, S.; Miller, D. T., Phase-Sensitive Imaging of the Outer Retina Using Optical Coherence Tomography and Adaptive Optics. *Biomedical Optics Express* **2012,** *3* (1), 104-124.

257. Desissaire, S.; Schwarzhans, F.; Steiner, S.; Vass, C.; Fischer, G.; Pircher, M.; Hitzenberger, C. K., Temporal Phase Evolution Oct for Measurement of Tissue Deformation in the Human Retina in-Vivo. *Biomedical Optics Express* **2021,** *12* (11), 7092-7112.

258. Hu, C. F.; Zhu, S. S.; Gao, L.; Popescu, G., Endoscopic Diffraction Phase Microscopy. *Optics Letters* **2018,** *43* (14), 3373-3376.

259. Costa, P. C.; Guang, Z.; Ledwig, P.; Zhang, Z. B.; Neill, S.; Olson, J. J.; Robles, F. E., Towards in-Vivo Label-Free Detection of Brain Tumor Margins with Epi-Illumination Tomographic Quantitative Phase Imaging. *Biomedical Optics Express* **2021,** *12* (3), 1621-1634.

260. Gordon, G. S. D.; Joseph, J.; Alcolea, M. P.; Sawyer, T.; Williams, C.; Fitzpatrick, C. R. M.; Jones, P. H.; di Pietro, M.; Fitzgerald, R. C.; Wilkinson, T. D.; Bohndiek, S. E., Quantitative Phase and Polarization Imaging through an Optical Fiber Applied to Detection of Early Esophageal Tumorigenesis. *Journal of Biomedical Optics* **2019,** *24* (12).

261. Kim, K.; Choe, K.; Park, I.; Kim, P.; Park, Y., Holographic Intravital Microscopy for 2-D and 3-D Imaging Intact Circulating Blood Cells in Microcapillaries of Live Mice. *Scientific Reports* **2016,** *6*.

262. Sung, Y. J.; Choi, W.; Fang-Yen, C.; Badizadegan, K.; Dasari, R. R.; Feld, M. S., Optical Diffraction Tomography for High Resolution Live Cell Imaging. *Optics Express* **2009,** *17* (1), 266-277.

263. Park, Y.; Popescu, G.; Badizadegan, K.; Dasari, R. R.; Feld, M. S., Diffraction Phase and Fluorescence Microscopy. *Optics Express* **2006,** *14* (18), 8263-8.

264. Lue, N.; Choi, W.; Popescu, G.; Yaqoob, Z.; Badizadegan, K.; Dasari, R. R.; Feld, M. S., Live Cell Refractometry Using Hilbert Phase Microscopy and Confocal Reflectance Microscopy. *J Phys Chem A* **2009,** *113* (47), 13327-30.

265. Chowdhury, S.; Eldridge, W. J.; Wax, A.; Izatt, J. A., Structured Illumination Multimodal 3d-Resolved Quantitative Phase and Fluorescence Sub-Diffraction Microscopy. *Biomedical Optics Express* **2017,** *8* (5), 2496-2518.

266. Kemper, B.; Schmidt, L.; Przibilla, S.; Rommel, C.; Vollmer, A.; Ketelhut, S.; Schnekenburger, J.; von Bally, G., Influence of Sample Preparation and Identification of Subcelluar Structures in Quantitative Holographic Phase Contrast Microscopy. *Biophotonics: Photonic Solutions for Better Health Care Ii* **2010,** *7715*.

267. Barroso, A.; Woerdemann, M.; Vollmer, A.; von Bally, G.; Kemper, B.; Denz, C., Three-Dimensional Exploration and Mechano-Biophysical Analysis of the Inner Structure of Living Cells. *Small* **2013,** *9* (6), 885-93.

268. Weaver, S. S.; Li, Y. F.; Foucard, L.; Majeed, H.; Bhaduri, B.; Levine, A. J.; Kilian, K. A.; Popescu, G., Simultaneous Cell Traction and Growth Measurements Using Light. *Journal of Biophotonics* **2019,** *12* (3).

269. Sridharan, S.; Li, Y. F.; Bhaduri, B.; Majeed, H.; Dupenloup, P.; Levine, A.; Kilian, K. A.; Popescu, G., Hilbert Phase Dynamometry (Hpd) for Real-Time Measurement of Cell Generated Forces. *Quantitative Phase Imaging Ii* **2016,** *9718*.

270. Chowdhury, S.; Eldridge, W. J.; Wax, A.; Izatt, J. A., Structured Illumination Microscopy for Dual-Modality 3d Sub-Diffraction Resolution Fluorescence and Refractive-Index Reconstruction. *Biomedical Optics Express* **2017,** *8* (12), 5776-5793.

271. Tamamitsu, M.; Toda, K.; Shimada, H.; Honda, T.; Takarada, M.; Okabe, K.; Nagashima, Y.; Horisaki, R.; Ideguchi, T., Label-Free Biochemical Quantitative Phase Imaging with Mid-Infrared Photothermal Effect. *Optica* **2020,** *7* (4), 359-366.

272. Jung, J.; Hong, S. J.; Kim, H. B.; Kim, G.; Lee, M.; Shin, S.; Lee, S.; Kim, D. J.; Lee, C. G.; Park, Y., Label-Free Non-Invasive Quantitative Measurement of Lipid Contents in Individual Microalgal Cells Using Refractive Index Tomography. *Scientific Reports* **2018,** *8*.

273. Schurmann, M.; Cojoc, G.; Girardo, S.; Ulbricht, E.; Guck, J.; Muller, P., Three-Dimensional Correlative Single-Cell Imaging Utilizing Fluorescence and Refractive Index Tomography. *Journal of Biophotonics* **2018,** *11* (3).

274. Kim, K.; Park, W. S.; Na, S.; Kim, S.; Kim, T.; Do Heo, W.; Park, Y., Correlative Three-Dimensional Fluorescence and Refractive Index Tomography: Bridging the Gap between Molecular Specificity and Quantitative Bioimaging. *Biomedical Optics Express* **2017,** *8* (12), 5688-5697.

275. Descloux, A.; Grussmayer, K. S.; Bostan, E.; Lukes, T.; Bouwens, A.; Sharipov, A.; Geissbuehler, S.; Mahul-Mellier, A. L.; Lashuel, H. A.; Leutenegger, M.; Lasser, T., Combined Multi-Plane Phase Retrieval and Super-Resolution Optical Fluctuation Imaging for 4d Cell Microscopy. *Nature Photonics* **2018,** *12* (3), 165-+.

276. Rinehart, M.; Zhu, Y.; Wax, A., Quantitative Phase Spectroscopy. *Biomedical Optics Express* **2012,** *3* (5), 958-965.

277. Jung, J. H.; Jang, J.; Park, Y., Spectro-Refractometry of Individual Microscopic Objects Using Swept-Source Quantitative Phase Imaging. *Anal Chem* **2013,** *85* (21), 10519-25.

278. Rinehart, M. T.; Park, H. S.; Walzer, K. A.; Chi, J. T.; Wax, A., Hemoglobin Consumption by P. Falciparum in Individual Erythrocytes Imaged Via Quantitative Phase Spectroscopy. *Sci Rep* **2016,** *6*, 24461.

279. Jung, J.; Kim, K.; Yoon, J.; Park, Y., Hyperspectral Optical Diffraction Tomography. *Opt Express* **2016,** *24* (3), 2006-12.

280. Baiz, C. R.; Blasiak, B.; Bredenbeck, J.; Cho, M.; Choi, J. H.; Corcelli, S. A.; Dijkstra, A. G.; Feng, C. J.; Garrett-Roe, S.; Ge, N. H.; Hanson-Heine, M. W. D.; Hirst, J. D.; Jansen, T. L. C.; Kwac, K.; Kubarych, K. J.; Londergan, C. H.; Maekawa, H.; Reppert, M.; Saito, S.; Roy, S.; Skinner, J. L.; Stock, G.; Straub, J. E.; Thielges, M. C.; Tominaga, K.; Tokmakoff, A.; Torii, H.; Wang, L.; Webb, L. J.; Zanni, M. T., Vibrational Spectroscopic Map, Vibrational Spectroscopy, and Intermolecular Interaction. *Chem Rev* **2020,** *120* (15), 7152-7218.

281. Kang, J. W.; Lue, N.; Kong, C. R.; Barman, I.; Dingari, N. C.; Goldfless, S. J.; Niles, J. C.; Dasari, R. R.; Feld, M. S., Combined Confocal Raman and Quantitative Phase Microscopy System for Biomedical Diagnosis. *Biomedical Optics Express* **2011,** *2* (9), 2484-92.

282. Singh, S. P.; Kang, S.; Kang, J. W.; So, P. T. C.; Dasari, R. R.; Yaqoob, Z.; Barman, I., Label-Free Characterization of Ultra Violet-Radiation-Induced Changes in Skin Fibroblasts with Raman Spectroscopy and Quantitative Phase Microscopy. *Scientific Reports* **2017,** *7* (1), 10829.

283. Dubey, V.; Ahmad, A.; Butola, A.; Qaiser, D.; Srivastava, A.; Mehta, D. S., Low Coherence Quantitative Phase Microscopy with Machine Learning Model and Raman Spectroscopy for the Study of Breast Cancer Cells and Their Classification. *Applied Optics* **2019,** *58* (5), A112-A119.

284. Prevedel, R.; Diz-Munoz, A.; Ruocco, G.; Antonacci, G., Brillouin Microscopy: An Emerging Tool for Mechanobiology. *Nat Methods* **2019,** *16* (10), 969-977.

285. Raghunathan, R.; Zhang, J.; Wu, C.; Rippy, J.; Singh, M.; Larin, K. V.; Scarcelli, G., Evaluating Biomechanical Properties of Murine Embryos Using Brillouin Microscopy and Optical Coherence Tomography. *J Biomed Opt* **2017,** *22* (8), 1-6.

286. Zhang, J.; Raghunathan, R.; Rippy, J.; Wu, C.; Finnell, R. H.; Larin, K. V.; Scarcelli, G., Tissue Biomechanics During Cranial Neural Tube Closure Measured by Brillouin Microscopy and Optical Coherence Tomography. *Birth Defects Res* **2019,** *111* (14), 991-998.

287. Schlüßler, R.; Kim, K.; Nötzel, M.; Taubenberger, A.; Abuhattum, S.; Beck, T.; Müller, P.; Maharana, S.; Cojoc, G.; Girardo, S.; Hermann, A.; Alberti, S.; Guck, J., Correlative All-Optical Quantification of Mass Density and Mechanics of Subcellular Compartments with Fluorescence Specificity. *ELife* **2022,** *11*, e68490.

288. Guo, S. M.; Yeh, L. H.; Folkesson, J.; Ivanov, I. E.; Krishnan, A. P.; Keefe, M. G.; Hashemi, E.; Shin, D.; Chhun, B. B.; Cho, N. H.; Leonetti, M. D.; Han, M. H.; Nowakowski, T. J.; Mehta, S. B., Revealing Architectural Order with Quantitative Label-Free Imaging and Deep Learning. *Elife* **2020,** *9*.

289. Jo, Y.; Cho, H.; Lee, S. Y.; Choi, G.; Kim, G.; Min, H.-s.; Park, Y., Quantitative Phase Imaging and Artificial Intelligence: A Review. *IEEE Journal of Selected Topics in Quantum Electronics* **2019,** *25* (1), 1-14.

290. Paine, S. W.; Fienup, J. R., Machine Learning for Improved Image-Based Wavefront Sensing. *Optics Letters* **2018,** *43* (6), 1235-1238.

291. Nishizaki, Y.; Valdivia, M.; Horisaki, R.; Kitaguchi, K.; Saito, M.; Tanida, J.; Vera, E., Deep Learning Wavefront Sensing. *Optics Express* **2019,** *27* (1), 240-251.

292. Zhou, Z.; Xia, J.; Wu, J.; Chang, C.; Ye, X.; Li, S.; Du, B.; Zhang, H.; Tong, G., Learning-Based Phase Imaging Using a Low-Bit-Depth Pattern. *Photonics Research* **2020,** *8* (10).

293. Wang, K.; Li, Y.; Kemao, Q.; Di, J.; Zhao, J., One-Step Robust Deep Learning Phase Unwrapping. *Optics Express* **2019,** *27* (10), 15100-15115.

294. Ronneberger, O.; Fischer, P.; Brox, T. In *U-Net: Convolutional Networks for Biomedical Image Segmentation*, Medical Image Computing and Computer-Assisted Intervention – MICCAI 2015, 2015; pp 234-241.

295. Midtvedt, B.; Helgadottir, S.; Argun, A.; Pineda, J.; Midtvedt, D.; Volpe, G., Quantitative Digital Microscopy with Deep Learning. *Applied Physics Reviews* **2021,** *8* (1).

296. Sheneman, L.; Stephanopoulos, G.; Vasdekis, A. E., Deep Learning Classification of Lipid Droplets in Quantitative Phase Images. *PLoS One* **2021,** *16* (4), e0249196.

297. Rivenson, Y.; Liu, T.; Wei, Z.; Zhang, Y.; de Haan, K.; Ozcan, A., Phasestain: The Digital Staining of Label-Free Quantitative Phase Microscopy Images Using Deep Learning. *Light: Science & Applications* **2019,** *8*, 23.

298. Nygate, Y. N.; Levi, M.; Mirsky, S. K.; Turko, N. A.; Rubin, M.; Barnea, I.; Dardikman-Yoffe, G.; Haifler, M.; Shalev, A.; Shaked, N. T., Holographic Virtual Staining of Individual Biological Cells. *Proc Natl Acad Sci U S A* **2020,** *117* (17), 9223-9231.

299. Ozaki, Y.; Yamada, H.; Kikuchi, H.; Hirotsu, A.; Murakami, T.; Matsumoto, T.; Kawabata, T.; Hiramatsu, Y.; Kamiya, K.; Yamauchi, T.; Goto, K.; Ueda, Y.; Okazaki, S.; Kitagawa, M.; Takeuchi, H.; Konno, H., Label-Free Classification of Cells Based on Supervised Machine Learning of Subcellular Structures. *PLoS One* **2019,** *14* (1), e0211347.

300. Jo, Y.; Cho, H.; Park, W. S.; Kim, G.; Ryu, D.; Kim, Y. S.; Lee, M.; Park, S.; Lee, M. J.; Joo, H.; Jo, H.; Lee, S.; Lee, S.; Min, H. S.; Heo, W. D.; Park, Y., Label-Free Multiplexed Microtomography of Endogenous Subcellular Dynamics Using Generalizable Deep Learning. *Nat Cell Biol* **2021,** *23* (12), 1329-1337.

301. Kandel, M. E.; He, Y. R.; Lee, Y. J.; Chen, T. H.-Y.; Sullivan, K. M.; Aydin, O.; Saif, M. T. A.; Kong, H.; Sobh, N.; Popescu, G., Phase Imaging with Computational Specificity (Pics) for Measuring Dry Mass Changes in Sub-Cellular Compartments. *Nature Communications* **2020,** *11* (1).

302. Javidi, B.; Moon, I.; Yeom, S.; Carapezza, E., Three-Dimensional Imaging and Recognition of Microorganism Using Single-Exposure on-Line (Seol) Digital Holography. *Optics Express* **2005,** *13* (12), 4492-4506.

303. Moon, I.; Javidi, B., Volumetric Three-Dimensional Recognition of Biological Microorganisms Using Multivariate Statistical Method and Digital Holography. *Journal of Biomedical Optics* **2006,** *11* (6), 064004.

304. Jo, Y.; Park, S.; Jung, J.; Yoon, J.; Joo, H.; Kim, M.-h.; Kang, S.-J.; Choi, M. C.; Lee, S. Y.; Park, Y., Holographic Deep Learning for Rapid Optical Screening of Anthrax Spores. *Science Advances* **2017,** *3* (8), e1700606.

305. Jo, Y.; Jung, J.; Kim, M. H.; Park, H.; Kang, S. J.; Park, Y., Label-Free Identification of Individual Bacteria Using Fourier Transform Light Scattering. *Optics Express* **2015,** *23* (12), 15792-805.

306. Barker, K. L.; Boucher, K. M.; Judson-Torres, R. L., Label-Free Classification of Apoptosis, Ferroptosis and Necroptosis Using Digital Holographic Cytometry. *Applied Sciences* **2020,** *10* (13).

307. Butola, A.; Popova, D.; Prasad, D. K.; Ahmad, A.; Habib, A.; Tinguely, J. C.; Basnet, P.; Acharya, G.; Senthilkumaran, P.; Mehta, D. S.; Ahluwalia, B. S., High Spatially Sensitive Quantitative Phase Imaging Assisted with Deep Neural Network for Classification of Human Spermatozoa under Stressed Condition. *Scientific Reports* **2020,** *10* (1), 13118.

308. Mirsky, S. K.; Barnea, I.; Levi, M.; Greenspan, H.; Shaked, N. T., Automated Analysis of Individual Sperm Cells Using Stain-Free Interferometric Phase Microscopy and Machine Learning. *Cytometry A* **2017,** *91* (9), 893-900.

309. Singh, V.; Srivastava, V.; Mehta, D. S., Machine Learning-Based Screening of Red Blood Cells Using Quantitative Phase Imaging with Micro-Spectrocolorimetry. *Optics and Laser Technology* **2020,** *124*.

310. Kim, G.; Jo, Y.; Cho, H.; Min, H. S.; Park, Y., Learning-Based Screening of Hematologic Disorders Using Quantitative Phase Imaging of Individual Red Blood Cells. *Biosensors & Bioelectronics* **2019,** *123*, 69-76.

311. Javidi, B.; Markman, A.; Rawat, S.; O'Connor, T.; Anand, A.; Andemariam, B., Sickle Cell Disease Diagnosis Based on Spatio-Temporal Cell Dynamics Analysis Using 3d Printed Shearing Digital Holographic Microscopy. *Optics Express* **2018,** *26* (10), 13614-13627.

312. Go, T.; Kim, J. H.; Byeon, H.; Lee, S. J., Machine Learning-Based in-Line Holographic Sensing of Unstained Malaria-Infected Red Blood Cells. *Journal of Biophotonics* **2018,** *11* (9), e201800101.

313. Pasquale, M.; Vittorio, B.; Pierluigi, C.; Andouglas Goncalves da Silva, J.; Luiz Marcos Garcia, G.; Francesco, M.; Melania, P.; Cosimo, D.; Pietro, F. In *Identification and Classification of Biological Micro-Organisms by Holographic Learning*, Proc.SPIE, 2019.

314. Lam, V.; Nguyen, T.; Bui, V.; Chung, B. M.; Chang, L. C.; Nehmetallah, G.; Raub, C., Quantitative Scoring of Epithelial and Mesenchymal Qualities of Cancer Cells Using Machine Learning and Quantitative Phase Imaging. *Journal of Biomedical Optics* **2020,** *25* (2), 1-17.

315. Lam, V. K.; Nguyen, T.; Phan, T.; Chung, B. M.; Nehmetallah, G.; Raub, C. B., Machine Learning with Optical Phase Signatures for Phenotypic Profiling of Cell Lines. *Cytometry A* **2019,** *95* (7), 757-768.

316. Nguyen, T. H.; Sridharan, S.; Macias, V.; Kajdacsy-Balla, A.; Melamed, J.; Do, M. N.; Popescu, G., Automatic Gleason Grading of Prostate Cancer Using Quantitative Phase Imaging and Machine Learning. *Journal of Biomedical Optics* **2017,** *22* (3), 36015.

317. Pavillon, N.; Hobro, A. J.; Akira, S.; Smith, N. I., Noninvasive Detection of Macrophage Activation with Single-Cell Resolution through Machine Learning. *Proceedings of the National Academy of Sciences of the United States of America* **2018,** *115* (12), E2676-E2685.

318. Paidi, S. K.; Raj, P.; Bordett, R.; Zhang, C.; Karandikar, S. H.; Pandey, R.; Barman, I., Raman and Quantitative Phase Imaging Allow Morpho-Molecular Recognition of Malignancy and Stages of B-Cell Acute Lymphoblastic Leukemia. *Biosensors & Bioelectronics* **2021,** *190*, 113403.

Chapter 5. Conclusion

The works presented in this thesis are just two ways to approach modeling biomechanical properties with QPI. The first study looked at using mass redistribution as measured with QPI via autocorrelation and modeling with a simple viscoelastic mechanical model to generate information on stiffness and viscosity for a variety of cell lines along with molecular perturbations and biological transition. The second study examined how information extracted from QPI could be used to quantify the amount of work cells were used for mass accumulation versus that of motion through a series of mechanical derivations. Finally, this thesis presented a comprehensive review of the QPI with respect with to its' usage in biomedicine.

FUTURE DIRECTIONS

Expansion on the preexisting work in this thesis can be found applying various QPR models of viscoelasticity to interrogate other biological questions. An example would be applying these QPR techniques to measure the changes in viscoelasticity during differentiation or immune responses, it also be explored how chemical or biological perturbations on viscoelasticity during such scenarios may affect the outcome or survival of certain cells as they differentiate or are targeted by an immune response. Other biological relevant question would be how mtDNA damage or mutantation may facilitate cascading signals that modulate cellular viscoelasticity. The same approach could be applied to the studies on cellular work, where there is a great deal of interest on how cells undergoing different germ lineage differentiation end up partitioning their energy usage in terms of mass accumulation vs. motion as well as during other biological transitions.

Besides further perturbation of these established biomechanical properties or exploration of other ways to dissect out more information from QPI data, there are four broad directions that QPI is

expanding towards. This thesis had already extensively examined them in the previous section but to summarize they are quantitative phase tomography, QPI in tissues and *in vivo*, multimodality approaches, and machine learning. Each approach expands the limits of QPI either by unlocking more questions to which QPI can be applied or the amount of information QPI could generate.

A simple advancement of QPI is the application into 3D structures through quantitative phase tomography which makes use of the already extensive possibilities of QPI with the added effect of extra axis in space. Where 2D QPI measured the integral of the refractive index of the sample through the thickness of the sample at each imaging pixel, quantitative phase tomography does same but within each voxel. These QPI tomography are developed from phase shifting interferometry[1], and light-emitting diode (LED) array microscopy[2, 3]. This transition into 3D allows QPI to probe mass within multicellular specimens, such as whole animals[1] or 3D organoids which are *in vitro* models of development or disease[4] expanding the range of biological questions QPI can tackle.

On topic of animal models is the efforts to apply QPI to tissue slices and the *in vivo* environment due confounding effects of studying cell behavior *in vitro*. The approaches to this is to either modify techniques of *in vivo* imaging for phase retrieval like with optical coherence tomography[5] or use *in vitro* QPI and translate for the *in vivo* setting through miniaturization. An example would be moving the QPI diffraction phase microscopy system into an endoscope[6]. This would allow for more invasive studies in living organism instead of being confined to structures closer to the regions close to the surface of the skin[7].

Another approach is to simply combine QPI with other imaging or measurement modality in QPI multimodality approaches. The most widely used multimodality QPI approach is QPI with fluorescence detection[8], while more obscure ones are QPI molecular vibrational spectroscopy approaches[9] including QPI Raman[10] and Brillouin[11, 12]. This allows QPI to probe and dissect more information from the data collected by using the second imaging modality in order to segment or parse out structure, cellular state, or even chemical composition enabling QPI to answer even more mechanistically intensive questions.

Incorporation of machine learning into QPI is another promising approach with studies already using them to ease image processing[13] and post-processing[14] steps for QPI. A popular approach to machine learning with QPI is to use the algorithm for classification using QPI[15, 16]. With the increasing numbers of biomechanical properties that can be measured with QPI including QPR viscoelasticity and cellular work, machine learning algorithm be better positioned to identify and classify cells in even more ambiguous cases. A novel approach for QPI machine learning can be using machine learning algorithm to fish for properties that are pertinent in identifying differences between cell types or state and then modeling what biological relevance such properties would have.

CONCLUSIONS

The studies covered in this dissertation show the ability of QPI to tease apart biophysical properties of the cell through examination of cellular biomass and its' associated properties. These studies demonstrate that even through a multitude of biological processes and transition QPI still retains its' ability to dissect and model cellular properties through their relation to biomass regardless of cellular state or process. How cells and other biological samples produce and consume biomass is integral to biology and thus QPI with its' ability to interrogate this property and the vast interaction underpinning is integral to answering questions in biology.

REFERENCES

1. Choi, W.; Fang-Yen, C.; Badizadegan, K.; Oh, S.; Lue, N.; Dasari, R. R.; Feld, M. S., Tomographic Phase Microscopy. *Nature Methods* **2007,** *4* (9), 717-9.

2. Tian, L.; Waller, L., 3d Intensity and Phase Imaging from Light Field Measurements in an Led Array Microscope. *Optica* **2015,** *2* (2), 104-111.

3. Chen, M.; Tian, L.; Waller, L., 3d Differential Phase Contrast Microscopy. *Biomedical Optics Express* **2016,** *7* (10), 3940-3950.

4. Ledwig, P.; Robles, F. E., Epi-Mode Tomographic Quantitative Phase Imaging in Thick Scattering Samples. *Biomedical Optics Express* **2019,** *10* (7), 3605-3621.

5. Joo, C.; Akkin, T.; Cense, B.; Park, B. H.; de Boer, J. E., Spectral-Domain Optical Coherence Phase Microscopy for Quantitative Phase-Contrast Imaging. *Optics Letters* **2005,** *30* (16), 2131-2133.

6. Hu, C. F.; Zhu, S. S.; Gao, L.; Popescu, G., Endoscopic Diffraction Phase Microscopy. *Optics Letters* **2018,** *43* (14), 3373-3376.

7. Kim, K.; Choe, K.; Park, I.; Kim, P.; Park, Y., Holographic Intravital Microscopy for 2-D and 3-D Imaging Intact Circulating Blood Cells in Microcapillaries of Live Mice. *Scientific Reports* **2016,** *6*.

8. Chowdhury, S.; Eldridge, W. J.; Wax, A.; Izatt, J. A., Structured Illumination Multimodal 3d-Resolved Quantitative Phase and Fluorescence Sub-Diffraction Microscopy. *Biomedical Optics Express* **2017,** *8* (5), 2496-2518.

9. Jung, J. H.; Jang, J.; Park, Y., Spectro-Refractometry of Individual Microscopic Objects Using Swept-Source Quantitative Phase Imaging. *Anal Chem* **2013,** *85* (21), 10519-25.

10. Singh, S. P.; Kang, S.; Kang, J. W.; So, P. T. C.; Dasari, R. R.; Yaqoob, Z.; Barman, I., Label-Free Characterization of Ultra Violet-Radiation-Induced Changes in Skin Fibroblasts with Raman Spectroscopy and Quantitative Phase Microscopy. *Scientific Reports* **2017,** *7* (1), 10829.

11. Raghunathan, R.; Zhang, J.; Wu, C.; Rippy, J.; Singh, M.; Larin, K. V.; Scarcelli, G., Evaluating Biomechanical Properties of Murine Embryos Using Brillouin Microscopy and Optical Coherence Tomography. *J Biomed Opt* **2017,** *22* (8), 1-6.

12. Zhang, J.; Raghunathan, R.; Rippy, J.; Wu, C.; Finnell, R. H.; Larin, K. V.; Scarcelli, G., Tissue Biomechanics During Cranial Neural Tube Closure Measured by Brillouin Microscopy and Optical Coherence Tomography. *Birth Defects Res* **2019,** *111* (14), 991-998.

13. Wang, K.; Li, Y.; Kemao, Q.; Di, J.; Zhao, J., One-Step Robust Deep Learning Phase Unwrapping. *Optics Express* **2019,** *27* (10), 15100-15115.

14. Midtvedt, B.; Helgadottir, S.; Argun, A.; Pineda, J.; Midtvedt, D.; Volpe, G., Quantitative Digital Microscopy with Deep Learning. *Applied Physics Reviews* **2021,** *8* (1).

15. Javidi, B.; Moon, I.; Yeom, S.; Carapezza, E., Three-Dimensional Imaging and Recognition of Microorganism Using Single-Exposure on-Line (Seol) Digital Holography. *Optics Express* **2005,** *13* (12), 4492-4506.

16. Moon, I.; Javidi, B., Volumetric Three-Dimensional Recognition of Biological Microorganisms Using Multivariate Statistical Method and Digital Holography. *Journal of Biomedical Optics* **2006,** *11* (6), 064004.

Appendix I. 3D Printed Electromagnet Compatible QPM System

Cellular viscoelasticity is an important property that can serve as biomarkers of disease[1] and is usually defined via two parameters stiffness and viscosity characterizing either the elastic or dissipative components of a cell's response to stress[2]. The elastic component has been widely used as a biomarker for cancer cells[3], metastatic potential[4], and cell migratory pattern[5]. The viscosity portion has been linked to multiple biological processes, including diffusion[6, 7], and cell disease state[8, 9].

Components that contribute most to cellular viscosity in mammalian cells are the various cellular cytoskeletal components from the lipid bilayer to the actin cortex. These components include things like microfilaments, microtubules, motor proteins, and various other structures. These structures are implicated in a host of different processes from adhesion[10] to differentiation[11]. Although there are approaches to measuring cell viscoelastic properties including induced deformations[12] or probes[13]. There are concerns on how these mechanical forces propagate throughout the cell[14] or cell interactions with a probe[15].

There has been great interest using a contact-free, non-invasive approach that can accurately measures cell viscoelastic properties, one of which is based on quantitative phase imaging (QPI). QPI[16] is a microscopy technique that measures the phase-shift of light due to its interactions with the non-aqueous biomass of a cell[17], through experimentally determined cell-average specific refractive index, we can relate the phase shift of light to cell biomass[18, 19]. QPI has traditionally been used to study cell growth[20], death[21], and responses to chemotherapeutics or targeted inhibitors[22-24].

Previous work[25] by Reed et al. has shown that that it entirely possible to such mass information from the various organelle components of the cell as displacement probes. With the use of force perturbation via magnetic breads on the QPI, Reed et al. was also able to show how localized stress affected the mass distribution and rearrangement. Here we show a modified version of the device introduced by Reed et al. fabricated using an electromagnet and 3D printed materials allowing for ease of fabrication and more control of the force generated via the magnetic beads.

Results

The device is a modified version of the one by Reed at al. (Fig. 1a) which makes use of an electromagnet instead of a magnet with a stepper motor. The body of the device was fabricated through 3D printing with ABS materials from a CAD file designed (Fig. 1b) through Solidworks. In order to accommodate the electromagnet, the body of the device (Fig. 1c) that sits below the cell sample is hollow so an electromagnet can be set within and sealed with a round coverslip. The 3D printed body is hollow due to the method of fabrication and so a heat conductive epoxy resin is used to fill up the hollow regions. A heat conductive base is then used to seal the bottom of the device with a hole to allow wiring to connect the electromagnet to a control device.

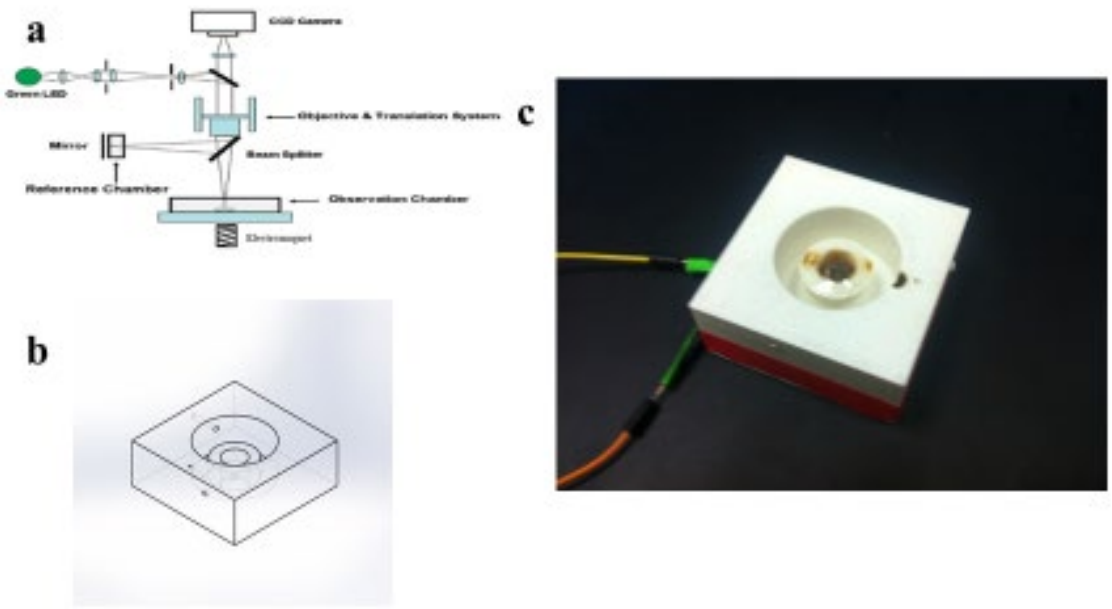

FIGURE 1 Schematic and example of electromagnet QPI setup. (**a**) A schematic using the base of the device fabricated by Reed et al. showing the substitution of an electromagnetic (Modified with permission from [25], © 2008 American Chemical Society). (**b**) CAD design of the body of the device generated via Solidworks. (**c**) Picture of a fully 3D printed and assembled device.

The device was then tested with nickel microspheres on cantilevers and imaged on a Michelson interferometer showing the change in displacement due to the magnet turned off (Fig. 1a) and on (Fig. 1b). The system was then setup for live cell experiments using MCF-7 cells with intensity images for the cell bread setup (Fig. 1c) and QPI phase shift images taken of the cells (Fig. 1d). Demonstrating the system was cell compatible and had a functioning electromagnet for activing the microsphere for probing capabilities.

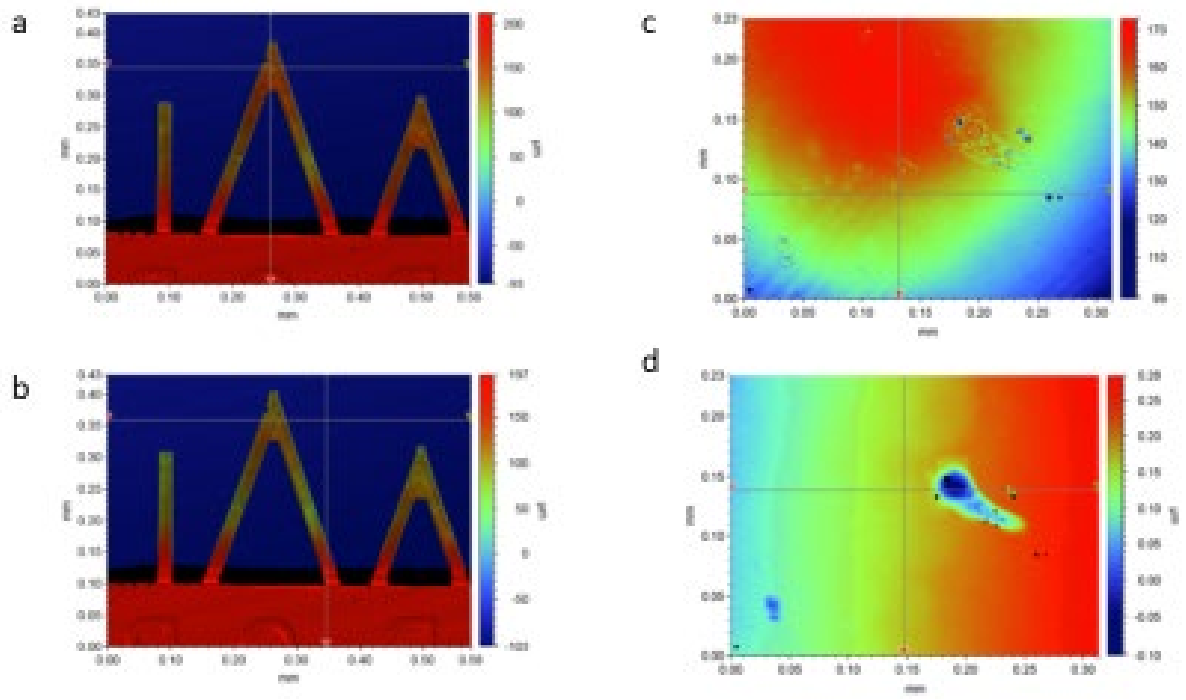

FIGURE 2 QPI images and data captured from electromagnet QPI setup. Distance distribution images of magnetic beads on cantilever (**a**) before and (**b**) activation of electromagnet. (**c**) Intensity and (**d**) phase images of MCF-7 cells with nickel microspheres.

References

1. Bao, G.; Suresh, S., Cell and Molecular Mechanics of Biological Materials. *Nat Mater* **2003,** *2* (11), 715-25.

2. Moeendarbary, E.; Harris, A. R., Cell Mechanics: Principles, Practices, and Prospects. *Wiley Interdiscip Rev Syst Biol Med* **2014,** *6* (5), 371-88.

3. Cross, S. E.; Jin, Y. S.; Rao, J.; Gimzewski, J. K., Nanomechanical Analysis of Cells from Cancer Patients. *Nature nanotechnology* **2007,** *2* (12), 780-3.

4. Xu, W. W.; Mezencev, R.; Kim, B.; Wang, L. J.; McDonald, J.; Sulchek, T., Cell Stiffness Is a Biomarker of the Metastatic Potential of Ovarian Cancer Cells. *PLOS One* **2012,** *7* (10), e46609.

5. Barriga, E. H.; Franze, K.; Charras, G.; Mayor, R., Tissue Stiffening Coordinates Morphogenesis by Triggering Collective Cell Migration in Vivo. *Nature* **2018,** *554* (7693), 523-527.

6. Einstein, A., The Motion of Elements Suspended in Static Liquids as Claimed in the Molecular Kinetic Theory of Heat. *Ann Phys-Berlin* **1905,** *17* (8), 549-560.

7. Wojcieszyn, J. W.; Schlegel, R. A.; Wu, E. S.; Jacobson, K. A., Diffusion of Injected Macromolecules within the Cytoplasm of Living Cells. *P Natl Acad Sci-Biol* **1981,** *78* (7), 4407-4410.

8. Eze, M. O., Membrane Fluidity, Reactive Oxygen Species, and Cell-Mediated-Immunity - Implications in Nutrition and Disease. *Med Hypotheses* **1992,** *37* (4), 220-224.

9. Zakim, D.; Kavecansky, J.; Scarlata, S., Are Membrane Enzymes Regulated by the Viscosity of the Membrane Environment. *Biochemistry* **1992,** *31* (46), 11589-11594.

10. Chicurel, M. E.; Singer, R. H.; Meyer, C. J.; Ingber, D. E., Integrin Binding and Mechanical Tension Induce Movement of Mrna and Ribosomes to Focal Adhesions. *Nature* **1998,** *392* (6677), 730-733.

11. Felsenfeld, D. P.; Choquet, D.; Sheetz, M. P., Ligand Binding Regulates the Directed Movement of Beta 1 Integrins on Fibroblasts. *Nature* **1996,** *383* (6599), 438-440.

12. Lekka, M.; Laidler, P.; Gil, D.; Lekki, J.; Stachura, Z.; Hrynkiewicz, A. Z., Elasticity of Normal and Cancerous Human Bladder Cells Studied by Scanning Force Microscopy. *Eur. Biophys. J.* **1999,** *28* (4), 312-6.

13. Wirtz, D., Particle-Tracking Microrheology of Living Cells: Principles and Applications. *Annual review of biophysics* **2009,** *38*, 301-26.

14. Van Vliet, K. J.; Bao, G.; Suresh, S., The Biomechanics Toolbox: Experimental Approaches for Living Cells and Biomolecules. *Acta Materialia* **2003,** *51* (19), 5881-5905.

15. Squires, T. M.; Mason, T. G., Fluid Mechanics of Microrheology. *Annual Review of Fluid Mechanics* **2010,** *42*, 413-438.

16. Popescu, G.; Park, Y., Quantitative Phase Imaging in Biomedicine. *J. Biomed. Opt.* **2015,** *20* (11), 111201.

17. Zangle, T. A.; Teitell, M. A., Live-Cell Mass Profiling: An Emerging Approach in Quantitative Biophysics. *Nat. Methods* **2014,** *11* (12), 1221-8.

18. Davies, H. G.; Wilkins, M. H. F., Interference Microscopy and Mass Determination. *Nature* **1952,** *169* (4300), 541-541.

19. Barer, R., Interference Microscopy and Mass Determination. *Nature* **1952,** *169* (4296), 366-367.

20. Mir, M.; Wang, Z.; Shen, Z.; Bednarz, M.; Bashir, R.; Golding, I.; Prasanth, S. G.; Popescu, G., Optical Measurement of Cycle-Dependent Cell Growth. *Proc. Natl. Acad. Sci. USA* **2011,** *108* (32), 13124-9.

21. Pavillon, N.; Kuhn, J.; Moratal, C.; Jourdain, P.; Depeursinge, C.; Magistretti, P. J.; Marquet, P., Early Cell Death Detection with Digital Holographic Microscopy. *PLoS One* **2012,** *7* (1), e30912.

22. Hejna, M.; Jorapur, A.; Song, J. S.; Judson, R. L., High Accuracy Label-Free Classification of Single-Cell Kinetic States from Holographic Cytometry of Human Melanoma Cells. *Scientific reports* **2017,** *7* (1), 11943.

23. Reed, J.; Chun, J.; Zangle, T. A.; Kalim, S.; Hong, J. S.; Pefley, S. E.; Zheng, X.; Gimzewski, J. K.; Teitell, M. A., Rapid, Massively Parallel Single-Cell Drug Response Measurements Via Live Cell Interferometry. *Biophys. J.* **2011,** *101* (5), 1025-31.

24. Mir, M.; Bergamaschi, A.; Katzenellenbogen, B. S.; Popescu, G., Highly Sensitive Quantitative Imaging for Monitoring Single Cancer Cell Growth Kinetics and Drug Response. *PLoS One* **2014,** *9* (2), e89000.

25. Reed, J.; Troke, J. J.; Schmit, J.; Han, S.; Teitell, M. A.; Gimzewski, J. K., Live Cell Interferometry Reveals Cellular Dynamism During Force Propagation. *Acs Nano* **2008,** *2* (5), 841-846.

Appendix II. Type V Collagen in Scar Tissue Regulates the Size of Scar after Heart Injury

Cell

Article

Type V Collagen in Scar Tissue Regulates the Size of Scar after Heart Injury

Graphical Abstract

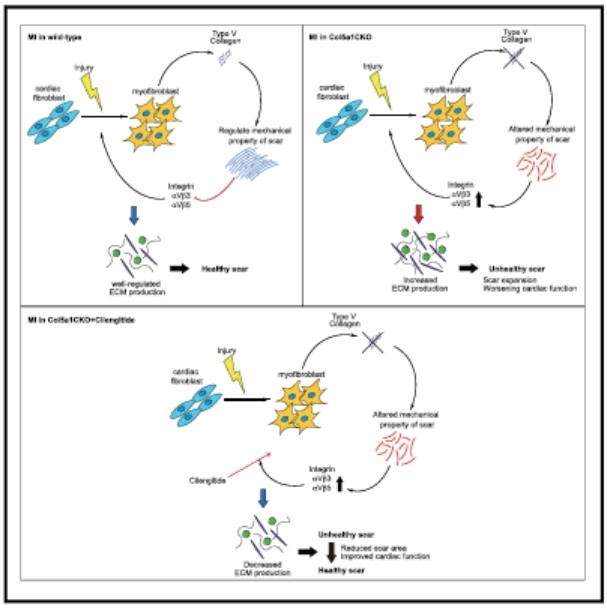

Highlights

- Collagen V deficiency increases scar size after acute heart injury
- Mechanical properties of scars are altered with Col V deficiency
- Altered mechanosensitive cues augment myofibroblast formation in scar
- Inhibition of specific integrins rescues increased scarring in Col-V-deficient states

Authors

Tomohiro Yokota, Jackie McCourt, Feiyang Ma, ..., Marcus Seldin, Aldons J. Lusis, Arjun Deb

Correspondence

adeb@mednet.ucla.edu

In Brief

Scar tissue size following heart injury is a predictor of cardiovascular outcomes. Yokota et al. find that a specific collagen, type V, plays a paradoxical role in limiting scar size by altering the mechanical properties of developing scar tissue.

Yokota et al., 2020, Cell *182*, 545–562
August 6, 2020
https://doi.org/10.1016/j.cell.2020.06.030

CellPress

Cell

CellPress

Article

Type V Collagen in Scar Tissue Regulates the Size of Scar after Heart Injury

Tomohiro Yokota,[1,2,3,4,5,6] Jackie McCourt,[7] Feiyang Ma,[3,4,5] Shuxun Ren,[5,8] Shen Li,[1,2,3,4,5,6] Tae-Hyung Kim,[7] Yerbol Z. Kurmangaliyev,[9] Rohollah Nasiri,[6,10,11] Samad Ahadian,[6,10,12] Thang Nguyen,[10] Xing Haw Marvin Tan,[6,10,15] Yonggang Zhou,[1,2,3,4,5,6] Rimao Wu,[1,2,3,4,5,6] Abraham Rodriguez,[1,2,3,4,5,6] Whitaker Cohn,[16] Yibin Wang,[5,8] Julian Whitelegge,[16] Sergey Ryazantsev,[6] Ali Khademhosseini,[6,10,12,13,14] Michael A. Teitell,[10,18] Pei-Yu Chiou,[6,10,15] David E. Birk,[19] Amy C. Rowat,[7,10] Rachelle H. Crosbie,[4,5,7] Matteo Pellegrini,[3,4,5] Marcus Seldin,[17] Aldons J. Lusis,[1,20] and Arjun Deb[1,2,3,4,5,6,21,*]

[1]Division of Cardiology, Department of Medicine, David Geffen School of Medicine, University of California, Los Angeles, CA 90095, USA
[2]UCLA Cardiovascular Theme, David Geffen School of Medicine, University of California, Los Angeles, CA 90095, USA
[3]Department of Molecular, Cell and Developmental Biology, College of Letters and Sciences, University of California, Los Angeles, CA 90095, USA
[4]Eli & Edythe Broad Center of Regenerative Medicine and Stem Cell Research, University of California, Los Angeles, CA 90095, USA
[5]Molecular Biology Institute, University of California, Los Angeles, CA 90095, USA
[6]California Nanosystems Institute, University of California, Los Angeles, CA 90095, USA
[7]Department of Integrative Biology and Physiology, University of California, CA 90095, USA
[8]Department of Anesthesiology, David Geffen School of Medicine, University of California, Los Angeles, CA 90095, USA
[9]Department of Biological Chemistry, David Geffen School of Medicine, Los Angeles, CA 90095, USA
[10]Department of Bioengineering, School of Engineering, University of California, Los Angeles, CA 90095, USA
[11]Department of Mechanical Engineering, Sharif University of Technology, Tehran 11365-11155, Iran
[12]Terasaki Institute for Biomedical Innovation (TIBI), Los Angeles, CA 90024, USA
[13]Department of Chemical Engineering, School of Engineering, University of California, Los Angeles, CA 90095, USA
[14]Department of Radiology, David Geffen School of Medicine, University of California, Los Angeles, CA 90095, USA
[15]Department of Mechanical and Aerospace Engineering, University of California, Los Angeles, CA 90095, USA
[16]Passarow Mass Spectrometry Laboratory, Semel Institute for Neuroscience and Behaviour, David Geffen School of Medicine, Los Angeles, CA 90095, USA
[17]Department of Biological Chemistry and Center for Epigenetics and Metabolism, University of California, Irvine, CA 92697, USA
[18]Department of Pathology and Laboratory Medicine, University of California, Los Angeles, CA 90095, USA
[19]University of South Florida College of Medicine, Tampa, FL 33612, USA
[20]Department of Genetics, David Geffen School of Medicine, Los Angeles, CA 90095, USA
[21]Lead Contact
*Correspondence: adeb@mednet.ucla.edu
https://doi.org/10.1016/j.cell.2020.06.030

SUMMARY

Scar tissue size following myocardial infarction is an independent predictor of cardiovascular outcomes, yet little is known about factors regulating scar size. We demonstrate that collagen V, a minor constituent of heart scars, regulates the size of heart scars after ischemic injury. Depletion of collagen V led to a paradoxical increase in post-infarction scar size with worsening of heart function. A systems genetics approach across 100 in-bred strains of mice demonstrated that collagen V is a critical driver of postinjury heart function. We show that collagen V deficiency alters the mechanical properties of scar tissue, and altered reciprocal feedback between matrix and cells induces expression of mechanosensitive integrins that drive fibroblast activation and increase scar size. Cilengitide, an inhibitor of specific integrins, rescues the phenotype of increased post-injury scarring in collagen-V-deficient mice. These observations demonstrate that collagen V regulates scar size in an integrin-dependent manner.

INTRODUCTION

Following acute myocardial infarction (MI), dead cardiac muscle is replaced by scar tissue. Clinical studies demonstrate that scar size in patients with prior MI is an independent predictor of mortality and outcomes, even when normalized with respect to cardiac function (Gulati et al., 2013). Despite the immense pathophysiologic importance of scar burden, little is known about factors that regulate scar size after ischemic cardiac injury (Frangogiannis, 2017).

To identify factors determining scar size after MI, we subjected animals to ischemic cardiac injury and performed transcriptional

profiling of heart scars isolated from 3 days to 6 weeks post injury. We observed that scars rapidly attained transcriptional maturity, and there were minimal transcriptional changes in the maturing scar tissue beyond 2 weeks of injury. We thus hypothesized that genes that regulate scar size are likely to be differentially expressed early after ischemic injury. Collagens were one of the most highly differentially upregulated genes in the injured heart early after ischemic cardiac injury. Collagens I and III are the most abundant collagens present in the uninjured heart, comprising approximately 90%–95% of all cardiac collagens (Bashey et al., 1992; Frangogiannis, 2017; Weber, 1989). They belong to the family of fibrillar collagens that are thought to confer mechanical strength to the cardiac matrix. However, more than 26 different types of collagens have been described in mammals, and we observed a large number of collagens that are minimally expressed in the uninjured heart to be robustly induced following injury. The physiological necessity for the heterogeneity of collagen expression in scar tissue is unclear.

In this report, we demonstrate that collagen V (Col V), a fibrillar collagen that is minimally expressed in the uninjured heart and a minor component of scar tissue, limits scar size after ischemic cardiac injury. Animals lacking Col V in scar tissue exhibit a significant and paradoxical increase in scar size after ischemic injury. In the absence of Col V, scars exhibit altered mechanical properties that drive integrin-dependent mechanosensitive feedback on fibroblasts, augmenting fibroblast activation, extracellular matrix (ECM) secretion, and increase in scar size. Modulation of such mechanosensitive feedback cues rescues the Col-V-deficient phenotype of increased scarring. These findings provide insight into the physiological role of Col V in regulating scar size and have implications for the treatment of dysregulated wound healing in genetic diseases caused by mutations in Col-V-encoding genes.

RESULTS

Heart Scars Attain Transcriptional Maturity Early after Acute Ischemic Cardiac Injury

We subjected adult C57BL/6 mice to ischemic cardiac injury (Ubil et al., 2014) by permanent ligation of the left anterior descending coronary artery and observed acute and progressive loss of cardiac function (Figure S1A). Hearts were harvested at 3, 7, 14, 21, and 42 days after ischemic injury, and the fibrotic scar tissue in the injured and the region remote to the area of injury were dissected from the same heart for RNA sequencing (RNA-seq) to quantify temporal changes in gene expression. Principal-component analysis (PCA) showed samples from remote regions at all time points clustered together (Figure 1A). Principal component 1 (PC1) separated transcriptional signatures of injured and uninjured regions across all time points examined (Figure 1A), suggesting that gene expression differences continue to persist between the injured and uninjured regions. PC2 separated the samples of scar tissue in a temporal manner following injury (Figure 1A). In particular, significant differences were observed between scar tissue harvested at 3 and 7 days following injury, as well as between that harvested at 7 days and subsequent time points. However, the transcriptional signatures of the injured region of the hearts at 14, 21, and 42 days after injury clustered together, demonstrating that most transcriptional changes occur within 2 weeks of injury (Figure 1A). Analysis of differentially expressed genes (DEGs) demonstrated that the largest number of DEGs occurred between injured and uninjured samples at each analyzed time point (from 1,210 to 1,931) (Figure 1B; Table S1). Comparisons between time points of injured regions detected 247 and 100 DEGs between days 3 and 7, and days 7 and 14, respectively. Almost no differences were detected between scar tissue harvested at later time points (Figure 1B). These data demonstrate that major transcriptional changes within scar tissue occur early after injury and further maturation of scar tissue beyond 2 weeks is not associated with significant transcriptional changes.

We hypothesized that genes that directly regulate scar size are upregulated early after ischemic cardiac injury. Collagens were one of the most differentially upregulated genes in the injured region early after injury. We examined expression patterns of genes encoding obligatory subunits of all types of collagen (Figure 1C). In addition to type I and III collagens, we observed genes encoding for various subunits of Col V, VI, VIII, XI, XII, XIV, XV, XVI, and XVIII to be significantly induced after heart injury (Figure 1C) with expression of most collagens increasing by 3 days, peaking at 7 days, and declining by 42 days after injury (Figure 1C). Next, to confirm our findings, we performed qPCR for the principal genes encoding all mammalian collagens (Figure 1D, Figure S1B). *Col1a1* and *Col3a1* demonstrated the most robust gene expression changes after acute injury, consistent with them being the principal cardiac collagens (Figure 1D). Collagen-encoding genes that are known to be abundantly expressed in extra-cardiac tissues such as *Col2a1*, *Col7a1*, and *Col9a2* demonstrated dynamic expression changes (Figure S1B), but absolute levels of expression were low (Figure S1C). Taken together, these data demonstrate that a diverse set of collagen genes, including several that are minimally expressed in the uninjured heart, are robustly induced early after acute ischemic cardiac injury.

Col5a1 Expression Overlaps *Col1a1* and *Col3a1* Expression in the Infarcted Region with a Single Cardiac Fibroblast Expressing All Three Collagens

We next dissected the nascent scar tissue at 7 days following injury and first performed proteomic analysis of the collagens differentially expressed between the scar and uninjured tissue (Figure 2A). We confirmed increased levels of the fibrillar collagen peptide chains COL1A1, COL3A1, and COL5A1 and other collagen peptides (Figure 2A). *Col1a1* and *Col3a1* genes were the most abundantly expressed fibrillar collagen genes in scar tissue at 7 days following injury (Figure 2B). Out of other fibrillar collagens (II, V, XI), *Col5a1* was the only one that was induced robustly early in scar tissue (Figure 2B).

We next examined the spatial expression of the fibrillar collagens Col I, III, and V. The objective of this experiment was to determine whether the same cell expressed all three fibrillar collagens (I, III, and V) or whether the collagens were expressed by different cells in scar tissue. To prevent cross reactivity of antibodies to different collagens and to facilitate accurate fluorophore colocalization, we chose to perform RNA fluorescence *in situ* hybridization (RNA-FISH) to determine the spatial

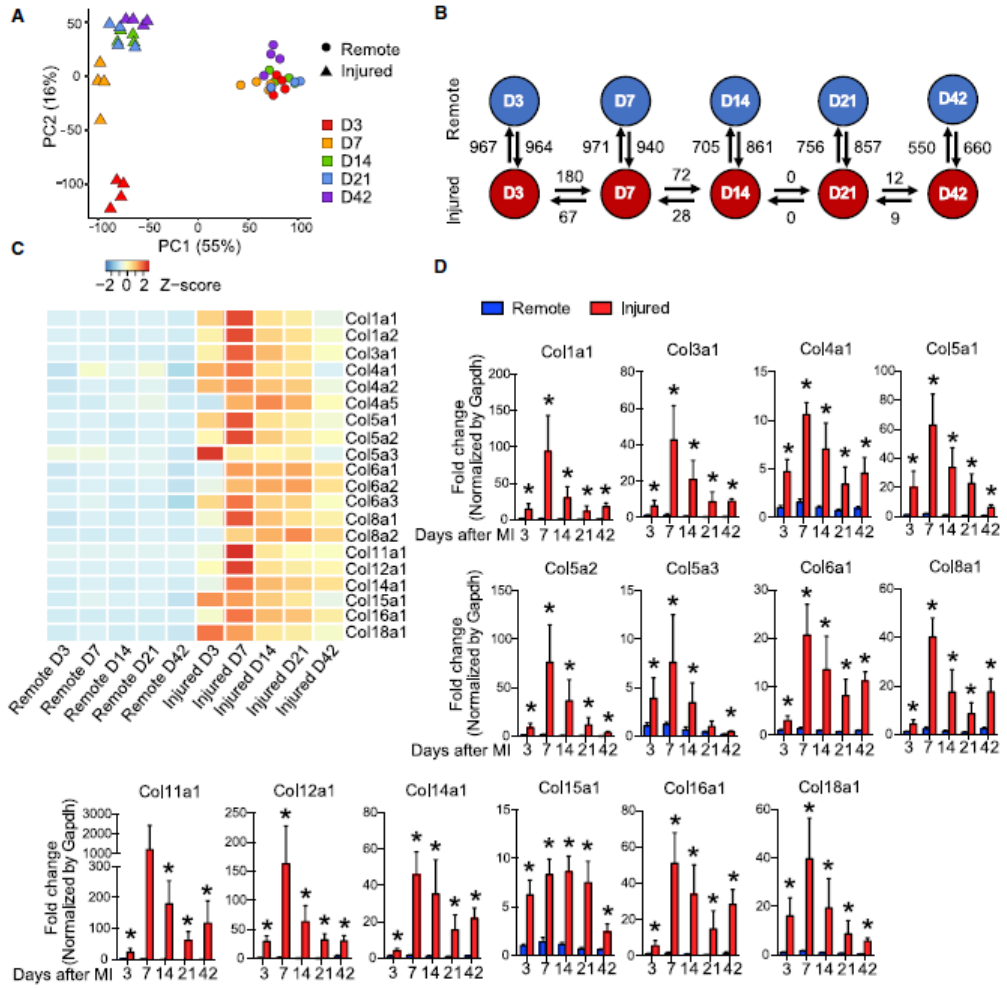

Figure 1. Temporal Changes in Gene Expression of Scar Tissue following Acute Ischemic Cardiac Injury

(A) Principal-component analysis based on expression profiles of all genes (n = 4).

(B) Summary of differential gene expression analysis. Arrows and numbers indicate direction and numbers of differentially expressed genes detected in each pairwise comparison (false discovery rate [FDR] 1%, fold change > 4).

(C) Heatmap with expression patterns of collagen genes (n = 4).

(D) Expression of collagen genes encoding for obligatory units of the respective collagen by qPCR (mean ± SD, *p < 0.05, n = 5).

See also Figure S1.

expression of *Col5a1* versus *Col1a1* or *Col3a1* post injury. RNA-FISH demonstrated robust and overlapping expression of *Col5a1* with either *Col3a1* or *Col1a1* mRNA in the injured region of the heart (Figure 2C), and we observed the same cell to express both *Col5a1* and *Col3a1*/*Col1a1* (Figure 2D). To confirm these observations, we performed RNA-FISH in mice with genetically labeled cardiac fibroblasts. For this purpose, mice expressing fibroblast Cre drivers (Col1a2CreERT or TCF21MerCreMer) were crossed with the lineage reporter Rosa26tdTomato mice (Acharya et al., 2011; Pillai et al., 2017; Zheng et al., 2002) and tamoxifen was administered to induce genetic labeling of cardiac fibroblasts (Pillai et al., 2017; Ubil

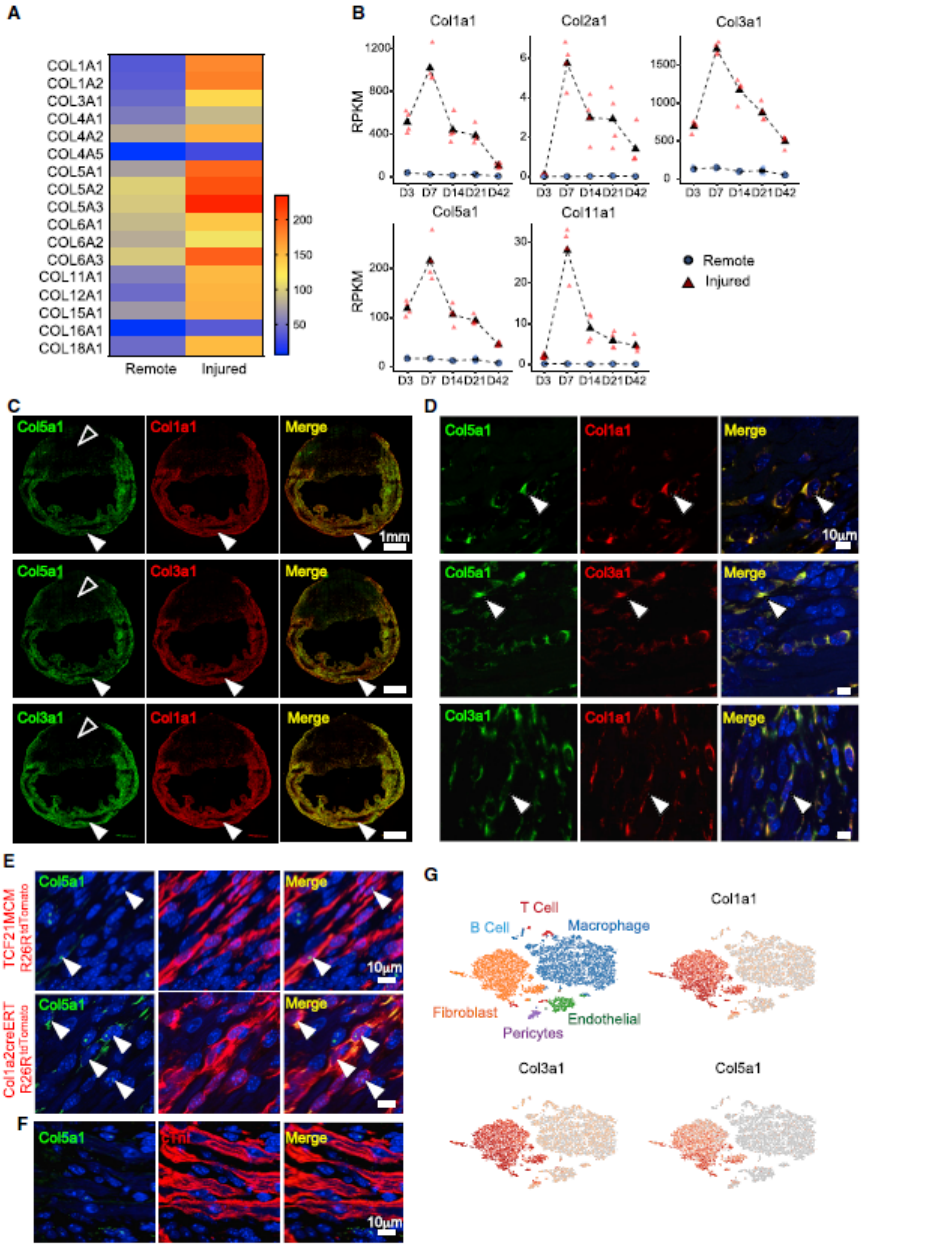

(legend on next page)

et al., 2014). RNA-FISH on hearts harvested at 7 days post injury demonstrated tdTomato-labeled cardiac fibroblasts to express *Col5a1* (Figure 2E). As cardiomyocytes are known to express collagens (Heras-Bautista et al., 2019), we performed immunostaining for cardiac troponin I, but did not observe cardiomyocytes to express *Col5a1* (Figure 2F). To provide corroborative evidence, we next performed single-cell RNA-seq (scRNA-seq) of the non-myocyte cell fraction of the injured region of the heart at 7 days post injury and observed significant overlap between *Col5a1* expression and *Col3a1* and *Col1a1* expression (Figure 2G). Taken together, these observations demonstrate that Col I, III, and V have overlapping expression in the area of injury and that a single cardiac fibroblast has the ability to produce both Col V and Col I/III.

Mice Deficient in Type V Collagen Exhibit a Paradoxical Increase in Fibrosis and Scar Size after Heart Injury

Homozygous deletion of the *Col5a1* gene results in absence of functional Col V protein in tissues and causes early embryonic lethality (Wenstrup et al., 2004). Mice heterozygous for Col5a1 deficiency exhibit increased fibrosis in their valves and myocardium at birth, suggestive of a role of Col V in regulating ECM output (Lincoln et al., 2006). To determine the functional role of Col V in the injured heart, we first crossed the Col1a2CreERT mice with *Col5a1* floxed mice (Sun et al., 2011). We administered tamoxifen to progeny mice for 5 days prior to injury and continued for seven days post injury to maximize labeling and generate Col5a1CKO (conditional knockout) mice. Control animals included littermates that lacked the Cre transgene but had both *Col5a1* alleles floxed and were injected with tamoxifen in an identical manner. RNA-FISH on the Col5a1CKO hearts demonstrated 66.6% ± 17.8% reduction of *Col5a1* expression (mean ± SD, $^*p < 0.05$) (Figures S2A and S2B). We observed significant depression of cardiac contractile performance (ejection fraction [EF] and fractional shortening [FS]) by 7 days in the Col5a1CKO group following ischemic injury, which persisted throughout the next 6 weeks (mean ± SD, $^*p < 0.05$) (Figures 3A and 3B), and this was associated with a strong trend toward chamber dilatation ($p = 0.06$ for LVID(d) at 6 weeks post MI) (Figure 3B). Histology demonstrated that the area of fibrotic scar tissue was significantly greater by 1.5-fold in the Col5a1CKO compared to wild-type littermates (mean ± SD, $^*p < 0.05$) (Figures 3C and 3D). To further analyze the wound healing response in Col5a1CKO animals, we determined the fraction of animals that exhibited mild, moderate, or severe fibrosis after ischemic injury. We defined mild, moderate, and severe fibrosis as scar surface area less than 20%, between 20% and 40%, and greater than 40% of the left ventricular surface area, respectively, measured at 6 weeks following injury, and observed that greater than 58% of the Col5a1CKO animals had severe fibrosis compared to approximately 12% of animals in control littermates (Figure 3E). There were no significant differences in interstitial fibrosis of the uninjured myocardium in Col5a1CKO and control mice (Figure S2C). As scars mature, collagen fibrils undergo crosslinking within scar tissue and become less soluble. We found that the amount of insoluble collagen (surrogate for crosslinked collagen) was increased by 254% ± 64% (mean ± SD, $^*p < 0.05$) in the Col5a1CKO group at 6 weeks post injury (Figure 3F). Col V is thought to initiate organization of Col I and III fibrils in the ECM and is intercalated between the staggered arrangement of Col I and III fibrils maintaining organization of the ECM (Wenstrup et al., 2004). We performed toluidine blue staining and observed the typical wavy nature of collagen fibrils compactly arranged in parallel in the injured control animal hearts, but the hearts from the Col5a1CKO animals showed a loose arrangement of collagen fibers (Figure 3G). We performed transmission electron microscopy, and instead of the smooth parallel arrangement of collagen fibrils in scars of control animals, we observed fibrillar disarray with fibrils running at orthogonal axes to each other in the Col5a1CKO scars (Figures 3H and 3I). Collagen fibril diameters were significantly greater (Figures 3J and 3K), and a histogram of the numbers of collagen fibrils versus their diameter demonstrated a rightward shift of the curve in Col5a1CKO mice (Figure 3L). Finally, we performed electron tomography and observed shorter length, irregular fibrillar structure and breaks in collagen fibrils in the Col5a1CKO scar compared to wild-type scar (Figures 3M and 3N). Taken together, these observations demonstrate that deletion of type V collagen leads not only to increased scar size, but also results in grossly abnormal scar architecture.

As increased scar size in the post-infarcted heart is associated with adverse phenotypes such as hypertrophy of cardiomyocytes in the border zone (Frangogiannis, 2017, 2019), we harvested hearts at 6 weeks following injury and observed significantly greater heart-weight/body-weight ratios of Col5a1CKO hearts compared to control littermates (mean ± SD, $^*p < 0.05$) with no significant differences in body weight alone (Figures S2D and S2E). Immunostaining for cardiac troponin I confirmed robust hypertrophy of cardiomyocytes abutting the margins of the scar (border zone) in Col5a1CKO animals (Figures S2F and S2G).

Figure 2. Expression of Col5a1 in Relation to Col1a1 and Col3a1

(A) Proteomic analysis of individual collagen chains in injured and remote region of myocardium at 7 days post MI (n = 3).

(B) Normalized expression levels (reads per kilobase of transcript, per million mapped reads [RPKM]) for selected collagen genes. Average expression levels across time points are shown in black symbols and dashed lines. Expression levels for individual replicates are shown in colored symbols (n = 4).

(C) RNA-FISH to demonstrate expression of *Col5a1*, *Col1a1*, and *Col3a1* in the heart at 7 days post MI (solid arrowhead, representative images, n = 4, unfilled arrowhead indicates remote region, images were acquired and stitched together using Nikon software).

(D) Higher magnification demonstrating co-localization of Col5a1 with Col1a1 and Col3a1 within the same cell (arrows, representative images, n = 4).

(E and F) Expression of *Col5a1* in cardiac fibroblasts genetically labeled by the TCF21 or Col1a2 label (E) but not in cardiomyocytes (Troponin I stained) in the injury region (F) (arrows, representative images, n = 3).

(G) Single cell RNA-seq of non-myocytes at 7 days post MI demonstrating typical cell phenotypes in clusters and distribution of *Col1a1*, *Col3a1*, and *Col5a1* (n = 3).

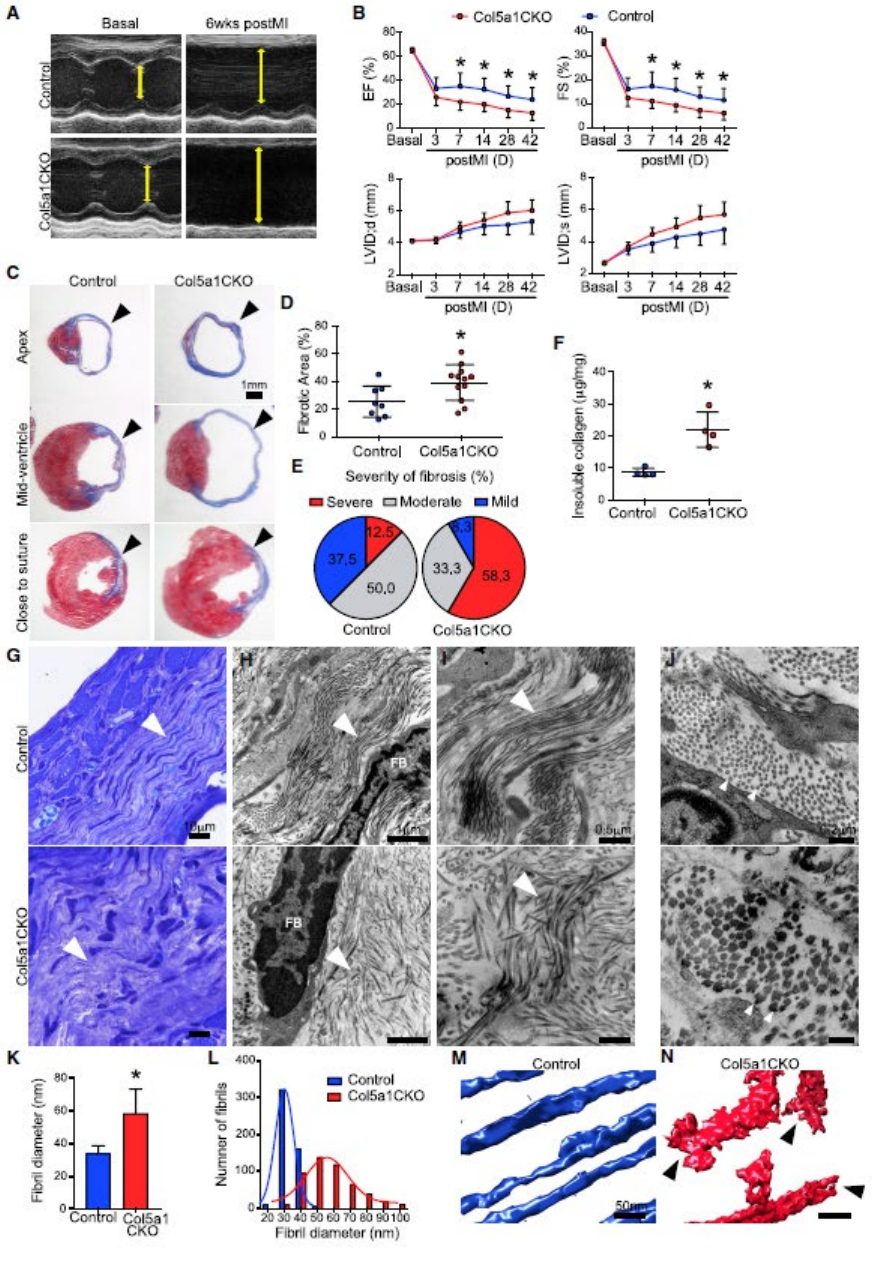

(legend on next page)

Validation of Phenotype of Collagen V Deficiency in the Injured Heart Using an Alternative Cre Driver

To validate our observations noted with the Col1a2Cre driver, we generated another CKO of the *Col5a1* gene using the Tcf21MerCreMer driver (Tcf21MCM), Tcf21 being a specific marker of cardiac fibroblasts in the adult heart (Acharya et al., 2011; Kanisicak et al., 2016). The Tcf21MCM mice were crossed with the Col5a1 floxed mice and tamoxifen-administered 5 days prior to injury and for 7 days following injury to create Tcf21MCM:Col5a1CKO mice. Controls included littermate animals that had both *Col5a1* alleles floxed but lacked the Cre transgene and were injected with tamoxifen in an identical manner. At 7 days post injury, *Col5a1* expression in the injury region of Tcf21MCM:Col5a1CKO decreased by almost 60.1% ± 10.1% (mean ± SD, $^*p < 0.05$) (Figures S3A and S3B). Tcf21MCM:Col5a1CKO mice exhibited significant decline in cardiac contractile function by 7 days of injury that persisted for the next 6 weeks (Figures S3C and S3D), and this was also associated with a trend toward greater chamber size (LVID) (Figure S3D). We observed a significant 1.5-fold increase in scar size in Tcf21MCM:Col5a1CKO animals versus control littermates (mean ± SD, $^*p < 0.05$) (Figures S3E and S3F). The fraction of animals that exhibited severe fibrosis (>40% surface area) was 40% in the Tcf21MCM:Col5a1CKO animals compared to approximately 11% in the control littermates (Figure S3G). The Tcf21MCM:Col5a1CKO animals exhibited significantly greater heart-weight/body-weight ratios at 6 weeks after injury (no change in body weight) (Figures S3H and S3I), and histology confirmed significantly greater myocyte hypertrophy (mean ± SD, $^*p < 0.05$) (Figures S3J and S3K). To exclude a potential role of tamoxifen in contributing to post-injury contractile dysfunction, tamoxifen was administered in an identical manner to TCF21MCM mice but without the Col5a1 floxed alleles. No differences in cardiac function were observed within 1 and 2 weeks of injury following tamoxifen administration (Figure S4A). Taken together, these observations using an independent Cre driver mirror and provide compelling evidence that deletion of type V collagen leads to an exacerbated fibrotic repair response.

To complement these observations, we subjected the Col5a1 heterozygous KO mice (Col5a1$^{+/-}$) (Wenstrup et al., 2004) to ischemic cardiac injury. Compared to wild-type littermates, the heterozygote Col5a1KO exhibited a significant reduction in cardiac contractile function by 1 and 2 weeks of injury and exhibited greater degree of cardiac hypertrophy as assessed by heart-weight/body-weight ratios (Figures S4B–S4D). The data presented earlier show that scars rapidly attain transcriptional maturity, and cardiac function is significantly compromised within 7 days of injury in the Col5a1CKO mice. Considering these observations, we postulated that the effects of Col5a1 deficiency on cardiac function early after cardiac injury may be related to its role in mediating an acute fibrotic repair response. To investigate this, we deleted Col5a1 after the acute phase of injury by administering tamoxifen from post-injury day 4 for 10 days. We observed that the TCF21MCM:Col5a1CKO animals (with deletion of Col5a1 after the acute injury response) did not exhibit a reduction in cardiac function at 2 weeks after injury (Figure S4E). These observations suggest that type V collagen affects post-injury cardiac function by playing a critical role in the early fibrotic repair response.

Col5a1 Is a Critical Determinant of Post-Injury Heart Function vis-à-vis Other ECM Genes

A large number of collagens and other ECM proteins are upregulated in the region of scarring (in addition to Col V), and an argument can be made of the functional importance of Col V vis-à-vis other ECM proteins. We adopted a population genetics approach to determine the relative functional importance of Col V in driving post-injury cardiac function vis-à-vis other ECM genes. The hybrid mouse diversity panel (HMDP) comprises approximately 100 diverse inbred and recombinant strains of mice, and each strain can be subjected to an identical environmental perturbation to determine the genetic factors underlying responses (Ghazalpour et al., 2012; Lusis et al., 2016). The individual mouse strains in the HMDP were subjected to continuous isoproterenol infusion for 3 weeks that induces a chronic form of cardiac injury characterized by cardiomyocyte hypertrophy and interstitial fibrosis (Wang et al., 2016). Key traits of cardiac function such as cardiac contractility, chamber size, and fibrosis were followed over 3 weeks. Gene expression changes in the heart following isoproterenol infusion were determined in each strain, and these were statistically integrated with clinical traits to identify key loci or genes involved (Figure 4A) (Rau et al., 2017; Rau et al., 2015). We first analyzed a set of

Figure 3. Animals with *Col5a1* Deletion in Cardiac Fibroblasts Exhibit a Paradoxical Increase in Scar Tissue after Heart Injury

(A) M-mode echocardiogram demonstrating left ventricular (LV) walls and internal dimension (yellow line) prior to basal and 6 weeks post MI (representative images).

(B) Ejection fraction (EF), fractional shortening (FS), LV dimensions in end diastole (LVIDd), and end systole (LVIDs) at different time points post MI (n = 12/control and 27/CKO at basal, n = 10/control and 22/CKO at 3 days, n = 9/control and 15/CKO at 1 week, n = 9/control and 13/CKO at 2 weeks, n = 8/control and 12/CKO at 4 and 6 weeks post MI).

(C) Masson trichrome staining of hearts sectioned at the base (just distal to suture line) at mid-ventricle and apex 6 weeks post MI (representative images).

(D) Quantification of surface area of scar normalized to the surface area of the ventricle (n = 8/control and 12/CKO).

(E) Fraction of animals demonstrating mild/moderate or severe scarring at 6 weeks post MI.

(F) Measurement of insoluble collagen in scar tissue at 4 weeks post MI (n = 4)

(G) Toluidine blue staining of scar tissue at 4 weeks post MI (arrowhead, representative images, n = 2)

(H) Transmission electron microscopy (TEM) of scar area showing fibrillar disarray in the Col5a1CKO (arrowhead, FB = fibroblast)

(I) Higher magnification with TEM demonstrating fibrillar disarray with fibrils running in orthogonal axes to each other in the Col5a1CKO scar (arrowhead).

(J) Cross-sectional TEM view demonstrating fibril diameter size (arrowheads, n = 2 for all TEM).

(K) Average collagen fibril diameter in scars (n = 2).

(L) Histogram of collagen fibril diameters demonstrates a clear shift to the right in Col5a1CKO (n = 2).

(M and N) Electron tomogram of scar area from (M) control and (N) Col5a1CKO animal. Data shown as mean ± SD, $^*p < 0.05$.

See also Figures S2, S3, and S4.

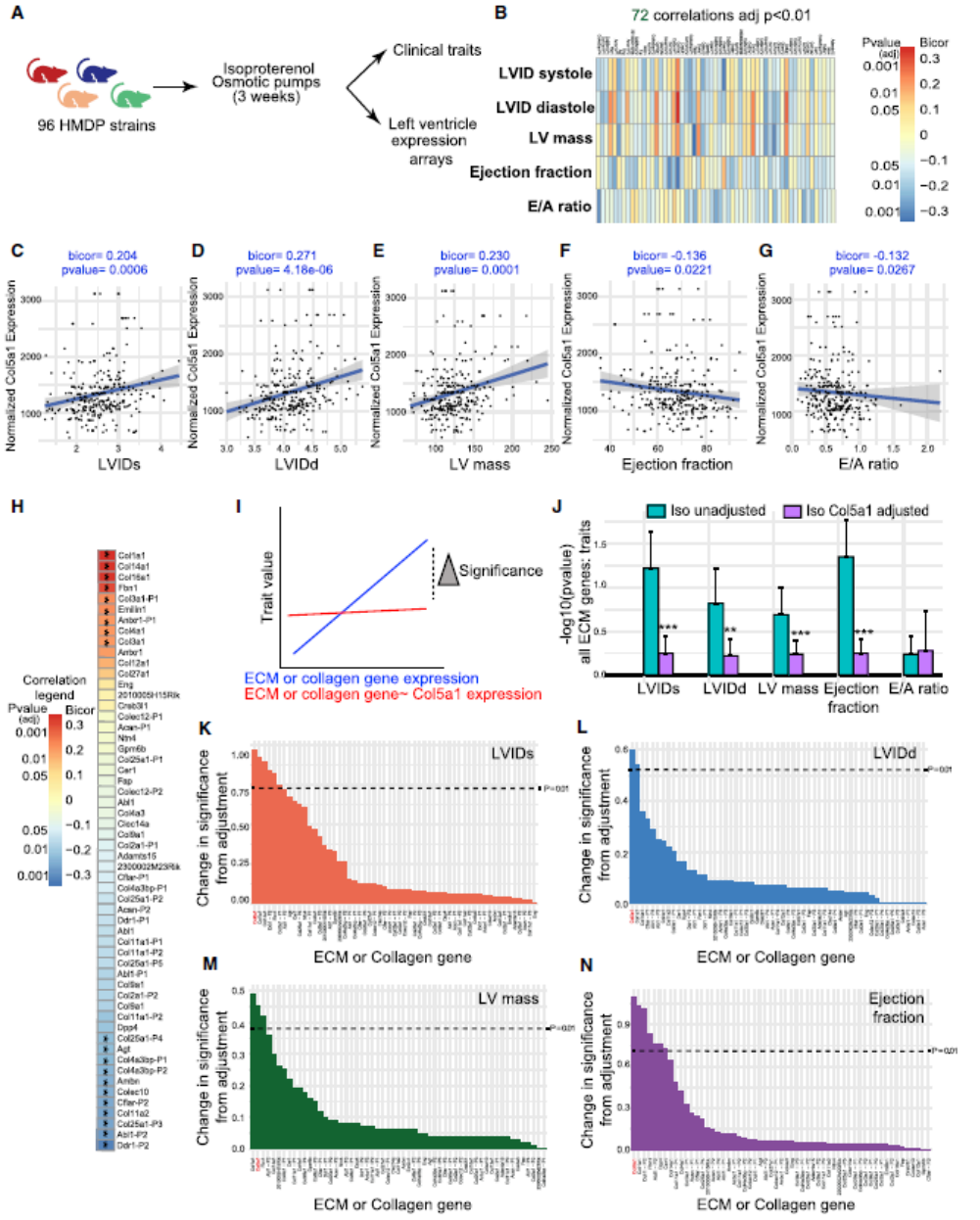

(legend on next page)

ECM genes including collagens (Extracellular Matrix - GO:0031012 or Collagen Network - GO:0098645) that are abundantly expressed in the heart (Figure S4F) for correlations with clinical traits mentioned above (Figure 4B). *Col5a1* expression significantly correlated with cardiac traits of chamber size (LVID systole or diastole), cardiac hypertrophy (LV mass), and systolic and diastolic function (EF and E/A ratios) (Figures 4C–4G). We also observed genetic variation in the average expression of Col5a1 across the strains in the HMDP (Figure S4G). We next analyzed the strength of association between *Col5a1* gene expression and the abovementioned set of ECM genes after isoproterenol. While several significant relationships were observed between *Col5a1* and ECM genes, there did not appear to be consistent patterns of overall positive or negative concordance (Figure 4H; Table S2). Given that (1) ECM genes strongly correlate with clinical traits and (2) *Col5a1* gene expression strongly correlates with a subset of ECM genes, we performed conditional analyses to evaluate the functional importance of *Col5a1* in mediating ECM:trait correlations. If *Col5a1* significantly contributed to the strength of correlation between ECM genes and traits, then adjustment for *Col5a1* expression should reduce the overall significance of correlations (Figure 4I). Conditioning on *Col5a1* expression led to a significant reduction in the overall strength of the association between rest of ECM genes and cardiac traits of chamber size, LV mass, and EF, while measures of diastolic compliance (E/A ratio) were not affected following *Col5a1* adjustment (Figure 4J). To test whether the correlation was specifically dependent on *Col5a1*, we conditioned on each of the other ECM genes and then assessed the change in significance of the correlations. As can be seen in Figures 4K–4N, while conditioning on several genes reduced the strength of the correlations, *Col5a1* showed the highest changes in significance following adjustment for LVID (systole), LVID (diastole), and ejection fraction. Only for cardiac mass was *Col5a1* in ranked second after *Col1a1* (Figure 4M). Using alternative cardiac injury models and complementary genetics approaches, these data support our principal observations of the physiological importance of Col V in regulating heart repair.

Collagen V Deficiency Increases Myofibroblast Formation and Expression of Extracellular Matrix Genes in Scar Tissue

We next investigated mechanisms by which *Col5a1* deficiency leads to increase in scar size and examined whether the deficiency of *Col5a1* altered cell populations in the scar or affected their transcriptional signatures. As maximal changes in transcriptional signatures of scars occur within the first few days after cardiac injury (Figure 1A), we harvested injured and uninjured regions of hearts, isolated non-myocyte cells, and subjected the cells to scRNA-seq using the 10x Genomics platform. A tSNE (t-distributed stochastic neighbor embedding) plot demonstrated the major cell populations in the injured region at 7 days (Figures 5A and S5A). We next determined the fraction of cells contributing to each cluster in the Col5a1CKO and wild-type controls (Figure 5B) and observed a comparable distribution of cells across fibroblast, endothelial, smooth muscle, and other cell populations with a slightly higher number of macrophages (Figures 5B and S5B). As *Col5a1* was deleted principally in cardiac fibroblasts, we focused on DEGs in the cardiac fibroblast cell cluster and first confirmed decreased expression of *Col5a1* in fibroblasts from Col5a1CKO mice (Figure 5C). We observed that fibroblasts from Col5a1CKO hearts exhibited significantly greater expression of *Acta 2* (αsmooth muscle actin or αSMA) (Figure 5D), a gene that is not expressed by cardiac fibroblasts in the uninjured heart, but is a marker of myofibroblasts, a population of activated fibroblasts expressing smooth muscle contractile proteins (Frangogiannis, 2019). Myofibroblasts exhibit a synthetic and contractile phenotype and are thought to be the principal cells that secrete ECM proteins to form scar tissue (van den Borne et al., 2010). Other smooth-muscle-specific contractile proteins (*Cnn2* [calponin] and *Actn1* [Actinin 1]), markers of smooth muscle differentiation SM22α (*Tagln*), proteins regulating smooth-muscle contraction such as regulatory myosins (*Myl 6* and *Myl9*), or calcium handling during smooth muscle contraction (*S100a4* and *s100a6*) were also significantly upregulated in fibroblasts of Col5a1CKO animals, suggestive of broad cytoskeletal organization and activation of fibroblasts (Figures 5E and S5C). Lysyl oxidase (*Lox*), which mediates crosslinking of collagen, was also upregulated (Figure S5C), consistent with increased amounts of insoluble collagen in scar tissue of Col5a1CKO hearts. We next examined the subsets of fibroblasts residing within the fibroblast cluster (Figure 5F) and observed that *αSMA* was abundantly expressed in Cluster 0, identifying that cluster as a population enriched in myofibroblasts (Figures 5G and 5H). We observed that the number of myofibroblasts (defined as fibroblasts expressing *αSMA*) (Cluster 0) was significantly increased by 33% in the Col5a1CKO animals (Figure 5I). To confirm these findings, we performed double immunofluorescence staining for αSMA and vimentin (fibroblast marker) on hearts of Col5a1CKO mice and observed that the number of myofibroblasts (defined as the fraction of αSMA+vimentin+/total

Figure 4. Importance of *Col5a1* in Regulating Cardiac Function Post Injury vis-à-vis Other ECM Genes

(A) HMDP comprising 96 strains of mice were subjected to continuous isoproterenol infusion for 3 weeks.

(B) Gene X trait analysis demonstrating strength of association between individual ECM genes and cardiac traits.

(C–G) Scatterplots show correlation of Col5a1 expression with traits of (C) LVIDs, (D) LVIDd, (E) LV mass, (F) EF, and (G) E/A ratio following isoproterenol injection across all HMDP strains.

(H) Strength of association between Col5a1 expression and that of ECM genes (*$p < 0.01$).

(I) Hypothesis of how adjustment for Col5a1 could significantly change the strength of association between ECM genes and cardiac traits.

(J) Conditional analysis demonstrating the strength of correlation (-log p value) between ECM genes and different cardiac traits following adjustment for Col5a1 expression (***$p < 0.005$,**$p < 0.01$, compared to isoproterenol unadjusted).

(K–N) Change in significance of rest of ECM genes and specific trait (K) LVIDs, (L) LVIDd, (M) LV mass, and (N) EF following adjustment for specific gene (horizontal dotted line shows a cut-off p value = 0.01).

See also Figure S4.

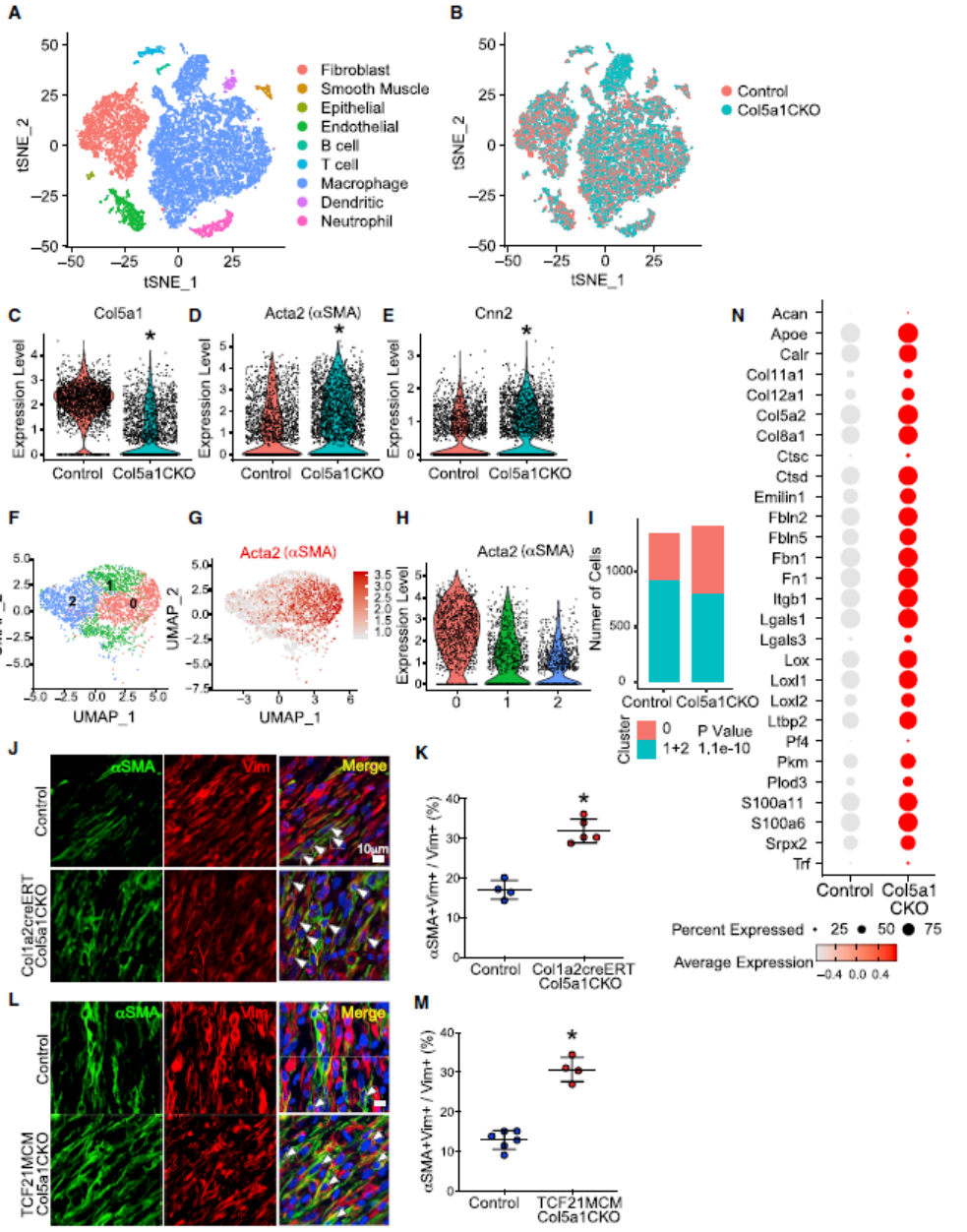

(legend on next page)

number of vimentin+ cells) was 2- to 2.5-fold greater in the scar tissue of Col5a1CKO mice (Figures 5J and 5K) or that of Tcf21MCM:Col5a1CKO mice (Figures 5L and 5M) (mean ± SD,*p < 0.05). Analysis of differentially expressed ECM genes demonstrated a large number of ECM genes to be significantly upregulated in Col5a1CKO fibroblasts, including several collagens (*Col8a1* and *Col11a1*), *fibronectin*, *osteopontin*, and *fibrillin* (Figure 5N). Our data suggest that increased numbers of myofibroblasts along with increased expression of myofibroblast markers and other ECM genes in cardiac scar tissue of Col5a1CKO animals contribute to the increase in scar size. We next determined whether increased myofibroblast numbers in Col5a1CKO scar tissue were secondary to increased proliferation. We examined the expression of cell cycle genes that regulate S/G1 as well as G2/M transitions of the cell cycle in cluster 0 (myofibroblast population) (Figures S6A and S6B), but the average expression of such genes did not show any difference between the myofibroblasts of control and Col5a1CKO animals (Figure S6C). We performed immunostaining for a marker of proliferation (Ki67), but also did not observe any significant differences between the fraction of fibroblasts expressing Ki67 (Figure S6D). Collectively, these observations suggest that increased myofibroblast differentiation or formation, rather than myofibroblast proliferation, likely underlies the increased myofibroblast numbers observed in Col5a1CKO scar tissue compared to that of control littermates.

Collagen V Deficiency Alters Mechanical Properties of Fibroblasts and Matrix in Scar Tissue

We next explored the molecular underpinnings of increased myofibroblast differentiation and hypothesized that altered mechanical properties of the matrix could be driving feedback cues to drive myofibroblast differentiation. We first performed atomic force microscopy (AFM) to determine the stiffness of mid-ventricular scar tissue 7 days post injury and observed that the Young's modulus was significantly decreased by 15% in the Col5a1CKO animals (Figures 6A–6D) and a less-stiff scar is more prone to expansion by hemodynamic forces. Scar contraction is another major determinant of scar size. During wound healing, contractile forces generated by cardiac fibroblasts shrink the size of the scar, but if the surrounding matrix is less stiff, this would decrease the forces transduced through scar tissue. We explored this hypothesis by examining force contraction relationships of mutant and control fibroblasts isolated from scar tissue at 7 days following injury. We fabricated a device with polydimethyl siloxane (PDMS) posts, isolated cardiac fibroblasts from infarcted hearts, incorporated the fibroblasts into a collagen hydrogel to form tissue scaffolds, and subsequently suspended the fibroblast-embedded hydrogel between two PDMS posts (Figure 6E). We observed a significantly lower displacement of the PDMS posts with the Col5a1CKO fibroblasts that reflects decreased contractile ability of Col5a1CKO fibroblasts (approximately 34% reduction, *p < 0.05) (Figures 6F–6H). Next, we isolated cardiac fibroblasts from Col5a1 floxed mice and infected the cardiac fibroblasts *in vitro* with a lentivirus encoding Cre recombinase gene or GFP as control (Figure 6I). To minimize artifacts from repeated passaging, we immortalized the isolated Col5a1fl/fl cardiac fibroblasts by infecting them with a lentivirus encoding the SV40 large T cell antigen prior to infecting the cells with Cre recombinase or control GFP virus (Mali et al., 2008; Welm et al., 2008). Cells infected by Cre recombinase lentivirus (Truitt et al., 2016) were identified by co-expression of GFP fluorescence and sorted by flow cytometry, and we found an approximately 60% ± 20% decrease in *Col5a1* expression (mean ± SD, *p < 0.05). Successfully transduced cells were then incorporated into collagen hydrogels and suspended between PDMS posts in a similar manner. We observed a significant reduction in pillar displacement and hydrogel contraction, suggestive that the deficiency of ColV is sufficient to affect fibroblast contractile forces (Figures 6J and 6K). Taken together, these experiments show that ColV depletion leads to decreased scar stiffness and attenuated tissue scaffold contraction by fibroblasts, which could both contribute to increased scar size.

To assay the mechanical properties of fibroblasts, we subjected the Col5a1floxed cardiac fibroblasts (following lenti Cre infection) to a cell deformability assay. In this assay, cell deformability is determined by parallel microfiltration (PMF), where the ability of cells to filter through a porous membrane over the timescale of seconds in response to an applied pressure is determined (Kim et al., 2016, 2019; Qi et al., 2015). More deformable cells will filter more quickly through the pores, resulting in a lower volume of cell suspension retained in the top well (Figure 6L). We observed that Col5a1CKO fibroblasts are significantly less deformable (Figure 6M), while there were no significant differences in cell size or viability between lenti Cre or lenti GFP

Figure 5. Single-Cell RNA-Seq of Non-myocytes of Control and Col5a1CKO Hearts Harvested at 7 Days following Injury

(A) tSNE plot demonstrating non-myocyte cell populations of the heart at 7 days post MI.
(B) Distribution of non-myocyte cells from injured control and Col5a1CKO hearts across these clusters.
(C–E) Violin plot demonstrating expression of (C) Col5a1, (D) Acta2 (αSMA), and (E) Cnn2 (Calponin) in fibroblast clusters.
(F) Sub-clustering of fibroblast population.
(G) UMAP plot with expression of αSMA in fibroblast subclusters.
(H) Expression of Acta2 in subclusters of fibroblasts.
(I) Cell numbers in cluster 0 (myofibroblasts) versus clusters 1 and 2 (non-myofibroblasts).
(J) Immunostaining for αsmooth muscle actin (αSMA) and vimentin (Vim) in the scar of Col5a1CKO at 7 days post MI (arrows, representative images).
(K) Quantitation of the number of αSMA expressing myofibroblasts (n = 4/control and 5/CKO).
(L) Immunostaining for αSMA and Vim in the scar of TCF21MCM:Col5a1CKO hearts at 7 days post MI (arrows, representative images).
(M) Quantitation of the number of αSMA expressing myofibroblasts (n = 6/control and 4/CKO).
(N) Dot plot representing expression of ECM genes that are significantly upregulated in fibroblasts of Col5a1CKO hearts at 7 days post MI (adjusted p value < 0.05). Data shown as mean ± SD, *p < 0.05.
See also Figures S5 and S6.

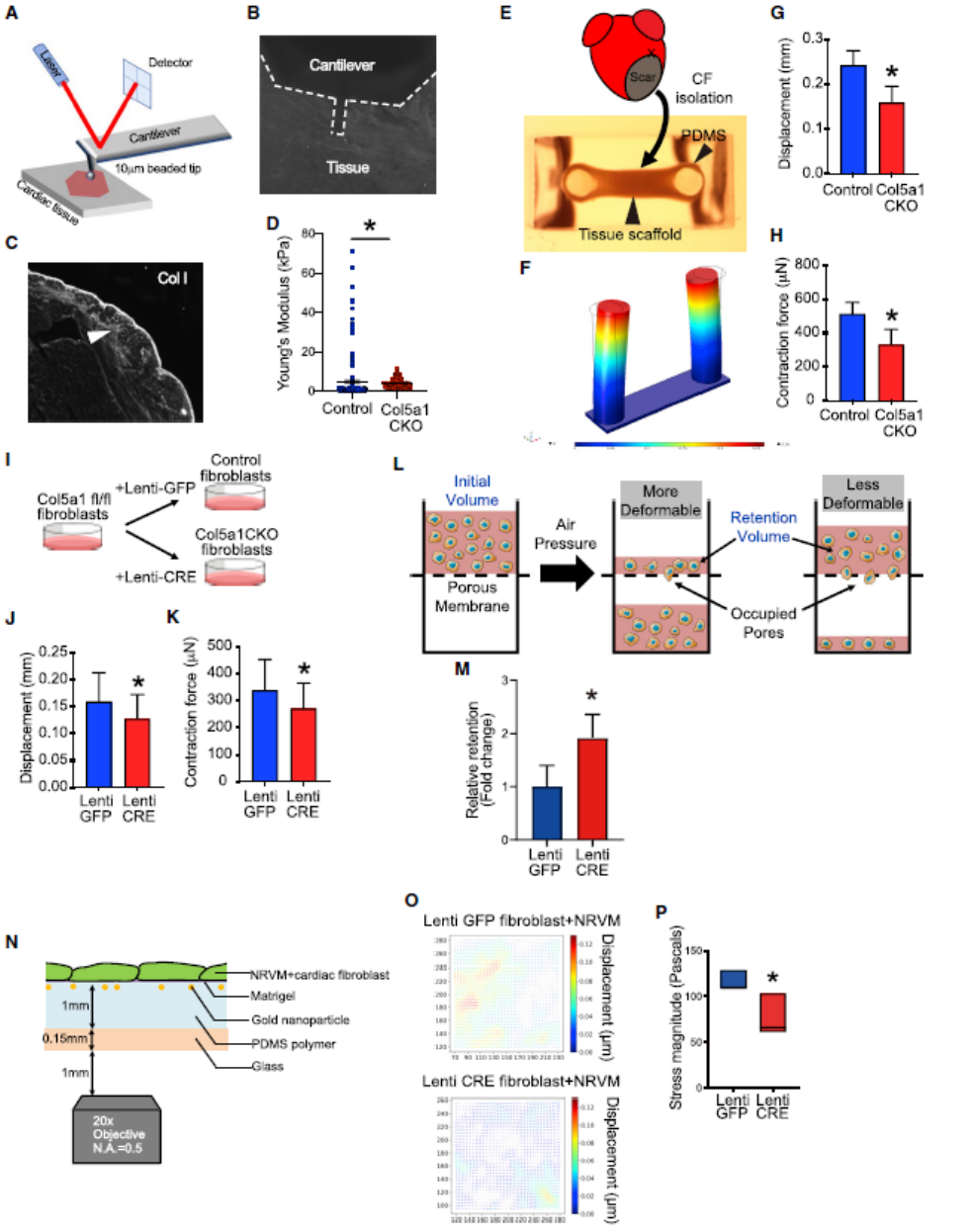

(legend on next page)

cardiac fibroblasts (Figures S7A and S7B). To further investigate the altered physical properties of Col5a1CKO fibroblasts, we performed quantitative phase microscopy (QPM) to measure the rate at which biomass redistributes within individual cells (decorrelation rate). We observed that the decorrelation rate was faster (approximately 2-fold higher) in Col5a1CKO fibroblasts versus control-GFP virus infected fibroblasts; mean ± SD, *$p < 0.05$) (Figures S7C–S7E), further substantiating the altered physical properties of Col5a1CKO fibroblasts.

We next examined whether stiffer cardiac fibroblasts affect cardiomyocyte contractile forces, thereby reducing cardiac function. We co-cultured neonatal rodent ventricular cardiomyocytes (NRVMs) with Col5a1-deficient or control cardiac fibroblasts generated *in vitro*. We performed traction force microscopy to determine myocyte contractile forces generated in the presence of control of Col5a1CKO cardiac fibroblasts. A co-culture of cardiomyocytes and control or Col5a1CKO cardiac fibroblasts was seeded onto a Matrigel surface on a PDMS scaffold containing gold-labeled nano-particles (Figure 6N). As the myocytes contract, the movement or displacement of the gold particles is captured, and machine learning approaches are utilized to calculate contractile forces (Figure 6O). Using this approach, we observed that the stress generated by myocytes in the presence of Col5a1CKO fibroblasts is significantly decreased (mean ± SD, *$p < 0.05$) (Figure 6P). These observations are consistent with our *in vivo* findings of decreased cardiac contractile forces in Col5a1CKO hearts following ischemic cardiac injury.

Collagen V Deficiency Induces Myofibroblast Formation via Altered Integrin Expression on Cardiac Fibroblasts

Given the abnormal biomechanical properties of the scar, we hypothesized that altered mechanical cues were driving a myofibroblast gene expression program and increasing myofibroblast formation. First, we determined whether the deficiency of Col5a1 in cardiac fibroblasts was sufficient to induce myofibroblast differentiation and expression of ECM genes. To address this question, we again generated Col5a1-deficient cardiac fibroblasts by lentiviral Cre transduction and observed significant upregulation of canonical myofibroblast and ECM genes such as *αSMA*, *periostin*, *Col3a1*, *Myh11*, etc. (Figure 7A). These observations demonstrate that the loss of *Col5a1* is sufficient to induce activation of a myofibroblast gene expression program. Integrins are mechanosensitive receptors on the cell surface, and alterations in mechanical properties of the extracellular environment can lead to rapid changes in integrin profile. Moreover, integrins are known to regulate key cellular events such as cell survival, proliferation, and differentiation (Hynes, 2002; Katsumi et al., 2004). We hypothesized that augmentation of a myofibroblast gene expression program in Col5a1CKO fibroblasts could be secondary to altered integrin expression on the *Col5a1*CKO fibroblasts. We performed flow cytometry on *Col5a1*-deficient cardiac fibroblasts and observed that a significantly greater fraction of *Col5a1*-deficient cardiac fibroblasts expressed the integrins αvβ3 and αvβ5 (Figures 7B and 7C). In contrast, β1, β2, α5, and αv integrins did not show any changes in expression (Figures S7F–S7I). These integrins were chosen as they have shown to affect smooth muscle and fibroblast function (Deb et al., 2004; Ieda et al., 2009; Liu et al., 2010), and particularly for αvβ3/αvβ5, there is evidence that these integrins promote myofibroblast differentiation by modulating latent TGFβ signaling (Asano et al., 2005; Lygoe et al., 2004; Sarrazy et al., 2014).

Immunostaining demonstrated robust expression of αvβ3 and αvβ5 integrins in cardiac fibroblasts of Col5a1CKO scar tissue compared to that of control littermates (Figures 7D and 7E). Myocardium remote to the area of injury did not show any expression of αvβ3 and αvβ5 integrins (Figure S8A). Given the upregulation of αvβ3 and αvβ5 integrins in Col5a1CKO cardiac fibroblasts, we next determined whether there was a causal relationship between these differentially expressed integrins and myofibroblast differentiation. To address this question, we adopted a pharmacologic loss-of-function approach by using the drug cilengitide, a specific inhibitor of αvβ3 and αvβ5 integrins. Cilengitide is a cyclic Arg-Gly-Asp peptide that has been used in human clinical trials of various malignancies, such as gliomas, and is a specific inhibitor of the αvβ3 and αvβ5 integrins (Belvisi et al., 2005; Dechantsreiter et al., 1999; Scaringi et al., 2012). We infected the Col5a1 floxed cardiac fibroblasts with a lentiviral Cre or control GFP and added cilengitide to cardiac fibroblasts at the same time. After 7 days, expression of myofibroblast markers was significantly increased in the Col5a1CKO fibroblasts, but the addition of cilengitide significantly reduced expression of myofibroblast markers (Figure 7F).

Figure 6. Col5a1CKO Fibroblasts Exhibit Altered Mechano-biological Properties

(A) Schematic illustration of atomic force microscopy (AFM) instrumentation.

(B) Representative image of AFM probe and cantilever over tissue section.

(C) Representative image of collagen I (Col I) indirect immunofluorescence detection in scar region (arrow) that was probed with AFM.

(D) Young's Modulus measurements from injured regions (mean ± SEM, *$p < 0.05$, $n = 3$).

(E–H) Determination of mutant or control cardiac fibroblasts (CFs) to generate contractile forces. (E) CFs were isolated at 7 days post MI and incorporated into hydrogel scaffolds and suspended between PDMS posts. (F) Contraction of CFs determined from displacement of PDMS posts. (G) Displacement of PDMS posts by CF tissue scaffold ($n = 3$). (H) Contraction forces generated by either control or Col5a1CKO CFs ($n = 3$).

(I–K) Determination of contractile forces by generating Col5a1CKO CFs *ex vivo*. (I) CFs from hearts of Col5a1fl/fl mice were infected with a lentiviral Cre or GFP virus to create Col5a1 deficient CFs. (J) Displacement of the PDMS posts and (K) contractile forces generated by Col5a1CKO CFs ($n = 3$).

(L) Schematic illustration of parallel microfiltration (PMF) assay.

(M) Relative retention of cells measured by PMF assay and normalized to the control (Lenti-GFP) CFs ($n = 3$).

(N) Schematic of set up of traction force microscopy where myocytes and CFs are seeded onto a matrigel layer containing gold-labeled nanoparticles.

(O and P) Heatmaps demonstrating displacement of clusters of contracting myocytes (O) and determination of stress forces generated by myocytes in the presence of Col5a1CKO CFs (P) ($n = 3$). Data, unless otherwise stated, shown as mean ± SD, *$p < 0.05$.

See also Figure S7.

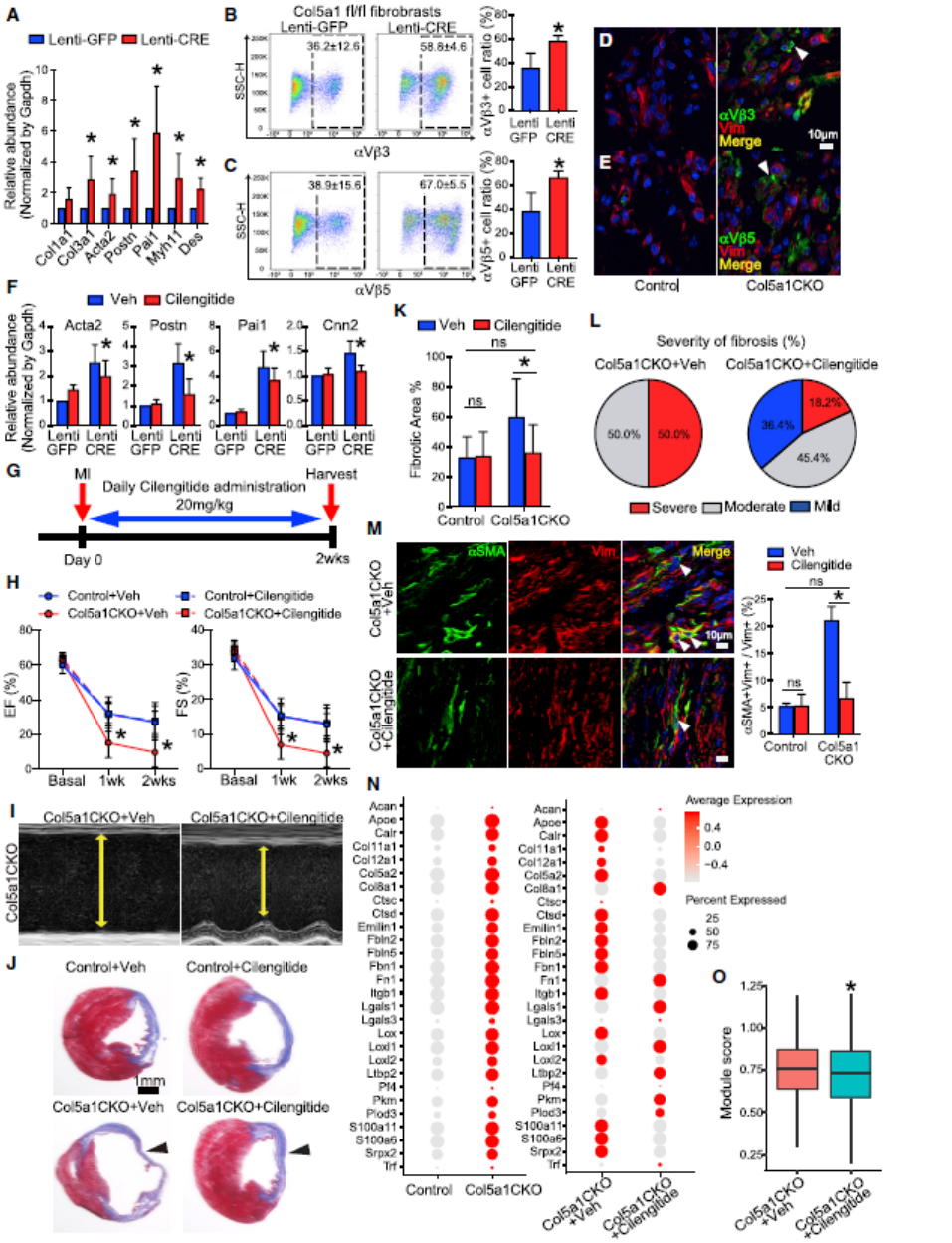

(legend on next page)

Considering these observations, we investigated the effects of injecting cilengitide *in vivo* to Col5a1CKO animals to determine effects on post-injury scar size and cardiac function. We subjected Col5a1CKO to ischemic cardiac injury and injected cilengitide or vehicle at 20mg/kg daily (Bagnato et al., 2018) for 14 days starting from the day of injury (Figure 7G). We observed that the Col5a1CKO animals injected with vehicle exhibited a significant decline in post-injury cardiac function, but the Col5a1CKO animals treated with cilengitide had a complete rescue of function and the post-injury heart function was not significantly different from the control littermates (Cre(-) Col5a1$^{fl/fl}$) (Figures 7H and 7I). In contrast, cilengitide infusion did not affect post-injury cardiac function of control (Cre(-)Col5a1$^{fl/fl}$) littermate animals (Figure 7H). Histology demonstrated significant reduction in scar size in Col5a1CKO animals injected with cilengitide compared to vehicle-injected Col5a1CKO animals (Figures 7J and 7K). To demonstrate that the benefits of cilengitide on post-injury cardiac function of Col5a1CKO animals was secondary to its effect on the infarcted region, we performed myocardial strain imaging. Longitudinal strain generated by different segments of myocardial walls is a surrogate for contractile forces generated. With MI, the basal segment of the myocardium close to the suture line was relatively unaffected compared to the anterior apical wall (Figures S8B and S8C). Following cilengitide administration, the functional improvement was restricted to the apical segment and not the basal segment, demonstrating that the beneficial effects of cilengitide were not secondary to augmentation of contractile forces of the non-injured myocardium (Figure S8D). Cilengitide did not affect the scar size of control animals (Cre(-)Col5a1$^{fl/fl}$) following injury (Figures 7J and 7K). The Col5a1CKO animals injected with cilengitide had a much lower fraction of animals exhibiting severe fibrosis (Figure 7L). We next examined the numbers of myofibroblasts in the scars of Col5a1CKO animals and observed that the number of myofibroblasts was significantly reduced in the cilengitide group (Figure 7M). We subsequently determined whether cilengitide reversed increased expression of ECM genes in cardiac fibroblasts of Col5a1CKO animals. We examined the set of ECM genes that were upregulated in cardiac fibroblasts in Col5a1CKO hearts at 7 days following injury. scRNA-seq of fibroblasts isolated from Col5a1CKO hearts following 7 days of cilengitide therapy demonstrated reversion of expression of these genes, and average expression of this module of genes was significantly lower in cardiac fibroblasts following cilengitide treatment ($p = 9.3e-7$) (Figures 7N and 7O). The degree of myocyte hypertrophy was also substantially reduced in the cilengitide-injected Col5a1CKO animals (Figures S8E and S8F). Taken together, these experiments demonstrate that the differential expression of αvβ3 and αvβ5 integrins in cardiac fibroblasts of Col5a1CKO animals drives myofibroblast differentiation, and pharmacologic inhibition of such integrins is sufficient to rescue the phenotype.

DISCUSSION

Our data can be used to construct a collagen-V-dependent model of cardiac wound healing where Col V regulates wound healing at least in part by modulating the mechanical properties of the scar. In the absence of Col V, the scar is less stiff, and less-stiff scars are prone to sudden scar expansion (Rog-Zielinska et al., 2016). In addition, the reduced scar stiffness drives integrin-mediated mechanical feedback cues that promote myofibroblast differentiation, further ECM production, and scar size. The feedback response is critical to the phenotype as modulation of specific integrin signaling reverses increased ECM gene expression and rescues the phenotype.

Our findings could also have implications for Ehlers Danlos syndrome (EDS), a heterogeneous group of connective tissue disorders characterized by abnormalities in skin extensibility, joint hypermobility, and tissue fragility (Ghali et al., 2019). Individuals with classical EDS (cEDS) most commonly have mutations in genes encoding for type V collagen (*Col5a1* and *Col5a2*) (Wenstrup et al., 2000). Although there is scant clinical data on the prognosis of MI and heart scarring in these patients (owing to the relatively rare nature of the disease), patients with cEDS have abnormal mechanical properties of the ECM and exhibit dysregulated wound healing with increased scar size. Moreover, fibroblasts isolated from skin of patients with cEDS demonstrate increased expression of αvβ3 integrins (Zoppi et al., 2018) that is thought to reflect a response to abnormal ECM and raise the

Figure 7. Inhibition of αvβ3 and αvβ5 Integrins Rescues Increased Scarring and Cardiac Dysfunction in Col5a1CKO Animals

(A) Expression of ECM and myofibroblast genes in Col5a1CKO CFs generated *ex vivo* (n = 6).

(B and C) Flow cytometry to determine expression of (B) αvβ3 and (C) αvβ5 integrins on Col5a1CKO CFs (n = 6).

(D and E) Immunostaining for Vim, (D) αvβ3, and (E) αvβ5 in scar tissue at 7 days post MI (arrows, representative images).

(F) Expression of key myofibroblast genes in Col5a1CKO CFs in the presence or absence of cilengitide (n = 6).

(G) Experimental design to treat animals with daily cilengitide (20mg/kg).

(H) EF and FS in control and Col5a1CKO injected with cilengitide or vehicle (*Col5a1CKO+Cilengitide [red dotted line] versus Col5a1CKO+Veh [red solid line], n = 13/CKO+Cilengitide 10/other groups at basal, n = 12/CKO+Cilengitide, 6/CKO+Veh, 9/Control+Cilengitide, 7/Control+Veh at 2 weeks post MI).

(I) Representative images of M-mode echocardiogram (yellow line indicates end systolic diameter).

(J) Masson trichrome staining of mid-ventricle at 2 weeks post MI to show scar size (arrowhead, n = same number at 2 weeks post MI, as above).

(K) Quantitation of fibrotic area (n = same number as above).

(L) Fraction of Col5a1CKO animals demonstrating mild, moderate, and severe fibrosis following vehicle or cilengitide infusion

(M) Immunostaining for αSMA and Vimentin in hearts of Col5a1CKO receiving vehicle or cilengitide and quantitation of the fraction (arrows, representative images, n = 10/CKO+Cilengitide, n = 6/CKO+Veh, n = 6/animals for all other groups).

(N) Dot plot representing expression of ECM genes that are upregulated in CFs of Col5a1CKO hearts at 7 days post MI compared to controls (left panel). The same genes were shown in fibroblasts from Col5a1CKO+Vehicle and Col5a1CKO+Cilengitide samples (right panel).

(O) Boxplot showing the module scores of 28 genes from (N) in fibroblasts from Col5a1CKO+Veh and Col5a1CKO+Cilengitide. Data shown as mean ± SD, *$p < 0.05$, ns: not significant.

See also Figures S7 and S8.

possibility that inhibitors of specific integrins such as cilengitide may have a role in mitigating dysregulated wound healing in cEDS.

In summary, we demonstrate that a feedback mechanism between the mechanical properties of scar tissue and cardiac fibroblasts are pivotal to the regulation of scar size. Teleologically, such a feedback loop provides an efficient way to integrate the output of ECM and strength of scars. Our observations illustrate a model of wound healing in which the structural constituents of scar tissue function to limit the size of scar itself.

STAR★METHODS

Detailed methods are provided in the online version of this paper and include the following:

- KEY RESOURCES TABLE
- RESOURCE AVAILABILITY
  - Lead Contact
  - Materials Availability
  - Data and Code Availability
- EXPERIMENTAL MODEL AND SUBJECT DETAILS
  - Animal care and use
  - Generation of animals with genetically labeled cardiac fibroblasts and fibroblast specific deletion of Col5a1
  - Murine models of acute ischemic cardiac injury
  - Echocardiogram
- METHOD DETAILS
  - Antibodies and probes
  - Bulk RNA-seq, single-cell RNA-seq and qPCR
  - Col5a1 correlation with extracellular matrix pathway accounts for clinical trait association in the HMDP
  - Proteomic analysis of scar tissue
  - Histological studies
  - RNA-Fluorescence *in situ* hybridization
  - Insoluble collagen assay
  - Transmission electron microscopy
  - Tomography of collagen fibers
  - Plasmid construction and Lentivirus preparation
  - Isolation of primary culture adult cardiac fibroblast
  - Generation of Col5a1 deficient immortalized cardiac fibroblast
  - Flow cytometry
  - Measurement of force generated by Col V deficient cardiac fibroblasts
  - Measurement of decorrelation rate of Col V deficient cardiac fibroblasts
  - Traction force measurement of neonatal rat ventricle myocyte and fibroblast co-culture
  - Parallel microfiltration
  - Atomic force microscopy
- QUANTIFICATION AND STATISTICAL ANALYSIS

SUPPLEMENTAL INFORMATION

Supplemental Information can be found online at https://doi.org/10.1016/j.cell.2020.06.030.

ACKNOWLEDGMENTS

We thank Dr. Eric Olson, University of Texas Southwestern Medical Center and Dr. Andrew Leask, University of Western Ontario, Canada for providing us the TCF21 MerCreMer and Col1a2CreERT mice, respectively. We thank Dr. Siobhan Braybrook (UCLA) and Dr. Dan Cohn (UCLA) for AFM and ECM expertise. This work was funded by grants from the National Institutes of Health, U.S.A. (HL129178, HL137241, AR075867, HL126204, and HL147883), Department of Defense, U.S.A. (W81XWH-17-1-0464 and W81XWH-20-1-0238), National Science Foundation, U.S.A. (BMMB-1906165), grants from the Eli and Edythe Broad Stem Cell Center at UCLA and California Nanosystems Institute (BSCRC/CNSI innovation award), and James Eason Cardiovascular Discovery funds. This research was also partly supported by NIH National Center for Advancing Translational Science (NCATS) UCLA Clinical and Translational Science Institute (CTSI), U.S.A. (grant number UL1TR001881). J.L.M. was supported by UPLIFT: UCLA Postdocs' Longitudinal Investment in Faculty (NIH K12 GM106996).

AUTHOR CONTRIBUTIONS

T.Y. performed the majority of experiments and analyzed data including cardiac imaging. S.L., Y.Z., R.W., and A.R. assisted in bench experiments. S.R. and Y.W. performed animal surgeries. Y.Z.K., F.M., and M.P. analyzed RNA-seq and scRNA-seq. J.M. and R.H.C. performed, analyzed, and interpreted AFM experiments. T.N. and M.A.T. performed and analyzed QPM experiments. T.-H.K. and A.C.R. performed and interpreted PMF experiments. X.H.M.T. and P.Y.-C. performed and interpreted traction force microscopy experiments. R.N., S.A., and A.K. performed and analyzed contraction of tissue scaffolds. W.C. and J.W. performed mass spectroscopy experiments. M.S. and A.J.L. analyzed HMDP data. S.R. performed TEM. D.E.B. provided key reagents and contributed toward discussion. A.D. conceptualized the project, supervised data collection and analysis, and wrote the manuscript.

DECLARATION OF INTERESTS

The authors declare no competing interests. Based on this work, patent no: 63/002,828 "Compositions and methods for treating dysregulated wound healing" has been filed and assigned to the Regents of the University of California.

Received: November 15, 2019
Revised: March 17, 2020
Accepted: June 18, 2020
Published: July 3, 2020

REFERENCES

Acharya, A., Baek, S.T., Banfi, S., Eskiocak, B., and Tallquist, M.D. (2011). Efficient inducible Cre-mediated recombination in Tcf21 cell lineages in the heart and kidney. Genesis *49*, 870–877.

Asano, Y., Ihn, H., Yamane, K., Jinnin, M., Mimura, Y., and Tamaki, K. (2005). Increased expression of integrin alpha(v)beta3 contributes to the establishment of autocrine TGF-beta signaling in scleroderma fibroblasts. J. Immunol. *175*, 7708–7718.

Bagnato, G.L., Irrera, N., Pizzino, G., Santoro, D., Roberts, W.N., Bagnato, G., Pallio, G., Vaccaro, M., Squadrito, F., Saitta, A., et al. (2018). Dual αvβ3 and αvβ5 blockade attenuates fibrotic and vascular alterations in a murine model of systemic sclerosis. Clin. Sci. (Lond.) *132*, 231–242.

Barer, R. (1952). Interference microscopy and mass determination. Nature *169*, 366–367.

Bashey, R.I., Martinez-Hernandez, A., and Jimenez, S.A. (1992). Isolation, characterization, and localization of cardiac collagen type VI. Associations with other extracellular matrix components. Circ. Res. *70*, 1006–1017.

Belvisi, L., Riccioni, T., Marcellini, M., Vesci, L., Chiarucci, I., Efrati, D., Potenza, D., Scolastico, C., Manzoni, L., Lombardo, K., et al. (2005). Biological and molecular properties of a new alpha(v)beta3/alpha(v)beta5 integrin antagonist. Mol. Cancer Ther. *4*, 1670–1680.

Bendat, J.S., and Piersol, A.G. (2013). Random data: analysis and measurement procedures (Wiley-Interscience).

Beussman, K.M., Rodriguez, M.L., Leonard, A., Taparia, N., Thompson, C.R., and Sniadecki, N.J. (2016). Micropost arrays for measuring stem cell-derived cardiomyocyte contractility. Methods *94*, 43–50.

Bon, P., Maucort, G., Wattellier, B., and Monneret, S. (2009). Quadriwave lateral shearing interferometry for quantitative phase microscopy of living cells. Opt. Express *17*, 13080–13094.

Brown, X.Q., Ookawa, K., and Wong, J.Y. (2005). Evaluation of polydimethylsiloxane scaffolds with physiologically-relevant elastic moduli: interplay of substrate mechanics and surface chemistry effects on vascular smooth muscle cell response. Biomaterials *26*, 3123–3129.

Crocker, J.C., and Grier, D.G. (1996). Methods of digital video microscopy for colloidal studies. J. Colloid Interface Sci. *179*, 298–310.

Davies, H.G., and Wilkins, M.H. (1952). Interference microscopy and mass determination. Nature *169*, 541.

Deb, A., Skelding, K.A., Wang, S., Reeder, M., Simper, D., and Caplice, N.M. (2004). Integrin profile and in vivo homing of human smooth muscle progenitor cells. Circulation *110*, 2673–2677.

Dechantsreiter, M.A., Planker, E., Mathä, B., Lohof, E., Hölzemann, G., Jonczyk, A., Goodman, S.L., and Kessler, H. (1999). N-Methylated cyclic RGD peptides as highly active and selective alpha(V)beta(3) integrin antagonists. J. Med. Chem. *42*, 3033–3040.

Dobin, A., Davis, C.A., Schlesinger, F., Drenkow, J., Zaleski, C., Jha, S., Batut, P., Chaisson, M., and Gingeras, T.R. (2013). STAR: ultrafast universal RNA-seq aligner. Bioinformatics *29*, 15–21.

Frangogiannis, N.G. (2017). The extracellular matrix in myocardial injury, repair, and remodeling. J. Clin. Invest. *127*, 1600–1612.

Frangogiannis, N.G. (2019). The Extracellular Matrix in Ischemic and Nonischemic Heart Failure. Circ. Res. *125*, 117–146.

Ghali, N., Sobey, G., and Burrows, N. (2019). Ehlers-Danlos syndromes. BMJ *365*, l4966.

Ghazalpour, A., Rau, C.D., Farber, C.R., Bennett, B.J., Orozco, L.D., van Nas, A., Pan, C., Allayee, H., Beaven, S.W., Civelek, M., et al. (2012). Hybrid mouse diversity panel: a panel of inbred mouse strains suitable for analysis of complex genetic traits. Mamm. Genome *23*, 680–692.

Gulati, A., Jabbour, A., Ismail, T.F., Guha, K., Khwaja, J., Raza, S., Morarji, K., Brown, T.D., Ismail, N.A., Dweck, M.R., et al. (2013). Association of fibrosis with mortality and sudden cardiac death in patients with nonischemic dilated cardiomyopathy. JAMA *309*, 896–908.

Heras-Bautista, C.O., Mikhael, N., Lam, J., Shinde, V., Katsen-Globa, A., Dieluweit, S., Molcanyi, M., Uvarov, V., Jütten, P., Sahito, R.G.A., et al. (2019). Cardiomyocytes facing fibrotic conditions re-express extracellular matrix transcripts. Acta Biomater. *89*, 180–192.

Hinkel, R., Ball, H.L., DiMaio, J.M., Shrivastava, S., Thatcher, J.E., Singh, A.N., Sun, X., Faskerti, G., Olson, E.N., Kupatt, C., and Bock-Marquette, I. (2015). C-terminal variable AGES domain of Thymosin β4: the molecule's primary contribution in support of post-ischemic cardiac function and repair. J. Mol. Cell. Cardiol. *87*, 113–125.

Hynes, R.O. (2002). Integrins: bidirectional, allosteric signaling machines. Cell *110*, 673–687.

Ieda, M., Tsuchihashi, T., Ivey, K.N., Ross, R.S., Hong, T.T., Shaw, R.M., and Srivastava, D. (2009). Cardiac fibroblasts regulate myocardial proliferation through beta1 integrin signaling. Dev. Cell *16*, 233–244.

Kanisicak, O., Khalil, H., Ivey, M.J., Karch, J., Maliken, B.D., Correll, R.N., Brody, M.J., J Lin, S.C., Aronow, B.J., Tallquist, M.D., and Molkentin, J.D. (2016). Genetic lineage tracing defines myofibroblast origin and function in the injured heart. Nat. Commun. *7*, 12260.

Katsumi, A., Orr, A.W., Tzima, E., and Schwartz, M.A. (2004). Integrins in mechanotransduction. J. Biol. Chem. *279*, 12001–12004.

Kim, T.H., Gill, N.K., Nyberg, K.D., Nguyen, A.V., Hohlbauch, S.V., Geisse, N.A., Nowell, C.J., Sloan, E.K., and Rowat, A.C. (2016). Cancer cells become less deformable and more invasive with activation of β-adrenergic signaling. J. Cell Sci. *129*, 4563–4575.

Kim, T.H., Ly, C., Christodoulides, A., Nowell, C.J., Gunning, P.W., Sloan, E.K., and Rowat, A.C. (2019). Stress hormone signaling through β-adrenergic receptors regulates macrophage mechanotype and function. FASEB J. *33*, 3997–4006.

Kremer, J.R., Mastronarde, D.N., and McIntosh, J.R. (1996). Computer visualization of three-dimensional image data using IMOD. J. Struct. Biol. *116*, 71–76.

Lincoln, J., Florer, J.B., Deutsch, G.H., Wenstrup, R.J., and Yutzey, K.E. (2006). ColVa1 and ColXIa1 are required for myocardial morphogenesis and heart valve development. Dev. Dyn. *235*, 3295–3305.

Liu, S., Xu, S.W., Blumbach, K., Eastwood, M., Denton, C.P., Eckes, B., Krieg, T., Abraham, D.J., and Leask, A. (2010). Expression of integrin beta1 by fibroblasts is required for tissue repair in vivo. J. Cell Sci. *123*, 3674–3682.

Lusis, A.J., Seldin, M.M., Allayee, H., Bennett, B.J., Civelek, M., Davis, R.C., Eskin, E., Farber, C.R., Hui, S., Mehrabian, M., et al. (2016). The Hybrid Mouse Diversity Panel: a resource for systems genetics analyses of metabolic and cardiovascular traits. J. Lipid Res. *57*, 925–942.

Lygoe, K.A., Norman, J.T., Marshall, J.F., and Lewis, M.P. (2004). AlphaV integrins play an important role in myofibroblast differentiation. Wound Repair Regen. *12*, 461–470.

Ma, X., Dewan, S., Liu, J., Tang, M., Miller, K.L., Yu, C., Lawrence, N., McCulloch, A.D., and Chen, S. (2019). 3D printed micro-scale force gauge arrays to improve human cardiac tissue maturation and enable high throughput drug testing. Acta Biomater. *95*, 319–327.

Mali, P., Ye, Z., Hommond, H.H., Yu, X., Lin, J., Chen, G., Zou, J., and Cheng, L. (2008). Improved efficiency and pace of generating induced pluripotent stem cells from human adult and fetal fibroblasts. Stem Cells *26*, 1998–2005.

Otsu, N. (1979). Threshold Selection Method from Gray-Level Histograms. IEEE Transactions on Systems, Man, and Cybernetics *9*, 62–66.

Oyunbaatar, N.E., Lee, D.H., Patil, S.J., Kim, E.S., and Lee, D.W. (2016). Biomechanical Characterization of Cardiomyocyte Using PDMS Pillar with Microgrooves. Sensors (Basel) *16*. https://doi.org/10.3390/s16081258.

Pettersen, E.F., Goddard, T.D., Huang, C.C., Couch, G.S., Greenblatt, D.M., Meng, E.C., and Ferrin, T.E. (2004). UCSF Chimera–a visualization system for exploratory research and analysis. J. Comput. Chem. *25*, 1605–1612.

Pillai, I.C., Li, S., Romay, M., Lam, L., Lu, Y., Huang, J., Dillard, N., Zemanova, M., Rubbi, L., Wang, Y., et al. (2017). Cardiac Fibroblasts Adopt Osteogenic Fates and Can Be Targeted to Attenuate Pathological Heart Calcification. Cell Stem Cell *20*, 218–232.e5.

Qi, D., Kaur Gill, N., Santiskulvong, C., Sifuentes, J., Dorigo, O., Rao, J., Taylor-Harding, B., Ruprecht Wiedemeyer, W., and Rowat, A.C. (2015). Screening cell mechanotype by parallel microfiltration. Sci. Rep. *5*, 17595.

Rappsilber, J., Mann, M., and Ishihama, Y. (2007). Protocol for micro-purification, enrichment, pre-fractionation and storage of peptides for proteomics using StageTips. Nat. Protoc. *2*, 1896–1906.

Rau, C.D., Wang, J., Avetisyan, R., Romay, M.C., Martin, L., Ren, S., Wang, Y., and Lusis, A.J. (2015). Mapping genetic contributions to cardiac pathology induced by Beta-adrenergic stimulation in mice. Circ Cardiovasc Genet *8*, 40–49.

Rau, C.D., Romay, M.C., Tuteryan, M., Wang, J.J., Santolini, M., Ren, S., Karma, A., Weiss, J.N., Wang, Y., and Lusis, A.J. (2017). Systems Genetics Approach Identifies Gene Pathways and Adamts2 as Drivers of Isoproterenol-Induced Cardiac Hypertrophy and Cardiomyopathy in Mice. Cell Syst. *4*, 121–128.e4.

Ren, J., Zhang, S., Kovacs, A., Wang, Y., and Muslin, A.J. (2005). Role of p38alpha MAPK in cardiac apoptosis and remodeling after myocardial infarction. J. Mol. Cell. Cardiol. *38*, 617–623.

Ribeiro, A.J., Denisin, A.K., Wilson, R.E., and Pruitt, B.L. (2016). For whom the cells pull: Hydrogel and micropost devices for measuring traction forces. Methods *94*, 51–64.

Robinson, M.D., McCarthy, D.J., and Smyth, G.K. (2010). edgeR: a Bioconductor package for differential expression analysis of digital gene expression data. Bioinformatics *26*, 139–140.

Rog-Zielinska, E.A., Norris, R.A., Kohl, P., and Markwald, R. (2016). The Living Scar–Cardiac Fibroblasts and the Injured Heart. Trends Mol. Med. *22*, 99–114.

Sarrazy, V., Koehler, A., Chow, M.L., Zimina, E., Li, C.X., Kato, H., Caldarone, C.A., and Hinz, B. (2014). Integrins αvβ5 and αvβ3 promote latent TGF-β1 activation by human cardiac fibroblast contraction. Cardiovasc. Res. *102*, 407–417.

Scaringi, C., Minniti, G., Caporello, P., and Enrici, R.M. (2012). Integrin inhibitor cilengitide for the treatment of glioblastoma: a brief overview of current clinical results. Anticancer Res. *32*, 4213–4223.

Sneddon, I.N. (1965). The relation between load and penetration in the axisymmetric boussinesq problem for a punch of arbitrary profile. International Journal of Engineering Science *3*, 47–57.

Sun, M., Chen, S., Adams, S.M., Florer, J.B., Liu, H., Kao, W.W., Wenstrup, R.J., and Birk, D.E. (2011). Collagen V is a dominant regulator of collagen fibrillogenesis: dysfunctional regulation of structure and function in a corneal-stroma-specific Col5a1-null mouse model. J. Cell Sci. *124*, 4096–4105.

Truitt, J.M., Blednov, Y.A., Benavidez, J.M., Black, M., Ponomareva, O., Law, J., Merriman, M., Horani, S., Jameson, K., Lasek, A.W., et al. (2016). Inhibition of IKKβ Reduces Ethanol Consumption in C57BL/6J Mice. eNeuro *3*. https://doi.org/10.1523/ENEURO.0256-16.2016.

Ubil, E., Duan, J., Pillai, I.C., Rosa-Garrido, M., Wu, Y., Bargiacchi, F., Lu, Y., Stanbouly, S., Huang, J., Rojas, M., et al. (2014). Mesenchymal-endothelial transition contributes to cardiac neovascularization. Nature *514*, 585–590.

van den Borne, S.W., Diez, J., Blankesteijn, W.M., Verjans, J., Hofstra, L., and Narula, J. (2010). Myocardial remodeling after infarction: the role of myofibroblasts. Nat. Rev. Cardiol. *7*, 30–37.

Wang, Z., Volinsky, A.A., and Gallant, N.D. (2014). Crosslinking effect on polydimethylsiloxane elastic modulus measured by custom-built compression instrument. J. Appl. Polym. Sci. *131*.

Wang, J.J., Rau, C., Avetisyan, R., Ren, S., Romay, M.C., Stolin, G., Gong, K.W., Wang, Y., and Lusis, A.J. (2016). Genetic Dissection of Cardiac Remodeling in an Isoproterenol-Induced Heart Failure Mouse Model. PLoS Genet. *12*, e1006038.

Weber, K.T. (1989). Cardiac interstitium in health and disease: the fibrillar collagen network. J. Am. Coll. Cardiol. *13*, 1637–1652.

Welm, B.E., Dijkgraaf, G.J., Bledau, A.S., Welm, A.L., and Werb, Z. (2008). Lentiviral transduction of mammary stem cells for analysis of gene function during development and cancer. Cell Stem Cell *2*, 90–102.

Wenstrup, R.J., Florer, J.B., Willing, M.C., Giunta, C., Steinmann, B., Young, F., Susic, M., and Cole, W.G. (2000). COL5A1 haploinsufficiency is a common molecular mechanism underlying the classical form of. Am. J. Hum. Genet. *66*, 1766–1776.

Wenstrup, R.J., Florer, J.B., Brunskill, E.W., Bell, S.M., Chervoneva, I., and Birk, D.E. (2004). Type V collagen controls the initiation of collagen fibril assembly. J. Biol. Chem. *279*, 53331–53337.

Xiao, F., Wen, X., Tan, X.H.M., and Chiou, P.-Y. (2018). Plasmonic micropillars for precision cell force measurement across a large field-of-view. Appl. Phys. Lett. *112*, 033701.

Zangle, T.A., Burnes, D., Mathis, C., Witte, O.N., and Teitell, M.A. (2013a). Quantifying biomass changes of single CD8+ T cells during antigen specific cytotoxicity. PLoS ONE *8*, e68916.

Zangle, T.A., Chun, J., Zhang, J., Reed, J., and Teitell, M.A. (2013b). Quantification of biomass and cell motion in human pluripotent stem cell colonies. Biophys. J. *105*, 593–601.

Zangle, T.A., Teitell, M.A., and Reed, J. (2014). Live cell interferometry quantifies dynamics of biomass partitioning during cytokinesis. PLoS ONE *9*, e115726.

Zheng, B., Zhang, Z., Black, C.M., de Crombrugghe, B., and Denton, C.P. (2002). Ligand-dependent genetic recombination in fibroblasts : a potentially powerful technique for investigating gene function in fibrosis. Am. J. Pathol. *160*, 1609–1617.

Zoppi, N., Chiarelli, N., Ritelli, M., and Colombi, M. (2018). Multifaced Roles of the αvβ3 Integrin in Ehlers-Danlos and Arterial Tortuosity Syndromes' Dermal Fibroblasts. Int. J. Mol. Sci. *19* https://doi.org/10.3390/ijms19040982.

STAR★METHODS

KEY RESOURCES TABLE

REAGENT or RESOURCE	SOURCE	IDENTIFIER
Antibodies		
Rabbit anti-Vimentin	Abcam	Cat# ab47003; RRID: AB_2257290
Mouse anti-smooth muscle actin	Dako	Cat# M0851; RRID: AB_2223500
Mouse anti-integrin αVβ3	Abcam	Cat# ab7166; RRID: AB_305742
Mouse anti-integrin αVβ5	R&D	Cat# MAB2528; RRID: AB_2280706
Rabbit anti-cardiac troponin I	Abcam	Cat# ab47003; RRID: AB_869982
Rabbit Anti-Mouse Collagen Type I	Cedarlane Laboratories	Cat# CL50151AP; RRID: AB_10061240
Rabbit anti-RFP	Rockland	Cat# 600-402-379; RRID: AB_828391
Rat anti-integrin αV, PE-conjugated	Invitrogen	Cat# 12-0512-82; RRID: AB_465704
Rat anti-integrin α5, PE-conjugated	BioLegend	Cat# 103805; RRID: AB_313054
Rat anti-integrin β1, PE-conjugated	Invitrogen	Cat# 12-0181-82; RRID: AB_465572
American hamster anti-integrin β2, PE-conjugated	Invitrogen	Cat# 12-0291-82; RRID: AB_763478
Rabbit anti-integrin αVβ3	ThermoFisher Scientific	Cat# MA5-32195; RRID: AB_2809482
Rabbit anti-integrin αVβ5	Bioss Antibodies	Cat# bs-1356R; RRID: AB_10853044
Alexa Flour 594 conjugated WGA	Invitrogen	W11262
Chemicals, Peptides, and Recombinant Proteins		
Cilengitide	MCE	HY-16141
Tamoxifen	Sigma	T5648
Human basic fibroblast growth factoor	Millipore	GF003
Protease Inhibitor Cocktail	Sigma	P8340
Critical Commercial Assays		
RNAscope Multiplex FL reagent kit v2	ACD bio	323100
Sircol Insoluble Collagen Assay Kit	Biocolor	S2000
RNeasy Mini Kit	QIAGEN	74104
Masson Trichrome Stain Kit	Thermo Fisher Scientific	87019
Pierce Quantitative Colorimetric Peptide Assay	Thermo Fisher Scientific	23275
M.O.M Immunodetection Kit, Basic	Vector	BMK-2202
Avidin/Biotin blocking kit	Vector	SP-2001
Fluorescein avidin DCS	Vector	A-2001
Deposited Data		
HMDP ventricular expression array data	Rau et al., 2017	GSE48760
Myocardial infarction RNaseq data	This paper	GSE151834
Myocardial infarction single cell RNaseq data from wild-type mouse	This paper	GSE152122
Myocardial infarction single cell RNaseq data from Col5a1CKO mouse	This paper	GSE151695
Myocardial infarction single cell RNaseq data from Col5a1CKO mouse treated with cilengitide	This paper	GSE151695
Figures for STAR Methods	This paper	Mendeley Data https://doi.org/10.17632/z3vsb9yvks.2
Experimental Models: Cell Lines		
Mouse: immortalized Col5a1 fl/fl cardiac fibroblast	This paper	N/A
Mouse: primary cardiac fibroblast	This paper	N/A

(Continued on next page)

Continued

REAGENT or RESOURCE	SOURCE	IDENTIFIER
Experimental Models: Organisms/Strains		
Mouse: Col5a1 fl/fl: C57BL/6	Sun et al., 2011	PMID: 22159420
Mouse: Col1a2-CreERT: C57BL/6	Zheng et al., 2002	PMID: 12000713
Mouse: TCF21-MerCreMer: C57BL/6	Acharya et al., 2011	PMID: 21432986
Mouse: R26RtdTomato: C57BL/6	The Jackson Laboratory	007914
Mouse: C57BL/6	The Jackson Laboratory	000664
Mouse: Col5a1 KO: C57BL/6	Wenstrup et al., 2004	PMID: 15383546
Oligonucleotides		
Mouse Col1a1-C1 probe	ACD bio	319371
Mouse Col3a1-C2 probe	ACD bio	455771-C2
Mouse Col5a1-C3 probe	ACD bio	521291-C3
Quantitative real-time PCR Primers	Table S3	N/A
Recombinant DNA		
Ef1a_Large T-antigen_Ires_Puro	Mali et al., 2008	Addgene#18922
Lenti-pHIV-EGFP	Welm et al., 2008	Addgene#21373
psPAX2	Trono Lab Packaging and Envelope Plasmids (unpublished)	Addgene#12260
pMD.G2	Trono Lab Packaging and Envelope Plasmids (unpublished)	Addgene#12259
pLV-EGFP-Cre	Truitt et al., 2016	Addgene#86805
Software and Algorithms		
Vevo LAB	VisualSonics	https://www.visualsonics.com/product/software/vevo-lab
ImageJ	NIH	https://imagej.nih.gov/ij/
FolwJo	FolwJo	https://www.flowjo.com
Cellranger mkfastq	10x Genomics	3.0.2
R package Seurat	Bioconductor	3.0.2
Proteome Discoverer	Thermo Fisher Scientific	2.2
WGCNA	CRAN	https://cran.r-project.org/web/packages/WGCNA/index.html
pheatmap	CRAN	https://cran.r-project.org/web/packages/pheatmap/index.html
Prism 8	GraphPad	N/A
JPKSPM Data Processing	Bruker, JPK	N/A
UCSF Chimera	RBVI, UCSF	http://www.cgl.ucsf.edu/chimera/
Other		
Nikon Eclipse Ti2 confocal microscopy	Nikon	https://www.microscope.healthcare.nikon.com/products/inverted-microscopes/eclipse-ti2-series
Vevo 2100 Imaging System	VisualSonics	https://www.visualsonics.com/product/imaging-systems/vevo-2100
Q Exactive Plus Hybrid Quadrupole-Orbitrap Mass Spectrometer	Thermo Fisher Scientific	IQLAAEGAAPFALGMBDK
JEM1200EX transmission electron microscope	JEOL	https://www.jeolusa.com/PRODUCTS/Transmission-Electron-Microscopes-TEM
TF20 TEM	FEI	https://www.felmi-zfe.at/instrumentation/tem/fei-tecnai-f20/
SHOCONGG-TL AFM Probes	AppNano	SHOCONGG-TL
JPK Nanowizard 4A BioAFM	Bruker, JPK	https://usa.jpk.com/products/atomic-force-microscopy/nanowizard-ultra-speed-2

RESOURCE AVAILABILITY

Lead Contact

Further information and requests for resources and reagents should be directed to and will be fulfilled by the Lead Contact, Arjun Deb (adeb@mednet.ucla.edu)

Materials Availability

This study did not generate new reagents.

Data and Code Availability

The accession number for the bulk RNA sequencing and single-cell RNA sequencing in this paper are available in NCBI GEO dataset. Myocardial infarction bulk RNaseq data: GSE151834, Myocardial infarction sc RNaseq data: GSE152122, Myocardial infarction sc RNaseq data from Col5a1CKO/Control mouse: GSE151695, Myocardial infarction sc RNaseq data from Col5a1CKO mouse treated with cilengitide or vehicle: GSE151695.

Figures for STAR Methods are available in Mendeley data (https://doi.org/10.17632/z3vsb9yvks.2)

EXPERIMENTAL MODEL AND SUBJECT DETAILS

Animal care and use

All animal studies were approved by the Animal Research Committee, University of California, Los Angeles. All animals were maintained at the UCLA vivarium according to the policies instituted by the American Association for Accreditation of Laboratory Animal Care. Sample size was estimated based on published literatures on murine myocardial infarction models (Hinkel et al., 2015; Ren et al., 2005). Male and female animals aged between 10 and 14 weeks were used in the study. All animals belonged to the C57BL/6 strain, were healthy, immune-free, and drug or test naive and were not involved in other experimental procedures. Littermates were used as controls for all experiments.

Generation of animals with genetically labeled cardiac fibroblasts and fibroblast specific deletion of Col5a1

Col1a2CreERT (B6 background) and TCF21MerCreMer (B6 background) animals were crossed with the lineage reporter Rosa26tdtomato (B6 background) animals to generate progeny animals as described (Pillai et al., 2017). Tamoxifen was administered for 10 days prior to ischemic cardiac injury followed by RNA-FISH to determine whether genetically labeled fibroblasts co-expressed the RNA signal. For generation of Col5a1CKO mice, Col1a2CreERT or TCF21MerCreMer mice were crossed with the Col5a1 floxed (B6 background) mice (Sun et al., 2011) and progeny mice were administered tamoxifen (1 mg IP daily) for 5 days prior to ischemic injury and continued for 7 days following injury. For the experiment on TCF21MerCreMer mice to demonstrate an effect of Cre recombinase on heart function and fibrosis, these mice were administered tamoxifen for 5 days prior to ischemic injury and continued for 7 days following injury as as for generating Col5a1CKO mice. For experiments related to administration of tamoxifen after acute injury, TCF21MerCreMer mice crossed with the Col5a1 floxed mice were administered tamoxifen from 4 days to 14 days post injury. Col5a1(+/−) heterozygous KO (B6 background) mice (Lincoln et al., 2006) were used for experiments to confirm Col5a1CKO post infarction phenotype.

Murine models of acute ischemic cardiac injury

All animal studies were approved by the Animal Research Committee, University of California, Los Angeles. Myocardial infarction was performed by ligating the left anterior descending (LAD) coronary artery following open thoracotomy as described (Pillai et al., 2017; Ubil et al., 2014). Briefly, Mice were anesthetized with ketamine (80 mg/kg)/xylazine (20 mg/kg) by intraperitoneal injection. Respiration was provided by mechanical ventilation with 95% O2 (tidal volume 0.5 ml, 130 breaths/min). The LAD coronary artery was ligated intramurally 2mm from its origin with a 9-0 proline suture.

For experiments related to use of cilengitide, 20mg/kg of Cilengitide diluted in PBS was administered by intraperitoneal injection every day until harvest and PBS was used as vehicle as a control.

Echocardiogram

Animals was assessed at pretreatment baseline and at the time point of 3 day, 1 week, 2 weeks, 3 weeks, 4 weeks, and 6 weeks post-Myocardial infarction. Animals were continuously anesthetized with 1.5% isoflurane and 95% O2. Vevo2100 imaging system and a 30-mHz scan head (Toronto, Canada) were used to acquire short/long axis B-mode and M-mode images. Long axis B-mode view was used for analyzing peak longitudinal strain rate. All measurements and calculations were conducted using Vevo2100 software.

METHOD DETAILS

Antibodies and probes

The following primary antibodies, reagents, or probes were used for immunostaining: rabbit anti-Vimentin (1:100, Abcam, ab45939); mouse anti-smooth muscle actin (1:100, Dako, M0851); anti-cardiac Troponin I (1:100, Abcam, ab47003); mouse anti-integrin αVβ3 (1:50, Abcam, ab7166); mouse integrin αVβ5 (1:20, R&D, MAB2528); Alexa Fluor 594 conjugated WGA (5μg/mL, Invitrogen, W11262). For dual RNA-FISH/immunostaining: rabbit anti-RFP (1:50, Rockland, 600-401-379). For flowcytometry: rabbit anti-integrin αVβ3(CD51/CD61) (1:100, ThermoFisher, MA5-32195); rabbit anti-integrin αVβ5 (1:30, Bioss, bs-1356R); PE-conjugated rat anti-integrin αV (1:20, Invitrogen, 12-0512-82); PE-conjugated rat anti-integrin β1 (1:20, Invitrogen, 12-0181-82); PE-conjugated american hamster anti-integrin β2 (1:20, Invitrogen, 12-0291-82); PE-conjugated rat anti-integrin α5 (1:100, BioLegend, 103805); PE-conjugated rat IgG isotype control (same dilution for target antibody, BioLegend, 400508). For RNA-FISH: mouse Col1a1-C1 probe (1:50, ACD, 319371); mouse Col3a1-C2 probe (1:50, ACD, 455771-C2); mouse Col5a1-C3 probe (1:50, ACD, 521291-C3).

Bulk RNA-seq, single-cell RNA-seq and qPCR

For bulk RNA-seq, the injured and uninjured regions of the heart were harvested at different time points following injury, total RNA extracted using RNeasy Mini kit (QIAGEN) and used to generate RNA-Seq libraries followed by sequencing using Illumina 4000 platform (single-end, 65bp). Reads were aligned to the mouse reference genome (mm10) using STAR aligner (Dobin et al., 2013), and used to quantify normalized expression values (RPKM) for annotated genes (Ensembl v.86). RPKM values were used for principal component analysis (PCA) and gene expression visualizations. Differential expression analysis was performed using edgeR quasi-likelihood pipeline (Robinson et al., 2010). Differential expressed genes (DEGs) were identified at FDR 1% and minimum fold-change value of 4.

For sc- RNA-seq, 1wk post MI hearts were harvested and digested by liberase as described later. After digestion, cells were incubated with 10μM Calcein AM (Abcam, ab141420) and flow sorted to identify live cells followed by library preparation. Library was generated by Chromium Single Cell 3′ Library Construction (10x Genomics) and sequenced by Illumina NextSeq 500 Sequencing System. After sequencing, fastq files were generated using Cellranger mkfastq (version 3.0.2). The raw reads were mapped to human reference genome (refdata-cellranger-mm10-3.0.0) using cellranger count. Digital expression matrix was extracted from the filtered_feature_bc_matrix folder outputted by the cell ranger count pipeline. Multiple samples were aggregated by cellranger aggr. To identify different cell types and find signature genes for each cell type, the R package Seurat (version 3.0.2) was used to analyze the digital expression matrix. Cells with less than 500 unique molecular identifiers (UMIs) or less than 100 genes, or greater than 50% mitochondrial expression were removed, resulting in a final dataset of 17,826 cells and 21,447 genes for further analysis. The Seurat function NormalizeData was used to normalize the raw counts. Variable genes were identified using the FindVariableFeatures function. The ScaleData function was used to scale and center expression values in the dataset, the number of unique molecular identifiers (UMI) was regressed against each gene. Principal component analysis (PCA), t-distributed stochastic neighbor embedding (tSNE), and uniform manifold approximation and projection (UMAP) were used to reduce the dimensions of the data, and the first 2 dimensions were used in the plots. The FindClusters function was sued cluster the cells. Marker genes were found using the FindAllMarkers function for each cluster. Cell types were annotated based on the marker genes and their match to canonical markers.

For qPCR, For RNA-seq, the injured and uninjured regions of the heart were harvested at different time points following injury, RNA extracted using RNeasy Mini kit (QIAGEN). cDNAs were generated using iScript cDNA Synthesis Kit (BioRad) and qPCR performed.

Col5a1 correlation with extracellular matrix pathway accounts for clinical trait association in the HMDP

The data used for analysis, including left ventricle expression arrays and clinical traits can be found using the GEO accession: GSE48760 and within the following studies [5, 6]. Midweight bicorrelation coefficients and corresponding p values were generated from HMDP data using the R package WGGNA. To calculate adjusted regressions using the same approaches and compare directly, residuals from each ECM gene correlated with Col5a1 were extracted from the regression using the base lm() function in R. These residuals were then integrated with original expression values and correlated against indicated traits also using WGCNA to enable direct comparisons. For purposes of comparisons, we also adopted a similar approach by collapsing all ECM genes into eigengenes using WGCNA and correlated with either traits or traits adjusted for Col5a1 expression. Distributions of p values resulting from these analyses were compared using a Student's t test (two-way). Plots for visualization were made sing either ggplot2 or pheatmap packages in R.

Proteomic analysis of scar tissue

Injured and uninjured regions of the mouse heart at Day 7 following injury were dissected and homogenized in lysis buffer (200 uL, 12 mM sodium lauroyl sarcosine, 0.5% sodium deoxycholate, 50 mM triethylammonium bicarbonate (TEAB)), Sigma Protease Inhibitor Cocktail (0.89 mg/mL final concentration)), then subjected to bath sonication (10 min, Bioruptor Pico, Diagenode Inc. (Denville, NJ)) and heated (95°C, 5 min). An aliquot of the resulting solution (9 uL) was taken for measurement of total protein concentration (bicinchoninic acid assay; Micro BCA Protein Assay Kit, Thermo Fisher Scientific, Waltham, MA, using BSA as a standard). The remaining samples were diluted to 0.5 mg protein/mL with lysis buffer, and an aliquot of each (100 uL) was treated with tris(2-carbox-

yethyl) phosphine (10 uL, 55 mM in 50 mM TEAB, 30 min, 37°C) followed by treatment with chloroacetamide (10 uL, 120 mM in 50 mM TEAB, 30 min, 25°C in the dark). They were then diluted 5-fold with aqueous 50 mM TEAB, and incubated overnight with Sequencing Grade Modified Trypsin (1 ug in 10 uL of 50 mM TEAB; Promega, Madison, WI) following which an equal volume of ethyl acetate/trifluoroacetic acid (TFA, 100/1, v/v) was added. After vigorous mixing (5 min) and centrifugation (13,000 x g, 5 min), the supernatants were discarded and the lower phases were dried in a centrifugal vacuum concentrator. The samples were then desalted using a modified version of Rappsilber's protocol (Rappsilber et al., 2007) in which the dried samples were reconstituted in acetonitrile/water/TFA (solvent A, 100 uL, 2/98/0.1, v/v/v) and then loaded onto a small portion of a C18-silica disk (3M, Maplewood, MN) placed in a 200 uL pipette tip. Prior to sample loading the C18 disk was prepared by sequential treatment with methanol (20 uL), acetonitrile/water/TFA (solvent B, 20 uL, 80/20/0.1, v/v/v) and finally with solvent A (20 uL). After loading the sample, the disc was washed with solvent A (20 uL, eluent discarded) and eluted with solvent B (40 uL). The collected eluent was dried in a centrifugal vacuum concentrator. The samples were then chemically modified using a TMT10plex Isobaric Label Reagent Set (Thermo Fisher Scientific) as per the manufacturer's protocol. The TMT-labeled peptides were dried and reconstituted in solvent A (50 uL), and an aliquot (2 uL) was taken for measurement of total peptide concentration (Pierce Quantitative Colorimetric Peptide, Thermo Fisher Scientific). The samples were then pooled according to protein content (10 ug of peptide from each sample; 100 ug total), and desalted using the modified Rappsilber's protocol described above. The dried multiplexed pooled sample was reconstituted in water/acetonitrile with 10mM ammonium bicarbonate (solvent C, 5uL, 98/2, v/v, pH10) prior to fractionation (2.7 uL injection) via high pH reversed-phase chromatography using a 1260 Infinity LC System (Agilent Technologies, Santa Clara, CA) and a ZORBAX 300 Extend-C18 column (Agilent Technologies, 0.3 × 150 mm, 3.5 μm) equilibrated in solvent C and eluted (6 uL/min) with an increasing concentration of solvent D (acetonitrile/water with 10mM ammonium bicarbonate, 80/20, v/v, pH10: min/% D; 0/0, 5/14, 65/60, 75/0, 95/0). The fractions were eluted into a 96-well plate with 20 uL of 5% formic acid (FA) in each well over the course of 68 min. The 96 fractions were then condensed into 12 fractions prior to another desalting again using the modified Rappsilber's protocol described above. The eluants were then dried and reconstituted in water/acetonitrile/FA (solvent E, 10 uL, 98/2/0.1, v/v/v), and aliquots (5 uL) were injected onto a reverse phase nanobore HPLC column (AcuTech Scientific, C18, 1.8um particle size, 360 um x 20 cm, 150 um ID), equilibrated in solvent E and eluted (500 nL/min) with an increasing concentration of solvent F (acetonitrile/water/FA, 98/2/0.1, v/v/v: min/% F; 0/0, 5/3, 18/7, 74/12, 144/24, 153/27, 162/40, 164/80, 174/80, 176/0, 180/0) using an Eksigent NanoLC-2D system (Sciex (Framingham, MA)). The effluent from the column was directed to a nanospray ionization source connected to a hybrid quadrupole-Orbitrap mass spectrometer (Q Exactive Plus, Thermo Fisher Scientific) acquiring mass spectra in a data-dependent mode alternating between a full scan (*m/z* 350-1700, automated gain control (AGC) target 3×10^6, 50 ms maximum injection time, FWHM resolution 70,000 at m/z 200) and up to 10 MS/MS scans (quadrupole isolation of charge states $\geq$ 2, isolation width 1.2 Th) with previously optimized fragmentation conditions (normalized collision energy of 32, dynamic exclusion of 30 s, AGC target 1×10^5, 100 ms maximum injection time, FWHM resolution 35,000 at *m/z* 200). The raw data was analyzed in Proteome Discoverer 2.2, which provided measurements of relative abundance of the identified peptides.

Histological studies

Hearts were harvested under anesthesia and perfused with PBS followed by fixation in 4% formaldehyde in PBS at 4þC for 24 h, and subsequently subjected to dehydration in sucrose solution. Then the hearts were embedded in Tissue-Tek O.C.T compound (SAKURA, Finetek, USA) and sectioned with 10μm-thickness.

For immunostaining, tissue sections were incubated with pre-chilled acetone at −20þC for 10 min, blocked in 10% species-specific normal serum in 1% BSA/PBS for 1 h, and primary antibodies diluted in 1% BSA/PBS at 4þC overnight. Secondary antibodies were diluted in PBS and incubated with the sections for 1 h. Samples were counterstained with DAPI (1μg/mL, Invitrogen, D3571) and mounted with SlowFade Gold Antifade reagent (Invitrogen, S36936). Images were taken using Nikon Eclipse Ti2 confocal microscopy (Nikon,USA) and analyzed in NIS Element AR software (Nikon). For detection of αsmooth muscle actin, integrin αVβ3, and αVβ5, M.O.M immunodetection kit (Vector) was used. Breifly, tissue sections were incubated with pre-chilled acetone at −20þC for 10 min, incubated with Avidin/Biotin blocking buffer (Vector) for 15 min, M.O.M blocking buffer for 1 h, and primary antibodies diluted in M.O.M diluent at 4þC overnight. Biotinylated 2nd antibody against mouse (Vector) was diluted in M.O.M diluent (1:250) and incubated with the sections for 10 min. Samples were incubated with diluted fluorescien avidin DCS (1:60) for 5 min. Samples were counterstained with DAPI (1μg/mL, Invitrogen, D3571) and mounted with SlowFade Gold Antifade reagent (Invitrogen, S36936).

For Masson Trichrome staining, sections were stained using Masson Trichrome Stain kit (Thermo Scientific, 87019). Images were taken in heart sections from apex, mid-ventricle, and close to suture and fibrotic area analyzed from apex to mid-ventricle. Scar tissue area was calculated as the fraction of left ventricular surface area occupied by the scar tissue. Severity of fibrosis was classified as sample showed > 40% fibrotic area as "severe," 20%–40% as "moderate," or < 20% as "mild" for 6wks post MI hearts and > 50% fibrotic area as "severe," 30%–50% as "moderate," or < 30% as "mild" for 2wks post MI hearts.

RNA-Fluorescence *in situ* hybridization

RNA-FISH was performed using RNAscope Multiplex Fluorescent reagent kit v2 (ACD Inc, USA) as per manufacturer instructions. Tissue sections were incubated with hydrogen peroxide for 15 min followed by incubation with RNAscope Target Retrieval Reagent at 99þC for 5 min. Then the section was incubated with Protease III reagent at 40þC for 30 min in HybEZ II oven (ACDInc). After pretreatment steps, RNAscope probes were hybridized at 40þC for 2 h, AMP1 for 30 min, AMP2 for 30 min, AMP3 for 15 min, channel-

specific HRP reagent for 15 min, diluted TSA Plus fluorophores (PerkinElmer,USA) in RNAscope TSA dilution buffer (1:1000 dilution) for 30 min, HRP-blocker reagent for 15 min. Stained section was counterstained with DAPI solution and mounted in SlowFade Gold Antifade reagent (Invitrogen, S36936).

For dual RNA-FISH and immunostaining, tissue sections were pre-treated, and signals developed as described above. Following RNA-FISH, the sections were blocked with 10% normal goat serum/1%BSA in PBS, incubated with anti-RFP (1:50, Rockland, 600-401-379) or anti-cTnI (1:50, Abcam, ab47003) at 4þC overnight, HRP-conjugated secondary antibodies against rabbit (1:200, Invitrogen, #31470) for 30 min, diluted TSA Plus TMR (1:300, PerkinElmer, FP1169) in RNAscope TSA buffer for 15 min, and counterstained with DAPI.

Insoluble collagen assay

Insoluble collagen assay was conducted using Sircol Insoluble Collagen Assay Kit (Biocolor, S2000). The injured regions of the heart were harvested at 4 weeks following injury and weight their wet weight. Tissues were homogenized in 0.1mg/mL pepsin/0.5M acetic acid and incubated overnight at 4þC. lysates were centrifuged at 12K r.p.m for 10min and supernatants were transfer to new tubes. Tissue residues were incubated with Fragmentation Reagent at 65þC for 2 h with vortex every 30 min during incubation, centrifuged at 12K r.p.m for 10 min, and supernatants were transferred into new tubes. Supernatants were mixed with 1ml of Sircol Dye Reagent and incubated for 30 min with gentle shaking. Precipitates were collected by centrifuge at 12K r.p.m for 10 min and washed with 750μl of ice-cold Acid-Salt Wash Reagent. Washed precipitates were dissolved in 500μl of Alkali Reagent, transferred 200μl of each sample and collagen standards into a 96-well plate, and measured absorbance at 550nm using Synergy H1 microplate reader (BioTeK).

Transmission electron microscopy

Samples were fixed in 2% glutaraldehyde in PBS at 4oC for 3 h. Fixed samples were embedded in low-viscosity resin (Agar, UK) as following: samples were osmicated using 1% OsO4; stained with 3% uranyl-acetate; dehydrated in 30-50-70-95%–100% ethanol and embedded in low-viscosity resin (Agar, UK). Plastic-embedded samples were sectioned using UCT ultramicrotome (Leica, Austria) and diamond knife (Diatome, Austria). Sections 50-55nm thick were mounted on home-made EM grid(s) with plastic-carbon support film, stained with saturated uranyl-acetate and Sato's lead-citrate. Sections were imaged using JEM1200EX transmission electron microscope (JEOL, Japan) at 80 kV equipped with BioScan600W digital camera (Gatan, USA). Images were prepared for publication using a Photoshop (Adobe, USA). Approximately 500 fibrils were measured by ImageJ for analyzing fibril diameter in each group.

Tomography of collagen fibers

Sections 200 nm thick were mounted on 150 mesh hexagonal copper grids (Ted Pella, USA). Thereafter, grids with attached sections were stained with saturated uranyl acetate, lead citrate, 10nm gold from both sides. Layer of carbon was evaporated on top of the section. Grids were loaded into high-resolution tomography holder Model 2020 (Fischione, USA) and imaged with TF20 TEM (FEI, Netherlands) at 200 kV. To collect tomograms, FEI Batch Tomography software was used. The tomograms were processed using IMOD software (Kremer et al., 1996). Alignment of the stack was performed using fiducial markers (10 nm gold) on both sides of the tomogram. The final 3d model calculation was performed by SIRT (IMOD). Obtained 3d models were visualized in Chimera (Pettersen et al., 2004). They were filtered with Gaussian filter and segmented in Segger, part of Chimera package. Final models were imaged in Chimera also.

Plasmid construction and Lentivirus preparation

pLenti-Largen T antigen (Cat#18922), Lenti-pHIV-eGFP (Cat#21373), PSPAX2 (Cat#12260), PMD.G2 (Cat#12259), pLV-eGFP-Cre (Cat#86805) were purchased from Addgene. Total 13ug pasmids (object gene, PSPAX2, PMD.G2) was co-transfected into 75cm^2 flask with 293T cells in 10 mL DMEM Medium, 6-7ml fresh DMEM medium were changed after plasmids co-transfected 8-10 h. The medium was collected and centrifuged at 4°C in 500x g for 10 min after transfected 72 h. The medium with virus was aliquoted and stored at −80þC.

Isolation of primary culture adult cardiac fibroblast

5-7 hearts were harvested from wild-type C57BL/6 mice or Col5a1 floxed mice. Valves and atriums were removed from the hearts, and the hearts rinsed in ice-cold HBSS. The hearts were chopped into 1mm square pieces, suspended in 0.1μg/mL liberase TH (Sigma, 5401151001) in Tyrodes buffer (136mM NaCl, 5.4mM KCl, 0.33mM NaH_2PO_4, 1mM $MgCl_2$, 10mM HEPES, 0.18% Glucose), and incubated with shaking incubator at 37þC for 30 min at 80 rpm. Digested hearts were filtered with a 40μm cell strainer (Fisher, 22363547), centrifuged at 200x g for 5 min, resuspended cells with 10ml of 20%FBS in F12K medium, and seeded the cells into 100mm^2 dish. After 2 h, medium was changed to human basic FGF (10ng/mL, Millipore, GF003) containing 20%FBS in F12K medium. Isolated cardiac fibroblast was used for experiments in 2nd or 3rd passage.

Generation of Col5a1 deficient immortalized cardiac fibroblast

Cardiac fibroblasts were isolated from Col5a1 fl/fl mouse as described above. These cells were infected with Lentivirus-Large T antigen in presence of polybrene (8μg/mL) for 16 h, treated with puromycin (2μg/mL) for selection of infected cells. Immortalized cells

were cultured with 10%FBS containing high glucose DMEM. Cells so immortalized were then infected with Lentivirus-Cre recombinase or lentivirus-GFP to generate Col5a1 deficient cardiac fibroblast or control cardiac fibroblast, respectively. These cells were cultured for 6-7 days and used for each experiment to determine effects on gene expression. To determine an effect of Cilengitide on these cells, Col5a1fl/fl cardiac fibroblasts were pretreated with Cilengitide (1μM) in 10%FBS containing high glucose DMEM for 1 h before infection with lentivirus-Cre recombinase or lentivirus-GFP. These cells were treated with Cilengitide/vehicle for 7 days and medium was changed every 2 days.

Flow cytometry

For cultured cardiac fibroblasts, cells were harvested and fixed in 4% formaldehyde/PBS for 10min on ice, incubated for primary antibodies diluted in 1%BSA/PBS for 1 h on ice. For unconjugated antibodies, cells were incubated with diluted Alex Fluor 594 secondary antibody (1:200, Invitrogen). Data was analyzed using Flowjo software.

Measurement of force generated by Col V deficient cardiac fibroblasts

Device fabrication

The device to make microtissues was designed using AutoCAD software (Autodesk Inc., USA). STAR Methods Figure 1A shows the three-dimensional (3D) design of master mold. STAR Methods Figure 1B shows the 3D schematic of the replicated design with wells and two microposts. The top view of the replicated design is shown in STAR Methods Figure 1C. By using a laser cutter with a fine-tuned laser power and speed, poly(methyl methacrylate) (PMMA) master molds were fabricated as shown in STAR Methods Figure 1D. After sticking the mold to a Petri dish with glue, a mixture of polydimethylsiloxane (PDMS) prepolymer and its curing agent with the mass ratio of 20:1 was prepared and poured on the mold. After removing bubbles and curing at 80°C for 2 h, the PDMS was peeled off from the mold as shown in STAR Methods Figure 1E.

Fabrication of microtissues

In order to make microtissues, after sterilizing the PDMS platform, a collagen hydrogel at density of 3 mg/mL was prepared. Cardiac fibroblasts were mixed with the gel at density of 5 Million cells/mL. The small well around microposts was filled with the cell-laden gel and then incubated for 1 h to encourage the gel formation. After the incubation, sufficient cell culture media was added to the samples.

Measurement of contraction force of microtissues

The pictures of tissues were taken on days 1, 2, and 3 of culture by using ToupView microscope integrated with SeBaView software. The images were then analyzed with ImageJ software to measure the deflection of microposts due to the tissue contraction. The cantilever beam theory was used to quantify tissue force. This theory correlates the tissue force to small deflection of microposts as shown in STAR Methods Figure 1F. The stiffness of microposts can be calculated by Equation 1 and the contraction force can be calculated by Equation 2 by measuring the deflection of the free end of each micropost as follows:

$$k = \frac{3\pi E d^4}{64 L^3} \qquad \text{Equation 1}$$

$$F = k\delta \qquad \text{Equation 2}$$

where k is the stiffness of each micropost that is a function of length (L), diameter (d), and Young's modulus of PDMS post (E). The Young's modulus of PDMS was considered to be 1.1 MPa (Brown et al., 2005; Wang et al., 2014). In the Equation (2), F is the contraction force, δ is the deflection of free end of the micropost (Beussman et al., 2016; Ma et al., 2019; Oyunbaatar et al., 2016; Ribeiro et al., 2016).

Numerical simulation

To confirm the measurements of PDMS deflection and contraction force, finite element analysis (FEA) implemented in COMSOL Multiphysics 5.3 software was used. The FEM model consisted of two cylindrical PDMS microposts with the post height of 3.1 mm and diameter of 0.8 mm inside a well. The microposts were fixed to the well and deemed as a cantilever beam. The PDMS assembly was modeled as linear elastic material with a uniform Young's modulus of 1.1 MPa. After setting appropriate boundary conditions and by applying a single force to the free end of the microposts, the displacement distribution of the microposts were determined as illustrated in STAR Methods Figure 1G. Moreover, the simulation showed a linear relationship between the applied force and micropost deflection, which is in agreement with the cantilever beam theory (STAR Methods Figure 1H).

Measurement of decorrelation rate of Col V deficient cardiac fibroblasts

Quantitative phase microscopy (QPM) was used to determine decorrelation rate as follows. Cardiac fibroblasts were isolated from Col5a1 floxed mice, immortalized and then treated with a Cre expressing or GFP lentivirus to generate Col5a1CKO or control fibroblasts. Cells were imaged every 5 min for 20 h at 20x with a SID-4 Bio (Phasics) camera to acquire QPM data via quadriwave lateral shearing interferometry(Bon et al., 2009). This was on an Axio-vision Observer Z1 (Zeiss) equipped 0.4 numerical aperture objective lens with illumination was provided by a 660 nm center wavelength collimated LED (Thorlabs). The Col5a1CKO fibroblasts and the

control fibroblasts were imaged with enough spacing between cells to allow for automated particle tracking (Crocker and Grier, 1996; Zangle et al., 2013a) and cell or cell cluster segmentation (Otsu, 1979; Zangle et al., 2013b). Automated detection of cell division events were done by pattern matching (Zangle et al., 2014) of quantitative phase images. Using experimentally determined cell average specific refractive index, quantitative phase shifts is related to the dry biomass of cells (Barer, 1952; Davies and Wilkins, 1952). All image processing was performed using custom MATLAB (MathWorks) scripts.

QPM decorrelation rate via temporal autocorrelation

We quantified the rate of biomass redistribution by examining the similarity of the QPM data over time through an unbiased estimate of autocorrelation (Bendat and Piersol, 2013) of the phase shift signal. The temporal autocorrelation was normalized with respect to the number of data points used in each autocorrelation window, referenced to the end of the time shift window (t_0), and defined as:

$$C_{\phi\phi}(x,y,t_0,\tau) = \frac{w}{\left(w-\frac{\tau}{\Delta t}\right)}\cdot\frac{\sum_{i=0}^{w-\tau/\Delta t}\phi(x,y,t_0-i\Delta t)\cdot\phi(x,y,t_0-i\Delta t-\tau)}{\sum_{i=0}^{w}\left[\phi(x,y,t_0-i\Delta t)\right]^2}$$

Where x and y are the spatial positions after removing rigid translational motion of the cell cluster, t_0 is the time, ϕ is phase shift, w is the number of images used to calculate the signal, and τ is time lag. The autocorrelation was then averaged over the cell or cluster area as:

$$\overline{C_{\phi\phi}(t_0,\tau)} = \frac{1}{A}\sum_{\text{all } x,y \text{ in } A} C_{\phi\phi}(x,y,t_0,\tau)$$

where A is the area of the cell or cluster in pixels. The slope of a linear least-squares fit to the averaged autocorrelation from $\tau = 0$ to $\tau =$ 1 h (12 frames) was defined as the decorrelation rate and used to quantify the biomass redistribution rate within cell clusters. Any decorrelation rate measurements that included images with mitotic cells were excluded.

Traction force measurement of neonatal rat ventricle myocyte and fibroblast co-culture

Fabrication of bio-sensor devices

The bio-sensor devices were fabricated by first spin coating a layer of photoresist (AZ 4620, 2500rpm, 60 s) onto a glass slide, and baking it at 90 Celsius for 3 min. Then, gold nanoparticles suspended in citrate buffer (Sigma-Alrich 742090) were deposited onto the photoresist and left to dry in a vacuum desiccator (Thermo Scientific 53100250) overnight, as illustrated in STAR Methods Figure 2A. A mixture of polydimethylsiloxane (PDMS) comprising 1 part of Sylgard 184 (Dow Corning) with 6 parts of Sylgard 527 (Dow Corning) was then poured onto the surface of dried gold nanoparticles. The Sylgard mixture was put under vacuum to remove the air bubbles before a coverslip glass was put on top of it, as shown in STAR Methods Figure 2B. The devices were then left to cure in the oven at 60 Celsius for 12 h. Thereafter, the devices were released by immersing them into acetone overnight to dissolve the photoresist. This reveals the final structure shown in STAR Methods Figure 2C.

Cell Seeding and Microscopy

Matrigel (at concentration of 83μg/mL) was then coated for 12 h on the surface of the PDMS devices. On day 1, neonatal rat ventricular cardiomyocytes (NRVMs) were seeded at 75% confluence on the devices for the mutant group, and at 90% confluence on the devices for the control group. The confluence in the 2 groups was made different in order to account for the fact that each mutant fibroblast occupies 3 times more area than each control fibroblast. On day 2, control and mutant fibroblasts were separately seeded onto their respective devices. On day 3, the cells were stained with Calcein AM (Invitrogen), before they were imaged under dark field and fluorescence microscopy (Zeiss AxioScope A1, EC Epiplan-Neofluar, 20x, N.A. = 0.5). The gold nanoparticles were also imaged under dark field microscopy. The gold nanoparticles moved when the cells were beating, due to the mechanical coupling between the cells and the substrate.

Machine Learning Model

Before we could process the images obtained from microscopy, the numerical model needed to be built. The numerical model was built by first generating 1000 different random continuous stress distributions in COMSOL (finite element software) by using 2-dimensional random functions. An example of the stress distribution is shown in STAR Methods Figure 2D. The stress distributions were applied as boundary loads onto the top surface of the device in COMSOL. Stationary studies were done in COMSOL to solve for the equilibrium displacement of the PDMS surface. One example of the displacement of the PDMS surface is shown in STAR Methods Figure 2E. Thereafter, the 1000 different cases of stresses and displacements were used to train the linear regression machine learning model (scikit-learn).

Processing of Experimental Images

An area spanning 200μm by 200μm was selected from the video taken by a 20x magnification objective lens under a dark field microscope (Zeiss AxioScope A1, EC Epiplan-Neofluar, 20x, N.A. = 0.5). Two image frames were used to calculate the displacement of the gold nanoparticles. The reference frame was chosen as the frame in which the cells were not beating. The peak frame was chosen as the frame in which the cells and gold nanoparticles had the largest displacement. The positions of the gold nanoparticles were

determined using the Gaussian fitting method as described(Xiao et al., 2018). The displacement was taken to be the difference in the positions of the gold nanoparticles between the peak frame and the reference frame. STAR Methods Figures 2F and 2G show the displacement of each of the gold nanoparticles. The displacements in STAR Methods Figures 2F and 2G were then interpolated and a two-dimensional Fourier transform filter was applied to process the interpolated data to eliminate the components of high spatial frequencies. The resulting interpolated displacements after Fourier filtering are shown in STAR Methods Figures 2H and 2I. The displacements from STAR Methods Figures 2H and 2I were then input into the machine learning model. The machine learning model then output the stress distributions as shown in STAR Methods Figures 2J and 2K. The predicted stress distributions were then inputted back into the COMSOL software to confirm that the simulated displacements (STAR Methods Figure 2L) match with the interpolated displacements (STAR Methods Figure 2H) with an overall error of 2% for the control group. The overall error of the displacements was 10% for the mutant group (STAR Methods Figures 2I and 2M). The errors were calculated by the expression:

$$\sigma = \frac{\sum_{x,y}(u_{simulated}(x,y) - u_{actual}(x,y))^2 + \sum_{x,y}(v_{simulated}(x,y) - v_{actual}(x,y))^2}{\sum_{x,y}(u_{actual}(x,y))^2 + \sum_{x,y}(v_{actual}(x,y))^2}$$

where $u_{simulated}(x,y)$ and $v_{simulated}(x,y)$ are the x and y vector components of the simulated displacement from COMSOL in STAR Methods Figure 2L, and $u_{actual}(x,y)$ and $v_{actual}(x,y)$ are the x and y vector components of the displacement in STAR Methods Figure 2H. Note that the displacements are functions over space (x,y). It can be seen that the magnitude of the stresses is larger for the control group STAR Methods Figure 2J as compared to the mutant group STAR Methods Figure 2K.

Parallel microfiltration

To measure the deformability of wild-type and *Col5a1* null fibroblasts, we used parallel microfiltration (PMF) as described in our previous studies(Kim et al., 2016; Kim et al., 2019; Qi et al., 2015) to assess the ability of cells in a suspended state to filter through 10 μm pores of a membrane in response to applied pressure. The volume of retained cell suspension retained in the top well indicates the number of pores that are occluded, which is largely determined by cell deformability: lower retention indicates a sample with more deformable cells. Polycarbonate membranes with 10 μm pore size (TCTP14250, Millipore) were used for all filtration experiments. Prior to the PMF assay, trypsinized cells were rested 20 m at room temperature, counted using an automated cell counter (TC20, Bio-Rad), and resuspended in medium to a density of 5×10^5 cells/mL. Cell suspensions (400 μL) were loaded into each well of a 96-well plate sample loading plate (4 wells per sample). We measured cell viability by staining cells with Trypan Blue (T8154, Sigma) and verified that cell suspensions prior to filtration consisted of single cells; therefore, the filtration behavior is largely determined by the occlusion of viable single cells rather than apoptotic cells or larger aggregates of cells. Since cell size can also impact occlusion, we measured cell size distributions and confirmed there were no significant size differences between wild-type and knock-out cells in a suspended state (Figure S7A). To drive cell suspensions to filter through the 10 μm pores, we applied an air pressure of 2.0 kPa for 30 s. To quantify retention volume, we transferred the cell suspension retained in the top well after filtration to a 96-well plate and measured the absorbance of phenol red at 562 nm using a plate reader (SpectraMax M2, Molecular Devices). Using a standard curve, we calculated the retained volume. Retention was determined by the volume of cell suspension that remains in the top well after filtration divided by the initial volume loaded ($Volume_{final}/Volume_{initial}$).

Atomic force microscopy

For atomic force microscopy (AFM) experiments, PBS-perfused hearts were dissected and mounted in OCT (Tissue-Tek, Sakura Finetek, Torrance, CA, USA) and flash frozen in liquid nitrogen-cooled isopentane. Cardiac tissue cryosections (30 μm) were mounted onto microscope slides with an adhesive coating (#SUMGP14 Matsunami Glass Ind. Ltd., Kishiwada, Osaka, Japan). Cardiac sections were incubated in rabbit anti-mouse collagen type I antibody (CL50151AP-1; 1:250; Cedarlane Labs) in PBS at 4°C overnight and were detected by indirect immunofluorescence using Alexa Fluor 488 goat anti-rabbit secondary antibody (AB150156; 1:500; Abcam). AFM measurements were performed on each section in PBS using a JPK Nanowizard 4A BioAFM with a 200x200x200 μm HybridStage (Bruker/JPK BioAFM, Billerica, MA, USA) coupled to a Leica M205 stereoscope (Leica Microsystems, Wetzlar, Germany). Scar regions were identified by collagen I dense immunofluorescence signal which was used as a guide for overlaying the AFM cantilever for force spectroscopy (Figures 6B and 6C). Non-scar regions were selected in areas where collagen I signal was confined to the interstitial matrix surrounding cardiomyocytes and at least 1000 μm away from a scar region. Both scar regions and non-scar regions were probed with AppNano SHOCONGG-TL cantilevers with a 10 μm silicon dioxide sphere (nominal freq (kHz) = 21(8-38), k(N/m) = 0.14 (0.01-0.6); AppNano, Mountain View, CA, USA). The sensitivity and spring constant of each probe were calibrated before each experiment using the contact-free calibration method. All measurements were taken in force spectroscopy mode and force-versus-indentation curves were generated from an average of 200 points/sample. Approach and retraction speeds for all force measurements were 2 μm/sec with a setpoint force of 2.5 nN and a retraction distance of 10 μm. Data analysis was performed using JPKSPM Data Processing software. To evaluate tissue stiffness, Young's modulus was calculated from > 100 AFM force curves, using the Hertz-Sneddon model (Sneddon, 1965). Young's modulus data were plotted and statistics calculated in GraphPad (Prism) software using the Kolmogorov-Smirnov nonparametric test.

QUANTIFICATION AND STATISTICAL ANALYSIS

All data is presented as mean ± standard deviation (SD) except Figure 6D (mean ± SEM) and mentioned in the figure legends. The exact value of n is mentioned in the figure legends and always stands for separate biological replicates. Statistical analysis was performed using GraphPad (Prism) software using Student's t test (Two tailed) and one-way ANOVA with Tukey's multiple comparison analysis as appropriate. A P value < 0.05 was considered as statistically significant. For analysis of strain imaging data, outlier identification was conducted in ROUT (Q = 2%) method using GraphPad (Prism) software. The values identified as outlier were excluded from statistical analysis.

Supplemental Figures

A

	Basal	3D	7D	14D	21D	42D
EF (%)	65.2±4.6	36.9±11.6	37.3±16.6	33.6±12.2	27.2±10.0	24.3±11.9
FS (%)	35.4±3.5	17.8±6.1	18.3±8.9	16.2±6.3	12.8±4.9	11.4±5.8

B

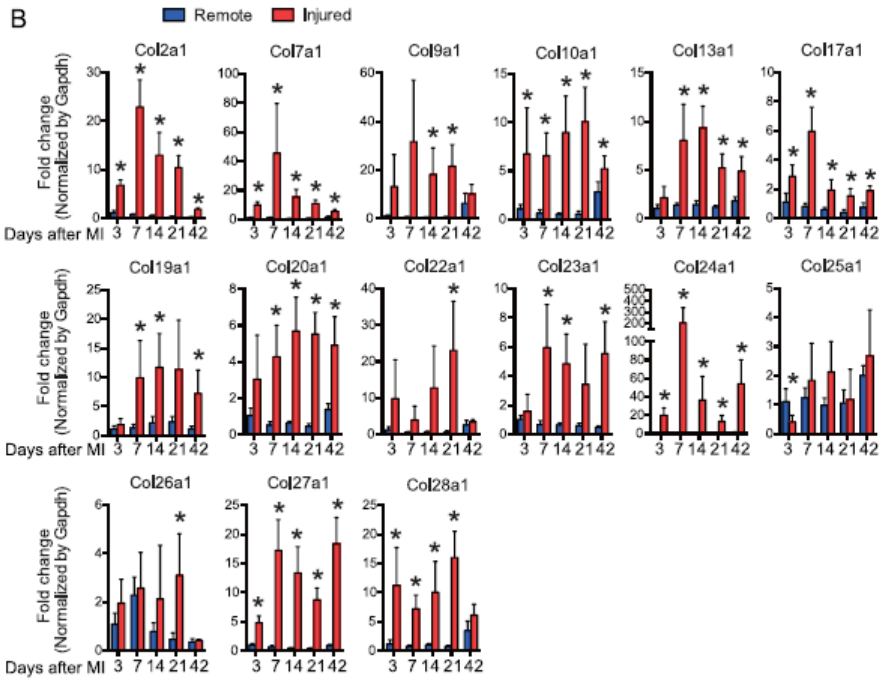

C

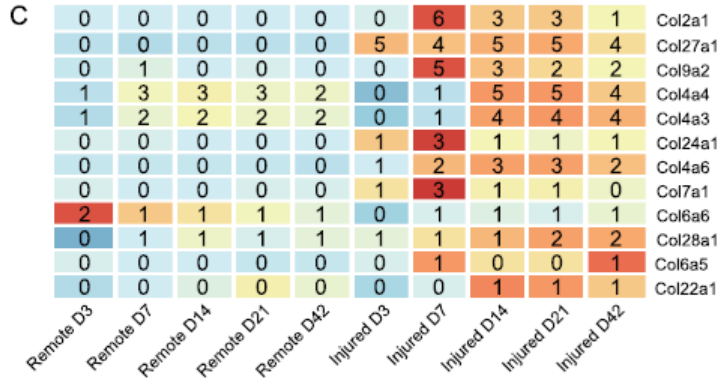

(legend on next page)

Figure S1. Dynamic Changes in Expression of Collagen Genes following Injury, Related to Figure 1

(A) Temporal changes in ejection fraction (EF) and fractional shortening (FS) after ischemic cardiac injury (data shown as mean ± S.D., n = 8 animals/group/time point (B) qPCR demonstrating temporal changes in collagen genes that are not abundantly expressed in the heart (data shown as mean ± S.D., n = 5 animals/group/time point, *$p < 0.05$, compared to expression of respective collagen gene in uninjured region at that time point) (C) Heatmap demonstrating temporal changes in collagen genes (that are usually expressed in extra cardiac tissues) as well as RPKM values from RNA-seq of injured and uninjured region of heart demonstrating low expression of such collagen genes.

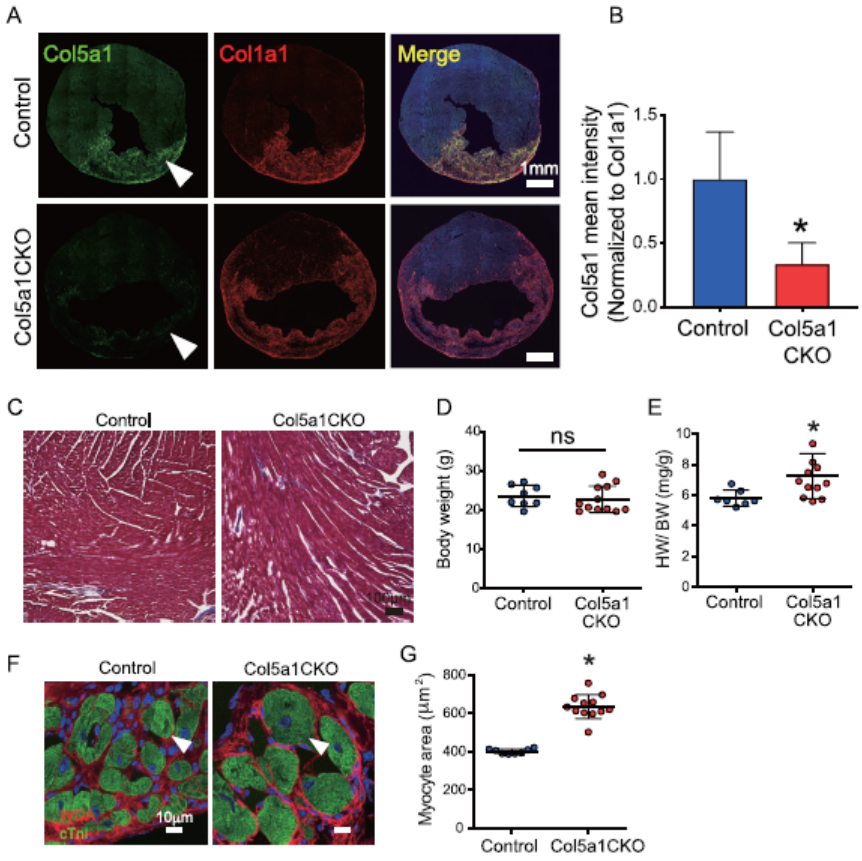

Figure S2. Col5a1CKO Animals Exhibit Decreased Col5a1 Expression and Have Myocardial Hypertrophy after Ischemic Cardiac Injury, Related to Figure 3

(A) Conditional deletion of Col5a1 (Col5a1CKO mice) was performed by crossing mice harboring the Col1a2CreERT driver with Col5a1 floxed mice. RNA-FISH demonstrating decreased expression of Col5a1 in Col5a1CKO mice compared to control littermates at 7 days following injury (arrows, representative images, images were acquired and stitched together with Nikon software). The decrease in intensity is compared to Col1a1 in Col5a1 CKO and control littermates. (B) mean intensity of Col5a1 expression normalized to Col1a1 expression in the Col5a1CKO and control animals (mean ± S.D., *$p < 0.05$, n = 9 Control and 15 CKO) (C) Masson trichrome staining in remote area of Col5a1CKO and Control animals at 6wks post MI demonstrates minimal fibrosis in both groups. (D) Body weight and (E) Heart weight body weight ratio of Col5a1CKO and control animals at 6 weeks post injury (mean ± S.D., *$p < 0.05$, n = 8 control and 12/CKO, ns: not significant). (F) Immunostaining for cardiac troponin I and wheat germ agglutinin (WGA) demonstrates increased myocyte surface area in Col5a1CKO animals at 6 weeks following injury (arrows, representative images, same number of animals as above) (G) Quantitation of myocyte surface area in border zone region of Col5a1CKO and Control animals (mean ± S.D., *$p < 0.05$, n = 8 control and 12/CKO).

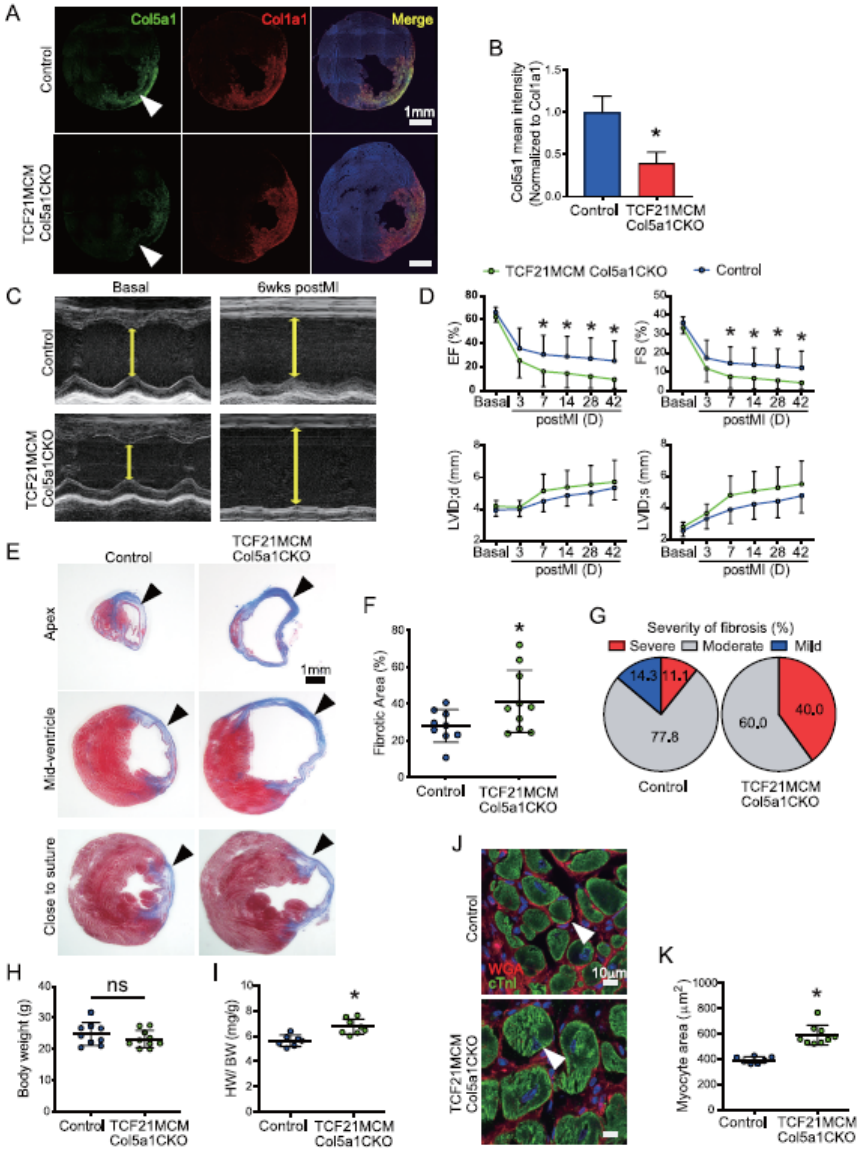

Figure S3. Col5a1CKO Mice Generated by Using the TCF21MerCreMer Driver Also Exhibit Increased Scarring following Ischemic Heart Injury, Related to Figure 3

(A) TCF21MCM:Col5a1CKO mice were generated by crossing the TCF21MerCreMer mice with the Col5a1 floxed mice. Expression of Col5a1 in the injury region by RNA-FISH in TCF21MCM:Col5a1CKO animals compared to control littermates at 7 days post MI (arrows, representative images, images were acquired and stitched together with Nikon software). (B) Quantitative decrease in Col5a1 expression in TCF21MCM:Col5a1CKO mice compared to control littermates (mean ± SD., *$p < 0.05$, n = 6 animals/Control and 4/CKO). (C) M mode echocardiogram demonstrating left ventricular walls and internal dimension (yellow line) prior to (basal) and 6 weeks following injury in TCF21MCM:Col5a1CKO and control littermates (representative images, n = 12 Control and 18 CKO at basal. n = 9 Control

(legend continued on next page)

and 10 CKO at 6wks post MI). (D) Ejection fraction and Fractional shortening in TCF21MCM:Col5a1CKO and control littermates at different time points following injury (mean ± S.D., *p < 0.05, n = 12 animals/Control and 18/CKO at basal, n = 9/Control and 14/CKO at 3D post MI. n = 9/Control and 12/CKO at 1wk postMI, n = 9/Control and 10/CKO at 2-6wks post MI). Left ventricular dimensions in end diastole (LVIDd) and end systole (LVIDs) at different time points following injury (E) Masson trichrome staining of hearts of TCF21MCM:Col5a1CKO and control littermates sectioned at the base (just distal to suture line) at mid ventricle and apex 6 weeks following injury (representative images shown, n = 9 animals/Control and 10/CKO) (F) Quantification of surface area of scar normalized to the surface area of the left ventricle (mean ± S.D., *p < 0.05, n = 9 animals/Control and 10/CKO). (G) Fraction of animals in the TCF21MCM:Col5a1CKO and control groups that demonstrate mild/moderate or severe scarring at 6 weeks following injury. (mild scarring < 20% of surface area, moderate between 20 and 40% of ventricular surface area and severe > 40% of surface area). (H) Body weight in TCF21MCM:Col5a1CKO and control animals at 6 weeks following injury. (mean ± S.D., n = 9 Control and 8 CKO) (I) Heart weight/body weight ratio in TCF21MCM:Col5a1CKO and control animals at 6 weeks following injury. (mean ± S.D., *p < 0.05, n = 9 Control and 8 CKO) (J) Immunostaining of mid ventricular heart sections of TCF21MCM:Col5a1CKO and control littermates with Troponin I and Wheat germ agglutinin (WGA) at 6 weeks following injury to determine surface area (cross sectional area, arrowhead) of cardiomyocytes (representative images, n = 7 animals/Control and 9/CKO) (K) Quantitation of surface area of individual cardiomyocytes between TCF21MCM:Col5a1CKO and Control groups at 6 weeks following injury (mean ± S.D., *p < 0.05, n = 7 animals/Control and 9/CKO).

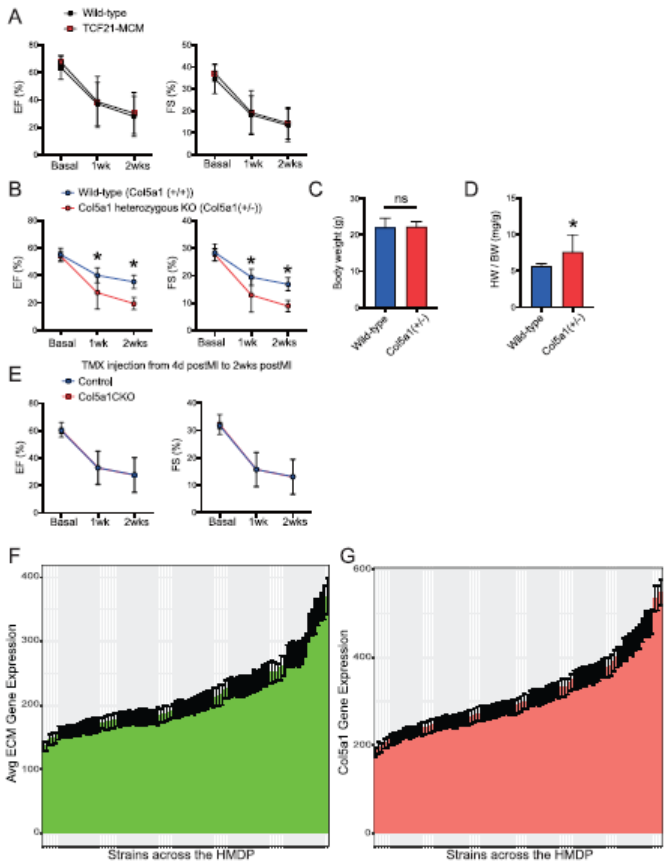

Figure S4. Cardiac Function and Scarring in TCF21MCM, Col5a1 Heterozygous KO, and TCF21MCM:Col5a1CKO Animals, But with Tamoxifen Administered from Day 4 Onward, and Expression of ECM Genes and Col5a1 across All Strains in the HMDP following Isoproterenol Infusion for 3 weeks, Related to Figures 3 and 4

(A) TCF21MCM animals and wild type animals were administered tamoxifen and subjected to ischemic cardiac injury. Cardiac contractile function in TCF21MCM and wild type littermates 1 and 2 weeks following injury ($p > 0.05$) ($n = 4$ for each group)

(B–D) Col5a1 heterozygous KO mice or wild type littermates were subjected to cardiac injury and (B) cardiac function (EF,FS) determined at 1 and 2 weeks after injury (*$p < 0.05$, $n = 8$ wild-type $n = 6$ Col5a1 heterozygous KO animals at basal, $n = 7$ wild-type $n = 4$ Col5a1 heterozygous KO animals at 1 and 2 weeks after injury) and (C and D) Cardiac hypertrophy assessed by heart weight/body weight ratios (*$p < 0.05$, $n = 7$ wild-type $n = 4$ Col5a1 heterozygous animals, ns: not significant) (E) TCF21MCM:Col5a1CKO or control littermates were subjected to ischemic injury but tamoxifen administered for 10 days starting at 4 days after injury. Cardiac contractile function between groups at 1 and 2 weeks after injury ($n = 8$ control $n = 7$ Col5a1CKO animals at basal, $n = 6$ control $n = 6$ TCF21MCM:Col5a1CKO animals at 1 and 2 weeks after injury, $p > 0.05$).

Average expression of ECM and Col5a1 genes (y axis) versus approximately 96 strains of mice on the x axis. Each data point refers to the average gene expression for ECM genes (F) or Col5a1 (G) in the left ventricle of that particular strain following isoproterenol infusion.

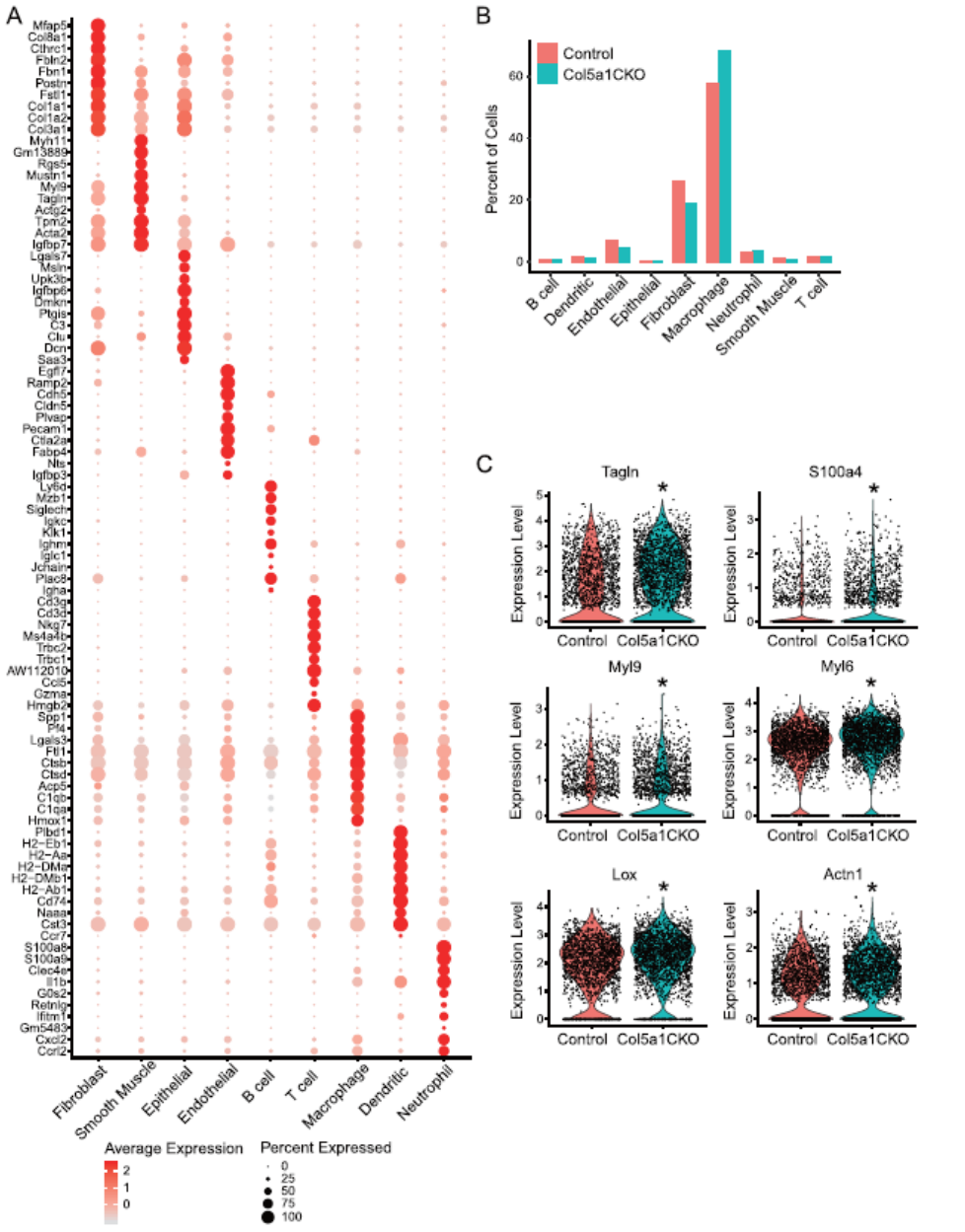

(legend on next page)

Figure S5. Identification of Cell Phenotypes According to Expression of Canonical Genes and Numbers of Cells in Each Phenotype in Col5a1CKO and Control Animals from scRNA-Seq Analysis Performed on Non-myocytes at Day 7 following Injury, and Expression of Myofibroblast Genes in Control and Col5a1CKO Cardiac Fibroblasts from Analysis of scRNA-Seq data, Related to Figure 5

(A) Illustration of clusters of canonical genes used to identify various cell phenotypes of non-myocytes in the heart at 7 days following injury. (B) Fraction of cells in either Col5a1CKO or control animals belonging to each phenotype. (n = 3 samples/group). (C) Expression of smooth muscle contractile proteins or calcium regulatory proteins in cardiac fibroblasts of Control or Col5a1CKO animals. Single cell RNA-seq data analysis demonstrating expression of Tagln (p = 1.86E-121), S100a4 (FSP1, p = 7.38E-20), Myl9 (p = 1.72E-129, Myl6 (p = 2.82E-107, Lox (p = 3.68E-37) and Actn1 (p = 7.11E-45) in cardiac fibroblasts in Col5a1CKO and control hearts harvested at 7 days following injury

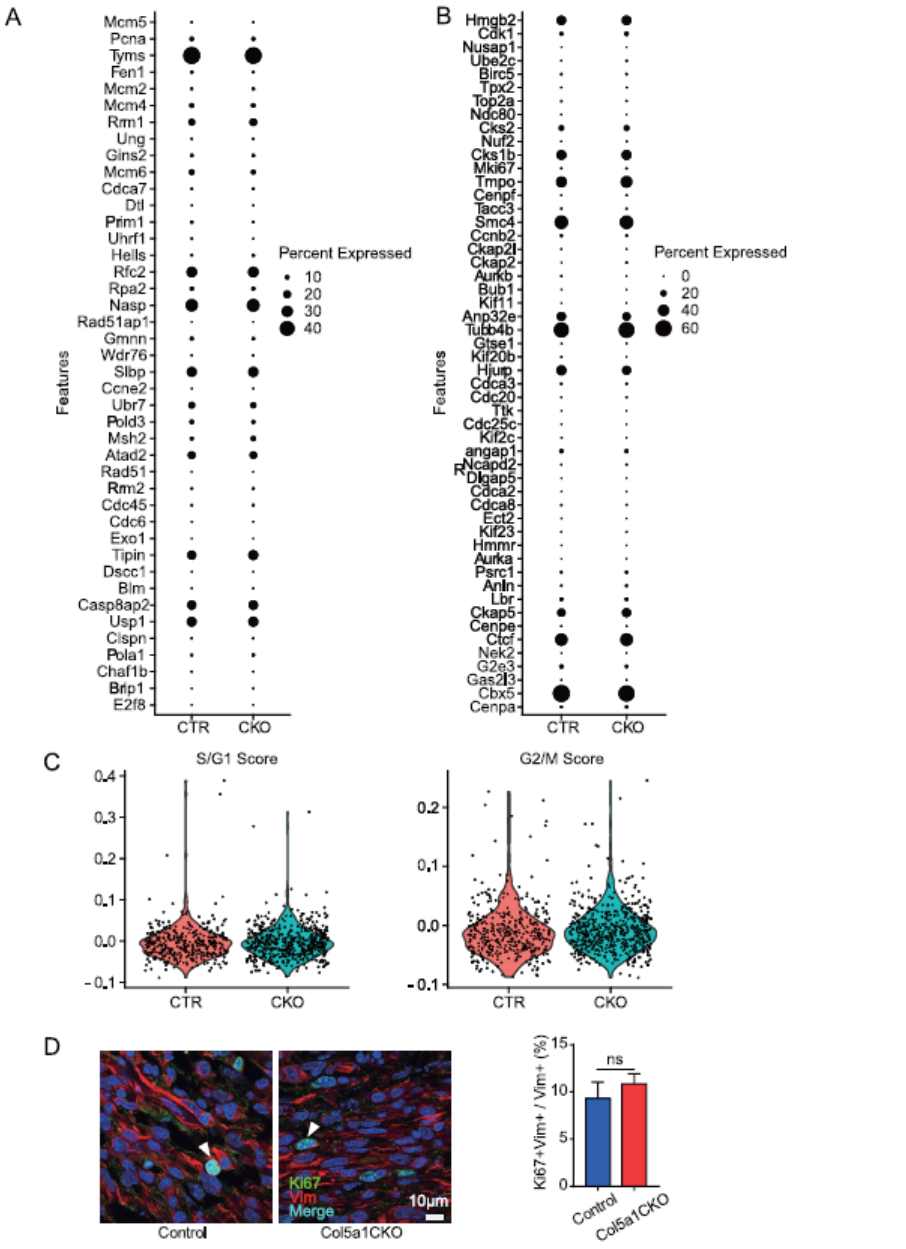

(legend on next page)

Figure S6. Myofibroblasts in Hearts of Col5a1CKO Animals Do Not Display Higher Rates of Proliferation Compared to That in Control Littermate Animals, Related to Figure 5

Cluster 0 (myofibroblast population) in both control and Col5a1 CKO animals were analyzed for expression of cell cycle genes at 7 days following injury. (A and B) Dot blot demonstrating expression of (A) cell cycle genes regulating S/G1 phase and (B) G2/M phase in both control and CKO animals (C) Violin plot demonstrating average expression of genes regulating S/G1 and G2/M phases in myofibroblasts of Col5a1 CKO and control littermates; A score denoting average expression of all cycle genes in S/G1 or G2/M was used and there were no significant differences in expression of genes between the groups. (D) Immunostaining for vimentin and Ki67 (marker of proliferation) in scar tissue of hearts of Col5a1 CKO and control animals at 7 days following injury and quantitation of the fraction of proliferating fibroblasts (Ki67+Vimentin+/Vimentin+) (mean ± S.D., ns = not significant, representative images shown, n = 6 Control n = 4 CKO)

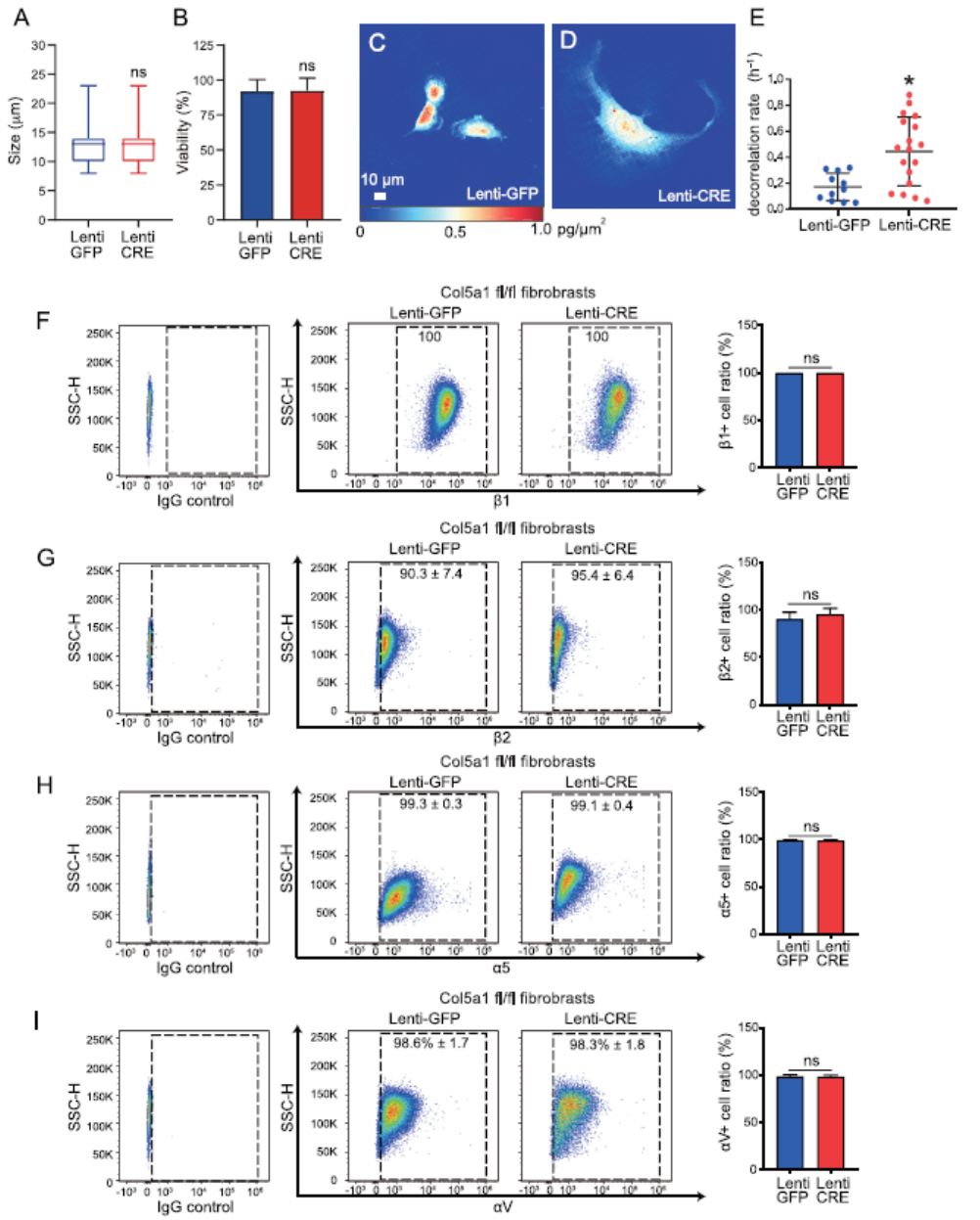

(legend on next page)

Figure S7. Cell Deformability and Decorrelation Rate of Col5a1CKO and Wild-Type Cardiac Fibroblasts, and Flow Cytometry Demonstrating Expression of Integrins on Col5a1CKO Fibroblasts Generated *Ex Vivo* by Lentiviral Transduction, Related to Figures 6 and 7

(A) Cell size (n > 600) measured right before the PMF assay. Boxplot shows the minimum and maximum with median (line) and whiskers. (B) Cell viability measured by Trypan Blue staining right before the PMF assay. (mean ± SD n = 3 independent experiments, ns: not significant). (C-E) Quantitative phase microscopy (QPM) to determine cell stiffness of Col5a1CKO cardiac fibroblasts and control cardiac fibroblasts. (C and D) Representative QPM images demonstrating heatmap of mass/density in (C) control and (D) Col5a1CKO fibroblasts and (E) decorrelation rate of control and Col5a1CKO fibroblasts (mean ± S.D., $^*p < 0.05$, n = 3 independent experiments with 11 cell clusters examined/control and 18 cell clusters/Col5a1CKO).

Col5a1fl/fl cardiac fibroblasts were infected with Cre or GFP lentivirus and then flow sorted based on GFP expression and then subjected to flow cytometry to determine expression of (F) β1 (G) β2 (H) α5 (I) αv integrins (mean ± S.D, ns = not significant, n = 3 independent experiments)

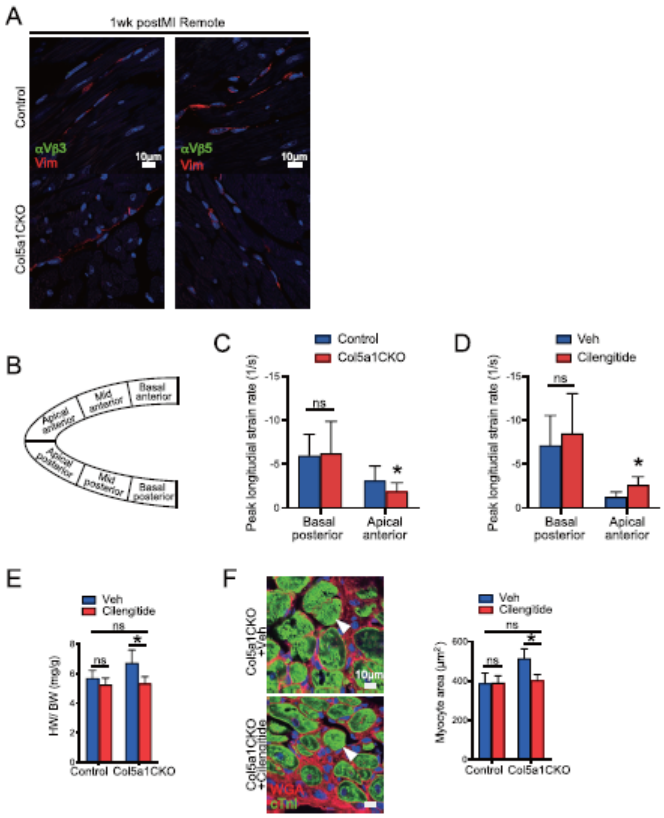

Figure S8. Effect of Cilengitide on Injured/Uninjured Myocardium and Cardiac Hypertrophy following Ischemic Cardiac Injury, Related to Figure 7

(A) Immunostaining for vimentin and αvβ3 or αvβ5 in remote tissue of Col5a1 CKO and control littermate heart at 7 days following injury (representative images). (B) A schematic of myocardial regions identified from the parasternal long axis view. (C) Peak longitudinal strain rate of basal posterior and apical anterior region from Col5a1CKO and control littermate at 7 days following injury (mean ± S.D., *p < 0.05, basal posterior; n = 18 animals/Control and 25/CKO apical anterior; n = 20 animals/Control and 22/CKO). (D) Peak longitudinal strain rate of basal posterior and apical anterior region from Col5a1CKO treated with vehicle or cilengitide at 7 days following injury (mean ± S.D., *p < 0.05, basal posterior; n = 12 animals/vehicle and 18/cilengitide. apical anterior; n = 10 animals/vehicle and 18/cilengitide, outliers in the strain imaging data were excluded after identifying them with Prism 8 (ROUT (Q = 2%)). (E) Heart weight/body weight of hearts harvested at 2 weeks following injury (mean ± S.D., *p < 0.05, n = 12 CKO animals receiving cilengitide, n = 6 CKO animals injected with vehicle, n = 9 control animals receiving cilengitide, n = 7 control animals injected with vehicle) (F) Immunostaining for cardiac troponin and WGA to determine myocyte surface area as a surrogate for hypertrophy in the border zone region of Col5a1CKO animals injected with vehicle or cilengitide (arrows, representative images, mean ± S.D., *p < 0.05, n = 10/CKO+Cilengitide, n = 6/CKO+Veh, n = 6/animals for all other groups).

Table S1, Related to Figure 1. Bulk RNA-seq of injured and uninjured hearts at various time points after ischemic cardiac injury.					
gene	remote	injured	logFC	PValue	padj
Eci1	212.485	10.5747	-4.3262	2.3E-13	1.9E-09
Hopx	137.718	4.90668	-4.8158	4E-13	1.9E-09
Coq10a	85.4086	5.20377	-4.0414	5E-13	1.9E-09
Sord	65.3544	4.87722	-3.7407	7.6E-13	2.1E-09
C3ar1	3.16885	33.7355	3.41109	1.2E-12	2.1E-09
Pxmp2	48.7392	1.54707	-4.9802	1.3E-12	2.1E-09
Pla2g5	14.1208	0.32171	-5.4446	1.7E-12	2.1E-09
Lilrb4a	7.45589	76.312	3.35256	2E-12	2.1E-09
Efnb3	22.12	0.28632	-6.262	2.4E-12	2.1E-09
Epha4	15.8721	1.31671	-3.5891	2.8E-12	2.1E-09
Arhgap20	5.69792	0.42001	-3.7712	2.8E-12	2.1E-09
Plin5	62.3632	1.83697	-5.1019	2.9E-12	2.1E-09
Slc16a3	0.73492	13.9908	4.2392	3.6E-12	2.1E-09
Nnt	96.8762	7.29169	-3.736	3.6E-12	2.1E-09
Uqcr11	544.224	63.4257	-3.1005	4.3E-12	2.1E-09
Ndufa12	133.209	18.2867	-2.8636	4.4E-12	2.1E-09
Tcap	796.169	26.3537	-4.9385	4.5E-12	2.1E-09
Ndufa5	339.506	30.495	-3.4807	4.7E-12	2.1E-09
Tcirg1	3.28181	28.4011	3.11918	5.1E-12	2.1E-09
Hadh	132.494	8.68993	-3.937	5.1E-12	2.1E-09
Tecr	116.96	14.8088	-2.9837	5.1E-12	2.1E-09
Mgst3	194.348	13.8882	-3.8161	5.7E-12	2.1E-09
0610009O20Rik	62.4813	10.4165	-2.5847	5.7E-12	2.1E-09
Gcdh	30.6936	4.00038	-2.9401	5.7E-12	2.1E-09
Ech1	614.676	31.1068	-4.2992	6E-12	2.1E-09
Fitm1	97.0067	2.6166	-5.2313	6E-12	2.1E-09
Adamts4	1.02968	20.3908	4.31557	6.2E-12	2.1E-09
Tcea3	70.8157	5.2562	-3.7522	6.3E-12	2.1E-09
Ndufs3	88.0693	11.3406	-2.9583	6.8E-12	2.1E-09
Pink1	232.258	17.5277	-3.7189	7E-12	2.1E-09
Gstk1	48.4676	3.10138	-3.9818	7.2E-12	2.1E-09
Mylk4	12.0123	0.20432	-5.8988	7.5E-12	2.1E-09
Csf2ra	2.28256	26.4183	3.53019	7.7E-12	2.1E-09
Itgb3	0.83645	9.88875	3.56389	7.8E-12	2.1E-09
Abhd18	10.1543	0.78878	-3.6927	8.1E-12	2.1E-09
Hsdl2	126.304	10.8197	-3.552	8.1E-12	2.1E-09
Ppa2	10.5046	1.75347	-2.5824	8.4E-12	2.1E-09
Dnajc28	19.6975	1.25348	-3.9743	8.4E-12	2.1E-09

Table S2, Related to Figure 4. Correlation of Col5a1 with ECM genes and Col5a1 and ECM genes with traits following isoproterenol infusion.			
probe	gene	Col5a1_bicor	Iso Col5a1 pvalue adj
ILMN_1234774	2010005H15Rik	0.294440677	0.004171698
ILMN_2683656	2300002M23Rik	0.023567252	0.822577053
ILMN_2639818	Acan	-0.019844226	0.850248691
ILMN_2645654	Acan	0.180855727	0.082765999
ILMN_3161887	Adamts15	0.032593912	0.756442651
ILMN_1227398	Agt	-0.169998965	0.103287676
ILMN_1243738	Abl1	-0.078599441	0.453921288
ILMN_2675551	Abl1	-0.040132175	0.702505671
ILMN_2742730	Abl1	-0.267783645	0.009457366
ILMN_2796842	Abl1	0.10410819	0.320658177
ILMN_1240933	Ambn	-0.200332189	0.054182927
ILMN_1226183	Antxr1	0.60274776	1.63E-10
ILMN_1229643	Antxr1	0.591077748	4.45E-10
ILMN_2759144	Col2a1	-0.084161864	0.422509566
ILMN_2759142	Col2a1	0.035669596	0.734277633
ILMN_2606039	Col11a1	-0.040706995	0.698448722
ILMN_1217703	Col11a1	-0.141365222	0.176491302
ILMN_2776931	Col11a1	-0.05249345	0.617267558
ILMN_2623644	Colec10	-0.202631179	0.051422863
ILMN_2862538	Col12a1	0.533157083	3.76E-08
ILMN_2706693	Col9a1	-0.098325727	0.348414406
ILMN_2939882	Col9a1	-0.083046934	0.428703354
ILMN_2706692	Col9a1	0.066444358	0.526864347
ILMN_1256550	Clec14a	0.093987331	0.370194975
ILMN_2683958	Col3a1	0.593583534	3.60E-10
ILMN_1258629	Col3a1	0.627965127	1.61E-11
ILMN_2884751	Cer1	0.134958447	0.197120262
ILMN_2865074	Col11a2	-0.236260663	0.022608851
ILMN_2711663	Colec12	0.185145159	0.07561398
ILMN_2613636	Col4a3bp	-0.172712496	0.097819328
ILMN_1245536	Col4a3bp	-0.1955361	0.060332789
ILMN_2902575	Col4a3bp	0.011120238	0.915746943
ILMN_1257219	Colec12	0.104403433	0.31928022
ILMN_2595260	Creb3l1	0.292162225	0.004487587
ILMN_2591027	Col14a1	0.813262976	4.07E-23
ILMN_1248099	Col16a1	0.811726321	5.70E-23
ILMN_1257585	Ddr1	-0.329677718	0.001250875
ILMN_2713898	Ddr1	-0.027380759	0.794456434

Table S3, Related to Key resources. Primer sequences for qPCR

Mouse Col1a1 primer Forward: GAAACCCGAGGTATGCTTGA
Mouse Col1a1 primer Reverse: GGGTCCCTCGACTCCTACAT
Mouse Col2a1 primer Forward: GGGAATGTCCTCTGCGATGAC
Mouse Col2a1 primer Reverse: GAAGGGGATCTCGGGGTTG
Mouse Col3a1 primer Forward: GCACAGCAGTCCAACGTAGA
Mouse Col3a1 primer Reverse: TCTCCAAATGGGATCTCTGG
Mouse Col4a1 primer Forward: CTGGCACAAAAGGGACGAG
Mouse Col4a1 primer Reverse: ACGTGGCCGAGAATTTCACC
Mouse Col5a1 primer Forward: TTCCAGGCCAAACGGTACAT
Mouse Col5a1 primer Reverse: TGAGACACTGTTACAACGATTCCT
Mouse Col5a2 primer Forward: TTGGAAACCTTCTCCATGTCAGA
Mouse Col5a2 primer Reverse: TCCCCAGTGGGTGTTATAGGA
Mouse Col5a3 primer Forward: CGGGGTACTCCTGGTCCTAC
Mouse Col5a3 primer Reverse: GCATCCCTACTTCCCCCTTG
Mouse Col6a1 primer Forward: TGGCTCACCTGAGCTCCTAT
Mouse Col6a1 primer Reverse: ACGGATAGGTTAGGGGCAGT
Mouse Col7a1 primer Forward: GCCCAGAGATAGAGTGACCTG
Mouse Col7a1 primer Reverse: CGCACTTCTCGAAAGTTGCTG
Mouse Col8a1 primer Forward: ACTCTGTCAGACTCATTCAGGC
Mouse Col8a1 primer Reverse: CAAAGGCATGTGAGGGACTTG
Mouse Col9a1 primer Forward: CGACCGACCAGCACATCAA
Mouse Col9a1 primer Reverse: AGGGGGACCCTTAATGCCT

Mouse Col10a1 primer Forward: TTCTGCTGCTAATGTTCTTGACC
Mouse Col10a1 primer Reverse: GGGATGAAGTATTGTGTCTTGGG
Mouse Col11a1 primer Forward: ACAAAACCCCTCGATAGAAGTGA
Mouse Col11a1 primer Reverse: CTCAGGTGCATACTCATCAATGT
Mouse Col12a1 primer Forward: AAGTTGACCCACCTTCCGAC
Mouse Col12a1 primer Reverse: GGTCCACTGTTATTCTGTAACCC
Mouse Col13a1 primer Forward: GGAGCACCTGGACTAGACG
Mouse Col13a1 primer Reverse: GCCTTGGACTGGTAAGCCAT
Mouse Col14a1 primer Forward: TTTGGCGGCTGCTTGTTTC
Mouse Col14a1 primer Reverse: CGCTTTTGTTGCAGTGTTCTG
Mouse Col15a1 primer Forward: CCCAGGGAAGAATGGAGAAGT
Mouse Col15a1 primer Reverse: CCAGAGCCTTCAATCTCAAATCC
Mouse Col16a1 primer Forward: GAGAGCGAGGATACACTGGC
Mouse Col16a1 primer Reverse: CTGGCCTTGAAATCCCTGG
Mouse Col17a1 primer Forward: GAAAGGAGACAAAGGTGACCA
Mouse Col17a1 primer Reverse: CGGCTTGATGGCAATACTTC
Mouse Col18a1 primer Forward: GGGGAAAGGATTCTTGCCTATG
Mouse Col18a1 primer Reverse: GAAGGAACAGAGAGTAAACCGTG
Mouse Col19a1 primer Forward: GGCTCTTGGAAATTGTGGACC
Mouse Col19a1 primer Reverse: AGCACACTTCCCAACTTGAAA
Mouse Col20a1 primer Forward: AGCCGACTCATTTGCCAAAAA
Mouse Col20a1 primer Reverse: GGGTGGGTATAAGGCTGGAG
Mouse Col22a1 primer Forward: GGGGAACCTGGATACGCTAAA

Mouse Col22a1 primer Reverse: CAAAGTACGCACACTGGGAG
Mouse Col23a1 primer Forward: CCCCATCTGAGTGCATCTGTC
Mouse Col23a1 primer Reverse: CTTGCCGTCCAGACCTAGAG
Mouse Col24a1 primer Forward: TTCACTGTCTAAACACCCCAAGG
Mouse Col24a1 primer Reverse: CCATCCTGAATCTTGCAGTCAT
Mouse Col25a1 primer Forward: TTCCATCCGCTGTCTGACAC
Mouse Col25a1 primer Reverse: CCTGGCCGTTCTTATTTTAGCC
Mouse Col26a1 primer Forward: GCCATCACACGGTGACAAG
Mouse Col26a1 primer Reverse: GAGTCCTGTAACTCACGAGGT
Mouse Col27a1 primer Forward: CCTTCCCGTAGGGACTCCAT
Mouse Col27a1 primer Reverse: GGCACAGTAATTGTGAGCGAC
Mouse Col28a1 primer Forward: AGCAGCGGGTCAAGTCTCT
Mouse Col28a1 primer Reverse: ACGCCATCTTTACGCCCTTC
Mouse Acta2 primer Forward: CCTTCGTGACTACTGCCGAG
Mouse Acta2 primer Reverse: ATAGGTGGTTTCGTGGATGC
Mouse Postn primer Forward: CGAATCATTACAGACACACCTGC
Mouse Postn primer Reverse: ACGGCCTTCTCTTGATCGTC
Mouse Pai1 primer Forward: CCGATGGGCTCGAGTATGAC
Mouse Pai1 primer Reverse: TTCTCAAAGGGTGCAGCGAT
Mouse Myh11 primer Forward: AAGCTGCGGCTAGAGGTCA
Mouse Myh11 primer Reverse: CCCTCCCTTTGATGGCTGAG
Mouse Des primer Forward: GTGGATGCAGCCACTCTAGC
Mouse Des primer Reverse: TTAGCCGCGATGGTCTCATAC

Mouse Cnn2 primer Forward: AGGAAGCAGAACTCCGAAGC
Mouse Cnn2 primer Reverse: CCAGTTCTGCATAGAGCGGT
Mouse Gapdh primer Forward: ACAACTTTGGCATTGTGGAA
Mouse Gapdh primer Reverse: GATGCAGGGATGATGTTCTG

Appendix III. Pressure-Driven Mitochondrial Transfer Pipeline Generates Mammalian Cells of Desired Genetic Combinations and Fates

Cell Reports

Resource

Pressure-Driven Mitochondrial Transfer Pipeline Generates Mammalian Cells of Desired Genetic Combinations and Fates

Graphical Abstract

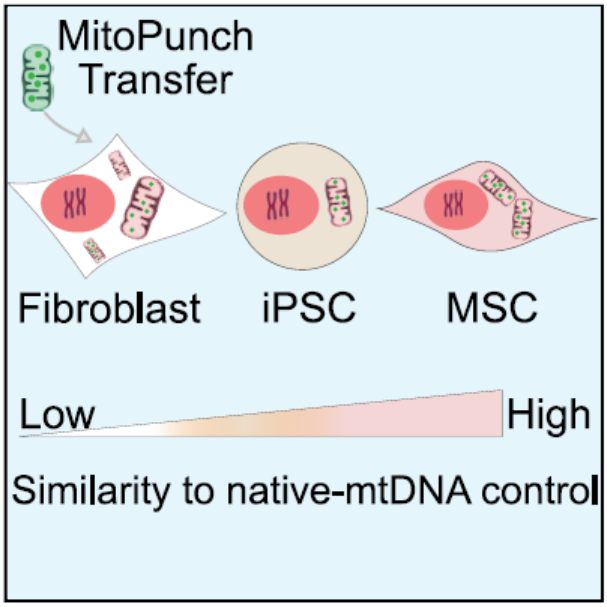

Authors

Alexander N. Patananan, Alexander J. Sercel, Ting-Hsiang Wu, ..., Kayvan R. Niazi, Pei-Yu Chiou, Michael A. Teitell

Correspondence

mteitell@mednet.ucla.edu

In Brief

Patananan and colleagues demonstrate a pipeline for transferring isolated mitochondria into mtDNA-deficient recipient cells. mtDNA-depleted fibroblasts permanently retain acquired non-native mtDNA through cell fate transitions. Initially, mitochondrial recipients show mtDNA-deficient cell transcriptome and metabolome profiles, with improvement to control profiles by reprogramming to pluripotency and subsequent differentiation.

Highlights

- We report a "proof-of-principle" mitochondrial transfer pipeline by MitoPunch
- MitoPunch generates cells with unique mtDNA-nDNA pairs, regardless of cell source
- Replacement mtDNA in non-immortal cells remains stable with cell fate conversions
- Enables studies of mtDNA-nDNA interactions with reprogramming and differentiation

Patananan et al., 2020, Cell Reports *33*, 108562
December 29, 2020
https://doi.org/10.1016/j.celrep.2020.108562

CellPress

Cell Reports

CellPress
OPEN ACCESS

Resource

Pressure-Driven Mitochondrial Transfer Pipeline Generates Mammalian Cells of Desired Genetic Combinations and Fates

Alexander N. Patananan,[1,16] Alexander J. Sercel,[2,16] Ting-Hsiang Wu,[3,16] Fasih M. Ahsan,[1] Alejandro Torres, Jr.,[1] Stephanie A.L. Kennedy,[1] Amy Vandiver,[4] Amanda J. Collier,[5,6,7] Artin Mehrabi,[3] Jon Van Lew,[3] Lise Zakin,[8] Noe Rodriguez,[8] Marcos Sixto,[8] Wael Tadros,[8] Adam Lazar,[8] Peter A. Sieling,[8] Thang L. Nguyen,[9] Emma R. Dawson,[1] Daniel Braas,[10] Justin Golovato,[11] Luis Cisneros,[11] Charles Vaske,[11] Kathrin Plath,[5,6,7] Shahrooz Rabizadeh,[3,8] Kayvan R. Niazi,[3,8] Pei-Yu Chiou,[9,12,13] and Michael A. Teitell[1,6,7,13,14,15,17,*]

[1]Department of Pathology and Laboratory Medicine, David Geffen School of Medicine, University of California, Los Angeles, Los Angeles, CA 90095, USA
[2]Molecular Biology Interdepartmental Program, University of California, Los Angeles, Los Angeles, CA 90095, USA
[3]NanoCav LLC, Culver City, CA 90232, USA
[4]Division of Dermatology, University of California, Los Angeles, Los Angeles, CA 90095, USA
[5]Department of Biological Chemistry, University of California, Los Angeles, Los Angeles, CA 90095, USA
[6]Molecular Biology Institute, University of California, Los Angeles, Los Angeles, CA 90095, USA
[7]Eli and Edythe Broad Center of Regenerative Medicine and Stem Cell Research, University of California, Los Angeles, Los Angeles, CA 90095, USA
[8]NantWorks, LLC, Culver City, CA 90232, USA
[9]Department of Bioengineering, University of California, Los Angeles, Los Angeles, CA 90095, USA
[10]UCLA Metabolomics Center, University of California, Los Angeles, Los Angeles, CA 90095, USA
[11]NantOmics, LLC, Culver City, CA 90232, USA
[12]Department of Mechanical and Aerospace Engineering, University of California, Los Angeles, Los Angeles, CA 90095, USA
[13]California NanoSystems Institute, University of California, Los Angeles, Los Angeles, CA 90095, USA
[14]Department of Pediatrics, David Geffen School of Medicine, University of California, Los Angeles, Los Angeles, CA 90095, USA
[15]Jonsson Comprehensive Cancer Center, David Geffen School of Medicine, University of California, Los Angeles, Los Angeles, CA 90095, USA
[16]These authors contributed equally
[17]Lead Contact
*Correspondence: mteitell@mednet.ucla.edu
https://doi.org/10.1016/j.celrep.2020.108562

SUMMARY

Generating mammalian cells with desired mitochondrial DNA (mtDNA) sequences is enabling for studies of mitochondria, disease modeling, and potential regenerative therapies. MitoPunch, a high-throughput mitochondrial transfer device, produces cells with specific mtDNA-nuclear DNA (nDNA) combinations by transferring isolated mitochondria from mouse or human cells into primary or immortal mtDNA-deficient (ρ0) cells. Stable isolated mitochondrial recipient (SIMR) cells isolated in restrictive media permanently retain donor mtDNA and reacquire respiration. However, SIMR fibroblasts maintain a ρ0-like cell metabolome and transcriptome despite growth in restrictive media. We reprogrammed non-immortal SIMR fibroblasts into induced pluripotent stem cells (iPSCs) with subsequent differentiation into diverse functional cell types, including mesenchymal stem cells (MSCs), adipocytes, osteoblasts, and chondrocytes. Remarkably, after reprogramming and differentiation, SIMR fibroblasts molecularly and phenotypically resemble unmanipulated control fibroblasts carried through the same protocol. Thus, our MitoPunch "pipeline" enables the production of SIMR cells with unique mtDNA-nDNA combinations for additional studies and applications in multiple cell types.

INTRODUCTION

Mammalian mitochondria are cellular power plants with additional roles in apoptosis, reactive oxygen species (ROS) and Fe-S cluster generation, Ca^{2+} regulation, and metabolite production (Patananan et al., 2018). Each mitochondrion contains >1,100 nucleus-encoded and imported proteins (Calvo et al., 2016) with numerous copies of a circular ~16.5-kilobase pair (kbp) mitochondrial genome (mtDNA) encoding 13 proteins required for electron transport chain (ETC) activity and

respiration. As many as 1:5,000 people have mtDNA mutations that impair high-energy-demand tissues and contribute to debilitating diseases, including cancer, diabetes, and metabolic syndromes (Schaefer et al., 2004). In addition, cells may contain a mixture of different mtDNA sequences, a situation termed heteroplasmy, with up to 1 in 8 asymptomatic individuals carrying an unsuspected pathogenic mtDNA mutation (Elliott et al., 2008; Rebolledo-Jaramillo et al., 2014). Thus, an ability to controllably manipulate mtDNA sequences could enable studies of mitochondria and potentially develop disease models or therapies for mtDNA disorders.

In human reproduction, several types of mitochondrial replacement strategies were developed to exchange pathogenic mtDNA in a zygote with non-detrimental mtDNA from a healthy donor oocyte. These approaches have potential for preventing transmission of mtDNA disorders from carrier mothers to their children (Wolf et al., 2015; Wolf et al., 2019). However, *in vitro* methods to change mtDNA sequences within somatic cells and tissues remain limited (Patananan et al., 2016). Cell fusions that produce "cybrids" permanently retain donor mitochondria (Wong et al., 2017), although fusion partners are typically transformed cells that cannot be reprogrammed. Also, endonucleases imported into mitochondria can shift heteroplasmy ratios to alter mitochondria and cell functions by targeting specific sequences for destruction. However, these endonucleases are laborious to produce, are limited to certain mtDNA sequences, are inefficient, and do not yield homoplasmy (Campbell et al., 2018; Yahata et al., 2017; Yang et al., 2018). Of note, a recent and exciting development using a bacterial cytidine deaminase, DddA, to edit mtDNA single-base sequences is tempered by low efficiency and an undesirable off-target rate (Mok et al., 2020).

Several methods transfer isolated mitochondria into mtDNA-deficient cells, known as ρ0 (rho null) cells, to restore respiration (Kim et al., 2018; Nzigou Mombo et al., 2017). In addition, some studies reported endoyctosis of mitochondria by mammalian cells (Clark and Shay, 1982; Kesner et al., 2016). However, these studies were not concerned with rescuing ρ0 cells and generating stable isolated mitochondrial recipient (SIMR) clones that permanently retain donor mtDNA (Kesner et al., 2016; Kitani et al., 2014; Sun et al., 2019). A recent study did produce a limited number of SIMR clones by coincubating high concentrations of isolated HEK293T donor mitochondria with ρ0 osteosarcoma cells (Patel et al., 2017). We (Dawson et al., 2020) and others (Ali Pour et al., 2020) have recently reported similar findings in which cells are capable of endocytosing exogenous mitochondria and even altering metabolic functions for a limited period of time (~1 week), but these exogenous mtDNAs are lost over time. To address this problem, we previously developed a photothermal nanoblade to stably transfer small quantities of isolated mitochondria into ρ0 osteosarcoma cells (Wu et al., 2016). Unfortunately, the nanoblade is laborious and low throughput, and two of three SIMR clones reported did not reset the ρ0 cell metabolome. A technique that generates many non-transformed stable clones is desirable to examine novel mtDNA-nuclear DNA (nDNA) combinations through reprogramming to pluripotency and differentiation into multiple cell types.

Here, we describe a simple-to-use mitochondrial transfer technique called "MitoPunch" to rapidly generate numerous non-transformed SIMR clones. We apply MitoPunch to implement a pipeline that demonstrates donor mtDNA functions in recipient host primary cells at different cell fates. Our study establishes this resource pipeline to generate primary SIMR cells using non-immortalized materials. We also measure the status of the metabolome, transcriptome, and biophysical properties of SIMR cells with defined mtDNA-nDNA combinations to guide future studies generating somatic cells with desired mtDNA-nDNA combinations.

RESULTS

MitoPunch Generates SIMR Cells with a Range of Cell Types and mtDNAs

MitoPunch is a massively parallel, pressure-driven, large cargo transfer platform based on prior photothermal nanoblade and biophotonic laser-assisted cell surgery tool (BLAST) technologies (Sercel et al., 2020; Wu et al., 2016; Wu et al., 2015). MitoPunch uses a mechanical plunger to physically deform a pliable polydimethylsiloxane (PDMS) reservoir containing isolated mitochondria suspended in phosphate-buffered saline (1× PBS [pH 7.4]) (Figure 1A). Plunger activation propels the suspended cargo within the PDMS delivery chamber through a porous membrane containing numerous 3-μm-diameter holes on which a confluent layer of adherent cells is grown. This action directly forces isolated mitochondria into the cytosol of recipient cells.

To demonstrate MitoPunch generation of SIMR cells, we transferred isolated mitochondria from ~1.5 × 10^7 HEK293T cells into ~2 × 10^5 143BTK− ρ0 osteosarcoma cells. Post-transfer, we select for and isolate SIMR colony clones with permanently retained donor mtDNA using uridine-deficient media. This selection is enabling because respiration-defective ρ0 cells have inactive dihydroorate dehydrogenase and depend on exogenous uridine or restored respiration for pyrimidine biosynthesis (Grégoire et al., 1984). Compared to the coincubation of the same amount of isolated mitochondria with cells (Clark and Shay, 1982; Kesner et al., 2016), only 143BTK− ρ0 cells with HEK293T mitochondria from MitoPunch transfer (143BTK− ρ0+HEK293T) permanently retained donor mtDNA and survived uridine-deficient media selection (Figure 1B). In a representative set of mitochondrial transfer experiments, MitoPunch generated ~75 independent crystal-violet-stained SIMR clones in comparison to no clones obtained by coincubation (Figure 1B).

We next examined whether MitoPunch could generate SIMR clones with defined mtDNA-nDNA pairs that transfer features of mitochondrial disease. We isolated mitochondria from cybrid cells containing either an A3243G mtDNA substitution commonly associated with mitochondrial encephalopathy, lactic acidosis, and stroke-like episodes (MELAS) or wild-type (WT), non-mutant mtDNA from the same individual (Picard et al., 2014). The A3243G point mutation is in the $tRNA^{LEU}$ gene and results in altered production and assembly of ETC complexes with impaired oxidative phosphorylation (Chomyn et al., 1992; Sasarman et al., 2008). Following MitoPunch into 143BTK− ρ0 recipients and 2 weeks of selection, two of several dozen independent SIMR clones that permanently retained MELAS (143BTK− ρ0+MELAS) or WT (143BTK− ρ0+WT) mtDNA were tested for oxygen consumption rate (OCR) using the Seahorse

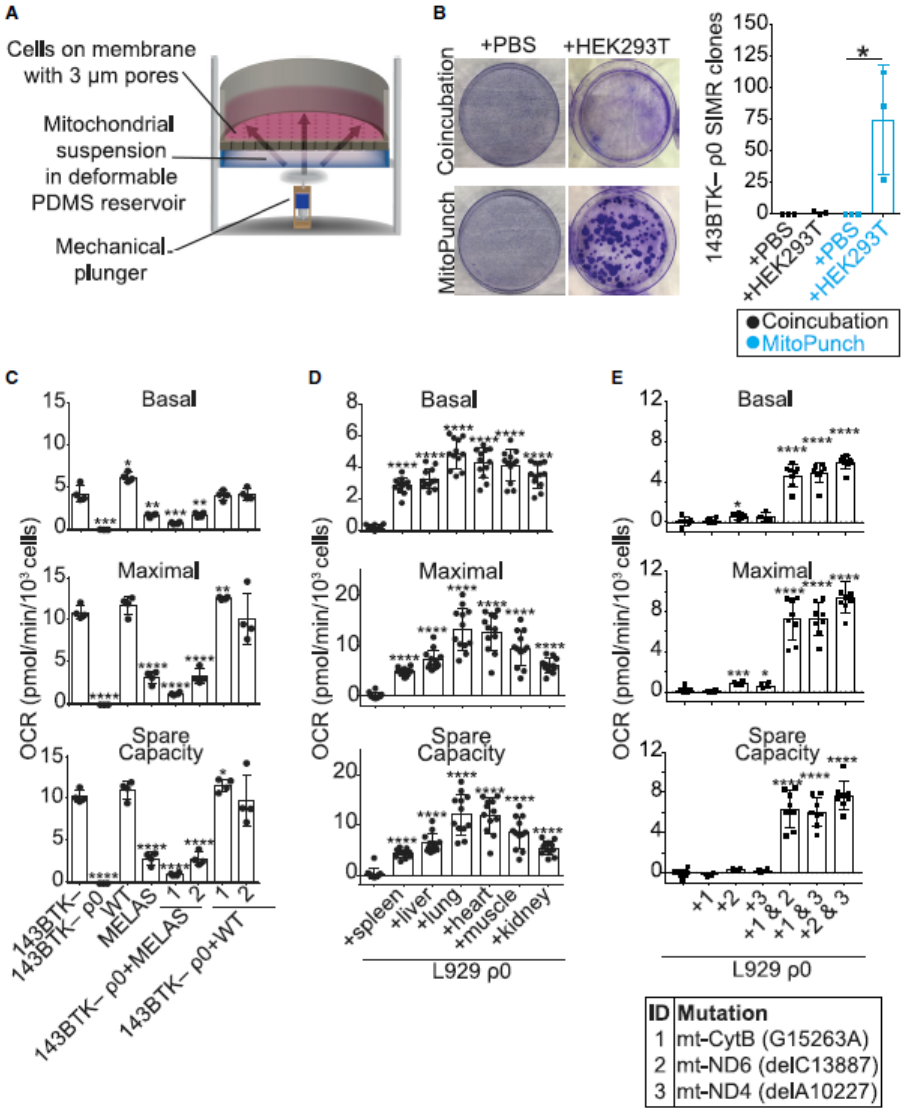

Figure 1. MitoPunch Is a Versatile Mitochondrial Transfer Technology

(A) Schematic representation of the MitoPunch mitochondrial transfer platform.

(B) Images of crystal-violet-stained SIMR colonies from coincubation or MitoPunch delivery of either 1× PBS (pH 7.4) (sham control) or isolated HEK293T cell mitochondria into 143BTK– ρ0 osteosarcoma cells after selection in uridine-depleted medium. Data are the means ± SD of three technical replicates.

(C) OCR measurements for ~1.5 × 10^4 143BTK–, 143BTK– ρ0, WT cybrid, MELAS cybrid, 143BTK– ρ0+MELAS SIMR, and 143BTK– ρ0+WT SIMR cells by Seahorse XF96 Extracellular Flux Analyzer. Values were calculated by standard procedures (see STAR Methods). Data are the means ± SD of four technical replicates.

(legend continued on next page)

Extracellular Flux Analyzer. Results showed 143BTK− ρ0+MELAS clones had significantly impaired basal respiration, maximal respiration, and spare respiratory capacity compared to patient-matched 143BTK− ρ0+WT and native 143BTK− control cells (Figure 1C), indicating stable mtDNA transfer of the primary metabolic deficit of the MELAS phenotype.

We then expanded mitochondrial donor and recipient cell pairings beyond these initial studies to demonstrate the versatility of MitoPunch. As examples, mitochondria were isolated from harvested C57BL/6 mouse tissues and MitoPunch transferred into C3H/An-derived L929 ρ0 immortalized fibroblasts. Two weeks of selection yielded dozens of SIMR clones from each mitochondrial source. SIMR clones generated with high-energy-demand heart, lung, or muscle-derived mitochondria showed the most robust respiratory profiles, in contrast to SIMR clones that received low-energy-demand spleen- or kidney-derived mitochondria (Figure 1D). We also evaluated MitoPunch delivery of heteroplasmic mtDNA mixtures into cells. Mitochondria isolated from mouse cybrid lines containing mtDNA mutations in the cytochrome B (*mt-Cytb*), NADH dehydrogenase subunit 4 (*mt-nd4*), and NADH dehydrogenase subunit 6 (*mt-nd6*) genes were MitoPunch transferred individually or in 1:1 mixtures by protein content into L929 ρ0 fibroblasts. SIMR cells with a single source of mutant mtDNA continued to show severe respiratory impairments (Figure 1E). In contrast, SIMR cells with a mixture of non-overlapping mutant mtDNAs showed markedly improved respiratory profiles, strongly suggesting that both mtDNAs were stably maintained (Figure 1E). Thus, MitoPunch and selection is a versatile approach for generating human or mouse SIMR cells with desired mtDNA-nDNA pairs. Co-transfer of multiple mtDNA types into the same recipient cell also provides a simple method to examine complementation for mutant mtDNA mixtures.

MitoPunch Generates Non-Transformed, Non-Malignant SIMR Cells

To obtain SIMR cells with mtDNA-nDNA combinations using non-immortalized recipient cells, we established a human fibroblast mitochondrial recipient pipeline. Hayflick-limited BJ foreskin (BJ) fibroblasts, neonatal dermal fibroblasts (NDFs), and adult dermal fibroblasts (ADFs) were treated for 3 weeks with FDA-approved 2′,3′-dideoxycytidine (ddC) (Nelson et al., 1997) to deplete endogenous mtDNA. Primary ρ0 human fibroblasts had undetectable mtDNA (Figures S1A and S1B) and cellular respiration (Figures S1C and S1D) by qPCR and Seahorse assay, respectively. Because ddC could cause nDNA alterations, we examined BJ ρ0 fibroblasts by whole-genome sequencing and identified only a few non-synonymous mutations at 0.6 mutations per megabase, on average, with no chromosomal breaks and no changes in DNA copy number (Table S1).

Subsequently, mitochondria isolated from a human peripheral blood mononuclear cell lot (PBMC1) were transferred into fresh ρ0 fibroblasts, followed by an empirical and reproducible selection protocol with uridine-deficient galactose medium. From 5–10 BJ fibroblasts, NDFs, or ADFs, ρ0+PBMC1 SIMR clones were isolated that showed the correct mtDNA-nDNA sequence pairs and human leukocyte antigen (HLA) recipient cell haplotypes (Figures 2A–2C). Primary, non-immortal SIMR clones were also obtained from independent PBMC2 and HEK293T cell mitochondrial transfers. We observed variable efficiencies for HEK293T cell and the PBMC2 mitochondrial transfers, whereas ADFs ρ0+PBMC2 did not yield clones (Figure S1E). Analysis of the bulk culture representing 23 BJ ρ0+HEK293T SIMR clones confirmed the correct mtDNA-nDNA pairing and HLA haplotype (Figures S1F and S1G).

We examined the respiratory function of BJ ρ0+PBMC1 and BJ ρ0+HEK293T SIMR fibroblasts by Seahorse assay, which showed statistically improved basal and maximal respiration and spare respiratory capacity for both SIMR cell types compared to BJ ρ0 fibroblasts, albeit remaining lower than levels for control BJ fibroblasts (Figures 2D and S1H). Immunofluorescence (IF) microscopy showed BJ ρ0 fibroblasts with a fragmented mitochondrial network morphology lacking mtDNA-containing nucleoids, as observed previously for ρ0 cells (Kukat et al., 2008) (Figure 2E). In contrast, native BJ fibroblasts showed a reticular mitochondrial network with dozens of nucleoids per cell (Figure 2E). By IF nucleoid speckle numbers, both BJ ρ0+PBMC1 and BJ ρ0+HEK293T SIMR cells appeared to restore mtDNA content to levels equivalent to or exceeding that of native BJ fibroblasts (Figures 2E and S1I). SIMR cell mitochondria showed a reticular mitochondrial network morphology similar to that of native BJ fibroblasts, although with denser and more swollen mitochondria (Figures 2E and S1I). Despite SIMR fibroblasts permanently retaining donor mtDNA, OCR and IF suggest that assimilation of transferred mtDNA results in cells with features in between those of BJ ρ0 and native BJ fibroblasts.

SIMR Fibroblasts Are Reprogrammable

We reprogrammed BJ ρ0+PBMC1 and BJ ρ0+HEK293T SIMR fibroblasts along with native BJ fibroblasts using *OCT4*, *SOX2*, *KLF4*, *cMYC*, *NANOG*, and *LIN28* RNAs and quantified for TRA-1-60$^+$ staining clones. In two independent experiments, native BJ fibroblasts yielded an average of 136 reprogrammed TRA-1-60$^+$ clones (0.068% efficiency), compared to 21 (0.011%) and three (0.0015%) clones for BJ ρ0+PBMC1 and BJ ρ0+HEK293T cells, respectively (Figures 3A and S1J). Three unique reprogrammed clones of BJ ρ0+PBMC1-iPSCs (1, 2, and 11) and BJ ρ0+HEK293T-iPSCs (1, 2, and 4) were tested for pluripotency biomarkers and stained positive for OCT3/4 and SOX2 transcription factors by flow cytometry, as did BJ-induced pluripotency stem cell (iPSC) control, but not native BJ fibroblasts, as expected (Figures 3B and S1K). Conversely, the differentiated cell biomarker CD44 (Quintanilla et al., 2014) was negative in all reprogrammed BJ ρ0+PBMC1-iPSC, BJ ρ0+HEK293T-iPSC, and control BJ-iPSC clones and immunostained only the native BJ fibroblasts

(D) OCR measurements for ~1.5 × 10^4 L929 ρ0 and L929 ρ0 SIMR cells generated with mitochondria from C57BL/6 mouse tissues. Data are the means ± SD of 12 technical replicates (L929 ρ0 cells had four technical replicates).
(E) OCR measurements for ~1.5 × 10^4 L929 ρ0 and L929 ρ0 SIMR cells generated by transferring isolated mitochondria alone or in combinations from mouse cybrids with non-overlapping mtDNA mutations (Mito 1, Mito 2, and Mito 3). Data are the means ± SD of eight technical replicates.
Statistical significance for (B)–(E) by unpaired, two-tailed Student's t test. *p ≤ 0.05; **p ≤ 0.01; ***p ≤ 0.001; ****p ≤ 0.0001. See also Figure S1.

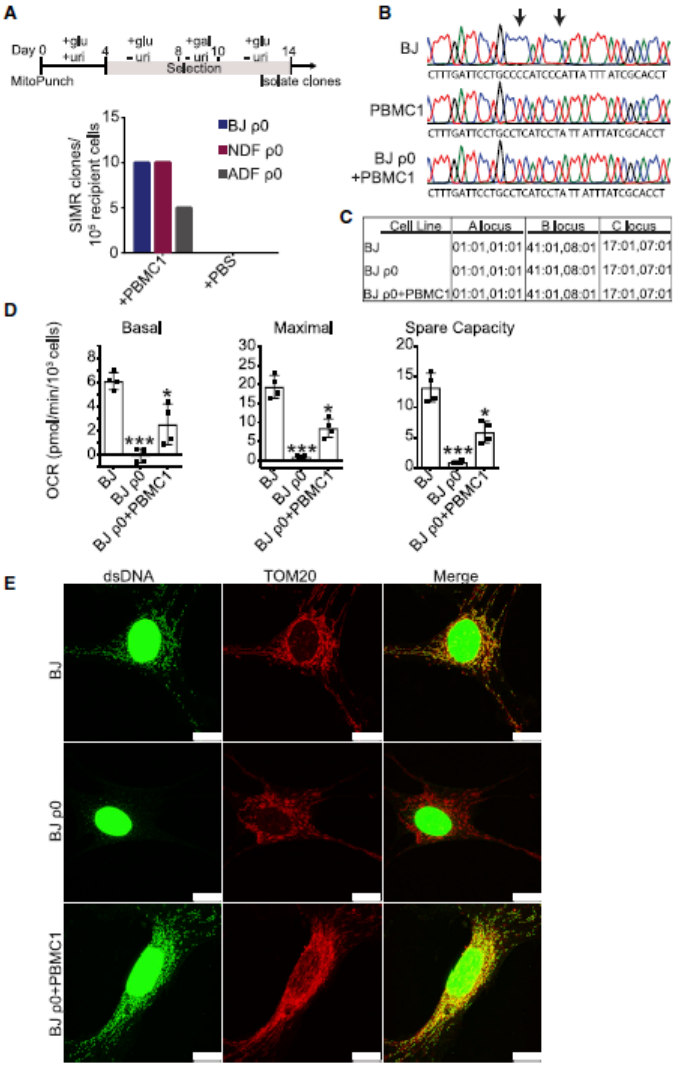

Figure 2. Generation of SIMR Fibroblasts

(A) Selection workflow (in days) for generating SIMR cells from ρ0 primary human fibroblasts and SIMR clone generation efficiency data. Mitochondria from ~3 × 10^7 peripheral blood mononuclear cells (PBMC1) were MitoPunch transferred into BJ ρ0, NDF ρ0, or ADF ρ0 recipient fibroblasts. After selection, SIMR colonies were stained with crystal violet and quantified. Clone counts from a single representative mitochondrial transfer into ~1 × 10^5 recipient ρ0 fibroblasts are indicated.

(B) D-loop hypervariable region mtDNA sequences from native BJ, PBMC1, and BJ ρ0+PBMC1 SIMR fibroblasts. Arrows denote single-nucleotide polymorphisms.

(C) Major histocompatibility complex (MHC) class I HLA A, B, and C locus genotyping using One Lambda Type v.1.3.1 for native BJ, BJ ρ0, and BJ ρ0+PBMC1 SIMR fibroblasts.

(D) OCR measurements for ~1.5 × 10^4 native BJ, BJ ρ0, and BJ ρ0+PBMC1 SIMR fibroblasts by the Seahorse XF96 Extracellular Flux Analyzer. Values were calculated by standard procedures (see STAR Methods). Data are the means ± SD of four technical replicates. Statistical significance by unpaired, two-tailed Student's t test. *$p \leq 0.05$; ***$p \leq 0.001$

(E) Representative images of native BJ, BJ ρ0, and BJ ρ0+PBMC1 SIMR fibroblasts immunostained for double-stranded DNA (dsDNA) (green) and TOM20 (red) with colocalization indicated (yellow). Images (100×) were acquired on a Leica SP8 confocal microscope. Scale bars, 15 μm.

See also Figure S1 and Table S1.

(Figures 3B and S1K). BJ-iPSC and all SIMR-iPSC reprogrammed clones were also SSEA-4$^+$ (Abujarour et al., 2013) and OCT4$^+$ by IF (Figures 3C and S1L). Seahorse assays of BJ ρ0+PBMC1-iPSC and BJ ρ0+HEK293T-iPSC clones showed minimal or no statistical differences in basal respiration, maximal respiration, and spare respiratory capacity compared to the native BJ-iPSC control (Figures 3D and S1M). Thus, SIMR fibroblast reprogramming generated iPSCs with donor mtDNA.

Other studies have shown iPSC reprogramming of fibroblasts from individuals with pathogenic mtDNA mutations (Cherry et al., 2013; Folmes et al., 2013; Hämäläinen et al., 2013; Kang et al., 2016; Kodaira et al., 2015; Ma et al., 2015; Matsubara et al., 2018; Pek et al., 2019; Perales-Clemente et al., 2016; Russell et al., 2018; Yang et al., 2018), but this has not been attempted for SIMR fibroblasts with donated, non-native mutant mtDNA. Therefore, mitochondria containing an A3243G MELAS mtDNA mutation or WT mtDNA were isolated, followed by MitoPunch transfer into BJ ρ0 fibroblasts and selection. BJ ρ0+MELAS SIMR fibroblasts showed impaired proliferation during reprogramming and did not yield iPSCs (data not shown). Therefore, we switched to NDF ρ0 recipient fibroblasts and generated SIMR fibroblasts using isolated MELAS (NDF ρ0+MELAS), WT (NDF ρ0+WT), or NDF (NDF ρ0+NDF) mitochondria. Seahorse assays showed that NDF ρ0+MELAS fibroblasts had a significant reduction in basal respiration, maximal respiration, and spare respiratory capacity compared to native NDF, NDF ρ0+NDF, and NDF ρ0+WT

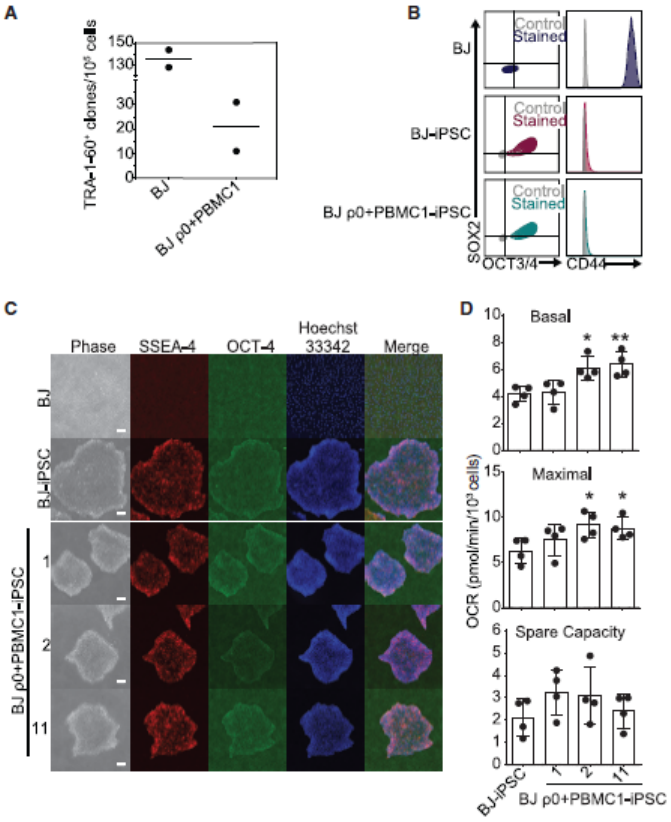

Figure 3. SIMR Fibroblasts Can Be Reprogrammed

(A) Native BJ and SIMR fibroblasts reprogrammed to iPSCs with TRA-1-60+ clones counted by microscopy. Data are the means of biological duplicates. Data for BJ fibroblast control are the same data as in Figure S3A.

(B) Flow cytometry of pluripotency biomarkers SOX2 and OCT3/4, and fibroblast biomarker CD44. Immunostained samples are shown in color with isotype negative controls in gray. Representative data for native BJ fibroblasts and BJ-iPSCs, and for BJ ρ0+PBMC1-iPSC cells. Data for the native BJ fibroblasts and BJ-iPSCs shown here are the same as in Figure S3B.

(C) Representative phase contrast and IF microscopy images of native BJ fibroblast (negative control), BJ-iPSC (positive control), and three BJ ρ0+PBMC1-iPSC clones immunostained for pluripotency biomarkers SSEA-4 and OCT4. Scale bars, 100 μm.

(D) OCR measurements for ~1.5 × 10^4 native BJ-iPSCs and BJ ρ0+PBMC1-iPSC clones 1, 2, and 11. Data for BJ-iPSC control are the same as in Figure S3D. Data are the means ± SD of four technical replicates. Statistical significance by unpaired, two-tailed Student's t test. *$p \leq 0.05$; **$p \leq 0.01$

See also Figure S1 and Table S2.

fibroblasts (Figure S1N). Restriction fragment length polymorphism (RFLP) PCR analyses confirmed the generation of homoplasmic NDF ρ0+MELAS SIMR fibroblasts (Figure S1O). We also generated ~25%–50% heteroplasmic NDF ρ0+MELAS/WT fibroblasts, which was verified by RFLP analyses (Figure S1O). Homoplasmic NDF ρ0+MELAS fibroblasts underwent RNA-based reprogramming as described earlier, but all developing iPSC clones spontaneously differentiated (Figure S1P). Reprogramming of NDF ρ0+MELAS/WT heteroplasmic fibroblasts (Figures S1O) yielded 20 iPSC clones, but all clones retained only WT mtDNA by RFLP analysis (Figures S1P and S1Q). To examine whether the reprogramming method influenced mutant mtDNA SIMR-iPSC generation, NDF ρ0+MELAS fibroblasts underwent integrating DNA, lentiviral, and Sendai virus reprogramming strategies. In all cases, NDF ρ0+MELAS cells spontaneously differentiated despite early signs of reprogramming (Table S2). In addition, no NDF ρ0+MELAS-iPSCs were obtained when reprogramming was performed with additional uridine supplementation, antioxidant N-acetylcysteine, a Rho-associated protein kinase (ROCK) inhibitor, or low oxygen tension (data not shown). Similar results were also obtained with all four reprogramming strategies for NDF ρ0 SIMR fibroblasts containing additional mtDNA mutations including a cytochrome B deletion, a Kearns-Sayre common deletion, and A8344G or T8993G mtDNA substitutions (Table S2). Thus, SIMR fibroblasts readily maintain a large variety of mtDNA sequences, in contrast to SIMR-iPSCs, which can be generated only with non-detrimental mtDNA sequences. Further biochemical investigations are needed to determine how mtDNA sequences dictate SIMR reprogramming, whereas native mutant mtDNA fibroblasts can be reprogrammed (Hämäläinen et al., 2013; Ma et al., 2015; Pek et al., 2019).

SIMR-iPSCs Produce Functional, Differentiated Cell Types

We next determined whether SIMR-iPSCs with isogenic nuclei and non-native donor mtDNAs could differentiate. We chose to examine defined medium differentiation of mesenchymal stem cells (MSCs) because of their relevance to potential therapies and current use in over 850 clinical trials (Hsu et al., 2016). A BJ-iPSC control, BJ ρ0+PBMC1-iPSCs, and BJ ρ0+HEK293T-iPSCs were differentiated into MSCs and validated with an antibody panel against surface biomarkers established by the International Society for Cellular Therapy (ISCT) (Dominici et al., 2006). Flow cytometry verified that the BJ-MSC control, BJ

ρ0+PBMC1-MSC clones, and BJ ρ0+HEK293T-MSC clones were positive for MSC biomarkers CD73, CD90, and CD105, and negative for a cocktail of non-MSC biomarkers, including CD11b, CD19, CD34, CD45, and HLA-DR (Figures 4A and S1R). BJ-MSCs and all SIMR-MSC clones from both mtDNA donors adhered to plastic, consistent with ISCT criteria for MSCs (Figures 4B and S1S).

Seahorse assays of BJ-MSC control, BJ ρ0+PBMC1-MSC clones, and BJ ρ0+HEK293T-MSC clones revealed no or mild differences in basal respiration, maximal respiration, and spare respiratory capacity, indicating that respiratory changes are mutable for ρ0 fibroblasts after MitoPunch with reprogramming and differentiation (Figures 4C and S1T). Quantitative phase microscopy (QPM) was used to examine key cellular biophysical properties in SIMR MSCs and detected minimal to no differences in cell growth rate, area, and biomass among the BJ-MSC control, BJ ρ0+PBMC1-MSC clones, and BJ ρ0+HEK293T-MSC clones (Figures 4D and S1U). The function of SIMR-MSC clones and the BJ-MSC control was compared by co-culture with human PBMC-isolated T cells in a standard immunosuppression assay, which measures MSC clinical immunomodulatory performance (Djouad et al., 2003; Ghannam et al., 2010). All BJ ρ0+PBMC1-MSC and BJ ρ0+HEK293T-MSC clones repressed T cell proliferation (Figures 4E and S1V). BJ ρ0+PBMC1-MSC clone 11 showed the greatest immunosuppression and reduction in T cell proliferation, whereas no large differences were detected between the remaining SIMR-MSC clones and the BJ-MSC control. Finally, we performed directed trilineage differentiation of SIMR-MSCs into adipocytes, osteoblasts, and chondrocytes to demonstrate the clinical potential of MitoPunch-engineered lines. The BJ-MSC control, BJ ρ0+PBMC1-MSCs, and BJ ρ0+HEK293T-MSCs all formed these three MSC-differentiated lineages (Figures 4F and S1W). Adipocytes and chondrocytes were phenotypically similar between the BJ control and SIMR clones, whereas SIMR osteoblasts tended to qualitatively produce more calcium deposits. Thus, our mitochondrial transfer strategy enables the generation of iPSCs, MSCs, and further differentiated cell types from ρ0 fibroblasts by stable incorporation of specific, non-detrimental, and non-native donor mtDNAs.

SIMR Cell Metabolism and RNA Transcript Changes with Fate Transitions

We used ultra-high-performance liquid chromatography-mass spectrometry (UPHLC-MS) to quantify 154 steady-state metabolites in native BJ, BJ ρ0, BJ ρ0+PBMC1 clones, and BJ ρ0+HEK293T clones at fibroblast, iPSC, and MSC fates. Hierarchical clustering showed distinct, grouped profiles for fibroblasts, iPSCs, and MSCs independent of mitochondrial transfer status (Figures S2A and S2B; Table S3). Principal component analysis (PCA) of metabolite data also showed three main clusters representing fibroblast, iPSC, and MSC fates but no clear differences between SIMR and native control cells within each fate (Figures S2C and S2D). Metabolite set variation analysis (MSVA) and Euclidean distance analysis of the BJ ρ0+PBMC1-iPSC and BJ ρ0+PBMC1-MSC clones showed similar metabolite pathway profiles to themselves and to their respective BJ-iPSC and BJ-MSC controls (Figures S2A, S2E, and S2F). In contrast, BJ ρ0+HEK293T-iPSC clones 1 and 2 clustered separately from clone 4 and the BJ-iPSC control for several metabolic pathways, particularly purine, pyrimidine, glutathione, and ethanol metabolism (Figures S2B, S2E, and S2F). This separation in BJ ρ0+HEK293T-iPSC clones was no longer present upon further differentiation to BJ ρ0+HEK293T-MSC clones (Figures S2B, S2E, and S2F). In summary, steady-state metabolite analyses showed that SIMR cells are comparable to native control cells, with only a few differences that are resolved upon iPSC reprogramming and differentiation to MSCs.

We utilized RNA sequencing (RNA-seq) to evaluate whole-transcriptome profiles for SIMR cells at fibroblast, iPSC, and MSC fates. DESeq2 was used to identify significant differentially expressed genes (DEGs), defined as genes showing an absolute log 2-fold change > 0.5 and adjusted $p < 0.05$. For both BJ ρ0+PBMC1 and BJ ρ0+HEK293T SIMR cells, the greatest number of DEGs compared to native BJ control cells with an adjusted $p < 0.05$ occurred at the fibroblast fate (Figures 5A and S3A). RNA-seq identified 1741, 194, and 224 elevated and 1827, 68, and 115 repressed DEGs by comparing BJ ρ0+PBMC1 cells to native BJ parent cells at the fibroblast, iPSC, and MSC fates, respectively (Figure 5A; Table S4). Transcriptomic analysis of the independently generated BJ ρ0+HEK293T cells similarly identified 1,377, 537, and 239 elevated and 1,564, 648, and 210 repressed DEGs compared to native BJ parent cells at fibroblast, iPSC, and MSC fates, respectively (Figure S3A; Table S4).

Reactome pathway enrichment analysis of DEGs showed diverse pathways altered in SIMR fibroblast transcript profiles compared to those in native BJ fibroblasts, including those associated with extracellular matrix organization and the complement cascade (Figure S3B; Table S5). Differential expression and pathway enrichment analyses comparing all SIMR-iPSCs and SIMR-MSCs to native BJ-iPSC and BJ-MSC controls, respectively, identified a dramatically smaller number of DEGs, with overrepresented pathways driven primarily by a cluster of histone transcripts (Figures S3C and S3D; Table S5).

Further detailed transcriptome analyses uncovered metabolic pathway differences based on cell condition and fate. Somatic cell reprogramming to iPSCs requires a metabolic shift from predominantly oxidative phosphorylation to mainly glycolysis, which corresponds with all BJ ρ0+PBMC1-iPSC and BJ ρ0+HEK293T-iPSC clones showing elevated expression of glycolysis-associated transcripts by gene set variation analysis (GSVA) (Figures S4A and S4B). Additionally, GSVA showed increased expression of ETC transcripts in BJ ρ0, BJ ρ0+PBMC1, and BJ ρ0+HEK293T SIMR fibroblasts compared to that in native BJ fibroblasts (Figures S4A and S4B). However, immunoblots for succinate dehydrogenase (SDHB; complex II), ubiquinol-cytochrome *c* reductase core protein 2 (UUQCRC2; complex III), cytochrome C oxidase II (MT-COXII; complex IV), and ATP synthase F1 subunit alpha (ATP5A; complex V) demonstrated the opposite result, with ETC proteins in SIMR fibroblasts reduced compared to those in the native BJ fibroblast control (Figure S4C). Overall, whole-transcriptome data analysis showed that initial large differences between SIMR clones and native control cells at the fibroblast fate progressively dissipated during reprogramming and differentiation.

We examined the RNA transcript levels of 1,158 nuclear genes listed in the MitoCarta2.0 database that encode proteins that

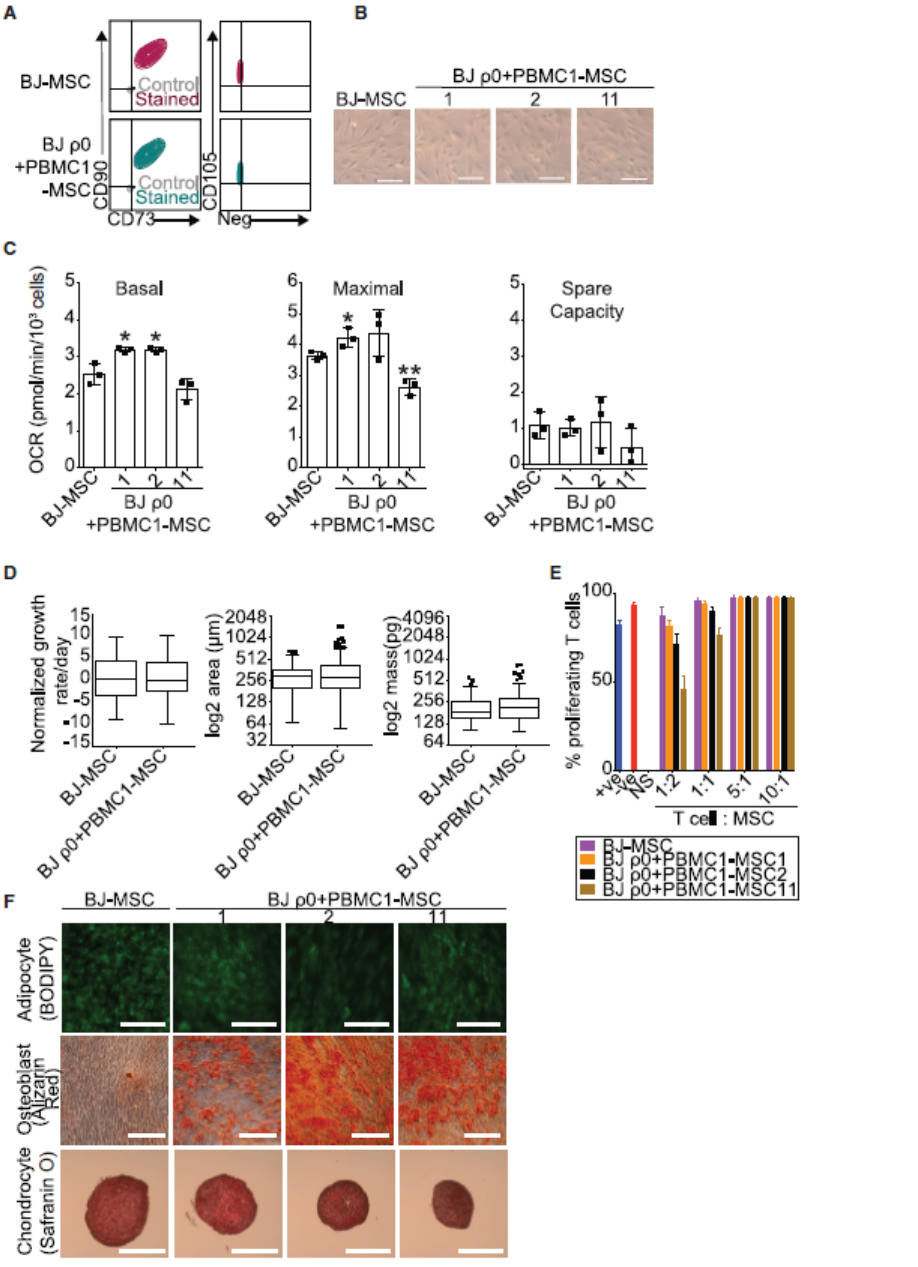

(legend on next page)

localize to the mitochondria. Hierarchical clustering analysis of transcripts from these genes identified a separation of BJ ρ0+PBMC1, BJ ρ0+HEK293T, and BJ ρ0 transcripts away from the native BJ transcripts at the fibroblast fate (Figures 5B and S3B). Pathway analysis of DEGs between these two groups showed an enrichment for genes encoding ETC proteins in the native BJ fibroblasts (Table S4). Of note, this differential clustering was not observed at the iPSC and MSC fates (Figures 5B and S5A).

Closer examination of mtDNA-encoded transcripts only demonstrated, as anticipated, that BJ ρ0 cells have dramatically lowered expression of all 13 coding gene transcripts compared to transcripts from SIMR and native fibroblast cells (Figures 5C and S5B). Additionally, both BJ ρ0+PBMC1 and BJ ρ0+HEK293T fibroblasts showed significantly reduced expression of the 13 mtDNA-encoded genes compared to native BJ fibroblasts (Figures 5C and S5B). By contrast, no significant difference was observed in mtDNA transcript levels after reprogramming SIMR and control fibroblasts to iPSCs, followed by differentiation to MSCs (Figures 5C and S5B).

We then used the MitoXplorer pipeline (Yim et al., 2020) to quantify the representation of 38 distinct mitochondrial processes within the identified DEGs. As anticipated from abolished respiration, BJ ρ0 fibroblasts showed DEGs for 29 mitochondrial processes compared to native BJ fibroblasts, especially within oxidative phosphorylation, mitochondrial genome translation, and amino acid metabolism processes (Figure 5D). Similarly, BJ ρ0+PBMC1 and BJ ρ0+HEK293T fibroblasts had altered gene expression profiles in 30 and 29 mitochondrial processes, respectively, in comparison to native BJ fibroblasts (Figures 5D and S5C). Further analysis at this fate using MitoXplorer highlighted differences between the two SIMR lines, as the BJ ρ0+PBMC1 had fewer DEGs for mtDNA-associated oxidative phosphorylation and mitochondrial genome translation compared to BJ ρ0+HEK293T fibroblasts. Furthermore, both SIMR fibroblast lines had more DEGs associated with nuclear-encoded mitochondrial translation and calcium signaling and transport than the BJ ρ0 line, when compared to native BJ fibroblasts. Of note, the number of affected mitochondrial processes was dramatically reduced by reprogramming, with only 7 and 16 processes exhibiting DEGs in BJ ρ0+PBMC1-iPSCs and BJ ρ0+HEK293T-iPSCs, respectively (Figures 5D and S5C). Finally, BJ ρ0+PBMC1-MSCs and BJ ρ0+HEK293T-MSCs exhibited only 3 and 8 mitochondrial processes with DEGs, respectively, with only ROS defense similarly altered between the two SIMR-MSC lines and MSC control (Figures 5D and S5C). These data uncover transcriptomic alterations to translation, among additional mitochondrial processes, at the fibroblast fate as a potential difference maker for exogenous mtDNA function in SIMR cells. Combined, the results show that, although SIMR cell mitochondrial function becomes more similar to that of the BJ control with reprogramming and differentiation, differences still exist that are based on the transferred mtDNA sequence.

DISCUSSION

Here, we use MitoPunch to report on a rapid, versatile pipeline to generate transformed or non-immortal cells with specific mtDNA-nDNA combinations, an advance with certain advantages over cybrid technology (Patananan et al., 2016; Wong et al., 2017), uncontrolled selection in physiologic mitochondrial "bottlenecks" (Latorre-Pellicer et al., 2019), or time-consuming screens for cells with desired mtDNA mutations (Fayzulin et al., 2015; Lorenz et al., 2017). We show that the transcriptome and metabolome of SIMR fibroblasts resemble those of ρ0 matched recipient cells and that reprogramming to pluripotency followed by differentiation resets these profiles to closely resemble those of unmanipulated control cells. Our studies would be difficult or impossible using other mitochondrial transfer approaches, such as those that use immortal cell lines incapable of reprogramming. Although it is also possible to generate SIMR cells with the nanoblade and microinjection, these low-throughput methods suffer practical and experimental limitations. In contrast, MitoPunch is an accessible approach to generate numerous clones with desired, stable mtDNA-nDNA combinations within 2 weeks.

SIMR clone formation was achieved for all ρ0 recipient fibroblasts studied. Of note, some mtDNA-nDNA combinations produced SIMR clones at lower efficiencies than other combinations, which could only be detected using a high-throughput platform like MitoPunch. In contrast to 143BTK− ρ0+HEK293T

Figure 4. SIMR iPSCs Produce MSCs with Trilineage Differentiation Potential

(A) Flow cytometry of MSC biomarkers CD73, CD90, and CD105, and a cocktail of negative MSC biomarkers. Immunostained samples are indicated in color, with isotype negative controls in gray. Data for BJ-MSC control are the same data as in Figure S5A. Representative clones for native BJ-MSCs and BJ ρ0+PBMC1-MSCs are indicated.

(B) Bright-field microscopy showing unmanipulated BJ-MSC and BJ ρ0+PBMC1-MSC clones 1, 2, and 11 adhering to plastic at 20× magnification (scale bars, 100 μm). Data for BJ-MSC control are the same data as in Figure S5B.

(C) OCR measurements for ~1.5 × 10^4 native BJ-MSCs and BJ ρ0+PBMC1-MSC clones 1, 2, and 11. Data for BJ-MSC control are the same as in Figure S5C. Data are the means ± SD of three technical replicates. Statistical significance by unpaired, two-tailed Student's t test. *$p \leq 0.05$; **$p \leq 0.01$.

(D) Quantitative phase microscopy of native BJ-MSCs and a 1:1:1 mix of BJ ρ0+PBMC1-MSC clones 1, 2, and 11. Data for BJ-MSC control are the same as in Figure S5D. Shown are box-and-whisker Tukey plots with outliers identified. Data were averaged from 77 and 172 cells for native BJ-MSCs and BJ ρ0+PBMC1-MSCs, respectively. Statistical significance by Welch's t test.

(E) T cells were added into native BJ-MSC or BJ ρ0+PBMC1-MSC clone 1, 2, or 11 cultures at 1:2, 1:1, 5:1, and 10:1 T cell:MSC ratios. After 5 days of co-culture, T cell proliferation was measured using a CFSE dye dilution assay by flow cytometry. The data labeled "NS" (no stimulus) denote T cells without CD3/CD28 bead activation. The data labeled "-ve" (negative) denote no addition of MSCs to stimulated T cells. The data labeled "+ve" (positive) denote a 1:1 addition of myeloid-derived suppressor cells to T cells. Data are the means ± SD of three technical replicates.

(F) Trilineage differentiation of native BJ-MSCs and BJ ρ0+PBMC1-MSC clones 1, 2, and 11. Representative sections were fixed and stained with 1 μM Bodipy 493/503, 1% alizarin red S, and 0.1% Safranin O, respectively. Shown are adipocytes (first row, 20×; scale bars, 100 μm), osteocytes (second row, 20×; scale bars, 200 μm), and chondrocytes (fourth row, 5×; scale bars, 500 μm).

See also Figure S1.

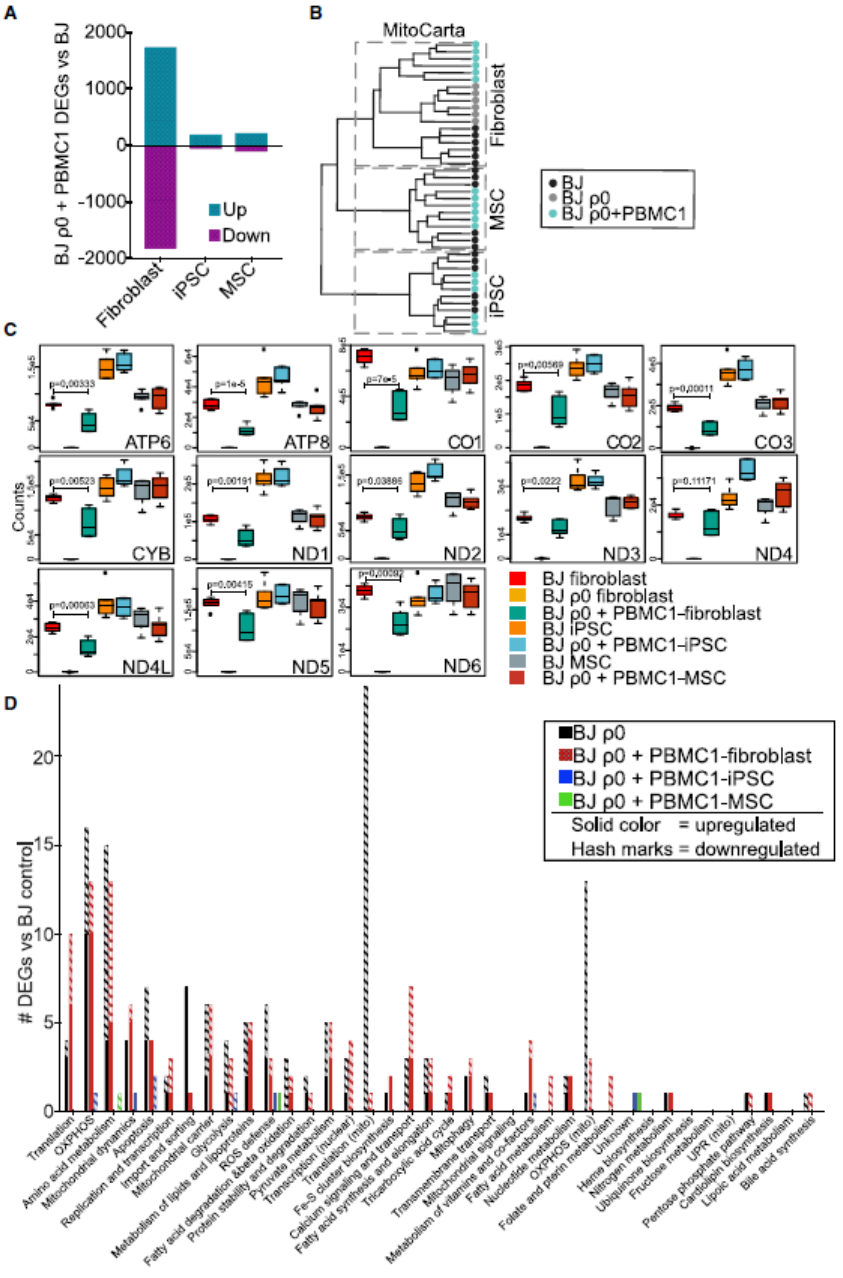

(legend on next page)

SIMR cells that produced ~75 clones, MitoPunch transfers into primary fibroblasts yielded fewer SIMR clones, possibly related to the Hayflick limit or a sub-optimal response to the MitoPunch procedure. For example, ADF ρ0 recipients grew the slowest, reached senescence shortly after mtDNA depletion (data not shown), and resulted in the fewest SIMR clones. On average, twice as many BJ ρ0+HEK293T clones were obtained compared to BJ ρ0+PBMC1 clones, which may be from a more compatible mtDNA-nDNA pairing and more favorable metabolic profile (Latorre-Pellicer et al., 2016). SIMR fibroblasts also showed a 10-fold reduction in reprogramming efficiency compared to native fibroblast controls. A similar reduction was observed in mouse embryo fibroblast reprogramming with non-native mtDNA, perhaps from a lower mtDNA-nDNA compatibility (Latorre-Pellicer et al., 2019).

Evidence for incomplete mtDNA-nDNA assimilation in SIMR fibroblasts was observed in transcriptome data that showed hundreds of DEGs between SIMR and unmanipulated fibroblasts. Also, MitoCarta2.0- and mtDNA-encoded transcripts were most similar for SIMR and ρ0 fibroblasts, despite SIMR cell culture in restrictive medium requiring ETC activity for growth and survival. These data suggest that exogenous mtDNA in SIMR fibroblasts do not fully communicate and influence the nDNA, despite being able to support a selectable level of ETC activity and adequate synthesis of metabolites for cell proliferation. Supporting evidence for this suggestion includes that ddC exposure yielded minimal nDNA damage and that the metabolome and transcriptome profiles of SIMR fibroblasts are mostly reset to unmanipulated BJ-iPSC profiles in SIMR-iPSCs. Our results agree with a report showing that ρ0 cells have altered metabolism and an epigenome that can only be partially reset by cybrid formation (Smiraglia et al., 2008). Our study provides a platform for investigating the resetting of ρ0 cell transcription and metabolism after stable mtDNA transplantation and subsequent cell fate changes. Further work is needed to determine whether cells that receive exogenous mtDNA by other forms of mitochondrial transfer also have disrupted mtDNA transcription profiles.

In summary, we provide a proof-of-principle mitochondrial transfer pipeline to generate cells of different fates with specific mtDNA-nDNA combinations, including clonal lines with genome pairings not found in nature. Future studies will generate SIMR-derived cells representing high-energy-demand tissues, such as cardiomyocytes or neurons, and will investigate the current inability to generate SIMR-iPSCs containing mutant mtDNAs to enable patient-specific disease and drug screening models with isogenic nuclei for mtDNA diseases. Furthermore, our results show that the interpretation of mitochondrial transfer experiments must consider that cells initially generated may not show complete mtDNA-nDNA integration and subsequent restoration of cellular pathways. This is particularly salient for cells that lack subsequent reprogramming potential, such as transient or transformed mitochondrial transfer cell lines, since our results show that reprogramming and differentiation are required for resetting the nDNA expression profile. Finally, this mitochondrial transfer pipeline bypasses the evolutionary pairwise selection of mtDNAs and nDNAs in cells to expand upon the repertoire of genomic combinations present in the human population and generates a library of cells at various fates with defined mtDNA-nDNA combinations and unique functional properties for research and potential therapeutic applications.

STAR★METHODS

Detailed methods are provided in the online version of this paper and include the following:

- KEY RESOURCES TABLE
- RESOURCE AVAILABILITY
  - Lead Contact
  - Materials Availability
  - Data and Code Availability
- EXPERIMENT MODEL AND SUBJECT DETAILS
  - Cell Lines
  - Human Tissues
- METHOD DETAILS
  - mtDNA Depletion and qPCR Verification
  - Mitochondrial Transfer into ρ0 Recipients
  - Confocal microscopy
  - Mitochondrial Oxygen Consumption Measurements
  - Mitochondrial Isolation from Mouse Tissues and Delivery
  - iPSC Reprogramming
  - MSC Differentiation
  - Human mtDNA D-Loop Sequencing
  - ROS Quantification
  - iPSC Flow Cytometry
  - MSC Flow Cytometry
  - Fluorescence Microscopy
  - MSC Immunosuppression Assay
  - Tri-lineage Differentiation
  - Tri-lineage Differentiation Analyses
  - UPHLC-MS Metabolomics Processing
  - RNA Extraction
  - RNA-Seq Library Preparation
  - Restriction-Fragment Length Polymorphism Heteroplasmy Assay

Figure 5. Transcriptome Features of SIMR and Native mtDNA Cells

(A) Number of DEGs for BJ ρ0+PBMC1 cells compared to native BJ cells at fibroblast, iPSC, and MSC fates.

(B) Hierarchical clustering of nuclear-encoded MitoCarta2.0 database genes from native BJ, BJ ρ0, and BJ ρ0+PBMC1 cells at fibroblast, iPSC, and MSC fates.

(C) Normalized, batch-adjusted read counts shown as box-and-whisker Tukey plots for 13 MitoCarta2.0-annotated mtDNA-encoded genes for native BJ, BJ ρ0, and BJ ρ0+PBMC1 cells at the fibroblast, iPSC, and MSC fates. Statistical significance was by Welch's t test.

(D) MitoXplorer-categorized DEGs for BJ ρ0+PBMC1 compared to native BJ cells at the fibroblast, iPSC, and MSC fates divided into the 38 mitochondrial processes.

See also Figures S2, S3, S4, and S5 and Tables S3, S4, and S5.

- QUANTIFICATION AND STATISTICAL ANALYSIS
  - mtDNA Depletion and qPCR Verification
  - Mitochondrial Oxygen Consumption Rate Measurements
  - Metabolomics Data Analysis
  - RNA-Seq Pre-Processing
  - Differential Gene Expression Analysis
  - MitoXplorer Analysis
  - Gene Expression PCA and hierarchal clustering
  - Metabolic Transcript Gene Set Variation Analysis (GSVA)
  - Gene Set Overrepresentation Analysis (ORA)
  - HLA Class I Genotyping

SUPPLEMENTAL INFORMATION

Supplemental Information can be found online at https://doi.org/10.1016/j.celrep.2020.108562.

ACKNOWLEDGMENTS

A.N.P. is supported by the NIH (T32CA009120) and American Heart Association (18POST34080342). A.J.S. is supported by the NIH (T32GM007185 and T32CA009120). K.P. is supported by the Broad Center of Regenerative Medicine and Stem Cell Research at UCLA, the David Geffen School of Medicine, the NIH (P01GM099134), and a Faculty Scholar grant from the HHMI. M.A.T. is supported by the Air Force Office of Scientific Research (FA9550-15-1-0406), the NIH (R01GM114188, R01GM073981, R01CA185189, R21CA227480, R01GM127985, and P30CA016042), and CIRM (RT3-07678). We thank Rebeca Acin-Perez, Linsey Stiles, and Orian Shirihai of the UCLA Metabolomics Core for help with Seahorse XF Analyzer assays. We thank Felicia Codrea from the UCLA Flow Cytometry Core, in addition to Laurent Bentolila and Matthew Schibler from the California Nanosystems Institute Advanced Light Microscopy/Spectroscopy Laboratory for their insight and assistance. We thank Jonathan Wanagat for his critical insights during manuscript preparation. We also acknowledge Drs. Idoya Lahortiga and Luk Cox for their Library of Science and Medical Illustrations (https://www.somersault1824.com/).

AUTHOR CONTRIBUTIONS

Conceptualization: A.N.P., A.J.S., T.-H.W., S.R., K.R.N., and M.A.T.; Methodology: A.N.P., A.J.S., T.-H.W., F.M.A., A.M., J.V.L., S.R., K.R.N., P.-Y.C., and M.A.T.; Software: T.L.N., F.M.A., A.V., J.G., and D.B.; Formal Analysis: A.N.P., A.J.S., F.M.A., A.V., T.L.N., and D.B.; Investigation: A.N.P., A.J.S., T.-H.W., F.M.A., A.V., S.A.L.K., T.N., A.T., A.J.C., E.R.D., A.M., J.V.L., L.Z., N.R., M.S., W.T., A.L., P.A.S., D.B., J.G., and C.V.; Resources: A.N.P., A.J.S., T.-H.W., and F.M.A.; Data Curation: A.N.P., F.M.A., A.V., D.B., and C.V.; Writing – Original Draft: A.N.P., A.J.S., and F.M.A.; Writing – Review & Editing: A.N.P., A.J.S., F.M.A., A.V., T.-H.W., K.R.N., and M.A.T.; Validation: A.N.P. and A.J.S.; Visualization: A.N.P., A.J.S., T.L.N., F.M.A., and A.V.; Supervision: A.N.P. and T.-H.W.; Project Administration: A.N.P. and T.-H.W.; Funding Acquisition: A.N.P., A.J.S., S.R., K.R.N., P.-Y.C., K.P., and M.A.T.

DECLARATION OF INTERESTS

M.A.T. and P.-Y.C. are co-founders, board members, shareholders, and consultants for NanoCav, a private start-up company working on mitochondrial transfer and quantitative phase microscopy techniques and applications. T.-H.W. was an employee of NanoCav and is employed by ImmunityBio, and S.R. and K.R.N. are board members of NanoCav and employed by ImmunityBio. The other authors report no competing interests.

Received: July 18, 2020
Revised: October 29, 2020
Accepted: December 6, 2020
Published: December 29, 2020

REFERENCES

Abujarour, R., Valamehr, B., Robinson, M., Rezner, B., Vranceanu, F., and Flynn, P. (2013). Optimized surface markers for the prospective isolation of high-quality hiPSCs using flow cytometry selection. Sci. Rep. *3*, 1179.

Ali Pour, P., Kenney, M.C., and Kheradvar, A. (2020). Bioenergetics Consequences of Mitochondrial Transplantation in Cardiomyocytes. J. Am. Heart Assoc. *9*, e014501.

Benjamini, Y., and Hochberg, Y. (1995). Controlling the false discovery rate - a practical and powerful approach to multiple testing. J. R. Stat. Soc. Series B Methodol. *57*, 289–300.

Calvo, S.E., Clauser, K.R., and Mootha, V.K. (2016). MitoCarta2.0: an updated inventory of mammalian mitochondrial proteins. Nucleic Acids Res. *44* (*D1*), D1251–D1257.

Campbell, J.M., Perales-Clemente, E., Ata, H., Vidal-Folch, N., Liu, W., Clark, K.J., Xu, X., Oglesbee, D., Nelson, T.J., and Ekker, S.C. (2018). Engineering targeted deletions in the mitochondrial genome. bioRxiv. https://doi.org/10.1101/287342.

Cherry, A.B., Gagne, K.E., McLoughlin, E.M., Baccei, A., Gorman, B., Hartung, O., Miller, J.D., Zhang, J., Zon, R.L., Ince, T.A., et al. (2013). Induced pluripotent stem cells with a mitochondrial DNA deletion. Stem Cells *31*, 1287–1297.

Chomyn, A., Martinuzzi, A., Yoneda, M., Daga, A., Hurko, O., Johns, D., Lai, S.T., Nonaka, I., Angelini, C., and Attardi, G. (1992). MELAS mutation in mtDNA binding site for transcription termination factor causes defects in protein synthesis and in respiration but no change in levels of upstream and downstream mature transcripts. Proc. Natl. Acad. Sci. USA *89*, 4221–4225.

Clark, M.A., and Shay, J.W. (1982). Mitochondrial transformation of mammalian cells. Nature *295*, 605–607.

Dawson, E.R., Patananan, A.N., Sercel, A.J., and Teitell, M.A. (2020). Stable retention of chloramphenicol-resistant mtDNA to rescue metabolically impaired cells. Sci. Rep. *10*, 14328.

Djouad, F., Plence, P., Bony, C., Tropel, P., Apparailly, F., Sany, J., Noël, D., and Jorgensen, C. (2003). Immunosuppressive effect of mesenchymal stem cells favors tumor growth in allogeneic animals. Blood *102*, 3837–3844.

Dominici, M., Le Blanc, K., Mueller, I., Slaper-Cortenbach, I., Marini, F., Krause, D., Deans, R., Keating, A., Prockop, D.j., and Horwitz, E. (2006). Minimal criteria for defining multipotent mesenchymal stromal cells. The International Society for Cellular Therapy position statement. Cytotherapy *8*, 315–317.

Elliott, H.R., Samuels, D.C., Eden, J.A., Relton, C.L., and Chinnery, P.F. (2008). Pathogenic mitochondrial DNA mutations are common in the general population. Am. J. Hum. Genet. *83*, 254–260.

Fayzulin, R.Z., Perez, M., Kozhukhar, N., Spadafora, D., Wilson, G.L., and Alexeyev, M.F. (2015). A method for mutagenesis of mouse mtDNA and a resource of mouse mtDNA mutations for modeling human pathological conditions. Nucleic Acids Res. *43*, e62.

Folmes, C.D.L., Martinez-Fernandez, A., Perales-Clemente, E., Li, X., McDonald, A., Oglesbee, D., Hrstka, S.C., Perez-Terzic, C., Terzic, A., and Nelson, T.J. (2013). Disease-causing mitochondrial heteroplasmy segregated within induced pluripotent stem cell clones derived from a patient with MELAS. Stem Cells *31*, 1298–1308.

Ghannam, S., Bouffi, C., Djouad, F., Jorgensen, C., and Noël, D. (2010). Immunosuppression by mesenchymal stem cells: mechanisms and clinical applications. Stem Cell Res. Ther. *1*, 2.

Grègoire, M., Morais, R., Quilliam, M.A., and Gravel, D. (1984). On auxotrophy for pyrimidines of respiration-deficient chick embryo cells. Eur. J. Biochem. *142*, 49–55.

Hämäläinen, R.H., Manninen, T., Koivumäki, H., Kislin, M., Otonkoski, T., and Suomalainen, A. (2013). Tissue- and cell-type-specific manifestations of

heteroplasmic mtDNA 3243A>G mutation in human induced pluripotent stem cell-derived disease model. Proc. Natl. Acad. Sci. USA *110*, E3622–E3630.

Hänzelmann, S., Castelo, R., and Guinney, J. (2013). GSVA: gene set variation analysis for microarray and RNA-seq data. BMC Bioinformatics *14*, 7.

Harrow, J., Frankish, A., Gonzalez, J.M., Tapanari, E., Diekhans, M., Kokocinski, F., Aken, B.L., Barrell, D., Zadissa, A., Searle, S., et al. (2012). GENCODE: the reference human genome annotation for The ENCODE Project. Genome Res. *22*, 1760–1774.

Hsu, P.J., Liu, K.J., Chao, Y.Y., Sytwu, H.K., and Yen, B.L. (2015). Assessment of the immunomodulatory properties of human mesenchymal stem cells (MSCs). J. Vis. Exp. (*106*), e53265.

Hsu, Y.C., Wu, Y.T., Yu, T.H., and Wei, Y.H. (2016). Mitochondria in mesenchymal stem cell biology and cell therapy: From cellular differentiation to mitochondrial transfer. Semin. Cell Dev. Biol. *52*, 119–131.

Huber, W., Carey, V.J., Gentleman, R., Anders, S., Carlson, M., Carvalho, B.S., Bravo, H.C., Davis, S., Gatto, L., Girke, T., et al. (2015). Orchestrating high-throughput genomic analysis with Bioconductor. Nat. Methods *12*, 115–121.

Husson, F. (2020). FactoMineR v2.2 (RDocumentation).

Kanehisa, M., Goto, S., Sato, Y., Furumichi, M., and Tanabe, M. (2012). KEGG for integration and interpretation of large-scale molecular data sets. Nucleic Acids Res. *40*, D109–D114.

Kang, E., Wang, X., Tippner-Hedges, R., Ma, H., Folmes, C.D., Gutierrez, N.M., Lee, Y., Van Dyken, C., Ahmed, R., Li, Y., et al. (2016). Age-related accumulation of somatic mitochondrial DNA mutations in adult-derived human iPSCs. Cell Stem Cell *18*, 625–636.

Kankainen, M., Gopalacharyulu, P., Holm, L., and Oresic, M. (2011). MPEA–metabolite pathway enrichment analysis. Bioinformatics *27*, 1878–1879.

Kassambara, A. (2017). R package ggpubr v0.1.6 (RDocumentation).

Kassambara, A. (2019). factoextra v1.0.6 (RDocumentation).

Kesner, E.E., Saada-Reich, A., and Lorberboum-Galski, H. (2016). Characteristics of Mitochondrial Transformation into Human Cells. Sci. Rep. *6*, 26057.

Kim, M.J., Hwang, J.W., Yun, C.K., Lee, Y., and Choi, Y.S. (2018). Delivery of exogenous mitochondria via centrifugation enhances cellular metabolic function. Sci. Rep. *8*, 3330.

Kitani, T., Kami, D., Matoba, S., and Gojo, S. (2014). Internalization of isolated functional mitochondria: involvement of macropinocytosis. J. Cell. Mol. Med. *18*, 1694–1703.

Kodaira, M., Hatakeyama, H., Yuasa, S., Seki, T., Egashira, T., Tohyama, S., Kuroda, Y., Tanaka, A., Okata, S., Hashimoto, H., et al. (2015). Impaired respiratory function in MELAS-induced pluripotent stem cells with high heteroplasmy levels. FEBS Open Bio *5*, 219–225.

Kolde, R. (2015). Package 'pheatmap' - Pretty Heatmaps (CRAN: R-Project).

Kukat, A., Kukat, C., Brocher, J., Schäfer, I., Krohne, G., Trounce, I.A., Villani, G., and Seibel, P. (2008). Generation of rho0 cells utilizing a mitochondrially targeted restriction endonuclease and comparative analyses. Nucleic Acids Res. *36*, e44.

Kumar, L., and Futschik, M.E. (2007). Mfuzz: a software package for soft clustering of microarray data. Bioinformation *2*, 5–7.

Latorre-Pellicer, A., Moreno-Loshuertos, R., Lechuga-Vieco, A.V., Sánchez-Cabo, F., Torroja, C., Acin-Pérez, R., Calvo, E., Aix, E., González-Guerra, A., Logan, A., et al. (2016). Mitochondrial and nuclear DNA matching shapes metabolism and healthy ageing. Nature *535*, 561–565.

Latorre-Pellicer, A., Lechuga-Vieco, A.V., Johnston, I.G., Hämäläinen, R.H., Pellico, J., Justo-Méndez, R., Fernández-Toro, J.M., Claveria, C., Guaras, A., Sierra, R., et al. (2019). Regulation of Mother-to-Offspring Transmission of mtDNA Heteroplasmy. Cell Metab. *30*, 1120–1130.e5.

Li, H., and Durbin, R. (2010). Fast and accurate long-read alignment with Burrows-Wheeler transform. Bioinformatics *26*, 589–595.

Lorenz, C., Lesimple, P., Bukowiecki, R., Zink, A., Inak, G., Mlody, B., Singh, M., Semtner, M., Mah, N., Auré, K., et al. (2017). Human iPSC-Derived Neural Progenitors Are an Effective Drug Discovery Model for Neurological mtDNA Disorders. Cell Stem Cell *20*, 659–674.e9.

Love, M.I., Huber, W., and Anders, S. (2014). Moderated estimation of fold change and dispersion for RNA-seq data with DESeq2. Genome Biol. *15*, 550.

Ma, H., Folmes, C.D., Wu, J., Morey, R., Mora-Castilla, S., Ocampo, A., Ma, L., Poulton, J., Wang, X., Ahmed, R., et al. (2015). Metabolic rescue in pluripotent cells from patients with mtDNA disease. Nature *524*, 234–238.

Matsubara, M., Kanda, H., Imamura, H., Inoue, M., Noguchi, M., Hosoda, K., Kakizuka, A., and Nakao, K. (2018). Analysis of mitochondrial function in human induced pluripotent stem cells from patients with mitochondrial diabetes due to the A3243G mutation. Sci. Rep. *8*, 949.

Miyata, N., Steffen, J., Johnson, M.E., Fargue, S., Danpure, C.J., and Koehler, C.M. (2014). Pharmacologic rescue of an enzyme-trafficking defect in primary hyperoxaluria 1. Proc. Natl. Acad. Sci. USA *111*, 14406–14411.

Mok, B.Y., de Moraes, M.H., Zeng, J., Bosch, D.E., Kotrys, A.V., Raguram, A., Hsu, F., Radey, M.C., Peterson, S.B., Mootha, V.K., et al. (2020). A bacterial cytidine deaminase toxin enables CRISPR-free mitochondrial base editing. Nature *583*, 631–637.

Mudge, J.M., and Harrow, J. (2015). Creating reference gene annotation for the mouse C57BL6/J genome assembly. Mamm. Genome *26*, 366–378.

Nelson, I., Hanna, M.G., Wood, N.W., and Harding, A.E. (1997). Depletion of mitochondrial DNA by ddC in untransformed human cell lines. Somat. Cell Mol. Genet. *23*, 287–290.

Nzigou Mombo, B., Gerbal-Chaloin, S., Bokus, A., Daujat-Chavanieu, M., Jorgensen, C., Hugnot, J.P., and Vignais, M.L. (2017). MitoCeption: Transferring isolated human MSC mitochondria to glioblastoma stem cells. J. Vis. Exp. (*120*), 55245.

Patananan, A.N., Wu, T.H., Chiou, P.Y., and Teitell, M.A. (2016). Modifying the mitochondrial genome. Cell Metab. *23*, 785–796.

Patananan, A.N., Sercel, A.J., and Teitell, M.A. (2018). More than a powerplant: the influence of mitochondrial transfer on the epigenome. Curr. Opin. Physiol. *3*, 16–24.

Patel, D., Rorbach, J., Downes, K., Szukszto, M.J., Pekalski, M.L., and Minczuk, M. (2017). Macropinocytic entry of isolated mitochondria in epidermal growth factor-activated human osteosarcoma cells. Sci. Rep. *7*, 12886.

Patro, R., Duggal, G., Love, M.I., Irizarry, R.A., and Kingsford, C. (2017). Salmon provides fast and bias-aware quantification of transcript expression. Nat. Methods *14*, 417–419.

Pek, N.M.Q., Phua, Q.H., Ho, B.X., Pang, J.K.S., Hor, J.H., An, O., Yang, H.H., Yu, Y., Fan, Y., Ng, S.Y., and Soh, B.S. (2019). Mitochondrial 3243A > G mutation confers pro-atherogenic and pro-inflammatory properties in MELAS iPS derived endothelial cells. Cell Death Dis. *10*, 802.

Perales-Clemente, E., Cook, A.N., Evans, J.M., Roellinger, S., Secreto, F., Emmanuele, V., Oglesbee, D., Mootha, V.K., Hirano, M., Schon, E.A., et al. (2016). Natural underlying mtDNA heteroplasmy as a potential source of intra-person hiPSC variability. EMBO J. *35*, 1979–1990.

Picard, M., Zhang, J., Hancock, S., Derbeneva, O., Golhar, R., Golik, P., O'Hearn, S., Levy, S., Potluri, P., Lvova, M., et al. (2014). Progressive increase in mtDNA 3243A>G heteroplasmy causes abrupt transcriptional reprogramming. Proc. Natl. Acad. Sci. USA *111*, E4033–E4042.

Quintanilla, R.H., Jr., Asprer, J.S.T., Vaz, C., Tanavde, V., and Lakshmipathy, U. (2014). CD44 is a negative cell surface marker for pluripotent stem cell identification during human fibroblast reprogramming. PLoS ONE *9*, e85419.

R Core Team (2017). R: A Language and Environment for Statistical Computing (R Foundation for Statistical Computing).

Rebolledo-Jaramillo, B., Su, M.S., Stoler, N., McElhoe, J.A., Dickins, B., Blankenberg, D., Korneliussen, T.S., Chiaromonte, F., Nielsen, R., Holland, M.M., et al. (2014). Maternal age effect and severe germ-line bottleneck in the inheritance of human mitochondrial DNA. Proc. Natl. Acad. Sci. USA *111*, 15474–15479.

Ritchie, M.E., Phipson, B., Wu, D., Hu, Y., Law, C.W., Shi, W., and Smyth, G.K. (2015). limma powers differential expression analyses for RNA-sequencing and microarray studies. Nucleic Acids Res. *43*, e47.

Russell, O.M., Fruh, I., Rai, P.K., Marcellin, D., Doll, T., Reeve, A., Germain, M., Bastien, J., Rygiel, K.A., Cerino, R., et al. (2018). Preferential amplification of a human mitochondrial DNA deletion in vitro and in vivo. Sci. Rep. *8*, 1799.

Sasarman, F., Antonicka, H., and Shoubridge, E.A. (2008). The A3243G tRNA-Leu(UUR) MELAS mutation causes amino acid misincorporation and a combined respiratory chain assembly defect partially suppressed by overexpression of EFTu and EFG2. Hum. Mol. Genet. *17*, 3697–3707.

Schaefer, A.M., Taylor, R.W., Turnbull, D.M., and Chinnery, P.F. (2004). The epidemiology of mitochondrial disorders–past, present and future. Biochim. Biophys. Acta *1659*, 115–120.

Sercel, A.J., Patananan, A.N., Man, T., Wu, T.-H., Yu, A.K., Guyot, G.W., Rabizadeh, S., Niazi, K.R., Chiou, P.-Y., and Teitell, M.A. (2020). Stable transplantation of human mitochondrial DNA by high-throughput, pressurized mitochondrial delivery. bioRxiv. https://doi.org/10.1101/2020.09.15.298174.

Smiraglia, D.J., Kulawiec, M., Bistulfi, G.L., Gupta, S.G., and Singh, K.K. (2008). A novel role for mitochondria in regulating epigenetic modification in the nucleus. Cancer Biol. Ther. *7*, 1182–1190.

Smith, A.C., and Robinson, A.J. (2016). MitoMiner v3.1, an update on the mitochondrial proteomics database. Nucleic Acids Res. *44* (*D1*), D1258–D1261.

Soneson, C., Love, M.I., and Robinson, M.D. (2015). Differential analyses for RNA-seq: transcript-level estimates improve gene-level inferences. F1000Res. *4*, 1521.

Sun, C., Liu, X., Wang, B., Wang, Z., Liu, Y., Di, C., Si, J., Li, H., Wu, Q., Xu, D., et al. (2019). Endocytosis-mediated mitochondrial transplantation: Transferring normal human astrocytic mitochondria into glioma cells rescues aerobic respiration and enhances radiosensitivity. Theranostics *9*, 3595–3607.

Szolek, A., Schubert, B., Mohr, C., Sturm, M., Feldhahn, M., and Kohlbacher, O. (2014). OptiType: precision HLA typing from next-generation sequencing data. Bioinformatics *30*, 3310–3316.

Warnes, G., Bolker, B., Bonebakker, L., Gentleman, R., Huber, W., Liaw, A., Lumley, T., Maechler, M., Magnusson, A., Moeller, S., et al. (2016). gplots: Various R Programming Tools for Plotting Data (CRAN: R-Project).

Wickham, H. (2019). ggplot2 v3.2.0 (RDocumentation).

Wolf, D.P., Mitalipov, N., and Mitalipov, S. (2015). Mitochondrial replacement therapy in reproductive medicine. Trends Mol. Med. *21*, 68–76.

Wolf, D.P., Mitalipov, P.A., and Mitalipov, S.M. (2019). Principles of and strategies for germline gene therapy. Nat. Med. *25*, 890–897.

Wong, R.C.B., Lim, S.Y., Hung, S.S.C., Jackson, S., Khan, S., Van Bergen, N.J., De Smit, E., Liang, H.H., Kearns, L.S., Clarke, L., et al. (2017). Mitochondrial replacement in an iPSC model of Leber's hereditary optic neuropathy. Aging (Albany NY) *9*, 1341–1350.

Wu, Y.C., Wu, T.H., Clemens, D.L., Lee, B.Y., Wen, X., Horwitz, M.A., Teitell, M.A., and Chiou, P.Y. (2015). Massively parallel delivery of large cargo into mammalian cells with light pulses. Nat. Methods *12*, 439–444.

Wu, T.H., Sagullo, E., Case, D., Zheng, X., Li, Y., Hong, J.S., TeSlaa, T., Patananan, A.N., McCaffery, J.M., Niazi, K., et al. (2016). Mitochondrial transfer by photothermal nanoblade restores metabolite profile in mammalian cells. Cell Metab. *23*, 921–929.

Xiao, G., Chan, L.N., Klemm, L., Braas, D., Chen, Z., Geng, H., Zhang, Q.C., Aghajanirefah, A., Cosgun, K.N., Sadras, T., et al. (2018). B-cell-specific diversion of glucose carbon utilization reveals a unique vulnerability in B cell malignancies. Cell *173*, 470–484.e18.

Yahata, N., Matsumoto, Y., Omi, M., Yamamoto, N., and Hata, R. (2017). TALEN-mediated shift of mitochondrial DNA heteroplasmy in MELAS-iPSCs with m.13513G>A mutation. Sci. Rep. *7*, 15557.

Yang, Y., Wu, H., Kang, X., Liang, Y., Lan, T., Li, T., Tan, T., Peng, J., Zhang, Q., An, G., et al. (2018). Targeted elimination of mutant mitochondrial DNA in MELAS-iPSCs by mitoTALENs. Protein Cell *9*, 283–297.

Yim, A., Koti, P., Bonnard, A., Marchiano, F., Dürrbaum, M., Garcia-Perez, C., Villaveces, J., Gamal, S., Cardone, G., Perocchi, F., et al. (2020). mitoXplorer, a visual data mining platform to systematically analyze and visualize mitochondrial expression dynamics and mutations. Nucleic Acids Res. *48*, 605–632.

Yu, G., and He, Q.Y. (2016). ReactomePA: an R/Bioconductor package for reactome pathway analysis and visualization. Mol. Biosyst. *12*, 477–479.

Yu, G., Wang, L.G., Han, Y., and He, Q.Y. (2012). clusterProfiler: an R package for comparing biological themes among gene clusters. OMICS *16*, 284–287.

STAR★METHODS

KEY RESOURCES TABLE

REAGENT or RESOURCE	SOURCE	IDENTIFIER
Antibodies		
OCT3/4	BD Bioscience	Cat#561628, RRID: AB_10895977
SOX2	BD Bioscience	Cat#561610, RRID: AB_10712763
Mouse IgG1 κ Isotype Control	BD Bioscience	Cat#557782, RRID: AB_396870
Mouse IgG1, κ Isotype Control	BD Bioscience	Cat#560373, RRID: AB_1645606
SSEA4	eBioscience	Cat#12-8843-42, RRID: AB_11151520
OCT4	eBioscience	Cat#53-5841-82, RRID: AB_1210530
TRA-1-60	Stemgent	Cat#09-0068, RRID: AB_2233143
TOMM20	Abcam	Cat#ab78547 RRID: AB_2043078
dsDNA	Abcam	Cat#ab27156 RRID: AB_470907
Biological Samples		
LP351 Human PBMCs (PBMC1)	HemaCare	Donor ID: D326351
LP298 Human PBMCs (PBMC2)	HemaCare	Donor ID: D316153
Chemicals, Peptides, and Recombinant Proteins		
2',3'-dideoxycytidine	Sigma	D5782, CAS 7481-89-2
Dialyzed FBS	Life Technologies	Cat#26400-044
DMEM without glucose	GIBCO	Cat#11966025
Matrigel	Corning	Cat#356234
Lipofectamine RNAiMAX	ThermoFisher	Cat#13778100
mTeSR 1	StemCell Technologies	Cat#85850
Phusion high-fidelity PCR master mix with HF buffer	NEB	Cat#M0531S
Gentle Cell Dissociation Reagent	StemCell Technologies	Cat#07174
Accutase	BD Biosciences	Cat#561527
Hoechst 33342	ThermoFisher	Cat#R37605
Apa1	NEB BioLabs	Cat#R0114S
Critical Commercial Assays		
DNeasy Blood & Tissue kit	QIAGEN	Cat#69504
SYBR Select Master Mix for CFX	Life Technologies	Cat#4472942
Qproteome Mitochondria Isolation kit	QIAGEN	Cat#37612
StemRNA-NM Reprogramming kit		
ReproRNA-OKSGM	Stem Cell Technologies	Cat#05930
STEMCCA Constituitive Polycistronic (OKSM) Lentivirus Reprogramming kit	MilliporeSigma	Cat#SCR510
CytoTune-iPS 2.0 Sendai Reprogramming kit	Fisher Scientific	Cat#A16517
STEMdiff Mesenchymal Progenitor Kit	StemCell Technologies	Cat#05240
QIAGEN QIAQuick Gel Extraction kit	QIAGEN	Cat#28704
Fixation/Permeabilization Solution Kit with BD GolgiPlug	BD Bioscience	Cat#555028
Human MSC Analysis Kit	BD Bioscience	Cat#562245
V3 96-well plate	Agilent	Cat#101085-004
CD4+ T cell isolation kit	Miltenyi Biotec	Cat#130-096-533
Vybrant CFDA SE. Cell Tracer Kit	ThermoFisher	Cat#V12883

(Continued on next page)

Continued

REAGENT or RESOURCE	SOURCE	IDENTIFIER
Dynabeads Human T-activator CD3/CD28	ThermoFisher	Cat#11131D
MesenCult-ACF Basal Medium	StemCell Technologies	Cat#05449
MesenCult Adipogenic Differentiation Kit	StemCell Technologies	Cat#05412
MesenCult Osteogenic Differentiation medium	StemCell Technologies	Cat#05465
ACF Enzymatic Dissociation/Inhibition Solutions	StemCell Technologies	Cat#05426
MesenCult-ACF Chondrogenic Differentiation Medium	StemCell Technologies	Cat#05455
Y-27632	Stem Cell Technologies	Cat#72304
BCA protein assay	ThermoFisher	Cat#23225
CellROX Green Flow Cytometry Assay Kit	ThermoFisher	Cat#C10492
KAPA Stranded RNA-Seq Kit with Ribo-Erase	Kapa Biosystems, Roche	Cat#07962304001
Deposited Data		
RNaseq count matrices and raw reads	This paper	GEO: GSE115871
Metabolite relative amounts	This paper	N/A
Experimental Models: Cell Lines		
HEK293T	ATCC	Cat#CRL-3216
BJ Foreskin Fibroblast	ATCC	Cat#CRL-2522
Primary Dermal Fibroblast; Normal, Human, Adult	ATCC	Cat#PCS-201-012
Primary Dermal Fibroblast Normal; Human, Neonatal	ATCC	Cat#PCS-201-010
Leigh Syndrome ATP Synthase 6 (T8993G) Fibroblast	Coriell Institute	Cat#GM13411
Kearns-Sayre Syndrome (common deletion) Fibroblast	Coriell Institute	Cat#GM06225
MELAS (A3243G) Cybrid (CL3)	Gift from Douglas Wallace (Children's Hospital of Philadelphia Research Institute)	N/A
Wildtype Cybrid (CL9)	Gift from Douglas Wallace (Children's Hospital of Philadelphia Research Institute)	N/A
MELAS (A3243G) Cybrid	Gift from Carlos Moraes (University of Miami)	N/A
MERRF (A8344G) Cybrid	Gift from Carlos Moraes (University of Miami)	N/A
Δ Cytochrome B 3.0 Cybrid	Gift from Carlos Moraes (University of Miami)	N/A
L929 ρ0 Mouse Fibroblast	Gift from Jose Antonio Enriquez Dominguez (Centro Nacional de Investigaciones Cardiovasculares Carlos III (CNIC))	N/A
Oligonucleotides		
ND1 forward -CCCTA AAACCCGCCACATCT	IDT	N/A
ND1 reverse - CGAT GGTGAGAGCTAAGGTC	IDT	N/A
GAPDH Forward - TGCAC CACCAACTGCTTAGC	IDT	N/A
GAPDH Reverse - GGCA TGGACTGTGGTCATGAG	IDT	N/A
RPLP0 Forward -CGA CCTGGAAGTCCAACTAC	IDT	N/A

(*Continued on next page*)

Continued

REAGENT or RESOURCE	SOURCE	IDENTIFIER
RPLP0 Reverse -ATCT GCTGCATCTGCTTG	IDT	N/A
D Loop Forward - TTCCAA GGACAAATCAGAGAAAAAGT	IDT	N/A
D Loop Reverse - AGCC CGTCTAAACATTTTCAGTGTA	IDT	N/A
RFLP Forward - CCTC GGAGCAGAACCCAACCT	IDT	N/A
RFLP Reverse - CGAA GGGTTGTAGTAGCCCGT	IDT	N/A
Software and Algorithms		
FlowJo Software Version 10.4.2	FlowJo, LLC	N/A
Salmon v0.9.1	(Harrow et al., 2012; Mudge and Harrow, 2015; Patro et al., 2017)	https://github.com/COMBINE-lab/salmon/releases
Statistical Language R v3.6.0	(R Core Team, 2017)	https://www.r-project.org/
Bioconductor v3.9.0	(Huber et al., 2015)	https://bioconductor.org/news/bioc_3_3_release/
R Bioconductor package tximport v1.12.3	(Soneson et al., 2015)	https://support.bioconductor.org/p/106345/
R Bioconductor package DESeq2 v1.24.0	(Huber et al., 2015; Love et al., 2014)	https://bioconductor.org/packages/release/bioc/html/DESeq2.html
R package ggpubr v0.1.6	(Kassambara, 2017)	https://www.rdocumentation.org/packages/ggpubr/versions/0.1.6
R package pheatmap v1.0.12	(Warnes et al., 2016)	https://www.rdocumentation.org/packages/pheatmap/versions/1.0.8
R package gplots v3.0.1	(Kolde, 2015)	https://cran.r-project.org/web/packages/gplots/index.html
R package FactoMineR v2.2	(Husson, 2020)	https://www.rdocumentation.org/packages/FactoMineR/versions/1.34
R package factoextra v1.0.6	(Kassambara, 2019)	https://www.rdocumentation.org/packages/factoextra/versions/1.0.5
R Bioconductor package Mfuzz v2.38.0	(Kumar and Futschik, 2007)	https://bioc.ism.ac.jp/packages/3.6/bioc/html/Mfuzz.html
R package ggplot2 v3.2.0	(Wickham, 2019)	https://cran.r-project.org/web/packages/ggplot2/index.html
R Bioconductor package GSVA v1.32.0	(Hänzelmann et al., 2013)	https://anaconda.org/bioconda/bioconductor-gsva
R Bioconductor package limma v3.40.6	(Benjamini and Hochberg, 1995; Ritchie et al., 2015)	https://www.bioconductor.org/install/
R Bioconductor package clusterProfiler v3.12.0	(Yu and He, 2016)	https://bioconductor.org/packages/3.7/bioc/vignettes/clusterProfiler/inst/doc/clusterProfiler.html
R Bioconductor package ReactomePA v1.28.0	(Yu et al., 2012)	https://anaconda.org/bioconda/bioconductor-reactomepa
TraceFinder v3.3	ThermoFisher	Cat#OPTON-30493
MitoXplorer 1.0	(Yim et al., 2020)	http://mitoxplorer.ibdm.univ-mrs.fr

RESOURCE AVAILABILITY

Lead Contact

Further information and requests for resources and reagents should be directed to and will be fulfilled by the Lead Contact, Dr. Michael A. Teitell (mteitell@mednet.ucla.edu).

Materials Availability

All materials generated in this study are available upon reasonable request to the Lead Contact, Dr. Michael A. Teitell.

Data and Code Availability

All raw RNA-Seq reads, transcript abundance values, and processed gene count matrices are submitted to the NCBI Gene Expression Omnibus (GEO). The accession number for the RNA-seq reads reported in this paper is GEO: GSE115871. All other data are available upon request. All software used is available either commercially or as freeware. All custom code is available on GitHub at https://bitbucket.org/ahsanfasih/mitoDesigner/src/master/.

EXPERIMENT MODEL AND SUBJECT DETAILS

Cell Lines

HEK293T cells expressing mitochondria-targeted DsRed protein (pMitoDsRed, Clontech Laboratories) were made as previously described (Miyata et al., 2014). Primary, non-transformed human fibroblast sources include BJ (ATCC, Cat. # CRL-2522), ADF (ATCC, Cat. # PCS-201-012), and NDF (ATCC, Cat. # PCS-201-010). Isogenic cybrid cell lines derived from the same patient containing either the homoplasmic A3243G MELAS substitution or homoplasmic WT sequence were obtained from Douglas Wallace (Children's Hospital of Philadelphia Research Institute). An alternative A3243G MELAS cybrid cell line, in addition to A8344G MERRF and Δcytochrome B 3.0 cybrid cell lines, were from Carlos Moraes (University of Miami). Two primary A3243G MELAS fibroblast lines were from Anu Suomalainen Wartiovaara (University of Helsinki). Primary fibroblasts associated with Leigh Syndrome (T8993G, Cat. # GM13411) and Kearns Sayre Syndrome (common deletion, Cat. # GM06225) were obtained from the Coriell Repository.

BJ, NDF, ADF, and HEK293T-DsRed cells were grown at 37°C and 5% CO_2 in complete media containing DMEM (Corning, Cat. # 10013CV) supplemented with 10% Fetal Bovine Serum (FBS, Hyclone, Cat. # SH30088.03HI0), penicillin-streptomycin (Corning, Cat. # 30-002-CI), GlutaMax (ThermoFisher, Cat. # 35050-061), and non-essential amino acids (MEM NEAA, ThermoFisher, Cat. # 11-140-050). BJ ρ0, NDF ρ0, ADF ρ0, MELAS, MERRF, Δcytochrome B 3.0, Leigh Syndrome, and Kearns Sayre Syndrome cells were grown in complete media supplemented with 50 μg/ml uridine (Sigma, Cat. # U3003). iPSCs were grown on matrigel (Corning, Cat. # 356234) coated plates in mTeSR1 media (StemCell Technologies, Cat. # 85850) according to the manufacturer's protocol. MSCs were grown in defined, MesenCult-ACF media (StemCell Technologies, Cat. # 05449) following the manufacturer's protocol. Cells tested negative repeatedly for mycoplasma using a universal mycoplasma detection kit (ATCC, Cat. # 30-1012K).

Human Tissues

The following human tissues were used: PBMC1 (PBMCs from leukopak donor 351, Caucasian female, 42 year old, Donor ID: D326351, HemaCare Corp) and PBMC2 (PBMCs from leukopak donor 298, Hispanic/Latino male, 25 year old, Donor ID: D316153, HemaCare Corp).

METHOD DETAILS

mtDNA Depletion and qPCR Verification

A 1000x stock of ddC (Sigma, Cat. # D5782) was prepared in water and added to BJ, ADF, and NDF cells grown in complete media with 50 μg/ml uridine to an appropriate final concentration. Cells were passaged every 3-4 d with fresh ddC added over 3 weeks. Following ddC treatment, total DNA was extracted (QIAGEN, Cat. # 69504) and mtDNA quantified using SYBR Select Master Mix for CFX (Life Technologies, Cat. # 4472942). mtDNA-encoded *MT-ND1* was amplified with the following primers: forward: CCCTAAAACCCGCCACATCT; reverse: CGATGGTGAGAGCTAAGGTC. mtDNA levels were normalized to nucleus-encoded *GAPDH* using the following primers: forward: TGCACCACCAACTGCTTAGC; reverse: GGCATGGACTGTGGTCATGAG. RPLP0 served as an alternative nucleus-encoded gene for normalization using the following primers: forward: CGACCTGGAAGTCCAACTAC; reverse: ATCTGCTGCATCTGCTTG. qPCR was run on a BioRad CFX Thermal Cycler using the following protocol: 1) 50°C for 2 min, 2) 95°C for 2 min, and 3) 40 cycles at 95°C for 10 s and 60°C for 45 s. Samples were compared by calculating ΔΔCT and fold differences.

Mitochondrial Transfer into ρ0 Recipients

Mitochondria were harvested from HEK293T-DsRed cells, PBMCs (PBMC1 or PBMC2), or other cell types using a Qproteome Mitochondria Isolation Kit (QIAGEN, Cat. # 37612) following the manufacturer's protocol. Mitochondrial pellets were re-suspended in 1x PBS, pH 7.4, at 1 mg total protein/ml. Mitochondrial suspensions were delivered into ρ0 cells using MitoPunch.

The MitoPunch platform is a force-based mitochondrial transfer device. Briefly, a 5V solenoid (Sparkfun, Cat. # ROB-11015) is mounted on a threaded plug (Thor Labs, Cat. # SM1PL) and inserted into a threaded cage plate (Thor Labs, Cat. # CP02T). Above the solenoid, assembly rods (Thor Labs, Cat. # ER3) support an upper plate (Thor Labs, Cat. # CP02). The upper plate holds a custom machined aluminum washer (outer diameter, 25 mm; inner diameter, 10 mm) that supports a deformable PDMS (10:1 ratio of Part A base: Part B curing agent) fluid reservoir above the solenoid. The PDMS reservoir is composed of a bottom circular layer (25 mm diameter, 0.67 mm height) chemically bonded to an upper circular ring layer (outer diameter, 25 mm; inner diameter, 10 mm; height,

1.30 mm) and can hold approximately 120 μl of isolated mitochondrial suspension. Cells are seeded onto a porous membrane with 3 μm pores (Corning, Cat. # 353181) 24 h prior to mitochondrial transfer.

To perform mitochondrial transfer, this membrane with adherent cells is secured on top of the PDMS reservoir using an upper plate (Thor Labs, Cat. # CP02). The solenoid is controlled by a 5V power supply mini board (Futurlec, Cat. # MINIPOWER) and powered by a 12V, 3 Amp DC power supply (MEAN WELL, Cat. # RS-35-12). The activated solenoid strikes the center of the PDMS chamber, deforming the bottom circular layer by approximately 1.3 mm. This deformation rapidly injects the mitochondrial suspension through the membrane and into the monolayer cell culture on the opposite side. A tunable MitoPunch prototype was developed by NanoCav LLC with variable plunger force which improves SIMR generation efficiency especially in replication-limited fibroblasts.

As a comparison to MitoPunch, we performed isolated mitochondria coincubation control experiments. An equal number of co-incubation recipient cells were seeded alongside MitoPunch recipients in 12 well dishes instead of the porous membrane. After ~24 h, an equal volume of mitochondrial isolate as loaded into the PDMS reservoir for MitoPunch was pipetted into the cell medium of each coincubation recipient well and incubated at 37°C for 2 h before being released, collected, and plated on 10 cm dishes for selection as described below.

For human fibroblasts and mouse recipients, cells were grown in complete media with 50 μg/mL uridine for 4 d following mitochondria delivery and on day 5 post-delivery, cells were shifted to uridine-free complete media prepared with 10% dialyzed FBS (Life Technologies, Cat. # 26400-044). On day 8 post-delivery, cells were shifted to glucose-free, galactose-containing medium (DMEM without glucose, GIBCO, Cat. # 11966025) supplemented with 10% dialyzed FBS and 4.5 g/l galactose. Colonies emerged at approximately 10 d post-delivery and cells were shifted back to uridine-free medium before colonies were counted by microscopy or isolated using cloning rings. For human 143BTK– ρ0 recipients, cells were grown in complete media with 50 μg/mL uridine following mitochondria delivery and shifted to uridine-free complete media prepared with 10% dialyzed FBS on day 3 post-delivery, and clones emerged approximately 10 d post-delivery and were quantified.

Confocal microscopy

Cells, ~1x10^5, were plated on glass coverslips (Zeiss, Cat. # 474030-9000) in 6 well dishes in 2 mL of media and cultured for approximately 24 h. The media was aspirated and cells then fixed by incubation of 1 mL freshly diluted 4% paraformaldehyde (Thermo Fisher Scientific, Cat. # 28906) in 1x PBS, pH 7.4, for 15 min at RT. Paraformaldehyde was removed and cells were washed 3x with PBS, and then washed 3x with PBS with 5 min RT incubation during each wash. Cells were permeabilized by a 10 min RT incubation with 0.1% Triton X-100 (Sigma, Cat. # X100). Permeabilized cells were washed 3x with PBS and then blocked by incubation for 1 h at RT with 2% bovine serum albumin (BSA) dissolved in PBS. After blocking, cells were incubated with primary antibodies at 1:1000 dilution in 2% BSA blocking buffer against dsDNA (Abcam, Cat. # ab27156) and TOM20 (Abcam, Cat. # ab78547), and then washed 3x with 5 min RT incubation with PBS. After washing, cells were incubated for 1 h with secondary antibodies (Invitrogen, Cat. #'s A31573 and A21202) diluted 1:100 in 2% BSA blocking buffer protected from light at RT, and washed 3x with 5 min incubations with PBS. To mount coverslips on slides, samples were removed from the 6 well dish, dipped in deionized water, dried with a Kimwipe, and mounted using ProLong Gold Antifade Mountant with DAPI (Invitrogen, Cat. # P3691) on microscope slides (VWR, Cat. # 48311-601). Mounted samples were allowed to dry protected from light at RT for 48 h prior to imaging with a Leica SP8 confocal microscope.

Mitochondrial Oxygen Consumption Measurements

OCR was measured using a Seahorse XF96 Extracellular Flux Analyzer (Agilent). For fibroblasts or MSCs, 1 – 2 x10^5 cells per well were seeded onto a V3 96-well plate (Agilent, Cat. # 101085-004) and grown overnight before analysis. iPSCs were treated similarly but plated on matrigel-coated V3 plates. A mitochondrial stress test quantified OCR at basal respiration and after the sequential addition of mitochondrial inhibitors oligomycin, carbonyl cyanide-p-trifluoromethoxyphenylhydrazone (FCCP), and rotenone.

Mitochondrial Isolation from Mouse Tissues and Delivery

Spleen, liver, lung, bone marrow, heart, skeletal muscle, and kidney were harvested from an ~8 month-old female C57BL/6 mouse. Briefly, tissue was dissociated by passage through a cell strainer using the plunger of a syringe, and mitochondria were isolated from dissociated tissue using the Qproteome Mitochondria Isolation Kit (QIAGEN, Cat. # 37612) following the manufacturer's protocol. Mitochondrial suspensions were delivered into L929 ρ0 fibroblasts using MitoPunch. L929 ρ0 recipient cells were grown in complete media supplemented with 50 μg/mL uridine for 4 d following mitochondria delivery. On day 5 post-delivery, cells were shifted to uridine-free complete media prepared with 10% dialyzed FBS (Life Technologies, Cat. # 26400-044). On day 8 post-delivery, cells were shifted to glucose-free, galactose-containing medium (DMEM without glucose, GIBCO, Cat. # 11966025) supplemented with 10% dialyzed FBS and 4.5 g/l galactose. Colonies emerged at approximately 10 d post-delivery and cells were shifted back to uridine-free medium before colonies were counted by microscopy or isolated using cloning rings.

iPSC Reprogramming

Reprogramming of fibroblast lines to iPSCs was done using the StemRNA-NM Reprogramming kit (Stemgent, Cat. # 00-0076) following the manufacturer's protocol. Briefly, fibroblasts were plated on a matrigel (Corning, Cat. # 356234) coated 6-well plate at 2x10^5 cells/well on 0 d. Daily transfections of non-modified (NM)-RNA reprogramming cocktail were performed for 4 d using Lipofectamine RNAiMAX (ThermoFisher, Cat. # 13778100). On 10-12 d, iPSC colonies were identified by staining with TRA-1-60

antibody (Stemgent, Cat. # 09-0068). TRA-1-60$^+$ iPSC colonies were picked and re-plated on matrigel coated 12-well plates and maintained in mTeSR 1 medium (StemCell Technologies, Cat. # 85850). Alternative reprogramming strategies for fibroblasts included using ReproRNA-OKSGM (Stem Cell Technologies, Cat. # 05930), STEMCCA Lentiviral (MilliporeSigma, Cat. #SCR510), and CytoTune-iPS 2.0 Sendai (Fisher Scientific, Cat. # A16517) kits according to the manufacturers' protocols.

MSC Differentiation

MSC lines were generated from iPSCs using the STEMdiff Mesenchymal Progenitor Kit (StemCell Technologies, Cat. # 05240) following the manufacturer's protocol over the course of 21 d. Briefly, iPSCs were dispersed as single cells, plated at ~5 × 10^4 cells/cm^2, and cultured for 2 d on Matrigel with mTeSR1 medium before the medium was changed to STEMdiff -ACF Mesenchymal Induction Medium. STEMdiff -ACF Mesenchymal Induction Medium was changed daily for 3 d, and on day 4, the medium was changed to MesenCult -ACF Plus Medium. Cells were fed again with MesenCult -ACF Plus Medium on day 5. On day 6, cells were collected with Gentle Cell Dissociation Reagent (StemCell Technologies, Cat. # 07174) and passaged onto plastic plates with MesenCult -ACF Plus Medium with 10 μM ROCK inhibitor (Y-27632; Stem Cell Technologies, Cat. # 72304). Daily half-medium changes were made for ~1 week when cells were ~80% confluent. Cells were further passaged by dissociation with ACF Enzymatic Dissociation Solution and resuspended in MesenCult -ACF Plus Medium before further analysis.

Human mtDNA D-Loop Sequencing

Total DNA was extracted from 1x10^6 cells using the QIAGEN DNasy Blood and Tissue kit. PCR was performed using Phusion high-fidelity PCR master mix with HF buffer (NEB, Cat. # M0531S) and the following primers: forward – TTCCAAGGACAAATCAGAGAAAAAGT, reverse – AGCCCGTCTAAACATTTTCAGTGTA. PCR was run on an Eppendorf vapo.protect thermal cycler at 1) 98°C for 2 min, 2) 30 cycles at 98°C for 15 s, 58°C for 30 s, 72°C for 30 s, and 3) 72°C for 5 min. PCR products were run on a 0.8%–1% agarose TAE gel, extracted with the QIAGEN QIAQuick Gel Extraction kit (QIAGEN, Cat. # 28704), and Sanger sequenced using the same PCR primers.

ROS Quantification

CellROX Green Flow Cytometry Assay Kit (ThermoFisher, Cat. # C10492) was used according to the manufacturer's protocol. Briefly, 7.5x10^4 cells were plated in a 6-well plate ~24 h prior to measurements. 250 μM tert butyl hydroperoxide (TBHP) and 750 μM CellROX reagent were added to the cells ~2 h and 1 h prior to quantification, respectively. Cells were released using Accutase, washed once with FACS buffer (5% FBS in 1x DPBS, pH 7.4), and quantified using a LSRFortessa flow cytometer (BD Bioscience).

iPSC Flow Cytometry

iPSCs were harvested by 15 min RT incubation with Gentle Cell Dissociation Reagent. Cells were centrifuged at 300 x g for 5 min, washed in 1ml DPBS + 10% FBS, and re-suspended in 100 μL BD Perm/Fix Buffer (BD Bioscience). Cells were incubated at 4°C for 15 min and washed twice in DPBS + 10% FBS. Following the second wash, cells were incubated in 50μl DPBS + 10% FBS containing conjugated antibodies. Antibodies used were OCT3/4 AlexaFluor488 (BD Bioscience 561628 1:10), SOX2 V450 (BD Bioscience 561610 1:10), Mouse IgG1 κ Isotype Control AlexaFluor488 (BD Biosciences 557782 1:10), Mouse IgG1, κ Isotype Control V450 (BD Bioscience 560373 1:10), and CD44 PE (BD Bioscience 562245 1:21). Cells were incubated with conjugated antibodies for 30 min and then washed twice in DPBS + 10% FBS. Data was acquired on a LSRFortessa flow cytometer (BD Bioscience) and analyzed using FlowJo software (FlowJo, LLC).

MSC Flow Cytometry

MSCs were harvested by 5 min, 37°C incubation with Accutase (BD Biosciences). Cells were centrifuged at 300 x g for 5 min, washed in 1ml DPBS + 10% FBS, and re-suspended in DPBS + 10% FBS at 5x10^6 cells/ml. Cells were incubated in 100μl DPBS + 10% FBS for 30 min at 4°C with the antibodies provided in the Human MSC Analysis Kit (BD Biosciences, Cat. # 562245) for 30 min and then washed twice in DPBS + 10% FBS. Data was acquired on a LSRFortessa flow cytometer (BD Bioscience) and analyzed using FlowJo software (FlowJo, LLC).

Fluorescence Microscopy

iPSCs were cultured on matrigel-coated 6-well plates and fixed with 4% paraformaldehyde for 10 min. Blocking was done for 1 h in 1x PBS, pH 7.4, with 5% FBS and 0.3% Triton X-100. Cells were stained with SSEA4 (eBioscience, Cat. # 12-8843-42) and OCT4 (eBioscience, Cat. # 53-5841-82) antibodies, and Hoechst 33342 dye (ThermoFisher, Cat. # R37605) overnight at 4°C in blocking buffer. Phase contrast and fluorescence images were obtained with a Zeiss Axio Observer Z1 microscope and Hamamatsu EM CCD camera (Cat. # C9100-02).

MSC Immunosuppression Assay

MSC inhibition of T cell proliferation was performed as described previously (Hsu et al., 2015). Briefly, MSCs were plated in a 12-well plate the day before assay. PBMCs were isolated by Ficoll gradient from a healthy de-identified leukopak donor. CD4$^+$ T cells were isolated from PBMCs using the CD4$^+$ T cell Isolation Kit (Miltenyi Biotec, Cat. # 130-096-533) and labeled with CFDA SE

(ThermoFisher, Cat. #V12883). Labeled $CD4^+$ T cells were stimulated with Dynabeads Human T-activator CD3/CD28 (ThermoFisher, Cat. # 11131D) at a ratio of one bead per T cell. T cells were added into MSC cultures at the following T cell:MSC ratios: 1:2, 1:1, 5:1, and 10:1. After 5 d of co-culture, T cell proliferation was measured using CFSE signature dye dilution by flow cytometry.

Tri-lineage Differentiation

Adipocytes, osteoblasts, and chondrocytes were generated from MSCs. For adipocyte differentiation, MSCs between passages 3 – 4 were plated on 6-well plates with MesenCult-ACF Basal Medium (StemCell Technologies, Cat. # 05449) at $4 – 5 \times 10^5$ cells per well. Differentiation was performed using the MesenCult Adipogenic Differentiation Kit (StemCell Technologies, Cat. # 05412) according to the manufacturer's protocol. Media changes were done every 3 – 4 d until 13 d. For osteogenic lineage differentiation, MSCs between passages 3 – 4 were plated on a 6-well plate with MesenCult-ACF Basal Medium (StemCell Technologies) at $3 – 4 \times 10^4$ cells per well. Differentiation was performed using MesenCult Osteogenic Differentiation medium (StemCell Technologies, Cat. # 05465) according to the manufacturer's protocol. Medium changes were done every 3 – 4 d until 13 d. For 3-D pellet chondrogenic differentiation, MSCs were first released from T25 flasks using ACF Enzymatic Dissociation/Inhibition Solution (StemCell Technologies, Cat. # 05426) and collected in polypropylene tubes at $2.5 – 3 \times 10^6$ cells per tube with MesenCult-ACF Chondrogenic Differentiation Medium (StemCell Technologies, Cat. # 05455) according to the manufacturer's protocol. Medium changes were done every 3 – 4 days until 13 d.

Tri-lineage Differentiation Analyses

Osteogenic differentiation was assayed by staining cells with 1% Alizarin Red solution. Medium was removed from cells grown on 6-well plates and cells were washed 3 times with 1X DPBS. Cells were fixed in 4% PFA in 1X DPBS at 4°C for 15 min prior to 15 min incubation with 1% alizarin red at RT. Alizarin red solution was aspirated and the cells were imaged using a standard inverted microscope.

Adipogenic differentiation was assayed by staining cells with 0.1% Bodipy solution. Medium was removed from cells grown on 6-well plates and cells were washed 3x with 1X DPBS. Cells were fixed in 4% PFA in 1X DPBS at 4°C for 15 min and washed twice with 1X DPBS prior to a 10 min incubation with 0.1% Bodipy at RT. Bodipy solution was aspirated and the cells were washed with 1X DPBS prior to acquiring phase contrast and fluorescence images with a Zeiss Axio Observer Z1 microscope and Hamamatsu EM CCD camera (Cat. # C9100-02).

Chondrocyte differentiation was assayed by staining chondrogenic spheroids and spheroid sections with 0.1% Safranin O solution. For staining whole spheroids, the medium was removed from the spheroids and they were fixed in 4% PFA for 15 min at RT. The spheroids were washed twice with 1x PBS, pH 7.4, before 15 min incubation with 0.1% Safranin O solution at RT. The stained spheroids were washed twice with 1ml water and transferred by serological pipette to a 48-well dish for imaging. For spheroid section staining, spheroids were fixed in 10% formalin for 18 h, washed twice in water, and placed in 70% ethanol. Spheroids were microtome sectioned by the UCLA Translational Pathology Core Laboratory, tissue placed on microscope slides. Sections were deparaffinized and rehydrated by washes in xylenes, ethanol, and water. Unstained sections were stained with hematoxylin and eosin or 0.1% Safranin O for 10 min at RT prior to washing in ethanol. Sections were imaged under a standard inverted microscope.

UPHLC-MS Metabolomics Processing

Ultra-high-performance liquid chromatography mass spectrometry (UHLPC-MS) was performed as described previously (Xiao et al., 2018) to quantify metabolites from ~$7x10^5$ cells. Briefly, cells were rinsed with cold 150 mM ammonium acetate, pH 7.3, followed by addition of ice-cold 80% methanol. Cells were detached with scrapers, transferred into microcentrifuge tubes, and 1 nmol D/L-norvaline added. After vortexing, the suspension was centrifuged at 4°C at maximum speed. The supernatant was transferred into a glass vial, metabolites dried down under vacuum using an EZ-2Elite evaporator at 30°C, and re-suspended in 70% acetonitrile. To normalize samples, pellets were re-suspended in 58 mM Tris-HCl, pH 6.8, 5% glycerol, and 17 mg/ml sodium dodecyl sulfate and quantified by BCA protein assay (ThermoFisher, Cat. # 23225).

Metabolites were separated on a Luna NH2 (150 mm x 2 mm, Phenomenex) column using 5 mM NH_4AcO, pH 9.9 (buffer A), acetonitrile (buffer B), and the following gradient: initially at 15% buffer B, 18 min gradient to 90% buffer B, 9 min isocratic at 90% buffer B, 7 min isocratic at 15% buffer B. Samples were analyzed with an UltiMate 3000RSLC (Thermo Scientific) coupled to a Q Exactive mass spectrometer (Thermo Scientific) run with polarity switching (+3.50 kV / −3.50 kV) in full scan mode and m/z range of 65-975. Metabolites were quantified with TraceFinder 3.3 using accurate mass measurements ($\leq$3 ppm) and retention times of pure standards.

RNA Extraction

Fibroblasts, iPSCs, and MSCs were grown in biological triplicates and technical duplicates to 70 – 80% confluence and purified using the RNeasy Mini Kit (QIAGEN, Cat. # 74104) and RNase-free DNase (QIAGEN, Cat. # 79254) following the manufacturer's protocols. All samples showed a A260/280 ratio > 1.99 (Nanodrop; Thermo Scientific). Prior to library preparation, quality control of the RNA was performed using the Advanced Analytical Technologies Fragment Analyzer (Advanced Analytical, Inc.) and analyzed using PROSize 2.0.0.51 software. RNA Quality Numbers (RQNs) were computed per sample between 8.1 and 10, indicating intact total RNA per sample prior to library preparation.

RNA-Seq Library Preparation

Strand-specific ribosomal RNA (rRNA) depleted RNA-Seq libraries were prepared from 1 μg of total RNA using the KAPA Stranded RNA-Seq Kit with Ribo-Erase (Kapa Biosystems, Roche). Briefly, rRNA was depleted from total RNA samples, the remaining RNA was heat fragmented, and strand-specific cDNA was synthesized using a first strand random priming and second strand dUTP incorporation approach. Fragments were then A-tailed, adapters were ligated, and libraries were amplified using high-fidelity PCR. All libraries were prepared in technical duplicates per sample (n = 60 samples, 120 libraries total), and resulting raw sequencing reads merged for downstream alignment and analysis. Libraries were paired-end sequenced at 2x150 bp on an Illumina NovaSeq 6000.

Restriction-Fragment Length Polymorphism Heteroplasmy Assay

To quantify relative levels of mtDNA containing the A3243G substitution, total DNA was isolated from cells using the DNeasy Blood and Tissue kit (QIAGEN, Cat. # 69504). PCR amplification of the MELAS region to generate a 634 bp product was performed using the following primers: forward – CCTCGGAGCAGAACCCAACCT and reverse – CGAAGGGTTGTAGTAGCCCGT. ApaI digestion (NEB Biolabs, Cat. # R0114S) of the PCR product was performed according to manufacturer's protocol for 2 h at 25°C, and deactivated at 65°C for 20 min. Sample was separated on a 2.5% agarose gel at 100V for 1 h.

QUANTIFICATION AND STATISTICAL ANALYSIS

mtDNA Depletion and qPCR Verification

Statistical details are provided in each figure legend.

Mitochondrial Oxygen Consumption Rate Measurements

Statistical details are provided in each figure legend.

Metabolomics Data Analysis

Data analysis, including principal components analysis (PCA) and clustering, was performed using the statistical language R v3.6.0 and Bioconductor v3.9.0 packages (Huber et al., 2015; R Core Team, 2017). Metabolite abundance was normalized per μg of protein content per metabolite extraction, and metabolites not detected were set to zero. Metabolite normalized amounts were log transformed and then scaled and centered into Z-scores for relative comparison using R base function *scale()* with parameters *"scale = TRUE, center = TRUE"*. Heatmaps and Euclidean distance similarity plots were created using the Z-scores in R package pheatmap v1.0.12, and hierarchical clustering was performed using the Euclidean distance measure.

PCA was performed using R packages FactoMineR v2.2 and factoextra v1.0.6. PC scores computed from normalized metabolite counts with function *PCA()* using parameters *"scale.unit = TRUE, ncp = 10, graph = FALSE"*.

Pathway-level metabolite set enrichment analysis was performed using R Bioconductor package GSVA v1.32.0 (Hänzelmann et al., 2013). Metabolite normalized abundances were standardized using a log2(normalized amounts + 1) transformation, and metabolites per sample were converted to a pathways per sample matrix using function *gsva()* with parameters *"method = gsva, maseq = FALSE, abs.ranking = FALSE, min.sz = 5, max.sz = 500"*. GSVA pathway enrichment scores were then extracted and significance testing for multiple transfer conditions was calculated using R Bioconductor package limma v3.40.6, as described above. Pathway metabolite sets were constructed using the KEGG Compound Database and derived from the existing Metabolite Pathway Enrichment Analysis (MPEA) toolbox (Kanehisa et al., 2012; Kankainen et al., 2011).

RNA-Seq Pre-Processing

Fibroblasts, iPSCs, and MSCs were each sequenced in biological triplicates and technical duplicates (n = 60 total samples) to account for variation in extraction and culturing. Raw sequencing reads were converted into fastq files and filtered for low quality reads and Illumina sequencing adaptor contamination using bcl2fastq (Illumina). Reads were then quasi-mapped and quantified to the *Homo sapiens* GENCODE 28 (GRCh38.p12, Ensembl 92, April 2018) transcriptome using the alignment-free transcript level quantifier Salmon v0.9.1 (Harrow et al., 2012; Mudge and Harrow, 2015; Patro et al., 2017). A quasi-mapping index was prepared using parameters *"salmon index -k 31 –type quasi"*, and comprehensive transcript level estimates were calculated using parameters *"salmon quant -l A –seqBias –gcBias–discardOrphansQuasi"*. Transcript level counts were collapsed to gene level (HGNC) counts, transcripts per million abundances (TPM) and estimated lengths using R Bioconductor package tximport v1.12.3 (Soneson et al., 2015).

Differential Gene Expression Analysis

The resulting sample gene count matrix was size factor normalized and analyzed for pairwise differential gene expression using R Bioconductor package DESeq2 v1.18.1. Expression changes were estimated using an empirical Bayes procedure to generate moderated fold change values with design "~ Batch + Sample," modeling batch effect variation due to day of RNA extraction (Huber et al., 2015; Love et al., 2014). Significance testing was performed using the Wald test, and resulting *P values* were adjusted for multiple testing using the Benjamini-Hochberg procedure (Benjamini and Hochberg, 1995). DEGs were filtered using an adjusted false discovery rate (FDR) q value < 0.05 and an absolute $\log_2$ transformed fold-change > 0.05.

MitoXplorer Analysis

Differential expression analysis was performed using DESeq2, specifying an absolute log2 transformed fold change threshold > 0.5. Result lists including all genes were uploaded to the MitoXplorer 1.0 pipeline (http://mitoxplorer.ibdm.univ-mrs.fr/index.php) comparing SIMR-fibroblasts, -iPSCs, or -MSCs to the corresponding cell fate of the BJ control. DEGs were filtered using a $\log_2$ transformed fold-change threshold of 0.05. Subsequently, the number of upregulated and downregulated DEGs for each mitochondrial process were counted.

Gene Expression PCA and hierarchal clustering

Variance stabilized transform (VST) values in the gene count matrix were calculated and plotted for PCA using R Bioconductor packages DESeq2, FactoMineR, and factoextra, as described in the metabolomics methods (Huber et al., 2015; Love et al., 2014). For PCA of nucleus-encoded mitochondrial protein and mtDNA transcripts, relevant transcripts were extracted using localization evidence derived from MitoMiner v4.0, subsetting VST matrices using genes listed in MitoCarta 2.0 (Calvo et al., 2016; Smith and Robinson, 2016). Clonal heatmaps were prepared using R Bioconductor packages pheatmap v1.0.8 and gplots v3.0.1 (Warnes et al., 2016; Kolde, 2015). Heirarchal clustering was performed using R based function hclust and plotted using the dendextend package.

Metabolic Transcript Gene Set Variation Analysis (GSVA)

GSVA on metabolic transcripts was performed similarly to metabolomics data as noted above. Pathway-level metabolic gene set enrichment analysis was performed using R Bioconductor package GSVA v1.32.0 function *gsva()* with parameters *"method = gsva, rnaseq = FALSE, abs.ranking = FALSE, min.sz = 5, max.sz = 500"* using a $\log_2$(TPM + 1) transformed gene expression matrix (Hänzelmann et al., 2013). GSVA pathway enrichment scores per sample were extracted and assessed for significance using R Bioconductor package limma v3.40.0, as described above except with a Benjamini-Hochberg adjusted *P value* threshold = 0.01. Pathway metabolite sets were constructed using the KEGG PATHWAY Database, utilizing gene sets annotated to the metabolic pathways overview map HSA01100 (Kanehisa et al., 2012). Significance testing across clones and conditions for each gene set were calculated using Kruskal-Wallis ANOVA.

Gene Set Overrepresentation Analysis (ORA)

DEGs were extracted and analyzed for pathway/gene ontology (GO) term overrepresentation using the R Bioconductor package clusterProfiler v3.12.0 and ReactomePA v1.28.0, using a background gene set of all genes expressed with at least one read count in the sample gene count matrix (Yu and He, 2016; Yu et al., 2012). Overrepresented Reactome/KEGG pathways and GO terms were identified across DEG lists and conditions using clusterProfiler function *compareCluster()* with significance testing cutoffs of $p < 0.05$, and an adjusted FDR < 0.25.

HLA Class I Genotyping

MHC Class I HLA genotypes were identified using OptiType v1.3.1 (Szolek et al., 2014). All raw RNA-Seq sample FASTQs were aligned to the HLA Class I reference transcriptome packaged in OptiType using BWA MEM v0.7.17 with standard parameters (Li and Durbin, 2010). HLA subset reads were then analyzed for Class I genotype using OptiType in paired-end RNA mode with standard parameters.

Cell Reports, Volume *33*

Supplemental Information

Pressure-Driven Mitochondrial Transfer Pipeline Generates Mammalian Cells of Desired Genetic Combinations and Fates

Alexander N. Patananan, Alexander J. Sercel, Ting-Hsiang Wu, Fasih M. Ahsan, Alejandro Torres Jr., Stephanie A.L. Kennedy, Amy Vandiver, Amanda J. Collier, Artin Mehrabi, Jon Van Lew, Lise Zakin, Noe Rodriguez, Marcos Sixto, Wael Tadros, Adam Lazar, Peter A. Sieling, Thang L. Nguyen, Emma R. Dawson, Daniel Braas, Justin Golovato, Luis Cisneros, Charles Vaske, Kathrin Plath, Shahrooz Rabizadeh, Kayvan R. Niazi, Pei-Yu Chiou, and Michael A. Teitell

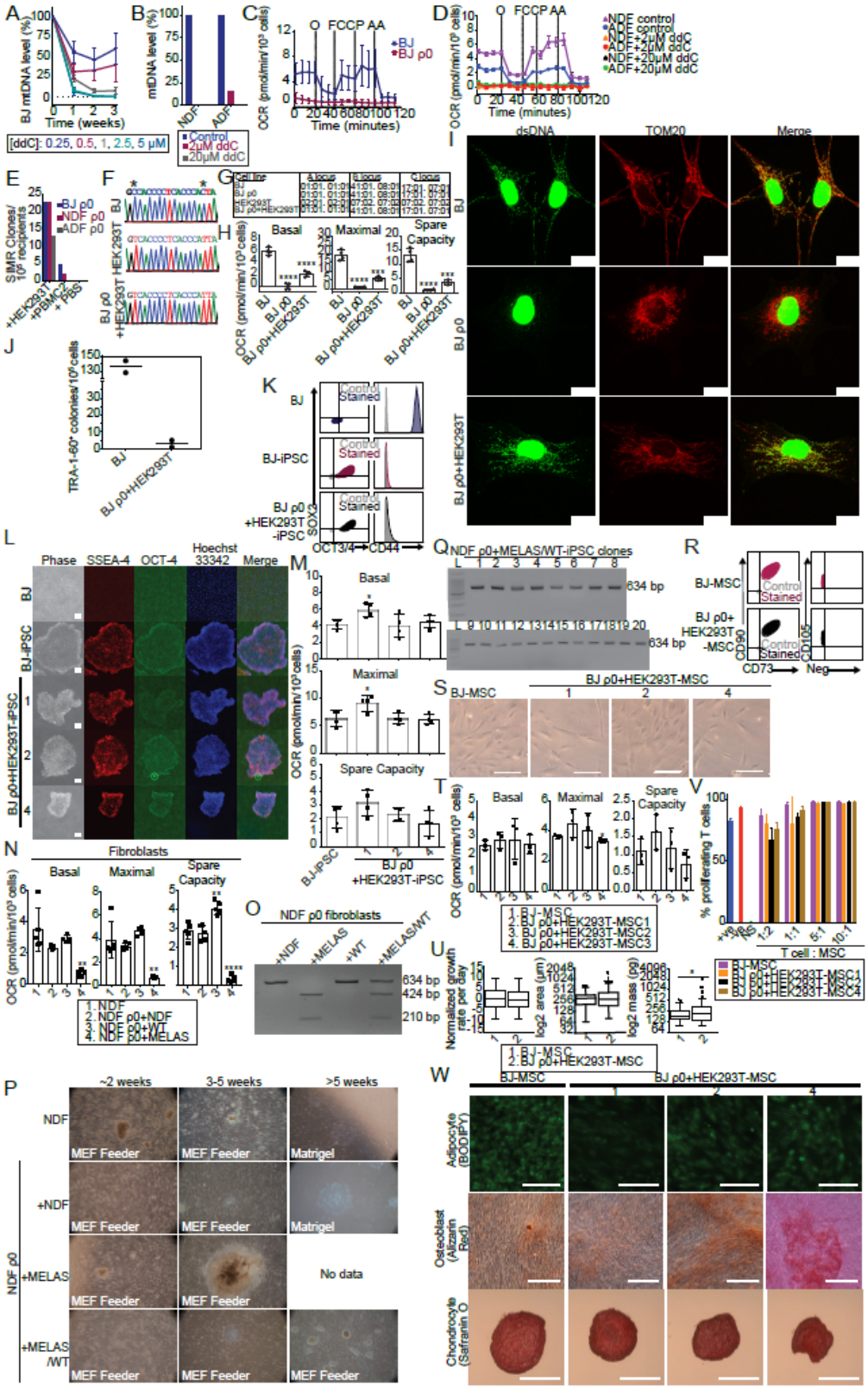
A
BJ mtDNA level (%)
Time (weeks)
[ddC]: 0.25, 0.5, 1, 2.5, 5 μM
B
mtDNA level (%)
NDF
ADF
Control
2μM ddC
20μM ddC
C
OCR (pmol/min/10³ cells)
O FCCP AA
BJ
BJ ρ0
Time (minutes)
D
OCR (pmol/min/10³ cells)
O FCCP AA
NDF control
ADF control
ADF+2μM ddC
ADF+2μM ddC
NDF+20μM ddC
ADF+20μM ddC
Time (minutes)
E
SMR Clones/ 10⁶ recipients
BJ ρ0
NDF ρ0
ADF ρ0
+HEK293T
+PBMC-2
+ PBS
F
BJ
HEK293T
BJ ρ0 +HEK293T
G
Cell line
A locus
B locus
C locus
BJ
BJ ρ0
HEK293T
BJ ρ0+HEK293T
H
Basal
Maximal
Spare Capacity
OCR (pmol/min/10³ cells)
BJ
BJ ρ0
BJ ρ0+HEK293T
I
dsDNA
TOM20
Merge
BJ
BJ ρ0
BJ ρ0+HEK293T
J
TRA-1-60⁺ colonies/10⁶ cells
BJ
BJ ρ0+HEK293T
K
BJ
BJ-iPSC
BJ ρ0 +HEK293T -iPSC
Control
Stained
SOX2
OCT3/4
CD44
L
Phase
SSEA-4
OCT-4
Hoechst 33342
Merge
BJ
BJ-iPSC
BJ ρ0HEK293T-iPSC
1
2
4
M
Basal
Maximal
Spare Capacity
OCR (pmol/min/10³ cells)
BJ-iPSC
BJ ρ0 +HEK293T-iPSC
N
Fibroblasts
Basal
Maximal
Spare Capacity
OCR (pmol/min/10³ cells)
1: NDF
2: NDF ρ0+NDF
3: NDF ρ0+WT
4: NDF ρ0+MELAS
O
NDF ρ0 fibroblasts
+NDF
+MELAS
+WT
+MELAS/WT
634 bp
424 bp
210 bp
Q
NDF ρ0+MELAS/WT-iPSC clones
L 1 2 3 4 5 6 7 8
634 bp
L 9 10 11 12 13 14 15 16 17 18 19 20
634 bp
R
BJ-MSC
BJ ρ0+HEK293T-MSC
Control
Stained
CD90
CD105
CD73
Neg
S
BJ-MSC
BJ ρ0+HEK293T-MSC
1
2
4
T
Basal
Maximal
Spare Capacity
OCR (pmol/min/10³ cells)
1: BJ-MSC
2: BJ ρ0+HEK293T-MSC1
3: BJ ρ0+HEK293T-MSC2
4: BJ ρ0+HEK293T-MSC3
U
Normalized growth rate per day
log2 area (μm²)
log2 mass (pg)
1: BJ-MSC
2: BJ ρ0+HEK293T-MSC
BJ-MSC
BJ ρ0+HEK293T-MSC1
BJ ρ0+HEK293T-MSC2
BJ ρ0+HEK293T-MSC4
V
% proliferating T cells
+VE
-VE
1:2
1:1
5:1
10:1
T cell : MSC
P
~2 weeks
3-5 weeks
>5 weeks
NDF
+NDF
+MELAS
+MELAS /WT
NDF ρ0
MEF Feeder
Matrigel
No data
W
BJ-MSC
BJ ρ0+HEK293T-MSC
1
2
4
Adipocyte (BODIPY)
Osteoblast (Alizarin Red)
Chondrocyte (Safranin O)

Figure S1. The MitoPunch Pipeline Generates Functional Cells with Unique mtDNA-nDNA Pairings, Related to Figures 1, 2, 3, and 4.

(A) Native BJ fibroblasts were exposed to the indicated doses of ddC for three weeks. mtDNA levels were quantified by qPCR using primers for MT-ND1 and normalized to GAPDH. Data are the mean ± SD of three independent biological replicates.

(B) Native ADF and NDF cells were exposed to the indicated doses of ddC for three weeks. mtDNA levels were quantified by qPCR using primers for MT-ND1 and normalized to RPLP0. Data represents the mean of three technical replicates.

(C) OCR measurements for ~$2.0x10^4$ native BJ and BJ ρ0 fibroblasts. Agents injected were oligomycin (O), Carbonyl cyanide-p-trifluoromethoxyphenylhydrazone (FCCP), and antimycin A (AA) at the indicated time points. Data are the mean ± SD of five technical replicates.

(D) OCR measurements for $1.5 – 2.0x10^4$ NDF, ADF, NDF ρ0, and ADF ρ0 (by exposure to the indicated amounts of ddC) fibroblasts. Data are the mean ± SD of four technical replicates.

(E) Mitochondria from HEK293T cells and from ~$3x10^7$ peripheral blood mononuclear cells (PBMC2) were MitoPunch transferred into BJ ρ0, NDF ρ0, or ADF ρ0 recipient fibroblasts. Following selection, SIMR colonies were stained with crystal violet and quantified. Clone counts from a single representative mitochondria transfer into ~$1x10^5$ recipient ρ0 fibroblasts are shown.

(F) D-loop hypervariable region mtDNA sequences from native BJ, HEK293T cell, and BJ ρ0+PBMC2 SIMR fibroblasts. Stars denote single nucleotide polymorphisms.

(G) MHC Class I HLA A, B, and C locus genotyping using OptiType v1.3.1 for native BJ, BJ ρ0, HEK293T, and BJ ρ0+HEK293T SIMR cells.

(H) OCR measurements for ~$1.5x10^4$ native BJ, BJ ρ0, and BJ ρ0+HEK293T SIMR fibroblasts. Data are the mean ± SD of four technical replicates. Statistical significance for by unpaired, two-tailed Student's t test. ***$p \leq 0.001$; ****$p \leq 0.0001$

(I) Representative images of native BJ, BJ ρ0, and BJ ρ0+HEK293T SIMR fibroblasts immunostained for dsDNA (green) and TOM20 (red) with co-localization indicated (yellow). Images (100X) acquired on a Leica SP8 confocal microscope. Scale bars are 15 µm.

(J) Native BJ and BJ SIMR fibroblasts reprogrammed to iPSCs with TRA-1-60$^+$ clones counted by microscopy. Data is the mean of biological duplicates. BJ fibroblast control shows the same data used in Figure 3A.

(K) Flow cytometry of pluripotency biomarkers SOX2 and OCT3/4, and fibroblast biomarker CD44. Immunostained samples are shown in color with isotype negative controls in grey. Representative data for native BJ fibroblasts and BJ-iPSCs, and for BJ ρ0+HEK293T-iPSC cells. The native BJ fibroblast and BJ-iPSC data shown here is the same as in Figure 3B.

(L) Representative phase contrast and IF microscopy images of unmodified BJ fibroblast (negative control), BJ-iPSCs (positive control), and three BJ ρ0+HEK293T-iPSC clones immunostained for pluripotency biomarkers SSEA-4 and OCT4. Scale bar is 100 µm.

(M) OCR measurements for ~$1.5x10^4$ native BJ-iPSCs and BJ ρ0+HEK293T-iPSC clones 1, 2, and 4. BJ-iPSC control shows the same data used in Figure 3D. Data are the mean ± SD of four technical replicates. Statistical significance was by unpaired, two-tailed Student's t test. *$p \leq 0.05$

(N) OCR measurements for ~$1.5x10^4$ native NDF, NDF ρ0+NDF, NDF ρ0+WT, and NDF ρ0+MELAS SIMR fibroblasts. Data are the mean ± SD of five technical replicates.
Statistical significance was by unpaired, two-tailed Student's t test. **$p \leq 0.01$; ****$p \leq 0.0001$

(O) RFLP analysis of mtDNA from homoplasmic NDF ρ0+NDF, NDF ρ0+MELAS, and NDF ρ0+WT SIMR fibroblasts, and 1:1 heteroplasmic NDF ρ0+MELAS/WT SIMR fibroblasts. ApaI restriction enzyme cleaves the 634 bp amplicon into 424 bp and 210 bp bands when the MELAS A3243G sequence is present.

(P) Representative phase contrast images (4X) of native NDF, NDF ρ0+NDF, NDF ρ0+MELAS, and NDF ρ0+MELAS/WT cells during reprogramming to iPSCs. Exposure and tint adjusted for subpanel consistency.

(Q) RFLP analysis of mtDNA from 20 independent, 1:1 heteroplasmic NDF ρ0+MELAS/WT-iPSC clones. ApaI restriction enzyme cleaves the 634 bp amplicon into 424 bp and 210 bp bands when the MELAS A3243G sequence is present.

(R) Flow cytometry of MSC biomarkers CD73, CD90, CD105, and a mix of negative MSC biomarkers. Immunostained samples are shown in color with isotype negative controls in grey. BJ-MSC control shows the same data used in Figure 4A. Representative clones for native BJ-MSCs and BJ ρ0+HEK293T-MSCs are shown.

(S) Brightfield microscopy showing native BJ-MSC, BJ ρ0+HEK293T-MSC clones 1, 2, and 4 adhering to plastic at 20X (scale bar, 100 µm) magnifications. BJ-MSC control shows the same data used in Figure 4B.

(T) OCR measurements for ~$1.5x10^4$ native BJ-MSCs and BJ ρ0+HEK293T-MSC clones 1, 2, and 4. BJ-MSC control shows the same data used in Figure 4C. Data are the mean ± SD of three technical replicates. Statistical significance was by unpaired, two-tailed Student's t test. *$p \leq 0.05$
(U) Quantitative phase microscopy of unmodified BJ-MSCs and a 1:1:1 mix of BJ ρ0+HEK293T-MSC clones 1, 2, and 4. BJ-MSC control shows the same data used in Figure 4D. Shown are box-and-whisker Tukey plots with outliers identified. Data was averaged from 77 and 124 cells for native BJ-MSCs and BJ ρ0+HEK293T-MSCs, respectively. Statistical significance was by Welch's T test. *$p \leq 0.05$
(V) T cells were added into native BJ-MSC or BJ ρ0+HEK293T-MSC clone 1, 2, or 4 cultures at 1:2, 1:1, 5:1, and 10:1 T cell: MSC ratios. After 5 days of co-culture, T cell proliferation was measured using a CFSE dye dilution assay by flow cytometry. The data labeled "NS" (no stimulus) denotes T cells without CD3/CD28 bead activation. The data labeled "-ve" (negative) denotes no addition of MSCs to stimulated T cells. The data labeled "+ve" (positive) denotes a 1:1 addition of MDSCs to T cells. Data are the mean ± SD of three technical replicates.
(W) Tri-lineage differentiation of native BJ-MSCs and BJ ρ0+HEK293T-MSC clones 1, 2, and 4. Representative sections were fixed and stained with 1 μM Bodipy 493/503, 1% alizarin red S, and 0.1% Safranin O, respectively. Shown are adipocytes (first row 20X; scale bar 100 μm), osteocytes (second row 20X; 200 μm), and chondrocytes (third row 5X; 500 μm).

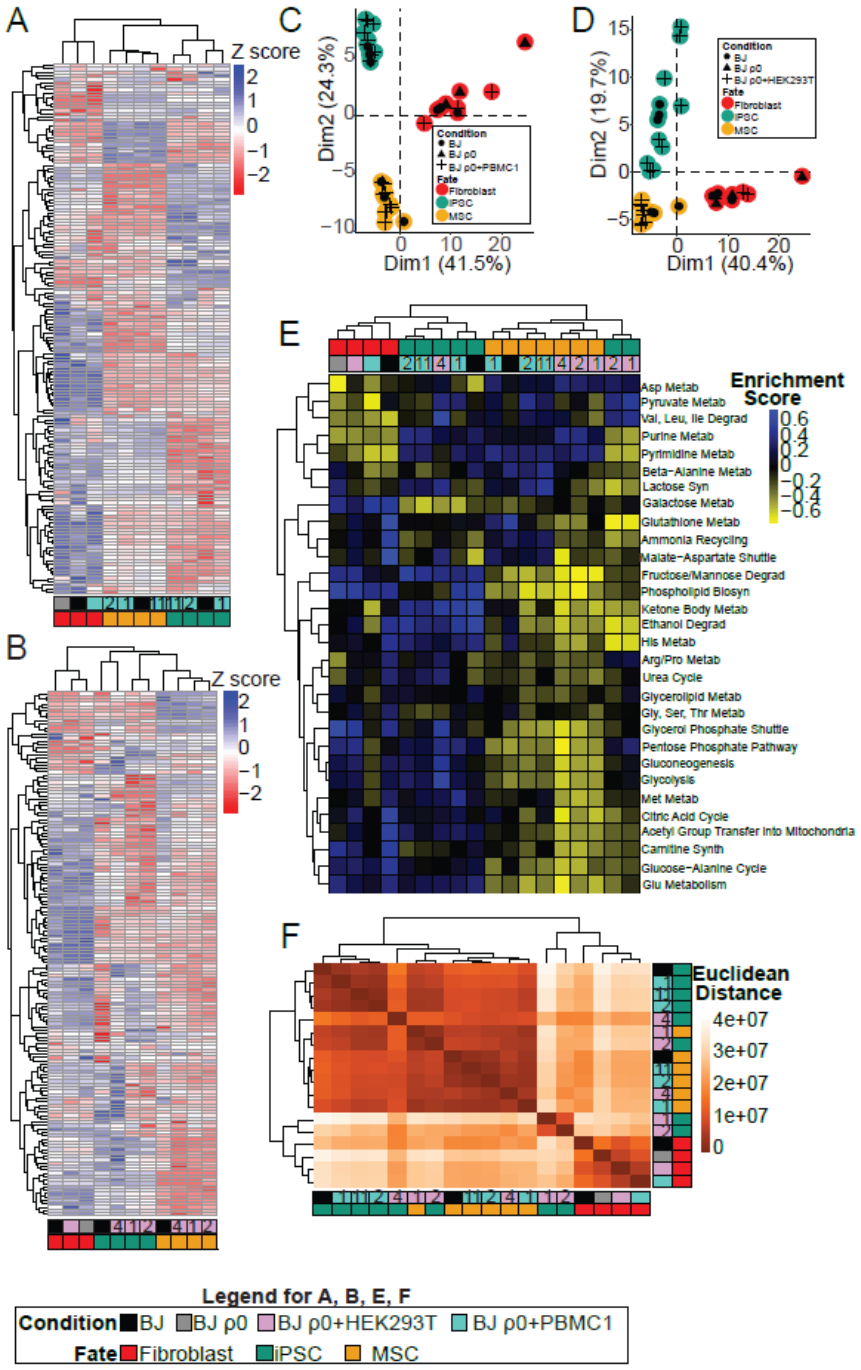

Figure S2. SIMR Metabolome Tracks Mainly with Cell Fate, Related to Figure 5.
(A) Quantification of 154 metabolites in native BJ, BJ ρ0, and BJ ρ0+PBMC1 cells by UHPLC-MS. Z-scores were calculated from the normalized, log transformed abundance of metabolites across averaged samples. Samples were clustered by similarity using an unbiased approach.

(B) Quantification of 154 metabolites in native BJ, BJ ρ0, and BJ ρ0+HEK293T cells by UHPLC-MS. Z-scores were calculated from the normalized, log transformed abundance of metabolites across averaged samples. Samples were clustered by similarity using an unbiased approach.
(C) PCA of normalized metabolite abundance. Colors denote fibroblasts (red), iPSCs (green), and MSCs (yellow), whereas shapes denote native BJ control (•), BJ ρ0 (▲), and BJ ρ0+PBMC1 (+) cells. Scatter plot shows the first (Dim1) and second (Dim2) principal components along the x- and y- axes, respectively.
(D) PCA of normalized metabolite abundance. Colors denote fibroblasts (red), iPSCs (green), and MSCs (yellow), whereas shapes denote native BJ control (•), BJ ρ0 (▲), and BJ ρ0+HEK293T (+) cells. Scatter plot shows the first (Dim1) and second (Dim2) principal components along the x- and y- axes, respectively.
(E) Metabolite set variation analysis (MSVA) indicating metabolite pathway enrichment across averaged samples. Rows indicate independent KEGG metabolic pathways analyzed. Higher MSVA enrichment scores indicate elevated pathway enrichment relative to all samples, lower MSVA enrichment scores indicate reduced pathway enrichment relative to all samples. Samples annotation is by cell fate (top row) and by mtDNA transfer condition (second row). Clone number for BJ ρ0+PBMC1 and BJ ρ0+HEK293T SIMR cells are indicated by a number in the transfer condition row.
(F) Euclidean distance similarity matrix of whole metabolite profiles across all sample comparisons. Heatmap values indicate the Euclidean distance between the two indicated samples (n = 54).

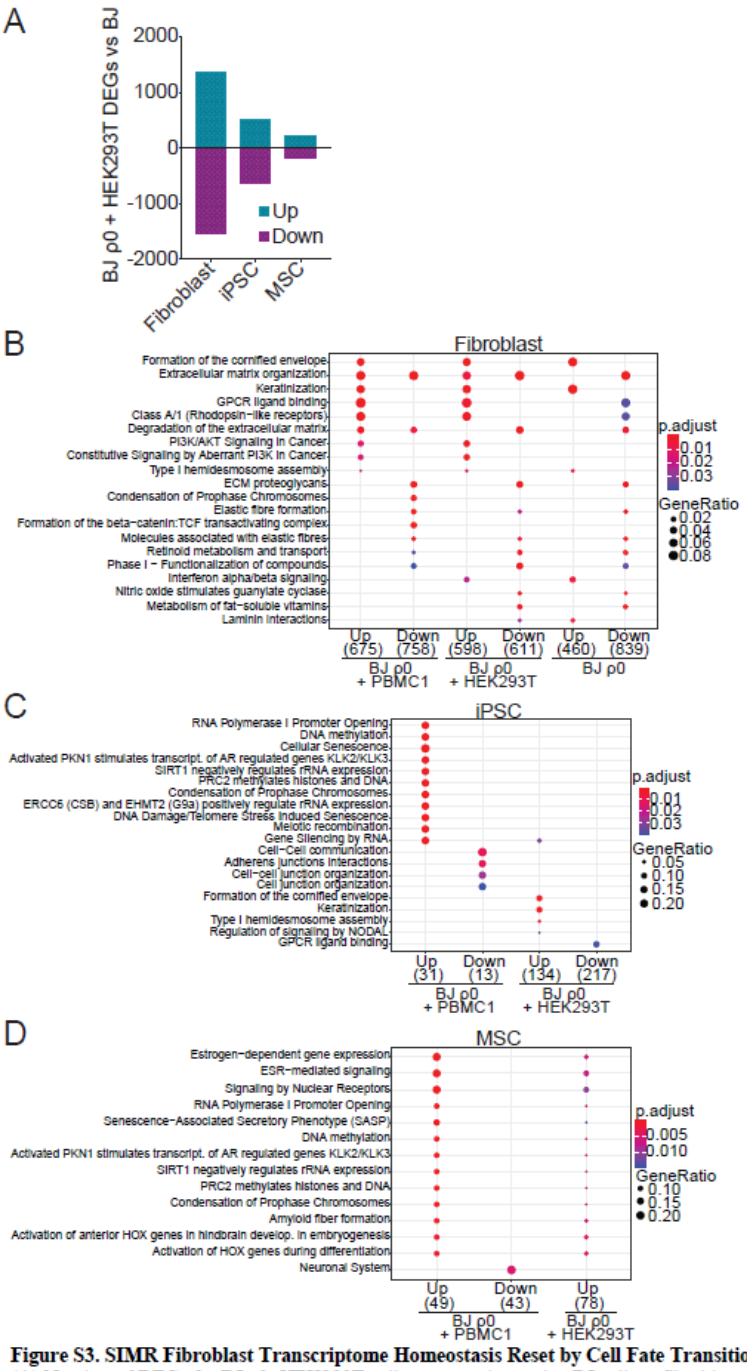

Figure S3. SIMR Fibroblast Transcriptome Homeostasis Reset by Cell Fate Transitions, Related to Figure 5.
(A) Number of DEGs for BJ ρ0+HEK293T cells compared to native BJ cells at fibroblast, iPSC, and MSC fates.
(B) Reactome pathway database overrepresentation analyses (ORA) of BJ ρ0+PBMC1, BJ ρ0+HEK293T, and BJ ρ0 compared to native BJ fibroblasts.

(C) Reactome pathway database ORA of BJ ρ0+PBMC1, BJ ρ0+HEK293T, and BJ ρ0 compared to native BJ iPSCs.
(D) Reactome pathway database ORA of BJ ρ0+PBMC1, BJ ρ0+HEK293T, and BJ ρ0 compared to native BJ MSCs.

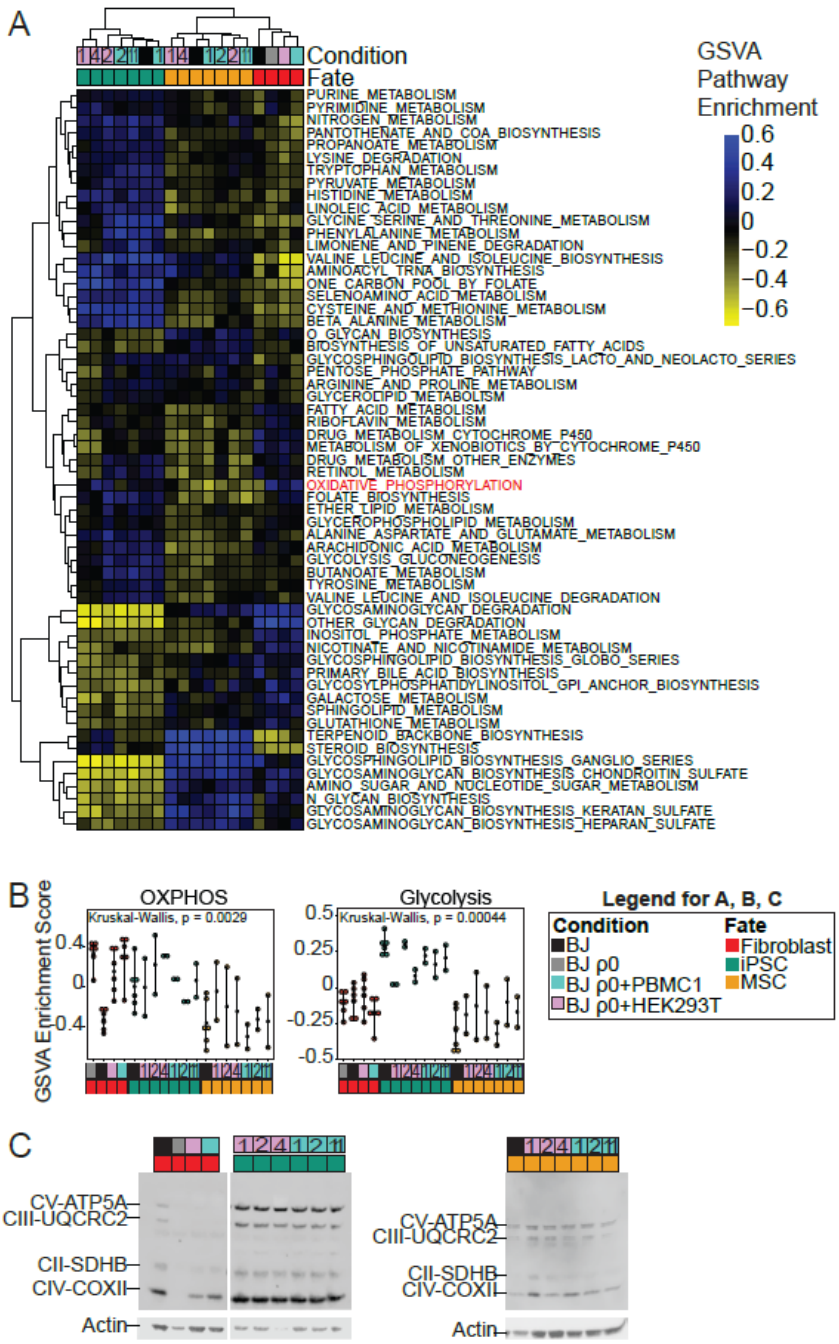

Figure S4. SIMR Cell Pathway Analysis Through Fate Transition, Related to Figure 5.
(A) Heatmap of gene set variation analysis (GSVA) showing enrichments for transcripts that encode metabolic pathways between averaged clones. Rows indicate independent KEGG metabolic pathways analyzed (HSA01100).

(B) Means of individual GSVA scores averaged for all 18 sample and clone fates and conditions (n = 6 for BJ samples; n = 2 for each SIMR clone) for enrichments of oxidative phosphorylation and glycolysis-gluconeogenesis encoding pathway genes.
(C) Immunoblots of ETC complex proteins for native BJ and BJ ρ0 control cells with BJ ρ0+PBMC1 and BJ ρ0+HEK293T SIMR cells at fibroblast, iPSC, and MSC fates.

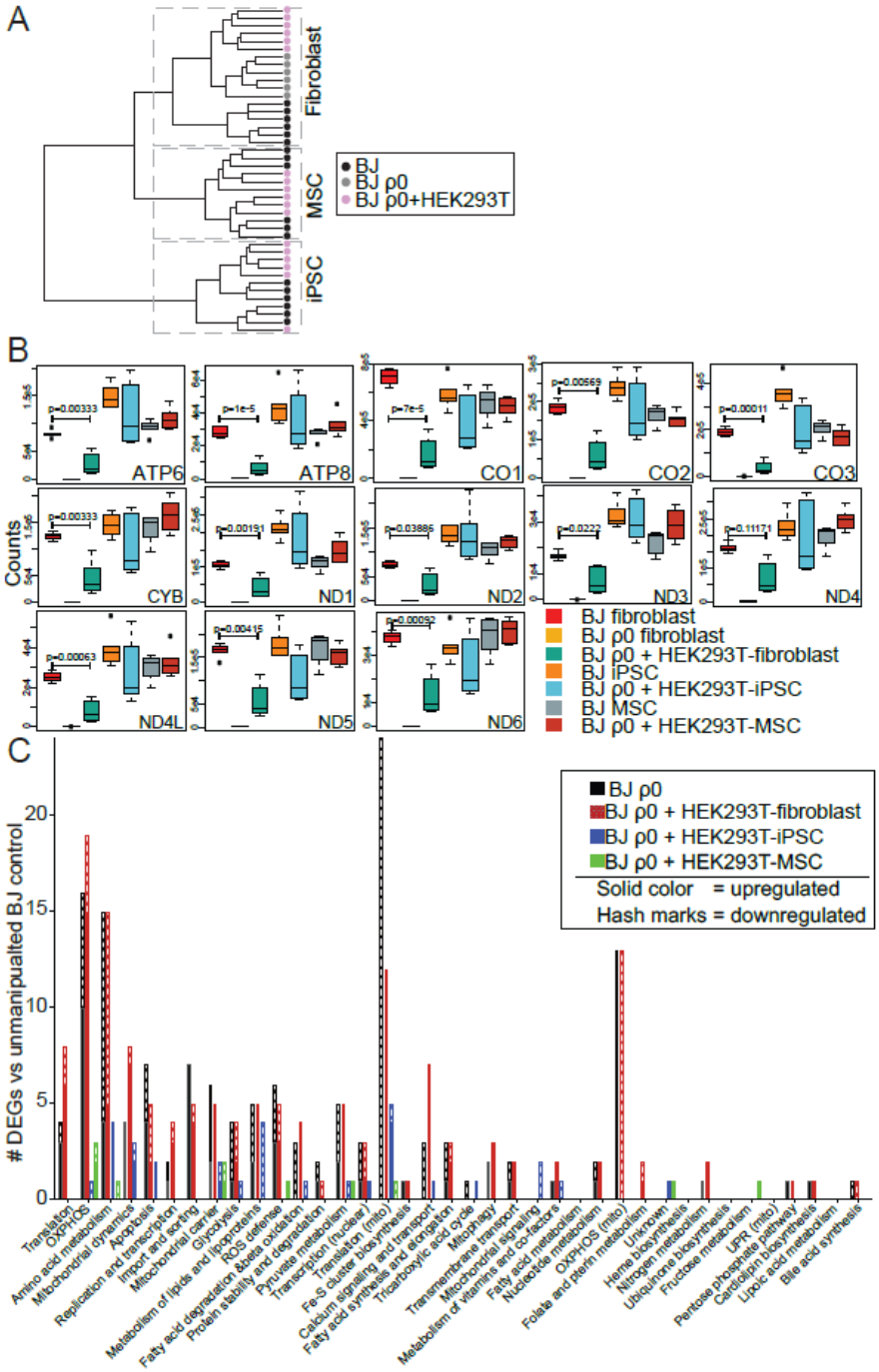

Figure S5. Mitochondrial-Associated Transcriptional Changes, Related to Figure 5.
(A) Hierarchical clustering of MitoCarta 2.0 database genes from native BJ, BJ ρ0, and BJ ρ0+HEK293T cells at fibroblast, iPSC, and MSC fates.

(B) Normalized, batch adjusted read counts shown as box-and-whisker Tukey plots for 13 MitoCarta annotated mtDNA-encoded genes for native BJ, BJ ρ0, and BJ ρ0+HEK293T cells at the fibroblast, iPSC, and MSC fates. Statistical significance was by Welch's T test.
(C) MitoXplorer categorized DEGs for BJ ρ0+HEK293T compared to native BJ cells at the fibroblast, iPSC, and MSC fates divided into the 38 mitochondrial processes.

Patananan, et. al. 2020
(Submitted - Cell Reports)
Supplementary Table S1:
ddC induced mutations
Related to Figures 2 and S1

Table of Contents

1. ddC Fibroblast Mutational Report

The following samples were sequenced to >30x average coverage. Data quality was within standard parameters for all samples. The following "contrast" was created to find novel variations in the treated sample vs. the control:

	control	treated
Cell line	BJ	BJ 5uM DDC

Since there was no clonal selection after treatment, it's extremely important to note the limit of detection for all of our assays. For whole genome sequencing, that's typically 15%. So if there was a variant of interest here, it would have to be present in at least 15% of the population before we could report anything.

2. Provenance

All treated cell lines shared 100% of markers with control, indicating that all samples were properly matched.

3. Variant Summary

Variant Type	BJ Count
Intergenic	8931
Intron	5134
NonCoding	835

Missense	22
Silent	10

Variant locations and sums were within close to each other.
Median allele fraction of variants ranged from 0.15 - 0.17 for the contrast.

4. Non-synonymous SNV Mutations

Single nucleotide variations were not abundant.

contrast	non-synonymous mutations	mutation rate
BJ 5uM DDC vs. BJ	26	0.6/MB

5. Mutational Signatures

SNVs are associated with a "mutational signature" denoting the mutational context around a particular transition or transversion.
There was little difference between the various contrasts on total number of variants.
For each variant, we measure the VAF (variant allele fraction). For all samples, these were mostly uniformly distributed in (0.0, 0.3), with a small number near 1.0 (likely artifacts).

BJ vs BJ 5uM DDC mutational signatures

Signature	# SNVs	% of Total	Caused by	Associated with	Common tumor types
Signature 5	2,230	42	Unknown	Transcriptional strand bias for T>C mutations	All
Signature 8	873	16	Unknown	Weak strand bias for C>A mutations	Breast, Medulloblastoma
Signature 9	854	16	DNA repair by polymerase eta	Activity of AID during somatic hypermutations	CLL, B-Cell Lymphoma

Signature 18	471	9	Unknown		Neuroblastoma
Signature 16	200	4	Unknown	Strong transcriptional strand bias for T>C mutations	Liver

6. Chromosomal breaks

No chromosomal breaks were detected in any of the samples.

7. Copy number and heterozygosity

No changes in copy number were observed.
There are some low confidence calls for loss of heterozygosity:

Contrast	Est. Population Prevalence	(Major, Minor) #	Size (Mb)	Cytoband(s)	State
BJ	38%	(2, 0)	20.88	21p11.2 - 21q21.3	CN-LOH

Patananan, et. al. 2020 (Submitted - Cell Reports)
Supplementary Table S2:
SIMR cell lines generated
Related to Figures 3 and S1

Mitochondrial Recipient	Mitochondrial Donor	Generate engineered fibroblast?	Reprogram into iPSC?	Reprogramming strategy
143BTK- ρ0	none	No	N/A	N/A
143BTK- ρ0	HEK293dsRED	Yes	N/A	N/A
143BTK- ρ0	Cybrid with MELAS-mutation (CL3); Gift from Mondira Kundu (Saint Jude Children's Research Hospital)	Yes	N/A	N/A
143BTK- ρ0	Control cybrid without MELAS mutaiton (CL9); Gift from Mondira Kundu (Saint Jude Children's Research Hospital)	B	N/A	N/A
L929 ρ0	Mitochondria from different mouse tissue	Yes	N/A	N/A
BJ ρ0 fibroblast	None (phosphate buffer saline control)	No	No	N/A
BJ ρ0 fibroblast	HEK293dsRED	Yes	Yes	StemRNA-NM Reprogramming kit; ReproRNA™-OKSGM

BJ ρ0 fibroblast	LP298 (PBMC)	Yes	N/A	StemRNA-NM Reprogramming kit; ReproRNA™-OKSGM
BJ ρ0 fibroblast	LP351 (PBMC) Cybrid with MELAS-mutation (CL3); Gift from Mondira Kundu (Saint Jude Children's Research Hospital)	Yes	Yes	StemRNA-NM Reprogramming kit; ReproRNA™-OKSGM
BJ ρ0 fibroblast	Control cybrid without MELAS mutaiton (CL9); Gift from Mondira Kundu (Saint Jude Children's Research Hospital)	Yes	No	StemRNA-NM Reprogramming kit; ReproRNA™-OKSGM
NDF ρ0 fibroblast	None (phosphate buffer saline control)	No	No	Lenti; CytoTune™-iPS 2.0 Sendai Reprogramming Kit
NDF ρ0 fibroblast	NDF (ATCC PCS-201-010)	Yes	Yes	Lenti; CytoTune™-iPS 2.0 Sendai Reprogramming Kit
NDF ρ0 fibroblast	HEK293dsREd Cybrid with MELAS-mutation (CL3); Gift from Mondira Kundu (Saint Jude Children's	Yes	No	Lenti; CytoTune™-iPS 2.0 Sendai Reprogramming Kit

	Research Hospital)			
NDF ρ0 fibroblast	Control cybrid without MELAS mutaiton (CL9); Gift from Mondira Kundu (Saint Jude Children's Research Hospital)	Yes	Yes	Lenti; CytoTune™-iPS 2.0 Sendai Reprogramming Kit
NDF ρ0 fibroblast	Alternative cybrid line with MELAS mutation	Yes	No	Lenti; CytoTune™-iPS 2.0 Sendai Reprogramming Kit
NDF ρ0 fibroblast	Heteroplasmic mixture of isolated mitochondria derived from CL3 and CL9 MERRF; Gift from Carlos Moraes (University of Miami);	Yes	Yes, but no detrimental mutation detected	Lenti; CytoTune™-iPS 2.0 Sendai Reprogramming Kit
NDF ρ0 fibroblast	A8344G subsitution	Yes	No	CytoTune™-iPS 2.0 Sendai Reprogramming Kit
NDF ρ0 fibroblast	Δ cytochrome B 3.0 cybrid; Gift from Carlos Moraes (University of Miami);	Yes	No	CytoTune™-iPS 2.0 Sendai Reprogramming Kit
NDF ρ0 fibroblast	Leigh syndrome primary fibroblast; Coriell Repository GM13411;	Yes	No	CytoTune™-iPS 2.0 Sendai Reprogramming Kit

NDF ρ0 fibroblast	T8993G substitution Primary MELAS fibroblast	Yes	No	CytoTune™-iPS 2.0 Sendai Reprogramming Kit
NDF ρ0 fibroblast	Kearns Sayre Syndrome; Coriell Repository GM06225; Common deletion	Yes	No	CytoTune™-iPS 2.0 Sendai Reprogramming Kit

Patananan, et. al. 2020 (Submitted - Cell Reports)
Supplementary Table S3:
Metabolomics Principal Components Analysis (PCA) and Pathway Analysis Related to STAR Methods (Metabolomics Data Analysis) and Figure S2

Accession Information:

To Be Added

Table of Contents:

Condition Code:

BJ
BJ rho null (BJρ0)
BJ HEK (BJρ0+HEK293T)
BJ LP351 (BJρ0+PBMC1)

Section I: Metadata for all metabolite samples processed (n = 54 total)

Condition_Exp	Condition	Fate	Transfer	Condition Fate
bj fibroblast_Exp1	BJ	Fibroblast	None	BJ Fibroblast
bj fibroblast_Exp2	BJ	Fibroblast	None	BJ Fibroblast
bj fibroblast_Exp3	BJ	Fibroblast	None	BJ Fibroblast
bj ipsc_Exp1	BJ iPSC	iPSC	None	BJ iPSC iPSC
bj ipsc_Exp2	BJ iPSC	iPSC	None	BJ iPSC iPSC
bj ipsc_Exp3	BJ iPSC	iPSC	None	BJ iPSC iPSC
bj MSC_Exp1	BJ MSC	MSC	None	BJ MSC MSC
bj MSC_Exp2	BJ MSC	MSC	None	BJ MSC MSC
bj MSC_Exp3	BJ MSC	MSC	None	BJ MSC MSC

bj rho 0 + hek mitos fibroblasts_Exp1	BJ HEK Fibroblast	Fibroblast	HEK Transfer	BJ HEK Fibroblast Fibroblast
bj rho 0 + hek mitos fibroblasts_Exp2	BJ HEK Fibroblast	Fibroblast	HEK Transfer	BJ HEK Fibroblast Fibroblast
bj rho 0 + hek mitos fibroblasts_Exp3	BJ HEK Fibroblast	Fibroblast	HEK Transfer	BJ HEK Fibroblast Fibroblast
bj rho 0 + hek mitos iPSC clone1_Exp1	BJ HEK IPSC Clone 1	iPSC	HEK Transfer 1	BJ HEK IPSC Clone 1 iPSC
bj rho 0 + hek mitos iPSC clone1_Exp2	BJ HEK IPSC Clone 1	iPSC	HEK Transfer 1	BJ HEK IPSC Clone 1 iPSC
bj rho 0 + hek mitos iPSC clone1_Exp3	BJ HEK IPSC Clone 1	iPSC	HEK Transfer 1	BJ HEK IPSC Clone 1 iPSC
bj rho 0 + hek mitos iPSC clone2_Exp1	BJ HEK IPSC Clone 2	iPSC	HEK Transfer 2	BJ HEK IPSC Clone 2 iPSC
bj rho 0 + hek mitos iPSC clone2_Exp2	BJ HEK IPSC Clone 2	iPSC	HEK Transfer 2	BJ HEK IPSC Clone 2 iPSC
bj rho 0 + hek mitos iPSC clone2_Exp3	BJ HEK IPSC Clone 2	iPSC	HEK Transfer 2	BJ HEK IPSC Clone 2 iPSC
bj rho 0 + hek mitos iPSC clone4_Exp1	BJ HEK IPSC Clone 4	iPSC	HEK Transfer 4	BJ HEK IPSC Clone 4 iPSC
bj rho 0 + hek mitos iPSC clone4_Exp2	BJ HEK IPSC Clone 4	iPSC	HEK Transfer 4	BJ HEK IPSC Clone 4 iPSC
bj rho 0 + hek mitos iPSC clone4_Exp3	BJ HEK IPSC Clone 4	iPSC	HEK Transfer 4	BJ HEK IPSC Clone 4 iPSC
bj rho 0 + hek mitos msc clone1_Exp1	BJ HEK MSC Clone 1	MSC	HEK Transfer 1	BJ HEK MSC Clone 1 MSC
bj rho 0 + hek mitos msc clone1_Exp2	BJ HEK MSC Clone 1	MSC	HEK Transfer 1	BJ HEK MSC Clone 1 MSC
bj rho 0 + hek mitos msc clone1_Exp3	BJ HEK MSC Clone 1	MSC	HEK Transfer 1	BJ HEK MSC Clone 1 MSC
bj rho 0 + hek mitos msc clone2_Exp1	BJ HEK MSC Clone 2	MSC	HEK Transfer 2	BJ HEK MSC Clone 2 MSC
bj rho 0 + hek mitos msc clone2_Exp2	BJ HEK MSC Clone 2	MSC	HEK Transfer 2	BJ HEK MSC Clone 2 MSC
bj rho 0 + hek mitos msc clone2_Exp3	BJ HEK MSC Clone 2	MSC	HEK Transfer 2	BJ HEK MSC Clone 2 MSC
bj rho 0 + hek mitos msc clone4_Exp1	BJ HEK MSC Clone 4	MSC	HEK Transfer 4	BJ HEK MSC Clone 4 MSC
bj rho 0 + hek mitos msc clone4_Exp2	BJ HEK MSC Clone 4	MSC	HEK Transfer 4	BJ HEK MSC Clone 4 MSC
bj rho 0 + hek mitos msc clone4_Exp3	BJ HEK MSC Clone 4	MSC	HEK Transfer 4	BJ HEK MSC Clone 4 MSC
bj rho 0 + LP351 mitos fibroblast_Exp1	BJ LP351 Fibroblast	Fibroblast	LP351 Transfer	BJ LP351 Fibroblast Fibroblast
bj rho 0 + LP351 mitos fibroblast_Exp2	BJ LP351 Fibroblast	Fibroblast	LP351 Transfer	BJ LP351 Fibroblast Fibroblast

bj rho 0 + LP351 mitos fibroblast_Exp3	BJ LP351 Fibroblast	Fibroblast	LP351 Transfer	BJ LP351 Fibroblast Fibroblast
bj rho 0 + LP351 mitos iPSC clone 1_Exp1	BJ LP351 IPSC Clone 1	iPSC	LP351 Transfer 1	BJ LP351 iPSC Clone 1 iPSC
bj rho 0 + LP351 mitos iPSC clone 1_Exp2	BJ LP351 IPSC Clone 1	iPSC	LP351 Transfer 1	BJ LP351 iPSC Clone 1 iPSC
bj rho 0 + LP351 mitos iPSC clone 1_Exp3	BJ LP351 IPSC Clone 1	iPSC	LP351 Transfer 1	BJ LP351 iPSC Clone 1 iPSC
bj rho 0 + LP351 mitos iPSC clone 11_Exp1	BJ LP351 IPSC Clone 11	iPSC	LP351 Transfer 11	BJ LP351 iPSC Clone 11 iPSC
bj rho 0 + LP351 mitos iPSC clone 11_Exp2	BJ LP351 IPSC Clone 11	iPSC	LP351 Transfer 11	BJ LP351 iPSC Clone 11 iPSC
bj rho 0 + LP351 mitos iPSC clone 11_Exp3	BJ LP351 IPSC Clone 11	iPSC	LP351 Transfer 11	BJ LP351 iPSC Clone 11 iPSC
bj rho 0 + LP351 mitos iPSC clone 2_Exp1	BJ LP351 IPSC Clone 2	iPSC	LP351 Transfer 2	BJ LP351 iPSC Clone 2 iPSC
bj rho 0 + LP351 mitos iPSC clone 2_Exp2	BJ LP351 IPSC Clone 2	iPSC	LP351 Transfer 2	BJ LP351 iPSC Clone 2 iPSC
bj rho 0 + LP351 mitos iPSC clone 2_Exp3	BJ LP351 IPSC Clone 2	iPSC	LP351 Transfer 2	BJ LP351 iPSC Clone 2 iPSC
bj rho 0 + LP351 mitos msc clone 1_Exp1	BJ LP351 MSC Clone 1	MSC	LP351 Transfer 1	BJ LP351 MSC Clone 1 MSC
bj rho 0 + LP351 mitos msc clone 1_Exp2	BJ LP351 MSC Clone 1	MSC	LP351 Transfer 1	BJ LP351 MSC Clone 1 MSC
bj rho 0 + LP351 mitos msc clone 1_Exp3	BJ LP351 MSC Clone 1	MSC	LP351 Transfer 1	BJ LP351 MSC Clone 1 MSC
bj rho 0 + LP351 mitos msc clone 11_Exp1	BJ LP351 MSC Clone 11	MSC	LP351 Transfer 11	BJ LP351 MSC Clone 11 MSC
bj rho 0 + LP351 mitos msc clone 11_Exp2	BJ LP351 MSC Clone 11	MSC	LP351 Transfer 11	BJ LP351 MSC Clone 11 MSC
bj rho 0 + LP351 mitos msc clone 11_Exp3	BJ LP351 MSC Clone 11	MSC	LP351 Transfer 11	BJ LP351 MSC Clone 11 MSC
bj rho 0 + LP351 mitos msc clone 2_Exp1	BJ LP351 MSC Clone 2	MSC	LP351 Transfer 2	BJ LP351 MSC Clone 2 MSC
bj rho 0 + LP351 mitos msc clone 2_Exp2	BJ LP351 MSC Clone 2	MSC	LP351 Transfer 2	BJ LP351 MSC Clone 2 MSC
bj rho 0 + LP351 mitos msc clone 2_Exp3	BJ LP351 MSC Clone 2	MSC	LP351 Transfer 2	BJ LP351 MSC Clone 2 MSC
bj rho 0 fibroblast_Exp1	BJ Rho Null Fibroblast	Fibroblast	Rho Null	BJ Rho Null Fibroblast Fibroblast

bj rho 0 fibroblast_Exp2	BJ Rho Null Fibroblast	Fibroblast	Rho Null	BJ Rho Null Fibroblast Fibroblast
bj rho 0 fibroblast_Exp3	BJ Rho Null Fibroblast	Fibroblast	Rho Null	BJ Rho Null Fibroblast Fibroblast

Section II: Euclidean distance similarity mapping values across samples. (n = 54 total)

bj rho 0 + hek mitos fibroblasts	bj rho 0 + hek mitos iPSC clone 1	bj rho 0 + hek mitos iPSC clone 2	bj rho 0 + hek mitos iPSC clone 4	bj rho 0 + hek mitos msc clone 1	bj rho 0 + hek mitos msc clone 2	bj rho 0 + hek mitos msc clone 4	bj rho 0 + LP351 mitos fibroblast	bj rho 0 + LP351 mitos iPSC clone 1	bj rho 0 + LP351 mitos iPSC clone 11	bj rho 0 + LP351 mitos iPSC clone 2	bj rho 0 + LP351 mitos msc clone 1	bj rho 0 + LP351 mitos msc clone 11	bj rho 0 + LP351 mitos msc clone 2	bj rho 0 fibroblast
11218493.2	34361331.6	29275696.9	19321441.9	23949499.5	24836220.4	22399675.1	14709602.3	25454374.9	24853435.5	25204240.9	21248383.1	19528751.3	20028268.3	16351937
34333209.6	40747338.9	31309512.9	17379143.2	7715139.97	8483484.94	12863149.4	34581462.2	3590765.46	5780836.57	4754482.09	10667059.3	13702412	13159180.1	39246005.6
24436329.8	33046083.7	24298210.5	11240414.1	7095378.98	8354738.9	6835089.06	24455319.3	10907688.9	10078654.5	9946458.73	4180820.79	2397500.93	3269869.33	29283528.9
0	31060971.5	27846027.3	22781194.2	29556967.7	30338518	26505944.7	64228 98.39	31688782.8	30816462.4	31108197.5	26666926.1	24110040.2	24531328.5	7742173.78
31060971.5	0	10452117	26333777.6	35229725.8	34152710.8	29477418.3	28736039.8	38803305.9	36000160.8	36576920.4	33113477.8	31108045.7	30833727.1	32584312.9
27846027.3	10452117	0	19054233.2	25875173.2	24625514.1	20265207.1	25320023.9	29617694.8	26813231.7	27223425.2	24245616.3	22457047.2	22053925.2	30908192.5
22781194.2	26333777.6	19054233.2	0	12979920.6	12996685.7	9602310.34	23333851.1	14541127.8	12430030	13282975.8	10344085.2	9665311.14	9316374.91	26828866.9
29556967.7	35229725.8	25875173.2	12979920.6	0	26663 73.86	6023709.93	29452817.9	6657376.36	5124695.76	4868339.07	4083144.39	7263537.38	6372316.47	34470507.4
30338518	34152710.8	24625514.1	12996685.7	26663 73.86	0	5823278.66	30100836.8	7614390.95	5261960.15	5166714.4	5225239.7	8072046.52	7194186.89	35198058.1
26505944.7	29477418.3	20265207.1	9602310.34	6023709.93	5823278.66	0	25941824.2	11307711.3	8854663.91	9065976.21	4972567.14	5445843.93	4027730.12	31286535.3
64228 98.39	28736039.8	25320023.9	23333851.1	29452817.9	30100836.8	25941824.2	0	32154175.6	31098732.8	31258075.3	26813062	24039991.2	24355337.8	11192914.9
31688782.8	38803305.9	29617694.8	14541127.8	6657376.36	7614390.95	11307711.3	32154175.6	0	3527468.1	2926832.07	8720449.87	1158581.3	1110086.8	36475703.3
30816462.4	36000160.8	26813231.7	12430030	5124695.76	5261960.15	8854663.91	31098732.8	3527468.1	0	1588957.14	7159737.82	1016271.3	9416031.48	35548852
31108197.5	36576920.4	27223425.2	13282975.8	4868339.07	5166714.4	9065976.21	31258075.3	2926832.07	1588957.14	0	7314077.56	1023143.5	9559691.53	35951652.5
26666926.1	33113477.8	24245616.3	10344085.2	4083144.39	5225239.7	4972567.14	26813062	8720449.87	7159737.82	7314077.56	0	3726240.41	3217915.83	31469837
24110040.2	31108045.7	22457047.2	9665311.14	7263537.38	8072046.52	5445843.93	24039991.2	1158581.3	1016271.3	1023143.5	3726240.41	0	1784072.15	28894901.6
24531328.5	30833727.1	22053925.2	9316374.91	6372316.47	7194186.89	4027730.12	24355337.8	1110086.8	9416031.48	9559691.53	3217915.83	1784072.15	0	29314951
7742173.78	32584312.9	30908192.5	26828866.9	34470507.4	35198058.1	31286535.3	11192914.9	36475703.3	35548852	35951652.5	31469837	28894901.6	29314951	0

Section III: Protein content-normalized metabolite abundance amounts for 154 metabolites identified across samples. Samples where the metabolite was not identified are set to zero for PCA.

	bj fibroblast_Exp1	bj fibroblast_Exp2	bj fibroblast_Exp3
13BPG	9176.144184	11700.87272	9391.573081
2-Aminobutyrate	4128.129589	11091.731	6761.849595
2-HG	27478.87339	26991.90197	31260.18648
3-Hydroxy-3-methylglutarate	12923.52802	14746.17585	12370.56507
3PG	17468.17677	19539.86949	16155.92188
5M-thioadenosine	249227.5419	233207.5542	235287.9864
6P-gluconate	21515.75119	24062.42841	19635.77405
A	3746.621922	44769.98783	23198.96408
a-KG	37516.62163	36627.44972	46883.17557
Ac-carnitine	5086002.319	6079936.983	5506851.349
Ac-choline	371101.8904	433863.5794	373542.9374
Acetyl-CoA	2668.286015	3255.861408	3312.056712
Aconitate	52637.7177	72842.03114	58443.67779
Adenine	1155.969991	464.9802245	1860.013109
ADP	121692.7217	133624.5741	121719.3581
ADP/ATP	0.269161839	0.231662892	0.25617419
Ala	1032478.258	1917438.175	1175615.894
AMP	43102.36867	30422.86394	27096.91841
AMP/ATP	0.095334484	0.052743657	0.057028982
Arg	1187951.769	1382977.299	1188053.59
Arg-Succ	2802.097381	2624.624211	3282.600215
Asn	365239.5502	376744.6922	418948.8479
Asp	2019413.705	2127602.421	2227314.106
ATP	452117.2919	576806.1209	475142.9411
C	28474.84839	31375.91244	34176.00169
Carbamoyl-Asp	430.5184167	1306.546709	594.5297479
Carbamoyl-P	491.5775736	807.6006776	2347.435903
Carnitine	1757892.775	2406271.465	1905888.868
CDP	8692.182791	8566.361528	9104.761054
CDP-choline	931.294132	294.8437002	612.1935391
CDP-EtA	1068.176277	1223.01544	1530.374052
Cholesterol sulfate	5221.701032	6492.181233	8870.273425
Choline	303609.9361	492059.1157	274327.6426
Cit	3014872.403	3894972.4	3471953.498
Citrulline	47370.40826	55177.10956	49464.20378
CMP	1657.21834	1389.752465	2082.952727
CoA	1379.634553	1940.383566	1523.405068
Creatine	3754773.863	6295403.235	4160678.59

Creatine/P-Creatine	12.93548496	16.04741302	11.31838306
Creatinine	848251.242	1234596.734	950745.1892
CTP	26979.70426	37536.49693	31051.46015
Cystathionine	90601.62199	95603.9623	95828.10632
Cystine	1809.643864	2337.858467	1476.273513
Cytosine	4664.491613	6651.401745	5322.135615
dA	1459.91466	1363.670287	1343.810256
dAMP	0	0	0
dATP	0	0	0
dC	3749.782913	5313.766592	7388.325829
dCDP	0	0	0
dCMP	136.3108457	0	151.884048
dCTP	0	120.0845773	0
dG	0	0	0
dGDP	3213.742117	2525.578278	2897.739038
dGTP	392.4905231	0	800.9387498
DHAP	10066.3149	10356.1832	10599.77717
Dihydroorotate	469.8373332	210.5717929	757.0203292
Dihydrouracil	35115.24124	35632.64303	40736.53389
dTMP	64.3088462	0	0
dTTP	61.71614964	150.7897791	138.6461449
dU	5272.997027	1835.429729	6955.80865
dUMP	91.30292716	128.5612781	140.7902857
F16BP	107695.2033	141080.6923	119044.5242
Folate	27629.54078	27346.66944	22568.53568
Fru	219818.8523	218346.8447	228764.1483
Fum	96130.73257	96281.82176	110018.3277
G	9106.065675	9008.865843	11122.15318
G3P	9170.425576	10408.98339	9890.394083
GABA	10425.637	16575.91802	14985.17261
GDP	15244.48073	15320.41879	15328.19331
GDP-Mannose	2747.626887	3443.664709	1512.153846
Glc	5684162.069	6030124.282	6244393.187
GlcN	3391270.208	3793938.812	2939780.518
GlcN-6P	4627.927693	3700.759208	5001.710891
GlcNAc-6P	2587.448679	4008.223687	3931.78205
Gln	15476349.47	16117522.95	18661339.13
Glu	11569747.8	12546400.48	12958205.19
GlucA	9701.375148	10918.85694	11977.9248
Gluconate	441310.0251	342153.4094	486982.382

GluNAc	15439.62917	14877.91476	17094.21994
Gly	204781.0486	379589.2035	243936.9712
Glycerate	3839.910239	4364.786583	4152.354162
Glycerol	2070.985508	4450.022052	781.4446711
Glycerol-3P	11767.25966	15934.93687	17626.1409
Glyoxylate	20071.02467	31682.1392	22000.77667
GMP	3604.902923	4274.08302	3461.023458
GSH	859822.0992	962515.9429	1042640.933
GSH/GSSG	4.756664129	7.118226848	8.494762309
GSSG	180761.5749	135218.498	122739.2709
GTP	58411.25324	76025.88167	61222.56163
Guanine	0	0	88.66682856
H6P	67837.46235	67295.62692	77618.89049
His	1350470.674	1603061.904	1454789.663
HMG-CoA	148.6409334	170.8545756	195.6209712
Hypotaurine	123975.3712	208280.6972	144309.6284
Hypoxanthine	0	0	110.3712261
IMP	870.5850291	343.1311404	503.3889275
Inosine	9726.439315	7381.579705	6698.914835
Inositol	5457294.036	4683577.607	5829280.556
Isobutyryl-carnitine	574063.4613	636290.7061	605426.9723
Isobutyryl-CoA	27.74292313	36.21018135	35.27345876
Lac	1330936.116	1799007.21	1369074.73
Leu/Ile	7098445.924	11458445.01	8259474.038
Lys	368490.8459	556127.1393	422404.4548
Mal	1262308.63	1320189.141	1467620.611
Malonyl-CoA	1085.738293	1127.371105	1159.513549
Met	1778601.48	2597620.077	2016920.781
Methionine sulfoxide	158260.1806	175316.166	170955.8315
Mevalonate	56793.22821	98905.73994	38817.48916
NAD+	247464.1858	251385.1345	261986.2413
NADH	4307.302324	4854.544778	4898.691935
NADP+	5491.10247	3482.223414	3100.795658
NADPH	0	86.70529552	121.0744833
Nicotinamide	314482.0564	445896.2986	291377.4263
Ornithine	6485.009872	13270.25497	8451.593469
P-Choline	843561.097	1026531.022	1022246.149
P-Creatine	290269.2767	392300.1935	367603.6205
P-EtA	1630.719807	1450.69231	1291.939806
P-Ser	5596.551565	7816.4688	6270.488661

Palmitate	5917136.018	6217974.752	7603970.555
Pantothenate	3445851.435	3506865.635	3343816.151
PEP	1264.633085	1320.315145	790.2969397
Phe	11979569.15	13584529.33	12840251.65
Pro	4005383.139	6799089.918	4699086.584
Pro-OH	112921.1396	165765.4037	120818.388
PRPP	1358.502302	1558.080328	1329.198311
Pyridoxine	220250.7379	234040.2438	246989.0089
R5P	1257.131961	1167.940166	1891.424429
Rib	142.5434698	88.11189614	0
S7P	3281.25761	3319.067889	4053.037894
SAH	19138.61027	27113.55381	17579.73451
SAM	195358.4404	161175.6934	201123.1414
Sarcosine	126135.6867	233387.794	174639.421
Ser	79431.56136	103540.9474	89266.46195
Sorbitol	8348.178669	10714.18925	10536.42018
Succ	74893.17033	86280.77891	82665.03364
Succ-Semialdehyde	3597.095324	3459.379368	3856.136378
T	4453.30615	3678.467623	4328.167803
Taurine	10031978.87	9373887.502	0
Thr	906350.0294	1468802.694	1060591.641
Thymine	53445.28786	52929.86692	64545.72805
Trp	1881348.892	2309815.539	2061540.158
Tyr	3295588.376	3650293.37	3637942.31
Tyramine	4117.461855	3951.461728	3355.619905
U	23422.07398	21735.27907	26842.04248
UDP	29021.9419	25548.81045	25885.214
UDP-Glc	153255.3157	193627.7436	189722.9254
UDP-GlcNAc	0	204093.6876	103470.7199
UDP-GlucA	17223.93999	22220.36457	18594.44334
UMP	13637.8724	12295.25343	8066.163599
Uracil	33261.66156	29615.95277	30420.97386
Uric Acid	52246.76175	44009.79208	44769.09187
UTP	54191.03695	66586.51634	58895.49872
Val	4520825.093	15567296.69	8638120.491
Xanthine	220778.875	156911.7041	206006.1801

Section IV: Metabolite pathway sets identified as significantly enriched across one or more sample conditions (using an F statistic adjusted P value threshold of 0.05)

Metabolite Set	SampleMatrix.ConditionBJ	SampleMatrix.ConditionBJ.HEK.Fibroblast	SampleMatrix.ConditionBJ.HEK.IPSC.Clone.1
Pyrimidine Metabolism	-0.51538394	-0.34956396	-0.48290558
Fructose and Mannose Degradation	0.0992071	0.46852084	-0.12942882
Purine Metabolism	-0.37433988	-0.37170344	-0.4317121
Phospholipid Biosynthesis	0.48986329	0.58289533	-0.12215524
Glycolysis	0.24899897	0.26098391	0.10917707
Glycerol Phosphate Shuttle	0.46217707	0.54860994	0.03590357
Histidine Metabolism	0.49997077	0.15637439	-0.57346662
Ethanol Degradation	0.48991104	0.23696437	-0.54020909
Methionine Metabolism	0.33261675	0.13857708	-0.04284158
Carnitine Synthesis	0.5682723	0.32776831	-0.17232526
Galactose Metabolism	0.55261701	0.29101932	0.10011369
Gluconeogenesis	0.2902023	0.31653097	0.1083967
Pentose Phosphate Pathway	0.08366097	0.44945871	0.36756683
Ketone Body Metabolism	0.10552495	0.07226798	-0.37867993
Lactose Synthesis	-0.03009259	-0.08373244	-0.36306761
Glutamate Metabolism	0.42231192	0.2411559	-0.09436682
Valine, Leucine and Isoleucine Degradation	-0.52972944	-0.26272282	0.47516545
Glucose-Alanine Cycle	0.53604876	0.33611159	-0.17372736
Aspartate Metabolism	-0.08909138	-0.04112353	0.24864894
Transfer of Acetyl Groups into Mitochondria	0.5934011	0.22214384	-0.20078139
Citric Acid Cycle	0.63535047	0.34229721	-0.12780337
Arginine and Proline Metabolism	0.38027877	0.08241091	0.23925691
Malate-Aspartate Shuttle	0.7695959	0.22315709	-0.06485613
Pyruvate Metabolism	0.11313918	-0.16774511	0.54864097
Glutathione Metabolism	0.7219193	0.22932919	-0.64485934
Ammonia Recycling	0.59680642	0.2118832	-0.29424831
Beta-Alanine Metabolism	-0.27237943	-0.01064737	-0.22835947
Urea Cycle	0.37903996	0.14991337	0.07338484
Glycerolipid Metabolism	0.15613818	0.0738998	0.15832478
Glycine, Serine and Threonine Metabolism	0.33170956	0.19629219	0.02972197

Section V: List of metabolites (KEGG COMPOUND ID) associated with each metabolic pathway for GSVA analysis.

Metabolite Pathway	Metabolites (KEGG COMPOUND ID) Associated						
Alanine Metabolism	C00026	C00022	C00025	C00041	C00036	C00037	C00048

Amino Sugar Metabolism	C00085	C05345	C06023	C00329	C00352	C00357	C01674
Ammonia Recycling	C00064	C00001	C00026	C00022	C00025	C00014	C00002
Arginine and Proline Metabolism	C00025	C00014	C00169	C00077	C00086	C00062	C00122
Aspartate Metabolism	C00122	C03406	C00049	C00327	C00036	C00099	C00152
Beta-Alanine Metabolism	C00049	C00864	C00099	C01262	C00386	C02229	C05665
Carnitine Synthesis	C00001	C00026	C00047	C00037	C00011	C00007	C00004
Citric Acid Cycle	C00001	C00026	C00022	C00288	C00002	C00008	C00122
Ethanol Degradation	C00001	C00002	C00020	C00010	C00024	C00007	C00027
Fructose and Mannose Degradation	C00111	C00085	C05345	C00354	C05378	C00119	C00661
Galactose Metabolism	C00446	C00052	C00029	C00103	C00137	C00668	C00116
Gluconeogenesis	C00001	C00026	C00022	C00002	C00008	C00036	C00597
Glucose-Alanine Cycle	C00001	C00026	C00022	C00025	C00014	C00041	C00004
Glutamate Metabolism	C00064	C00026	C00025	C00014	C00169	C00003	C00669
Glutathione Metabolism	C00025	C00097	C00037	C00669	C01879	C01419	C00051
Glycerol Phosphate Shuttle	C00004	C00003	C00093	C00111	C00118	C00661	C00236
Glycerolipid Metabolism	C00002	C00008	C00258	C00597	C00004	C00003	C00006
Glycine, Serine and Threonine Metabolism	C00022	C00014	C00258	C00597	C03232	C00065	C01005
Glycolysis	C00001	C00022	C00002	C00008	C00597	C00004	C00003
Histidine Metabolism	C00025	C00002	C00008	C00020	C00101	C00011	C00386
Ketone Body Metabolism	C00011	C00164	C00010	C00024	C00004	C00003	C00332
Lactose Synthesis	C00002	C00008	C00446	C00052	C00029	C00103	C00105
Malate-Aspartate Shuttle	C00026	C00025	C00049	C00036	C00004	C00003	C00018
Methionine Metabolism	C00002	C00065	C00097	C02291	C05330	C00101	C00037
Pentose Phosphate Pathway	C00011	C00668	C01172	C00198	C00085	C05345	C00672
Phospholipid Biosynthesis	C00416	C00093	C00154	C00111	C01996	C00114	C00307
Purine Metabolism	C00064	C00002	C00008	C00020	C00044	C00144	C00117
Pyrimidine Metabolism	C00064	C00169	C00099	C02642	C00429	C00106	C00105

Pyruvate Metabolism	C00022	C00036	C00546	C00024	C00083	C00332	C00074
Spermidine and Spermine Biosynthesis	C00002	C00077	C00073	C00170	C00315	C00134	C01137
Transfer of Acetyl Groups into Mitochondria	C00001	C00022	C00002	C00008	C00036	C00011	C00010
Urea Cycle	C00064	C00001	C00026	C00022	C00025	C00014	C00288
Valine, Leucine and Isoleucine Degradation	C00164	C00024	C00100	C06002	C02170	C00183	C00332

Patananan, et. al. 2020 (Submitted - Cell Reports)
Supplementary Table S4:
Transcriptomics Principal Components Analysis (PCA) and select gene expression.
Related to Figures 5 and S3, S4, S5.

Accession Information:
GSE115871

Table of Contents:

Condition Code:
BJ
BJ rho null (BJρ0)
BJ HEK (BJρ0+HEK293T)
BJ LP351 (BJρ0+PBMC1)

Section I: Metadata for all samples collected for bulk RNA-sequencing analysis (n = 60 total).

File	Sample	Clone	Batch	Condition	Transfer	ClonalInfo
b8a9e771-5e64-4973-a459-f2de0182d439.rsem.txt.gz	BJ Rho Null Fibs	0	1	Fibs	Rho Null	BJ Rho Null Fibroblast
255d874b-6966-4235-b809-d26a97fc4b52.rsem.txt.gz	BJ Rho Null Fibs	0	1	Fibs	Rho Null	BJ Rho Null Fibroblast
73c987bf-fdd2-4674-a3c5-3352c8f7e96a.rsem.txt.gz	BJ Rho Null Fibs	0	1	Fibs	Rho Null	BJ Rho Null Fibroblast
d8e86411-8f83-44ab-a4e0-be587a3e69a5.rsem.txt.gz	BJ Fibs	0	1	Fibs	BJ	BJ Fibroblast
c9d94a14-38ea-4ef4-8045-1f68b6ca36e0.rsem.txt.gz	BJ Fibs	0	1	Fibs	BJ	BJ Fibroblast
1bd36e15-65bc-475f-9b59-024ac2038dae.rsem.txt.gz	BJ Fibs	0	1	Fibs	BJ	BJ Fibroblast

1ad3cd29-2eda-4a71-9c7d-deaa3cc6ab6f.rsem.txt.gz	HEK Transfer Fibs	0	1	Fibs	HEK Transfer	HEK Transfer Fibroblast
a9cdeb6a-0b30-4bcd-8d91-73bffed920fd.rsem.txt.gz	HEK Transfer Fibs	0	1	Fibs	HEK Transfer	HEK Transfer Fibroblast
36659ffa-4d9d-48b6-9af7-ee69add64a31.rsem.txt.gz	HEK Transfer Fibs	0	1	Fibs	HEK Transfer	HEK Transfer Fibroblast
158c0cda-a7f9-4a0f-81e3-50d946a1452f.rsem.txt.gz	LP351 Transfer Fibs	0	1	Fibs	LP351 Transfer	LP351 Transfer Fibroblast
d094adc5-496c-45c1-8da9-fc61204b3ee6.rsem.txt.gz	LP351 Transfer Fibs	0	1	Fibs	LP351 Transfer	LP351 Transfer Fibroblast
7cfb6f23-8670-43e2-ac43-9b9cb27de3e8.rsem.txt.gz	LP351 Transfer Fibs	0	1	Fibs	LP351 Transfer	LP351 Transfer Fibroblast
96c524a0-9ec2-4af4-a29f-e5b58171da84.rsem.txt.gz	BJ iPSC	0	1	iPSC	BJ	BJ iPSC
90fe80c9-2f5d-4faa-9b6e-aa52ef99acfb.rsem.txt.gz	BJ iPSC	0	1	iPSC	BJ	BJ iPSC
d09bdbb2-0881-4ba5-b77f-38e1a39fe29a.rsem.txt.gz	BJ iPSC	0	1	iPSC	BJ	BJ iPSC
d0a731cc-9d22-411f-bef9-c2ee1207f745.rsem.txt.gz	HEK Transfer iPSC	1	1	iPSC	HEK Transfer	HEK Transfer iPSC Clone 1
c9a75556-39c7-44e8-8ec1-9b88bf79ce37.rsem.txt.gz	HEK Transfer iPSC	2	1	iPSC	HEK Transfer	HEK Transfer iPSC Clone 2
e0a67304-7019-44cf-a2c9-d5bf91c36ea7.rsem.txt.gz	HEK Transfer iPSC	4	1	iPSC	HEK Transfer	HEK Transfer iPSC Clone 4
a0db8844-9056-42dc-bf36-654061617b1b.rsem.txt.gz	LP351 Transfer iPSC	1	1	iPSC	LP351 Transfer	LP351 Transfer iPSC Clone 1
2c708981-49e5-4691-95d1-ed04676bcdc6.rsem.txt.gz	LP351 Transfer iPSC	2	1	iPSC	LP351 Transfer	LP351 Transfer iPSC Clone 2
0f9cb841-ff39-4b48-bfd5-faf2bad51109.rsem.txt.gz	LP351 Transfer iPSC	11	1	iPSC	LP351 Transfer	LP351 Transfer iPSC Clone 11
fb4f8f80-ec69-4cae-a0c7-2f743b3844d7.rsem.txt.gz	BJ MSC	0	1	MSC	BJ	BJ MSC
7c463e9b-d7e7-46ad-af69-97efd6efb931.rsem.txt.gz	BJ MSC	0	1	MSC	BJ	BJ MSC
597999d5-2013-45a6-aa9d-2ad0c05cc4dd.rsem.txt.gz	BJ MSC	0	1	MSC	BJ	BJ MSC
7feb6877-39dc-445b-bfb5-f6755851592d.rsem.txt.gz	HEK Transfer MSC	1	1	MSC	HEK Transfer	HEK Transfer MSC Clone 1
49a57add-fd64-4609-937c-7b8bef7ee7f4.rsem.txt.gz	HEK Transfer MSC	2	1	MSC	HEK Transfer	HEK Transfer MSC Clone 2

5245244d-170b-4258-ba53-b6fe1398349e.rsem.txt.gz	HEK Transfer MSC	4	1	MSC	HEK Transfer	HEK Transfer MSC Clone 4
bec88e7e-17ac-40b8-901f-eb9143c2ae49.rsem.txt.gz	LP351 MSC	1	1	MSC	LP351 Transfer	LP351 Transfer MSC Clone 1
c7432564-97f0-45e6-b332-3e2753ee08ed.rsem.txt.gz	LP351 MSC	2	1	MSC	LP351 Transfer	LP351 Transfer MSC Clone 2
52f558cb-1b97-4f8d-81be-13b8a0e9732c.rsem.txt.gz	LP351 MSC	11	1	MSC	LP351 Transfer	LP351 Transfer MSC Clone 11
5491c6d3-31f1-483c-b4f7-b778e10c4272.rsem.txt.gz	BJ Rho Null Fibs	0	2	Fibs	Rho Null	BJ Rho Null Fibroblast
cd3c684e-26fe-4ea8-81df-fffc3dff959b.rsem.txt.gz	BJ Rho Null Fibs	0	2	Fibs	Rho Null	BJ Rho Null Fibroblast
15cd734e-a53d-4033-b103-415614b373b4.rsem.txt.gz	BJ Rho Null Fibs	0	2	Fibs	Rho Null	BJ Rho Null Fibroblast
0a788839-3eb4-4b27-9ad5-f8b23da97d67.rsem.txt.gz	BJ Fibs	0	2	Fibs	BJ	BJ Fibroblast
94799a70-74de-411e-bff1-e6c4ed715f0d.rsem.txt.gz	BJ Fibs	0	2	Fibs	BJ	BJ Fibroblast
81198c14-b0ef-45ad-9042-cb7821bb64b0.rsem.txt.gz	BJ Fibs	0	2	Fibs	BJ	BJ Fibroblast
33cd518a-88f7-4984-941a-bbdf4c00a1d7.rsem.txt.gz	HEK Transfer Fibs	0	2	Fibs	HEK Transfer	HEK Transfer Fibroblast
5cd6540c-abe9-4768-ac60-d34f39047287.rsem.txt.gz	HEK Transfer Fibs	0	2	Fibs	HEK Transfer	HEK Transfer Fibroblast
2012771c-8d8d-426e-b083-3393e44c31df.rsem.txt.gz	HEK Transfer Fibs	0	2	Fibs	HEK Transfer	HEK Transfer Fibroblast

Section II: Transcript per million (TPM) normalized expression values for summarized HGNC gene-level counts per sample.

	b8a9e771-5e64-4973-a459-f2de0182d439	**255d874b-6966-4235-b809-d26a97fc4b52**	**73c987bf-fdd2-4674-a3c5-3352c8f7e96a**	**d8e86411-8f83-44ab-a4e0-be587a3e69a5**	**c9d94a14-38ea-4ef4-8045-1f68b6ca36e0**	**1bd36e15-65bc-475f-9b59-024ac2038dae**	**1ad3cd29-2eda-4a71-9c7d-deaa3cc6ab6f**	**a9cdeb6a-0b30-4bcd-8d91-73bfed920fd**	**36659ffa-4d9d-48b6-9af7-ee69add64a31**	**158c0cda-a7f9-4a0f-81e3-50d946a1452f**	**d094adc5-496c-45c1-8da9-fc61204b3ee6**	**7cfb6f23-8670-43e2-ac43-9b9cb27de3e8**
A1BG	14.71145	12.949188	13.104916	16.929945	15.475654	15.945637	10.936097	8.275323	12.897414	11.904079	18.107024	14.897876
A1BG-AS1	4.245462	4.036122	4.043239	5.084312	4.697988	4.755244	4.455787	3.730475	4.129011	5.029377	4.629368	5.024089
A1CF	0.017163	0.010603	0.01625	0.018535	0.016516	0.01691	0.023875	0.022885	0.018575	0.031768	0.046778	0.036986

A2M	0.449387	0.420971	0.662334	35.620856	29.025254	27.858903	1.442073	1.330456	1.001217	0.344843	0.537272	0.375365
A2M-AS1	0.011713	0.022959	0.018091	0.315249	0.294279	0.380799	0.075833	0.061439	0.052727	0.213023	0.271593	0.215064
A2ML1	0.042829	0.246011	0.186717	0.104925	0.106611	0.103508	0.224339	0.213274	0.212727	0.119041	0.299965	0.201018
A2ML1-AS1	0	0	0	0	0	0	0	0	0	0.025804	0.072944	0.064965
A2ML1-AS2	0.055609	0.109415	0.02827	0.10853	0.030816	0.091248	0.026057	0.147111	0	0	0	0
A2MP1	0.009694	0	0	0.031045	0.053287	0.056661	0.014809	0.013247	0	0.031794	0.010916	0.002043
A3GALT2	0.008906	0.012841	0.015822	0.012193	0.013645	0	0.018318	0.008763	0.015394	0.031618	0.025894	0.042783
A4GALT	3.706751	3.373845	3.383823	7.052174	7.207618	5.994747	4.852479	3.469518	3.762685	6.274258	2.081367	1.896951
A4GNT	0.06875	0.182797	0.173168	0.299675	0.234351	0.330214	0.116862	0.128633	0.185514	0.085747	0.085106	0.107358
AAAS	11.08221	13.345913	13.714196	14.9848	14.005754	14.249459	12.051991	12.179488	12.93515	13.916387	13.618351	12.199545
AACS	5.909526	6.030743	5.96977	8.532159	7.406034	7.517313	7.843647	7.075549	6.687875	8.030247	7.377285	9.746318
AACSP1	0.006947	0.020813	0.022276	0.023235	0.011472	0.013699	0.022397	0.050506	0.029965	0.013673	0.020529	0.03826
AADAC	0	0	0.005778	0.037684	0	0.007421	0.01028	0.016158	0.03756	0.013263	0	0.040987
AADACL2	0.010026	0.007789	0.006315	0.021816	0.016643	0.003008	0.009446	0.009078	0	0.007597	0.005941	0.009048
AADACL2-AS1	0	0.03079	0.047075	0	0.069212	0	0	0.018477	0	0.154307	0	0
AADACL3	0	0.009049	0.006636	0.006198	0.001712	0.002508	0.005937	0.002486	0	0.006547	0.00485	0.013313
AADACL4	0.006997	0.009006	0.012276	0.083536	0.115	0.037002	0.010942	0	0	0.003989	0.004023	0.005428
AADACP1	0	0	0	0	0.023901	0	0.069528	0.05643	0.01562	0.065019	0.045876	0.020267
AADAT	1.921118	2.520221	2.39693	3.505138	3.126402	3.611132	2.066938	2.240401	2.259807	2.349226	2.774343	2.377316
AAED1	22.061451	18.114471	19.244842	25.156234	26.522667	28.687271	31.689267	20.417975	32.167744	37.025155	30.283419	42.389528
AAGAB	17.372031	14.925478	15.150327	14.515257	13.505598	13.600643	12.865706	11.495957	14.548645	15.091883	14.061894	14.533363
AAK1	35.913007	27.094496	27.303868	23.732019	23.528802	23.524057	25.448379	26.333253	29.681487	28.695617	26.727988	32.042458
AAMDC	16.113722	16.634054	14.995158	15.583793	15.139153	13.832916	17.794757	13.347927	19.786809	21.059537	34.801959	34.745579

AAMP	25.314632	23.749383	23.080166	19.565049	18.595221	17.995016	19.971725	15.696617	21.266506	18.478267	19.153806	18.798203
AAN AT	0.051799	0.078527	0.079841	0.072861	0.037087	0.019135	0.055723	0.085181	0.020526	0.0462	0.058525	0.066819
AAR2	8.445205	7.540654	7.684383	8.520969	8.310893	7.62049	7.092033	6.074537	7.310501	7.166396	9.114483	8.624774
AARD	12.129518	10.616825	5.717013	2.498242	4.404324	1.722773	3.839818	0.357323	3.928873	2.371112	1.338314	1.02623
AARS	45.234477	39.054864	37.622886	46.397072	44.468605	46.735761	20.168775	22.547849	23.97715	21.897541	27.148307	30.364171
AARS2	3.490587	3.687635	3.5387	2.96652	2.724064	2.589291	2.683927	2.707084	2.861904	2.563468	2.208929	2.073685
AARSD1	9.98744	12.071345	14.870814	11.443342	11.434516	12.385085	14.406906	10.73261	14.363246	11.458089	12.553704	13.686338
AARSP1	0	0	0	0	0	0	0	0	0	0	0	0.018019
AASDH	2.744812	3.07919	2.784752	3.872972	3.427548	3.643064	2.785321	2.384999	2.787806	2.62974	2.947115	2.817076
AASDHPT	13.129804	13.405754	12.944083	12.161022	11.652108	11.548747	11.395028	9.71118	13.070702	14.010083	14.02217	13.256166
AASS	3.864044	5.859395	6.775301	5.674089	5.769977	5.42302	4.583374	6.237094	5.636809	6.682701	4.398393	4.189875
AAT	0.078176	0.122511	0.11689	0.238395	0.154331	0.083399	0.151926	0.161073	0.210854	0.145745	0.150134	0.181106
BCAAT F	10.602794	10.766887	10.253891	10.425546	8.861772	8.705768	9.773732	9.618051	9.638878	9.683937	8.28359	8.129524

Section III - MitoMiner 4.0 gene lists (subset for MitoCarta 2.0 evidence) used for nuclear-encoded mitochondrial transcript analysis.

Ensembl Identifier	Entrez Gene	*HGNC Symbol*	Full gene description	Chromosome	MitoCarta 2.0 Evidence?	IMPI Evidence?	GO Term Evidence?	HPA Evidence?	iPSortMTS	MitoFatesMTS	MitoprotMTS	TargetPMTS
ENSMUSG00000024442	66839	*0610009O20Rik*	RIKEN cDNA 0610009O20 gene	18	TRUE	Known mitochondrial	TRUE		1	0.97	0.8369	0.906
ENSMUSG00000027637	67388	*1110008F13Rik*	RIKEN cDNA 1110008F13 gene	2	TRUE	Dubious gene	TRUE		0	0.014	0.0519	0.099
ENSMUSG00000021023	66132	*1110008L16Rik*	RIKEN cDNA 1110008L16 gene	12	TRUE	Known mitochondrial	TRUE		0	0.215	0.7446	0.385
ENSMUSG00000019797	67851	*1700021F05Rik*	RIKEN cDNA 1700021F05 gene	10	TRUE	Predicted mitochondrial	TRUE		1	0.192	0.8992	0.601
ENSMUSG00000038323	73467	*1700066M21Rik*	RIKEN cDNA 1700066M21 gene	1	TRUE	Known mitochondrial	FALSE		0	0.266	0.8348	0.706
ENSMUSG00000021290	70257	*2010107E04Rik*	RIKEN cDNA 2010107E04 gene	12	TRUE	Known mitochondrial	TRUE		0	0.069	0.0377	0.049

ENSMUSG0000032403	69478	*2300009A05Rik*	RIKEN cDNA 2300009A05 gene	9	TRUE	Known mitochondrial	FALSE	1	0.881	0.8764	0.893
ENSMUSG0000050705	69662	*2310061I04Rik*	RIKEN cDNA 2310061I04 gene	17	TRUE	Predicted mitochondrial	TRUE	1	0.195	0.866	0.816
ENSMUSG0000049760	224904	*2410015M20Rik*	RIKEN cDNA 2410015M20 gene	17	TRUE	Known mitochondrial	TRUE	0	0.022	0.7399	0.277
ENSMUSG0000010277	72503	*2610507B11Rik*	RIKEN cDNA 2610507B11 gene	11	TRUE	Predicted NOT mitochondrial	FALSE	0	0	0.83	0.102
ENSMUSG0000047635	72650	*2810006K23Rik*	RIKEN cDNA 2810006K23 gene	5	TRUE	Known mitochondrial	TRUE	0	0.421	0.9352	0.806
ENSMUSG0000084234	243996	*4933405O20Rik*	RIKEN cDNA 4933405O20 gene	7	TRUE		TRUE	0	0.059	0.6619	0.153
ENSMUSG0000048489	213393	*8430408G22Rik*	RIKEN cDNA 8430408G22 gene	6	TRUE	Predicted mitochondrial	TRUE	0	0.019	0.0803	0.252
ENSMUSG0000021185	217830	*9030617O03Rik*	RIKEN cDNA 9030617O03 gene	12	TRUE	Known mitochondrial	TRUE	1	0.993	0.9776	0.942
ENSMUSG0000033213		*AA467197*	expressed sequence AA467197	2	TRUE	Predicted NOT mitochondrial	TRUE	0	0	0.1577	0.049
ENSMUSG0000057228	23923	*Aadat*	aminoadipate aminotransferase	8	TRUE	Known mitochondrial	TRUE	1	0.934	0.939	0.815
ENSMUSG0000023938	224805	*Aars2*	alanyl-tRNA synthetase 2, mitochondrial	17	TRUE	Known mitochondrial	TRUE	1	0.777	0.9758	0.771
ENSMUSG0000029695	30956	*Aass*	aminoadipate-semialdehyde synthase	6	TRUE	Known mitochondrial	TRUE	1	0.998	0.9942	0.894
ENSMUSG0000057880	268860	*Abat*	4-aminobutyrate aminotransferase	16	TRUE	Known mitochondrial	TRUE	1	0.742	0.9754	0.877
ENSMUSG0000041797	217262	*Abca9*	ATP-binding cassette, sub-family A (ABC1), member 9	11	TRUE	Predicted mitochondrial	TRUE	0	0.261	0.9963	0.778
ENSMUSG0000031974	56199	*Abcb10*	ATP-binding cassette, sub-family B (MDR/TAP), member 10	8	TRUE	Known mitochondrial	TRUE	1	0.681	0.9962	0.907
ENSMUSG0000026198	74104	*Abcb6*	ATP-binding cassette, sub-family B (MDR/TAP), member 6	1	TRUE	Known mitochondrial	TRUE	0	0.003	0.0017	0.018
ENSMUSG0000031333	11306	*Abcb7*	ATP-binding cassette, sub-family B (MDR/TAP), member 7	X	TRUE	Known mitochondrial	TRUE	1	0.561	0.9351	0.503
ENSMUSG0000028973	74610	*Abcb8*	ATP-binding cassette, sub-family B (MDR/TAP), member 8	5	TRUE	Known mitochondrial	TRUE	1	0.867	0.393	0.87
ENSMUSG0000029408	56325	*Abcb9*	ATP-binding cassette, sub-family B (MDR/TAP), member 9	5	TRUE	Predicted NOT mitochondrial	FALSE	0	0.004	0.1498	0.063

ENSMUSG00000031378	11666	*Abcd1*	ATP-binding cassette, sub-family D (ALD), member 1	X		TRUE	Predicted mitochondrial	TRUE	1	0.092	0.9381	0.631
ENSMUSG00000055782	26874	*Abcd2*	ATP-binding cassette, sub-family D (ALD), member 2		15	TRUE	Predicted NOT mitochondrial	FALSE	0	0.939	0.9963	0.815
ENSMUSG00000028127	19299	*Abcd3*	ATP-binding cassette, sub-family D (ALD), member 3		3	TRUE	Predicted mitochondrial	TRUE	0	0.799	0.8169	0.841
ENSMUSG00000028953	27407	*Abcf2*	ATP-binding cassette, sub-family F (GCN20), member 2		5	TRUE	Predicted mitochondrial	TRUE	0	0	0.0717	0.167
ENSMUSG00000033157	213012	*Abhd10*	abhydrolase domain containing 10		16	TRUE	Known mitochondrial	TRUE	1	0.452	0.9971	0.943
ENSMUSG00000040532	68758	*Abhd11*	abhydrolase domain containing 11		5	TRUE	Known mitochondrial	TRUE	1	0.916	0.9929	0.913
ENSMUSG00000036138	113868	*Acaa1a*	acetyl-Coenzyme A acyltransferase 1A		9	TRUE	Predicted mitochondrial	TRUE	0	0.432	0.4131	0.834
ENSMUSG00000010651	235674	*Acaa1b*	acetyl-Coenzyme A acyltransferase 1B		9	TRUE		TRUE	0	0.175	0.1966	0.594
ENSMUSG00000036880	52538	*Acaa2*	acetyl-Coenzyme A acyltransferase 2 (mitochondrial 3-oxoacyl-Coenzyme A thiolase)		18	TRUE	Known mitochondrial	TRUE	1	0.989	0.4113	0.63
ENSMUSG00000020532	107476	*Acaca*	acetyl-Coenzyme A carboxylase alpha		11	TRUE		TRUE	0	0	0.1062	0.075
ENSMUSG00000042010	100705	*Acacb*	acetyl-Coenzyme A carboxylase beta		5	TRUE	Known mitochondrial	TRUE	0	0.005	0.219	0.025
ENSMUSG00000029456	71985	*Acad10*	acyl-Coenzyme A dehydrogenase family, member 10		5	TRUE	Known mitochondrial	TRUE	1	0.919	0.874	0.904
ENSMUSG00000090150	102632	*Acad11*	acyl-Coenzyme A dehydrogenase family, member 11		9	TRUE	Known mitochondrial	TRUE	0	0	0.0536	0.07
ENSMUSG00000042647		*Acad12*	acyl-Coenzyme A dehydrogenase family, member 12		5	TRUE		TRUE	1	0.732	0.9728	0.919

Section IV: Metabolic gene sets (derived from the KEGG Pathway database HSA01100) tested using metabolism transcript GSVA.

KEGG Metabolism Pathway Gene Sets	**KEGG Metabolism URL**	**Metabolism Genes**																							
KEGG_GLYCOLY	http://www.broadinstitute.org/gsea/	ACS	GCK	PG	PG	PD	PDH	PDH	PG	TP	ACS	FB	ADH	HK2	ADH	HK1	HK3	AD	PGA	AD	PGA	ADH	ALD	ALD	LDH

SIS_G	msigdb/car	S		K	K	H	A	A	M	I	S	P	1		1			H	M	H	M	1	O	H	A
LUCO	ds/KEGG_	2		2	1	B	1	2	2	1	1	1	B		C			4	2	5	1	A	C	7	L
NEOG	GLYCOLY																							A	6
ENESI	SIS_GLUC																							1	B
S	ONEOGEN																								
	ESIS																								
	http://www.								L		L														
	broadinstitu								O		O														
KEGG	te.org/gsea/								C		C														
_CITR	msigdb/car								6		2														
ATE_	ds/KEGG_	I						P	4	P	8					I									
CYCL	CITRATE_	D	D	P		P	P	D	2	D	3		S	O	S	D	S	I	I	A	A	M		M	D
E_TC	CYCLE_T	H	L	C		D	C	H	5	H	3		D	G	D	H	D	D	H	C	C	D	D	D	L
A_CY	CA_CYCL	3	S	K	C	H	K	A	0	A	9	F	H	D	H	3	H	H	1	O	L	H	L	H	A
CLE	E	B	T	2	S	B	1	1	2	2	8	H	D	H	B	A	C	2	1	1	Y	2	D	1	T
	http://www.																			L					
	broadinstitu																			O					
KEGG	te.org/gsea/																			C	P				
_PENT	msigdb/car									T										7	R				
OSE_P	ds/KEGG_					P				A			T			A	A	A		2	P	P			
HOSP	PENTOSE_		R	P	P	R	F	P	P	L		F	K		R	L	L	L	H	9	S	R	D	G	P
HATE	PHOSPHA	R	P	G	G	P	B	F	F	D	T	B	T	P	B	D	D	D	6	0	1	P	E	6	G
_PAT	TE_PATH	P	I	M	L	S	P	K	K	O	K	P	L	G	K	O	O	O	P	2	L	S	R	P	M
HWAY	WAY	E	A	2	S	2	2	M	L	1	T	1	2	D	S	A	C	B	D	0	1	1	A	D	1
KEGG	http://www.																								
_PENT	broadinstitu																								
OSE_A	te.org/gsea/														L										
ND_G	msigdb/car														O										
LUCU	ds/KEGG_	U					U								C		U			U					
RONA	PENTOSE_	G	U		U	U	G	U			U		U		7		G			G	A	U	U	U	U
TE_IN	AND_GLU	T	G		G	G	T	G	C		G		G		2		T			T	K	G	G	G	G
TERC	CURONAT	1	T		T	T	2	T	R	U	T	G	T	D	9	D	2	U	X	2	R	T	T	T	T
ONVE	E_INTERC	A	1	R	1	1	B	1	Y	G	2	U	1	C	0	H	B	G	Y	B	1	2	2	2	1
RSION	ONVERSI	1	A	P	A	A	2	A	L	D	A	S	A	X	2	D	1	P	L	1	B	B	B	A	A
S	ONS	0	8	E	7	6	8	5	1	H	1	B	9	R	0	H	1	2	B	0	1	7	4	3	4
	http://www.																								
KEGG	broadinstitu																								
_FRU	te.org/gsea/																								
CTOS	msigdb/car																	A							
E_AN	ds/KEGG_							P					P		P		P	K							
D_MA	FRUCTOS							F		M		P	F		F	M	F	R				M			
NNOS	E_AND_M		P	P	F	P	G	K	P	T	T	H	K		K	T	K	1	F		F	T			
E_ME	ANNOSE_	M	M	M	B	F	M	F	F	M	P	P	F	F	F	M	F	B	P	K	B	M	H	H	H
TABO	METABOL	P	M	M	P	K	D	B	K	R	I	T	B	U	B	R	B	1	G	H	P	R	K	K	K
LISM	ISM	I	2	1	2	M	S	4	L	6	1	1	3	K	2	1	1	0	T	K	1	2	2	3	1
	http://www.																								
KEGG	broadinstitu					B																			B
_GAL	te.org/gsea/					4																		A	4
ACTO	msigdb/car		G			G		L								G				G				K	G
SE_M	ds/KEGG_		A	G	G	A	P	A	P	P	M				G	6		G		A	G	U	P	R	A
ETAB	GALACTO	G	L	L	A	L	G	L	F	F	G	H	H	H	A	P	G	A	L	L	6	G	G	1	L
OLIS	SE_META	C	K	B	L	T	M	B	K	K	A	K	K	K	L	C	L	N	C	K	P	P	M	B	T
M	BOLISM	K	1	1	E	1	2	A	M	L	M	2	1	3	T	2	A	C	T	2	C	2	1	1	2
KEGG	http://www.	U	U	U	U	A	U	A	U	M	U	U	A	A	U	A	U	U	U	U	U	U	U	U	U
_ASC	broadinstitu	G	G	G	G	L	G	L	G	I	G	G	L	L	G	L	G	G	G	G	G	G	G	G	G

ORBATE_AND_ALDARATE_METABOLISM	te.org/gsea/msigdb/cards/KEGG_ASCORBATE_AND_ALDARATE_METABOLISM	T10	T18	T17	T16	DHB1B1	T2B28	DH2	T1A5	OX	DH	T2A1	DH9A1	DH3A2	T1A9	DHA7A1	T2B1	T2B1	T2B1	T2B7	T2B4	T2A3	T1A4	T1A1	T2B1	T1A3
KEGG_FATTY_ACID_METABOLISM	http://www.broadinstitute.org/gsea/msigdb/cards/KEGG_FATTY_ACID_METABOLISM	CPTA1	CPTA2	ACOX1	ADHB1	CACSB	ACDL	ALDH2	ACOX3	CYP4A	ACOX1	ACADVL	ACAT1	ACAT2	AHADH	HADHA	HADHB	CYP4A	AACS1	ADH7	ADH6	ADH1B	ADH1C	ADH4	ECHS1
KEGG_STEROID_BIOSYNTHESIS	http://www.broadinstitute.org/gsea/msigdb/cards/KEGG_STEROID_BIOSYNTHESIS	SOAT1	SLSE	SQLE	EBP	CYP51A1	DHCR7	CYP51B1	DHCR24	HSD17B7	MSMO1	FDFT1	SC5DL	LIPA	CEL	TM7SF2	NSDHL	SOAT2								
KEGG_PRIMARY_BILE_ACID_BIOSYNTHESIS	http://www.broadinstitute.org/gsea/msigdb/cards/KEGG_PRIMARY_BILE_ACID_BIOSYNTHESIS	CYP46A1	SLC27A5	BAAT	CYP7B1	AKR1C4	HSD3B7	SCP2	AKR1D1	ACOX2	HSD17B4	CYP27A1	AMACR	CYP7A1	CYP8B1	CYP39A1	CH25H									
KEGG_STEROID_HORMONE_BIOSYNTHESIS	http://www.broadinstitute.org/gsea/msigdb/cards/KEGG_STEROID_HORMONE_BIOSYNTHESIS	SARD1A	AKR1C3	CYP1A1	HSD3B2	UGT2B28	HSD3B1	CYP19A1	SULT1E1	CYP11A1	CYP17A1	CYP21A2	AKR1C4	HSD17B3	SULT2B1	HSD17B6	HSD17B2	HSD17B1	CYP1B1	HSD11B1	CYP11B1	CYP11B2	CYP1A2	HSD11B2	HSD17B11
KEGG_OXIDATIVE_PHOSPHORYLATION	http://www.broadinstitute.org/gsea/msigdb/cards/KEGG_OXIDATIVE_PHOSPHORYLATION	ATP6V1G1	UQCRC2	NDUFA5	NDUFB8	COX6B1	PPA2	ATP5J2	NDUFS7	CYC1	ATP6V0A1	ATP6V1G2	PPA1	ATP6V1C2	TCIRG1	COX5A	ATP6V0E2	ATP5O	COX7A1	COX5B	COX4I1	ATP5A1	ATP5J	NDUFB1	NDUFA4
KEGG_PURINE_METABOLISM	http://www.broadinstitute.org/gsea/msigdb/cards/KEGG_PURINE_METABOLISM	POLR1B	NT5C1A	POLR1C	ENTPD1	POLR2K	POLR2E	ENTPD5	XDH	POLR2H	POLR2L	PPAT	DGUOK	PAICS	DGUOK	AMPD3	MCM6	POLR2A	PKLR	POLR1D	DCK	POLR3B	POLR2J	AK1	MCM4	AK2

OLISM	ds/KEGG_PURINE_METABOLISM	2G	C2	2H	P3	2E	2F	P1		2I	2J	E3		S2			1D	T1	2K	1A	D3	2L		-NME2	
KEGG_PYRIMIDINE_METABOLISM	http://www.broadinstitute.org/gsea/msigdb/cards/KEGG_PYRIMIDINE_METABOLISM	NT5C2	POLR2G	POLR2H	POLR2E	POLR2F	POLR2I	POLR2J	POLE3	TYMS	TXNRD1	NME6	POLR1D	PNPT1	POLR2K	DHODH	POLD3	POLR2L	NME1-NME2	POLA2	UPRT	CANT1	NME4	NME1	NME2
KEGG_ALANINE_ASPARTATE_AND_GLUTAMATE_METABOLISM	http://www.broadinstitute.org/gsea/msigdb/cards/KEGG_ALANINE_ASPARTATE_AND_GLUTAMATE_METABOLISM	GLUD2	GFPT2	AGXT2	CPS1	GLS2	ABAT	ADSS	ADSL	GLUD1	GLS	ASL	IL4I1	GPT	GFPT1	GPT2	DDO	ADSSL1	ACY3	GAD1	GAD2	GOT2	AGXT	GLUL	NIT2
KEGG_GLYCINE_SERINE_AND_THREONINE_METABOLISM	http://www.broadinstitute.org/gsea/msigdb/cards/KEGG_GLYCINE_SERINE_AND_THREONINE_METABOLISM	ALAS1	ALAS2	GLYCTK	MAOB	AGXT2	MAOA	AOC2	GATM	SDS	AOC3	GNMT	SHMT1	GCAT	PHGDH	DMGDH	SHMT2	SRR	PSAT1	BHMT	GLDC	DLD	GAMT	PSPH	AGXT
KEGG_CYSTEINE_AND_METHIONINE_METABOLISM	http://www.broadinstitute.org/gsea/msigdb/cards/KEGG_CYSTEINE_AND_METHIONINE_METABOLISM	AMD1	SRM	ADI1	AHCY	DNMT1	SDS	TRDMT1	DNMT3A	DNMT3B	LDHC	IL4I1	SMS	LDHB	ENOPH1	BHMT	GOT2	CDO1	APIP	GOT1	LDHAL6B	TAT	AHCYL1	MTAP	MAT2B
KEGG_VALINE_LEUCINE_AND_ISOLEUCINE_DEG	http://www.broadinstitute.org/gsea/msigdb/cards/KEGG_VALINE_LEUCINE_AND_ISOLE	AOX1	ALDH1B1	ACADS	ACADSB	ABAT	ALDH2	ACADM	ACAT2	HSD17B10	ACAT1	OXCT1	ACAA2	IL4I1	HADH	MCEE	HADHB	DBT	HADHA	ALDH6A1	HMGCL	IVD	BCKDHB	ACAD8	ECHS1

RADATION	UCINE_DEGRADATION																								
KEGG_VALINE_LEUCINE_AND_ISOLEUCINE_BIOSYNTHESIS	http://www.broadinstitute.org/gsea/msigdb/cards/KEGG_VALINE_LEUCINE_AND_ISOLEUCINE_BIOSYNTHESIS	PDHB	VARS2	IARS2	PDHA1	PDHA2	LARS	LARS2	VARS	BCAT1	BCAT2	IARS													
KEGG_LYSINE_DEGRADATION	http://www.broadinstitute.org/gsea/msigdb/cards/KEGG_LYSINE_DEGRADATION	SUV39H2	AASDHPPT	DLST	ALDH1B1	AASDH	ALDH2	ACAT2	PLOD2	PLOD1	TMLHE	EHMT2	ACAT1	SETD8	HADH	SETMAR	OGDH	HADHA	BBOX1	AASS	ECHS1	ALDH9A1	ALDH3A2	SUV420H1	SUV39H1
KEGG_ARGININE_AND_PROLINE_METABOLISM	http://www.broadinstitute.org/gsea/msigdb/cards/KEGG_ARGININE_AND_PROLINE_METABOLISM	SRM	ADC	GLUD2	GLS2	ARG1	ARG2	GLUD1	GSS	ASL	CKMT1A	P4HA2	SMS	CKB	NOS3	NOS2	NOS1	GOT2	GLUL	P4HA1	ABP1	ALDH7A1	LAP3	AGMAT	GOT1
KEGG_HISTIDINE_METABOLISM	http://www.broadinstitute.org/gsea/msigdb/cards/KEGG_HISTIDINE_METABOLISM	CNDP1	MAOB	MAOA	ALDH1B1	ALDH2	METTL6	ALDH3A1	WBSCR22	HAL	HNMT	DDC	ACY3	ALDH1A3	METTL2B	ALDH3B1	ALDH3B2	ALDH9A1	ALDH3A2	HEMK1	LCMT2	UROC1	TRMT11	ABP1	ALDH7A1
KEGG_TYROSINE_METABOLISM	http://www.broadinstitute.org/gsea/msigdb/cards/KEGG_TYROSINE_METABOLISM	MAOB	MAOA	HPD	AOX1	AOC2	TYR	HGD	METTL6	ALDH3A1	COMT	AOC3	WBSCR22	IL4I1	GSTZ1	DDC	ADH7	DBH	ADH6	METTL2B	ADH1B	ALDH1A3	ADH1C	ALDH3B1	ADH4
KEGG_PHENYLALANINE_METABOLISM	http://www.broadinstitute.org/gsea/msigdb/cards/KEGG_PHENYLALANINE_	ALDH1A3	ALDH3B1	ALDH3B2	MAOB	MAOA	HPD	GOT2	AOC2	ALDH3A1	AOC3	PAH	GOT1	PRDX6	TAT	MIF	NAT6	IL4I1	DDC						

	METABOLISM http://www.																										
KEGG_TRYPTOPHAN_METABOLISM	broadinstitute.org/gsea/msigdb/cards/KEGG_TRYPTOPHAN_METABOLISM					ALDH1B1	AANAT	ALDH2	AWRS	IDO1		ACAT2	AACS1	ILVBL	HAAO	OGDH	TPH1	HIAA	DDC	AFMID	CYP1A1	CYP1A2	CYP1B1		ECHS1
KEGG_BETA_ALANINE_METABOLISM	http://www.broadinstitute.org/gsea/msigdb/cards/KEGG_BETA_ALANINE_METABOLISM				ALDH9A1	ALDH3A2				ALDH1B1	DHCR		EHHADH	ALDH3A1	ACOX1		ALDH7A1				MLYCD	HACD1			
KEGG_TAURINE_AND_HYPOTAURINE_METABOLISM	http://www.broadinstitute.org/gsea/msigdb/cards/KEGG_TAURINE_AND_HYPOTAURINE_METABOLISM	GCGT7	CSAD	GGAT5	GGAT1	GAD1	BAAT	GAAD2	GAGT6	CDO1	ADO														
KEGG_SELENOAMINO_ACID_METABOLISM	http://www.broadinstitute.org/gsea/msigdb/cards/KEGG_SELENOAMINO_ACID_METABOLISM	ME		WBSE	SE		SETD2	MEHL			LCMT1	PAPSS1	PAPSS2	TRMT1	MARS1		AHCY			MAT2A	MAT1A	LCMT2		AHCY	
KEGG_GLUTATHIONE_METABOLISM	http://www.broadinstitute.org/gsea/msigdb/cards/KEGG_GLUTATHIONE_METABOLISM	SRTM1	GSTP1	GSTT1	GSTT2	GSS1	GSS2	RRM2B			GSS1	GSS2	GMPS	GLYCTK	GART	MTHFD1L	GSS1	GSTT2B	GSTA4	GSR	GPX1	GSTA4	GSR	GCLC	GSS2	GSTM2
KEGG_STARCH_AND_SUCROSE_METABOLISM	http://www.broadinstitute.org/gsea/msigdb/cards/KEGG_STARCH_AND_SUCROSE_METABOLISM	EN		ENPP1	AMY2B	UGT2B28	PGM2	UXS1	UGDH	MGAM	GYS2	GYS1	HK2	HK3	HK1	GBA3	GUSB	TREH	AMY1A	AMY1B	AMY1C	AMY2A1	UGT2B4	PYGB	PYGM

	TABOLISM http://www.broadinstitute.org/gsea/msigdb/cards/KEGG_N_GLYCAN_BIOSYNTHESIS	ALG13	DOLPP1	RPN1	ALG14	MAN1B1	ALG3	B4GALT1	MGAT5	RPN2	STT3A	MGAT3	DAD1	MGAT2	ALG12	TUSC3	MAN1C1	DPM2	DPM1	GANAB	ALG1	MGAT4A	ALG10B	STT3B	MAN2A2
KEGG_OTHER_GLYCAN_DEGRADATION	http://www.broadinstitute.org/gsea/msigdb/cards/KEGG_OTHER_GLYCAN_DEGRADATION	ENGASE	NAGLB1	MAN2B1A	MAN2B1	NAGBA	NEU4	NEU2	NEU1	FUCA1	FUCA2	AGA	MAN2C1	MAN2B2	NEU3	HEXB	HEXA									
KEGG_O_GLYCAN_BIOSYNTHESIS	http://www.broadinstitute.org/gsea/msigdb/cards/KEGG_O_GLYCAN_BIOSYNTHESIS	GALNT4	GALNT2	GALNT5	GALNT6	GALNT5	GALNT1	GALNT6	GALNT3	GCNT3	GALNT1	GALNT10	GALNT1	GALNT19	GALNT7	GCNT4	GALNT11	GCNT1	GALNT18	GCNT1	GALNT14	C1GALT1	GALNT12	GALNT2	GALNT2	GALNT13
KEGG_AMINO_SUGAR_AND_NUCLEOTIDE_SUGAR_METABOLISM	http://www.broadinstitute.org/gsea/msigdb/cards/KEGG_AMINO_SUGAR_AND_NUCLEOTIDE_SUGAR_METABOLISM	MPI	GCK	GFPT2	GALK1	AMPD2	PMM2	PGM2	PMM1	AMDHD2	GNPDA2	GMDS	UXS1	GNPNAT1	NANS	UGDH	CYB5R3	GFPT1	FUK	NANP	CYB5R1	FPGT	HEXB	HEXA	HK2
KEGG_GLYCOSAMINOGLYCAN_DEGRADATION	http://www.broadinstitute.org/gsea/msigdb/cards/KEGG_GLYCOSAMINOGLYCAN_DEGRADATION	HS3ST3A1	HPSE2	HPSE	GLB1	GUSB	HYAL3	HYAL4	HYAL1	HYAL2	SPAM1	HS3ST1	GLCE	IDUA	HS3ST3B1	SGSH	NAGLU	HEXB	NAGA	HEXA	IDS	ARSB			
KEGG_GLYCOSAMINOGLYCAN_BIOSYNTHESIS_CHONDROITIN_SULFATE	http://www.broadinstitute.org/gsea/msigdb/cards/KEGG_GLYCOSAMINOGLYCAN_BIOSYNTHESIS_CHONDROITIN_SULFATE	DSE	B3GALT6	CHPF	XYLT2	CHSY1	XYLT1	CHSY3	B3GAT3	CHPF2	CHSY1	CHPF	HS6ST2	B4GALT7	CHST14	UST	HS6ST1	CHST11	CHST12	B3GAT1	CHST15	CSGALNACT1	CHST3	B3GAT2	

GLYC	ds/KEGG_		L		T	Y	T	1	T	Y	1	F	1	L	T		1	L	T	L	T	1	T
AN_BI	GLYCOSA		T		1	3	2	4	1	1	1	2	5	T	7		3	N	2	N	3	2	3
OSYN	MINOGLY		6											7				A		A			
THESI	CAN_BIOS																	C		C			
S_CH	YNTHESIS																	T		T			
ONDR	_CHONDR																	2		1			
OITIN	OITIN_SU																						
_SULF	LFATE																						
ATE																							
KEGG	http://www.																						
_GLY	broadinstitu																						
COSA	te.org/gsea/																						
MINO	msigdb/car																						
GLYC	ds/KEGG_																						
AN_BI	GLYCOSA					B		S	B	S	B	B		S									
OSYN	MINOGLY		B	B		4	B	T	4	T	4	4		T									
THESI	CAN_BIOS	C	3	3	C	G	3	3	G	3	G	G	C	3		C							
S_KER	YNTHESIS	H	G	G	H	A	G	G	A	G	A	A	H	G	F	H							
ATAN	_KERATA	S	N	N	S	L	N	A	L	A	L	L	S	A	U	S							
_SULF	N_SULFA	T	T	T	T	T	T	L	T	L	T	T	T	L	T	T							
ATE	TE	2	1	2	1	1	7	2	3	1	2	4	4	3	8	6							
KEGG	http://www.																						
_GLY	broadinstitu																						
COSA	te.org/gsea/																						
MINO	msigdb/car																						
GLYC	ds/KEGG_										H						H						
AN_BI	GLYCOSA										S					B			S			B		
OSYN	MINOGLY	H						B			3	H	H	B	H	3	H	H	3			4	B	
THESI	CAN_BIOS	S			N	X	X	3	N		S	S	S	3	S	G	S	S	S	N	N	G	3	E
S_HEP	YNTHESIS	3	E	E	D	Y	Y	G	D	G	T	2	6	G	3	A	3	6	T	D	D	A	G	X
ARAN	_HEPARA	S	X	X	S	L	L	A	S	L	3	S	S	A	S	L	S	S	3	S	S	L	A	T
_SULF	N_SULFA	T	T	T	T	T	T	T	T	C	B	T	T	T	T	T	T	T	A	T	T	T	T	L
ATE	TE	5	2	1	3	1	2	1	1	E	1	1	2	3	1	6	2	1	1	2	4	7	2	1
KEGG	http://www. broadinstitu te.org/gsea/																				P N	P N		
_GLY	msigdb/car	M							M					L			A		A	A	L	L		G
CERO	ds/KEGG_	B							B		D			D			G	A	G	K	I	I	P	D	L
LIPID	GLYCERO	O	G	L	D	D	D	D	O		G			H			P	W	P	R	P	P	N	G	Y
_MET	LIPID_ME	A	P	I	G	G	G	G	A		A	G	G	7	A	D	A	A	A	1	R	R	L	A	C
ABOLI	TABOLIS	T	A	P	K	K	K	K	T	G	T	K	L	A	G	A	T	T	T	B	P	P	I	T	T
SM	M	2	M	G	Z	E	D	H	1	K	2	2	A	1	K	K	3	2	4	1	2	1	P	1	K

Section V: Significantly enriched metabolic pathways across sample conditions identified using GSVA (using an F statistic adjusted P value threshold of 0.05).

	SampleMatrix.ClonalInfoBJ.Fibroblast	SampleMatrix.ClonalInfoBJ.iPSC	SampleMatrix.ClonalInfoBJ.MSC	SampleMatrix.ClonalInfoBJ.Rho.Null.Fibroblast

KEGG_GLYCOSAMINOGLYCAN_DEGRADATION	0.405813902	-0.55531956	0.16206836	0.36951536
KEGG_OTHER_GLYCAN_DEGRADATION	0.474766612	-0.48280539	-0.18262391	0.60932469
KEGG_GLYCOSPHINGOLIPID_BIOSYNTHESIS_GANGLIO_SERIES	0.382309082	-0.54846351	0.44537103	0.0578382
KEGG_GLYCINE_SERINE_AND_THREONINE_METABOLISM	-0.383649528	0.40109112	0.0764127	-0.26725939
KEGG_GLYCOSAMINOGLYCAN_BIOSYNTHESIS_CHONDROITIN_SULFATE	-0.052699356	-0.45450794	0.27339616	0.24174442
KEGG_CYSTEINE_AND_METHIONINE_METABOLISM	-0.396336915	0.35707445	-0.21197381	-0.25991657
KEGG_AMINO_SUGAR_AND_NUCLEOTIDE_SUGAR_METABOLISM	0.000668027	-0.35955462	0.06385756	0.28983686
KEGG_ONE_CARBON_POOL_BY_FOLATE	-0.24128595	0.44139376	-0.14850649	-0.3393163
KEGG_VALINE_LEUCINE_AND_ISOLEUCINE_BIOSYNTHESIS	-0.468182931	0.46403657	0.10976203	-0.29216111
KEGG_NITROGEN_METABOLISM	-0.050971916	0.21965976	0.03857841	-0.12463341
KEGG_TERPENOID_BACKBONE_BIOSYNTHESIS	-0.470311707	-0.1863855	0.47007272	-0.49893796
KEGG_BETA_ALANINE_METABOLISM	-0.251185103	0.36688292	-0.28747999	-0.19066366
KEGG_N_GLYCAN_BIOSYNTHESIS	-0.216661638	-0.36447541	0.12509319	0.18557465
KEGG_ALANINE_ASPARTATE_AND_GLUTAMATE_METABOLISM	-0.01577062	0.1992658	-0.30918366	0.04677447
KEGG_GALACTOSE_METABOLISM	0.091774469	-0.23914495	-0.15957031	0.24175358
KEGG_AMINOACYL_TRNA_BIOSYNTHESIS	-0.383620391	0.25067563	0.11462189	-0.06011311
KEGG_GLYCOSAMINOGLYCAN_BIOSYNTHESIS_KERATAN_SULFATE	-0.205296027	-0.2550607	0.22388406	0.05485028
KEGG_GLYCOSYLPHOSPHATIDYLINOSITOL_GPI_ANCHOR_BIOSYNTHESIS	-0.059839128	-0.31262592	-0.01253082	0.36172065
KEGG_INOSITOL_PHOSPHATE_METABOLISM	0.262690597	-0.24778133	-0.19549115	0.21435705

Section VI: Reactome pathway analaysis of the top 500 genes signficantly altered genes between BJ parent and the BJ rho nulls and SIMR cell lines.

	Cluster	ID	Description	GeneRatio	BgRatio	pvalue	p.adjust	qvalue	geneID	Count
1	Upregulated	R-HSA-1632000	Respiratory electron transport, ATP synthesis by chemiosmotic coupling, and heat production by uncoupling proteins.	12/115	123/10619	7.64E-09	2.50E-06	2.32E-06	COX1/COX3/ND3/ND2/ND6/CYTB/ND5/ATP6/ND1/ATP8/ND4/COX2	12
2	Upregulated	R-HSA-6121105	Respiratory electron transport	10/115	100/10619	1.14E-07	1.87E-05	1.73E-05	COX1/COX3/ND3/ND2/ND6/CYTB/ND5/ND1/ND4/COX2	10
3	Upregulated	R-HSA-1428517	The citric acid (TCA) cycle and respiratory electron transport	12/115	174/10619	3.65E-07	3.98E-05	3.69E-05	COX1/COX3/ND3/ND2/ND6/CYTB/ND5/ATP6/ND1/ATP8/ND4/COX2	12
4	Upregulated	R-HSA-6799198	Complex I biogenesis	6/115	55/10619	2.66E-05	0.001822	0.001689	ND3/ND2/ND6/ND5/ND1/ND4	6
5	Upregulated	R-HSA-4655427	SUMOylation of DNA methylation proteins	4/115	17/10619	2.79E-05	0.001822	0.001689	PHC1/CBX2/DNMT3B/DNMT3A	4
6	Upregulated	R-HSA-8964043	Plasma lipoprotein clearance	4/115	33/10619	0.000941	0.022843	0.021178	MYLIP/PCSK9/APOC1/APOE	4
7	Upregulated	R-HSA-2866423	Ephrin signaling	3/115	19/10619	0.000506	0.013549	0.012565	EFNB3/EPHB4/EPHB6	3
8	Downregulated	R-HSA-1474244	Extracellular matrix organization	18/183	301/10619	4.28E-06	0.000258	0.000241	ADAMTS2/SCUBE3/ITGB1/TIMP2/ADAMTS1/CD44/ITGA3/NTN4/ITGA2/LOX/LAMC1/SERPINE1/CTSK/CTSB/FGF2/LOXL2/MMP12/CD151	18
9	Downregulated	R-HSA-75205	Dissolution of Fibrin Clot	4/83	13/10619	5.40E-05	0.001163	0.001077	SERPINB2/SERPINB8/PLAT/SERPINE1	4

		R-HSA-					0.0	0.0		
	Down	2109			25/	5.7	11	10		
10	regulated	9191	Basigin interactions	5/183	106/19	8E-05	63.4	07.7	ITGB1/ITGA3/SLC16A3/CAV1/L1CAM	5
		R-HSA-								
		8874				0.0	0.0	0.0		
	Down	0808			30/	00	21	18		
11	regulated	1	MET activates PTK2 signaling	5/183	106/19	14 5	82.4	90.3	MET/ITGB1/ITGA3/ITGA2/LAMC1	5
		R-HSA-								
		9006	Signaling by			0.0	0.0	0.0		
	Down	9334	Receptor Tyrosine Kinases	19/183	458/619	00 34	41 44	35 89	MET/ATP6V0E1/ITGB1/PDGFC/ITGA3/ITGA2/SH3GL2/ VEGFC/CAV1/PLAT/LAMC1/BDNF/FGF5/FGF2/EGFR/ ATP6V1E1/EREG/ATP6V1A/ATP6AP1	19
12	regulated						3	2 5		

Patananan, et. al. 2020 (Submitted - Cell Reports)
Supplementary Table S5:
Transcriptomics overrepresentation and global pathway analysis.
Related to Figures 5 and S3, S4, and S5.

Accession Information:

GSE115871

Table of Contents:

Condition Code:

BJ
BJ rho null (BJρ0)
BJ HEK (BJρ0+HEK293T)
BJ LP351 (BJρ0+PBMC1)

Section I: List of differentially expressed genes between BJ ρ0 Fibroblasts (numerator) and

BJ Fibroblasts (denominator):

DEGs were calculated using an absolute log2FC > 1 and adjusted P value < 0.05

(Benjamini-Hochberg False Discovery Rate = 0.05)

HGNC Gene Name	Geometric Mean Expression Across Samples	Log2 Fold Change (p0 Fibroblast/BJ Fiborblast)	Log Fold Change Standard Error	Wald Test Statistic	Wald test *P* value	Adjusted *P* value
MT-CO1	433436.171	-9.4154576	0.2384446	-35.293135	7.48E-273	2.11E-268

MT-ND6	28408.1742	-8.5626792	0.2373881 9	-31.857857	1.02E-222	1.44E-218
MT-ND5	128222.532	-8.592825	0.2394386 3	-31.710944	1.10E-220	1.03E-216
MT-ND3	20672.2952	-8.4892744	0.2385692	-31.392461	2.56E-216	1.81E-212
MT-CO3	183615.539	-8.7161804	0.2531134 9	-30.485062	4.11E-204	2.32E-200
MT-CYB	111338.345	-8.6191694	0.2506297 1	-30.400104	5.48E-203	2.57E-199
MT-ND2	91210.5298	-8.1742957	0.2404914 8	-29.831808	1.51E-195	6.09E-192
MT-ND1	118333.647	-8.5303575	0.2705458 8	-27.833939	1.69E-170	5.94E-167
MT-ND4	178539.614	-8.1383759	0.2579176 6	-27.676956	1.32E-168	4.14E-165
MT-ATP6	87007.231	-8.2457387	0.2619612	-27.659587	2.14E-168	6.03E-165
MT-CO2	148722.339	-8.6924717	0.2782259 8	-27.648287	2.93E-168	7.50E-165
MT-ND4L	23790.3573	-8.6833802	0.2783504 3	-27.603263	1.02E-167	2.39E-164
MT-ATP8	25909.6871	-8.4843636	0.2934107 5	-25.508144	1.60E-143	3.47E-140
CPXM1	2397.31675	-6.8584727	0.2487428 9	-23.552322	1.19E-122	2.39E-119
MT-TY	1416.52297	-8.3629809	0.3226287 3	-22.821839	2.78E-115	5.23E-112
MT-TC	1169.04405	-7.2294925	0.2757945 2	-22.587441	5.76E-113	1.01E-109
MTATP6P 1	8287.40308	-7.3269131	0.3031666 9	-20.86942	1.02E-96	1.68E-93
EFNB3	665.027606	-4.6208549	0.179306	-20.193719	1.11E-90	1.74E-87
MT-TP	888.527422	-8.8272843	0.3903131 9	-20.053856	1.87E-89	2.77E-86
SMO	4056.6609	-4.0263527	0.1528967 1	-19.793446	3.39E-87	4.78E-84
KBTBD11	807.536057	-5.3985847	0.2287403 5	-19.229597	2.09E-82	2.81E-79
SOX11	6574.78325	-5.4796105	0.2329966 1	-19.226075	2.24E-82	2.87E-79
MT-TE	1187.20916	-9.2803678	0.4370425 9	-18.946363	4.73E-80	5.80E-77
KISS1	1810.96797	6.55059089	0.2952338 9	18.800656 1	7.46E-79	8.41E-76
PIM1	3077.83149	-3.1810617	0.1160055 3	-18.80136	7.36E-79	8.41E-76
SERPINF1	3957.51185	-4.3159212	0.1813707 7	-18.282556	1.14E-74	1.24E-71
EIF4E3	1151.76538	-3.4344114	0.1368848 2	-17.784378	9.34E-71	9.75E-68
NDN	1586.99448	-5.1683058	0.2347446 6	-17.756766	1.53E-70	1.54E-67

RGMA	1904.38441	-4.4507525	0.19778892	-17.446642	3.65E-68	3.55E-65
FGF7	471.18189	-5.5055707	0.25877592	-17.41109	6.80E-68	6.39E-65
LTBP4	7406.45918	-4.2461128	0.18764688	-17.29905	4.78E-67	4.35E-64
MYLIP	913.506414	-4.9057969	0.22629098	-17.260065	9.40E-67	8.28E-64
C10orf105	211.574659	-8.0416366	0.41866882	-16.81911	1.77E-63	1.51E-60
OLFM2	1652.49865	-4.2005636	0.19435482	-16.467632	6.27E-61	5.20E-58
MT-TA	464.838413	-7.7664229	0.41369379	-16.356114	3.93E-60	3.17E-57
VWA5A	736.053063	-3.5924924	0.16257463	-15.946476	3.01E-57	2.36E-54
COL5A3	2093.76657	-4.2311483	0.20890998	-15.466701	5.82E-54	4.43E-51
STK32B	1113.76259	-3.6755619	0.17627946	-15.177956	4.95E-52	3.67E-49
ARHGEF3	538.483341	-3.6845436	0.17716299	-15.152959	7.24E-52	5.23E-49

Section II: Fibroblast expression relative to BJ Fibroblast Reactome Overrepresentation Analysis (ORA) results:

DEGs across fibroblast transfer conditions were evaluated for ORA in the Reactome database using compareCluster() in R Bioconductor package ReactomePA. Overrepresented pathways are calculated with a P value threshold < 0.05 and an adjusted P value of 0.20 (BH FDR = 0.2)

	Cluster ID (Relative to BJ)	Reactome ID	Pathway Description	DEG Ratio	Background Gene Ratio	*P* value	Adjusted *P* value	Benjamini-Hochberg Corrected *q* value	*List of HGNC gene IDs*	Gene Hit Count
1	LP351 Upregulated	R-HSA-1474244	Extracellular matrix organization	20/173	301/10619	8.9E-08	4.7E-05	4.11E-05	SCUBE3/NCAM1/TGFB2/COL8A1/MMP12/SERPINE1/TLL2/MMP10/ELN/P4HA3/ITGA6/PLOD2/MMP3/ITGA4/COL10A1/ITGA3/ITGB5/SPP1/ITGB6/COMP	20

	LP351 Upregulated	R-HSA-6809371	Formation of the cornified envelope	11/173	129/10619	7.8E-06	0.001076	0.009076	0.029072	DSP/KRT81/DSG2/DSC3/KRT14/IVL/PKP1/KRT34/KRT5/SPRR1A/PI3	11
2											
	LP351 Upregulated	R-HSA-216083	Integrin cell surface interactions	9/173	85/10619	9.3E-06	0.001076	0.009076	0.029072	COL8A1/ITGA6/ITGA4/COL10A1/ITGA3/ITGB5/SPP1/ITGB6/COMP	9
3											
	LP351 Upregulated	R-HSA-6785807	Interleukin-4 and Interleukin-13 signaling	10/173	108/10619	9.9E-06	0.001076	0.009076	0.029072	CCND1/IL1A/GATA3/POMC/SAA1/MMP3/IL13RA2/PTGS2/CD36/IL1B	10
4											
	LP351 Upregulated	R-HSA-6805567	Keratinization	14/173	214/10619	1.0E-05	0.001076	0.009076	0.029072	DSP/KRT81/DSG2/KRTAP2-3/DSC3/KRT14/IVL/PKP1/KRT34/KRT5/KRTAP3-1/KRTAP21-2/SPRR1A/PI3	14
5											
	LP351 Upregulated	R-HSA-9009391	Non-genomic estrogen signaling	8/173	77/10619	3.4E-05	0.002068	0.023374	0.029072	CCND1/HBEGF/EREG/MMP3/TGFA/EPGN/GNAT3/GNAI1	8
6											
	LP351 Upregulated	R-HSA-963463	Estrogen-dependent nuclear events downstream of ESR-membrane signaling	5/173	24/10619	3.5E-05	0.002068	0.023374	0.029072	CCND1/HBEGF/EREG/TGFA/EPGN	5
7											
	LP351 Upregulated	R-HSA-180336	SHC1 events in EGFR signaling	4/173	13/10619	4.3E-05	0.002084	0.024768	0.029072	HBEGF/EREG/TGFA/EPGN	4
8											
	LP351 Upregulated	R-HSA-180336	SHC1 events in EGFR signaling	4/173	14/10619	6.0E-05	0.003049	0.030432	0.029072	HBEGF/EREG/TGFA/EPGN	4
9											
	LP351 Upregulated	R-HSA-182971	EGFR downregulation	5/173	31/10619	0.00013	0.006054	0.056978	0.029072	HBEGF/SH3GL2/EREG/TGFA/EPGN	5
10											
	LP351 Upregulated	R-HSA-180292	GAB1 signalosome	4/173	17/10619	0.00072	0.006054	0.056978	0.029072	HBEGF/EREG/TGFA/EPGN	4
11											
	LP351 Upregulated	R-HSA-888590	GABA synthesis, release, reuptake and degradation	4/173	19/10619	0.00011	0.006054	0.056978	0.029072	ALDH5A1/SYT1/RIMS1/GAD1	4
12											
	LP351 Upregulated	R-HSA-1474228	Degradation of the extracellular matrix	9/173	140/10619	0.00028	0.006054	0.057152	0.029072	SCUBE3/COL8A1/MMP12/TLL2/MMP10/ELN/MMP3/COL10A1/SPP1	9
13											
	LP351 Upregulated	R-HSA-1250196	PI3K events in ERBB4 signaling	3/173	10/10619	0.00046	0.006054	0.057152	0.029072	HBEGF/NRG1/EREG	3
14											

	gulated	1250342				878	941	9717			
	LP351	R-HSA-				0.000	0.019	0.0			
	Upregulated	3519067	Apoptotic cleavage of cell adhesion proteins	3/173	11/10619	6.8	1.17	1709	DSP/DSG2/PKP1		3
	LP351	R-HSA-				0.000	0.019	0.0			
	Upregulated	4464107	Type I hemidesmosome assembly	3/173	11/10619	6.8	1.17	1709	ITGA6/KRT14/KRT5		3
	LP351	R-HSA-				0.000	0.019	0.0			
	Upregulated	1474290	Collagen formation	7/173	90/10619	71.1	1.17	1709	COL8A1/TLL2/P4HA3/ITGA6/PLOD2/MMP3/COL10A1		7
	LP351	R-HSA-				0.000	0.019	0.0			
	Upregulated	1643713	Signaling by EGFR in Cancer	4/173	25/10619	86.7	1.17	1709	HBEGF/EREG/TGFA/EPGN		4
	LP351	R-HSA-				0.001	0.026	0.0			
	Upregulated	7527505	Dissolution of Fibrin Clot	3/173	13/10619	7.3	2.85	2266	SERPINB2/SERPINE1/PLAT		3

Section III: iPSC expression relative to BJ iPSC Reactome Overrepresentation Analysis (ORA) results. Results derived as above.

	Cluster ID (Relative to BJ)	**Reactome ID**	**Pathway Description**	**Background Genome Ratio**	***P* value**	**Adjusted *P* value**	**Benjamini-Hochberg Corrected *q* value**	***List of HGNC gene IDs***	**Gene Hit Count**	
1	LP351 Upregulated	R-HSA-7372	RNA Polymerase I Promoter Opening	18-May	63/1061	5.05E-08	2.05E-06	4.31E-07	HIST1H3A/HIST1H4A/HIST1H3C/HIST1H4F/HIST1H2BB	5
2	LP351 Upregulated	R-HSA-5334	DNA methylation	18-May	65/1061	5.92E-08	2.05E-06	4.31E-07	HIST1H3A/HIST1H4A/HIST1H3C/HIST1H4F/HIST1H2BB	5
3	LP351 Upregulated	R-HSA-5625	Activated PKN1 stimulates transcription of AR (androgen receptor) regulated genes KLK2 and KLK3	18-May	67/1061	6.91E-08	2.05E-06	4.31E-07	HIST1H3A/HIST1H4A/HIST1H3C/HIST1H4F/HIST1H2BB	5

4	LP351 Upregulated	R-HSA-427359	SIRT1 negatively regulates rRNA expression	18-May	68/1061	7.45E-08	2.05E-06	4.31E-07	HIST1H3A/HIST1H4A/HIST1H3C/HIST1H4F/HIST1H2BB	5
5	LP351 Upregulated	R-HSA-212300	PRC2 methylates histones and DNA	18-May	73/1061	1.07E-07	2.06E-06	4.33E-07	HIST1H3A/HIST1H4A/HIST1H3C/HIST1H4F/HIST1H2BB	5
6	LP351 Upregulated	R-HSA-2299718	Condensation of Prophase Chromosomes	18-May	74/1061	1.14E-07	2.06E-06	4.33E-07	HIST1H3A/HIST1H4A/HIST1H3C/HIST1H4F/HIST1H2BB	5
7	LP351 Upregulated	R-HSA-427389	ERCC6 (CSB) and EHMT2 (G9a) positively regulate rRNA expression	18-May	76/1061	1.31E-07	2.06E-06	4.33E-07	HIST1H3A/HIST1H4A/HIST1H3C/HIST1H4F/HIST1H2BB	5
8	LP351 Upregulated	R-HSA-912446	Meiotic recombination	18-May	86/1061	2.44E-07	3.16E-06	6.66E-07	HIST1H3A/HIST1H4A/HIST1H3C/HIST1H4F/HIST1H2BB	5
9	LP351 Upregulated	R-HSA-201722	Formation of the beta-catenin:TCF transactivating complex	18-May	91/1061	3.25E-07	3.16E-06	6.66E-07	HIST1H3A/HIST1H4A/HIST1H3C/HIST1H4F/HIST1H2BB	5
10	LP351 Upregulated	R-HSA-5250924	B-WICH complex positively regulates rRNA expression	18-May	91/1061	3.25E-07	3.16E-06	6.66E-07	HIST1H3A/HIST1H4A/HIST1H3C/HIST1H4F/HIST1H2BB	5
11	LP351 Upregulated	R-HSA-73772	RNA Polymerase I Promoter Escape	18-May	91/1061	3.25E-07	3.16E-06	6.66E-07	HIST1H3A/HIST1H4A/HIST1H3C/HIST1H4F/HIST1H2BB	5
12	LP351 Upregulated	R-HSA-1912408	Pre-NOTCH Transcription and Translation	18-May	93/1061	3.62E-07	3.16E-06	6.66E-07	HIST1H3A/HIST1H4A/HIST1H3C/HIST1H4F/HIST1H2BB	5
13	LP351 Upregulated	R-HSA-3214815	HDACs deacetylate histones	18-May	94/1061	3.82E-07	3.16E-06	6.66E-07	HIST1H3A/HIST1H4A/HIST1H3C/HIST1H4F/HIST1H2BB	5
14	LP351 Upregulated	R-HSA-5625740	RHO GTPases activate PKNs	18-May	95/1061	4.03E-07	3.16E-06	6.66E-07	HIST1H3A/HIST1H4A/HIST1H3C/HIST1H4F/HIST1H2BB	5
15	LP351 Upregulated	R-HSA-8936459	RUNX1 regulates genes involved in megakaryocyte differentiation and platelet function	18-May	97/1061	4.47E-07	3.28E-06	6.90E-07	HIST1H3A/HIST1H4A/HIST1H3C/HIST1H4F/HIST1H2BB	5
16	LP351 Upregulated	R-HSA-2559583	Cellular Senescence	18-Jun	195/106	5.49E-07	3.77E-06	7.94E-07	HIST1H3A/HIST1H4A/HIST1H1A/HIST1H3C/HIST1H4F/HIST1H2BB	6
17	LP351 Upregulated	R-HSA-	Positive epigenetic regulation of rRNA expression	18-May	106/106	6.97E-07	3.84E-06	8.08E-07	HIST1H3A/HIST1H4A/HIST1H3C/HIST1H4F/HIST1H2BB	5

18	LP351 Upregulated	5250913 R-HSA-5578749	Transcriptional regulation by small RNAs	18-May	106/10619	6.97E-07	3.84E-06	8.08E-07	HIST1H3A/HIST1H4A/HIST1H3C/HIST1H4F/HIST1H2BB	5
19	LP351 Upregulated	R-HSA-427413	NoRC negatively regulates rRNA expression	18-May	107/10619	7.30E-07	3.84E-06	8.08E-07	HIST1H3A/HIST1H4A/HIST1H3C/HIST1H4F/HIST1H2BB	5

Section IV: MSC expression relative to MSC iPSC Fibroblast Reactome Overrepresentation Analysis (ORA) results. Results derived as above.

	Cluster ID (Relative to BJ)	**Reactome ID**	**Pathway Description**	**Background Genome Ratio**	***P* value**	**Adjusted *P* value**	**Benjamini-Hochberg Corrected *q* value**	***List of HGNC gene IDs***	**Gene Hit Count**	
1	LP351 Upregulated	R-HSA-73728	RNA Polymerase I Promoter Opening	13-Apr	63/10619	7.73E-07	2.59E-05	5.46E-06	HIST1H3A/HIST1H4A/HIST1H3C/HIST1H2BB	4
2	LP351 Upregulated	R-HSA-5334118	DNA methylation	13-Apr	65/10619	8.77E-07	2.59E-05	5.46E-06	HIST1H3A/HIST1H4A/HIST1H3C/HIST1H2BB	4
3	LP351 Upregulated	R-HSA-5625886	Activated PKN1 stimulates transcription of AR (androgen receptor) regulated genes KLK2 and KLK3	13-Apr	67/10619	9.92E-07	2.59E-05	5.46E-06	HIST1H3A/HIST1H4A/HIST1H3C/HIST1H2BB	4
4	LP351 Upregulated	R-HSA-427359	SIRT1 negatively regulates rRNA expression	13-Apr	68/10619	1.05E-06	2.59E-05	5.46E-06	HIST1H3A/HIST1H4A/HIST1H3C/HIST1H2BB	4
5	LP351 Upregulated	R-HSA-212300	PRC2 methylates histones and DNA	13-Apr	73/10619	1.40E-06	2.59E-05	5.46E-06	HIST1H3A/HIST1H4A/HIST1H3C/HIST1H2BB	4
6	LP351 Upregulated	R-HSA-2299718	Condensation of Prophase Chromosomes	13-Apr	74/10619	1.48E-06	2.59E-05	5.46E-06	HIST1H3A/HIST1H4A/HIST1H3C/HIST1H2BB	4
7	LP351 Upregulated	R-HSA-427389	ERCC6 (CSB) and EHMT2 (G9a) positively regulate rRNA expression	13-Apr	76/10619	1.65E-06	2.59E-05	5.46E-06	HIST1H3A/HIST1H4A/HIST1H3C/HIST1H2BB	4
8	LP351 Upregulated	R-HSA-2559583	Cellular Senescence	13-May	195/10619	2.27E-06	2.96E-05	6.24E-06	HIST1H3A/HIST1H4A/HIST1H3C/HIST1H1A/HIST1H2BB	5

	LP351 Upregulated	R-HSA-912446	Meiotic recombination	13-Apr	86/1061 9	2.71E-06	2.96E-05	6.24E-06	HIST1H3A/HIST1H4A/HIST1H3C/HIST1H2BB	4
10	LP351 Upregulated	R-HSA-201722	Formation of the beta-catenin:TCF transactivating complex	13-Apr	91/1061 9	3.40E-06	2.96E-05	6.24E-06	HIST1H3A/HIST1H4A/HIST1H3C/HIST1H2BB	4
11	LP351 Upregulated	R-HSA-5250924	B-WICH complex positively regulates rRNA expression	13-Apr	91/1061 9	3.40E-06	2.96E-05	6.24E-06	HIST1H3A/HIST1H4A/HIST1H3C/HIST1H2BB	4
12	LP351 Upregulated	R-HSA-73772	RNA Polymerase I Promoter Escape	13-Apr	91/1061 9	3.40E-06	2.96E-05	6.24E-06	HIST1H3A/HIST1H4A/HIST1H3C/HIST1H2BB	4
13	LP351 Upregulated	R-HSA-1912408	Pre-NOTCH Transcription and Translation	13-Apr	93/1061 9	3.71E-06	2.96E-05	6.24E-06	HIST1H3A/HIST1H4A/HIST1H3C/HIST1H2BB	4
14	LP351 Upregulated	R-HSA-3214815	HDACs deacetylate histones	13-Apr	94/1061 9	3.87E-06	2.96E-05	6.24E-06	HIST1H3A/HIST1H4A/HIST1H3C/HIST1H2BB	4
15	LP351 Upregulated	R-HSA-5625740	RHO GTPases activate PKNs	13-Apr	95/1061 9	4.04E-06	2.96E-05	6.24E-06	HIST1H3A/HIST1H4A/HIST1H3C/HIST1H2BB	4
16	LP351 Upregulated	R-HSA-8936459	RUNX1 regulates genes involved in megakaryocyte differentiation and platelet function	13-Apr	97/1061 9	4.39E-06	3.02E-05	6.36E-06	HIST1H3A/HIST1H4A/HIST1H3C/HIST1H2BB	4
17	LP351 Upregulated	R-HSA-5250913	Positive epigenetic regulation of rRNA expression	13-Apr	106/106 19	6.26E-06	3.32E-05	7.00E-06	HIST1H3A/HIST1H4A/HIST1H3C/HIST1H2BB	4
18	LP351 Upregulated	R-HSA-5578749	Transcriptional regulation by small RNAs	13-Apr	106/106 19	6.26E-06	3.32E-05	7.00E-06	HIST1H3A/HIST1H4A/HIST1H3C/HIST1H2BB	4
19	LP351 Upregulated	R-HSA-427413	NoRC negatively regulates rRNA expression	13-Apr	107/106 19	6.50E-06	3.32E-05	7.00E-06	HIST1H3A/HIST1H4A/HIST1H3C/HIST1H2BB	4
20	LP351 Upregulated	R-HSA-1912422	Pre-NOTCH Expression and Processing	13-Apr	109/106 19	6.99E-06	3.32E-05	7.00E-06	HIST1H3A/HIST1H4A/HIST1H3C/HIST1H2BB	4

Appendix IV. Transcriptional, Electrophysiological, and Metabolic Characterizations of hESC-Derived First and Second Heart Fields Demonstrate a Potential Role of TBX5 in Cardiomyocyte Maturation

frontiers in Cell and Developmental Biology

ORIGINAL RESEARCH
published: 20 December 2021
doi: 10.3389/fcell.2021.787684

Transcriptional, Electrophysiological, and Metabolic Characterizations of hESC-Derived First and Second Heart Fields Demonstrate a Potential Role of TBX5 in Cardiomyocyte Maturation

Arash Pezhouman[1,2†], Ngoc B. Nguyen[1,2,3†], Alexander J. Sercel[4], Thang L. Nguyen[5], Ali Daraei[1], Shan Sabri[6], Douglas J. Chapski[7], Melton Zheng[1], Alexander N. Patananan[5], Jason Ernst[2,6,8,9], Kathrin Plath[2,6,9], Thomas M. Vondriska[7,10,11], Michael A. Teitell[5,8,9,12] and Reza Ardehali[1,2,3,6]*

[1]Division of Cardiology, Department of Internal Medicine, David Geffen School of Medicine, University of California, Los Angeles, Los Angeles, CA, United States, [2]Eli and Edythe Broad Stem Cell Research Center, University of California, Los Angeles, Los Angeles, CA, United States, [3]Molecular, Cellular and Integrative Physiology Graduate Program, University of California, Los Angeles, Los Angeles, CA, United States, [4]Molecular Biology Interdepartmental Doctoral Program, University of California, Los Angeles, Los Angeles, CA, United States, [5]Department of Bioengineering, University of California, Los Angeles, Los Angeles, CA, United States, [6]Department of Biological Chemistry, University of California, Los Angeles, Los Angeles, CA, United States, [7]Department of Anesthesiology and Perioperative Medicine, University of California, Los Angeles, Los Angeles, CA, United States, [8]Molecular Biology Institute, University of California, Los Angeles, Los Angeles, CA, United States, [9]Jonsson Comprehensive Cancer Center, David Geffen School of Medicine, University of California, Los Angeles, Los Angeles, CA, United States, [10]Department of Physiology, University of California, Los Angeles, Los Angeles, CA, United States, [11]Department of Medicine, University of California, Los Angeles, Los Angeles, CA, United States, [12]Department of Pediatrics, University of California, Los Angeles, Los Angeles, CA, United States

Background: Human embryonic stem cell-derived cardiomyocytes (hESC-CMs) can be used as a source for cell delivery to remuscularize the heart after myocardial infarction. Despite their therapeutic potential, the emergence of ventricular arrhythmias has limited their application. We previously developed a double reporter hESC line to isolate first heart field (FHF: *TBX5*$^{+}$*NKX2-5*$^{+}$) and second heart field (SHF: *TBX5*$^{-}$*NKX2-5*$^{+}$) CMs. Herein, we explore the role of TBX5 and its effects on underlying gene regulatory networks driving phenotypical and functional differences between these two populations.

Methods: We used a combination of tools and techniques for rapid and unsupervised profiling of FHF and SHF populations at the transcriptional, translational, and functional level including single cell RNA (scRNA) and bulk RNA sequencing, atomic force and quantitative phase microscopy, respirometry, and electrophysiology.

Results: Gene ontology analysis revealed three biological processes attributed to *TBX5* expression: sarcomeric structure, oxidative phosphorylation, and calcium ion handling. Interestingly, migratory pathways were enriched in SHF population. SHF-like CMs display less sarcomeric organization compared to FHF-like CMs, despite prolonged *in vitro* culture. Atomic force and quantitative phase microscopy showed increased cellular stiffness and decreased mass distribution over time in FHF compared to SHF populations, respectively. Electrophysiological studies showed longer plateau in action

OPEN ACCESS

Edited by:
Amaresh Ranjan, Midwestern University, United States

Reviewed by:
Aitor Aguirre, Michigan State University, United States
Ellen Poon, The Chinese University of Hong Kong, China
Sara Pahlavan, Royan Institute for Stem Cell Biology and Technology (RI-SCBT), Iran

***Correspondence:**
Reza Ardehali
RArdehali@mednet.ucla.edu

†These authors have contributed equally to this work

Specialty section:
This article was submitted to Stem Cell Research, a section of the journal Frontiers in Cell and Developmental Biology

Received: *01 October 2021*
Accepted: *25 November 2021*
Published: *20 December 2021*

Citation:
Pezhouman A, Nguyen NB, Sercel AJ, Nguyen TL, Daraei A, Sabri S, Chapski DJ, Zheng M, Patananan AN, Ernst J, Plath K, Vondriska TM, Teitell MA and Ardehali R (2021) Transcriptional, Electrophysiological, and Metabolic Characterizations of hESC-Derived First and Second Heart Fields Demonstrate a Potential Role of TBX5 in Cardiomyocyte Maturation. Front. Cell Dev. Biol. 9:787684. doi: 10.3389/fcell.2021.787684

potentials recorded from FHF-like CMs, consistent with their increased expression of calcium handling genes. Interestingly, both populations showed nearly identical respiratory profiles with the only significant functional difference being higher ATP generation-linked oxygen consumption rate in FHF-like CMs. Our findings suggest that FHF-like CMs display more mature features given their enhanced sarcomeric alignment, calcium handling, and decreased migratory characteristics. Finally, pseudotime analyses revealed a closer association of the FHF population to human fetal CMs along the developmental trajectory.

Conclusion: Our studies reveal that distinguishing FHF and SHF populations based on TBX5 expression leads to a significant impact on their downstream functional properties. FHF CMs display more mature characteristics such as enhanced sarcomeric organization and improved calcium handling, with closer positioning along the differentiation trajectory to human fetal hearts. These data suggest that the FHF CMs may be a more suitable candidate for cardiac regeneration.

Keywords: first and second heart fields, single cell RNA seq, action potential, hESC-derived cardiomyocyte, maturity, regenerative medicine, metabolism

INTRODUCTION

Cardiovascular disease is a leading cause of death worldwide (Benjamin et al., 2019). Due to the limited regenerative capacity of the heart, ischemic events such as myocardial infarction (MI) leads to permanent loss of CMs and replacement by scar tissue which can eventually result in heart failure (Laflamme and Murry, 2011). Despite the current standard strategies of revascularization to salvage myocardium, paradoxical effect of ischemia-reperfusion precipitates further injury of viable heart muscle (Selmer et al., 2005). Over the past 20 years, scientists have attempted many approaches to regenerate damaged heart tissue such as promoting the proliferation of endogenous CMs or direct reprogramming of resident cardiac fibroblasts into CMs (Cao et al., 2016). However, the application of these strategies has been limited due to the low proliferative capacity of adult CMs even upon exogenous stimulation as well as low efficiency of direct reprogramming (Ghiroldi et al., 2017). In recent years, pluripotent stem cell-based regenerative therapy has offered a great promise for cardiac repair. Several studies have shown that human embryonic stem cell-derived CMs (hESC-CMs) can improve cardiac function and remuscularize the heart after MI (Laflamme et al., 2007; Skelton et al., 2016a; Skelton et al., 2016b; Yanamandala et al., 2017; Liu et al., 2018). Despite the improvement in cardiac function, emergence of fatal ventricular arrhythmias has limited the application of hESC-CMs (Shiba et al., 2016). Electrophysiological studies on transplanted hESC-CMs also provide evidence that graft-induced arrhythmias may result from pacemaker-like activity rather than abnormal conduction (Liu et al., 2018).

Our group recently introduced a new approach to generate heart field-specific CMs from differentiating hESCs which can be used to provide insight into the emergence of fatal arrhythmias post-transplantation (Pezhouman et al., 2021). Using a double reporter system comprising of early cardiac transcription factors *TBX5* and *NKX2-5*, we were able to isolate first heart field (FHF) (*TBX5*$^+$/*NKX2-5*$^+$) and second heart field (SHF) (*TBX5*$^-$/*NKX2-5*$^+$) CMs while excluding pacemaker-like cells (*TBX5*$^+$/*NKX2-5*$^-$). Investigators have shown that within the heart, *TBX5* is predominately expressed in the primitive posterior heart tube, marking progenitors of the LV and atria, corresponding to the FHF (Bruneau et al., 1999; Liberatore et al., 2000; Bruneau et al., 2001; Sizarov et al., 2011; Xie et al., 2012; Später et al., 2013; Steimle et al., 2018). Our study showed that delineation of hESC-derived heart-field specific CMs using TBX5 roughly mirrored the previous *in vivo* models. Prior studies (Lundy et al., 2013; Lewandowski et al., 2018) have shown that prolonged *in vitro* culture of stem-cell derived CMs may lead to the maturation of their structural and contractile properties to a more adult-like phenotype. Interestingly, we found significant differences in electrophysiological properties of FHF- and SHF-like CMs. Given the persistent delay in maturation of SHF-like CMs, we hypothesized that these intrinsic differences between FHF- and SHF-like populations may be driven by early expression of TBX5 and its downstream effects on biological processes involved in cardiac maturation. The role of TBX5 in early cardiac development and chamber-specificity is well-studied; however, its effects on later stages of development and maturation of CMs remains unknown.

In this study, we used a stepwise approach to identify and validate underlying biological processes that lead to the phenotypical differences observed between FHF- and SHF-like CMs. Unsupervised differential gene expression analyses revealed four main biological processes including muscle cell development, oxidation phosphorylation, response to wounding, and calcium handling. We next conducted relevant biological and/or functional assays to validate these biological processes, including Seahorse Assay, atomic force microscopy, and optical mapping. We also performed pseudotime analyses of our FHF- and SHF-like CMs compared to human fetal CMs to determine where hESC-derived CMs are positioned along the developmental trajectory. Our study reveals that not only *TBX5*

expression is important for early cardiac development and chamber specification, but it may also play a role in later stages of differentiation and cardiac maturation by fine-tuning sarcomeric organization and calcium handling.

METHODS

Differentiation of Double Reporter hESC Line

We have previously generated hESC *TBX5-TdTomato*$^{+/W}$/*NKX2-5*$^{eGFP/W}$ double reporter using a HES3-*NKX2-5*$^{eGFP/W}$ line generously provided by E. Stanley and A. Elefanty (Monash University, Victoria, AU) (Elliott et al., 2011; Pezhouman et al., 2021). Monolayer cardiac differentiation was achieved using small molecule inhibitors of GSK3 and Wnt. HES3-*TBX5-TdTomato*$^{+/W}$/*NKX2-5*$^{eGFP/W}$ cells were expanded on Geltrex (Gibco™, A1413202) to 70–85% confluency then harvested as a single-cell suspension using Accutase [Gibco™, A1110501)] and resuspended in mTeSR plus (Stem Cell™ Technologies, 05826) containing 10 µM ROCK inhibitor Y-27632 (Tocris Biosciences, 1,254). Cells were counted using a Countess II Automated Cell Counter (Countess™, AMQAX1000) and re-plated onto Geltrex coated plates at 1×10^5 cells/cm^2 in mTeSR™ Plus containing 10 µM ROCK inhibitor Y-27632 (day -2 of differentiation). At day -1 media was changed to mTeSR™ Plus. At day 0 media was changed to RPMI (Gibco™, 11875093) containing B-27™ supplement, minus Insulin (Gibco™, A1895601) containing CHIR99021 (Tocris, 4,423) (10 µM). After 24 h (day 1) media was aspirated and replaced with RPMI B27 minus Insulin until day 3. On day 3 of differentiation media aspirated and replaced with RPMI B27 minus Insulin containing 5 µM IWP2 (Tocris, 3,533). At day 5, media was changed to RPMI B27 minus Insulin until day 7 when media was switched to RPMI containing B-27™ supplement (Gibco™, A3582801). Cells were maintained in this media and changed every 3 days thereafter.

Flow Cytometry and Cell Sorting

Differentiated hESCs were dissociated with Accutase™ (STEMCELL Technology, 07920) for 3–5 min at 37°C to form a single cell suspension. Cells were resuspended in FACS buffer (2% FBS, 1% BSA, 2 mM EDTA) containing 10 µM ROCK inhibitor Y-27632 and DAPI. Cells were sorted using a FACS-ARIA-H (BD Biosciences) into RPMI containing B-27™ supplement (Gibco™, A3582801) with 10 µM ROCK inhibitor Y-27632. FACS data were analyzed using FlowJo software (Tree Star Inc.).

Bulk RNA-Sequencing

FHF (TdTomato$^+$/GFP$^+$), SHF (TdTomato$^-$/GFP$^+$) cells were FACS sorted on day 20 of differentiation. RNA of the FHF and SHF cells was isolated using TRIZOL LS Reagent (Invitrogen™, 10296028), RNeasy Micro Kit (Qiagen, 74004) was used for purification. The quality of the RNA was assessed by Agilent 2,200 Tapestation. For library preparation, total RNA was fragmented and subjected to cDNA conversion, adapter ligation, and amplification using KAPA Stranded RNA-Seq Library Preparation Kit (KAPA Biosystems, KK8502) according to the manufacturer's instructions. The final library was quantified using Agilent 2,100 Bioanalyzer to evaluate its integrity. The deep sequencing for 2 × 150 bp paired-end reads was performed using Illumina Novaseq 6,000. For sample analysis, RNA-seq data was mapped to the reference genome (GRCh38) with OLego version 1.1.5 and normalized by using TPM (Transcripts per millions) analysis. Total number of reads mapped to a known transcript annotation was estimated using featureCounts version v1.5.0-p2. Expression levels for each transcript were determined by normalizing the counts returned by featureCounts using custom Perl scripts. Normalized expression levels for each transcript were determined by transforming the raw expression counts to TPM following log2 scaling. Gene Ontology (GO) enrichments were computed using Metascape (Zhou et al., 2019). RStudio was used to run custom R scripts to generate boxplots and heatmaps using "heatmaply" package.

Single Cell RNA Sequencing of Human Fetal Hearts and hESC-Derived CMs

Human fetal heart 6, 10, and 17 weeks of gestation was digested into single cell suspension using Collagenase II (Worthington, LS004176, 0.45 mg/ml) and Pancreatin (Sigma, P3292-25G, 1 mg/ml). Day 20 FHF and SHF cells were digested into single cell suspension using TrypLE. Single cells were captured using the 10X Genomics Chromium Single Cell v.2 platform. cDNA libraries derived from the FHF and SHF were independently generated and sequenced on the Illumina NextSeq, generating 490 million reads of FHF-derived samples and 466 million reads of SHF-derived libraries of which >97% passed quality control. cDNA libraries from human fetal heart were sequenced with the Illumina NovaSeq. Digital expression matrix was generated by de-multiplexing, barcode processing, and gene unique molecular index counting using the Cell Ranger v3.0 pipeline and the GRCh38 reference genome. Cells that express less than 200 genes, and genes detected in less than 3 cells were filtered out. The Seurat 4.0.4 R toolkit (Hao et al., 2021) for single cell genomics was used to analyze sequencing results. Downstream analysis was restricted to cells associated with at least 3,000 unique molecular identifiers (UMIs). For identification of cell clusters in the human fetal heart (*TNNT2*, *MYH7*) *(COL1A1, DDR2)*, and (*PECAM1, CDH5*) were used to identify cardiac, fibroblast, and endothelial cell clusters, respectively. The FeaturePlot, BoxPlot, and ViolinPlot functions of Seurat were used to visualize genes of interest.

Monocle Pseudotime Analysis

The Seurat object file was converted into a CellDataSet (CDS) for further analysis using the Monocle 3 software (Trapnell et al., 2014). Cell clusters and trajectories were visualized using the standard Monocle workflow. The first 20 PCs were used for pre-processing (preprocessCDS). Then, these lower-dimensional coordinates were used to initialize a nonlinear manifold learning algorithm implemented in Monocle 3 called "UMAP"

(*via* reduceDimension; Becht et al., 2018). This allows us to visualize the data in two dimensions. The "cluster_cells" function was used to identify clusters and then "learn_graph" was used to learn the sequence of gene expression changes of each cell to generate an overall trajectory. To mark the root of the pseudotime, we used the "order_cells" function to assign the starting root of pseudotime. Gene expression along pseudotime were plotted using the "plot_genes_in_pseudotime" function, with "color_cells_by" parameter set at "ID."

TBX5 and NKX2-5 Binding Simulation

To test whether TBX5 and NKX2-5 preferentially bind to FHF and SHF gene promoters, we first empirically defined gene markers for each cell population using the FindMarkers() function in Seurat with the following parameters: ident.1 = "TBX5+ CMs," ident.2 = "TBX5- CMs," and min.pct = 0.3. For this simulation, we defined FHF genes as the marker subset with avg_log2FC > 0, and SHF genes as the subset with avg_log2FC < 0. As a negative control, we randomly selected 10 subsets of 150 genes (excluding FHF and SHF genes) from the count matrix. We then downloaded fetal (E12.5) *TBX5* and *NKX2-5* bioChIP-seq peak sets from online dataset (Akerberg et al., 2019) and determined mm9 promoter coordinates of murine orthologs of the FHF, SHF, and random gene subsets. To test whether regions of *TBX5* or *NKX2-5* binding significantly overlap with our gene subsets, we used hypergeometric tests as in (Chapski et al., 2021). Because we performed a total of 12 statistical tests during each transcription factor simulation (FHF, SHF, and 10 random gene sets), we corrected the *p*-values using the Benjamini-Hochberg (Benjamini and Hochberg, 1995) method in R.

Immunocytochemistry

Immunocytochemical staining were performed on cells seeded onto Geltrex coated optical tissue culture chamber (Thermo Scientific Lab-Tek II Chamber Slide System, 154,526). Cells were fixed in 4% paraformaldehyde (PFA) in PBS for 15 min at RT followed by PBS washings. For staining, fixed cells were permeabilized with 0.2% Triton X-100 (Fisher Bioreagents, BP151) in PBS for 10 min prior to blocking non-specific binding with 10% normal serum in PBST (PBS with 0.1% Tween-20 (MP Biomedicals, 11TWEEN201) for 30 min. Cells were incubated with primary antibodies at 4°C overnight and then stained with secondary antibodies at room temperature for 1 h and mounted with VECTASHIELD Antifade Mounting Medium with DAPI (Vector Laboratories, H-1200). The stained cells were imaged with a Leica TCS SP5 microscope using LAS X software (Leica Biosystems) or an LSM 880 with Airyscan Confocal Microscope using ZEN software (Carl Zeiss Microscopy). The following primary antibodies were used: Rabbit anti-Cardiac Troponin T (Abcam, ab45932,1:400), Mouse anti-cardiac ACTN2 (Sigma, A7811, 1:300), Rabbit anti-TOMM20 (Abcam, ab2043078, 1:1,000), Mouse anti-dsDNA (Abcam, ab470907, 1:1,000).

OCR and ECAR Measurements

Oxygen consumption rate and extracellular acidification rate were quantified using an Agilent Seahorse XFe96 Extracellular Flux Analyzer. 2×10^4 cells were seeded on each well of a V3 96-well plate (Agilent, Cat#101085-004) and cultured for 2–3 days prior to analysis. The Agilent Seahorse mitochondrial stress test was used to measure basal OCR and ECAR as well as OCR and ECAR following sequential addition of the electron transport chain inhibitor drugs oligomycin, carbonyl cyanide-p-trifluoromethoxyphenylhydrazone (FCCP), and antimycin A. Results were normalized to cell count and analysed using the Agilent Wave 2.6.2 software package.

Quantitative Phase Microscopy and Cellular Motion Measurements

Quantitative phase images on FHF and SHF cells were obtained with 20 × 0.4 numerical aperture objective lens on an Axio Observer Z1 inverted microscope with a temperature and CO2 regulated stage-top cell incubation chamber (Zeiss). Quantitative phase data was obtained with a SID4Bio (Phasics) quadriwave lateral shearing interferometry (QWLSI) camera (Bon et al., 2009; Zhang et al., 2013) while fluorescence images were obtained on an EM-CCD C9100 camera (Hamamatsu Photonics). A 660 nm centred wavelength collimated LED (Thorlabs) was used as the *trans*-illumination source for QPM and an X-Cite Series 120 Q (Lumen Dynamics) source for fluorescence imaging. Image collection occurred every 10 min for over 2 d 14—20 imaging locations containing cells plated with sufficient spacing to enable automated image processing and biomass segmentation. All image processing was performed using custom MATLAB (MathWorks) scripts. Cells and clusters were identified and segmented using a local adaptive threshold based on Otsu's method (Otsu, 1979) with particle tracking code based on Grier *et al* (Zangle et al., 2013; Nguyen et al., 2020). Net positional displacement of cells were calculated based on the differences in cell position in tracks in one frame compared to the next while percent mass fluctuations was calculated based on the difference in mass distribution of cells normalized with regards to cellular mass from one frame compared to the next.

Atomic Force Microscopy

We have employed a combination of atomic force microscopy (AFM)/confocal microscopy techniques to determine the mechanical properties of FHF and SHF cells. The nanoindentation and data acquisition were performed using a JPK Nanowizard 4A Atomic force microscopy combined with a Zeiss LSM 510 confocal microscope. The stage is arranged so that we can independently control the AFM cantilever, sample, and confocal microscope objective. Using the confocal microscope, we verified that the cells chosen for the nanoindentation experiment are the FHF ($TBX5^{TdT+}/NKX2.5^{eGFP+}$) or the SHF ($TBX5^{TdT-}/NKX2\text{-}5^{eGFP+}$).

To do the nanoindentation experiment, a cell culture dish was mounted on the AFM stage (temperature = 36.5°C during the experiments) and the cantilever tip approaches the sample from a few microns above the sample (maximum applied force = 3 nN, indentation speed = 2 µm/s). A soft AFM probe (spring constant k = 0.286 nN/nm, Bruker, NY, United States) with a spherical tip of 10 µm diameter was used for this experiment. Indentation and retraction of cantilever was plotted and processed using JPK

analysis software. The built-in Hertz/Sneddon model fitting tool of the JPK software was used to compute Young's modulus values. Hertz model for a spherical tip was calculated using following equation.

$$F = \frac{4\sqrt{R}}{3}\frac{E}{1-\upsilon^2}\delta^{3/2}$$

(F = indentation force, R = radius of the cantilever tip, E = Young's modulus, υ = poison ration (0.5 in our experiment) and δ = indentation depth). The average stiffness of five local regions on top of the nucleus in each cell, is reported as the stiffness of the cell.

Monolayer Optical Mapping

FACS-isolated cells were suspended in RPMI B27 supplemented with ROCK inhibitor Y-27632 (10 μM) at 20-22 × 10 (Yanamandala et al., 2017) cells/ml. Drops of 25 μl of this cell suspension were applied to Geltrex-coated 5 mm coverslips (5 × 10 (Ghiroldi et al., 2017) cells/coverslip). The cells were incubated in the 25 μl volume for 8–12 h to facilitate cell attachment. Once spontaneous contractions were observed, cells were stained with voltage-sensitive dye, Di-8-ANEPPS (Invitrogen, D3167, 40 μM) and washed with normal Tyrode solution three times (Pezhouman et al., 2014; Pezhouman et al., 2015; Pezhouman et al., 2018; Pezhouman et al., 2021). Optical AP recording were made using MiCAM-Ultima CMOS camera at 500 frames per second (fps). Spontaneously occurring APs were recorded and APD_{30} and APD_{80} were measured using BV-Ana (1,604) software.

Data and Software Availability

The RNA-sequencing data has been deposited in the SRA repository with BioProject accession numbers PRJNA773814.

Study Approval

The collection and use of human fetal material were carried out following federal and local approval, including the United States Institutional Review Board (IRB 11-002504) to the Translational Pathology Core Laboratory of the Department of Pathology and Laboratory Medicine at UCLA. Cardiac tissues from human embryos were collected with informed consent following surgical termination of pregnancy and staged immediately by stereomicroscopy according to the Carnegie classification. All identifiers were removed before obtaining the samples.

Statistics

All data are represented as individual values. Due to the nature of the experiments, randomization was not performed, and the investigators were not blinded. Statistical significance was determined by using student's t test (unpaired, two-tailed) in GraphPad Prism 8 software. Results were significant at $p < 0.05$ (*), $p < 0.01$ (**), $p < 0.001$ (***), and $p < 0.0001$ (****). All statistical parameters are reported in the respective figures and figure legends. All error bars are depicted as SEM.

RESULTS

Biological Process Analyses Reveal Enrichment of Structural, Metabolic, and Calcium Handling Pathways Within FHF-Like Compared to SHF-Like CMs

We used our previously generated HES3-*TBX5-TdTomato*$^{+/W}$/*NKX2-5*$^{eGFP/W}$ double reporter line (Pezhouman et al., 2021) to isolate FHF (*TBX5*$^{+}$/*NKX2-5*$^{+}$) and SHF (*TBX5*$^{-}$/*NKX2-5*$^{+}$) CMs using a monolayer cardiac differentiation protocol (GSK3 inhibitor/Wnt inhibitor (GIWI)) (**Supplementary Figures S1A,B**). Fluorescent imaging showed clusters of cells that express both TdTomato and GFP (FHF) or solely GFP (SHF) (**Supplementary Figure S1C**). Fluorescence activated cell sorting (FACS) was used to isolate these two distinct populations using their respective fluorescent markers (**Supplementary Figure S1D**). We had previously shown that FHF-like CMs exhibit longer action potential duration compared to SHF, suggesting a potential role of TBX5 expression in orchestrating downstream signaling pathways that may lead to these functional and phenotypic differences. Here, we use the 10X Genomics (10X Genomics, 2020) and Seurat toolkits (Hao et al., 2021) to transcriptionally profile FACS-isolated FHF and SHF cells to unravel the contribution of TBX5 expression to cardiomyocyte maturation. After removal of low-quality cells, we obtained 9,883 SHF and 6,413 FHF single-cell transcriptomes for downstream analyses (**Figures 1A,B**). Principal component analysis revealed that PC1 separated these 2 cell populations, with correlated genes belonging to the structural proteins, including *MYH6*, *TNNT2*, and *TTN* (**Supplementary Figures S1E,F**). Because FHF-like CMs were selected based on expression of *TBX5*, we asked whether promoters of genes preferentially expressed in FHF-like CMs (FHF genes) have higher *TBX5* occupancy compared to that of SHF gene promoters. To test enrichment, we downloaded a murine *TBX5* bioChIP-seq peak set from fetal (E12.5) ventricles (Akerberg et al., 2019) and determined binding enrichment at murine orthologs of FHF and SHF genes using hypergeometric tests. Interestingly, both FHF and SHF genes are significantly bound by *TBX5* (corrected *p*-values of 9.71×10^{-12} and 2.18×10^{-7} for FHF and SHF genes, respectively) (**Supplementary Figure S1G**). Because both FHF- and SHF-like CMs express *NKX2-5* at some point in development, we also examined a murine *NKX2-5* bioChIP-seq dataset from the same study (Akerberg et al., 2019) and found significant enrichment of NKX2-5 occupancy at both promoter sets (corrected *p*-values of 2.21×10^{-22} and 9.50×10^{-12} for FHF and SHF gene promoters, respectively) (**Supplementary Figure S1H**). Notably, we did not observe enrichment of *TBX5* and *NKX2-5* at the promoters of random gene sets (**Supplementary Figures S1G,H**). Taken together, these data suggest that the FHF and SHF populations represent myocyte-like cells that express a set of genes preferentially bound by *TBX5* and *NKX2-5*.

To test the robustness of our approach in capturing pure CMs in both populations, we examined the expression of known cardiac cell type markers such as *MYH6* and *TNNT2* (cardiomyocyte), *DDR2* and *COL1A1* (fibroblast), and *CD31*

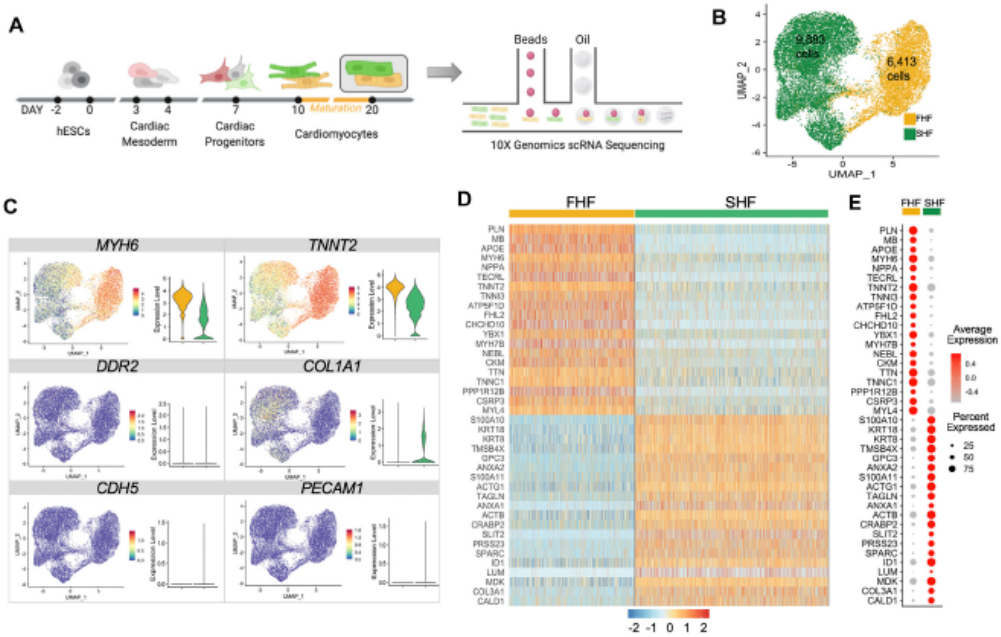

F

Top 100 Upregulated Genes in FHF

GO	Description	-Log10(P)
GO:0030049	muscle filament sliding *	28.21
GO:0006119	oxidative phosphorylation *	19.89
GO:0055001	muscle cell development	16.36
GO:0014888	striated muscle adaptation	9.83
GO:0010882	regulation of cardiac muscle contraction by calcium ion signaling*	8.75
GO:0032971	regulation of muscle filament sliding	6.57
GO:0032780	negative regulation of ATPase activity	6.33
GO:0000302	response to reactive oxygen species	6.31
GO:0042776	mitochondrial ATP synthesis coupled proton transport	5.74
GO:0070482	response to oxygen levels	4.44

G

Top 100 Upregulated Genes in SHF

GO	Description	-Log10(P)
GO:0009060	aerobic respiration	16.49
GO:0097435	supramolecular fiber organization	14.64
GO:0030049	muscle filament sliding	13.37
GO:0043462	regulation of ATPase activity	7.53
GO:0001667	ameboidal-type cell migration *	7.25
GO:0007015	actin filament organization	7.03
GO:0009611	response to wounding *	6.97
GO:0030855	epithelial cell differentiation	6.22
GO:0046677	response to antibiotic	6
GO:0030199	collagen fibril organization	5.59

FIGURE 1 | Single cell RNAseq of first and second heart field hESC-derived cardiomyocytes. **(A)**, Schematic representation of lineage commitment of hESCs into cardiomyocytes for single cell capture using 10X Genomics. **(B)**, Unsupervised clustering of FHF (yellow) and SHF (green) populations projected on a two-dimensional UMAP. **(C)**, UMAP and boxplots showing gene expression quantification for the cardiac genes (*MYH6*, *TNNT2*), fibroblast genes (*DDR2*, *COL1A1*), and endothelial genes (*CDH5*, *PECAM1*). **(D)**, The expression heatmap of top 20 differentially expressed genes in FHF and SHF. **(E)**, DotPlot analysis (average and percent expression) of top 20 differentially expressed genes in FHF and SHF populations. **(F)**, Gene Ontology analysis of the top 100 upregulated genes enriched in Day 20 FHF-like CMs. **(G)**, Gene Ontology analysis of the top 100 upregulated genes enriched in Day 20 SHF CMs.

and *CDH5* (endothelial). Only CM markers were expressed in these two populations, with higher expression of *MYH6* and *TNNT2* in FHF cells (**Figure 1C**). Heatmap analyses of the top 20 differentially expressed genes in FHF- and SHF-like CMs showed uniformity of gene expression within each population as well as distinct gene profiles between the two populations (**Figure 1D**). DotPlot analysis revealed that certain genes such as *TNNT2*, *MYL4*, *TTN*, and *TNNC1* have a high percent expression within both populations (i.e., percent of the cells that express the gene of interest); however, average expression levels are higher in FHF (i.e., average expression of gene of interest across all cells). On the other hand, genes such as *PLN*, *MB*, and *TNNI3*, exhibit both higher percent and average expression in FHF-like compared to SHF-like CMs (**Figure 1E**).

To unravel the biological processes enriched in FHF- and SHF-like CMs, we performed gene ontology (GO) analysis of the top 100 upregulated genes within each population using Metascape (Zhou et al., 2019). The top GO term categories within the FHF population revealed three main categories: muscle structure (muscle filament sliding, muscle cell development, striated muscle adaptation), metabolism (oxidative phosphorylation, mitochondrial ATP synthesis coupled proton transport), and calcium handling (regulation of cardiac muscle contraction by calcium ion signaling)

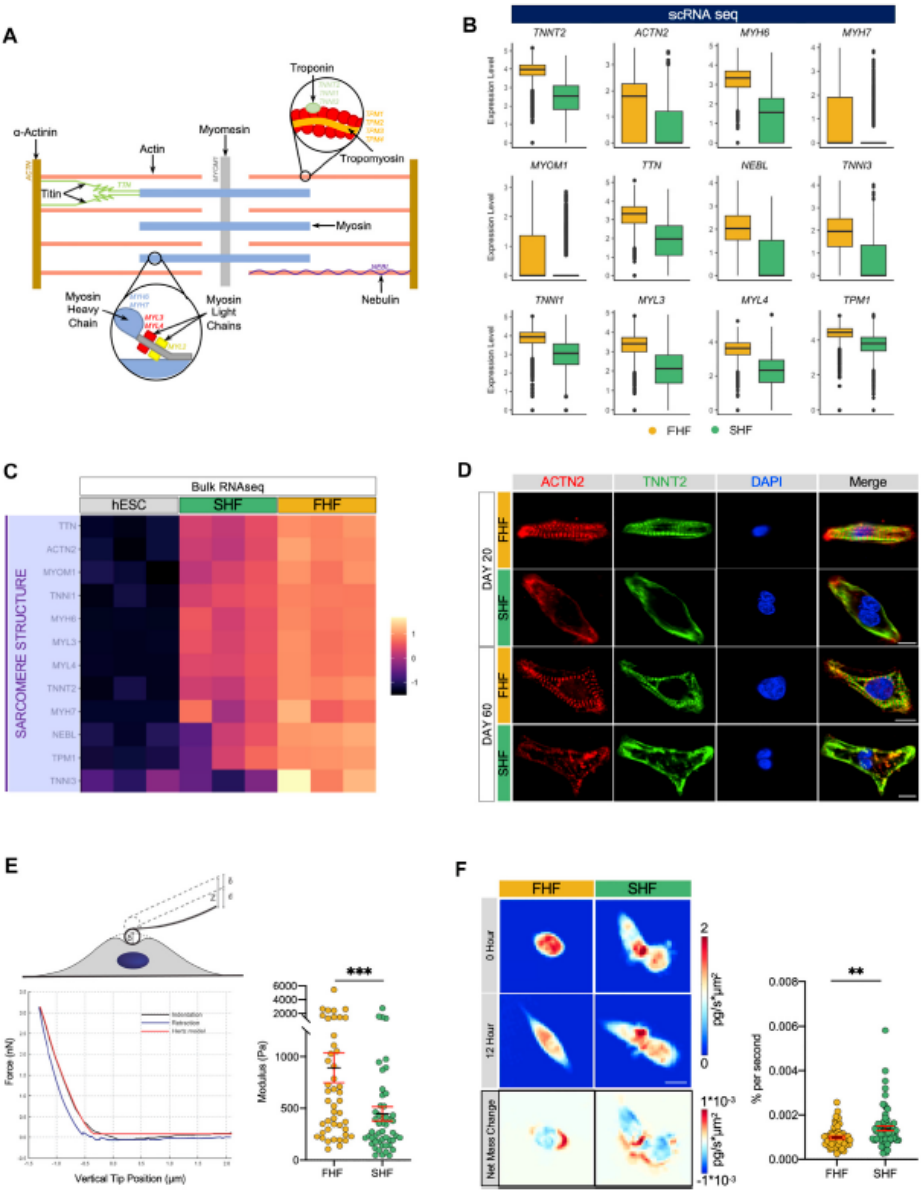

FIGURE 2| Differences in sarcomeric organization, cellular stiffness, and migration between FHF- and SHF-like CMs. **(A)**, Schematic of important structural and regulatory components of a cardiac sarcomeric unit. **(B)**, Boxplots of structural genes extracted from GO pathway "GO:0030049: muscle filament sliding" with higher average expression in FHF compared to SHF CMs. **(C)**, Heatmap of cardiac sarcomeric structural genes extracted from GO:0030049 using bulk RNA sequencing data of hESCs and FHF- and SHF-like CMs at Day 20. **(D)**, Immunocytochemistry of Day 20 **(top)** and Day 60 **(bottom)** FHF- and SHF-like CMs for cardiac structural markers ACTN2 and TNNT2. Nuclei were visualized with DAPI, scale = 10 μm. **(E)**, **(top)** Schematic of experimental indentation set-up. A cell is indented by an AFM cantilever with a spherical probe. The vertical position of the cantilever is moved by z; the cantilever bends by d; the cell is indented by δ; z = d + δ **(bottom left)** Example

(*Continued*)

FIGURE 2 | of a force vs. indentation (black) and retraction (blue) curves obtained by atomic force microscopy. The indentation data was fit using the Hertz model (red). **(right)** Dot plot of FHF ($n = 58$) and SHF ($n = 68$) Young's Modulus calculated from atomic force microscopy. **(F)**, **(top left)** Quantitative phase mass distribution images of FHF- and SHF-like CMs at the initial time of imaging and 12 h after **(bottom left)** Images showing the spatial redistribution of mass over the course of the 12-h period for the FHF- and SHF-like CM clusters shown above. Dot plot of FHF ($n = 58$) and SHF ($n = 68$) clusters' magnitude of net mass change derived from the averages of QPI mass redistribution images.

(**Figure 1F**). Interestingly, while SHF-like CMs shared structural (supramolecular fiber organization) and metabolism (aerobic respiration) related pathways, they were also distinctively enriched in cell migration and wound response pathways (**Figure 1G**). Given that structural, metabolic, and calcium handling categories enriched in the FHF population are important aspects of cardiac physiology, we further focused on the genes assigned to these pathways to better characterize the differences between FHF and SHF populations. This investigation would address our overall goal of determining whether *TBX5* expression in cardiac cells plays a role in mediating downstream signaling pathways leading to cardiac maturation.

Enhanced Sarcomeric Organization and Cellular Stiffness Within FHF-Like CMs

A prominent and unique feature of cardiac muscle is its sarcomeric strucutre. Sarcomeres give cardiac muscle their striated appearance and are the repeating segments that make up muscle filaments. In addition to actin and myosin, other proteins such as α-actinin (*ACTN*), myomesin (*MYOM1*), nebulin (*NEBL*), and titin (*TTN*) are important contributors in forming organized sarcomeric structures that are crucial for CM contractile function (**Figure 2A**). To determine structural differences between FHF and SHF populations, we compared the expression level of certain structural genes extracted from the GO pathway "GO:0030049: muscle filament sliding" from our single cell RNA sequencing dataset. Boxplot analysis revealed that expression of key structural-related genes such as *TTN, NEBL, MYOM1, MYH6, MYH7*, and *TNNT2* are higher within the FHF compared to SHF population (**Figure 2B**). Current scRNA-seq technology may have technical biases that if not correctly adjusted, can lead to severe type I error in differential expression analysis (Jia et al., 2017). To avoid this, we tested the average expression level of sarcomeric structure-related genes from GO:0030049 using bulk RNA sequencing (bulk RNA-seq), which were in alignment with our scRNA-seq data (**Figure 2C**), although some genes were more highly expressed in SHF (**Supplementary Figures S3A,B**). As gene-protein relationships are not always directly correlated, we next examined the structural organization of FHF and SHF populations using immunocytochemistry. Day 20 FACS sorted cells were replated and doubled stained with ACTN2 and TNNT2 (**Figure 2D**, top half). Interestingly, immunocytochemistry (ICC) of FHF-like CMs revealed enhanced alignment and organization of sarcomeres when compared to SHF populations. Studies have suggested that prolonged culture of hESC-derived CMs may promote their sarcomeric organization. To ensure that the structural differences observed between FHF and SHF are due to their intrinsic properties and not a time-dependent delay in the maturation of SHF CMs, we cultured both population of CMs for an additional 40 days. Although SHF-like CMs showed improvement in sarcomeric organization on Day 60 compared to Day 20, the extra time in culture did not result in similar extent of structural organization as FHF-like CMs (**Figure 2D**, bottom half). Previous studies have shown a direct correlation between sarcomeric structure organization and cellular stiffness (Akiyama et al., 2006). To investigate the surface rigidity of our heart field-specific CM populations, we used atomic force microscopy (AFM), a technique that employs a nanoscale tip to measure the tip-sample interaction force as a surrogate readout of cellular stiffness. Measurement of FHF-($n = 46$) and SHF-like CMs ($n = 51$) showed a significantly higher Young's Modulus in FHF-like compared to SHF-like CMs, illustrating a more cellular stiffness property of FHF-like CMs (**Figure 2E**).

Interestingly our GO term analysis of upregulated genes within SHF population revealed enrichment of migratory related pathways such as (GO:0001667: ameboidal-type cell migration and GO:0009611: response to wounding). Boxplot analysis revealed that expression of key genes associated with migratory processes such as *SLIT2, COL3A1, SPARC, ANAXA1, TUBA1A* are higher within the SHF compared to FHF population (**Supplementary Figures S3C,D**). To investigate intrinsic migratory characteristics of these two populations, we used quantitative phase microscopy (QPM). Time-lapsed images of quantitative phase data of FHF ($n = 58$) and SHF ($n = 68$) allow for measurements of cellular mass and motion. The identity of these cells was tracked using integrated fluorescent microscopy (**Supplementary Figure S3E**). Although there was no significant difference in mass nor in mass accumulation between these 2 cell types, images of mass redistribution from QPM revealed greater internal mass redistribution for the SHF CMs over those of the FHF-like CMs demonstrated by the darker blue and red regions in SHF CMs. Additionally, population average values showed that the SHF had significantly greater ($p < 0.01$) internal mass motion than cells of the FHF (**Figure 2F**; **Supplementary Video S1**). This greater mass movement within SHF cells indicates greater mass motility in line with our observations from the Young's Modulus data that SHF-like CMs are softer than FHF-like CMs *via* links between mass fluctuations and biophysical stiffness (Nguyen et al., 2020).

Optical Mapping Reveals Longer Phase 2 (Plateau) of Action Potentials Within FHF-Like Compared to SHF-Like CMs

Our GO term analyses revealed calcium ion signaling as one of the pathways enriched in FHF-like CMs. Indeed, calcium is a critical regulator of CM function, forming a link between electrical signals and mechanical contraction of CMs, a

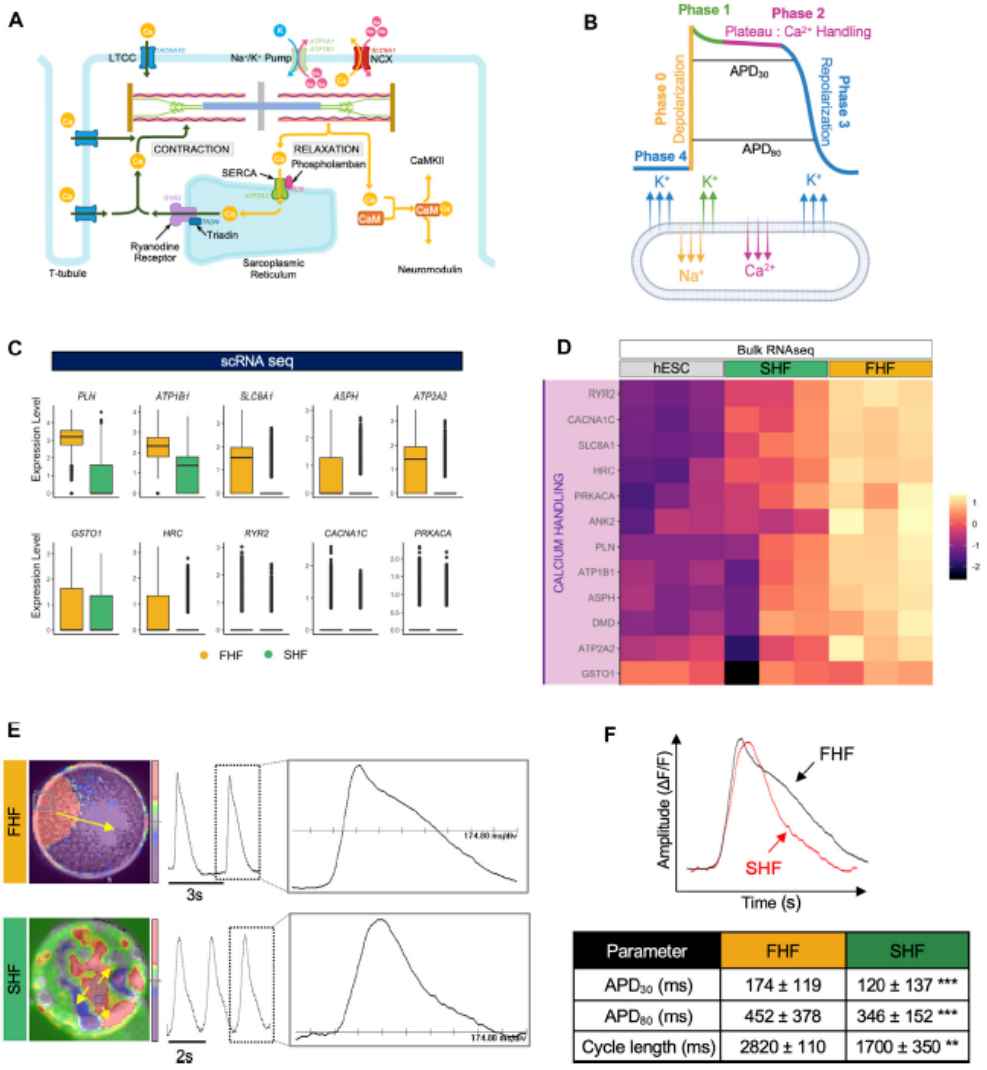

Parameter	FHF	SHF
APD_{30} (ms)	174 ± 119	120 ± 137 ***
APD_{80} (ms)	452 ± 378	346 ± 152 ***
Cycle length (ms)	2820 ± 110	1700 ± 350 **

FIGURE 3 | Optical mapping reveals longer phase 2 (plateau) of action potentials within FHF-like compared to SHF-like CMs. **(A)**, Schematic of calcium homeostasis within CMs. **(B)**, Schematic of action potential waveform separated by phase with corresponding ion flux. **(C)**, Boxplots of calcium handling-related genes extracted from GO term "GO:0010882: regulation of cardiac muscle contraction by calcium ion signaling" with higher average expression in FHF compared to SHF CMs. **(D)**, Heatmap of genes from panel C using bulk RNA sequencing data of hESCs and FHF- and SHF-like CMs at Day 20. **(E)**, Snapshot of optical mapping showing spontaneous APs which propagate across monolayer of FHF **(top)** and islands of SHF CMs **(bottom)**. The yellow arrow denotes direction of AP propagation. Single waveform magnified from dashed box inset scaled to 174.80 ms/div. **(F)**, **(top)** Superimposed APs from FHF- and SHF-like CMs showing longer APD in FHF-like CMs (bottom) Average values of APD_{30}, APD_{80}, and cycle length measured from FHF-like (n = 7,776) and SHF-like (n = 8,464) CMs.

process known as excitation-contraction coupling (EC coupling). Given their critical role in maintenance of normal cardiac rhythm, calcium ions are tightly regulated by a sophisticated machinery which consists of different channels [L-Type Ca (LTCC), ryanodine receptors (RYR2), and sarco/endoplasmic reticulum Ca2+ ATPase (SERCA)] as well as regulators

(phospholamban (PLN), triadin (TRDN), and calcium calmodulin-dependent protein kinase 2 (CaMKII)) (**Figure 3A**). An action potential (AP) waveform represents the net influence of different ions, such as Na^+, Ca^{2+}, and K^+ channels, of which the plateau portion of the AP reflects the Ca^{2+} handling machinery function and coordination (**Figure 3B**).

To determine calcium signaling differences between FHF and SHF populations, we compared the expression level of key calcium machinery genes extracted from the GO term "GO: 0010882: regulation of cardiac muscle contraction by calcium ion signaling" using our single cell RNA sequencing dataset. Boxplot analysis revealed that expression of key genes such as *PLN*, *ATP2A2* (SERCA), and *RYR2* (ryanodine receptor) are higher within the FHF compared to the SHF population (**Figure 3C**). These findings were confirmed in our bulk RNA-seq dataset (**Figure 3D**). Expression of genes such as *CALM1*, *CALM2*, and *CALM3* (calmodulin family) were also higher in SHF compared to FHF. Interestingly, bulk RNA-seq analysis of those genes shows high expression in undifferentiated hESCs as well (**Supplementary Figures S3A,B**).

To determine whether differences in calcium handling gene expression led to functional changes in action potential (AP) waveforms, particularly in the plateau phase, we used an optical mapping technique that enables the capture of electrical activity of thousands of cells simultaneously. FACS-isolated FHF- and SHF-like CMs were re-plated to form monolayers which were then optically mapped using voltage dye. FHF CMs showed uniform AP whereas, SHF CMs formed islands of cells in which APs propagated independently, but uniformly, in each island (Pezhouman et al., 2021). Spontaneous APs were recorded from FHF-like (**Figure 3E**, top) and SHF-like (**Figure 3E**, bottom) CMs. APD_{30} and APD_{80} distributions of FHF (n = 7,776) and SHF (n = 8,464) were measured and summarized in (**Supplementary Figures S3C,D**). APD_{30} (representative of net function of Ca^{2+} handling machinery) and APD_{80} (representative of Ca^{2+} handling and repolarization) analyses revealed that FHF-like CMs have significantly longer APD_{30} (45% increase) and APD_{80} (30% increase) durations compared to SHF population. Cycle length (representative of depolarization, repolarization, and diastolic interval) analysis revealed longer cycle length in FHF compared to SHF population (**Figure 3F**). These results suggest the presence of a more mature calcium handling machinery in FHF-like CMs as supported by our scRNA-seq results and enhanced sarcomeric structure observation, further supporting the likelihood that FHF-like CMs are more mature than SHF CMs.

FHF- and SHF-Like CMs Share Nearly Identical Mitochondrial Respiratory Profiles

So far, our study identified an increase in sarcomeric organization and cellular stiffness, a decrease in migratory properties, and prolonged phase 2 plateau (APD_{30}) of FHF compared to the SHF population. These results suggest that FHF population may represent a more mature state of CMs when compared to SHF cells. Another important parameter in CM maturation is the switch from glycolytic to fatty acid metabolism, with an increase in aerobic respiratory demand. Not surprisingly, our GO term analysis of top genes upregulated in FHF compared to SHF CMs showed an enrichment of GO:0006119: oxidative phosphorylation. Correspondingly, two independent gene expression analyses (scRNA and bulk RNA-seq) revealed that expression of key metabolic-related genes such as *CHCHD10, ATP5F1D, COX5A, and COX5B* were higher within the FHF compared to SHF population (**Figures 4A,B**).

To gain more insight into this process, we used respirometry to measure the levels of oxidative phosphorylation in the FHF and SHF populations. We performed a Seahorse Mitochondrial Stress Test using a Seahorse Extracellular Flux Analyzer to measure functional differences in respiration between FHF and SHF populations and found that the FHF- and SHF-like CMs show nearly identical respiratory profiles (**Figure 4C**). Among the respiratory parameters we measured with the mitochondrial stress test, we detected a significant difference only in oxygen consumption rate (OCR) contributed by ATP generation linked respiration for which FHF-like CMs showed greater OCR than SHF cells (**Figure 4D**). Additionally, we measured extracellular acidification rate (ECAR) from the same mitochondrial stress test as a proxy for glycolytic rate and found no significant differences between the FHF- and SHF-like CMs (**Supplementary Figures S5A,B**). Together, these data suggest that the FHF and SHF lineages share a common metabolic phenotype.

Finally, we visualized mitochondrial networks in FHF and SHF populations by confocal microscopy using antibodies against dsDNA and TOMM20. In both cell populations, we observed punctate mitochondrial networks (white arrows) with low nucleoid abundance. However, the FHF mitochondrial networks showed qualitatively higher numbers of filamentous mitochondrial (blue arrows) compared to the SHF networks (**Figures 4E,F**). In conclusion, our measurements suggest that the mitochondrial function and network morphology of FHF- and SHF-like CMs are highly similar despite the differences we observe in the transcription of several key metabolic genes.

Pseudotime Analysis Shows Closer Developmental Progression of FHF Population to Human Fetal CMs

Our findings thus far suggest that expression of TBX5 in hESC-derived CMs may play a role in their maturation process, as we observed more organized sarcomeric structure and stiffness along with enhanced calcium ion signaling in FHF-like CMs, characteristics previously attributed to more mature CMs (Jiang et al., 2018; Guo and Pu, 2020; Karbassi et al., 2020). Despite recent efforts, *in vitro* differentiation strategies do not yield mature CMs that exhibit similar phenotypes to their adult endogenous counterparts. To understand where our hESC-generated CMs are positioned on the trajectory of cardiomyocyte development, we compared our CM populations with human CMs isolated from fetal hearts at three timepoints; 6, 10, and 17 weeks of gestation. We isolated single fetal cardiac cells (6 wks: n = 1,048, 10 wks: n = 3,779, and 17 wks: n = 2,948) for scRNA-seq using the 10X Genomics

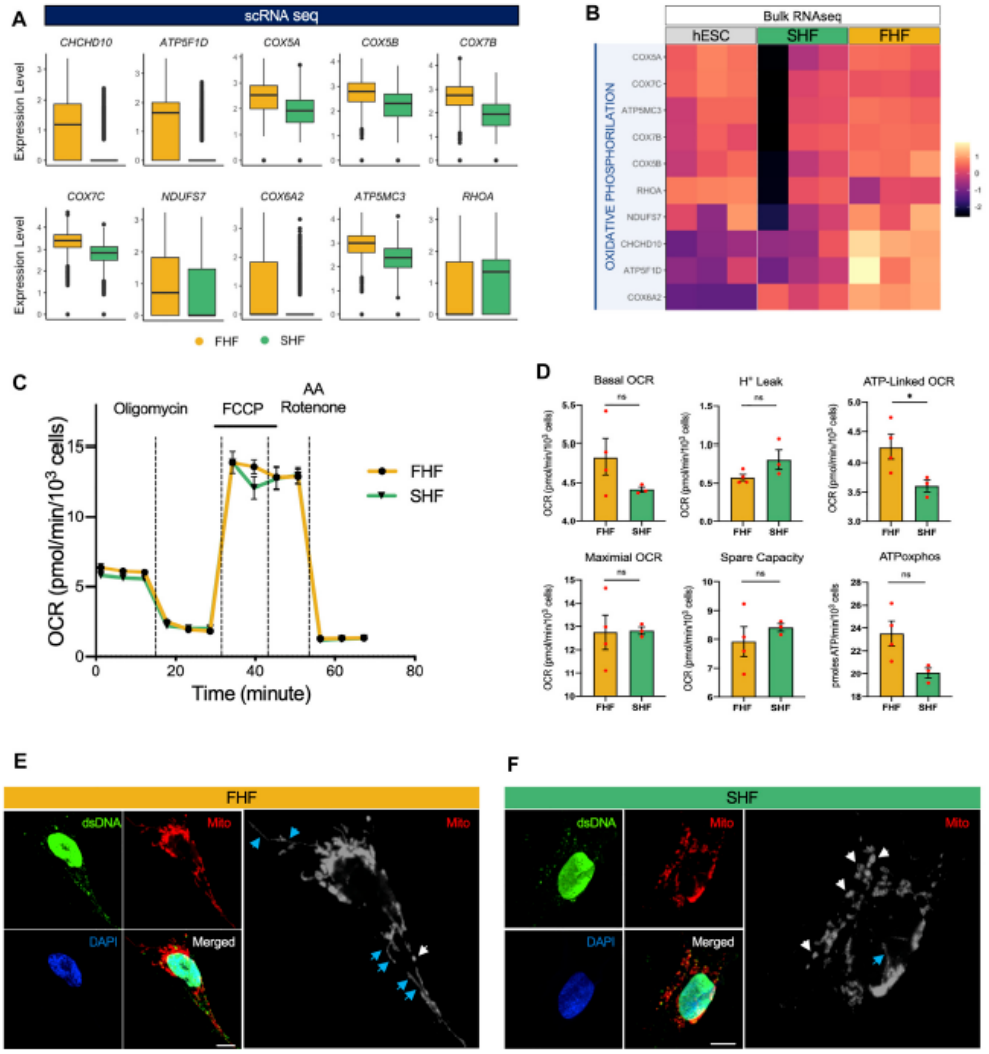

FIGURE 4 | Transcriptional and functional analyses of oxidative phosphorylation and mitochondrial networks in FHF- and SHF-like CMs. **(A)**, Boxplots of oxidative phosphorylation-related genes extracted from GO term "GO: 0006119: oxidative phosphorylation" with higher average expression in FHF compared to SHF CMs. **(B)**, Heatmap of genes from panel A using bulk RNA sequencing data of hESCs and FHF- and SHF-like CMs at Day 20. **(C)**, Seahorse Extracellular Flux Analysis comparing oxygen consumption profiles of FHF- and SHF-like CMs. **(D)**, Quantification of respiratory parameters in FHF- and SHF-like CMs. **(E)**, Immunocytochemical analyses for mitochondrial TOMM20 (red) in FHF-like CMs. Scale bar = 10 μm. **(F)**, Immunocytochemical analyses for mitochondrial TOMM20 (red) in SHF CMs. Scale bar = 5 μm. White and blue arrows denote punctate and filamentous mitochondria, respectively.

platform (**Supplementary Figure S5A**). We identified the CM cluster based on CM related genes such as *TNNT2* and *MYH7*. To avoid any contamination of other cells, we confirmed low or absent expression of fibroblast (*DDR2*, *COL1A1*) and endothelial markers (*CDH5*, *PECAM1*) within the isolated population (**Supplementary Figure S5B**). In addition, expression of key structural, calcium handling, and metabolic genes within these three fetal populations showed progressive increase with gestational age, confirming the influence of these pathways in the cardiac maturation process (**Supplementary Figure S5C**).

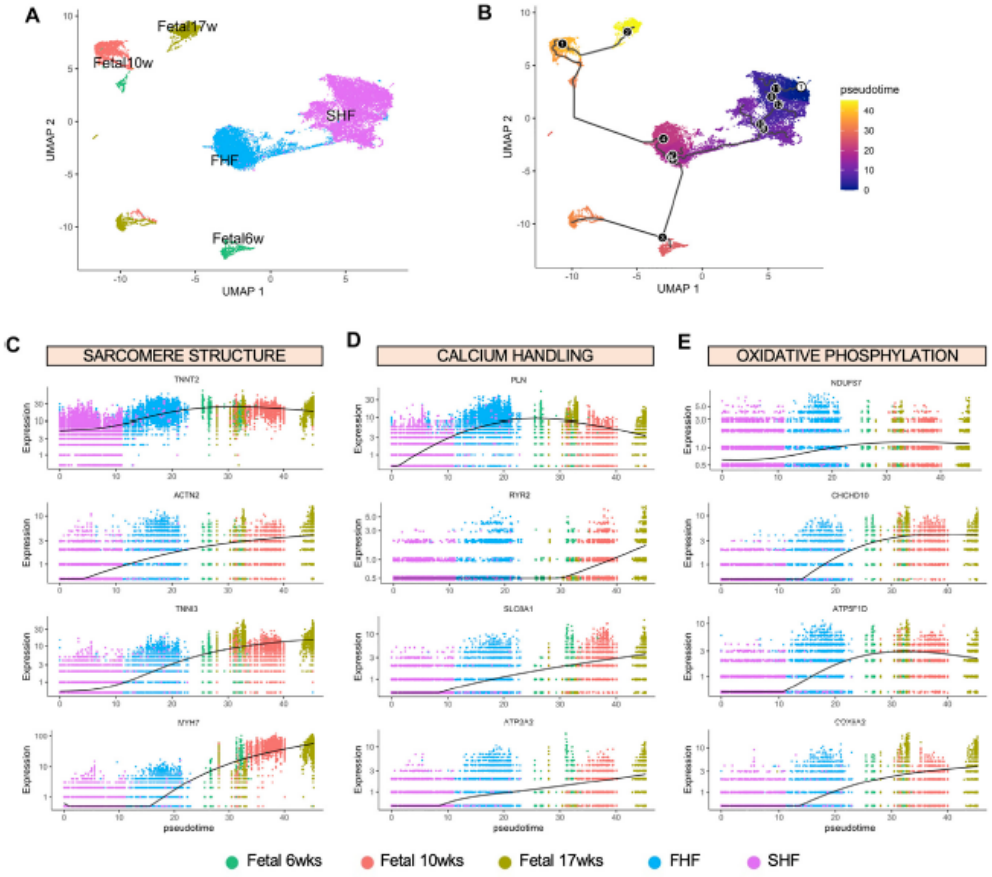

FIGURE 5 | Monocle pseudotime analysis of FHF- and SHF-like CMs with human fetal CMs at different gestational age. **(A)**, UMAP showing clusters of hESC-derived CMs and human fetal CMs. **(B)**, Ordering of hESC-derived and human fetal CMs based on pseudotime, constructed by Monocle. Black circles indicate branch points. Dynamics of expression over pseudotime of key genes from GO Term analyses relating to **(C)**, sarcomere structure, **(D)**, calcium handling, and **(E)**, oxidative phosphorylation.

To determine the maturity level of FHF- and SHF-like CM populations in comparison to human fetal CMs, we integrated these populations together into one large dataset for Monocle trajectory analysis (Trapnell et al., 2014). Confirming our prior analysis using Seurat, FHF- and SHF-like CMs constitute two distinct clusters as shown by UMAP analysis (**Figure 5A**). We then aligned these five populations in pseudotime to determine the relative developmental trajectory of our hESC-derived CM populations (**Figure 5B**). Not surprisingly, we found that FHF-like CMs aligned in closer proximity to the fetal CM populations compared to SHF CMs. Pseudotime analyses of key genes from each pathway (structural: *TNNT2*, *ACTN2*, *TNNI3*, *MYH7*; calcium handing: *PLN*, *RYR2*, *SLC8A1*, *ATP2A2*; metabolism: *NDUFS7*, *CHCHD10*, *ATP5F1D*, *COX6A2*) confirmed not only the closer alignment of FHF-like CMs to the fetal CM populations, but also higher overall expression of these genes compared to SHF CMs (**Figures 5C–E**). These findings further emphasize the important role of TBX5 expression in regulating the *in vitro* maturation process, particularly in structural and calcium handling pathways.

DISCUSSION

The heart is the first functional solid organ during embryogenesis. In early embryonic development, mesodermal cells under the

influence of secreted morphogens such as BMP4, Wnts and Activin A form the primitive streak (Galdos et al., 2017). Cardiac mesodermal cells migrate anterolaterally to form the cardiac crescent that gives rise to the primitive heart tube (Lescroart et al., 2014). These migratory cells include two heart-field specific progenitors known as FHF and SHF (Bruneau, 2013; Kelly et al., 2014). FHF progenitors mainly differentiate into CMs as they give rise to the left ventricle and part of atria (Bruneau et al., 1999). In contrast, SHF progenitors participate in elongation and looping of the heart tube, and because of their role, are highly proliferative and migratory. As these cells enter the heart tube to form the right ventricle, outflow tract, and atria, they differentiate into multiple cardiac cell types, such as CMs and smooth muscle cells (Kelly et al., 2014). Previous studies investigated the transcriptional profiles of these two populations and revealed that SHF progenitors are marked by the expression of *TBX1*, *FGF8*, *FGF10* and *SIX2* whereas FHF cells express *HCN4* and *TBX5* (Huynh et al., 2007; Watanabe et al., 2012; Später et al., 2013; Zhou et al., 2017).

Given the limited ability of adult CMs to proliferate in response to injury, much of effort has been focused on using human pluripotent stem cells to generate exogenous sources of CMs for cardiac cell-based regenerative therapy (Garbern and Lee, 2013). Our team (Pezhouman et al., 2021) and Zhang et al. (2019), for the first time, were able to isolate and characterize heart-field specific CMs from hESC and iPSCs, respectively. This is an important step in understanding early cardiac developmental processes as well as safer cell-based regenerative medicine, as prior transplantation studies used a heterogenous CM population which led to arrythmias (Liu et al., 2018; Romagnuolo et al., 2019). These prior studies focused on first isolating different subpopulations of CMs and nodal cells based on their expression of TBX5 or NKX2-5. This is followed by confirmation of their identify by profiling the expression of well-established transcriptional factors within each subpopulation. Although our previous study enabled us to separate FHF- from SHF-like CMs, using *TBX5* and *NKX2-5* expression, the role of TBX5 and its effects on underlying gene regulatory networks driving phenotypical and functional differences between these two populations remains unknown.

To uncover the underlying regulatory networks, we utilized techniques that enable rapid and unsupervised profiling of thousands of individual cells at the transcriptional, translational, and functional level, providing a more reliable representation of the differences between these two populations. First, we used scRNA-seq to obtain differentially expressed genes between FHF- and SHF-like CMs at the transcriptional level. Gene ontology analyses yielded four main biological processes including 1) muscle cell development (sarcomere structure), 2) oxidative phosphorylation (metabolism), 3) regulation of cardiac muscle contraction by calcium ion signaling (Ca^{2+} handling) and 4) response to wound healing (migration). We then used a variety of techniques such as Quantitative phase imaging, Seahorse assay, and Optical mapping to correlate gene expression differences to their structural and functional profiles.

Our structural analyses showed more mature sarcomeric organization in FHF- compared to SHF-like CMs, even in the presence of prolonged culture (i.e., up to 60 days), suggesting that intrinsic differences between these two populations may be the main drivers. Although the intrinsic differences can be attributed to many different processes, two categories that are known to regulate structural organization of CMs are genes that are directly involved in the formation of the sarcomeric unit (*TTN*, *NEBL*, *MYOM1*, and *ACTN2*) as well as genes involved in the regulation of the actin-myosin binding interactions (*MYL3*, *MYL4*, *MYH6*, and *MYH7*). The increased expression of these genes within FHF population can be associated with a higher degree of cellular stiffness we observed using atomic force microscopy. Prior studies have shown that cardiac muscle lacking nebulin (NEBL) resulted in variable lengths of thin filaments and lower isometric tension (Robinson and Winegrad, 1977; Robinson and Winegrad, 1979; Burgoyne et al., 2008) and that mutations in titin (TTN) can strongly affect cardiac muscle function due to changes in length-dependent activation of cross-bridges (Robinson and Winegrad, 1977; Robinson and Winegrad, 1979; Cazorla et al., 2001; Burgoyne et al., 2008; Granzier et al., 2009; Chung et al., 2013; Methawasin et al., 2014). Studies have also suggested that cardiac myofibrils are stiffer than skeletal myofibrils because Z-bands, titin filament networks, and other components of sarcomere structures within cardiac myofibrils are stronger than those of skeletal muscle (Akiyama et al., 2006). These data support our findings of increased expression and alignment of *ACTN2* and *MYOM1* in the FHF population, which forms the Z- and M-bands, respectively (Akiyama et al., 2006). Taken together, these data suggest that a downstream effect of TBX5 expression is the enhanced alignment and sarcomeric length regulation which leads to increased force generation, requisite for proper function of CMs from the left ventricle, primarily derived from the FHF population.

In addition to structural genes, our GO term analyses revealed differences in calcium signaling between the FHF and SHF populations. The action potential is central to CM function because it not only initiates but also regulates and coordinates excitation-contraction coupling. The morphology of APs reflects the net balance among ionic currents across the cell membrane. Among these ionic currents, calcium (Ca^{2+}) is a critical regulator of CM function and predominantly contributes to phase 2 (plateau) of AP morphology. Regulation of calcium current within CMs are mediated by a multitude of voltage channels and regulatory proteins such as LTCC, RYR2, SERCA, PLN, and TRDN. In alignment with our findings of enhanced sarcomeric organization, we observed higher expression of these key calcium handling genes within the FHF compared to SHF population.

Given the key role of calcium in excitation-contraction coupling, it is not surprising that subtle changes in these components can have profound consequences on AP plateau (which can be measured by APD_{30}) and contraction duration of CMs. To accurately quantify differences in AP plateau between our FHF and SHF population, we used a high-resolution imaging system (optical mapping) which allowed us to investigate the electrophysiological properties of thousands of cells within a large

population at once. Our functional studies showed prolonged APD_{30} in FHF-like CMs consistent with our gene expression analyses. The increase in APD_{30} can be, in part, attributed to higher expression of PLN, which exhibits an inhibitory effect on SERCA, leading to decreased re-uptake of intracellular calcium and prolonging the duration of AP depolarization (Fearnley et al., 2011).

As CMs differentiate and mature in the developing embryo, there are dramatic changes in energy sources and metabolism. During early cardiac development, glycolysis is a major source of energy for CM migration, proliferation, maturation, and contraction. As these cells mature, there is a switch from glycolytic to oxidative metabolism to support the increase in metabolic needs of functional CMs (Gaspar et al., 2014). This switch enables CMs to metabolize different carbon sources such as fatty acids, ketone bodies, and branched-chain amino acids to maintain cardiac function despite changes in substrate availability (Lloyd et al., 2004; Kolwicz et al., 2013). While our GO term analyses revealed potential metabolic differences between FHF- and SHF-like CMs, assessment of multiple aspects of oxidative phosphorylation revealed nearly identical respiratory profiles, albeit an increase in ATP-linked OCR within FHF-like CMs. There are a couple potential reasons that can be attributed to these findings. First, despite observing differences in structural proteins and calcium handling within FHF compared to SHF CMs, it is very likely that these two populations, having been derived *in vitro*, have not surpassed a maturation state beyond the embryonic period when compared to their *in vivo* counterparts. For this reason, both populations are still relatively immature and predominantly rely on glycolytic pathways. Indeed, prior work have shown that in contrast to their fetal counterparts, hiPSC-CMs have deficient fatty acid oxidation (FAO) despite expression of appropriate genes (Hui Zhang et al., 2020). Second, *in vitro* cardiac differentiation relies on specific media that is lipid-poor and glucose-rich (RPMI-B27) which has been shown to suppress FAO and may prevent the metabolic switch from glycolysis to oxidative phosphorylation (Saggerson, 2008; Lian et al., 2012; van Weeghel et al., 2018). Our study did not identify a role of TBX5 or its downstream mediators in coordinating the metabolic switch of hESC-derived CMs, although further studies are needed.

Despite uncovering differences between FHF and SHF populations, our study is limited by the use of *in vitro* hESC-derived CMs. Countless efforts to promote the maturation states of hESC-derived CMs have been unsuccessful thus far. Studies have shown that these cells are more similar to human embryonic CMs rather than their adult counterparts (Snir et al., 2003; Lieu et al., 2009). As our study yielded differences in sarcomeric structure and calcium handling suggestive of increased maturation in FHF compared to SHF CMs, we turned to human fetal heart samples and Monocle analyses to determine the proximity of FHF- and SHF-like CMs to endogenous fetal CMs along on the normal human cardiac development trajectory. Not surprisingly, trajectory analyses showed that SHF CMs were aligned earliest in pseudotime and that increased expression of sarcomeric proteins and calcium handling within FHF-like CMs resulted in a shift of this population farther along the development trajectory. As expected, these two populations lagged behind the human fetal heart samples on the trajectory inference, which were generally aligned accordingly to developmental age.

The role of TBX5 expression in cardiac development and heart field specification has been studied in detail. Here, we report isolation of FHF- and SHF-like CMs by differentiating our double reporter hESC line to uncover pivotal roles of TBX5 and its downstream effects on cardiac maturation. These effects include increased expression of key sarcomeric structure genes as well as calcium handling machinery. While metabolic differences may be attributable to *TBX5* expression, our study did not show respiratory distinctions between these two populations. These findings pave the way for further investigations into the modulation of *TBX5* expression as a potential method to regulate *in vitro* cardiac maturation which can serve as platforms for deeper understanding of the cardiac maturation process as well as development of more effective cardiac regenerative therapies.

DATA AVAILABILITY STATEMENT

The datasets presented in this study can be found in online repositories. The names of the repository/repositories and accession number(s) can be found in the article/**Supplementary Material**.

AUTHOR CONTRIBUTIONS

AP, NN, and RA contributed to the conception and design of the study. AP, NN, AS, TLN, AD, MZ, and ANP performed experiments. AP, NN, AS, TN, AD, SS, MZ, and DC performed the statistical analysis. AP, NN, and RA, wrote the first draft of the manuscript. AS, TN, AD, and DC, wrote sections of the manuscript. All authors contributed to manuscript revision, read, and approved 1580 the submitted version.

FUNDING

This work was supported in part by grants from the Eli and Edythe Broad Center of Regenerative Medicine and Stem Cell Research at UCLA Postdoctoral Fellowship (AP), Department of Defense Discovery Award (W81XWH-19-1-0244) (AP), Ruth L. Kirschstein Predoctoral Fellowship (HL144057) (NBN), California Institute for Regenerative Medicine (CIRM) (RN3-06378) (RA), National Institute of Health R01HL148714 (RA), and UCLA BSCRC-Rose Hills Foundation Research Award (RA), and the Eli and Edythe Broad Foundation Innovative Pilot Stem Cell Research Grant (RA), Air Force Office of Scientific Research (FA9550-15-1–0406) (MT), the Department of Defense

(W81XWH2110139) (MT and RA), and the NIH (R01GM073981, R01GM127985, and P30CA016042) (MT).

ACKNOWLEDGMENTS

We would like to acknowledge Drs. Hrayr S. Karagueuzian and James N. Weiss for the use of their electrophysiology instruments and consultation. We would also like to thank Drs. Adam Z. Stieg and Michael Lake from the California NanoSystems Institute (CNSI) as well as the UCLA BSCRC Microscopy and FACS Cores. Human fetal heart samples were generously provided by the Translational Pathology Core Laboratory of the Department of Pathology and Laboratory Medicine at UCLA.

SUPPLEMENTARY MATERIAL

The Supplementary Material for this article can be found online at: https://www.frontiersin.org/articles/10.3389/fcell.2021.787684/full#supplementary-material

Supplementary Figure S1 | Differentiation and isolation of FHF- and SHF-like CMs for scRNA-seq analysis. **(A)**, Schematic of the insertion of TdTomato and eGFP into the *TBX5* (Exon 9) and *NKX2-5* (Exon1) loci in previously generated hESC *TBX5-TdTomato*$^{+/W}$/*NKX2-5*$^{GFP/W}$ double reporter line. **(B)**, Schematic of monolayer cardiac differentiation protocol. **(C)**, Fluorescence microscopy of FHF (TdT$^+$/GFP$^+$) and SHF (TdT$^-$/GFP$^+$) optimized cardiac differentiations, scale bar = 100 µm. **(D)**, Representative flow cytometric analysis at Day 20 of cardiac differentiation showing the expression of TBX5 and NKX2-5. **(E)**, Top genes associated with principal components 1 and 2. **(F)**, DimPlot of FHF and SHF populations based on principal components 1 and 2. Hypergeometric tests show significant **(G)**, *TBX5* and **(H)**, *NKX2-5* occupancy at promoters of murine FHF and SHF gene orthologs when compared to 10 random sets of 150 genes that do not include FHF nor SHF genes (y-axis shows -$\log_{10}$(corrected p-value)). bioChIP-seq peaks from murine ventricles (E12.5) were used to define regions of *TBX5* or *NKX2-5* occupancy in the mm9 genome (Akerberg et al., 2019). Red dashed line crosses the y-axis at $-\log_{10}(0.05)$ as a reference point.

Supplementary Figure S2 | Differences in sarcomeric structure and cell migration between FHF- and SHF-like CMs. **(A)**, Boxplots of cardiac sarcomeric structural genes extracted from GO pathway "GO:0030049: muscle filament sliding" with higher average expression in SHF compared to FHF-like CMs. **(B)**, Heatmap of genes from panel A using bulk RNA sequencing data of hESCs and FHF- and SHF-like CMs at Day 20. **(C)**, Boxplots of migratory related-genes extracted from GO pathway "GO:0009611: response to wounding" with higher average expression in SHF compared to FHF-like CMs. **(B)**, Heatmap of genes from panel C using bulk RNA sequencing data of hESCs and FHF- and SHF-like CMs at Day 20. **(E)**, Quantitative phase imaging combined with fluorescent microscopy to identify and trace FHF-like (TdT$^+$/GFP$^+$) and SHF-like (TdT$^-$/GFP$^+$) CMs. Scale bar = 20 µm.

Supplementary Figure S3 | Transcriptional and functional analyses of calcium handling machinery in FHF- and SHF-like CMs. **(A)**, Boxplots of calcium handling-related genes extracted from GO term "GO:0010882: regulation of cardiac muscle contraction by calcium ion signaling" with higher average expression in SHF compared to FHF-like CMs. **(B)**, Heatmap of genes from panel A using bulk RNA sequencing data of hESCs and FHF- and SHF-like CMs at Day 20. **(C)**, APD_{50} (left) and APD80 (right) histograms of APs recorded from FHF-like CMs (n = 7,776 pixels). **(D)**, APD_{50} (left) and APD80 (right) histograms of APs recorded from SHF CMs (n = 8,464 pixels).

Supplementary Figure S4 | Extracellular acidification rate analyses in FHF- and SHF-like CMs. **(A)**, Seahorse assay measuring extracellular acidification rate (ECAR) profiles of FHF- and SHF-like CMs. **(B)**, Quantification of ECAR parameters between FHF-like and SHF-like CMs.

Supplementary Figure S5 | Single cell RNA sequencing analysis of human fetal CMs. **(A)**, UMAP showing clusters of 6, 10, and 17 weeks human fetal CMs. **(B)**, UMAP showing gene expression quantification for the cardiac genes (*TNNT2*, *MYH7*), fibroblast genes (*DDR2*, *COL1A1*), and endothelial genes (*CDH5*, *PECAM1*). **(C)**, Violin plots of expression of key genes from GO Term analyses relating to sarcomere structure, calcium handling, and oxidative phosphorylation.

REFERENCES

10X Genomics (2020). "Single-Library Analysis with Cell Ranger," in *10X Genomics*. Available at: https://support.10xgenomics.com/single-cell-gene-expression/software/pipelines/latest/using/count (Accessed May 17, 2020).

Akerberg, B. N., Gu, F., VanDusen, N. J., Zhang, X., Dong, R., Li, K., et al. (2019). A Reference Map of Murine Cardiac Transcription Factor Chromatin Occupancy Identifies Dynamic and Conserved Enhancers. *Nat. Commun.* 10 (1), 4907. doi:10.1038/s41467-019-12812-3

Akiyama, N., Ohnuki, Y., Kunioka, Y., Saeki, Y., and Yamada, T. (2006). Transverse Stiffness of Myofibrils of Skeletal and Cardiac Muscles Studied by Atomic Force Microscopy. *J. Physiol. Sci.* 56 (2), 145–151. doi:10.2170/physiolsci.RP003205

Becht, E., McInnes, L., Healy, J., Dutertre, C.-A., Kwok, I. W. H., and Ng, L. G. (2018). Dimensionality Reduction for Visualizing Single-Cell Data Using UMAP. *Nat. Biotechnol.* doi:10.1038/nbt.4314

Benjamin, E. J., Muntner, P., Alonso, A., Bittencourt, M. S., Callaway, C. W., Carson, A. P., et al. (2019). Heart Disease and Stroke Statistics-2019 Update: A Report from the American Heart Association. *Circulation* 139 (10), e56–e528. doi:10.1161/CIR.0000000000000659

Benjamini, Y., and Hochberg, Y. (1995). Controlling the False Discovery Rate: A Practical and Powerful Approach to Multiple Testing. *J. R. Stat. Soc. Ser. B (Methodological)* 57 (1), 289–300. doi:10.1111/j.2517-6161.1995.tb02031.x

Bon, P., Maucort, G., Wattellier, B., and Monneret, S. (2009). Quadriwave Lateral Shearing Interferometry for Quantitative Phase Microscopy of Living Cells. *Opt. Express* 17 (15), 13080–13094. doi:10.1364/oe.17.013080

Bruneau, B. G., Logan, M., Davis, N., Levi, T., Tabin, C. J., Seidman, J. G., et al. (1999). Chamber-specific Cardiac Expression of Tbx5 and Heart Defects in Holt-Oram Syndrome. *Dev. Biol.* 211 (1), 100–108. doi:10.1006/dbio.1999.9298

Bruneau, B. G., Nemer, G., Schmitt, J. P., Charron, F., Robitaille, L., Caron, S., et al. (2001). A Murine Model of Holt-Oram Syndrome Defines Roles of the T-Box Transcription Factor Tbx5 in Cardiogenesis and Disease. *Cell.* 106 (6), 709–721. doi:10.1016/s0092-8674(01)00493-7

Bruneau, B. G. (2013). Signaling and Transcriptional Networks in Heart Development and Regeneration. *Cold Spring Harb Perspect. Biol.* 5 (3), a008292. doi:10.1101/cshperspect.a008292

Burgoyne, T., Muhamad, F., and Luther, P. K. (2008). Visualization of Cardiac Muscle Thin Filaments and Measurement of Their Lengths by Electron Tomography. *Cardiovasc. Res.* 77 (4), 707–712. doi:10.1093/cvr/cvm117

Cao, N., Huang, Y., Zheng, J., Spencer, C. I., Zhang, Y., Fu, J.-D., et al. (2016). Conversion of Human Fibroblasts into Functional Cardiomyocytes by Small Molecules. *Science* 352 (6290), 1216–1220. doi:10.1126/science.aaf1502

Cazorla, O., Wu, Y., Irving, T. C., and Granzier, H. (2001). Titin-based Modulation of Calcium Sensitivity of Active Tension in Mouse Skinned Cardiac Myocytes. *Circ. Res.* 88 (10), 1028–1035. doi:10.1161/hh1001.090876

Chapski, D. J., Cabaj, M., Morselli, M., Mason, R. J., Soehalim, E., Ren, S., et al. (2021). Early Adaptive Chromatin Remodeling Events Precede Pathologic Phenotypes and Are Reinforced in the Failing Heart. *J. Mol. Cell Cardiol* 160, 73–86. doi:10.1016/j.yjmcc.2021.07.002

Chung, C. S., Hutchinson, K. R., Methawasin, M., Saripalli, C., Smith, J. E., 3rd, Hidalgo, C. G., et al. (2013). Shortening of the Elastic Tandem Immunoglobulin Segment of Titin Leads to Diastolic Dysfunction. *Circulation* 128 (1), 19–28. doi:10.1161/CIRCULATIONAHA.112.001268

Elliott, D. A., Braam, S. R., Koutsis, K., Ng, E. S., Jenny, R., Lagerqvist, E. L., et al. (2011). NKX2-5(eGFP/w) hESCs for Isolation of Human Cardiac

Progenitors and Cardiomyocytes. *Nat. Methods* 8 (12), 1037–1040. doi:10.1038/nmeth.1740

Fearnley, C. J., Roderick, H. L., and Bootman, M. D. (2011). Calcium Signaling in Cardiac Myocytes. *Cold Spring Harb Perspect. Biol.* 3 (11), a004242. doi:10.1101/cshperspect.a004242

Galdos, F. X., Guo, Y., Paige, S. L., VanDusen, N. J., Wu, S. M., and Pu, W. T. (2017). Cardiac Regeneration: Lessons from Development. *Circ. Res.* 120 (6), 941–959. doi:10.1161/CIRCRESAHA.116.309040

Garbern, J. C., and Lee, R. T. (2013). Cardiac Stem Cell Therapy and the Promise of Heart Regeneration. *Cell Stem Cell* 12 (6), 689–698. doi:10.1016/j.stem.2013.05.008

Gaspar, J. A., Doss, M. X., Hengstler, J. G., Cadenas, C., Hescheler, J., and Sachinidis, A. (2014). Unique Metabolic Features of Stem Cells, Cardiomyocytes, and Their Progenitors. *Circ. Res.* 114 (8), 1346–1360. doi:10.1161/CIRCRESAHA.113.302021

Ghiroldi, A., Piccoli, M., Ciconte, G., Pappone, C., and Anastasia, L. (2017). Regenerating the Human Heart: Direct Reprogramming Strategies and Their Current Limitations. *Basic Res. Cardiol.* 112 (6), 68. doi:10.1007/s00395-017-0655-9

Granzier, H. L., Radke, M. H., Peng, J., Westermann, D., Nelson, O. L., Rost, K., et al. (2009). Truncation of Titin's Elastic PEVK Region Leads to Cardiomyopathy with Diastolic Dysfunction. *Circ. Res.* 105 (6), 557–564. doi:10.1161/CIRCRESAHA.109.200964

Guo, Y., and Pu, W. T. (2020). Cardiomyocyte Maturation. *Circ. Res.* 126 (8), 1086–1106. doi:10.1161/CIRCRESAHA.119.315862

Hao, Y., Hao, S., Andersen-Nissen, E., Mauck, W. M., Zheng, S., Butler, A., et al. (2021). Integrated Analysis of Multimodal Single-Cell Data. *Cell* 184 (13), 3573–3587. doi:10.1016/j.cell.2021.04.048

Hui Zhang, M. G. B., Spiering, S., Divakaruni, A., Meurs, N. E., Yu, M. S., Colas, A. R., et al. (2020). Lipid Availability Influences the Metabolic Maturation of Human Pluripotent Stem Cell-Derived Cardiomyocytes. *bioRxiv*. doi:10.1101/2020.03.14.991927

Huynh, T., Chen, L., Terrell, P., and Baldini, A. (2007). A Fate Map of Tbx1 Expressing Cells Reveals Heterogeneity in the Second Cardiac Field. *Genesis* 45 (7), 470–475. doi:10.1002/dvg.20317

Jia, C., Hu, Y., Kelly, D., Kim, J., Li, M., and Zhang, N. R. (2017). Accounting for Technical Noise in Differential Expression Analysis of Single-Cell RNA Sequencing Data. *Nucleic Acids Res.* 45 (19), 10978–10988. doi:10.1093/nar/gkx754

Jiang, Y., Park, P., Hong, S. M., and Ban, K. (2018). Maturation of Cardiomyocytes Derived from Human Pluripotent Stem Cells: Current Strategies and Limitations. *Mol. Cells* 41 (7), 613–621. doi:10.14348/molcells.2018.0143

Karbassi, E., Fenix, A., Marchiano, S., Muraoka, N., Nakamura, K., Yang, X., et al. (2020). Cardiomyocyte Maturation: Advances in Knowledge and Implications for Regenerative Medicine. *Nat. Rev. Cardiol.* 17 (6), 341–359. doi:10.1038/s41569-019-0331-x

Kelly, R. G., Buckingham, M. E., and Moorman, A. F. (2014). Heart fields and Cardiac Morphogenesis. *Cold Spring Harb Perspect. Med.* 4 (10). doi:10.1101/cshperspect.a015750

Kolwicz, S. C., Jr., Purohit, S., and Tian, R. (2013). Cardiac Metabolism and its Interactions with Contraction, Growth, and Survival of Cardiomyocytes. *Circ. Res.* 113 (5), 603–616. doi:10.1161/CIRCRESAHA.113.302095

Laflamme, M. A., Chen, K. Y., Naumova, A. V., Muskheli, V., Fugate, J. A., Dupras, S. K., et al. (2007). Cardiomyocytes Derived from Human Embryonic Stem Cells in Pro-survival Factors Enhance Function of Infarcted Rat Hearts. *Nat. Biotechnol.* 25 (9), 1015–1024. doi:10.1038/nbt1327

Laflamme, M. A., and Murry, C. E. (2011). Heart Regeneration. *Nature* 473 (7347), 326–335. doi:10.1038/nature10147

Lescroart, F., Chabab, S., Lin, X., Rulands, S., Paulissen, C., Rodolosse, A., et al. (2014). Early Lineage Restriction in Temporally Distinct Populations of Mesp1 Progenitors during Mammalian Heart Development. *Nat. Cell Biol.* 16 (9), 829–840. doi:10.1038/ncb3024

Lewandowski, J., Rozwadowska, N., Kolanowski, T. J., Malcher, A., Zimna, A., Rugowska, A., et al. (2018). The Impact of *In Vitro* Cell Culture Duration on the Maturation of Human Cardiomyocytes Derived from Induced Pluripotent Stem Cells of Myogenic Origin. *Cell Transpl.* 27 (7), 1047–1067. doi:10.1177/0963689718779346

Lian, X., Hsiao, C., Wilson, G., Zhu, K., Hazeltine, L. B., Azarin, S. M., et al. (2012). Robust Cardiomyocyte Differentiation from Human Pluripotent Stem Cells via Temporal Modulation of Canonical Wnt Signaling. *Proc. Natl. Acad. Sci. U S A.* 109 (27), E1848–E1857. doi:10.1073/pnas.1200250109

Liberatore, C. M., Searcy-Schrick, R. D., and Yutzey, K. E. (2000). Ventricular Expression of Tbx5 Inhibits normal Heart Chamber Development. *Dev. Biol.* 223 (1), 169–180. doi:10.1006/dbio.2000.9748

Lieu, D. K., Liu, J., Siu, C. W., McNerney, G. P., Tse, H-F., Abu-Khalil, A., et al. (2009). Absence of Transverse Tubules Contributes to Non-uniform Ca(2+) Wavefronts in Mouse and Human Embryonic Stem Cell-Derived Cardiomyocytes. *Stem Cells Dev.* 18 (10), 1493–1500. doi:10.1089/scd.2009.0052

Liu, Y. W., Chen, B., Yang, X., Fugate, J. A., Kalucki, F. A., Futakuchi-Tsuchida, A., et al. (2018). Human Embryonic Stem Cell-Derived Cardiomyocytes Restore Function in Infarcted Hearts of Non-human Primates. *Nat. Biotechnol.* 36 (7), 597–605. doi:10.1038/nbt.4162

Lloyd, S. G., Wang, P., Zeng, H., and Chatham, J. C. (2004). Impact of Low-Flow Ischemia on Substrate Oxidation and Glycolysis in the Isolated Perfused Rat Heart. *Am. J. Physiol. Heart Circ. Physiol.* 287 (1), H351–H362. doi:10.1152/ajpheart.00983.2003

Lundy, S. D., Zhu, W. Z., Regnier, M., and Laflamme, M. A. (2013). Structural and Functional Maturation of Cardiomyocytes Derived from Human Pluripotent Stem Cells. *Stem Cells Dev.* 22 (14), 1991–2002. doi:10.1089/scd.2012.0490

Methawasin, M., Hutchinson, K. R., Lee, E. J., Saripalli, C., Smith, J. E., 3rd, Hidalgo, C. G., et al. (2014). Experimentally Increasing Titin Compliance in a Novel Mouse Model Attenuates the Frank-Starling Mechanism but Has a Beneficial Effect on Diastole. *Circulation* 129 (19), 1924–1936. doi:10.1161/CIRCULATIONAHA.113.005610

Nguyen, T. L., Polanco, E. R., Patananan, A. N., Zangle, T. A., and Teitell, M. A. (2020). Cell Viscoelasticity Is Linked to Fluctuations in Cell Biomass Distributions. *Sci. Rep.* 10 (1), 7403. doi:10.1038/s41598-020-64259-y

Otsu, N. (1979). A Threshold Selection Method from Gray-Level Histograms. *IEEE Trans. Syst. Man, Cybernetics* 9 (1), 62–66. doi:10.1109/TSMC.1979.4310076

Pezhouman, A., Cao, H., Fishbein, M. C., Belardinelli, L., Weiss, J. N., and Karagueuzian, H. S. (2018). Atrial Fibrillation Initiated by Early Afterdepolarization-Mediated Triggered Activity during Acute Oxidative Stress: Efficacy of Late Sodium Current Blockade. *J. Heart Health* 4 (1). doi:10.16966/2379-769X.146

Pezhouman, A., Engel, J. L., Nguyen, N. B., Skelton, R. J. P., Gilmore, W. B., Qiao, R., et al. (2021). Isolation and Characterization of hESC-Derived Heart Field-specific Cardiomyocytes Unravels New Insights into Their Transcriptional and Electrophysiological Profiles. *Cardiovasc. Res.* doi:10.1093/cvr/cvab102

Pezhouman, A., Madahian, S., Stepanyan, H., Ghukasyan, H., Qu, Z., Belardinelli, L., et al. (2014). Selective Inhibition of Late Sodium Current Suppresses Ventricular Tachycardia and Fibrillation in Intact Rat Hearts. *Heart rhythm* 11 (3), 492–501. doi:10.1016/j.hrthm.2013.11.026

Pezhouman, A., Singh, N., Song, Z., Nivala, M., Eskandari, A., Cao, H., et al. (2015). Molecular Basis of Hypokalemia-Induced Ventricular Fibrillation. *Circulation* 132 (16), 1528–1537. doi:10.1161/CIRCULATIONAHA.115.016217

Robinson, T. F., and Winegrad, S. (1979). The Measurement and Dynamic Implications of Thin Filament Lengths in Heart Muscle. *J. Physiol.* 286, 607–619. doi:10.1113/jphysiol.1979.sp012640

Robinson, T. F., and Winegrad, S. (1977). Variation of Thin Filament Length in Heart Muscles. *Nature* 267 (5606), 74–75. doi:10.1038/267074a0

Romagnuolo, R., Masoudpour, H., Porta-Sánchez, A., Qiang, B., Barry, J., Laskary, A., et al. (2019). Human Embryonic Stem Cell-Derived Cardiomyocytes Regenerate the Infarcted Pig Heart but Induce Ventricular Tachyarrhythmias. *Stem Cell Rep.* 12 (5), 967–981. doi:10.1016/j.stemcr.2019.04.005

Saggerson, D. (2008). Malonyl-CoA, a Key Signaling Molecule in Mammalian Cells. *Annu. Rev. Nutr.* 28, 253–272. doi:10.1146/annurev.nutr.28.061807.155434

Selmer, R., Halvorsen, S., Myhre, K. I., Wisløff, T. F., and Kristiansen, I. S. (2005). Cost-effectiveness of Primary Percutaneous Coronary Interventionversusthrombolytic Therapy for Acute Myocardial Infarction. *Scand. Cardiovasc. J.* 39 (5), 276–285. doi:10.1080/14017430510035988

Shiba, Y., Gomibuchi, T., Seto, T., Wada, Y., Ichimura, H., Tanaka, Y., et al. (2016). Allogeneic Transplantation of iPS Cell-Derived Cardiomyocytes Regenerates Primate Hearts. *Nature* 538 (7625), 388–391. doi:10.1038/nature19815

Sizarov, A., Devalla, H. D., Anderson, R. H., Passier, R., Christoffels, V. M., and Moorman, A. F. (2011). Molecular Analysis of Patterning of Conduction Tissues in the Developing Human Heart. *Circ. Arrhythm Electrophysiol.* 4 (4), 532–542. doi:10.1161/CIRCEP.111.963421

Skelton, R. J. P., Brady, B., Khoja, S., Sahoo, D., Engel, J., Arasaratnam, D., et al. (2016). CD13 and ROR2 Permit Isolation of Highly Enriched Cardiac Mesoderm from Differentiating Human Embryonic Stem Cells. *Stem Cel. Rep.* 6 (1), 95–108. doi:10.1016/j.stemcr.2015.11.006

Skelton, R. J. P., Khoja, S., Almeida, S., Rapacchi, S., Han, F., Engel, J., et al. (2016). Magnetic Resonance Imaging of Iron Oxide-Labeled Human Embryonic Stem Cell-Derived Cardiac Progenitors. *Stem Cells Translational Med.* 5 (1), 67–74. doi:10.5966/sctm.2015-0077

Snir, M., Kehat, I., Gepstein, A., Coleman, R., Itskovitz-Eldor, J., Livne, E., et al. (2003). Assessment of the Ultrastructural and Proliferative Properties of Human Embryonic Stem Cell-Derived Cardiomyocytes. *Am. J. Physiol. Heart Circ. Physiol.* 285 (6), H2355–H2363. doi:10.1152/ajpheart.00020.2003

Später, D., Abramczuk, M. K., Buac, K., Zangi, L., Stachel, M. W., Clarke, J., et al. (2013). A HCN4+ Cardiomyogenic Progenitor Derived from the First Heart Field and Human Pluripotent Stem Cells. *Nat. Cell Biol.* 15 (9), 1098–1106. doi:10.1038/ncb2824

Steimle, J. D., Rankin, S. A., Slagle, C. E., Bekeny, J., Rydeen, A. B., Chan, S. S-K., et al. (2018). Evolutionarily Conserved Tbx5- Wnt2/2b Pathway Orchestrates Cardiopulmonary Development. *Proc. Natl. Acad. Sci.* 115 (45), E10615. doi:10.1073/pnas.1811624115

Trapnell, C., Cacchiarelli, D., Grimsby, J., Pokharel, P., Li, S., Morse, M., et al. (2014). The Dynamics and Regulators of Cell Fate Decisions Are Revealed by Pseudotemporal Ordering of Single Cells. *Nat. Biotechnol.* 32 (4), 381–386. doi:10.1038/nbt.2859

van Weeghel, M., Abdurrachim, D., Nederlof, R., Argmann, C. A., Houtkooper, R. H., Hagen, J., et al. (2018). Increased Cardiac Fatty Acid Oxidation in a Mouse Model with Decreased Malonyl-CoA Sensitivity of CPT1B. *Cardiovasc. Res.* 114 (10), 1324–1334. doi:10.1093/cvr/cvy089

Watanabe, Y., Zaffran, S., Kuroiwa, A., Higuchi, H., Ogura, T., Harvey, R. P., et al. (2012). Fibroblast Growth Factor 10 Gene Regulation in the Second Heart Field by Tbx1, Nkx2-5, and Islet1 Reveals a Genetic Switch for Down-Regulation in the Myocardium. *Proc. Natl. Acad. Sci. U S A.* 109 (45), 18273–18280. doi:10.1073/pnas.1215360109

Xie, L., Hoffmann, A. D., Burnicka-Turek, O., Friedland-Little, J. M., Zhang, K., and Moskowitz, I. P. (2012). Tbx5-hedgehog Molecular Networks Are Essential in the Second Heart Field for Atrial Septation. *Dev. Cell* 23 (2), 280–291. doi:10.1016/j.devcel.2012.06.006

Yanamandala, M., Zhu, W., Garry, D. J., Kamp, T. J., Hare, J. M., Jun, H.-w., et al. (2017). Overcoming the Roadblocks to Cardiac Cell Therapy Using Tissue Engineering. *J. Am. Coll. Cardiol.* 70 (6), 766–775. doi:10.1016/j.jacc.2017.06.012

Zangle, T. A., Burnes, D., Mathis, C., Witte, O. N., and Teitell, M. A. (2013). Quantifying Biomass Changes of Single CD8+ T Cells during Antigen Specific Cytotoxicity. *PLoS One* 8 (7), e68916. doi:10.1371/journal.pone.0068916

Zhang, J. Z., Termglinchan, V., Shao, N. Y., Itzhaki, I., Liu, C., Ma, N., et al. (2019). A Human iPSC Double-Reporter System Enables Purification of Cardiac Lineage Subpopulations with Distinct Function and Drug Response Profiles. *Cell Stem Cell.* 24 (5), 802–811. doi:10.1016/j.stem.2019.02.015

Zhang, R., Han, P., Yang, H., Ouyang, K., Lee, D., Lin, Y-F., et al. (2013). *In Vivo* cardiac Reprogramming Contributes to Zebrafish Heart Regeneration. *Nature* 498 (7455), 497–501. doi:10.1038/nature12322

Zhou, Y., Zhou, B., Pache, L., Chang, M., Khodabakhshi, A. H., Tanaseichuk, O., et al. (2019). Metascape Provides a Biologist-Oriented Resource for the Analysis of Systems-Level Datasets. *Nat. Commun.* 10 (1), 1523. doi:10.1038/s41467-019-09234-6

Zhou, Z., Wang, J., Guo, C., Chang, W., Zhuang, J., Zhu, P., et al. (2017). Temporally Distinct Six2-Positive Second Heart Field Progenitors Regulate Mammalian Heart Development and Disease. *Cell Rep.* 18 (4), 1019–1032. doi:10.1016/j.celrep.2017.01.002

Conflict of Interest: The authors declare that the research was conducted in the absence of any commercial or financial relationships that could be construed as a potential conflict of interest.

Publisher's Note: All claims expressed in this article are solely those of the authors and do not necessarily represent those of their affiliated organizations, or those of the publisher, the editors, and the reviewers. Any product that may be evaluated in this article, or claim that may be made by its manufacturer, is not guaranteed or endorsed by the publisher.

Supplementary Figures

Supplementary Fig. 1: Differentiation and isolation of FHF and SHF CMs for scRNA seq analysis.

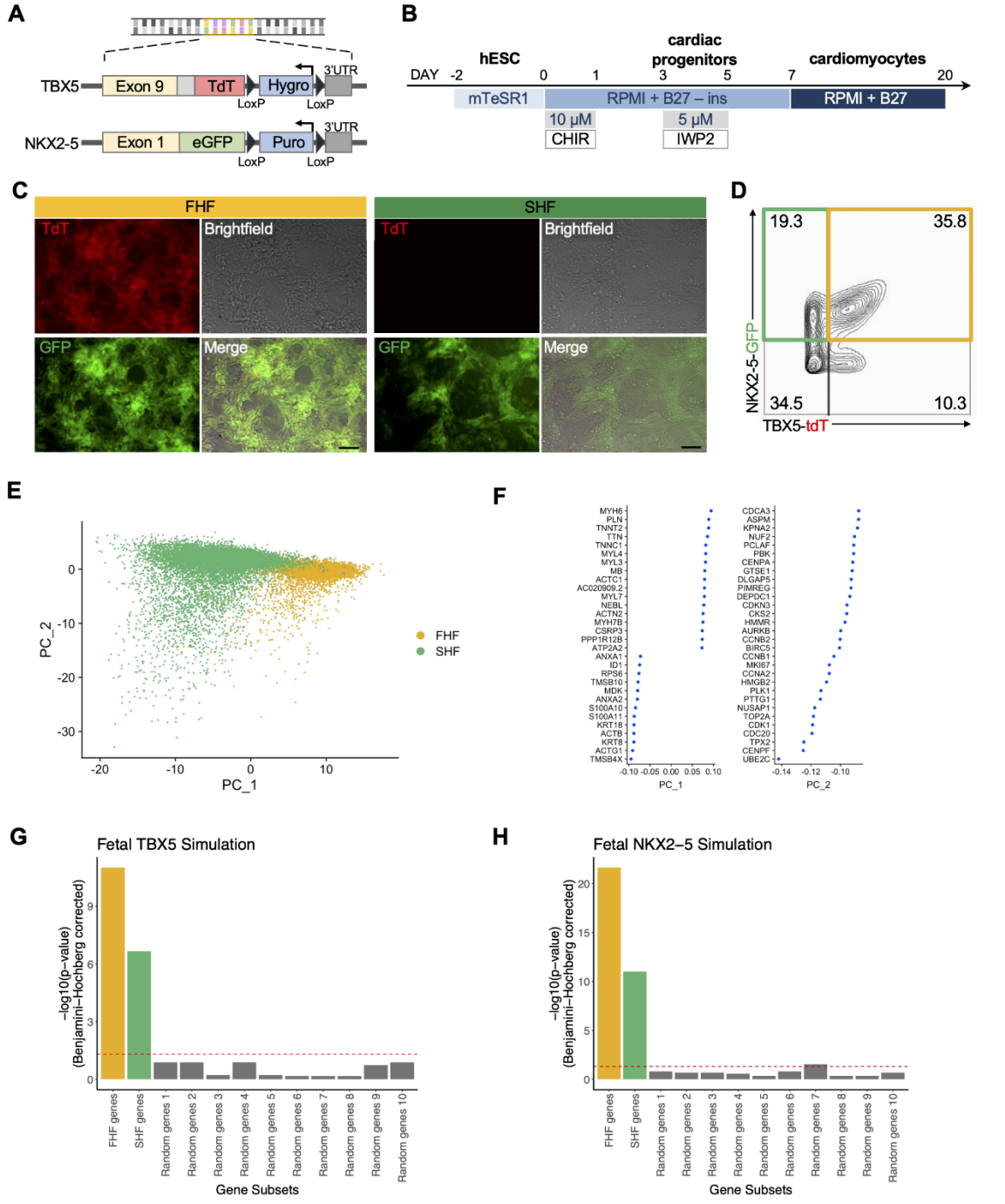

Supplementary Fig. 2: Differences in sarcomeric structure and cell migration between FHF and SHF CMs.

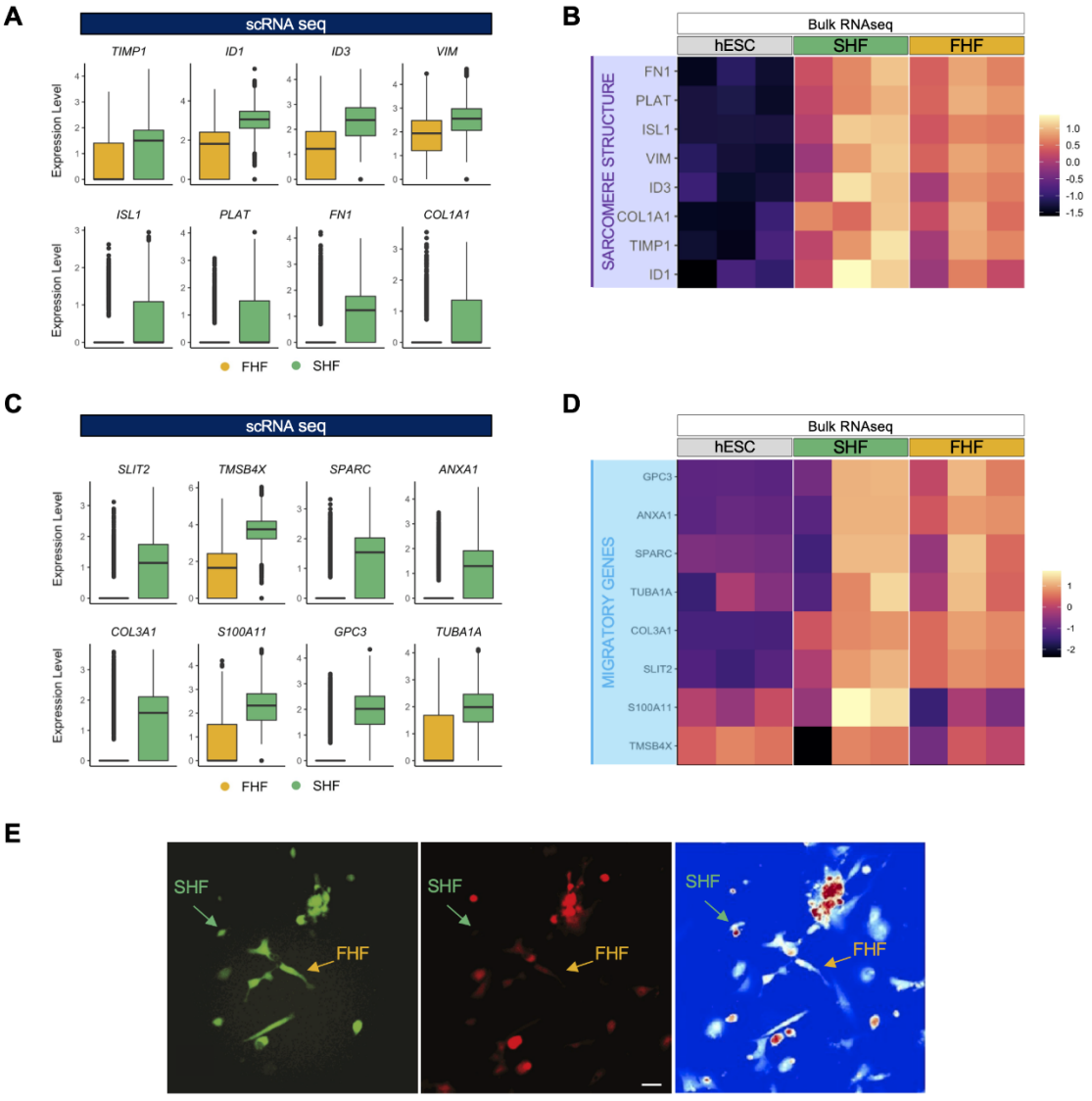

Supplementary Fig. 3: Electrophysiology and Calcium Signaling

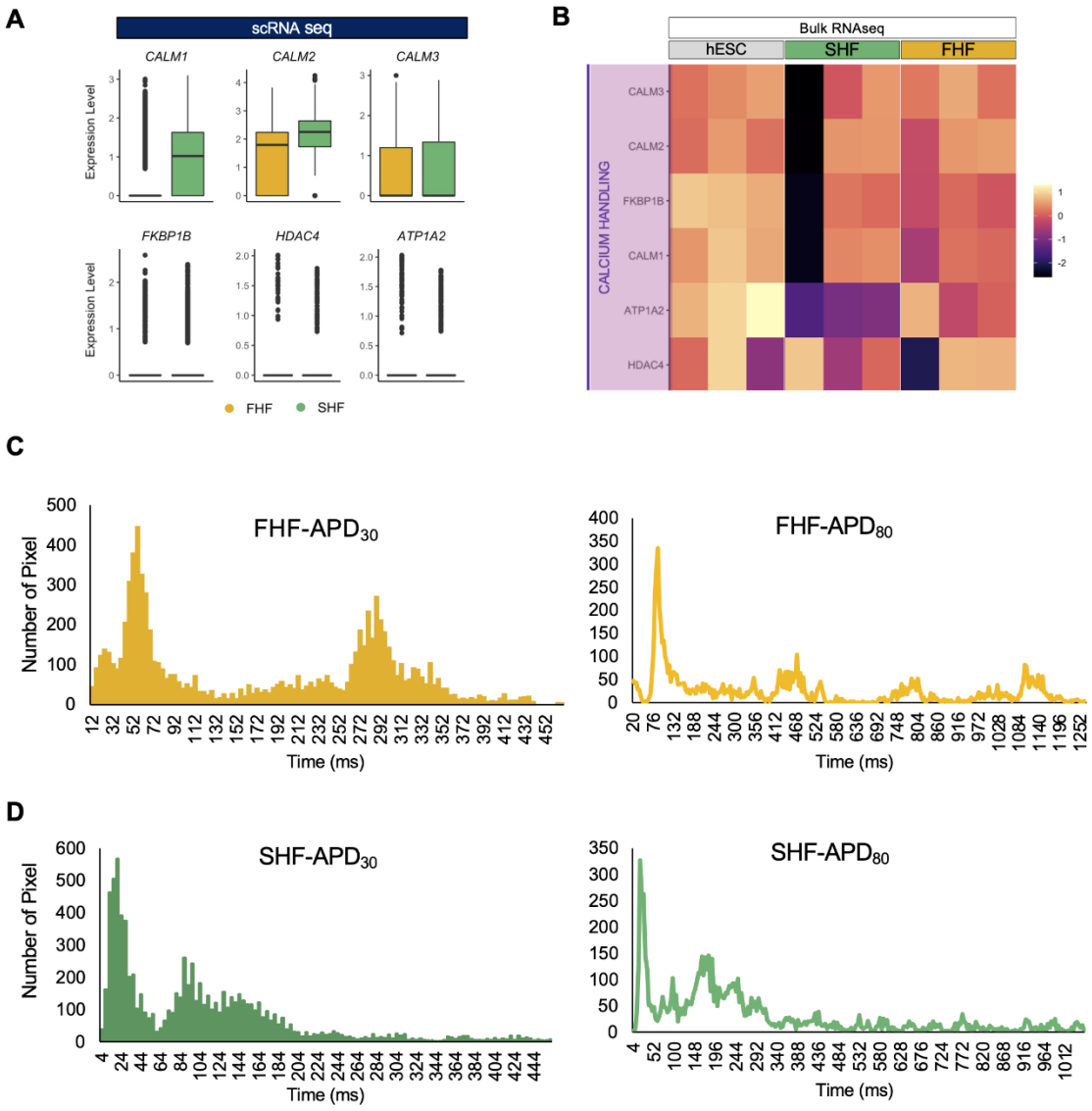

Supplementary Fig. 4: Metabolism

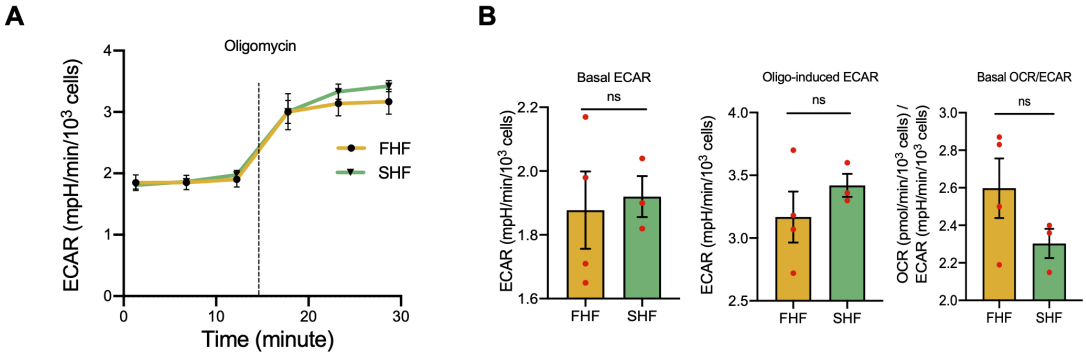

Supplementary Fig. 5: Monocle

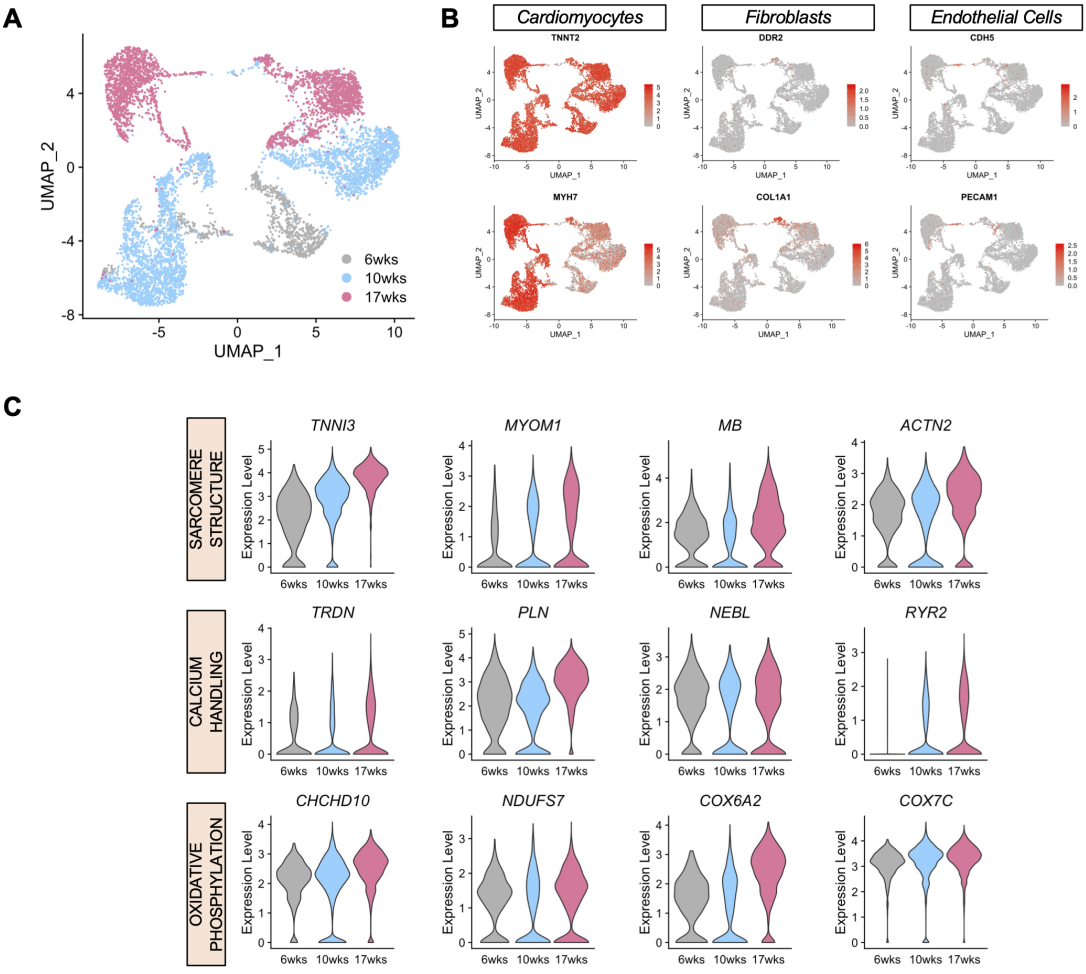

Appendix V. Topological Arrangement of Cardiac Fibroblasts Regulates Cellular Plasticity

Topological Arrangement of Cardiac Fibroblasts Regulates Cellular Plasticity

Jingyi Yu,* Marcus M. Seldin,* Kai Fu,* Shen Li, Larry Lam, Ping Wang, Yijie Wang, Dian Huang, Thang L. Nguyen, Bowen Wei, Rajan P. Kulkarni, Dino Di Carlo, Michael Teitell, Matteo Pellegrini, Aldons J. Lusis, Arjun Deb

Rationale: **Cardiac fibroblasts do not form a syncytium but reside in the interstitium between myocytes. This topological relationship between fibroblasts and myocytes is maintained throughout postnatal life until an acute myocardial injury occurs, when fibroblasts are recruited to, proliferate and aggregate in the region of myocyte necrosis. The accumulation or aggregation of fibroblasts in the area of injury thus represents a unique event in the life cycle of the fibroblast, but little is known about how changes in the topological arrangement of fibroblasts after cardiac injury affect fibroblast function.**

Objective: **The objective of the study was to investigate how changes in topological states of cardiac fibroblasts (such as after cardiac injury) affect cellular phenotype.**

Methods and Results: **Using 2 and 3-dimensional (2D versus 3D) culture conditions, we show that simple aggregation of cardiac fibroblasts is sufficient by itself to induce genome-wide changes in gene expression and chromatin remodeling. Remarkably, gene expression changes are reversible after the transition from a 3D back to 2D state demonstrating a topological regulation of cellular plasticity. Genes induced by fibroblast aggregation are strongly associated and predictive of adverse cardiac outcomes and remodeling in mouse models of cardiac hypertrophy and failure. Using solvent-based tissue clearing techniques to create optically transparent cardiac scar tissue, we show that fibroblasts in the region of dense scar tissue express markers that are induced by fibroblasts in the 3D conformation. Finally, using live cell interferometry, a quantitative phase microscopy technique to detect absolute changes in single cell biomass, we demonstrate that conditioned medium collected from fibroblasts in 3D conformation compared with that from a 2D state significantly increases cardiomyocyte cell hypertrophy.**

Conclusions: **Taken together, these findings demonstrate that simple topological changes in cardiac fibroblast organization are sufficient to induce chromatin remodeling and global changes in gene expression with potential functional consequences for the healing heart. (*Circ Res*. 2018;123:73-85. DOI: 10.1161/CIRCRESAHA.118.312589.)**

Key Words: cell biology ■ fibroblasts ■ fibrosis ■ hypertrophy ■ interferometry

Cardiac fibroblasts develop from epithelial–mesenchymal transition of epicardial cells during cardiac development.[1] After adoption of the mesenchymal phenotype, they migrate into the developing myocardium and as the myocardium compacts, they get trapped between the myocyte interstitium to become resident cardiac fibroblasts. This topological arrangement of fibroblasts and myocytes persists throughout postnatal life. However, this spatial relationship is disrupted after acute myocardial necrosis, when fibroblasts are recruited to, proliferate and aggregate in the region of injury, resulting in a much higher density of fibroblasts in the region of necrosis.[2] Aggregating fibroblasts in the region of injury are known to express gap junctions that facilitate intercellular communication between physically apposed fibroblasts.[3] Tumor cells and cancer cell lines, when cultured in 3-dimensional (3D) conditions to promote aggregation exhibit altered phenotypic features such as migration, proliferation, and chemo resistance associated with changes in gene expression

Editorial, see p 12
Meet the First Author, see p 3

Original received March 19, 2018; revision received April 17, 2018; accepted April 20, 2018. In March 2018, the average time from submission to first decision for all original research papers submitted to *Circulation Research* was 10.69 days.

From the Division of Cardiology, Department of Medicine (J.Y., M.M.S., S.L., P.W., Y.W., A.J.L., A.D.), Cardiovascular Research Laboratory (J.Y., M.M.S., S.L., P.W., Y.W., A.J.L., A.D.), Department of Molecular, Cell, and Developmental Biology (J.Y., K.F., S.L., L.L., P.W., Y.W., M.P., A.D.), Eli & Edythe Broad Center of Regenerative Medicine and Stem Cell Research (J.Y., K.F., S.L., L.L., P.W., Y.W., M.P., A.D.), Molecular Biology Institute (J.Y., K.F., S.L., L.L., P.W., Y.W., M.T., M.P., A.D.), Jonsson Comprehensive Cancer Center (J.Y., K.F., S.L., L.L., P.W., Y.W., R.P.K., D.D.C., M.T., M.P., A.D.), Departments of Human Genetics and Microbiology, Immunology and Molecular Genetics (M.M.S., A.J.L.), Department of Bioengineering (D.H., T.L.N., D.D.C.), Division of Dermatology, Department of Medicine, David Geffen School of Medicine (B.W., R.P.K.), and Department of Pathology and Laboratory Medicine, David Geffen School of Medicine (M.T.), University of California, Los Angeles.

*These authors contributed equally to this article.

The online-only Data Supplement is available with this article at http://circres.ahajournals.org/lookup/suppl/doi:10.1161/CIRCRESAHA.118.312589/-/DC1.

Correspondence to Arjun Deb, Department of Medicine, University of California, 3609A MRL, 675 Charles E Young Dr S, Los Angeles, CA 90095. E-mail adeb@mednet.ucla.edu

Novelty and Significance

What Is Known?

- Unlike cardiac myocytes, cardiac fibroblasts do not form a syncytium but reside in the interstitium among myocytes.
- This topological relationship is altered after heart injury when fibroblasts are recruited to an aggregate at the area of injury.
- Aggregation of fibroblasts after injury thus represents a unique event in the life cycle of the cardiac fibroblast but whether such topological rearrangement affects fibroblast function is not clear.

What New Information Does This Article Contribute?

- Aggregation of cardiac fibroblasts leads to global changes in gene expression and chromatin reorganization.
- Changes in the transcriptome are reversible on aggregation, disaggregation, and reaggregation of cardiac fibroblasts.
- Genes induced by fibroblast aggregation are expressed in the injured heart and correlate with poor cardiac outcomes in mouse models of hypertrophy and heart failure.
- The secretome of aggregated cardiac fibroblasts can induce hypertrophy of cardiac myocytes.

Cardiac fibroblasts reside in the interstitium of the heart and do not form a syncytium. After the injury, they, however, are recruited to aggregate in the area of injury, but the physiological significance of fibroblast aggregation remains unknown. Here, we demonstrate that simple aggregation of cardiac fibroblasts induces widespread changes in gene expression and chromatic reorganization. Such transcriptional changes are reversible when cardiac fibroblasts are disaggregated or subsequently reaggregated. Genes upregulated in the aggregated state are expressed in the region of injury and correlate with indices of adverse cardiac remodeling in murine models of cardiac hypertrophy and failure. Finally, we demonstrate that the secretome of aggregated cardiac fibroblasts induces hypertrophy of cardiac myocytes. Taken together these observations demonstrate that topological changes in the spatial organization of cardiac fibroblasts drives chromatin reorganization, gene expression patterns and has functional consequences for cardiac wound healing.

Nonstandard Abbreviations and Acronyms

Acta2	alpha-smooth muscle actin 2
ADAMTS15	metallopeptidase with thrombospondin motif 15
ATAC	assay for transposase accessible chromatin
Cnn2	calponin 2
CTGF	connective tissue growth factor
CTNNB1	beta-catenin
GPNMB	glycoprotein nonmetastatic B
HMDP	Hybrid Mouse Diversity Panel
MITF	microphthalmia-associated transcription factor
MMP	matrix metalloproteinase
NRVM	neonatal rat ventricular cardiomyocytes
PC	principle component
SRF	serum response factor

profiles.[4] However, little is known about how spatial rearrangement of fibroblasts such as that occurs after acute myocardial injury affects the cellular and genetic outputs of the fibroblast and the cardiac wound healing response.

Methods

All data and supporting materials are within the article and in the Online Data Supplement. In addition, RNA-seq and assay for transposase accessible chromatin (ATAC-seq) data for the study are available in National Center for Biotechnology Information's Gene Expression Omnibus and have been made publicly available through GEO series accession number GSE113277 at https://www.ncbi.nlm.nih.gov/geo/query/acc.cgi?acc=GSE113277.

Cardiac fibroblasts were isolated from adult wild-type mice (both male and female) as well as Col1a2CreERT:R26R^{tdtomato} and TCF21MerCreMer:R26R^{tdtomato} as described.[5] Isolated cardiac fibroblasts (<3 passages) were grown on standard polystyrene coated tissue culture plates (2D; plates not coated with collagen or other matrix proteins) or seeded onto ultra-low attachment plates (not coated with any extracellular matrix protein), whereby they formed spheres within 24 hours of seeding (3D). Subsequently, the cardiac fibroblasts were again transferred back to regular tissue culture plates, on which the spheres attached and fibroblasts migrated out of the spheres to form monolayers within 4 to 5 days (3D-2D). Reseeding of the fibroblasts onto ultra-low attachment plates again resulted in formation of spheres within 24 hours (3D-2D-3D). Fibroblasts in 2D or 3D maintained for 5 days served as temporally adjusted controls for 3D-2D states. 3D-2D fibroblasts trypsinized and reseeded onto 2D states served as additional controls for 3D-2D-3D states. RNA-seq and ATAC-seq were performed at each topological state of the cardiac fibroblast and on temporally adjusted controls for each time point. Transcripts upregulated in 3D states were correlated to clinical traits across a mouse population (Hybrid Mouse Diversity Panel [HMDP]) after isoproterenol infusion.[6] Cardiac fibroblasts were also seeded onto tissue culture plates of varying stiffness (0.5 kPa, 8 kPa, and 64 kPa elastic moduli) to determine whether 2D-3D gene expression changes were recapitulated by modulating substrate stiffness. Optical transparency of the heart was performed with solvent-based tissue clearing[7] and imaging performed with a Nikon C2+ confocal microscope. Immunofluorescent staining was performed using standard methods.[5] Conditioned medium was collected from 2D or 3D cardiac fibroblasts exactly 24 hours after initial seeding. Live cell interferometry was performed to track changes in cell biomass of single neonatal rat ventricular cardiomyocytes (NRVM) with 2D or 3D conditioned medium.

Results

To determine whether aggregation of cardiac fibroblasts affects the cellular phenotype, we first created a scaffold-free 3D system using ultra-low attachment tissue culture dishes where a covalently bonded hydrogel layer on the surface of the dish prevents cell attachment.[8] Cardiac fibroblasts were isolated from adult mice, and cells that had not undergone >3 passages were used for experiments. Seeding of primary adult mouse cardiac fibroblasts onto ultra-low attachment dishes resulted in fibroblasts aggregating together within 24 hours to form 3D spherical clusters (Figure 1A and 1B). To confirm that cardiac fibroblasts alone were capable of forming these spherical clusters, we next isolated cardiac fibroblasts from uninjured hearts of TCF21MerCreMer:R26R^{tdTomato} and Col1a2CreERT:R26R^{tdTomato} mice.[5,9,10] We and others have shown that the inducible Cre drivers are specific for genetic

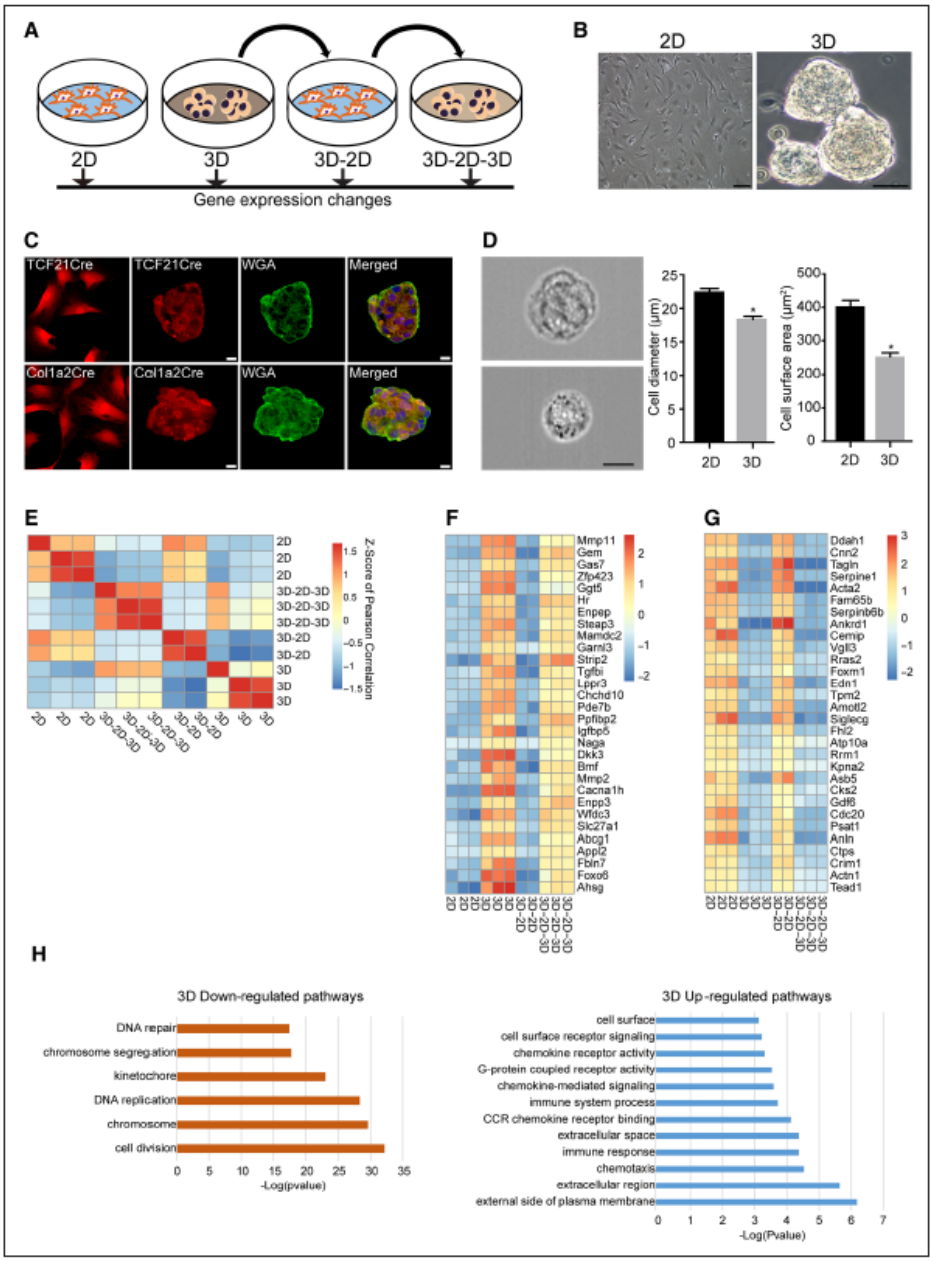

Figure 1. Cardiac fibroblasts exhibit dynamic changes in gene expression in different topological states. A, Schematic of how fibroblasts were transitioned from a 2-dimensional (2D) to 3D state and then back to 2D and 3D, respectively. For each topological state, fibroblasts were harvested for RNA-seq. **B**, Bright phase image of cardiac fibroblasts in 2D and 3D (scale bar: 50 μm). **C**, Pure population of genetically labeled (tdTomato) fibroblasts isolated by flow cytometry from hearts of TCF21MerCreMer:R26R^{tdtomato} or Col1a2CreERT:R26R^{tdtomato} mice were subjected to sphere formation (3D) and spheres stained with wheat germ agglutinin (WGA), that stains cell membranes (scale bar: 20 μm). **D**, Cardiac fibroblasts in 2D or 3D states dissociated and subjected to image flow cytometry showing representative image of fibroblast from 2D or 3D state (3000 cells imaged in each group, scale bar: 10 μm) and corresponding mean diameter and surface area of fibroblasts in 2D or 3D states (*P<0.001, mean±SEM, n=3). **E**, Heat map demonstrating clustering of sample correlations of fibroblasts (shown by Z scores) in different topological states. **F** and **G**, Heat map comparing (**F**) expression of the most upregulated 3D genes in different topological states and (**G**) 3D downregulated genes in different topological states (**H**) gene ontology analysis showing cellular pathways most affected by genes upregulated or downregulated in 2D/3D states.

labeling of cardiac fibroblasts after tamoxifen administration. Similar to cardiac fibroblasts from wild-type animals, genetically labeled cardiac fibroblasts within 24 hours of seeding onto ultra-low attachment plates also formed spherical clusters confirming the ability of cardiac fibroblasts to form 3D spherical aggregates under defined conditions (Figure 1C). Imaging Flow cytometry[11] demonstrated that aggregation into a 3D state resulted in significantly smaller small cell size (cell diameter: 22.45±0.30 um in 2D versus 18.41±0.26; mean±SEM; $P<0.001$) and surface area (449.85±3.05 µm2 in 3D versus 297.97±8 µm^2; mean±SEM; $P<0.001$; Figure 1D) suggestive of cellular remodeling as fibroblasts adopt the 3D state. To determine whether a switch from a 2D to a 3D state changes fibroblast phenotype, we first compared global gene expression changes by RNA-seq between cardiac fibroblasts cultured under standard 2D conditions on regular tissue culture dishes and 3D conditions as mentioned above (Figure 1A). For this purpose, cardiac fibroblasts were seeded onto standard tissue culture plates or ultra-low attachment plates with similar seeding density and identical cell culture medium and cells were harvested 24 hours later for gene expression analysis. To ask whether observed changes were reversible, we transferred 3D cardiac fibroblasts to regular tissue culture plates to put them back in 2D conditions (group termed 3D-2D; Figure 1A). Spherical clusters of 3D fibroblasts attached to regular tissue culture plates and the fibroblasts migrated from spherical cluster to a monolayer within 4 to 5 days. We again determined gene expression of 3D-2D fibroblasts (after transition from 3D to a monolayer) to determine whether the gene expression pattern reverted to that of the 2D state (Figure 1A). Finally, cardiac fibroblasts which had been grown under 3D conditions and then transferred to 2D conditions (3D-2D) were put back under 3D conditions (group termed 3D-2D-3D). Sphere formation occurred within 24 hours of reseeding on ultra-low attachment plates, and RNA-seq was performed to determine whether readoption of the 3D state was associated with gene expression signatures flipping back to the 3D state (Figure 1A). These experiments would thus determine whether changes in topological states or spatial arrangement of cardiac fibroblasts are associated with reversible and dynamic changes in gene expression. RNA-seq was performed for all the different topological states of the cardiac fibroblast and clustering of sample correlations demonstrated a grouping of all 2D fibroblast states and a separate grouping of 3D fibroblast states (Figure 1E). The gene expression profile of 2D cardiac fibroblasts was like that of the 3D-2D fibroblast group, whereas the gene expression profile of 3D fibroblasts was like that of the 3D-2D-3D group (Figure 1E). We observed a remarkable dynamic and reversible plasticity between the 2D and 3D states (Online Table I; Figure 1F and 1G). Out of 997 genes that were upregulated in 3D fibroblasts, expression of 996 genes reverted back when the 3D fibroblasts were transitioned back to the 2D state (3D-2D group) and reinduced after transition to 3D (3D-2D-3D group; Figure 1F). Similarly, genes downregulated in 3D state exhibited increased expression after transition to the 2D state (3D-2D group) and silencing on transitioning back to 3D (3D-2D-3D group; Figure 1G). To adjust for potential temporal changes in gene expression, the gene expression pattern of the 3D-2D group was also compared with that of 2D and 3D fibroblasts cultured for 5 days. A cluster analysis demonstrated distinct clustering of 2D and 3D states (Online Figure IA). In addition, for the 3D-2D-3D group, temporally adjusted controls of 3D-2D cells lifted and reseeded back onto 2D instead of 3D conditions was also used (Online Figure IB). Again, cluster analysis demonstrated distinct 2D and 3D states making it unlikely that differential gene expression was simply secondary to temporal dependent changes in gene expression of cardiac fibroblasts in culture.

We next examined whether dynamic changes in gene expression in different topological states can be simply explained by sudden changes in substrate stiffness as the fibroblasts transition from a 2D adherent state to a 3D spherical nonadherent state. To answer this question, we seeded cardiac fibroblasts onto tissue culture plates coated with biocompatible silicone controlled elastic moduli recapitulating environments similar to tissue.[12] We seeded cardiac fibroblasts on tissue culture plates with stiffness of 0.8 kPa, 8 kPa, and 64 kPa (Online Figure IIA) and following 24 hours of seeding, harvested the cells to compare changes in gene expression to that of 2D and 3D topological states. Analysis of global gene expression demonstrated a clustering of 2D states with that of cells seeded at different substrate stiffness (0.5, 8, and 64 kPa) and were distinct from gene expression signature of cardiac fibroblasts in 3D states (Online Figure IIB). We specifically examined the set of genes that displayed the highest degree of differential expression between 2D and 3D states and observed that the expression pattern of such genes was similar between cells seeded at 0.8, 8, and 64 kPa and 2D states and distinct from that seen in 3D states (Online Figure IIC and IID). Taken together, these observations suggest that topological changes in cardiac fibroblasts drive gene expression patterns and changes in substrate stiffness are unlikely to underlie differences in gene expression between 2D and 3D states. We next examined the pool of genes that were the most upregulated (Figure 1F) or downregulated (Figure 1G) in 3D versus 2D fibroblast states. Gene ontology analysis demonstrated that genes downregulated in the 3D state mainly comprised cell cycle processes such as DNA replication, chromosomal condensation/segregation, and cytokinesis (Figure 1H). Transcripts differentially upregulated in the 3D state involved pathways regulating extracellular matrix metabolism/proteolysis, surface proteins, chemotaxis, and immune response. (Figure 1H; Online Table II). We next specifically examined several genes which were highly differentially expressed between 3D versus 2D fibroblasts and that are also known to regulate extracellular matrix such as metalloproteinases/metallopeptidases, (*MMP11*, *MMP2* [matrix metalloproteinases 11 and 2], *ADAMTS15* [metallopeptidase with thrombospondin motif 15]), *CTGF* (connective tissue growth factor) and fibroblast contractility, *Acta2* (alpha-smooth muscle actin 2), *Cnn2* (calponin 2) and modulators of inflammatory response (*GPNMB* [glycoprotein nonmetastatic B]). Based on RNA-seq patterns, expression of these genes was reversible and highly dependent on the topological state of the fibroblast (Figure 2). For instance, *MMP11* and *MMP2* were highly induced after aggregation and sphere formation of fibroblasts, but expressions declined to 2D levels when the 3D fibroblasts

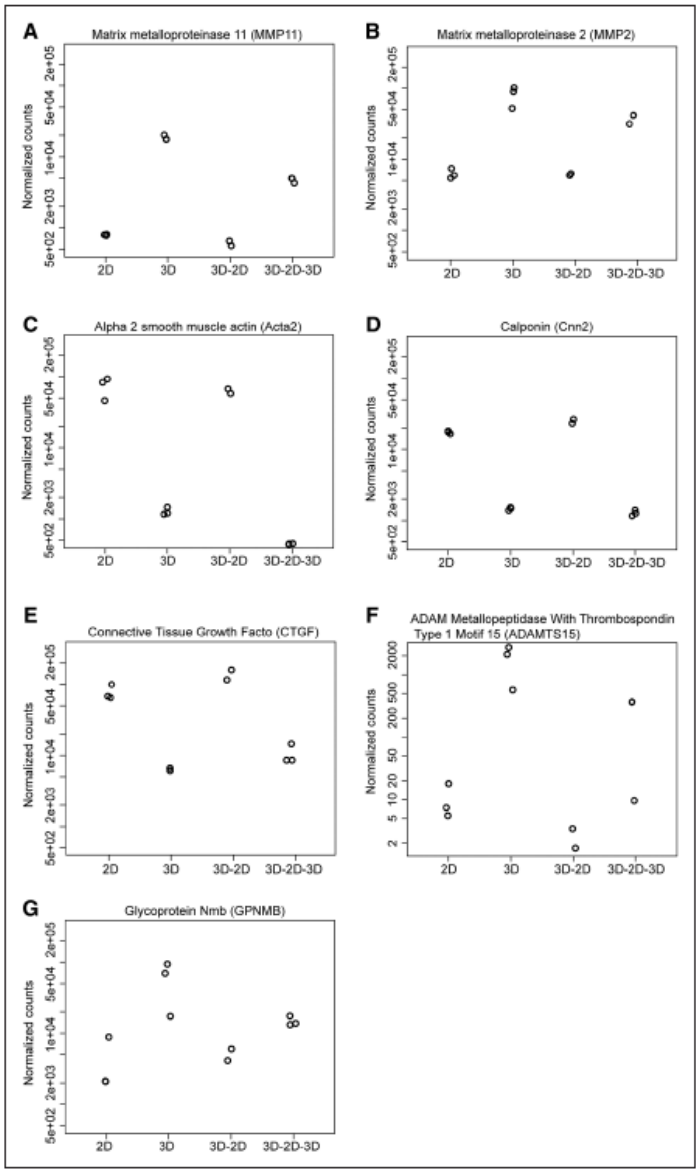

Figure 2. Dynamic changes in expression of myofibroblast and extracellular matrix genes between 2-dimensional (2D) and 3D cardiac fibroblast states. A and **B**, Normalized gene counts on RNA-seq demonstrating rapid changes in gene expression of (**A**) *MMP11* (matrix metalloproteinase 11), (**B**) *MMP2* (matrix metalloproteinase 2), (**C**) *Acta2* (alpha-smooth muscle actin 2), (**D**) *Cnn2* (calponin 2), (**E**) *CTGF* (connective tissue growth factor), (**F**) *ADAMTS15* (metallopeptidase with thrombospondin motif 15), and (**G**) *GPNMB* (glycoprotein nonmetastatic B) in cardiac fibroblasts in different topological states.

were allowed to attach and grow out as a monolayer for a few days (Figure 2A and 2B). However, reseeding the cells back to a 3D conformation led to rapid reinduction of *MMP2/MMP11* expression illustrating the dynamic plasticity of the system (Figure 2A and 2B). Gene expression of *Acta2*, *Cnn2*, *ADAMTS15*, *GPNMB*, and *CTGF*, which are thought to play a role in fibroblast contractility and regulation of inflammation and extracellular matrix, demonstrated similar patterns of changes of gene expression dependent on the topological state (Figure 2C through 2G).

To determine whether such gene expression changes are associated with changes in phenotype, we first determined changes in cardiac fibroblast proliferation in the 3D versus 2D state. For this purpose, cardiac fibroblasts either in the 2D or 3D state were treated with EdU for 4 hours followed by determination of EdU uptake by flow cytometry. Consistent with decreased expression of cell cycle genes in the 3D state, we observed that 5.47±1.4% of cardiac fibroblasts in the 2D state were cycling (EdU uptake) versus 0.15±0.05% in the 3D state (P<0.05; Figure 3A). Similarly, the fraction of

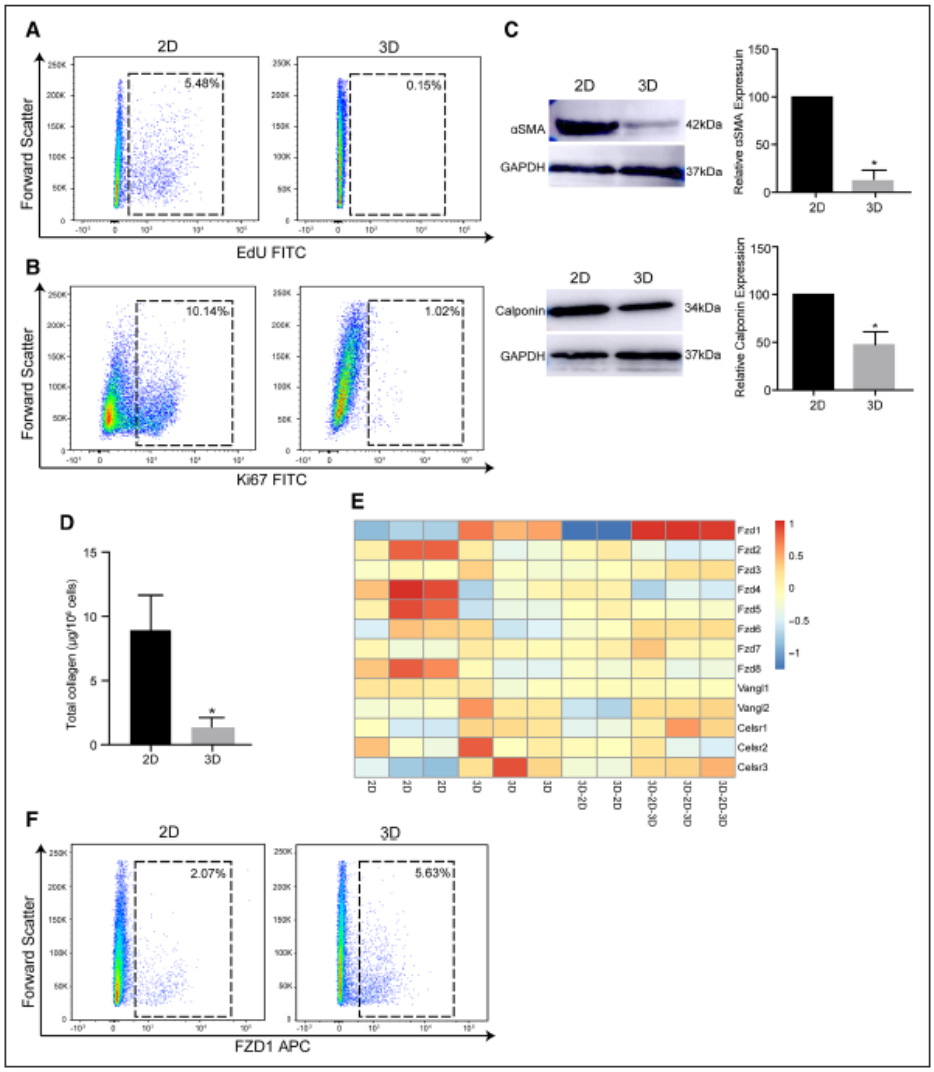

Figure 3. Changes in fibroblast phenotype in 3-dimensional (3D) vs 2D topological state. A and **B**, Flow cytometry to determine fraction of proliferating fibroblasts in 2D and 3D states by (**A**) EdU uptake (5.48±1.4% in 2D vs 0.15±0.05% in 3D, mean±SEM, $P<0.05$, n=3) or (**B**) Ki67 expression (10.14±3.0% in 2D vs 1.02±0.01% in 3D, mean±SEM, $P<0.05$, n=3). **C**, Western blotting and quantitative densitometry of expression of alpha-smooth muscle actin and calponin expression by cardiac fibroblasts in 2D or 3D states (mean±SEM, *$P<0.001$, n=3). **D**, Estimation of total collagen content of cardiac fibroblasts in 2D or 3D state (8.40±2.8 μg/106 cells in 3D vs 1.32±0.71/106 cells in 2D, mean±SEM, *$P<0.05$, n=3). **E**, Heat map demonstrating expression of members of the frizzled, Vangl, and Celsr family in different topological states of cardiac fibroblasts. **F**, Flow cytometry demonstrating Fzd1 (frizzled 1) expression in 3D vs 2D cardiac fibroblasts (2.07±0.33% in 2D vs 5.63±0.24% in 3D, mean±SEM, $P<0.05$, n=3).

cells expressing Ki67 (marker of proliferation) significantly decreased from 10.94±3.0% of cardiac fibroblasts in the 2D state to 1.0±0.08% in the 3D state ($P<0.05$; Figure 3B). Western blotting with quantitative densitometry demonstrated that fibroblasts in the 3D state exhibit decreased expression of contractile proteins alpha-smooth muscle actin (88±6% decrease in 3D versus 2D; $P<0.001$) and calponin (54±6% decrease in 3D versus 2D; $P<0.001$; Figure 3C), consistent with gene expression data demonstrating decreased expression of myofibroblast proteins. Differentially expressed genes between the 2D and 3D states included genes affecting extracellular matrix catabolism. Collagen is the most common abundant extracellular matrix protein secreted by cardiac fibroblasts, and we next determined how adoption of the 3D state affects collagen production. We measured total collagen using the Sircoll assay in 2D and 3D fibroblasts and observed

that the total cellular collagen content significantly decreased from 8.40±2.8 μg/10^6 cells in 3D states to 1.32±0.71/10^6 cells in 2D states (P<0.05; Figure 3D). Cardiac fibroblasts secrete extracellular matrix proteins but are also known to express matrix-degrading enzymes and can undergo dedifferentiation as well.[13] These data suggest that a transition from a 2D to a 3D state leads to a switch of cardiac fibroblast phenotype from a matrix synthetic to a nonsynthetic dedifferentiated state. Recent evidence suggests that aggregation of cardiac fibroblasts in the area of myocardial injury is associated with fibroblasts exhibiting evidence of polarization.[14] Polarization or alignment of cardiac fibroblasts is thought to play a critical role in appropriate cardiac wound healing.[15] We thus examined whether 3D cardiac fibroblasts exhibited any evidence of polarization compared with 2D fibroblasts. To address this question, we examined expression of genes that are members of the *Frizzled* (*Fzd*), *Van Gogh* (*Vangl* in vertebrates), and *Flamingo* (*Celsr* in vertebrates; Figure 3E). These families of genes initially identified in Drosophila are now known to play a critical role in planar cell polarity and cellular orientation in epithelial and mesenchymal cells of vertebrates as well.[16] Within this subset of genes known to regulate cellular polarity, we observed that Fzd1 (frizzled 1) expression was significantly higher in 3D compared with 2D states (Figure 3E). Fzd1 is a cell surface receptor and we performed flow cytometry to demonstrate that Fzd1 expression was significantly upregulated in 3D fibroblasts (Figure 3F) consistent with gene expression changes. Members of the frizzled family are known to be expressed in fibroblasts in the area of injury after myocardial injury and thought to contribute to cardiac remodeling and have been considered as therapeutic targets for augmenting cardiac repair.[14,17,18] In this regard, cardiac fibroblasts in 3D states recapitulate to a certain extent the expression of polarity genes known to be important for wound healing in vivo. Taken together, these observations demonstrate that aggregation and changes in spatial arrangement of cardiac fibroblasts can drive rapid, dynamic, and reversible expression of genes affecting a panoply of processes regulating wound healing such as fibroblast proliferation, activation, collagen content, and cell polarity.

We next investigated the mechanistic basis of such rapid and reversible changes in gene expression. We hypothesized that dynamic changes in chromatin structure may contribute at least in part to the rapid changes in gene expression seen after the transition of fibroblasts from a 2D to 3D state. Therefore, changes in chromatin organization and DNA accessibility (open and closed chromatin) were examined between cardiac fibroblasts in 2D versus 3D states by performing an ATAC-seq.[19] ATAC-seq enables identification of open and closed regions of chromatin across the genome and provides insights about regions of the genome that are more (open) or less accessible (closed) to transcription factors.[19] We observed that there were significant changes in global chromatin organization (Figure 4A). Approximately 23% of the genes differentially upregulated in fibroblast 3D states and 18% of the genes downregulated in fibroblast 3D state (ie, upregulated in 2D states) underwent significant changes in chromatin accessibility (Figure 4A) with remarkable concordance with their RNA-seq profiles. Both these values were significantly enriched over background levels as we observed that only 10% of all genes had differential ATAC-seq peaks on transition from a 2D to 3D state (Figure 4A). We next examined differential ATAC-seq peaks for specific genes such as *MMP2* and *CTGF* that demonstrated significant induction and silencing of gene expression respectively in the 3D state and observed significant differences in ATAC-seq peaks in their respective genomic loci, correlating with changes in gene expression (Figure 4B and 4C). These observations suggest that fibroblast aggregation and changes in spatial arrangement of cardiac fibroblasts are sufficient to induce changes in chromatin structure or organization that contributes to the global changes in genes expression between the 2D and 3D state.

Having demonstrated that changes in fibroblast aggregation and spatial arrangement are associated with concordant changes in the epigenome and gene expression, we next investigated the functional connotations of such global changes in gene expression for cardiac wound healing. Like humans, genetically diverse strains of mice differ in the degree of fibrosis or cardiac remodeling after pathological cardiac stressors and offer the advantage of tissue availability and experimental manipulation. The HMDP is a collection of genetically diverse mouse strains and allows sufficient power for genome-wide association analysis to determine how genetic architecture impacts phenotypic traits.[20–23] A single pathological stressor can be thus applied across all strains within the HMDP to perform genome-wide association studies and determine how genetic and environmental interactions contribute to global gene expression and clinical phenotypes.[24] In these studies, 96 strains of mice were administered a 3-week continuous infusion of isoproterenol via an osmotic pump.[6] Throughout the study, various physiological characteristics including cardiac functional indices (eg, ejection fraction, left ventricular internal dimensions in end systole and diastole), metabolic parameters and tissue weights (61 traits in all) were measured (Online Table III) and the left ventricle of each mouse strain was subjected to global expression arrays.[6,24] In this study, the mice responded dramatically to isoproterenol, as nearly every individual showed increased left ventricular mass after treatment. This data set enabled us to assess whether differentially expressed genes between 3D and 2D states of cardiac fibroblasts could inform phenotypic traits known to predict outcomes or disease severity in isoproterenol-induced cardiac hypertrophy and failure.

Initially, we asked whether significantly upregulated transcripts in all 3D fibroblast states (compared with 2D) were correlated with heart failure traits in the HMDP. By simply correlating individual 3D upregulated genes from our RNA-sequencing experiment across clinical traits in the mouse population (Online Figure III), we observed striking patterns of significance (Figure 5A). Because these patterns are difficult to interpret on a gene-by-gene basis, we used a data reduction method to establish vectors which represent 3D-specific gene signatures. Principle component (PC) approaches provide a means of data reduction whereby variation across any number of dimensions can be aggregated into single or multiple vectors. Similar approaches utilizing a PC to represent large gene sets are commonly utilized in population-based studies.[6,25] These produce a series of vectors which represent a given pattern of

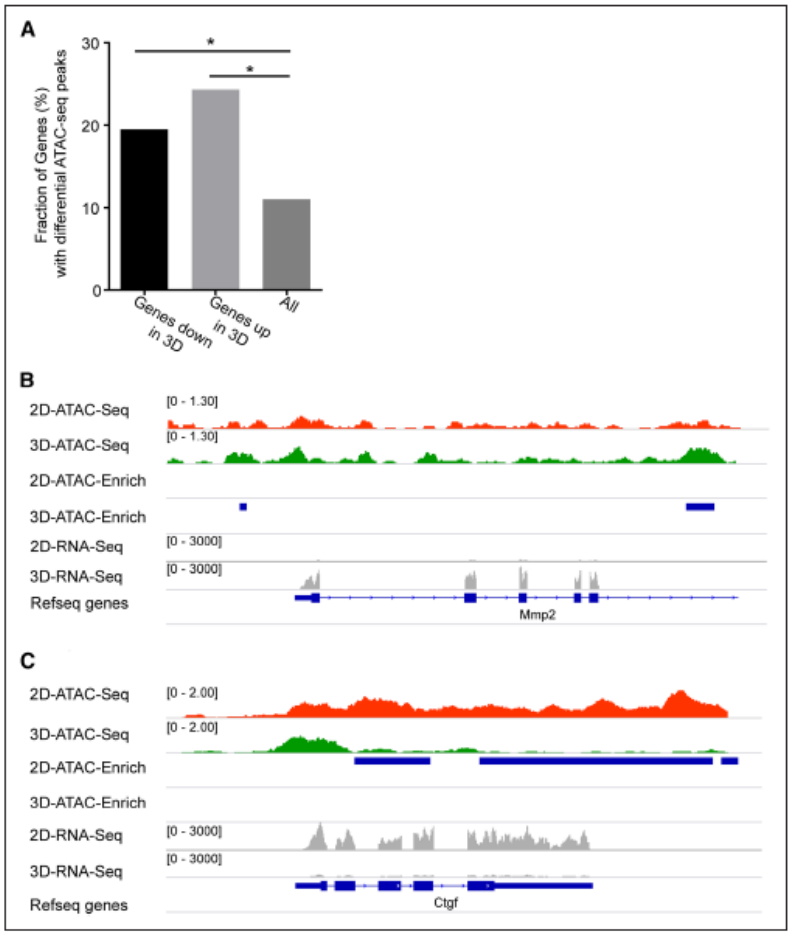

Figure 4. Chromatin changes underlie altered gene expression of fibroblasts in 3-dimensional (3D) vs 2D states. A, ATAC-seq (assay for transposase accessible chromatin) performed to demonstrate a fraction of genes demonstrating differential ATAC-seq peaks in either 2D or 3D cardiac fibroblast states. **B** and **C**, ATAC-seq peaks and RNA-seq showing expression of (**B**) *MMP2* (matrix metalloproteinase 2), and (**C**) *CTGF* (connective tissue growth factor) in 2D and 3D states demonstrating differential ATAC-seq peaks in loci of *MMP2* and *CTGF* genes (numbers listed refer to scales of enrichment).

variation, referred to as eigenvectors. Here, we applied this approach to gene expression, where the genes identified from the 2D versus 3D analysis were analyzed across a mouse population. We generated PC eigengenes which captured 14.4% (PC1) and 6.8% (PC2) of the variation of all 3D-upregulated transcripts within the HMDP expression arrays (Figure 5B). It is worth mentioning that these values are fairly typical when performing PC analysis on population-wide data (here, we use ≈600 genes within ≈100 strains of mice), especially given the significant variation observed in gene expression profiles. Using these eigengenes (PC1 and PC2) as signatures of 3D fibroblast genes, we plotted the position of each strain against various cardiac and noncardiac clinical traits. Cardiac fibroblasts are known to affect cardiac hypertrophy and play a major role in adverse cardiac remodeling and dilatation of the cardiac chambers, clinically determined by the left ventricular dimensions in end systole and diastole. Consistent with this notion, we observed highly significant positive correlations between 3D fibroblast-derived gene signatures and left ventricular dimensions in both end diastole (Figure 5C and 5D) and end systole (Figure 5E and 5F) as well as cardiac mass (Figure 5G and 5H). Notably, these 3D fibroblast eigengene signatures did not correlate with either heart rate (Figure 5I and 5J) or noncardiac traits such as plasma glucose (Figure 5K and 5L) demonstrating specificity of these eigengene signatures to cardiac remodeling traits. Collectively, these data show that 3D fibroblast-enriched transcripts show striking patterns of correlation with adverse cardiac indices such as cardiac hypertrophy and chamber dilatation across the murine population after isoproterenol infusion.

To date, our data demonstrate that cardiac fibroblasts exhibit a high degree of dynamic plasticity with induction and silencing of genes after transition from a 2D to 3D state. Genes induced in the 3D state significantly correlated with clinical indices of adverse ventricular remodeling. Therefore, we next determined whether genes differentially expressed in the 3D state were also upregulated in regions of fibroblast aggregation in vivo at the time of wound healing. For this purpose, we performed cryoinjury on hearts of Col1a2CreERT:R26R^{Idtomato} and TCF21MerCreMer:R26R^{Idtomato} mice after tamoxifen-mediated

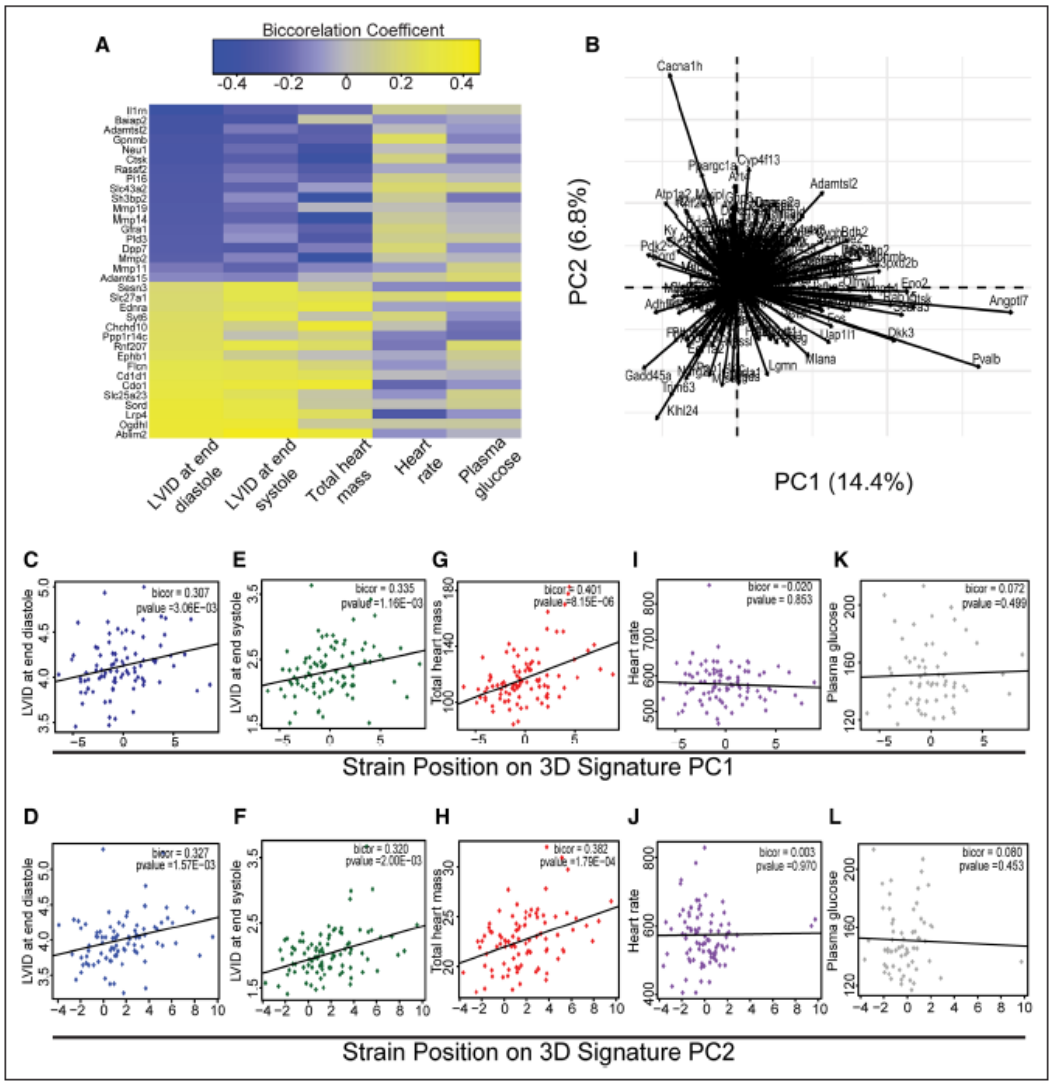

Figure 5. Genes enriched in 3-dimensional (3D) fibroblast states show significant correlation with indices of adverse ventricular modeling in HMDP (Hybrid Mouse Diversity Panel) studies after isoproterenol infusion. A, Correlation heat map (yellow: positive and blue: negative correlation) of top 15 differentially upregulated genes in 3D/2D states vs clinical traits of left ventricular dimensions, heart mass, plasma glucose and heart rate after infusion of isoproterenol. **B**, Individual gene contribution to eigengene signatures principle component (PC1 and PC2) using transcripts enriched in 3D states. **C–H**, Correlation of both eigengene signatures against cardiac and noncardiac traits with significant correlation between both eigengenes and (**C** and **D**) left ventricular internal diameter (LVID) at end diastole (**E** and **F**) LVID at end systole and (**G** and **H**) total heart mass with no significant correlation between either eigengene and (**I** and **J**) heart rate and (**K** and **L**) plasma glucose. bicor indicates bicorrelation coefficient.

labeling of cardiac fibroblasts. Tamoxifen was administered for 10 days to label the cardiac fibroblasts and stopped 5 days before cryoinjury. We chose cryoinjury as cryoinjury unlike ischemic myocardial injury creates a highly well-defined compact transmural scar on the left ventricle and the tdTomato labeling of cardiac fibroblasts can easily identify regions of compact scarring. Hearts were harvested at 7 days after cryoinjury and immunofluorescent staining performed to determine whether genes highly upregulated in 3D fibroblasts in vitro were expressed by labeled cardiac fibroblasts or expressed in abundance in the region of fibroblast aggregation. We observed abundant expression of MMP11 by tdTomato-labeled cardiac fibroblasts but minimal MMP11 expression in uninjured regions (Figure 6A through 6D). ADAMTS15, a

secreted protein that regulates extracellular matrix, is expressed in the developing heart and highly induced in the 3D fibroblast state (Online Table I), was also found to be abundantly present in the injured region and expressed by tdTomato-labeled fibroblasts (Figure 6E through 6H). To study the expression of 3D enriched transcripts in aggregating fibroblasts in regions

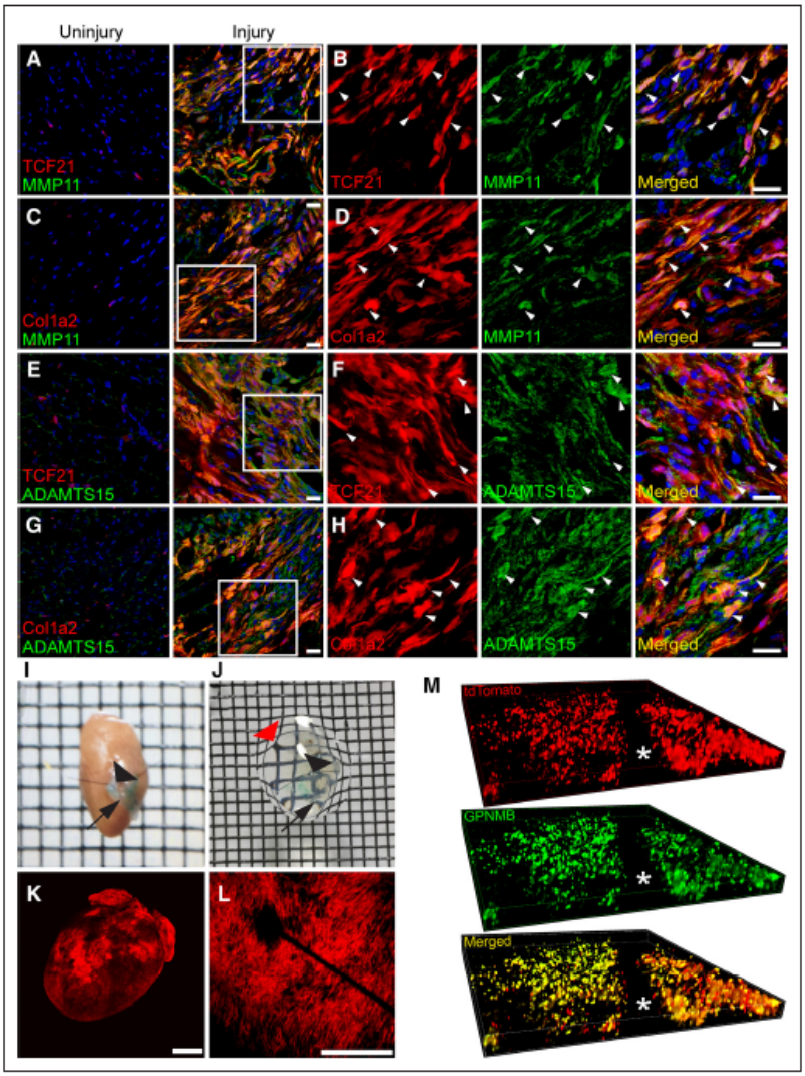

Figure 6. Genes enriched in 3-dimensional (3D) fibroblasts are expressed in vivo in regions of fibroblast aggregation after heart injury and affect cardiomyocyte hypertrophy. A–D, Immunofluorescent staining for MMP11 (matrix metalloproteinase 11) on uninjured and cryoinjured hearts of (**A** and **B**) TCF21MerCreMer:R26R^{tdtomato} and (**C** and **D**) Col1a2CreERT:R26R^{tdtomato} mice (**B** and **D**) area of injury shown in higher magnification demonstrating tdTomato-labeled fibroblasts expressing MMP11 (arrows). **E–H**, Immunofluorescent staining for ADAMTS15 (metallopeptidase with thrombospondin motif 15) on uninjured and cryoinjured hearts of (**E** and **F**) TCF21MerCreMer:R26R^{tdtomato} and (**G** and **H**) area of injury shown in higher magnification demonstrating tdTomato-labeled fibroblasts expressing ADAMTS15 (arrows; scale bars: 20 μm). **I** and **J**, Cryoinjured heart of Col1a2CreERT:R26R^{tdtomato} mouse (**I**) before and (**J**) after optical clearing (arrowhead points to suture for identifying injured region, arrow points to green dye to identify area adjacent to injury; note the wire mesh on which the heart lies is now visible through the transparent heart; red arrow). **K**, tdTomato fluorescence observed on cryoinjured Col1a2CreERT:R26R^{tdtomato} heart and (**L**) confocal image through an area of injury showing intense tdTomato fluorescence (scale bar: 500 μm). **M**, Immunofluorescent staining for GPNMB (glycoprotein nonmetastatic B) on optically cleared Col1a2CreERT:R26R^{tdtomato} heart after injury. The entire depth of the scar was imaged with a confocal microscope and sequential Z stack images are demonstrating the distribution of tdTomato (red), GPNMB (green) and merged (yellow) image demonstrating distribution of fluorophores across the depth of the scar (asterisk corresponds to position of suture). (*Continued*)

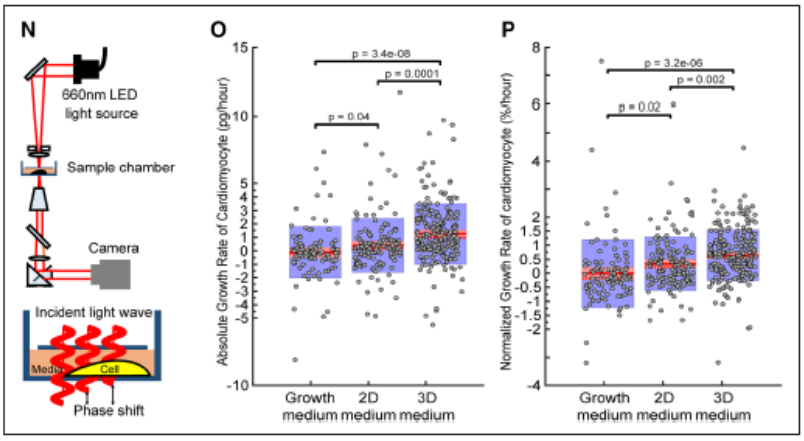

Figure 6 Continued. **N**, Set up of live cell interferometry with phase shift of light being a read out for changes in cell biomass (**O**) absolute and (**P**) normalized single cell cardiomyocyte (neonatal rat ventricular cardiomyocytes [NRVM]) biomass accumulation rates determined by serial measurements with interference microscopy >48 h after treatment of NRVM with growth medium (nonconditioned) or conditioned medium from fibroblasts in 2D or 3D state (each circle represents a single cardiomyocyte; number of single cardiomyocytes tracked: 103 for growth medium, 142 for 2D medium, and 231 for 3D medium).

of injury in greater detail, we subjected the harvested heart to solvent-based tissue clearing techniques to make the heart optically transparent.[7] This allows the entire 3D structure of the scar to be visualized in detail without having to extrapolate and reconstruct a 3D structure from conventional analysis of histological sections. We again performed cryoinjury on Col1a2CreERT:R26R^{tdtomato} mice after fibroblast labeling. We harvested the heart 7 days after cryoinjury and made them optically transparent and a nonabsorbable suture (placed at the time of injury) was used to identify an area of cryoinjury in the heart after tissue clearing (Figure 6I through 6K). The region of injury could be identified easily as an area with accumulation of tdTomato-labeled cardiac fibroblasts (Figure 6L). On the optically cleared heart, we performed immunostaining for another marker GPNMB, a gene upregulated in the 3D state, involved with immune response pathways and that strongly correlated with adverse cardiac remodeling indices in our murine model of isoproterenol-induced heart failure. Analysis of Z stacked confocal images taken sequentially through the whole depth of the scar demonstrated expression of GPNMB by tdTomato-labeled fibroblasts throughout the depth of the scar (Figure 6M). These observations demonstrate that genes expressed by aggregating fibroblasts in the region of injury at least partially recapitulate the gene expression signatures of 3D fibroblasts.

Fibroblasts are known to affect cardiac hypertrophy[26] and the gene expression signatures of 3D fibroblasts strongly correlated with clinical indices of heart mass and remodeling across mouse strains. We next investigated whether fibroblasts in 3D exert prohypertrophic effects on cardiomyocytes compared with fibroblasts cultured in 2D. For this purpose, we collected conditioned medium from fibroblasts grown in 3D or 2D conditions for 24 hours. We treated neonatal rat cardiomyocytes with 3D or 2D conditioned medium to determine effects on cardiomyocyte hypertrophy over the next 48 hours. Live cell interferometry, a validated version of quantitative phase microscopy[27,28] is an extremely sensitive tool for determining changes in total cellular biomass. Live cell interferometry is based on the principle that light slows as it interacts with matter. As light traverses through a cell that has greater biomass (ie, hypertrophied), the light slows and its waveform shifts in phase compared with light not passing through the cell[29] (Figure 6N). The change in phase shift over time is directly related to the change in biomass of the cell over time, and this quantitative phase shift has been used to precisely and reproducibly determine the dry biomass of cells including T cells, stem cells, cancer cells, and fibroblasts.[27,28] NRVM were treated with conditioned medium as above, and each cardiomyocyte was subjected to repeated measurements by live cell interferometry to obtain a growth rate. We observed that 2D conditioned medium significantly increased the rate of cardiomyocyte biomass accumulation compared with nonconditioned medium (0.4 picogram/h for 2D compared with −0.12 picogram/h for growth medium; P=0.04; Figure 6O). However, treatment with 3D conditioned medium tripled the rate of growth versus treatment with 2D conditioned medium (1.25 pg/h for 3D versus 0.4 pg/h for 2D; P=0.0001; Figure 6O). As cardiomyocytes after isolation can exhibit a significant difference in cell size, we normalized the growth rate of each cardiomyocyte to initial cell biomass. Again, we observed a significant 34% increase in cell biomass of NRVM after treatment with 2D conditioned medium compared with nonconditioned growth medium (0.34% for 2D versus −0.01% for growth medium; P=0.02; Figure 6P). However, 3D fibroblast conditioned medium significantly increased the cell biomass accumulation rate of NRVM by a further 88% compared with NRVM treated with 2D conditioned medium (0.64% for 3D versus 0.34% for 2D; P=0.002; Figure 6P). These observations demonstrate that the secretome of fibroblasts in 3D is sufficient to induce cardiomyocyte hypertrophy and are broadly consistent with the genome-wide association data shown earlier demonstrating a high correlation between

genes induced in the 3D state and indices of cardiac hypertrophy and remodeling after isoproterenol infusion. Our observations also suggest that the gene expression signatures adopted by aggregating fibroblasts may have a direct causal effect on a hypertrophic response after cardiac injury.

We next analyzed our RNA-seq data to obtain insight into transcription factors or transcriptional regulators that could be contributing to changes in gene expression between the 2D and 3D states and affecting myocyte hypertrophy. Genes differentially upregulated in the 3D versus 2D state were assayed for enrichment of upstream transcriptional factors or regulators using TRRUSTv2.[30] This analysis queries hundreds of published Chip-Seq and open chromatin data to infer regulatory elements from gene expression patterns. The 3D upregulated genes were used to identify enrichment of regulation by specific transcription factors or DNA binding elements known to regulate expression. We observed a significant representation of several transcription factors predicted to regulate 3D-specific genes (Online Figure IV) and some of these are also known to regulate or be associated with the cardiac hypertrophic response such as *MITF* (microphthalmia-associated transcription factor), *CTNNB1* (beta-catenin), and *SRF* (serum response factor).[31–33] Next, to obtain insight into secreted factors present in 3D conditioned medium that induced or contributed to myocyte hypertrophy, we filtered the differentially upregulated genes in the 3D state for secreted factors and observed expression of proteins known to affect the myocyte hypertrophic response such as angiotensinogen, pyrophosphatases affecting purinergic signaling (*ENPP3* [ectonucleotide pyrophosphatase/phosphodiesterase 3]) and members of the Wnt signaling family (*Dkk3* [dickkopf-related protein 3]; Online Table IV).[34–36]

Discussion

Cardiac fibroblasts are known to be highly plastic, and our study suggests that simple aggregation of fibroblasts may be sufficient to induce genome-wide changes in chromatin reorganization and gene expression. We show that gene expression signatures adopted by aggregating cardiac fibroblasts at least in part recapitulate changes in gene expression in the injured region in vivo and that such altered genetic outputs may have functional consequences for cardiac wound healing and remodeling. Cardiac fibroblasts are the principal contributors toward deposition of extracellular matrix but are also known to secrete metalloproteinases, and extracellular proteases that lead to degradation of extracellular matrix.[37] Acute myocardial injury is associated with significant upregulation in metalloproteinase activity[38] and MMP expression significantly increased in 3D cardiac fibroblasts mirroring such in vivo changes. A balance between the synthetic and proteolytic phenotype of the fibroblasts determines extracellular matrix content or burden of scar tissue in pathological states. Augmented matrix synthetic and matrix-degrading properties of cardiac fibroblasts can lead to high turnover of extracellular matrix, as seen in heart failure. Such fibroblast phenotypes with opposing effects on matrix synthesis and degradation, as seen in our 2D and 3D model could determine the burden of scar after acute and chronic injury and serve as a model for obtaining further mechanistic insight.[39] Although little is known about signaling mechanisms that regulate resolution of fibrosis, dedifferentiation of contractile elements of fibroblasts with decreased expression of alpha-smooth muscle actin is thought to represent a key event for fibrosis resolution.[40] In this regard, our model of fibroblast aggregation with decreased expression of smooth muscle actin and induction of various matrix-degrading enzymes demonstrates phenotypic features consistent with myofibroblast dedifferentiation and a proteolytic rather than a synthetic phenotype. The expression of alpha-smooth muscle actin and other contractile proteins in fibroblasts in the injury region allows for wound contraction in vivo, a mechanism that enables a reduction in the area of injury. Conversely, impaired expression of fibroblast contractile proteins or defects in fibroblast polarization in vivo can cause impaired wound contraction, dysregulated wound healing and lead to an expansion of the infarcted region, a dreaded complication after myocardial infarction. Our model that demonstrates a rapid and reversible expression of contractile proteins in fibroblasts could serve as a platform for investigating the molecular events that abruptly can switch a cardiac fibroblast from a synthetic and contractile phenotype to a proteolytic and dedifferentiated phenotype. Hypertrophy of surviving cardiac myocytes at the edges of the injured region occurs after myocardial infarction, and the 3D fibroblasts can serve as a platform for interrogating the paracrine effects of cardiac fibroblasts on myocyte hypertrophy. Given the global changes in gene expression and substantial changes in the 3D cardiac fibroblast secretome, it is likely that rather than a single driver, the activity of multiple transcription factors and secreted proteins synergistically affect gene expression changes and the myocyte hypertrophic response.

Study of cells in spheroids have been performed for cancer cells and cells with progenitor potential. Our study suggests that studying fibroblasts in a 3D state in contrast to the conventional analysis of 2D fibroblasts may be more informative of cellular changes in the injury region in vivo. Potentially, our model could also be used as a tool or a primary screening system to determine how drugs or small molecules affect changes in expression of specific genes that are upregulated in the 3D state or affect phenotypic transitions between matrix synthetic (2D) and matrix-degrading (3D) states of a cardiac fibroblast.

Acknowledgments

We thank the University of California, Los Angeles (UCLA) Heart Laboratory cell core for providing freshly isolated cardiomyocytes and the UCLA Clinical Microarray Core for RNA-sequencing. Imaging flow cytometry was performed in the UCLA Jonsson Comprehensive Cancer Center and Center for AIDS Research Flow Cytometry Core Facility. We thank Dr Eric Olson, University of Texas Southwestern Medical Center and Dr Andrew Leask, University of Western Ontario Canada for sharing the TCF21MerCreMer and Col1a2CreERT mice.

Sources of Funding

The project was supported by grants from the National Institutes of Health (NIH) HL129178, HL137241 to A. Deb, CA185189, GM073981, GM114188 to M. Teitell, HL30568 and HL123295 to A.J. Lusis, Department of Defense (PR152219, PR161247 to A. Deb), Air Force Office of Scientific Research (FA9550-15-1-0406 to M. Teitell), California Institute of Regenerative Medicine (DISC1-08790 to A. Deb), research award from the Eli and Edythe Broad Center of Regenerative Medicine and Stem Cell Research & Rose Hills

Foundation to A. Deb and planning award from the Eli and Edythe Broad Center of Regenerative Medicine and Stem Cell Research and California Nanosystems Institute at University of California, Los Angeles (UCLA) to A. Deb and D.D. Carlo. The project also received support from NIH/National Center for Advancing Translational Sciences UCLA CTSI (ULTR00024). Imaging flow cytometry at the UCLA Jonsson Comprehensive Cancer Center is supported by NIH awards P30 CA016042 and 5P30 AI028697.

Disclosures

None.

References

1. Männer J, Pérez-Pomares JM, Macías D, Muñoz-Chápuli R. The origin, formation and developmental significance of the epicardium: a review. *Cells Tissues Organs*. 2001;169:89–103. doi: 10.1159/000047867.
2. Christia P, Bujak M, Gonzalez-Quesada C, Chen W, Dobaczewski M, Reddy A, Frangogiannis NG. Systematic characterization of myocardial inflammation, repair, and remodeling in a mouse model of reperfused myocardial infarction. *J Histochem Cytochem*. 2013;61:555–570. doi: 10.1369/0022155413493912.
3. Camelliti P, Borg TK, Kohl P. Structural and functional characterisation of cardiac fibroblasts. *Cardiovasc Res*. 2005;65:40–51. doi: 10.1016/j.cardiores.2004.08.020.
4. Shoval H, Karsch-Bluman A, Brill-Karniely Y, Stern T, Zamir G, Hubert A, Benny O. Tumor cells and their crosstalk with endothelial cells in 3D spheroids. *Sci Rep*. 2017;7:10428. doi: 10.1038/s41598-017-10699-y.
5. Pillai ICL, Li S, Romay M, et al. Cardiac fibroblasts adopt osteogenic fates and can be targeted to attenuate pathological heart calcification. *Cell Stem Cell*. 2017;20:218–232.e5. doi: 10.1016/j.stem.2016.10.005.
6. Rau CD, Romay MC, Tuteryan M, Wang JJ, Santolini M, Ren S, Karma A, Weiss JN, Wang Y, Lusis AJ. Systems genetics approach identifies gene pathways and Adamts2 as drivers of isoproterenol-induced cardiac hypertrophy and cardiomyopathy in mice. *Cell Syst*. 2017;4:121–128.e4. doi: 10.1016/j.cels.2016.10.016.
7. Sung K, Ding Y, Ma J, Chen H, Huang V, Cheng M, Yang CF, Kim JT, Eguchi D, Di Carlo D, Hsiai TK, Nakano A, Kulkarni RP. Simplified three-dimensional tissue clearing and incorporation of colorimetric phenotyping. *Sci Rep*. 2016;6:30736. doi: 10.1038/srep30736.
8. Wang YJ, Bailey JM, Rovira M, Leach SD. Sphere-forming assays for assessment of benign and malignant pancreatic stem cells. *Methods Mol Biol*. 2013;980:281–290. doi: 10.1007/978-1-62703-287-2_15.
9. Ubil E, Duan J, Pillai IC, Rosa-Garrido M, Wu Y, Bargiacchi F, Lu Y, Stanbouly S, Huang J, Rojas M, Vondriska TM, Stefani E, Deb A. Mesenchymal-endothelial transition contributes to cardiac neovascularization. *Nature*. 2014;514:585–590. doi: 10.1038/nature13839.
10. Kanisicak O, Khalil H, Ivey MJ, Karch J, Maliken BD, Correll RN, Brody MJ, J Lin SC, Aronow BJ, Tallquist MD, Molkentin JD. Genetic lineage tracing defines myofibroblast origin and function in the injured heart. *Nat Commun*. 2016;7:12260. doi: 10.1038/ncomms12260.
11. Basiji D, O'Gorman MR. Imaging flow cytometry. *J Immunol Methods*. 2015;423:1–2. doi: 10.1016/j.jim.2015.07.002.
12. Gutierrez E, Groisman A. Measurements of elastic moduli of silicone gel substrates with a microfluidic device. *PLoS One*. 2011;6:e25534. doi: 10.1371/journal.pone.0025534.
13. Baudino TA, Carver W, Giles W, Borg TK. Cardiac fibroblasts: friend or foe? *Am J Physiol Heart Circ Physiol*. 2006;291:H1015–H1026. doi: 10.1152/ajpheart.00023.2006.
14. Blankesteijn WM, Essers-Janssen YP, Verluyten MJ, Daemen MJ, Smits JF. A homologue of Drosophila tissue polarity gene frizzled is expressed in migrating myofibroblasts in the infarcted rat heart. *Nat Med*. 1997;3:541–544.
15. Kong P, Shinde AV, Su Y, Russo I, Chen B, Saxena A, Conway SJ, Graff JM, Frangogiannis NG. Opposing actions of fibroblast and cardiomyocyte Smad3 signaling in the infarcted myocardium. *Circulation*. 2018;137:707–724. doi: 10.1161/CIRCULATIONAHA.117.029622.
16. Yang Y, Mlodzik M. Wnt-frizzled/planar cell polarity signaling: cellular orientation by facing the wind (Wnt). *Annu Rev Cell Dev Biol*. 2015;31:623–646. doi: 10.1146/annurev-cellbio-100814-125315.
17. Laeremans H, Hackeng TM, van Zandvoort MA, Thijssen VL, Janssen BJ, Ottenheijm HC, Smits JF, Blankesteijn WM. Blocking of frizzled signaling with a homologous peptide fragment of wnt3a/wnt5a reduces infarct expansion and prevents the development of heart failure after myocardial infarction. *Circulation*. 2011;124:1626–1635. doi: 10.1161/CIRCULATIONAHA.110.976969.
18. Daskalopoulos EP, Hermans KC, Janssen BJ, Matthijs Blankesteijn W. Targeting the Wnt/frizzled signaling pathway after myocardial infarction: a new tool in the therapeutic toolbox? *Trends Cardiovasc Med*. 2013;23:121–127. doi: 10.1016/j.tcm.2012.09.010.
19. Buenrostro JD, Giresi PG, Zaba LC, Chang HY, Greenleaf WJ. Transposition of native chromatin for fast and sensitive epigenomic profiling of open chromatin, DNA-binding proteins and nucleosome position. *Nat Methods*. 2013;10:1213–1218. doi: 10.1038/nmeth.2688.
20. Ghazalpour A, Rau CD, Farber CR, et al. Hybrid mouse diversity panel: a panel of inbred mouse strains suitable for analysis of complex genetic traits. *Mamm Genome*. 2012;23:680–692. doi: 10.1007/s00335-012-9411-5.
21. Lusis AJ, Seldin MM, Allayee H, et al. The hybrid mouse diversity panel: a resource for systems genetics analyses of metabolic and cardiovascular traits. *J Lipid Res*. 2016;57:925–942. doi: 10.1194/jlr.R066944.
22. Bennett BJ, Farber CR, Orozco L, et al. A high-resolution association mapping panel for the dissection of complex traits in mice. *Genome Res*. 2010;20:281–290. doi: 10.1101/gr.099234.109.
23. Patterson M, Barske L, Van Handel B, et al. Frequency of mononuclear diploid cardiomyocytes underlies natural variation in heart regeneration. *Nat Genet*. 2017;49:1346–1353. doi: 10.1038/ng.3929.
24. Wang JJ, Rau C, Avetisyan R, Ren S, Romay MC, Stolin G, Gong KW, Wang Y, Lusis AJ. Genetic dissection of cardiac remodeling in an isoproterenol-induced heart failure mouse model. *PLoS Genet*. 2016;12:e1006038. doi: 10.1371/journal.pgen.1006038.
25. Langfelder P, Horvath S. Eigengene networks for studying the relationships between co-expression modules. *BMC Syst Biol*. 2007;1:54. doi: 10.1186/1752-0509-1-54.
26. Fujiu K, Nagai R. Fibroblast-mediated pathways in cardiac hypertrophy. *J Mol Cell Cardiol*. 2014;70:64–73. doi: 10.1016/j.yjmcc.2014.01.013.
27. Zangle TA, Burnes D, Mathis C, Witte ON, Teitell MA. Quantifying biomass changes of single CD8+ T cells during antigen specific cytotoxicity. *PLoS One*. 2013;8:e68916. doi: 10.1371/journal.pone.0068916.
28. Zangle TA, Chun J, Zhang J, Reed J, Teitell MA. Quantification of biomass and cell motion in human pluripotent stem cell colonies. *Biophys J*. 2013;105:593–601. doi: 10.1016/j.bpj.2013.06.041.
29. Bon P, Maucort G, Wattellier B, Monneret S. Quadriwave lateral shearing interferometry for quantitative phase microscopy of living cells. *Opt Express*. 2009;17:13080–13094.
30. Han H, Cho JW, Lee S, et al. TRRUST v2: an expanded reference database of human and mouse transcriptional regulatory interactions. *Nucleic Acids Res*. 2018;46:D380–D386. doi: 10.1093/nar/gkx1013.
31. Tshori S, Gilon D, Beeri R, Nechushtan H, Kaluzhny D, Pikarsky E, Razin E. Transcription factor MITF regulates cardiac growth and hypertrophy. *J Clin Invest*. 2006;116:2673–2681. doi: 10.1172/JCI27643.
32. Bergmann MW. WNT signaling in adult cardiac hypertrophy and remodeling: lessons learned from cardiac development. *Circ Res*. 2010;107:1198–1208. doi: 10.1161/CIRCRESAHA.110.223768.
33. Madonna R, Geng YJ, Bolli R, Rokosh G, Ferdinandy P, Patterson C, De Caterina R. Co-activation of nuclear factor-κB and myocardin/serum response factor conveys the hypertrophy signal of high insulin levels in cardiac myoblasts. *J Biol Chem*. 2014;289:19585–19598. doi: 10.1074/jbc.M113.540559.
34. Burnstock G. Purinergic signaling in the cardiovascular system. *Circ Res*. 2017;120:207–228. doi: 10.1161/CIRCRESAHA.116.309726.
35. Wang AY, Chan JC, Wang M, Poon E, Lui SF, Li PK, Sanderson J. Cardiac hypertrophy and remodeling in relation to ACE and angiotensinogen genes genotypes in Chinese dialysis patients. *Kidney Int*. 2003;63:1899–1907. doi: 10.1046/j.1523-1755.2003.00933.x.
36. Foulquier S, Daskalopoulos EP, Lluri G, Hermans KCM, Deb A, Blankesteijn WM. WNT signaling in cardiac and vascular disease. *Pharmacol Rev*. 2018;70:68–141. doi: 10.1124/pr.117.013896.
37. Travers JG, Kamal FA, Robbins J, Yutzey KE, Blaxall BC. Cardiac fibrosis: the fibroblast awakens. *Circ Res*. 2016;118:1021–1040. doi: 10.1161/CIRCRESAHA.115.306565.
38. DeLeon-Pennell KY, Meschiari CA, Jung M, Lindsey ML. Matrix metalloproteinases in myocardial infarction and heart failure. *Prog Mol Biol Transl Sci*. 2017;147:75–100. doi: 10.1016/bs.pmbts.2017.02.001.
39. Fan D, Takawale A, Lee J, Kassiri Z. Cardiac fibroblasts, fibrosis and extracellular matrix remodeling in heart disease. *Fibrogenesis Tissue Repair*. 2012;5:15. doi: 10.1186/1755-1536-5-15.
40. Jun JI, Lau LF. Resolution of organ fibrosis. *J Clin Invest*. 2018;128:97–107. doi: 10.1172/JCI93563.

Supplementary Methods

Animal care and use

All experimental procedures involving animals in this study were approved by the Institutional Animal Care and Use Committee (IACUC) of University of California at Los Angeles (UCLA). All animals were maintained at the UCLA vivarium according to the policies instituted by the American Association for Accreditation of Laboratory Animal Care.

Isolation of cardiac fibroblasts

Cardiac fibroblasts were isolated as described(1, 2). Briefly, cardiac fibroblasts were isolated from explanted hearts of uninjured wild type or Col1a2CreERT:R26R^{tdTomato} and TCF21MerCreMer:R26R^{tdTomato} mice which previously injected with tamoxifen for 10 days. The hearts were explanted and washed three times with 1× HBSS (GIBCO) then minced into approximately 1mm^2 sized pieces and digested using 12.5 ml Liberase TH (SIGMA, CAT# 5401151001) digestion buffer [prepared by adding 5mg of liberase TH to 50ml Tyrodes buffer (136mM NaCl, 5.4mM KCl, 0.33mM NaH_2PO4, 1.0mM $MgCl_2$, 10mM HEPES with 1.8mg/L Glucose) to a final concentration of 0.1ug/ml]. Two sequential digestions were performed at 37°C. The cells were collected and passed through a 40µm strainer and plated in F12K medium (CORNING) with 1% penicillin/streptomycin, 20% Fetal Bovine Serum (FBS) (GIBCO) for 2 h at 37°C in a 5% CO2 incubator. After incubation for 2 hours, the medium was changed to F12K medium (GIBCO) supplemented with 20% FBS, 1% penicillin/streptomycin, 1,000 U/ml leukemia inhibitory factor (LIF) (Millipore) and 10 ng/ml basic fibroblast growth factor (bFGF) (Millipore). Cells were maintained under these conditions until they became confluent and used. All the cardiac fibroblast that had not undergone more than 3 passages were used for experiments

Cardiac fibroblast 2D/3D culture

For cardiac fibroblast sphere formation, the primary outgrowth of confluent monolayer cardiac fibroblasts from C57BL/6J, Col1a2CreERT:R26R^{tdTomato} or TCF21MerCreMer:R26R^{tdTomato} mice were harvested (0.25% trypsin-EDTA) and re-plated onto regular tissue culture dish (2D) (CORNING) or ultra-low attachment dish (3D) (CORNING) (CAT# 3261) at a density of 1-1.2 × 10^5 cells/cm^2. Both 2D and 3D cardiac fibroblasts were treated with identical cell culture medium [35% IMDM, 65% F12K, 3.5% FBS, 1% penicillin-streptomycin, 200mmol/L L-glutamine, 20ng/ml bFGF, 25ng/ml EGF (PEPROTECH), 1,000 U/ml LIF, 0.1mM 2-Mercaptoethanol (SIGMA)](3, 4). Under these conditions, cardiac fibroblasts seeded onto ultra -low attachment plates formed spherical clusters within 24 hours of seeding. After 24 h, the 3D spheres were collected and plated back onto a regular cell culture dish at 37°C 5%CO_2 for 5 days, with cell culture medium being changed every two days. The spherical clusters of cardiac fibroblasts attached and fibroblasts migrated out to form a monolayer by 5 days (3D-2D). Fibroblasts in 2D or 3D states maintained for 5 days served as controls. These cells were subsequently trypsinized and reseeded onto ultra-low attachment plates, where they again formed spherical clusters (3D-2D-3D) within 24 hours. Cells identically trypsinized but reseeded onto 2D conditions served as controls. Cardiac fibroblasts at different topological states were used for RNA-seq and ATAC-seq experiments. For WGS staining, cardiac fibroblasts isolated from Col1a2CreERT:R26R^{tdTomato} and TCF21MerCreMer: R26R^{tdTomato} were fixed in 2% paraformaldehyde for 15 min at 37°C, then stained with 1:200 diluted Wheat Germ Agglutinin Conjugates (WGA) stock solution 1.0mg/mL (Invitrogen) in HBSS for 10 min at room temperature (5). The cells were subsequently washed twice with HBSS and then permeabilized with 0.2% Triton X-1000 for 15min. Finally, the cells were mounted in slow fade gold anti-fade reagent with DAPI. Labeled cells were imaged with a confocal microscope (PROMO C2, NIKON).

To determine changes in gene expression of cardiac fibroblasts seeded onto substrates with varying elastic moduli (stiffness), cardiac fibroblasts ($5x10^5$ cells) were cultured on 6-well plates with various rigidities (0.5, 8, 64 kPa) at 37°C, 5%CO_2 for 24 hours according to the manufacturer's instruction (Advanced BioMatrix, CAT# 5145) (5, 6). All wells were pre-coated with type I collagen according to manufacturer's instructions (100μg/ml collagen Type I). Cardiac fibroblasts seeded onto regular tissue culture dishes precoated with type I collagen and at a similar seeding density served as controls. Cardiac fibroblasts seeded onto ultra-low attachment plates were used to create 3D fibroblast states for analyzing gene expression changes within the different groups. Following 24 hours of seeding, cells were harvested for RNA-seq.

RNA-seq and ATAC-seq

RNA was isolated from cardiac fibroblasts in different topological states, temporally adjusted controls as well as from cardiac fibroblasts seeded onto substrates of varying elastic moduli (0.5, 8, 64 kPa). RNA isolation was performed using PROMEGA RNA Isolation Kit (PROMEGA) and reverse transcription using Reverse Transcription System (PROMEGA). Libraries were constructed using standard Illumina RNA-seq library construction protocols and were sequenced on Illumina HiSeq 3000. For analysis of gene expression changes, we first mapped RNA-Seq reads of each sample to its corresponding genomic coordinates (mm10 genome version) with Tophat software (default parameters)(7). Next, we quantified the expression of each gene, i.e. the number of reads falling into each gene, with HTSeq-count software(8). We then performed the normalization and differential expressed genes (DEGs) analysis with DESeq2 software(9). The identified DEGs required a FDR value smaller than 0.01 and a log2 fold change larger than 1. Marker set enrichment analysis (MSEA) was performed on the DESeq2 output from RNA-sequencing, based on normalized fold-change expression in 3D/2D (3D up-regulated) and 2D/3D (3D down-regulated) conditions as well as for fibroblasts on substrates of varying stiffness. For pathway analysis, genes in each condition were weighted based on their fold-change, merged into modules based on Gene Ontology Terms and permuted 2000 times against transcripts detected across all RNA-seq samples to generate corresponding p-values(9, 10).

ATAC-seq was performed as described previously(11) using approximately 50,000 cells/sample. Cardiac fibroblasts harvested from all topological states (2D, 3D) were subjected to ATAC-seq. Samples were lysed with cold lysis buffer (10 mM Tris-HCl, pH 7.4, 10 mM NaCl, 3 mM $MgCl_2$ and 0.1% IGEPAL CA-630). Immediately following the nuclei preparation, the pellets were re-suspended in the transposase reaction mix (25μl 2×TD buffer, 2.5μl transposase (Illumina) and 22.5μl nuclease-free water). The transposition reaction was carried out for 30 min at 37°C. Directly following transposition, the samples were purified using a Qiagen MinElute kit. Following purification, the libraries were amplified using 1×NEB next PCR master mix and 1.25μM of custom Nextera PCR primers 1 and 2 (**Table 1**), using the following PCR conditions: 72°C for 5min; 98°C for 30 s; and thermocycling at 98°C for 10 s, 63°C for 30 s and 72°C for 1 min. Libraries were purified using a Qiagen PCR cleanup kit yielding a final library concentration of ~30nM in 20μl to remove primer dimers. Libraries were amplified for a total of 10–12 cycles. For analysis of ATAC-seq data, we first mapped ATAC-Seq reads of each sample to its corresponding genomic coordinates with Bowtie2 software, requiring no more than two mismatches(12). The uniquely mapped reads were then used for further analyses. We used MACS2 software to identify the enriched signal regions of ATAC-Seq peaks with default q-value cutoff(13). To compare the ATAC-Seq signals between different samples, we used MACS2 bdg diff function, requiring the identified differential regions were having a log10 likelihood of more than 5.

Expression overlay with hybrid mouse diversity panel

Differentially expressed transcripts from 2D vs 3D spheres were used for population-based analysis within the HMDP. We utilized gene expression arrays from left ventricle (GEO accession: GSE48760) among HMDP strains subjected to isoproterenol treatment. ALZET Model 1004 minipumps (Cupertino, CA, USA) were implanted intra-peritoneally to administered ISO, at a dose of 30 mg/kg body weight/day for 21 days. At the end of the protocol, mice were sacrificed by giving a sub-lethal dosage of inhaled isoflurane followed by cervical dislocation. LV tissues were collected and frozen immediately in liquid nitrogen. Data from HMDP populations administered isoproterenol were analyzed from the following studies(14, 15). From these arrays, all probes corresponding to the same genes were aggregated to a single gene by strain measurement. This gene-by-strain matrix was used for further analyses. Initially, individual differentially expressed genes were correlated with clinical traits from the corresponding isoproterenol study. For a larger sample size and consistency, we chose to measure echocardiogram traits following 14 days of isoproterenol infusion. Biweight midcorrelation values (bicor) were calculated using pairwise strains (70-96, depending on the trait assessed) in the R package WGCNA(16). From the matrix of gene-by-trait, biweight midcorrelation coefficients student p-values were calculated using the corresponding sample sizes. Following individual gene x trait correlations, the gene -by-strain matrix from HMDP study was used for eigengene construction. First, the matrix was narrowed down to genes only upregulated under 3D conditions by overlaying gene symbol of aggregated probes with the output from DESeq2 analysis on 3D fibroblast spheres. Next principal component analysis was performed on the remaining gene set (R package, prcomp) and score contributions for components were extracted for each strain. The score matrices for each PC and strain were then correlated against traits also using WGNCA as described above.

Flow cytometry analysis

Cultured Cardiac fibroblasts at different topological states were dissociated using 0.25% trypsin-EDTA solution (SIGMA), stained in FACS buffer (0.1%BSA PBS) with APC-conjugated anti-Frizzled-1 antibody (Miltenyi Biotec Inc. cat#130-112-398) or FITC conjugated anti-Ki67 antibody (eBioscience, cat#11-5698-82) for 30min at 4°C. After washing with FACS buffer twice, stained cells were analyzed on a flow cytometer. Unstained control cells were run first to establish gates followed by the cells stained with the primary antibody conjugated to the fluorophore. For EdU analysis, EdU was added to the cell culture medium at a final concentration of 10mM. After 4 hours incubation, the cells were dissociated with 0.25% trypsin-EDTA solution; cells were then fixed and permeabilized with 1x Click-iT saponin-based permeabilization and wash regent for 15min according to the manufacturing instruction of Click-iT™ Plus EdU Alexa Fluor™ 488 Flow Cytometry Assay Kit (Life technologies, cat#C10632). Subsequently Click-iT reaction cocktail was added to the cells and incubated for an additional 30 minutes at room temperature. After washing with1x Click-iT saponin-based permeabilization and wash regent twice, cells were analyzed on a flow cytometer.

Cell Cycle analysis using ImageStream

Cultured Cardiac fibroblasts at different topological states were dissociated as described above and fixed with 1% PFA on ice for 20min. Cells were washed twice with PBS/2%FBS twice, and then passed through a 70μm nylon mesh strainer. At least 1 million cells in 50μl were used for flowcytometry analyzing on the ImageStream system with bright field at 40x magnification (Amnis). Parameters including cell image, cell diameter, cell surface area were analyzed (n=3000 cells used for analysis) using the IDEAS™ post-acquisition analysis software (Amnis) (17, 18).

Immunoblotting analysis

Cultured Cardiac fibroblasts at different topological states were washed twice with ice-cold PBS and harvested in RIPA Lysis and Extraction Buffer (life technologies) plus Halt Protease Inhibitor Cocktail (life technologies) and Halt™ Phosphatase Inhibitor Cocktail (life technologies). Pierce™ BCA Protein Assay Kit was used for the colorimetric detection and quantitation of total protein (Life Technologies). Total 25µg protein was separated on 4-12% Tris-Glycine Mini Gels (Life Technologies) and transferred onto PVDF membranes (Merck Millipore). The membranes were probed with antibodies to alpha smooth muscle Actin (α SMA, 1:1000) (Abcam, cat# ab5694), calponin(1:1000)(Abcam, cat# ab46794), GAPDH(1:5000) (MilliporeSigma, cat# ABS16). Protein signals were detected using horseradish peroxidase (HRP)-conjugated secondary antibodies and enhanced chemiluminescence (ECL) western blotting detection regents (Thermo Fisher Scientific, MA, USA).

Sircol assay for determining collagen amounts

The Sircol collagen assay kit (Biocolor Ltd.,Newtownabbey, UK, CAT# CLRS4000) was used to quantify total collagen amounts in cardiac fibroblasts in 2D or 3D states according to the manufacturer's instructions. Collagen was measured only in 2D or 3D fibroblasts following harvest and collagen secreted from the cells onto the surface of the dish was thus not measured in this assay. In brief, collagen was extracted and digested overnight with 0.1 mg/ml pepsin in 5 M acetic acid. Soluble and insoluble collagen was measured according to the manufacturer's instructions using a standard curve of known concentrations of purified rat tail collagen to estimate total collagen content (19, 20).

Genetic labeling of cardiac fibroblasts

Col1a2CreERT:R26R^{tdTomato} and TCF21MerCreMer:R26R^{tdTomato} mice lines were obtained by crossing Collagen1a2CreERT and TCF21MerCreMer mice with the lineage reporter R26R ^{tdTomato} mice(1). Tamoxifen (1mg) (Sigma) was injected intraperitoneally for 10 days to induce Cre-mediated recombination in Col1a2CreERT:R26R^{tdTomato} and TCF21MerCreMer:R26R^{tdTomato} mice (8-10 weeks old). Five days following cessation of tamoxifen, animals were subjected to cardiac fibroblasts isolation or cardiac injury (myocardial cryoinjury). All mice were maintained on a C57BL/6 background. For isolation of tdTomato labeled cardiac fibroblasts, cultured cardiac fibroblasts isolated from non-transgenic mice were first run through the flow cytometer to establish gates. Next population of cultured cardiac fibroblasts isolated from Col1a2CreERT:R26R^{tdTomato} or TCF21MerCreMer:R26R^{tdTomato} mice hearts were run through the same gates to identify tdTomato labeled cells. All the tdTomato labeled cardiac fibroblast were sorted and collected for further culture and assays.

Murine Cardiac Cryo-injury

Mice (both male and female), 8–10 weeks old, were subjected to sham or myocardial cryoinjury as described(1). For cryoinjury, mice were initially anaesthetized with 3% isoflurane, maintained at 2% isoflurane, and intubated using a Harvard Rodent Volume-Cycled ventilator. A left thoracotomy was performed at the level of 2nd intercostal space and cardiac cryo-injury was performed by gently pressing a steel rod of 1mm diameter pre-cooled in dry ice against the exposed beating heart for 10 seconds. Freezing of cardiac tissue was confirmed by the rapid discoloration of the tissue. Seven days after injury, the hearts were harvested and processed for histological analysis.

Immunofluorescent staining and confocal microscopy

For harvesting the heart, the left ventricle was perfused with 5 ml PBS followed by 2 ml of 4%

paraformaldehyde (PFA). The hearts were post fixed in 4% PFA for additional 4 h and cryo-protected using 25% sucrose and embedded in OCT compound (TISSUE-TEK) (1). Immunofluorescent staining was performed on 7 mm frozen sections against markers that were upregulated in 3D spheres. Sections were washed and blocked using 10% normal donkey serum for 1 h and then stained with primary antibodies against MMP11 (ABCAM, AB119284), ADAMTS15 (R&D STSTEMS, AF5149) overnight at 4°C. After washing three times with PBS, sections were incubated in secondary antibodies for 1 h followed by washing an additional three times with PBS. Finally, the sections were mounted in slow fade gold anti-fade reagent with DAPI (LIFT TECHNOLOGIES, S36938). Labeled sections were imaged using a PROMO C2 inverted Laser Scanning Confocal Microscope (NIKON). For each sample, eight independent images within 100mm radius of the cryo injured region were used for quantitative analysis.

Mouse Heart Clearing using simplified CLARITY method (SCM) and Immunofluorescence Labeling

A simplified CLARITY method was used to perform cardiac tissue clearing as described(21). Mouse hearts were rinsed thoroughly with 1x Phosphate Buffered Saline (PBS) immediately following harvesting to remove residual blood from cardiac chambers. The hearts were subsequently fixed in 4% paraformaldehyde (PFA) overnight at 4°C. Following fixation, samples were rinsed with 1x PBS and then immersed in a solution of 4% acrylamide monomer (Bio-Rad) along with 0.625% w/v of the photoinitiator 2,2'-Azobis[2-(2-imidazolin-2-yl) propane] dihydrochloride (VA-044, Wako Chemicals USA). The tissues were then incubated overnight at 4°C. The following day, the tubes containing the hearts were incubated at 37°C for 3-4 hours, until the acrylamide solution became viscous. After polymerization, the tissues were rinsed with 1x PBS and then placed into a clearing solution comprised of 8% w/v sodium dodecyl sulfate (SDS, Sigma Aldrich) and 1.25% w/v boric acid (Fischer) (Ph8.4). Samples were incubated at 37°C until the desired transparency was reached, usually two weeks. Following incubation in clearing solution, the heart samples were washed with 1x PBS for one day and then blocked with bovine serum albumin (1x PBS, 1% BSA, 0.05% Tween-20) overnight prior to immunofluorescence applications. For immunofluorescence studies, the heart samples were incubated with GPNMB (R&D Systems, AF2550) primary antibody at 1:100 dilution for 24 hours. Samples were then rinsed with PBS for one day prior to the application of the appropriate Alexa 488-conjugated secondary antibody (Cell Signaling) for 24 hours at 1:100 dilution. To amplify the endogenous tdTomato signal when present, anti-td-Tomato primary antibody (Rockland) and appropriate Alexa 555-conjugated secondary antibody (Cell Signaling) were applied as described above. Following immunofluorescence labeling, the heart samples were placed in Refractive Index Matching Solution (RIMS) prior to imaging. To make 30 mL RIMS, 40 grams of Histodenz (Sigma-Aldrich) was dissolved in 1X PBS (Sigma) with 0.05% w/v sodium azide (Sigma) and syringe filtered through a 0.2 μm filter.

2D/3D conditioned medium experiments on neonatal rat ventricular myocytes

NRVMs were isolated from P1-P3 day old Sprague-Dawley rat pups of mixed gender as described previously (22) and plated with 700ul plating medium (DMEM, supplemented with 10% FBS and 1% penicillin/streptomycin) in a μ–Slide 4 well Ph+ (Phase contrast plus) (IBIDI) coated with 0.1% gelatin (104 cells /well). After resting overnight in plating medium, medium was changed to 700ul serum-free DMEM medium supplemented with 1% insulin-transferrin-selenium (ITS) (BD BIOSCIENCE) and 1% penicillin/streptomycin. Cells were incubated at 37°C, 5% CO_2. The medium was then replaced with conditioned medium obtained from 2D or 3D cardiac fibroblast cultures and myocyte mass measured over the next 48 hours.

Live cell Interferometry (LCI)

Cells were imaged every 30 min for up to 48 hours at 20x magnification using a 0.40 numerical aperture objective on an Axio Observer.A1 inverted microscope (Zeiss) in a temperature and CO2 regulated stage-

top cell incubation chamber. Quantitative phase microscopy (QPM) data was captured with a quadriwave lateral shearing interferometry (QWLSI) camera (SID4BIO, Phasics)(23). Illumination was provided by a 660nm center wavelength collimated LED (Thorlabs). In each experiment, QPM data was collected from 32 distinct locations for automated image processing and biomass segmentation analysis.

Quantitative phase microscopy (QPM) image analysis

All images were processed with custom MATLAB (MathWorks) scripts. Cells were identified and segmented using a local adaptive threshold based on Otsu's method (24) and tracked using particle tracking code based on Grier et al (25).

Biomass accumulation rate calculation

QPM biomass data was summed over the projected area of each cell to obtain total cell biomass at each collection time point. Biomass accumulation rates were calculated by fitting a first-order polynomial to each biomass versus time plot using MATLAB Polyfit (Math Works). Individual cell growth tracks were quality filtered using an upper cutoff of ± 5% uncertainty (s.d. of residuals) in the calculated growth rate, as determined by linear fitting the biomass versus time data.

Statistics

All data are presented as mean± standard error of the mean (S.E.M.). The value of n stated in the figure legends stands for independent biological replicates. Statistical analysis was performed using Graph Pad (Prizm) using student's t-test (two tailed). A P value <0.05 was considered significant and individual p values are mentioned in the figure/figure legend.

All computational procedures were carried out using R statistical software. For analysis of the Hybrid Mouse Diversity Panel (HMDP) and correlation of phenotypic traits with 3D upregulated genes, all computational procedures were carried out using R statistical software. The HMDP expression arrays were aggregated to average expression of each gene across multiple probes and used for correlation or principal component analysis. Correlations and associated p-values were calculated with the biweight midcorrelation, which is robust to outliers and associated pvalue (16). Principle component vectors were assigned using the R base function "prcomp" where strain position on corresponding vectors were used for correlation analysis also using WGCNA. Transcriptional Regulatory Relationships Unraveled by Sentence-based Text mining (TRRUSTv2) were interrogated for literature-based transcription factor (TF)-target interactions which persist in mice, focused on significance (FDR < 0.1) of TFs enriched among interactions with the set of 3D-enriched genes. Single comparisons between two groups were performed using two-tailed Student's *t* tests with 95% confidence intervals. To retrieve and overlay annotated secreted proteins, we used the list deposited in the Universal Protein resource (UniProt) as "secreted" localization annotations [SL-0243] for overlapping HUGO symbol in Mus musculus (Mouse) [10090].

Table 1: Oligo designs. A list of ATAC-seq oligos used for PCR.

Ad1_noMX:	AATGATACGGCGACCACCGAGATCTACACTCGTCGGCAGCGTCAGATGTG
Ad2.1_TAAGGCGA	CAAGCAGAAGACGGCATACGAGATTCGCCTTAGTCTCGTGGGCTCGGAGATGT
Ad2.2_CGTACTAG	CAAGCAGAAGACGGCATACGAGATCTAGTACGGTCTCGTGGGCTCGGAGATGT
Ad2.3_AGGCAGAA	CAAGCAGAAGACGGCATACGAGATTTCTGCCTGTCTCGTGGGCTCGGAGATGT
Ad2.4_TCCTGAGC	CAAGCAGAAGACGGCATACGAGATGCTCAGGAGTCTCGTGGGCTCGGAGATGT
Ad2.5_GGACTCCT	CAAGCAGAAGACGGCATACGAGATAGGAGTCCGTCTCGTGGGCTCGGAGATGT
Ad2.6_TAGGCATG	CAAGCAGAAGACGGCATACGAGATCATGCCTAGTCTCGTGGGCTCGGAGATGT
Ad2.7_CTCTCTAC	CAAGCAGAAGACGGCATACGAGATGTAGAGAGGTCTCGTGGGCTCGGAGATGT
Ad2.8_CAGAGAGG	CAAGCAGAAGACGGCATACGAGATCCTCTCTGGTCTCGTGGGCTCGGAGATGT
Ad2.9_GCTACGCT	CAAGCAGAAGACGGCATACGAGATAGCGTAGCGTCTCGTGGGCTCGGAGATGT
Ad2.10_CGAGGCTG	CAAGCAGAAGACGGCATACGAGATCAGCCTCGGTCTCGTGGGCTCGGAGATGT
Ad2.11_AAGAGGCA	CAAGCAGAAGACGGCATACGAGATTGCCTCTTGTCTCGTGGGCTCGGAGATGT
Ad2.12_GTAGAGGA	CAAGCAGAAGACGGCATACGAGATTCCTCTACGTCTCGTGGGCTCGGAGATGT
Ad2.13_GTCGTGAT	CAAGCAGAAGACGGCATACGAGATATCACGACGTCTCGTGGGCTCGGAGATGT
Ad2.14_ACCACTGT	CAAGCAGAAGACGGCATACGAGATACAGTGGTGTCTCGTGGGCTCGGAGATGT
Ad2.15_TGGATCTG	CAAGCAGAAGACGGCATACGAGATCAGATCCAGTCTCGTGGGCTCGGAGATGT
Ad2.16_CCGTTTGT	CAAGCAGAAGACGGCATACGAGATACAAACGGGTCTCGTGGGCTCGGAGATGT
Ad2.17_TGCTGGGT	CAAGCAGAAGACGGCATACGAGATACCCAGCAGTCTCGTGGGCTCGGAGATGT
Ad2.18_GAGGGGTT	CAAGCAGAAGACGGCATACGAGATAACCCCTCGTCTCGTGGGCTCGGAGATGT
Ad2.19_AGGTTGGG	CAAGCAGAAGACGGCATACGAGATCCCAACCTGTCTCGTGGGCTCGGAGATGT
Ad2.20_GTGTGGTG	CAAGCAGAAGACGGCATACGAGATCACCACACGTCTCGTGGGCTCGGAGATGT
Ad2.21_TGGGTTTC	CAAGCAGAAGACGGCATACGAGATGAAACCCAGTCTCGTGGGCTCGGAGATGT
Ad2.22_TGGTCACA	CAAGCAGAAGACGGCATACGAGATTGTGACCAGTCTCGTGGGCTCGGAGATGT
Ad2.23_TTGACCCT	CAAGCAGAAGACGGCATACGAGATAGGGTCAAGTCTCGTGGGCTCGGAGATGT
Ad2.24_CCACTCCT	CAAGCAGAAGACGGCATACGAGATAGGAGTGGGTCTCGTGGGCTCGGAGATGT

Supplemental References

1. Pillai IC, Li S, Romay M, Lam L, Lu Y, Huang J, et al. Cardiac Fibroblasts Adopt Osteogenic Fates and Can Be Targeted to Attenuate Pathological Heart Calcification. *Cell stem cell*. 2017;20:218-32 e5.
2. Pinz I, Zhu M, Mende U, and Ingwall JS. An improved isolation procedure for adult mouse cardiomyocytes. *Cell Biochem Biophys*. 2011;61:93-101.
3. Wang YJ, Bailey JM, Rovira M, and Leach SD. Sphere-forming assays for assessment of benign and malignant pancreatic stem cells. *Methods Mol Biol*. 2013;980:281-90.
4. Chen L, Pan Y, Zhang L, Wang Y, Weintraub N, and Tang Y. Two-step protocol for isolation and culture of cardiospheres. *Methods Mol Biol*. 2013;1036:75-80.
5. Gutierrez E, and Groisman A. Measurements of elastic moduli of silicone gel substrates with a microfluidic device. *PLoS One*. 2011;6:e25534.
6. Prager-Khoutorsky M, Lichtenstein A, Krishnan R, Rajendran K, Mayo A, Kam Z, et al. Fibroblast polarization is a matrix-rigidity-dependent process controlled by focal adhesion mechanosensing. *Nature cell biology*. 2011;13:1457-65.
7. Trapnell C, Roberts A, Goff L, Pertea G, Kim D, Kelley DR, et al. Differential gene and transcript expression analysis of RNA-seq experiments with TopHat and Cufflinks. *Nature protocols*. 2012;7:562-78.
8. Anders S, and Huber W. Differential expression analysis for sequence count data. *Genome biology*. 2010;11:R106.
9. Arneson D, Bhattacharya A, Shu L, Makinen VP, and Yang X. Mergeomics: a web server for identifying pathological pathways, networks, and key regulators via multidimensional data integration. *BMC genomics*. 2016;17(1):722.
10. Shu L, Zhao Y, Kurt Z, Byars SG, Tukiainen T, Kettunen J, et al. Mergeomics: multidimensional data integration to identify pathogenic perturbations to biological systems. *BMC genomics*. 2016;17:874.
11. Buenrostro JD, Giresi PG, Zaba LC, Chang HY, and Greenleaf WJ. Transposition of native chromatin for fast and sensitive epigenomic profiling of open chromatin, DNA-binding proteins and nucleosome position. *Nature methods*. 2013;10:1213-8.
12. Langmead B, and Salzberg SL. Fast gapped-read alignment with Bowtie 2. *Nature methods*. 2012;9(4):357-9.
13. Zhang Y, Liu T, Meyer CA, Eeckhoute J, Johnson DS, Bernstein BE, et al. Model-based analysis of ChIP-Seq (MACS). *Genome biology*. 2008;9:R137.
14. Rau CD, Wang J, Avetisyan R, Romay MC, Martin L, Ren S, et al. Mapping genetic contributions to cardiac pathology induced by Beta-adrenergic stimulation in mice. *Circulation Cardiovascular genetics*. 2015;8:40-9.
15. Wang JJ, Rau C, Avetisyan R, Ren S, Romay MC, Stolin G, et al. Genetic Dissection of Cardiac Remodeling in an Isoproterenol-Induced Heart Failure Mouse Model. *PLoS genetics*. 2016;12:e1006038.
16. Langfelder P, and Horvath S. Eigengene networks for studying the relationships between co-expression modules. *BMC Syst Biol*. 2007;1:54.

17. Basiji DA, Ortyn WE, Liang L, Venkatachalam V, and Morrissey P. Cellular image analysis and imaging by flow cytometry. *Clin Lab Med*. 2007;27:653-70, viii.

18. Hennig H, Rees P, Blasi T, Kamentsky L, Hung J, Dao D, et al. An open-source solution for advanced imaging flow cytometry data analysis using machine learning. *Methods*. 2017;112:201-10.

19. Shen C, Jiang L, Shao H, You C, Zhang G, Ding S, et al. Targeted killing of myofibroblasts by biosurfactant di-rhamnolipid suggests a therapy against scar formation. *Sci Rep*. 2016;6:37553.

20. Chu H, Shi Y, Jiang S, Zhong Q, Zhao Y, Liu Q, et al. Treatment effects of the traditional Chinese medicine Shenks in bleomycin-induced lung fibrosis through regulation of TGF-beta/Smad3 signaling and oxidative stress. *Sci Rep*. 2017;7:2252.

21. Sung K, Ding Y, Ma J, Chen H, Huang V, Cheng M, et al. Simplified three-dimensional tissue clearing and incorporation of colorimetric phenotyping. *Sci Rep*. 2016;6:30736.

22. Ota A, Zhang J, Ping P, Han J, and Wang Y. Specific regulation of noncanonical p38alpha activation by Hsp90-Cdc37 chaperone complex in cardiomyocyte. *Circ Res*. 2010;106:1404-12.

23. Bon P, Maucort G, Wattellier B, and Monneret S. Quadriwave lateral shearing interferometry for quantitative phase microscopy of living cells. *Opt Express*. 2009;17:13080-94.

24. Zangle TA, Chun J, Zhang J, Reed J, and Teitell MA. Quantification of biomass and cell motion in human pluripotent stem cell colonies. *Biophys J*. 2013;105::593-601.

25. Zangle TA, Burnes D, Mathis C, Witte ON, and Teitell MA. Quantifying biomass changes of single CD8+ T cells during antigen specific cytotoxicity. *PLoS One*. 2013;8::e68916.

Online Figure I

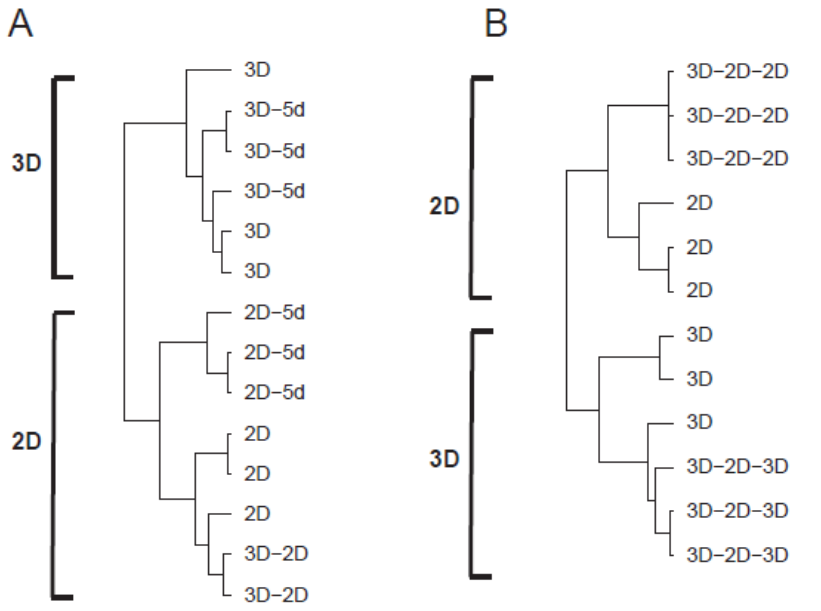

Online Figure I. Dendrogram demonstrating relationship of gene expression patterns of 3D-2D and 3D-2D-3D cardiac fibroblasts with temporally adjusted controls. (A) 3D-2D cardiac fibroblasts were generated by transferring the 3D cardiac fibroblasts to 2D conditions and maintaining the cells for 5 days (allowing the cells to migrate out from spheroids to a monolayer). For this purpose, additional temporally adjusted controls of 2D fibroblasts and 3D fibroblasts maintained in culture for 5 days (2D-5d; 3D-5d) and then subsequently harvested for RNA-seq were used. RNA-seq and gene expression analysis to construct dendrograms shows clustering of 3D-2D groups with 2D and 2D-5 day groups and are distinct from that of 3D or 3D-5 day groups. **(B)** Similarly, 3D-2D-3D fibroblasts were generated by transferring 3D-2D fibroblasts to an ultra-low attachment dish and harvesting the cells at 24 hours after initial seeding. A temporally adjusted control was generated by transferring the 3D-2D cells to a regular tissue culture dish and harvested 24 hours after seeding (3D-2D-2D). Dendrogram again shows clustering of the 3D-2D-3D gene expression pattern with that of the 3D and distinct from the 2D or 3D-2D-2D groups.

Online Figure II

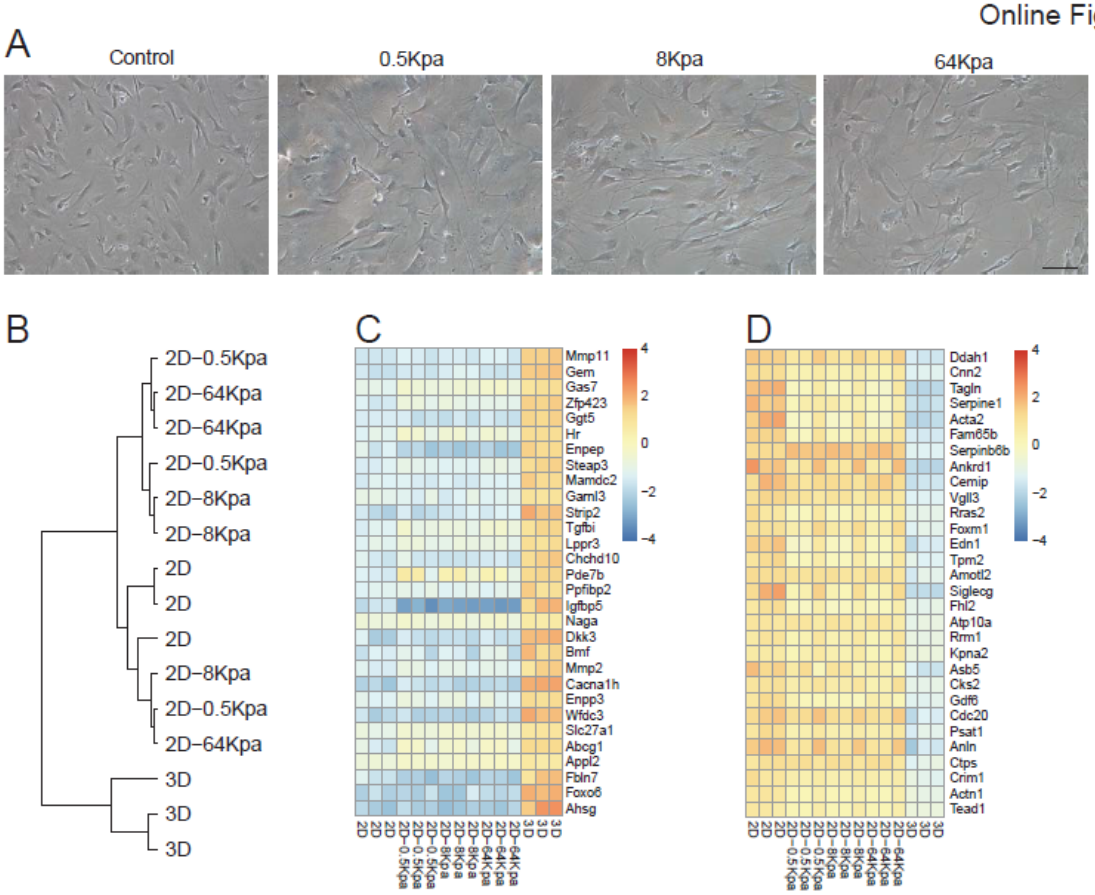

Online Figure II. Gene expression changes following seeding of cardiac fibroblasts onto tissue culture plates with stiffness of 0.5,8 and 64kPa. (A) Cardiac fibroblasts were seeded onto control (regular tissue culture plate or 2D group) or plates of 0.5kPA, 8kPa and 64kPa stiffness or ultra-low attachment plate (3D group) and cells harvested after 24 hours and RNA-seq performed. **(B)** Gene expression analysis and dendrogram demonstrates that the gene expression patterns of cardiac fibroblasts under different stiffness cluster together with that of the 2D group and are distinct from that of the 3D group. **(C,D)** Heat map demonstrating expression of the most highly **(C)** upregulated and **(D)** downregulated genes between the 3D and 2D groups across all the groups.

Online Figure III

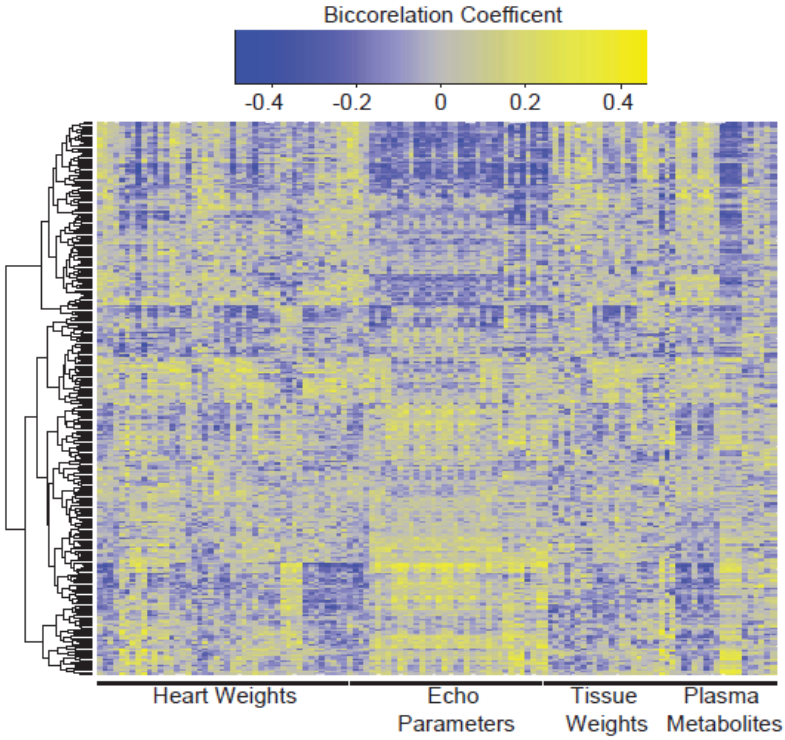

Online Figure III. Heat map of all 3D upregulated genes plotted against all cardiac and non-cardiac traits measured following infusion of isoproterenol in 96 strains of mice. Correlation heat map (yellow: positive and blue: negative correlation) of all differentially upregulated genes in 3D/2D states versus all cardiac and non-cardiac traits following infusion of isoproterenol.

Online Figure IV

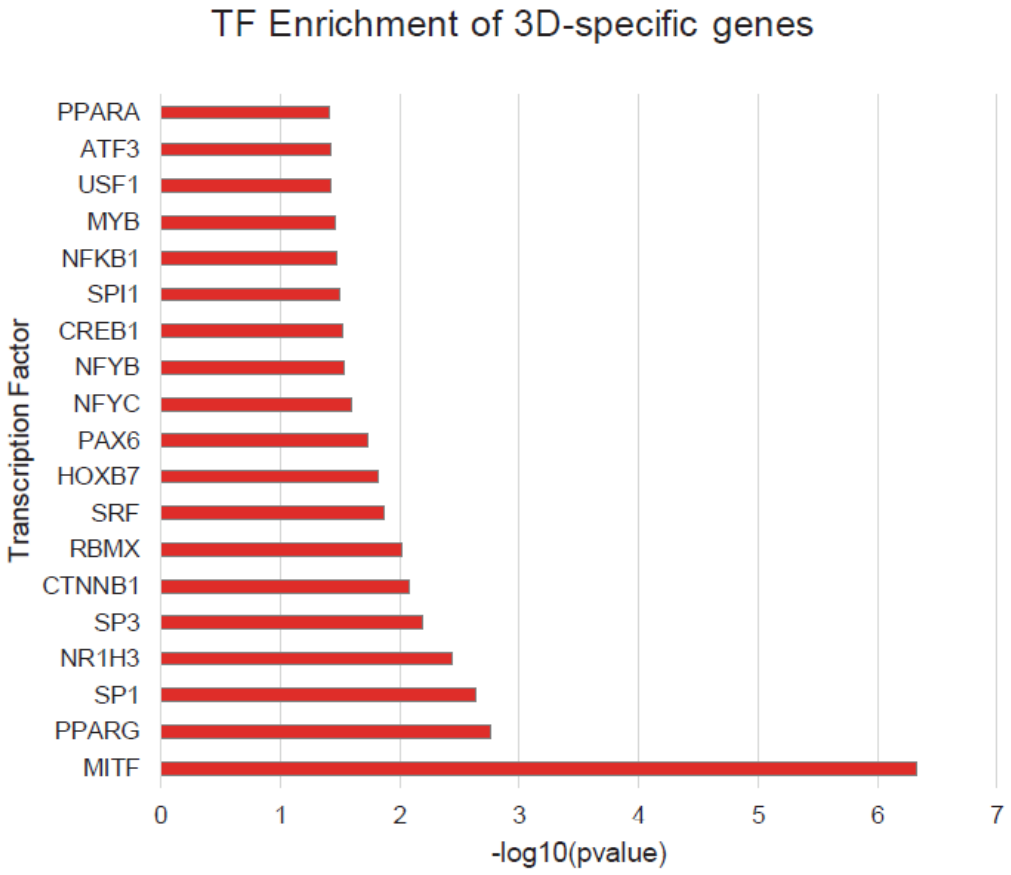

Online Figure IV. Predicted transcriptional regulators of 3D specific genes. Genes upregulated in 3D cardiac fibroblasts were assayed for enrichment of upstream transcriptional factors using TRRUSTv2. Significantly represented transcriptional components are plotted with corresponding p value enrichment among 3D genes.

Gene	3D-VS-2D	3D-2D-VS-2D	3D-2D-3D-VS-2D
Pvalb	10.05539546	2.042812383	6.148897168
Hmgcs2	8.176547545	0.434262448	5.246796241
Myrip	7.569744718	-0.96456143	3.535468722
Adamts15	7.428394976	-2.236678711	4.64226524
Ky	7.323873113	1.430596851	2.528030866
Ahsg	7.322443014	0.47445342	5.182554283
Lrrc4b	7.294700622	1.428847722	2.567511644
Ephb1	7.25185596	0.467220052	-1.277142321
Pnoc	7.062175922	-0.002789088	6.923764703
Syt6	7.046396418	0.562192577	5.349987257
Nt5c1a	7.006143756	3.298641568	9.242489561
Cacna1h	6.839489661	0.513723286	4.857629415
Slc25a34	6.73597135	1.193512673	5.411218678
Cilp	6.735065016	0.306014992	1.807565189
F7	6.634679275	1.477979591	2.769187831
Hpcal4	6.632336466	2.675310138	7.343315833
Plin1	6.447978021	-0.964554798	-0.315347653
5430431A17Rik	6.287056921	0.49926534	3.27757957
Cldn2	6.173261088	-0.351960129	7.343419587
Wfdc3	6.125032934	1.338744278	5.382560176
Fam71a	6.038721447	4.549254793	-0.315369125
Dct	6.029081483	1.453029962	3.342191267
Gcgr	6.015310487	0.46471614	1.160494986
Lrguk	5.968090507	4.237453053	5.277349871
Pde11a	5.911226392	-0.002767998	2.883438145
Doc2b	5.869156044	0.764404777	5.01155933
Adamts19	5.795304104	-0.002777597	-0.315363638
Ptgds	5.781639358	0.43945352	3.718051212
Cml5	5.765583486	-0.002775705	0.646431671
Aox3	5.75897692	0.086969067	3.393176203
Ctrb1	5.6872866	2.897731618	1.433115799
Ppp1r14c	5.623384744	-0.7608765	3.67798639
Foxo6	5.608402688	-2.447842636	3.573409712
Fndc5	5.587992716	-1.895141111	1.700377114
Slc24a4	5.561138758	-0.002769128	0.646438699
Agt	5.532807378	0.377688751	3.663862859
Npr1	5.500166531	-0.038330512	5.324854513
Fam163b	5.499889191	-0.002768895	3.889532941
Syt9	5.471852004	-1.834128988	6.367115106

Supplementary Table 1. Expression of genes in different topological states of cardiac fibroblasts. Differentially expressed genes in different topological states of cardiac fibroblasts expressed as a log2 fold change with respect to the 2D fibroblast state. The identified DEGs required a FDR value smaller than 0.01 and a log2 fold change larger than 1. (negative value refers to genes that are downregulated versus the 2D state while a positive value refers to genes that are upregulated versus the 2D state).

3D down-regulated pathways

MODULE	FDR	GENE	LOCUS	VALUE	Description
GO:0006281	0.00%	Pif1	Pif1	28.39	DNA repair
GO:0006281	0.00%	Exo1	Exo1	17.72	DNA repair
GO:0006281	0.00%	Neil3	Neil3	15.45	DNA repair
GO:0006281	0.00%	Clspn	Clspn	14.42	DNA repair
GO:0006281	0.00%	Polq	Polq	13.91	DNA repair
GO:0007059	0.00%	Ska1	Ska1	31.16	chromosome segregation
GO:0007059	0.00%	Kif2c	Kif2c	27.23	chromosome segregation
GO:0007059	0.00%	Cenpf	Cenpf	26.66	chromosome segregation
GO:0007059	0.00%	Nek2	Nek2	22.36	chromosome segregation
GO:0007059	0.00%	Cenpe	Cenpe	19.4	chromosome segregation
GO:0000776	0.00%	Ska1	Ska1	31.16	kinetochore
GO:0000776	0.00%	Kif2c	Kif2c	27.23	kinetochore
GO:0000776	0.00%	Cenpf	Cenpf	26.66	kinetochore
GO:0000776	0.00%	Nek2	Nek2	22.36	kinetochore
GO:0000776	0.00%	Plk1	Plk1	20.1	kinetochore
GO:0006260	0.00%	Pif1	Pif1	28.39	DNA replication
GO:0006260	0.00%	Dscc1	Dscc1	17.22	DNA replication
GO:0006260	0.00%	Rrm2	Rrm2	14.56	DNA replication
GO:0006260	0.00%	Polq	Polq	13.91	DNA replication
GO:0006260	0.00%	Ticrr	Ticrr	12.63	DNA replication
GO:0005694	0.00%	Ska1	Ska1	31.16	chromosome
GO:0005694	0.00%	Kif2c	Kif2c	27.23	chromosome
GO:0005694	0.00%	Kif4	Kif4	24.66	chromosome
GO:0005694	0.00%	Nek2	Nek2	22.36	chromosome
GO:0005694	0.00%	Plk1	Plk1	20.1	chromosome
GO:0051301	0.00%	Anln	Anln	36.4	cell division
GO:0051301	0.00%	Ska1	Ska1	31.16	cell division
GO:0051301	0.00%	Kif2c	Kif2c	27.23	cell division
GO:0051301	0.00%	Aspm	Aspm	27.05	cell division
GO:0051301	0.00%	Cdc20	Cdc20	26.59	cell division

3D upregulated pathways

MODULE	FDR	GENE	LOCUS	VALUE	Description
GO:0009986	2.88%	Adamts15	Adamts15	173.38	cell surface
GO:0009986	2.88%	Cd36	Cd36	19.93	cell surface
GO:0009986	2.88%	Ciita	Ciita	8.01	cell surface
GO:0009986	2.88%	Apoe	Apoe	6.74	cell surface
GO:0009986	2.88%	Adgrv1	Adgrv1	6.71	cell surface
GO:0007166	2.48%	Agt	Agt	44.71	cell surface receptor signaling pathway
GO:0007166	2.48%	Cd36	Cd36	19.93	cell surface receptor signaling pathway
GO:0007166	2.48%	Adgrf4	Adgrf4	9.34	cell surface receptor signaling pathway
GO:0007166	2.48%	Adgrg1	Adgrg1	9.16	cell surface receptor signaling pathway
GO:0007166	2.48%	Cd22	Cd22	7.5	cell surface receptor signaling pathway

GO:0004950	2.19%	Ccr1	Ccr1	5.68	chemokine receptor activity
GO:0004950	2.19%	Ccr3	Ccr3	4.67	chemokine receptor activity
GO:0004950	2.19%	Ccr5	Ccr5	4.64	chemokine receptor activity
GO:0004950	2.19%	Ackr2	Ackr2	4.34	chemokine receptor activity
GO:0004950	2.19%	Ccrl2	Ccrl2	3.66	chemokine receptor activity
GO:0004930	1.42%	Adra1a	Adra1a	18.01	G-protein coupled receptor activity
GO:0004930	1.42%	Ackr1	Ackr1	13.01	G-protein coupled receptor activity
GO:0004930	1.42%	Adgrf4	Adgrf4	9.34	G-protein coupled receptor activity
GO:0004930	1.42%	Adgrg1	Adgrg1	9.16	G-protein coupled receptor activity
GO:0004930	1.42%	Adgrv1	Adgrv1	6.71	G-protein coupled receptor activity
GO:0070098	1.36%	Ccl6	Ccl6	30.3	chemokine-mediated signaling pathway
GO:0070098	1.36%	Ccl8	Ccl8	14.23	chemokine-mediated signaling pathway
GO:0070098	1.36%	Ackr1	Ackr1	13.01	chemokine-mediated signaling pathway
GO:0070098	1.36%	Ccl19	Ccl19	6.62	chemokine-mediated signaling pathway
GO:0070098	1.36%	Ccr1	Ccr1	5.68	chemokine-mediated signaling pathway
GO:0002376	1.11%	C2	C2	8.87	immune system process
GO:0002376	1.11%	Cd7	Cd7	7.01	immune system process
GO:0002376	1.11%	Cd24a	Cd24a	6.4	immune system process
GO:0002376	1.11%	Cd1d1	Cd1d1	6.23	immune system process
GO:0002376	1.11%	Clec4d	Clec4d	5.63	immune system process
GO:0048020	0.49%	Ccl6	Ccl6	30.3	CCR chemokine receptor binding
GO:0048020	0.49%	Ccl8	Ccl8	14.23	CCR chemokine receptor binding
GO:0048020	0.49%	Ccl19	Ccl19	6.62	CCR chemokine receptor binding
GO:0048020	0.49%	Ccl3	Ccl3	5.46	CCR chemokine receptor binding
GO:0048020	0.49%	Ccl9	Ccl9	4.88	CCR chemokine receptor binding
GO:0005615	0.35%	Adamts15	Adamts15	173.38	extracellular space
GO:0005615	0.35%	Ahsg	Ahsg	143.77	extracellular space
GO:0005615	0.35%	Cilp	Cilp	101.07	extracellular space
GO:0005615	0.35%	Agt	Agt	44.71	extracellular space
GO:0005615	0.35%	Ccl6	Ccl6	30.3	extracellular space
GO:0006955	0.35%	Ccl6	Ccl6	30.3	immune response
GO:0006955	0.35%	Cd36	Cd36	19.93	immune response
GO:0006955	0.35%	Ccl8	Ccl8	14.23	immune response
GO:0006955	0.35%	Ccr1	Ccr1	5.68	immune response
GO:0006955	0.35%	Ccl3	Ccl3	5.46	immune response
GO:0006935	0.34%	Ccl6	Ccl6	30.3	chemotaxis
GO:0006935	0.34%	Ccl8	Ccl8	14.23	chemotaxis
GO:0006935	0.34%	Ccr1	Ccr1	5.68	chemotaxis
GO:0006935	0.34%	Ccl3	Ccl3	5.46	chemotaxis
GO:0006935	0.34%	Ccl9	Ccl9	4.88	chemotaxis
GO:0005576	0.03%	Adamts15	Adamts15	173.38	extracellular region
GO:0005576	0.03%	Ahsg	Ahsg	143.77	extracellular region
GO:0005576	0.03%	Cilp	Cilp	101.07	extracellular region
GO:0005576	0.03%	Angptl7	Angptl7	35.5	extracellular region
GO:0005576	0.03%	Ccl6	Ccl6	30.3	extracellular region
GO:0009897	0.01%	Cd36	Cd36	19.93	external side of plasma membrane
GO:0009897	0.01%	Anpep	Anpep	14.75	external side of plasma membrane

GO:0009897	0.01%	Abcg1	Abcg1	12.08	external side of plasma membrane
GO:0009897	0.01%	Cd22	Cd22	7.5	external side of plasma membrane
GO:0009897	0.01%	Ace	Ace	7.03	external side of plasma membrane

Online Table II. Gene Ontology (GO) enrichment of differentially expressed genes in 3D/2D fibroblast states using marker set enrichment analysis. Genes weighted by differential expression in 3D vs 2D conditions were used for pathway enrichment. The top 5 genes in each module (GO Term) are shown, as well as enrichment parameters used for marker set enrichment analysis.

Cardiac Traits	PC1 bicor	PC1 pvalue	PC2 bicor	PC2 pvalue
LVID at end diastole	0.307153722	0.003061476	0.323570986	0.00175629
LVID at end systole	0.335373707	0.001155294	0.31977809	0.00200237
total heart mass	0.401094007	8.15E-05	0.382985671	0.00017906
Heart rate	-0.096279289	0.363951754	0.012565032	0.90590092
left atrium mass	-0.207355374	0.04858779	-0.194756892	0.06432276
left atrium mass/body weight	0.234401802	0.02532589	-0.126156765	0.23342204
Mitral inflow E to A velocity ratio	0.206913009	0.049080681	-0.181414515	0.08525588
Mitral inflow E velocity	0.142027866	0.179288492	0.027156442	0.79832003
right atrium mass	0.141874927	0.17976205	-0.213481134	0.0421724
right ventricle mass	0.248416495	0.017580812	-0.136692434	0.19635339
PW thickening	-0.141602933	0.180606502	-0.027406706	0.79650139
IVS at end diastole	0.118263577	0.264212253	0.047024272	0.65803569
Fractional shortening	-0.117997784	0.265294858	0.069023215	0.51561902
Ejection fraction	-0.116547941	0.271253069	0.069464983	0.51292866
IVS to PW ratio at end systole	0.110277742	0.298052867	0.140994675	0.18250542
Mitral inflow A to E velocity ratio	-0.105389119	0.320114602	0.097216285	0.35927989
Velocity of circumferential shorteri	-0.092840053	0.381417667	0.020914209	0.84400568
Aortic valve ejection time	-0.041190146	0.698266367	-0.006581397	0.95063029
right atrium mass/body weight	-0.031229221	0.768863947	-0.162622492	0.12352472
Relative wall thickness at end diasto	0.021042494	0.843061023	0.004800975	0.96397537
Non-Cardiac Traits	**PC1 bicor**	**PC1 pvalue**	**PC2 bicor**	**PC2 pvalue**
glucose	0.071762413	0.49905418	0.079651552	0.45294327
liver mass	0.419959472	3.41E-05	-0.204154599	0.05224801
body weight	0.356474817	0.000523921	-0.217214	0.03862046
adrenal mass/body weight	0.017261024	0.870994403	-0.068477455	0.5189526
lung mass	0.314333443	0.002410094	-0.191032842	0.06969477
lung mass/body weight	0.028022775	0.792029117	-0.148271069	0.16072745
free fatty acids	0.261513514	0.012282178	-0.349471421	0.00068532
unesterified cholesterol	-0.001138736	0.991452678	-0.215058364	0.0406398
total cholesterol	0.058346891	0.582752968	-0.338164028	0.00104384
HDL	0.204694279	0.051615441	-0.340203757	0.00096866
trigycerides	0.197385148	0.060737614	-0.103279085	0.32995308
adrenal mass	0.159128625	0.131907152	-0.101031122	0.3406441
liver mass/body weight	0.237248848	0.023552203	-0.168058428	0.1113036

Online Table III. Traits measured in the HMDP following infusion of isoproterenol and their correlation with principal components based on genes upregulated in 3D fibroblasts. Individual cardiac and non-cardiac traits were plotted against the strain position on each component axis (as illustrated in Figure 3C-L). From these correlations, bicorrelation coefficients and corresponding p-values were calculated for each PC x trait relationship. Traits illustrated in Figure 3 are highlighted with a grey background.

Online Table IV

Gene	adjusted pvalue
Adamts15	6.26E-07
Ahsg	2.05E-21
Cilp	4.22E-06
Wfdc3	1.96E-25
Ptgds	4.14E-13
Ctrb1	5.63E-05
Fndc5	2.46E-07
Agt	2.79E-16
Angptl7	1.16E-07
Dkk3	5.87E-27
Fam180a	4.03E-12
Igfbp5	1.62E-28
Mmp11	2.03E-228
Htra3	1.39E-07
Penk	0.008313927
Emid1	0.005125138
Fbln7	8.73E-23
Plin4	1.19E-06
Ccl8	0.000140485
Mmp2	3.15E-26
Mamdc2	5.10E-38
Sparcl1	1.66E-05
Fam198a	2.13E-05
Tgfbi	2.13E-32
Fgl2	8.79E-09
Il1rn	0.009482538
Epor	0.001064303
Pik3ip1	4.01E-10
Enpp3	1.77E-25
Enpp2	7.36E-05
C2	0.0008716
Col9a2	0.001275955
Lpl	0.002443402
Mfap2	9.54E-11
Fbln1	0.000326378
Pamr1	0.000697679
Lgi4	1.64E-09
Smoc2	3.10E-05
Sepp1	5.53E-19
Adamtsl2	2.79E-11
C1ql1	0.000609573
Sned1	1.21E-05
Apoe	0.001412247
Iglon5	4.34E-11
Vash1	0.005782713
Clu	0.00605853

Dpt	0.008989791
Pla2g2e	0.000201816
Serpine2	4.13E-10
Dpp7	7.48E-19
Ssc5d	1.21E-06
Cpz	0.002400706
Islr	6.52E-06
Psap	0.008066424
Matn4	2.40E-09
Creg1	0.002226995
Ephb6	1.32E-08
Matn2	1.81E-05
Fam19a5	0.000596104
Sorl1	0.003374037
Slc17a5	0.000125364
Ctsl	3.23E-05
Hsd17b11	4.15E-18
Sord	2.79E-06
Ifi30	0.009015165
Sdc1	0.002285504
Tcn2	0.001758118
Gnptg	0.00861747
Grn	0.004461313
Txndc16	6.76E-07
Scpep1	3.31E-17
Mmp19	0.002352839
Glb1l	4.94E-05

Online Table IV. Genes upregulated in 3D cardiac fibroblasts filtered for secreted factors. Genes upregulated in the 3D cardiac fibroblast state were filtered for secreted factors by overlaying the gene symbol of 3D specific transcripts with deposited data of known secreted factors within the Universal Protein Resource (UniProt) using the following accessions: location:"Secreted [SL-0243]" type:component AND organism:"Mus musculus (Mouse) [10090]. The p values listed were generated from differential expression analysis of 3D vs 2D transcripts using a 10% FDR.